



HAL
open science

Elaboration of rigid-rigid block copolymers based on polymers absorbing in the near-infrared for organic electronics

Hisham Idriss

► **To cite this version:**

Hisham Idriss. Elaboration of rigid-rigid block copolymers based on polymers absorbing in the near-infrared for organic electronics. *Polymers*. Université de Pau et des Pays de l'Adour, 2020. English. NNT : 2020PAUU3017 . tel-03505895

HAL Id: tel-03505895

<https://theses.hal.science/tel-03505895>

Submitted on 1 Jan 2022

HAL is a multi-disciplinary open access archive for the deposit and dissemination of scientific research documents, whether they are published or not. The documents may come from teaching and research institutions in France or abroad, or from public or private research centers.

L'archive ouverte pluridisciplinaire **HAL**, est destinée au dépôt et à la diffusion de documents scientifiques de niveau recherche, publiés ou non, émanant des établissements d'enseignement et de recherche français ou étrangers, des laboratoires publics ou privés.

THÈSE

UNIVERSITE DE PAU ET DES PAYS DE L'ADOUR

École doctorale des sciences exactes et leurs applications

Soutenue le 02 Décembre 2020

Par **Hisham IDRIS**

Pour obtenir le grade de docteur
de l'Université de Pau et des Pays de l'Adour
Spécialité : Chimie et Physico-chimie des Polymères

Elaboration de copolymères à blocs rigide-rigide à base de polymères absorbant dans le proche infra-rouge pour l'électronique organique

Elaboration of rigid-rigid block copolymers based on polymers absorbing in the near-infrared for organic electronics

Devant le jury

Cyril BROCHON
Johann BOUCLE
Roger HIORNS
Lionel HIRSCH

Maître de Conférence - HDR / Université de Bordeaux
Maître de Conférence - HDR / Université de Limoges
Directeur de Recherche/ Université de Pau et des Pays de l'Adour
Directeur de Recherche/ Université de Bordeaux

Rapporteur
Rapporteur
Examineur
Examineur

Christine LARTIGAU- DAGRON
Iyad KARAME

Maître de Conférence - HDR/ Université de Pau et des Pays de l'Adour
Professeur/ Université Libanaise

Directrice de thèse
Co-Directeur de thèse



Acknowledgements

First and foremost, praises and thanks to GOD, the Almighty, for His showers of blessings throughout those years to successfully complete my research work.

I would like to express my warm appreciation to the members of the jury, Doctors Johann Bouclé, Cyril Brochon, Lionel Hirsch and Roger Hiorns. Thank you for attending my defense and for your evaluation.

I am deeply grateful to my supervisors, Dr. Christine Lartigau-Dagron, Dr. Antoine Bousquet and Dr. Iyad Karamah. Without their continuous optimism in this work, enthusiasm, encouragement and support, this study would hardly have been accomplished. Your guidance helped me throughout all this time.

I also owe a great debt of gratitude to Doctors Sylvain Chambon, Colin Bonduelle, Abdel Khoukh, Delphine Flahaut, Virginie Pellerin, and Sylvie blanc for their help.

I place on record, my sense of gratitude to all my friends who, directly or indirectly have lent their helping hand during those three years. And I take this opportunity to record my sincere thanks to all the members in the IPREM Laboratory for their help and encouragement. I am grateful to my labmates in the “IR-team”, Wissem Khelifi and Adèle Gapin, whom I have had the pleasure to work during this project. Many thanks for the lovely moments we have spent together.

A special mention to my friends, Fatima, Imad and Yasser, who have provided me through moral and emotional support. Thank you for being by my side.

I would like to thank my family members who were my life-coaches during the whole life. Many thanks to my dad “Kamel” and my mom “Badrieh” for greatly encouraging me to stay faithful in the eyes of GOD for it will bless me throughout my life. Special thanks to my brothers “Ahmad” and “Wissam”, my sisters “Ahlam” and “Salam” for their moral support. They all provided me with strong will and effort to overcome all the difficulties in my path. I dedicate all this work and efforts for the sake of their love and tender.

Last and not least, special thanks to my beloved wife, Dr. Riva, for supporting me spiritually throughout 8 years. My love, I won't be this stronger without you as you were the constant source of inspiration. You were the main reason why I keep pushing, I keep facing all the struggles and pains as I promised you with a bright future together with our future children. Honestly, I could not write this manuscript without being beside me. I promise to stick by you through my life as your smile will stay my priority. I love you to the moon and back.

Thank you all for your encouragement!

List of Abbreviations

OSC	Organic solar cell	GRIM	Grignard metathesis
HOMO	Highest occupied molecular orbital	CBCP	Conjugated block copolymer
LUMO	Lowest occupied molecular orbital	iPrMgCl₂	Isopropyl magnesium chloride
OPV	Organic photovoltaic	Mn	Number average molar mass
OLED	Organic light-emitting diode	NMR	Nuclear magnetic resonance
OFET	Organic field-effect transistors	SEC	Size exclusion chromatography
PANI	Polyaniline	Đ	Dispersity
PPy	Polypyrrole	NBS	N-bromosuccinimide
PT	Polythiophene	TLC	Thin layer chromatography
PPV	Poly(<i>p</i> -phenylene vinylene)	MeOH	Methanol
P3HT	Poly(3-hexylthiophene)	dppp	1,2-bis(diphenylphosphino)ethane
IP	Ionization potential	Pd₂dba₃	Tris (dibenzylidenacetone) dipalladium (0)
EA	Electron affinity	P(o-tolyl)₃	Tri (o-tolyl) phosphine
E_g	Energy bandgap	DOSY	Diffusion ordered spectroscopy
CV	Cyclic Voltammetry	RT	Room Temperature
D-A	Donor-Acceptor	Pt	Platinum
DTS	Dithieno[3,2-b:2',3'-d]silole	TGA	Thermo-gravimetric analysis
DAP	2,5-diazapentalene	DSC	Differential scanning calorimetry
DPP	Diketopyrrolopyrrole	GPC	Gel Permeation Chromatography
BT	Benzothiadiazole	T_c	Crystallization Temperature
QA	Quinoxaline	T_m	Melting temperature
II	Isoindigo	AFM	Atomic Force Microscopy
TPD	Thieno[3,4-c]pyrrole-4,6-dione	RR	Regioregularity
NIR	Near-infrared	DMF	Dimethylformamide
DP_n	Degree of polymerization	PPh₃	Triphenylphosphine
Ar	Aromatic	Pd(OAc)₂	Palladium(II) acetate
THF	Tetrahydrofuran	RMS	Root mean square roughness
BCP	Block copolymer	ITO	Indium tin oxide
BHJ	Bulk heterojunction	PSCs	Polymer solar cells
KCTP	Kumada catalyst-transfer polycondensation	ETL	Electron transport layer
P3AT	Poly(3-alkylthiophene)	HTL	Hole transport layer
Ni(dppp)Cl₂ nickel	1,2bis(diphenylphosphino)propane dichloro nickel		

ZnO	Zinc oxide	PEDOT:PSS	Poly(3,4-ethylenedioxythiophene) polystyrene sulfonate
TiO_x	Titanium oxide	MoO₃	Molybdenum oxide
PC₆₀BM	Phenyl C ₆₁ butyric acid methyl ester	CB	Conduction band
DIO	1,8-diiodoctane	VB	Valence band
CT	Charge transfer	NFA	Non-fullerene acceptor
V_{OC}	Open-circuit voltage	SAM	Self-assembled Monolayer
J_{SC}	Short-circuit current density	P3HT-Si	Triethoxysilane-terminated poly(3-hexylthiophene)
FF	Fill factor	PTES	1H,1H,2H,2H-perfluorooctyltriethoxysilane
R_S	Series resistance	XPS	X-Ray Photoelectron Spectroscopy
R_{SH}	Shunt resistance	SI-KCTP	Surface-initiated KCTP
J-V curve	Current-density-voltage curve	BLG	γ-benzyl-L-glutamate
WF	Work function		
PV	Photovoltaic		
DLS	Dynamic Light Scattering		
PCE	Power conversion efficiency		
EQE	External quantum efficiency		
NiO_x	Nickel oxide		
TFA-Lys	Trifluoroacetyl-L-lysine		
ROP	Ring opening polymerization		
NCA	N-carboxyanhydride		
PEIE	Polyethylenimine ethoxylated		
QE	Quantum efficiency		
V₂O₅	Vanadium oxide		
PL	Photoluminescence Spectroscopy		

Table of Contents

General Introduction.....	- 1 -
Introduction Générale	- 4 -
Chapter I:	- 8 -
Fundamental Concepts and Literature Review	- 8 -
I. Introduction	- 9 -
II. Origin of semiconducting behavior in organic semiconductors.....	- 9 -
III. π -Conjugated polymers.....	- 11 -
a. History of π -conjugated polymers	- 12 -
b. Properties of π -conjugated polymers	- 14 -
c. Relationship between chemical structure and properties of polymers.....	- 17 -
IV. Low-bandgap alternated Donor-Acceptor copolymers	- 21 -
a. General strategy	- 21 -
b. Donor monomers	- 23 -
c. Acceptor monomers	- 24 -
d. Examples of low-bandgap copolymers used in OPV devices	- 25 -
e. Near-infrared (NIR) absorbing molecules.....	- 28 -
V. Synthesis of low-bandgap D-A copolymers.....	- 34 -
a. Techniques of polymerization	- 34 -
b. Evolution in the synthetic procedures for conjugated polymers	- 36 -
c. Stille coupling polycondensation.....	- 38 -
VI. Rod-Rod block copolymers: interest and synthesis	- 41 -
a. Interest of rod-rod block copolymers in OPV	- 43 -
b. Synthesis of rod-rod block copolymers.....	- 50 -
VII. Poly(3-hexylthiophene) P3HT	- 56 -
a. Properties of P3HT	- 56 -
b. Regioregularity of P3ATs	- 56 -
c. Synthesis of poly(3-alkylthiophene) (P3AT)	- 57 -
VIII. Aim and strategy of this thesis.....	- 59 -
References.....	- 61 -
Chapter II:.....	- 69 -
Synthesis and Characterization of All-Conjugated Diblock Copolymers.....	- 69 -
I. Introduction	- 70 -
II. Objectives.....	- 72 -

III. Synthesis of molecular and macromolecular precursors	- 73 -
a. Synthesis and characterization of poly(3-hexylthiophene) (P3HT)	- 73 -
b. Synthesis of diketopyrrolopyrrole (DPP) monomer	- 79 -
c. Synthesis of 2,5-diazapentalene (DAP) monomer.....	- 85 -
d. Optical properties of DPP and DAP monomers	- 90 -
e. The donor monomer, DTS.....	- 91 -
IV. Synthesis and characterization of rod-rod block copolymers.....	- 92 -
a. Preliminary Stille coupling: P3HT-DPP	- 92 -
b. Synthesis of P(DTS-DPP) and P(DTS-DAP) alternated copolymers.....	- 95 -
c. Synthesis of conjugated diblock copolymers (CBCPs)	- 99 -
V. Optical properties of diblock copolymers	- 112 -
a. Optical behavior.....	- 112 -
b. Chromism	- 114 -
VI. Electrochemical characterizations	- 118 -
VII. Thermal characterizations	- 122 -
VIII. Morphological characterizations	- 127 -
IX. Conclusion.....	- 131 -
References.....	- 132 -
Chapter III:.....	- 136 -
Performances of Diblock Copolymer-Based Organic Solar Cells.....	- 136 -
I. Introduction	- 137 -
II. Organic photovoltaic cells.....	- 138 -
a. Concept of organic solar cells	- 138 -
b. Architecture of organic photovoltaic cells	- 138 -
c. Constituents of the photoactive blend.....	- 139 -
d. Blend morphology	- 141 -
e. General working principle of organic photovoltaic devices	- 141 -
f. Device characteristics.....	- 143 -
III. State of art.....	- 145 -
a. Optimizing the PCE of BHJ OPVs	- 146 -
IV. Objectives	- 149 -
V. Results and discussion	- 150 -
a. Architecture and constituents of the fabricated devices.....	- 150 -
b. Device performances using DPP-based block copolymers.....	- 153 -
c. Device performances using DAP-based block copolymers	- 174 -
VI. Conclusion	- 176 -
References.....	- 177 -

Chapter IV:	- 182 -
Elaboration of Self-Assembled Monolayers as Hole Transport Materials for OSCs	- 182 -
I. State of art	- 183 -
a. Hole transporting layers	- 183 -
II. Objectives.....	- 193 -
III. Elaboration of SAMs on ITO substrates.....	- 194 -
a. End-functionalization of P3HT to be grafted on ITO	- 194 -
b. Synthesis and characterization of triethoxysilane-terminated P3HT.....	- 196 -
c. Grafting of SAM molecules on ITO substrates	- 200 -
IV. Organic solar cells.....	- 215 -
a. Device architecture and fabrication	- 215 -
b. Photovoltaic performances	- 217 -
V. Conclusion.....	- 220 -
References.....	- 221 -
Chapter V:.....	- 224 -
Synthesis of Hybrid Block Copolymers Based on Polypeptide Segment	- 224 -
I. Introduction	- 225 -
a. Traditional methods for NCA polymerizations	- 227 -
b. Polypeptide-based block copolymers.....	- 229 -
II. Objectives.....	- 232 -
III. Synthesis of aniline-terminated P(DTS-DAP).....	- 233 -
IV. Diblocks with γ -Benzyl- <i>L</i> -Glutamate monomer unit.....	- 238 -
a. Synthesis of P(DTS-DAP)- <i>b</i> -P(BLG).....	- 238 -
b. Deprotection of P(DTS-DAP)- <i>b</i> -P(BLG)	- 241 -
V. Diblocks with TFA-Lysine NCA repetitive unit	- 242 -
a. Synthesis of P(DTS-DAP)- <i>b</i> -P(TFA-Lys)	- 242 -
b. Deprotection of P(DTS-DAP)- <i>b</i> -P(TFA-Lys).....	- 245 -
c. Photothermal effect of P(DTS-DAP)- <i>b</i> -P(Lys) in aqueous solution	- 248 -
VI. Conclusion	- 250 -
References.....	- 251 -
Chapter VI:	- 253 -
Experimental Procedures and Characterization Techniques	- 253 -
I. Materials.....	- 254 -
II. Synthetic procedures of Chapter II.....	- 254 -
a. Synthesis of P3HT-Br	- 254 -

b.	Synthesis of diketopyrrolopyrrole monomer (DPP)	- 255 -
c.	Synthesis of 2,5-diazapentalene monomer (DAP).....	- 256 -
d.	Synthesis of P(DTS-DPP) and P(DTS-DAP) copolymers	- 258 -
e.	Synthesis of all-conjugated block copolymers	- 259 -
III.	Synthetic procedures of Chapter IV	- 261 -
a.	Synthesis of allyl-terminated P3HT	- 261 -
b.	Synthesis of triethoxysilane-terminated P3HT (P3HT-Si).....	- 262 -
IV.	Synthetic procedures of Chapter V	- 262 -
a.	Synthesis of aniline-terminated P(DTS-DAP)	- 262 -
b.	Synthesis of Benzyl-L-Glutamate NCA-based hybrid copolymers.....	- 263 -
c.	Synthesis of TFA-Lysine NCA-based hybrid copolymers	- 264 -
V.	Fabrication of organic solar cells.....	- 265 -
a.	Preparation of ITO substrates	- 265 -
b.	Device fabrication.....	- 265 -
VI.	Characterization techniques	- 268 -
	References.....	- 277 -
	General Conclusion and Perspectives	- 278 -
	Conclusion Générale et Perspectives	- 281 -
	List of publications	- 284 -

General Introduction

With the increase of the global population and the hunt for higher life standards, the energy demand is continuously increasing. Nowadays, fossil fuels including oil, gas and coal deliver 84% of the energy needs. Aside from their limited earth-abundance, harmful greenhouse gas emissions such as carbon monoxide, carbon dioxide, nitric oxide and sulfur oxide are associated with their consumption. This causes pollution and irreversible climate changes, such as global warming.¹

Thus, the demand of renewable energy resources has been tremendously increased. Among them, solar energy is a promising alternative to the non-renewable energy sources because of its abundance and ease of accessibility. In this regard, numerous photovoltaic technologies exist for achieving solar electricity. Traditionally, solar cells are based on inorganic semiconductors, most prominently silicon. Recently, emerging technologies such as organic, perovskite and others have been widely studied.

Organic solar cells (OSCs), in particular based on or polymers have attracted significant attention as they meet requirements of cost-effective manufacturing, lightweight, flexibility and easy solution-processing. The active layer of such devices is composed of a bulk heterojunction of two components: electron donor and acceptor. Most of the couples used are constituted of a π -conjugated polymer as electron donor and a fullerene derivative acceptor. Organic solar cells have recently experienced efficiencies up to 18% showing that this technology becomes competitive to the inorganic field.² Whereas, much work has to be done to improve device efficiency and stability.

In general, this high increase in performance is attributed to several improvements such as the designation of new device architectures (inverted device structures, tandem cells...) ^{3,4} and the incorporation of suitable interfacial layers.⁵ Even though interfaces and architecture optimization govern the performance of solar cells, the components and the nanomorphology of the photoactive layer also play an important role in this regard. Thus, the incorporation of non-fullerene acceptor ³ and the usage of low-bandgap donor polymers that absorb more light in the visible and near-infrared region ⁶ can certainly improve device performances reaching high records.

During this PhD work, we mainly focused on the chemical design, synthesis and functionalization of conjugated polymers for the aim of enhancing photovoltaic performances, by improving the absorption of photon flux.

Conjugated polymers are characterized by their intrinsic electrical conductivity and therefore, are considered as an important class of organic semiconductors. Accordingly, they possess distinct advantages including light weight, environmentally friendly synthetic procedures and low processing cost. For this, they have been widely used in the field of organic electronics including organic photovoltaics (OPV), organic light-emitting diodes (OLED), organic field-effect transistors (OFET) and variety of sensors.

As low-bandgap polymers are well-known to improve photovoltaic performances, the most successful strategy used for lowering the bandgap is based on the elaboration of a polymer backbone using alternating moieties; an electron-rich monomer (donor) and an electron deficient one (acceptor). However, the morphological instability of blends containing D-A copolymers, drawn the attentions toward designing covalently linked donor and acceptor blocks. Generally, D-A block copolymers could be made up of either two rigid blocks (rod-rod) or one rigid and one flexible segment (rod-coil). The rod-rod block copolymers are interesting due to their self-assembly and electronic properties (such as tunable bandgaps).⁷ Another important criteria for the choice of rod-rod block copolymers is the complementary light absorption between the corresponding blocks. This eventually maximizes photon harvesting in the solar spectrum.

Thanks to these advantages and given the various available methods for their preparation, block copolymers can probably become a major material class to study for the future development of viable OPVs. Several strategies exist to produce all-conjugated diblock copolymers. Among them, the “end-functional coupling method” is very interesting because it is only a two-steps procedure allowing the combination of different polymerization mechanisms which implies a large choice of monomers. This method relies on the synthesis of a first block, bearing a functional group able either to initiate the chain polymerization of the second monomer⁸ or to react as a monofunctional macromonomer in a step-growth polycondensation.⁹

This manuscript consists of six main chapters. **Chapter I** presents the fundamental concepts behind π -conjugated polymers and their electronic properties. The recent developments in low-bandgap polymers and block copolymers are described to allow a better understanding of the path and choices established in this work. Additionally, an overview of the various synthetic methodologies of conjugated polymers is highlighted.

Chapter II is devoted to the synthesis of monomers and the corresponding rod-rod block copolymers *via* Stille coupling polycondensation. This chapter includes optical, electrical, thermal and morphological characterizations of the synthesized polymers.

The first part of **Chapter III** presents a general overview of the current energy situation and briefly describes the concepts of photovoltaics while highlighting the recent developments in this field. The second part of this chapter focuses on the incorporation of the synthesized block copolymers in inverted device structures of OSCs to study their efficiencies after optimization. The device fabrications were conducted at the IMS laboratory, Bordeaux, France.

Even though the photoactive layer certainly governs device performances, the interfacial layers sandwiching the active layer are of equal importance. The main roles of such materials are their capability to tune the energy level at the organic/electrode interface and to provide efficient charge carrier extraction towards the electrodes, thus avoiding losses such as non-ohmic contact, charge carrier recombination and exciton quenching at the interfaces.¹⁰

In this regard, modifying the ITO surface by self-assembled monolayers (SAMs), as PEDOT:PSS alternatives, *via* grafting onto technique is reported in **Chapter IV**. To do so, end-functional conjugated polymers have been synthesized. After characterizing the modified ITO surfaces, photovoltaic performances of normal device structures are studied and compared to those based on PEDOT:PSS hole transport layers.

Chapter V in its turn shows the possibility of synthesizing novel hybrid block copolymers constituting of a conjugated polymer, characterized with low-bandgap, and a polypeptide segment *via* ring opening polymerization of N-carboxyanhydrides (NCA) of the peptide monomer. The main aim of such study was achieving self-assembled nanostructures of polypeptides with an extended absorbance in the near-infrared region. Such properties make them efficient for photothermal applications. The experimental synthetic work of this chapter was conducted in the LCPO laboratory, Bordeaux, France.

Chapter VI is the experimental part that describes all the synthetic procedures, device fabrications and the characterization techniques used in this study.

Finally, some **conclusions** are presented along with **outlooks** into the future of the low-bandgap block copolymers in organic photovoltaic field and the further developments needed to better enhance device performances.

Introduction Générale

Avec l'augmentation de la population mondiale et la recherche d'un niveau de vie supérieur, la demande d'énergie ne cesse d'augmenter. De nos jours, les combustibles fossiles, notamment le pétrole, le gaz et le charbon, fournissent 84% des besoins énergétiques. Outre leur abondance terrestre limitée, les émissions nocives de gaz à effet de serre comme le monoxyde de carbone, le dioxyde de carbone, l'oxyde nitrique et l'oxyde de soufre sont associées à leur consommation. Cela entraîne une pollution et des changements climatiques irréversibles, comme le réchauffement climatique.¹

Ainsi, la production de ressources énergétiques propres et renouvelables est l'enjeu majeur de ce siècle. Parmi ces ressources, l'énergie solaire est une alternative prometteuse aux sources d'énergie non renouvelables en raison de son abondance et de sa facilité d'accès. À cet égard, les cellules solaires organiques (CSO), en particulier à base de polymères ont attiré une attention particulière car elles répondent aux exigences de fabrication rentable, de légèreté, de flexibilité. La couche active de tels dispositifs est composée d'une hétérojonction en volume de deux composants : donneur et accepteur d'électrons. La plupart des couples utilisés sont constitués d'un polymère π -conjugué comme donneur d'électrons et comme accepteur un dérivé de fullerène. Les cellules solaires organiques ont récemment connu des rendements prometteurs allant jusqu'à 18%, alors que beaucoup de travail doit encore être fait pour améliorer l'efficacité et la stabilité des dispositifs.²

D'une manière générale, cette forte augmentation des performances est attribuée à plusieurs améliorations telles que la conception de nouvelles architectures de dispositifs (structures de dispositifs inversées, cellules tandem ...) ^{3,4} et l'incorporation de couches interfaciales adaptées.⁵ Même si l'optimisation de l'interface et de l'architecture régit les performances des cellules solaires, les composants et la nanomorphologie de la couche photoactive jouent également un rôle important. Ainsi, l'incorporation d'accepteur non fullerène ³ ou l'utilisation de polymères donneurs à faible bande interdite qui absorbent plus de lumière dans la région du visible et proche infrarouge ⁶ peuvent certainement améliorer les performances du dispositif.

Dans ce travail de thèse, nous nous sommes principalement concentrés sur la conception chimique et la synthèse de polymères conjugués fonctionnels dans le but d'améliorer les performances photovoltaïques.

La stratégie la plus efficace et la plus utilisée pour abaisser la bande interdite, afin d'absorber plus de photons, est basée sur l'élaboration d'un squelette polymère utilisant l'alternance d'un monomère riche en électrons (donneur) et d'un monomère déficient en électrons (accepteur). Cependant, l'instabilité morphologique des mélanges contenant des copolymères D-A a attiré l'attention sur la conception de blocs donneurs et accepteurs liés de manière covalente. Ces copolymères à blocs rigide-rigide sont intéressants en raison de leur auto-assemblage et de leurs propriétés électroniques (telles que les bandes interdites modulables).⁷

Un critère important pour la synthèse de copolymères à blocs rigide-rigide est l'absorption de lumière complémentaire par les blocs correspondants. Cela maximise finalement la collecte des photons du soleil.

Plusieurs stratégies existent pour produire des copolymères diblocs entièrement conjugués. Parmi elles, la fonctionnalisation terminale est très intéressante car elle procède en seulement deux étapes, permettant la combinaison de différents mécanismes de polymérisation ce qui permet un large choix de monomères. Cette méthode repose sur la synthèse d'un premier bloc, portant un groupement fonctionnel capable soit d'initier la polymérisation en chaîne du second monomère,⁸ soit de réagir en macromonomère monofonctionnel dans une polycondensation.⁹

Ce manuscrit est composé de six chapitres. Le **Chapitre I** présente les concepts fondamentaux des polymères π -conjugués et leurs propriétés électroniques. Les développements récents des polymères à faible bande interdite et des copolymères à blocs sont décrits pour permettre une meilleure compréhension de la voie et des choix établis dans ce travail. De plus, un aperçu des diverses méthodologies de synthèse des polymères conjugués est mis en évidence.

Le **Chapitre II** est consacré à la synthèse des monomères et des copolymères à blocs rigide-rigide correspondants par polycondensation par couplage Stille. Ce chapitre comprend les caractérisations optiques, électriques, thermiques et morphologiques des polymères synthétisés.

La première partie du **Chapitre III** présente un aperçu général de la situation actuelle de l'énergie et décrit brièvement les concepts du photovoltaïque tout en mettant en évidence les développements récents dans ce domaine. La deuxième partie de ce chapitre se concentre sur l'incorporation des copolymères blocs synthétisés dans les structures de dispositifs inversés des OSC pour étudier leurs efficacités après l'optimisation de plusieurs paramètres. La fabrication du dispositif a été réalisée au laboratoire IMS, Bordeaux, France.

Même si la couche photoactive régit certainement les performances du dispositif, les couches interfaciales tenant en sandwich la couche active sont d'égale importance. Le rôle principal de ces matériaux est leur capacité à régler le niveau d'énergie à l'interface organique / électrode et à fournir une extraction efficace des porteurs de charge vers les électrodes, évitant ainsi les pertes telles que le contact non ohmique, la recombinaison des porteurs de charge et l'extinction des excitons aux interfaces.¹⁰ A cet égard, la modification de la surface ITO par des monocouches auto-assemblées (SAM), pour remplacer la couche hygroscopique de PEDOT:PSS, en utilisant la technique de « greffage sur » est décrite dans le **Chapitre IV**. Après avoir caractérisé les surfaces ITO modifiées, les performances photovoltaïques des structures de dispositif normal sont étudiées et comparées à celles basées sur des couches de transport de trous PEDOT : PSS.

Le **Chapitre V** montre à son tour la possibilité de synthétiser de nouveaux copolymères à blocs hybrides, constitué d'un polymère conjugué, caractérisé par une faible bande interdite et un segment polypeptidique, par polymérisation par ouverture de cycle de N-carboxyanhydrides (NCA) du monomère peptidique. L'objectif principal de cette étude était de réaliser des nanostructures auto-assemblées de polypeptides dans l'eau, présentant une absorbance étendue dans la région du proche infrarouge. Des telles propriétés les rendent efficaces pour les applications photothermiques. Les travaux de synthèse expérimentale des polypeptides de ce chapitre ont été réalisées au laboratoire LCPO, Bordeaux, France.

Le **Chapitre VI** expose la partie expérimentale, décrit toutes les procédures de synthèse, les fabrications de dispositifs et les techniques de caractérisation utilisées dans cette thèse.

Enfin, quelques **conclusions** sont présentées ainsi qu'une **perspective** sur l'avenir des copolymères blocs à faible bande interdite dans le domaine photovoltaïque organique et les développements ultérieurs nécessaires pour améliorer les performances.

References

- (1) Fisher, A. C.; Narain, U. Global Warming, Endogenous Risk, and Irreversibility. *Environ. Resour. Econ.* **2003**, *25* (4), 395–416.
- (2) Liu, Q.; Jiang, Y.; Jin, K.; Qin, J.; Xu, J.; Li, W.; Xiong, J.; Liu, J.; Xiao, Z.; Sun, K.; Yang, S.; Zhang, X.; Ding, L. 18% Efficiency Organic Solar Cells. *Sci. Bull.* **2020**, *65* (4), 272–275.
- (3) Cui, Y.; Yao, H.; Zhang, J.; Zhang, T.; Wang, Y.; Hong, L.; Xian, K.; Xu, B.; Zhang, S.; Peng, J.; Wei, Z.; Gao, F.; Hou, J. Over 16% Efficiency Organic Photovoltaic Cells Enabled by a Chlorinated Acceptor with Increased Open-Circuit Voltages. *Nat. Commun.* **2019**, *10*.
- (4) Liu, G.; Jia, J.; Zhang, K.; Jia, X.; Yin, Q.; Zhong, W.; Li, L.; Huang, F.; Cao, Y. 15% Efficiency Tandem Organic Solar Cell Based on a Novel Highly Efficient Wide-Bandgap Nonfullerene Acceptor with Low Energy Loss. *Adv. Energy Mater.* **2019**, *9* (11), 1803657.
- (5) Dkhil, S. B.; Pfannmöller, M.; Bals, S.; Koganezawa, T.; Yoshimoto, N.; Hannani, D.; Gaceur, M.; Videlot-Ackermann, C.; Margeat, O.; Ackermann, J. Square-Centimeter-Sized High-Efficiency Polymer Solar Cells: How the Processing Atmosphere and Film Quality Influence Performance at Large Scale. *Adv. Energy Mater.* **2016**, *6* (13), 1600290.
- (6) Sharma, G. D.; Reddy, M. A.; Ramana, D. V.; Chandrasekharam, M. A Novel Carbazole–Phenothiazine Dyad Small Molecule as a Non-Fullerene Electron Acceptor for Polymer Bulk Heterojunction Solar Cells. *RSC Adv.* **2014**, *4* (63), 33279–33285.
- (7) Zhang, Y.; Tajima, K.; Hirota, K.; Hashimoto, K. Synthesis of All-Conjugated Diblock Copolymers by Quasi-Living Polymerization and Observation of Their Microphase Separation. *J. Am. Chem. Soc.* **2008**, *130* (25), 7812–7813.
- (8) Wang, J.; Ueda, M.; Higashihara, T. Synthesis of All-Conjugated Donor–Acceptor–Donor ABA-Type Triblock Copolymers via Kumada Catalyst-Transfer Polycondensation. *ACS Macro Lett.* **2013**, *2* (6), 506–510.
- (9) Nakabayashi, K.; Mori, H. All-Polymer Solar Cells Based on Fully Conjugated Block Copolymers Composed of Poly(3-Hexylthiophene) and Poly(Naphthalene Bisimide) Segments. *Macromolecules* **2012**, *45* (24), 9618–9625.
- (10) Po, R.; Carbonera, C.; Bernardi, A.; Camaioni, N. The Role of Buffer Layers in Polymer Solar Cells. *Energy Environ. Sci.* **2011**, *4* (2), 285–310.

Chapter I:
Fundamental Concepts and
Literature Review

I. Introduction

The demand for energy has been increasing in the last decades, thus it is essential to seek for new energy sources other than the traditional non-renewable ones (such as fossil fuels)¹ having limited supplies. Additionally, the usage of non-renewable energy sources is associated with some environmental concerns such as climate changes and air pollution.² For this, solar energy is a promising alternative that converts light into electric energy with less expenses and unlimited supply.^{3,4} Among photovoltaics, organic solar cells (OSCs), dealing with organic semiconductors (conjugated polymers and/or small organic molecules) are targeted for their low cost,⁵ light weight, high flexibility and semi-transparency. Features that are highly desired for several applications including large-scale ones.⁶ Among organic semiconductors, conjugated polymers are interesting due to their ability in tuning the optoelectronic properties for the aim of optimizing the criteria needed for the corresponding application.⁷ Thus, most organic photovoltaic cells are polymer solar cells (PSCs). Specifically, polymers with low-bandgap form an interesting family of semiconductor materials and have proven their interest in the field of photovoltaics. Thus, the incorporation of low-bandgap polymers is a widely used strategy to improve device performances. Additionally, they can provide absorption in the entire visible region, possess high carrier mobilities and excellent power conversion efficiencies because of the controlled intramolecular charge transfer from donor to acceptor unit.⁸ Chemistry has also enabled the synthesis of conjugated polymers with very low-bandgap (less than 1.6 eV) absorbing in the near-infrared region.⁹ This was made possible by several polymerization techniques and strategies that are discussed in this chapter.

II. Origin of semiconducting behavior in organic semiconductors

In general, a semiconductor is a material that shows an intermediate electrical conductivity between conductors (metals) and insulators. When the bandgap of an organic or inorganic material becomes small enough (< 3.0 eV), the material is then categorized as a semiconductor. As this bandgap becomes smaller, an appreciable number of electrons in the valence band can “jump” the gap into the conduction band.¹⁰ Accordingly, the semiconductor physics is related to the quantum mechanics in explaining the charge carriers in any crystal lattice. Therefore, semiconductors can be categorized into three types: n-type (electron conduction), p-type (hole conduction) and ambipolar type (both electron and hole conduction).¹¹

Previously, researchers discovered that polycyclic aromatic compounds can form semiconducting charge-transfer complex salts with halogens.¹² Additionally, conjugated polymers possess a semiconducting behavior. Carbon atom (C-atom) is the main element constituting polymers in which the type of bonds between two adjacent carbon atoms determines the electronic properties of the material. The bonds could be saturated or unsaturated where the saturated gives the insulating properties (4 valence electrons used in the covalent bond formation *i.e.* sp^3 hybridization orbitals). On the other hand, the unsaturated conjugated structure causes the conductive polymer's property. Accordingly, an alternate single and double carbon-carbon bond is behind the electronic configuration of π -conjugated polymers.

Thus, the overlapping between molecular orbitals formed from the valence electrons of the bonded carbon atoms provides the semiconducting property of the conjugated polymers *i.e.* the main source of semi-conductivity is the π -delocalization of a single $2p_z$ valence electron along the polymer's backbone. A phenomenon taking place when one $2s$ orbital in the carbon atom is mixed with two of the $2p$ orbitals to form 3 sp^2 hybrid orbitals, thus, leaving one p orbital unhybridized in the carbon atom as shown in **Figure I-1a**. The sp^2 hybridization has one unpaired electron (π -electron) *per* C-atom. The three sp^2 hybrid orbitals of the carbon atom arrange themselves in a three-dimensional trigonal planer in a stable configuration with a bond of 120° between them. The $2p_z$ orbital then lays perpendicular to the plane of the three sp^2 hybrid orbitals (**Figure I-1b**).¹³

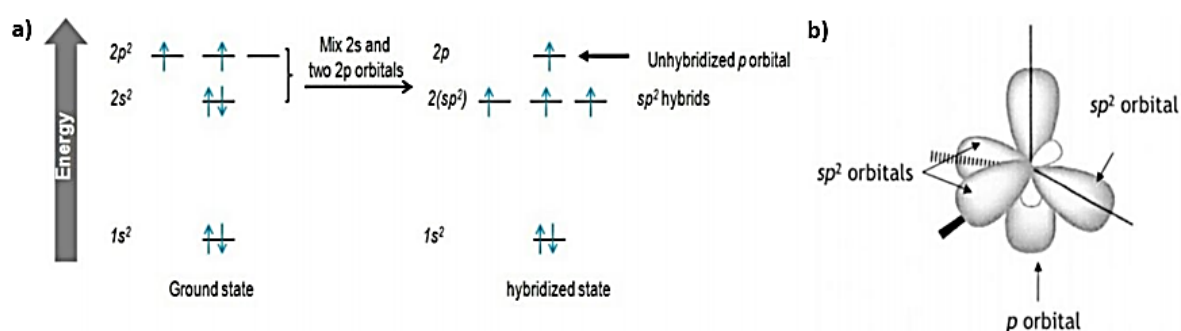


Figure I-1: (a) The sp^2 hybridization of the valence shell electrons of a carbon atom. (b) Spatial distribution of orbitals on an sp^2 hybridized carbon atom.¹³

For a C-C double bond, a sigma bond (σ -bond) is formed by overlapping one sp^2 orbital from each carbon atom while a π -bond is formed by the side-by-side overlap of two unhybridized $2p_z$ orbitals as shown in **Figure I-2**. A delocalized π -band stretched over the segment of the polymer chain is then formed and considered as the main basic source for the charge transport in the conjugated structures.^{14,15}

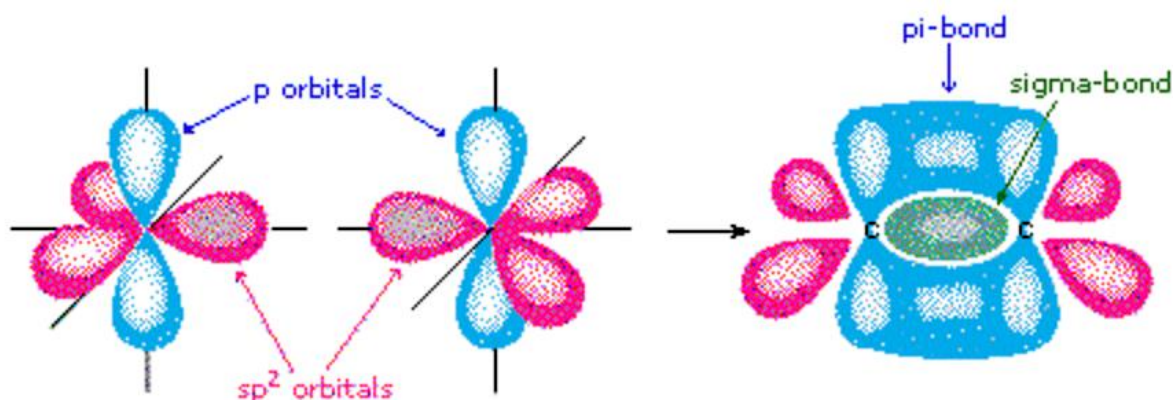


Figure I-2: The mechanism of the formation of π -bond.

For the energy band description, σ -bonds form completely filled bands, while π -bonds correspond to the half-filled states as shown in **Figure I-3**.¹⁶ In this regard, the filled bonding states eventually form π -orbitals, also called HOMO (Highest Occupied Molecular Orbital) levels and the empty anti-bonding states forms π^* -orbitals called LUMO (Lowest Unoccupied Molecular Orbital). The π electrons fill energy levels from the lowest level to highest one. Therefore, in a polymer, molecular orbitals form energy bands in a certain energy range.

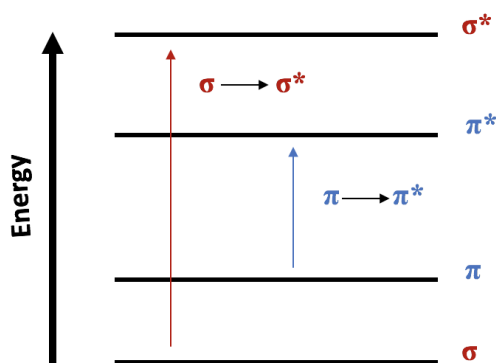
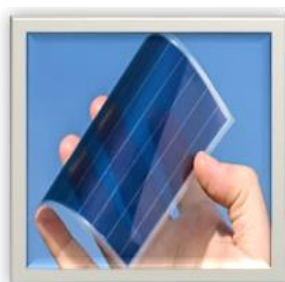


Figure I-3: Schematic energy bands of π -conjugated polymers.

III. π -Conjugated polymers

Conjugated polymers are organic materials characterized by a backbone made up of alternating single and double bonds allowing the delocalization of π -electrons. This is the reason behind their intrinsic electrical conductivity. Thus, conjugated polymers are considered as an important class of organic semiconductors.¹⁷

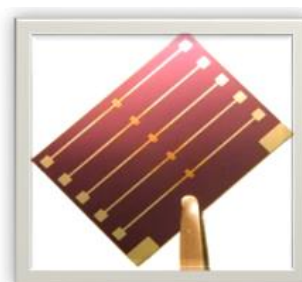
Compared to inorganic semiconductors, conjugated polymers possess distinct advantages of structural and functional versatility by molecular design, solution processability, light weight, environmentally friendly synthetic procedures and low processing cost. Thus, they are of great interest in the field of organic electronics such as organic photovoltaics (OPV). They are also used in organic light-emitting diodes (OLED), organic field-effect transistors (OFET), supercapacitors, batteries, and variety of sensors.¹⁸ **Figure I-4** shows some electronic devices based on organic semiconductors.



Organic photovoltaic (OPV)



Organic light-emitting diodes (OLED)



Organic field-effect transistors (OFET)

Figure I-4: Examples of some electronic devices based on organic semiconductors.

Although conjugated polymers show exciting advancement, they are still facing some limiting challenges. The most critical challenges in developing ideal materials are to synthesize and design conjugated polymers with presenting together strong absorption ability, high hole mobility, good film morphology and suitable HOMO-LUMO energy levels. Thus, a deep understanding of the molecular design allows to effectively tailor the intrinsic properties of conjugated polymers for serving the desired purpose and application.¹⁹

a. History of π -conjugated polymers

The discovery of the conjugated polymers returns back to the 19th century when Fritzsche reported the synthesis of polyaniline (PANI).²⁰ In the same period of time, Henry Letheby studied the electrochemical properties of PANI.²¹ Following, in 1958, Giulio Natta elaborated for the first time linear polyacetylene which have some limitations including low processability and insolubility.²² After this, Weiss and coworkers described the preparation of polypyrrole (PPy) at high conductivity degree in 1963.²³ However, an important development was the 2000's Nobel Prize in Chemistry for the discovery and development of conductive polymers in 1977.^{15,24} This price was awarded to Alan J. Heeger, Alan G. MacDiarmid and Hideki Shirakawa who stated that doping polyacetylene can change its behavior from semiconducting to metallic-like conducting. The promising features of those materials made their development grew rapidly. In addition to the nitrogen-containing polymers (PPy and PANI), sulfur-containing polymers, polythiophenes (PT) were also synthesized. Poly(3,4-ethylenedioxythiophene) (PEDOT) doped with poly(4-styrene sulfonate) (PSS) is among the most important conducting polymers in terms of conductivity, stability, transparency and biocompatibility. It has been widely used due to its intrinsically structural features, outstanding optical/electrical properties and potential applications.²⁵ Chemical structures of some synthesized conjugated polymers are shown in **Figure I-5**.

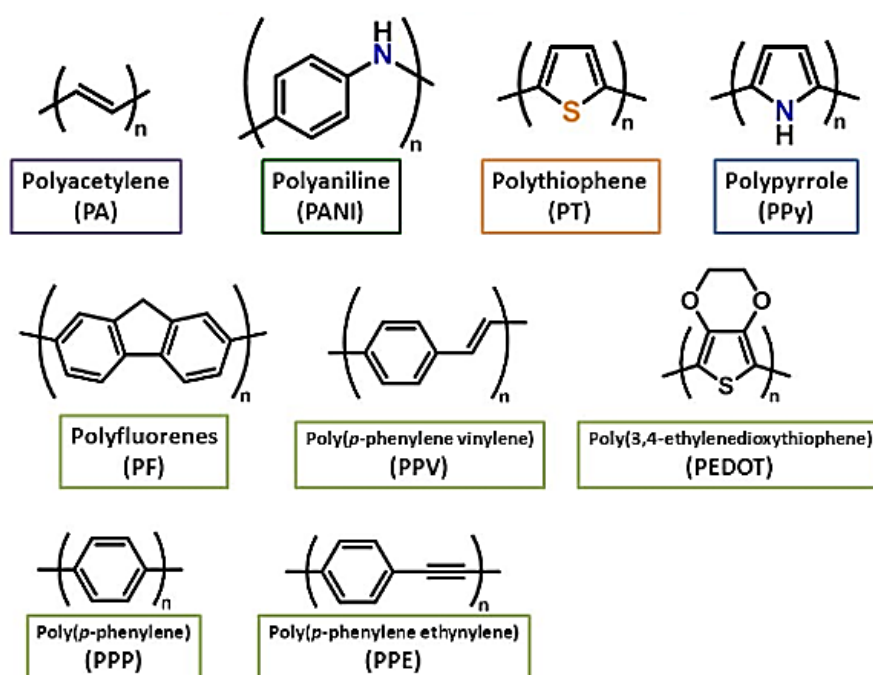


Figure I-5: Examples of some first-generation conjugated polymers.

Nevertheless, the lack of solubility of this first generation hindered some of their applications. Thus, to change their physical and chemical properties including solubility, variety of polymers were synthesized by chemically modifying the monomers through the addition of side chains (alkyl or alkoxy side chains groups) or functional groups.^{26,27} For example, since the discovery of poly(*p*-phenylene vinylene) (PPV) in 1990, it has been strongly used in LEDs and photovoltaic devices owing to the polymer's unique physical properties such as conductivity. However, the hyperbranched PPV has drawn much attention due to the improved solubility and thermal stability of PPV.²⁸ Additionally, the polymerization of alkyl pyrrole monomers resulted in the formation of soluble alkyl polypyrrole conducting polymers.²⁹ For the same purpose, substituted polythiophenes such as poly(3-hexylthiophene) (P3HT) were synthesized and showed tailored properties for various applications.³⁰ Those polymers were categorized as “second-generation conjugated polymers” (**Figure I-6**).

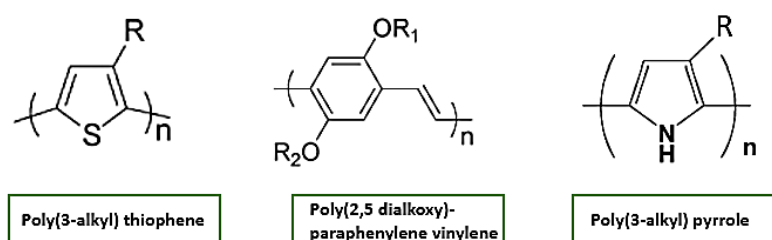


Figure I-6: Examples of some second-generation conjugated polymers.

A third-generation of conjugated polymers was then investigated to harvest more photons in the sun emission spectrum, driven by the photovoltaic emerging application. This generation is characterized by more complicated molecular structures with more atoms in the repetitive units. Those polymers such as the ever-growing class of alternated donor–acceptor copolymers shows enhanced electronic properties with tunable low-bandgap energy and a promising absorption in the range of visible and near-infrared regions (near-IR).^{31,32} Thus, these conjugated polymers are mainly used as solar cell active layer materials. Structures of some “third-generation” conjugated polymers are shown in **Figure I-7**.

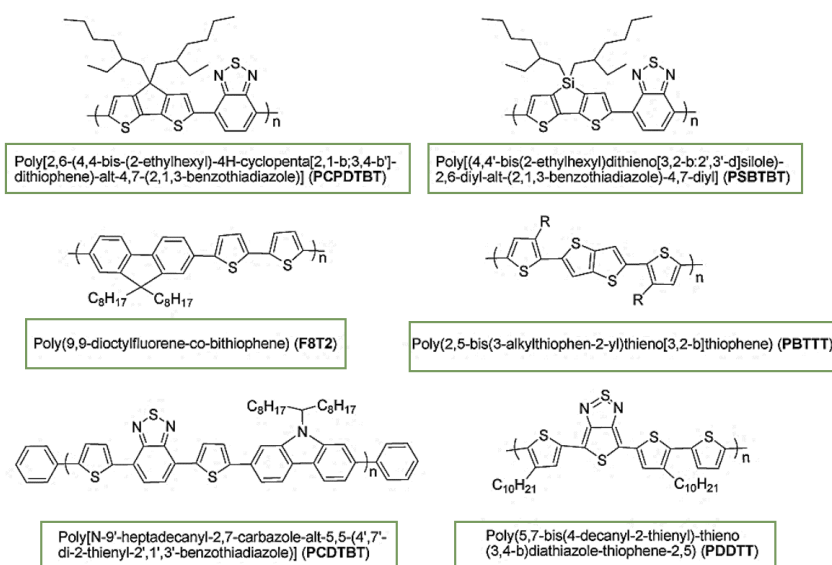


Figure I-7: Molecular structure of some of the studied third-generation conjugated polymers.³²

b. Properties of π -conjugated polymers

i. Electronic properties

Due to the low permittivity of the organic materials, an electron donor and acceptor couple is needed in photovoltaic active layer to dissociate the exciton created by the photon absorption. There are two types of semiconducting polymers depending on the position of their energy levels that determines the type of charge carriers that each material can conduct. Materials with high HOMO level are electron donor or p-type semiconductors, able to transport holes, thus they possess high hole mobility. On the contrary, those with low-lying LUMO level have high electron mobility and are known as electron acceptors or n-type semiconductors.³³

In general, HOMO and LUMO levels of an organic semiconductor are governed by the chemical functional groups in the π -conjugation.³⁴ This property makes organic semiconductors promising materials to study due to the variety of functional groups available. The HOMO and LUMO energy levels of a semiconducting polymer are related to their ionization potential (IP) and electron affinity (EA), respectively. As illustrated in **Figure I-8**, the position of the HOMO level relative to vacuum corresponds to the ionization potential (the energy required to remove an electron from the highest point). Similarly, the position of the LUMO level relative to vacuum corresponds to electron affinity (the energy required to inject an electron). The difference between the two mentioned energy levels is known as the π - π^* energy bandgap (E_g) measured in electron volt (eV).

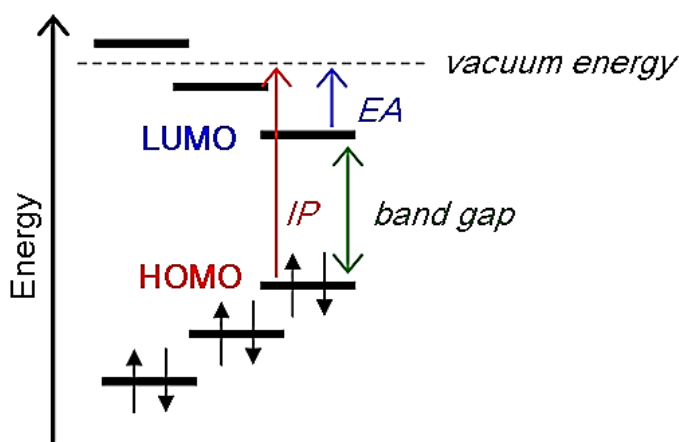


Figure I-8: The energy levels and bandgap of organic semiconductors.

The energy levels depend on the length of alternated sequence of single and double C-C bond, that defines the conjugation length. As shown in **Figure I-9**, the bandgap of an organic material changes in accordance to the number of carbon atoms participating to the conjugation length. Nevertheless, other parameters such as chain defects and metallic impurities can vary the bandgap value by affecting the energy levels alignments.

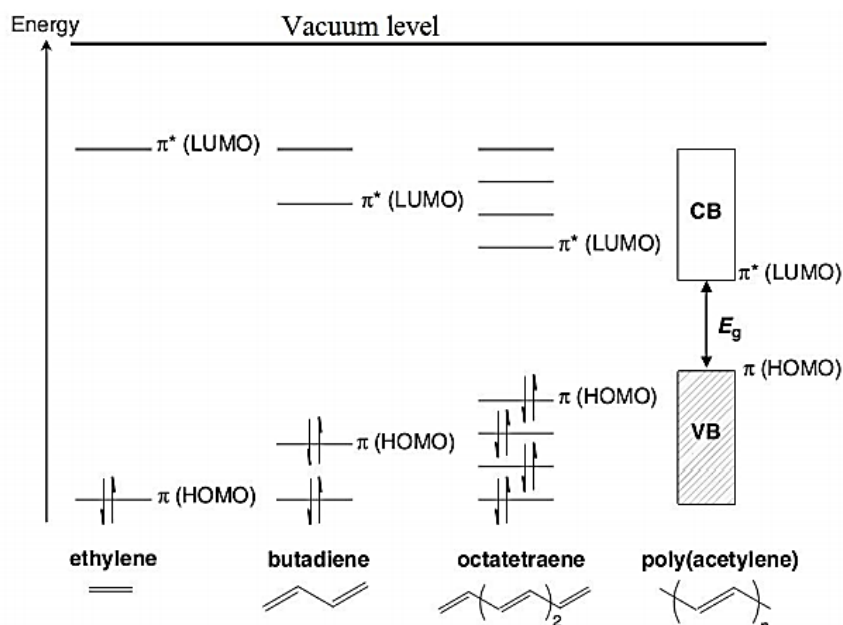


Figure I-9: Evolution of the molecular orbital diagram with the number of monomer units.³⁵

ii. Optical properties

When exciting a conjugated polymer by either a phonon (heat) or a photon (light), the occupied electrons in the HOMO level can be mobilized to the LUMO level. Such an electron transition requires a minimum amount of energy that differs between materials. It is worth mentioning that in semiconductors, there is a distinction difference between optical bandgap and electrical bandgap. The optical one, is the minimum energy needed for a photon to be absorbed and cause a transition while the electrical one is the threshold to create an electron-hole pair which are not bounded together.

Optical bandgap can be determined by Tauc's plot using **Equation 1**.³⁶

$$(\alpha h\nu)^{1/n} = A (h\nu - E_g^{(\text{opt})}) \quad \text{Equation 1}$$

Where $(\alpha h\nu)^{1/n}$ is plotted as function of photon energy ($h\nu$). The terms α , h , ν and $E_g^{(\text{opt})}$ are absorption coefficient, Planck constant, light frequency and optical bandgap energy, respectively, while A is a constant. The exponent n denotes the nature of the transition (0.5 for direct allowed transitions, 1.5 for direct forbidden transitions, 2 for indirect allowed transitions, and 3 for indirect forbidden transitions).^{36,37}

Another possible method for measuring the optical bandgap is by determining the absorption edge wavelength, λ_{edge} , directly from the UV-vis absorption spectrum of the material. Then, the gap is calculated using **Equation 2**.³⁸

$$E_g^{(\text{opt})} = h\nu = h.c/\lambda = 1240/\lambda_{\text{edge}} \quad \text{Equation 2}$$

Where c is the speed of light in vacuum.

On the other hand, the electrochemical bandgap of polymers can be estimated by cyclic voltammetry (CV) that helps in gaining information about the oxidation $E_{\text{onset}}^{\text{ox}}$ and reduction $E_{\text{onset}}^{\text{red}}$ potentials of materials. This analysis allows the determination of HOMO and LUMO energy levels, out of which the electrical bandgap can be estimated. The electrochemical bandgap is usually larger than the optical one because the electrochemical measurements require additional energy due to Coulomb interactions.³⁹

LUMO and HOMO energy levels can also be estimated by the mean of Inverse Photoelectron Spectroscopy (IPES) and Ultraviolet Photoelectron Spectroscopy (UPS), respectively.^{40,41}

Bandgaps for conjugated polymers are normally up to 3.0 eV.⁴² Thus, the absorption properties in the visible and near-infrared region are governed by the bandgap energy. The relationship between the energy bandgap and the absorbed wavelength is shown in **Figure I-10**.

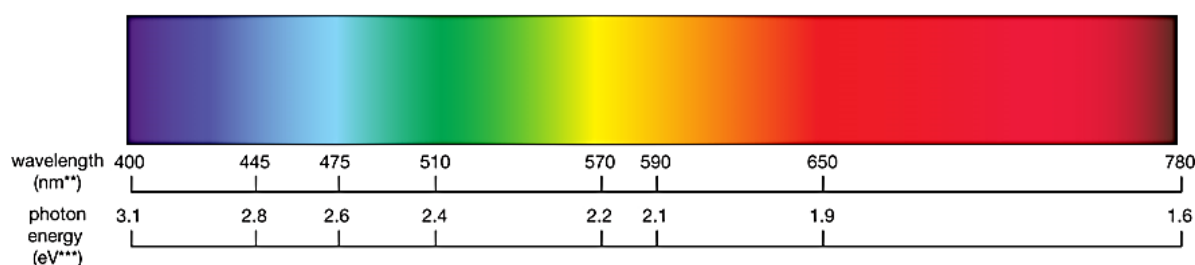


Figure I-10: Relationship between the bandgap energy and the absorbed wavelength.

iii. Charge transport properties

As previously mentioned, the conductivity in conjugated polymers arises from the π -electron delocalization along the carbon chains. When it comes to charge transport within the π -conjugated polymers, two important terms need to be identified, the intrachain transport and the interchain transport as shown in **Figure I-11**. Intrachain charge transport depends on the effective π -conjugation length along the polymer backbone. Therefore, for high coplanarity within the polymer backbone, effective π -conjugation and eventually enhanced intrachain charge transport take place. This type of charge transport is not sufficient for the displacement of charges over a macromolecular distance due to the presence of some structural defects. Thus, interchain charge transport is needed. This is related to the interchain distance where the charge transport between the polymer chains is highly anisotropic. In other words, the interchain charge transport allows charges to pass from one macromolecule to another. This mechanism is linked to the coupling between π orbitals of neighboring chains and depends mainly on the organization of the macromolecular chains with respect to each other. Thus, intrachain transport is faster than interchain transport which is considered as the rate limiting step.⁴³ Eventually, for totally disordered polymer films, charge mobility is relatively low while it increases in order of magnitudes for ordered structures.⁴⁴ Accordingly, amorphous or semi-crystalline polymers have low charge carrier mobilities ($1\text{-}15\text{ cm}^2\text{V}^{-1}\text{s}^{-1}$) compared to the polycrystalline inorganic material such as silicon ($1000\text{ cm}^2\text{V}^{-1}\text{s}^{-1}$).^{45,46}

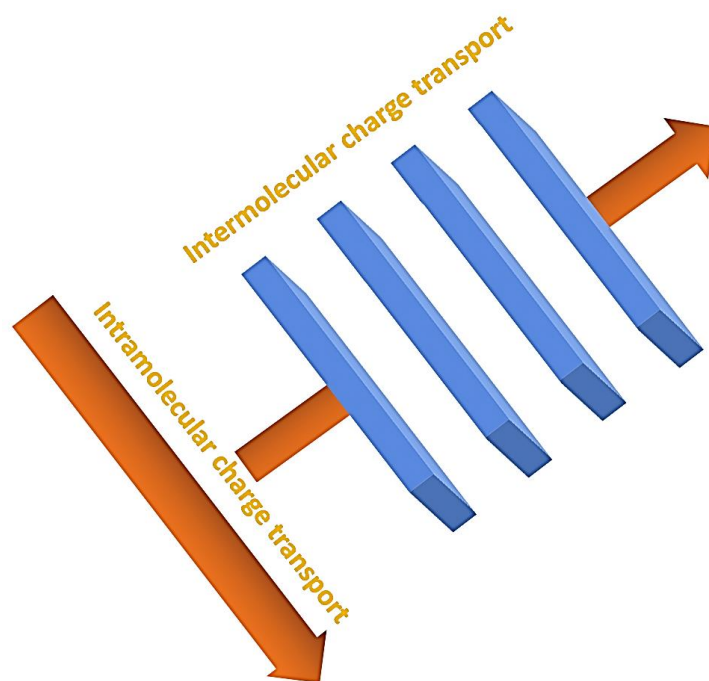


Figure I-11: Inter and intramolecular charge transport mechanism.

c. Relationship between chemical structure and properties of conjugated polymers

Electronic properties of a polymer are influenced by the bandgap and the HOMO/LUMO energy levels position. This position influences the range of light absorption and emission of the polymer and determines its electron donating/accepting behavior. Therefore, plenty of studies were investigated to understand the relationship between the chemical structure of a material and its corresponding properties including bandgap size and position. As previously mentioned, the HOMO-LUMO bandgap is decreased when the π -electron system is extended over the polymeric main chain. Accordingly, and as discussed by Briseno and co-workers, the increase in the chain length conjugation is a way to narrow the bandgap and thus bathochromically shift the corresponding absorbance.⁴⁷

Although the increase in the chain length conjugation can alter the properties, the maximum extent of conjugation between materials is different according to the employed heteroaromatic units. For instance, it was stated in literature that oligomers based on diketopyrrolopyrrole (DPP) and thiophene did not show any remarkable changes in the electronic properties beyond two repeating units.⁴⁸

A theoretical definition for the bandgap of an organic semiconductor was previously stated by Roncali in which it is expressed by the sum of five important contributions identified in **Equation 3**⁴⁹ and illustrated in **Figure I-12**.

$$E_g = E_{BLA} + E_{Sub} + E_{Res} + E_0 + E_{int} \quad \text{Equation 3}$$



Figure I-12: Structural parameters affecting the bandgap of conjugated materials.⁴⁹

E_{BLA} describes the contribution of the bond length alternation, E_{Sub} is the contribution of the substituent nature, E_{Res} is related to the aromatic resonance of the cycle, E_{θ} is the mean deviation from planarity and E_{int} represents the intermolecular or interchain coupling in the solid state such as π -stacking. Each of the mentioned parameters can be tuned by an appropriate design of monomer subunits.

i. Alternation of single and double bonds

Bond length alternation (BLA) represents the major contribution that can directly affect the magnitude of a bandgap. This contribution to E_g (E_{BLA}) is related to the difference between single and double bond length.

As discussed before, the semiconducting property is acquired when a material contains electrons that can move without destroying the chemical structure. Then, conjugation can be maintained when two or more π -bonds are adjacent and appropriately arranged in space in which π -electrons can be partially delocalized into the whole π -system. Thus, by increasing the number of alternating multiple bonds, a narrower bandgap can be obtained.

In some conjugated polymers, such as polyacetylene, a degenerate system is observed, in which two possible structures characterized to be energetically equivalent are obtained as shown in **Figure I-13a**. In other conjugated polymers, such as polyparaphenylene, a non-degenerate system is observed in which the two resonance forms are energetically different as shown in **Figure I-13b**. In this case, the second aromatic structure is called quinoid and usually possesses a low ionization potential and high electron affinity. This eventually lowers the bandgap of the corresponding polymer. Thus, it was demonstrated that in conjugated polymers based on aromatic rings, the bandgap decreases as function of both the bond length alternation (E_{BLA}) and the increased quinoid character of the polymer backbone.⁵⁰

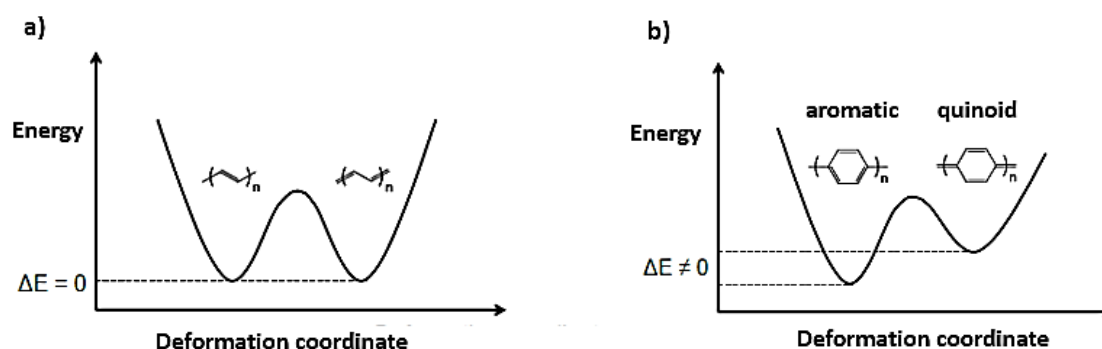


Figure I-13: The difference in the potential energy curve between the (a) degenerate and (b) non-degenerate systems.⁵¹

For example, poly(isothianaphtene), consisting of fused thiophene and benzene rings, is characterized by a bandgap of 1 eV. Since $E_{\text{Res}}(\text{benzene}) > E_{\text{Res}}(\text{thiophene})$, the benzene returns to the energetically favored aromatic structure. Thus, the thiophene ring adopts the quinoid configuration. Therefore, as previously explained, in the quinoid form, bond length alternation (E_{BLA}) is reduced and the electrons are less confined in the aromatic parts (low contribution from E_{Res}). In this case, the new π -bonds between the subunits force planarity of the whole backbone (E_{θ})⁵² as shown in **Figure I-14**.

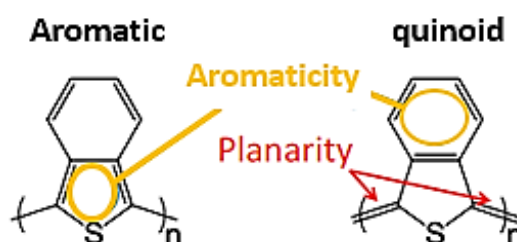


Figure I-14: Aromatic and quinoid forms of poly(isothianaphtene).⁵²

ii. Substituent effect

To overcome the solubility limitations of conjugated polymers in the most commonly used organic solvents, side chains were introduced into the main polymer backbone. Poly(3-alkylthiophene), poly(N-alkylpyrrole) and poly(*p*-phenylene vinylene) are among the studied examples on this concept. Another reason for grafting electron-donating (such as alkyl, alkoxy, etc.) or withdrawing substituents (cyano, thiadiazole, etc.) is to tune HOMO and LUMO levels, more specifically to increase HOMO or lower LUMO levels, respectively.⁴⁹ The effect of the substituent on the energy levels is summarized by donating or withdrawing electrons through mesomeric or inductive effects and therefore is represented by E_{Sub} in **Equation 3**. In addition to the nature of the substituent, its position is also important as it can lead to either steric hindrance or enhanced planarization. This can influence the length of conjugation and thus the bandgap. In its turn, steric hindrance between the subunits of the corresponding polymer chain can induce a higher torsion angle. Therefore, influencing the E_{θ} contribution.⁵³

Finally, substituents can also impact the properties of the material in the solid state by tuning the inter-molecular arrangement of the chain by either reducing the stacking and thus widening the bandgap or improving the solid-state ordering and π -stacking, thus narrowing the bandgap as in the case of regioregular polymers.⁵⁴

iii. Torsion angle

The existence of a single bond between aromatic cycles can play a role in inducing interannular rotations of aromatic rings through these single bonds connecting them. As the orbitals overlap can vary with the cosine of the twist angle (θ), therefore any deviation from coplanarity can result in increasing the bandgap.⁴⁹ In general, the large dihedral angle that exists between the subunits of a polymer chain and is attributed to the rotational freedom around σ bonds can break the planarity of the backbone. Thus, increasing the twist angle enlarges the corresponding bandgap through the contribution of E_θ . Therefore, variety of strategies were investigated for the aim of acquiring a more planar backbone as the planarization can directly affect the bandgap by reducing the contribution of E_θ .⁵⁵

For instance, poly(*para*-phenylene) (PPP) is one of the commonly known aromatic conjugated polymers in which its optical properties are limited by a strong torsion angle between the phenylene units.⁵⁶ Inserting double bonds between the phenyl units as in the case of poly(*p*-phenylenevinylene) (PPV) can reduce steric hindrance between the aromatic units, causing a more flattened structure. In this case, the conjugated system adopts a planar structure, thus narrowing the bandgap (**Figure I-15**). The same concept is observed when comparing poly(thiophene) (PT) to poly(thienylenevinylene) (PTV) (**Figure I-15**), in which the double bonds stop the rotational freedom around the thiophene-thiophene single bonds and lead also to a planar geometry.⁵⁷ Another important effect for the insertion of such double bonds is the decrease in the total aromaticity of the system, thus reducing the bandgap.

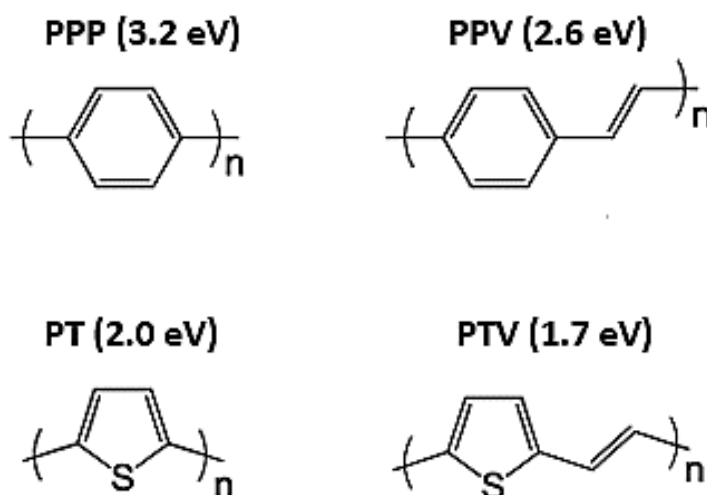


Figure I-15: The effect of double bond insertion between aromatic rings on the optical bandgap of phenyl and thiophene-based conjugated polymers.

iv. Interchain interactions

The interaction between molecules is responsible for their organization into a condensed phase. This intermolecular interaction is described by the parameter E_{int} and represents an important contribution for determining the bandgap as π -stacking can directly reduce it.⁵⁸ Consequently, the bandgap energy is narrower in the solid state than in solution due to the better organization and stacking of the molecular chains. This effect can be seen from absorption spectroscopy of a polymer by the red-shift occurring in the solid state when compared to the one in solution. This is caused by the stronger interchain interactions that are favored by more planar conformations.⁵⁹ For example, highly regioregular P3HT have enhanced stacking, therefore the corresponding bandgap is lower than the less regioregular P3HT chains.⁶⁰ As previously mentioned, bulky substituents in their turn can also reduce the interchain interactions in solid state due to the steric hindrance, resulting in a wider bandgap.⁶¹

IV. Low-bandgap alternated Donor-Acceptor copolymers

a. General strategy

As mentioned elsewhere, low-bandgap polymers form an interesting family of organic semiconductors that are widely used in electronic fields. The most successful strategy used for lowering the bandgap is based on the elaboration of polymer backbone using alternating moieties; an electron-rich monomer (donor) and an electron deficient one (acceptor). By combining donor-acceptor monomers with different forces, it is possible to modulate the absorption of the polymer at different wavelengths, to decrease the alternation of the bond length, and increase the flatness of the polymer. All of these characteristics tend to decrease the bandgap energy. Additionally, this strategy can eventually enhance the transport properties when compared to homopolymer materials.⁶²

In this alternated material, the bandgap decrease is explained by two distinct mechanisms. The first one is based on the delocalization of electrons along the conjugated polymer chain which is eventually responsible for the stabilization of the quinoid resonance structure.⁵⁰ The other proposed mechanism is explained by the hybridization of the frontier orbitals *i.e.* when different moieties are covalently bonded, HOMO and LUMO energy levels of the donor and the acceptor start to interact as shown in **Figure I-16**. As electrons are redistributed, new HOMO and LUMO levels are formed, thus lowering the bandgap.⁶³ In general, the formed HOMO energy level is affected by the donor material while the LUMO is affected by the acceptor material.^{19,64}

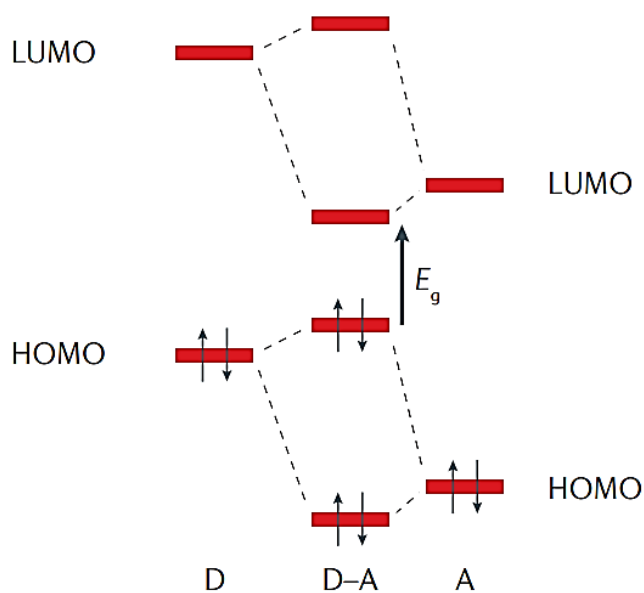


Figure I-16: Orbital interactions of donor (D) and acceptor (A) in donor-acceptor copolymers.⁶⁴

First in 1990, it was observed that intramolecular charge transfer is possible to occur in a polymer consisting of a thiophene donor and a pyridine acceptor in which this polymer showed a decrease in the bandgap observed as a red-shifted absorbance.⁶⁵

Later in 1993, semiconducting polymers based on polysquaraines and polycroconaines having low-bandgaps, even less than 0.5 eV, were synthesized. This reaction was based on a condensation between bifunctional donor moieties and acceptor-like moieties such as squaric acid or croconic acid.⁶⁶ In this regard, series of polymers containing aromatic donor and o-quinoid acceptor units were then prepared such as those based on thiophenes (aromatic donor) and benzo[1,2-c;3,4-c']bis[1,2,5]thiadiazole (o-quinoid-acceptor).⁶⁷

Following these pioneered studies, low-bandgap D-A copolymers emerged and broadened the boundaries of OPV technology in the past decade. Currently, there is a wide variety of donor and acceptor monomers which offer the possibility of a wide range of alternating D-A copolymers, with different alignment of HOMO-LUMO energy levels that eventually tunes the bandgap energies. In general, acceptor monomers are aryl or heteroaryls with one or more electronegative atoms. While donor monomers are generally based on thiophene and benzene substituted with donor groups such as alkoxy or alkyl. Some of the commonly used donors and acceptors are highlighted in the following section.

b. Donor monomers

Donor units are referred as electron-rich units. Among these units, thiophene and benzene are the most commonly used ones in which they can constitute the main fundamental building blocks of the synthesized donor materials. Accordingly, donor units formed from benzene or thiophene can be classified as: dibenzene bridged units, dithiophene bridged units and thiophene-benzene fused units as shown in **Figure I-17**.⁶⁸

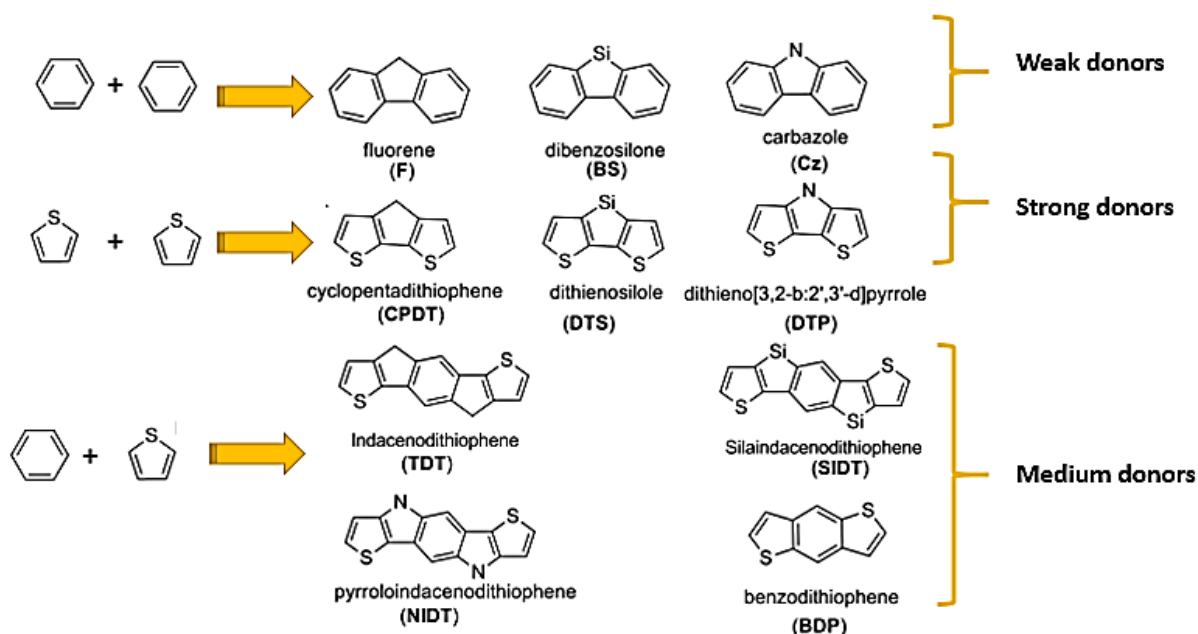


Figure I-17: Basic structures of some donor units.⁶⁸

When two benzene units are bridged by either carbon (C), silicon (Si) or nitrogen (N) atom, they form fluorene, dibenzosilole and carbazole, respectively. These donor units are classified as weak donors due to the electron-deficient nature of the benzene units. Since the dibenzene system is able to be fixed in one plane, the tricyclic system is efficient for constructing highly conjugated polymers in the presence of the bridging atoms which enhance the electronic properties. However, the benzene units lead to poor orbital mixing between those donors and acceptor units, thus widening the bandgaps.

Another class of donor materials was investigated based on dithiophene units bridged by either C, Si or N atom forming cyclopentadithiophene (CPDT), dithienosilole (DTS) and dithieno[3,2-b:20,30-d] pyrrole (DTP), respectively. These donor units are classified as strong donors. In general, dithiophene units are known to have stronger electron-delocalization ability, thus, they cause stronger orbital mixings with acceptors. This eventually narrows the bandgaps. Accordingly, the constructed donor-acceptor copolymers based on those donors possess higher planarity due to the less steric hindrance of the five-membered thiophenes with their neighbor blocks. However, the ideal donor units can be formed from the combination of the electron-deficient benzene units and the electron-rich thiophene units, a class known as benzene fused thiophene structures. In this case of medium donor units, electron-deficient benzene unit can assure a low HOMO energy level. This simultaneously narrows the bandgap. As an example, benzodithiophene (BDT) is a widely attractive donor unit.

c. Acceptor monomers

An acceptor unit is referred as electron-poor or electron-deficient unit that contains either the electron-withdrawing imine (C=N) such as benzothiadiazole (BT), quinoxaline (QA), naphtho[1,2-c:5,6-c]bis[1,2,5]thiadiazole (NT) and others or the electron withdrawing carbonyl group (C=O) such as diketopyrrolopyrrole (DPP), isoindigo (II), and thieno[3,4-c]pyrrole-4,6-dione (TPD). Generally speaking, most of these molecules are composed of fused rings with benzene that favors the quinoid form. The chemical structures of the most used acceptor units are shown in **Figure I-18**.

These acceptor units can be classified as weak, medium and strong acceptors depending on their electron-accepting abilities. More specifically, the lower the LUMO energy level, the stronger is the electron-accepting ability. This can be translated experimentally by studying the bandgap of the donor-acceptor copolymers. *i.e.* as the bandgap becomes narrower, the electron-accepting ability of the acceptor is stronger.

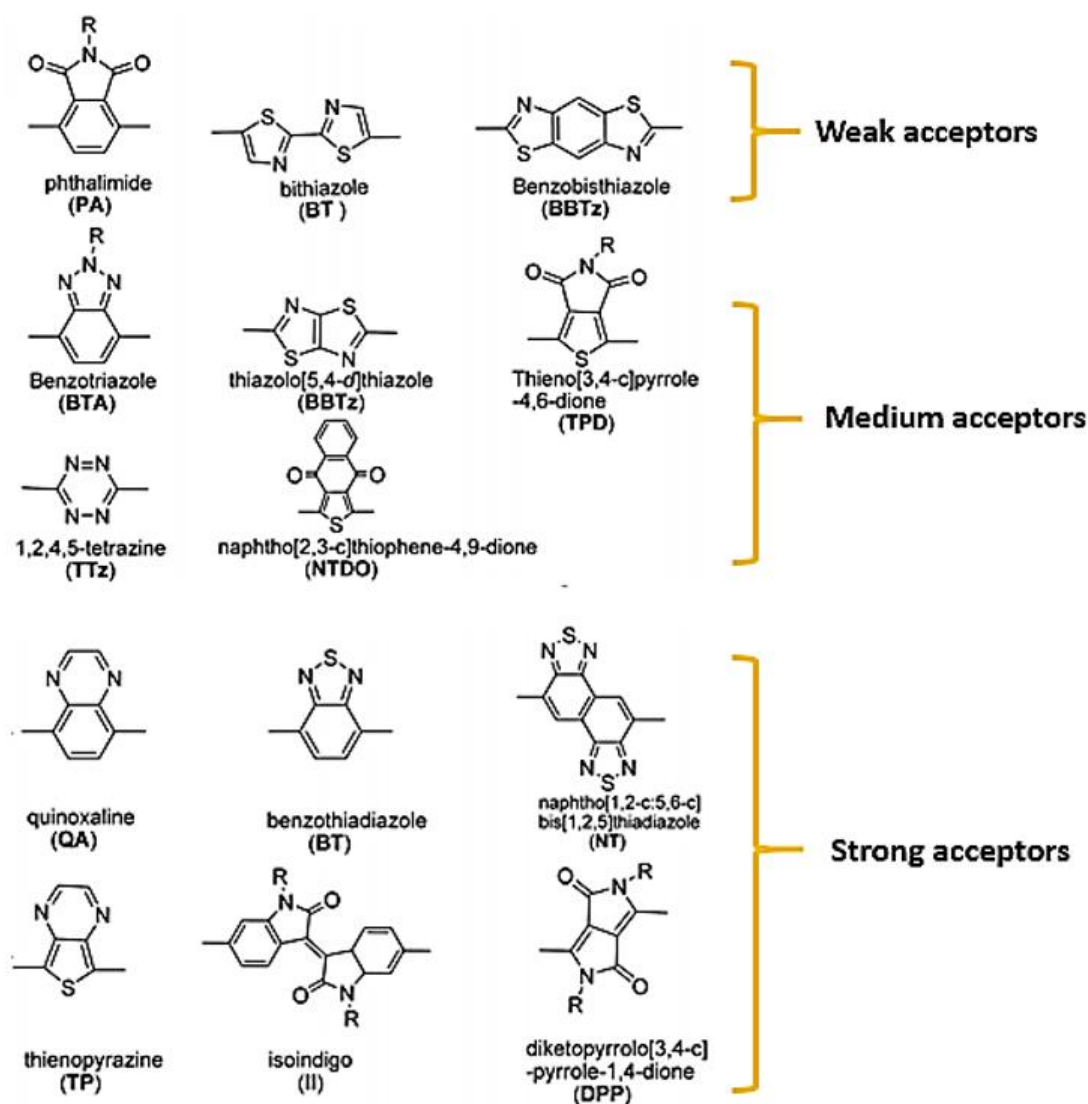


Figure I-18: Basic structures of some acceptor units ($R =$ alkyl chain).⁶⁸

d. Examples of low-bandgap copolymers used in OPV devices

Applying the D-A strategy while performing few modifications and combinations between the different building blocks, leads to design various copolymers having different bandgap values subjected toward different applications. Copolymers combining a donor (weak-medium) with an acceptor (weak-medium) generally give a large optical bandgap energy ($E_g \geq 1.8$ eV) and this is due to the poor overlap of the orbitals between the donor and acceptor units. However, for achieving really low-bandgap polymers, strong donors and acceptors are therefore needed.

It is worth mentioning that for solar cell applications, a bandgap less than 1.8 eV is desired for achieving high photocurrent. Additionally, copolymers with deep HOMO (~ -5.2 eV) and deep LUMO energy levels (deeper than -3.7 eV) are preferred for increasing the voltage of the solar devices and for efficient exciton dissociation, respectively.

A variety of copolymers showing high performances in photovoltaic devices are cited in the following section, along with their corresponding donor and acceptor moieties.

For instance, poly[(2,6-(4,8-bis(5-(2-ethylhexylthio)-4-fluorothiophen-2-yl)-benzo[1,2-b:4,5-b']dithiophene))-*alt*-(5,5-(1',3'-di-2-thienyl-5',7'-bis(2-ethylhexyl)benzo[1',2'-c:4',5'-c']dithiophene-4,8-dione)] (**PBDB-T-SF**) is a low-bandgap copolymer (1.8 eV) used in highly-efficient OPV devices (13% efficiency). It is a result of copolymerization between 2,6-bis(trimethyltin)-4,8-bis(5-(2-ethylhexylthio)-4-fluorothiophen-2-yl)benzo[1,2-b:4,5-b']dithiophene (BDTTDSFSn) electron-rich building block and 1,3-bis(5-bromothiophen-2-yl)-5,7-bis(2-ethylhexyl)benzo[1,2-c:4,5-c']dithiophene-4,8-dione (BDD) electron deficient building block (**Figure I-19**).⁶⁹

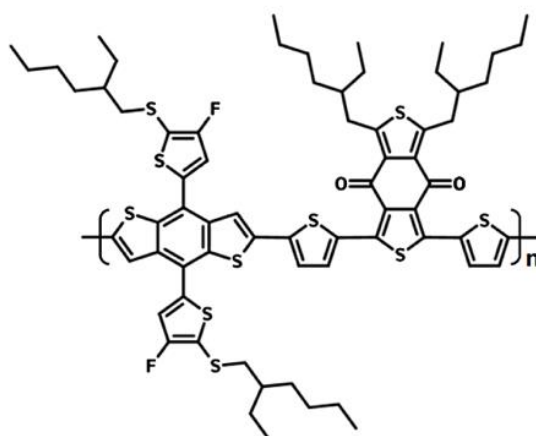


Figure I-19: Chemical structure of PBDB-T-SF copolymer.⁶⁹

Poly[(5,6-dihydro-5-octyl-4,6-dioxo-4H-thieno[3,4-c]pyrrole-1,3-diyl)[4,4-bis(2-ethylhexyl)-4H-silolo[3,2-b:4,5-b'];]dithiophene-2,6-diyl] (**PDTSTPD**), is another low-bandgap copolymer (1.73 eV) that shows high performances (up to 7%) in OPV devices. This copolymer has a thieno[3,4-c]pyrrole-4,6-dione (TPD) electron-deficient unit and dithienosilole (DTS) electron-rich unit (**Figure I-20**).^{70,71}

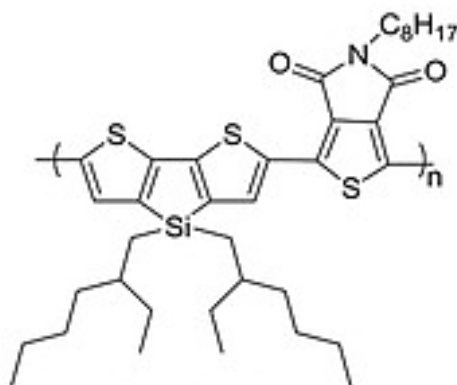


Figure I-20: Chemical structure of PDTSTPD copolymer.

Poly[(5,6-difluoro-2,1,3-benzothiadiazol-4,7-diyl)-*alt*-(3,3''-di(2-octyldodecyl)-2,2';5',2'';5'',2''''-quaterthiophen-5,5''''-diyl)] (**PffBT4T-2OD**) is another low-bandgap (1.65 eV) semiconducting polymer for organic photovoltaics (OPVs), which has reached very high power conversion efficiencies (PCEs) approaching 11%.⁷² This polymer was targeted by reacting 4,7-bis(5-bromo-4-(2-octyldodecyl)thiophen-2-yl)-5,6-difluorobenzo[c][1,2,5]-thiadiazole acceptor unit with 2,5-bis(trimethylstannyl)thieno[3,2-b]thiophene donor unit (**Figure I-21a**). Compared to PffBT4T-2OD, poly[(5,6-difluoro-2,1,3-benzothiadiazol-4,7-diyl)-*alt*-(3,3''-di(2-nonyltridecyl)-2,2';5',2'';5'',2''''-quaterthiophen-5,5''''-diyl)] (**PffBT4T-C9C13**) has a similar bandgap but larger side chains (**Figure I-21b**). This helps promote better solubility and film morphology. When using PffBT4T-C9C13 as a polymer donor with a fullerene acceptor, a certified efficiency of 11.5% was achieved.⁷³

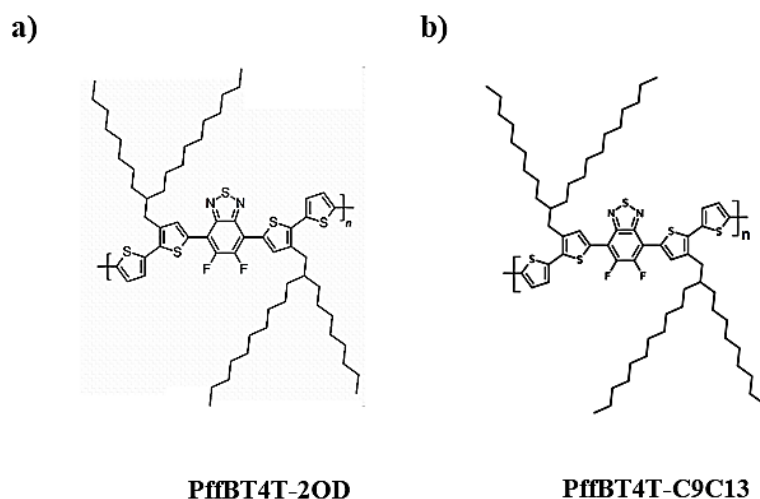


Figure I-21: Chemical structure of (a) PffBT4T-2OD and (b) PffBT4T-C9C13 copolymers.

One of the most successful low-bandgap polymers for solar cell applications were based on thieno[3,2-b]thiophene (TT) moiety. TT was investigated in 2009 and incorporated as acceptor units in the D-A strategy in which it was copolymerized with different donors yielding low-bandgap copolymers.

Among these copolymers, poly [[4,8-bis[(2-ethylhexyl)oxy]benzo[1,2-b:4,5-b']dithiophene-2,6-diyl][3-fluoro-2-[(2-ethylhexyl)carbonyl]thieno[3,4-b]thiophenediyl]] (**PTB7**) results from the copolymerization between BDT donor units and TT acceptor units (**Figure I-22a**). This low-bandgap PTB7 (1.6 eV) is a well-known donor polymer that is widely used in OPV applications yielding 9% efficiency.⁷⁴

Substituting BDT donor unit with alkylthienyl-substituted benzo[1,2-b:4,5-b']dithiophene (BDT-T) yields poly[4,8-bis(5-(2-ethylhexyl)thiophen-2-yl)benzo[1,2-b:4,5-b']dithiophene-2,6-diyl-*alt*-(4-(2-ethylhexyl)-3-fluorothieno[3,4-b]thiophene-)-2-carboxylate-2,6-diyl)] (**PTB7-Th**) shown in **Figure I-22b**. This polymer with a narrower bandgap (1.58 eV) possesses lower HOMO/LUMO levels and yields higher efficiencies when compared to PTB7-based devices.⁷⁵ The highest efficiency obtained so far for PTB7-Th:non-fullerene acceptor-based devices was 13%.⁷⁶

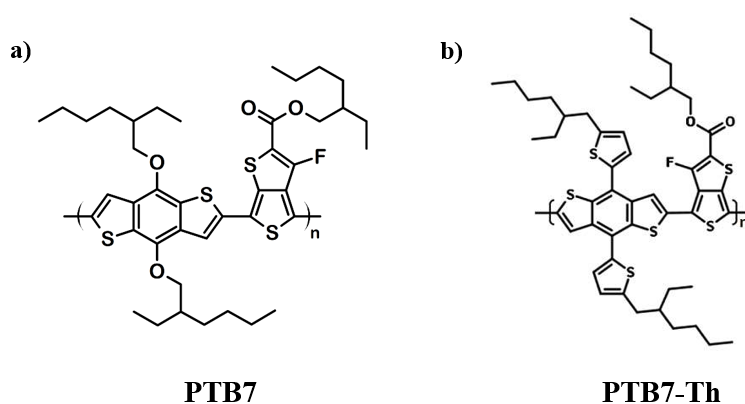


Figure I-22: Chemical structures of (a) PTB7 and (b) PTB7-Th copolymers.

Some other low-bandgap copolymers that were also used as donor materials in high-performance OPV devices are shown in **Figure I-23**.

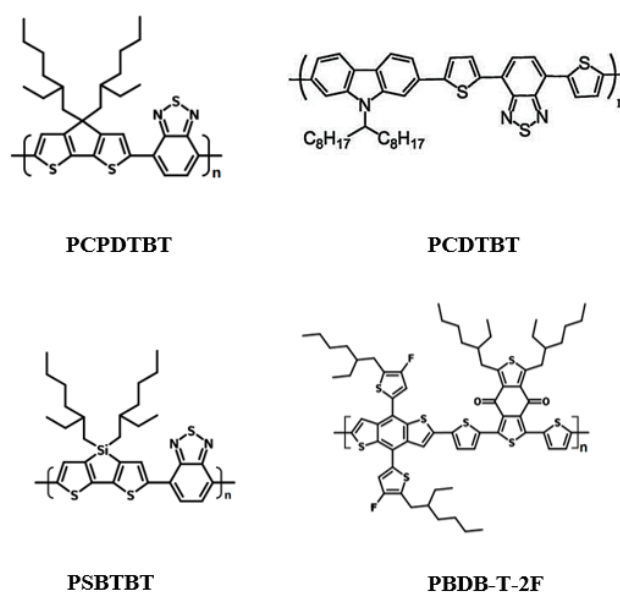


Figure I-23: Some low-bandgap copolymers used as donor materials in OPV devices.

Generally speaking, it was observed that performances of organic solar cells depend strongly on the intermolecular arrangements at the donor:fullerene interfaces. Thus, for a high performing D-A copolymer, the acceptor moiety should likely have less bulky or no alkyl substituents, whereas the donor moiety tend to have branched or bulkier alkyl substituents. This combination makes the acceptor moiety sterically accessible for interactions with the fullerene derivative while the donor has sterically hindered interactions with the fullerene molecule.⁷⁷

e. Near-infrared (NIR) absorbing molecules

NIR absorbing polymers represent a class of emerging materials that are widely used in different applications including photovoltaics and telecommunications.⁷⁸

In general, the power conversion efficiency in organic photovoltaics is enhanced by broadening the absorption band using materials with an absorption that matches the maximum solar flux region of the solar spectrum. Thus, as previously mentioned, low-bandgap polymers that absorb in the range of the maximum solar flux region (between 500 nm and 750 nm) are widely used.⁷⁹ However, power conversion efficiency in organic solar cells can be further enhanced by developing very low-bandgap polymers that extend absorption beyond 800 nm (**Figure I-24**). Typically, these NIR absorbing polymers possess bandgaps below 1.55 eV.

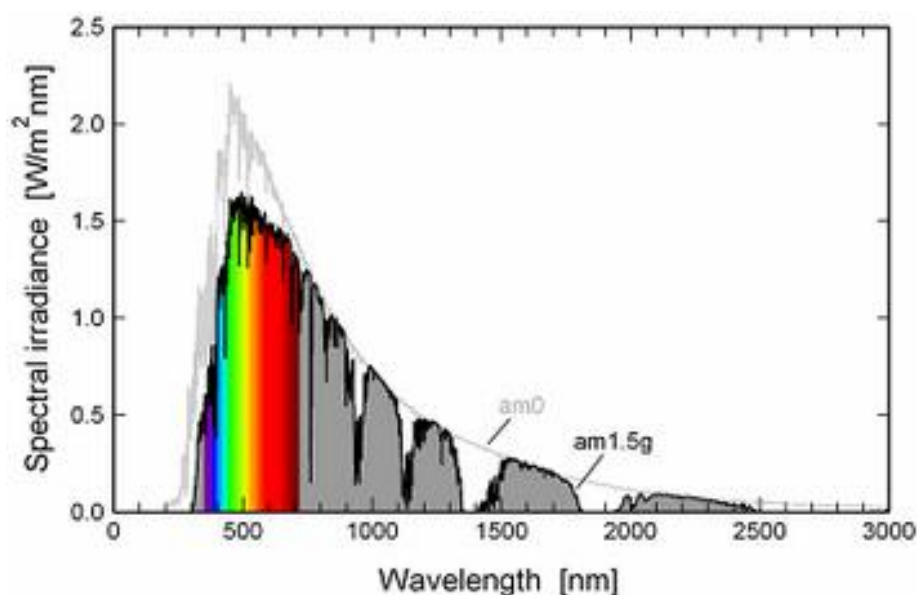


Figure I-24: Spectral irradiance of the AM 1.5G spectrum.

In this regard, one of the promising strategies is the incorporation of strong electron withdrawing materials such as diketopyrrolopyrole (DPP), thienoisindigo (TII) and other building blocks into the main polymer chain (strong electron donor). This tune the HOMO/LUMO energy levels and lower the bandgap. Eventually, this strategy enhances the optical and electronic properties of the resulting copolymers through intramolecular charge transfer from the donor to the acceptor.⁸⁰ Thus, in the following section, several examples of low-bandgap NIR absorbing copolymers are summarized based on the acceptor moieties used in the D-A strategy.

i. Examples of low-bandgap NIR absorbing D-A copolymers

1. Benzothiadiazole and difluorobenzothiadiazole-containing copolymers

Benzothiadiazole (BT) and its derivatives have been widely used as electron-deficient units in designing D-A copolymers as shown in **Figure I-25**. Poly[2,6-(4,4-bis(2-ethylhexyl)-4H-cyclopenta[2,1-b;3,4-b']dithiophene)-*alt*-4,7(2,1,3-benzothiadiazole)] (**PCPDTBT**) copolymer was previously synthesized by alternating cyclopenta[2,1-b;3,4-b']dithiophene (CPDT) donor units and BT acceptor units. This polymer possesses a low-bandgap of 1.4 eV. It was proven that replacing CPDT with the analogue silicon-substituted monomer, dithieno [3,2-b:2',3'-d]silole (DTS), has no effect on the bandgap of the obtained poly[(4,4-bis(2-ethylhexyl)-dithieno[3,2-b:2',3'-d]silole)-2,6-diyl-*alt*-(2,1,3-benzothiadiazole)-4,7-diyl] (**PSBTBT**) copolymer.⁶⁷ The same effect was recognized by replacing silicon (Si) with germanium (Ge) in the donor unit of poly[(4,4-bis(2-ethylhexyl)dithieno[3,2-b:2',3'-d]germole)-2,6-diyl-*alt*-(2,1,3-benzothiadiazole)-4,7-diyl] (**PGeBTBT**) copolymer.⁶⁸ However, the incorporation of an oxygen atom in the donor moiety, *i.e.* dithieno- [3,2-b:2',3'-d]pyran (DTP) alternating together with difluorobenzothiadiazole acceptor yields poly[2,7-(5,5-bis(3,7-dimethyloctyl)-5H-dithieno [3,2-b:2',3'-d]pyran)-*alt*-4,7-(5,6-difluoro-2,1,3-benzothiadiazole)] (**PDTP-DFBT**) copolymer having a slightly smaller bandgap (1.38 eV) with low-lying HOMO level and a near-IR charge collection when compared to the other obtained copolymers.⁸¹ All the mentioned copolymers were used as donor materials in organic solar cells.

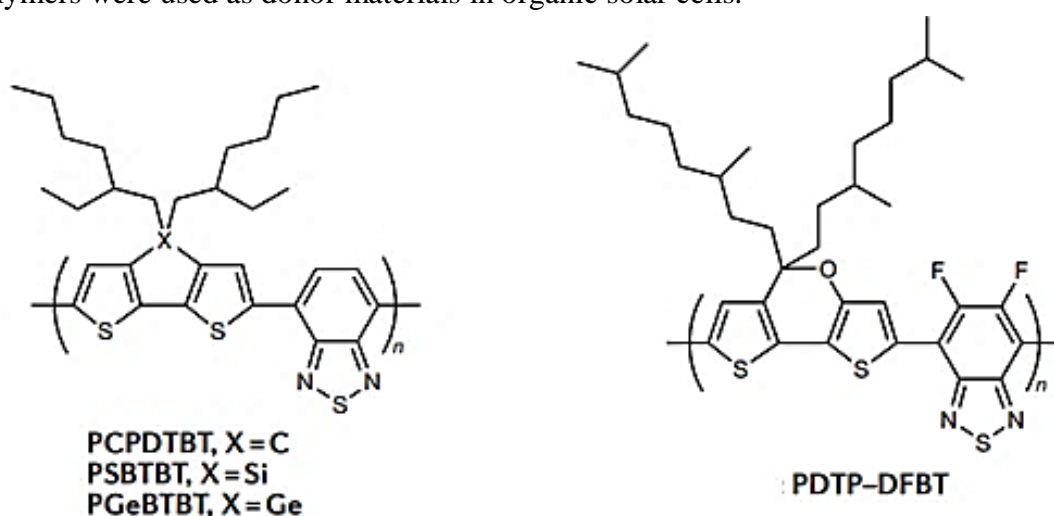


Figure I-25: Chemical structures of benzothiadiazole and difluorobenzothiadiazole-based copolymers.

2. Thiadiazoloquinoxaline-containing copolymers

Near-infrared absorbing copolymers based on 4,6,7,9-tetra(thiophen-2-yl)-[1,2,5]thiadiazolo [3,4-g]quinoxaline and 6,6',12,12'-tetraoctyl-6,12-dihydroindeno[1,2-b]fluorene (**PIFDQ**) or 9,9-dioctyl-9H fluorene (**PFDQ**) were previously synthesized and showed quite similar optical and electrochemical properties. The corresponding bandgaps (1.19 eV and 1.16 eV, respectively) were calculated from the onset wavelength of absorption that extended from 250 nm to 1100 nm in films (**Figure I-26**). The synthesized copolymers were used as photoactive materials when blended with PC₇₀BM in normal device structured OSCs.⁸²

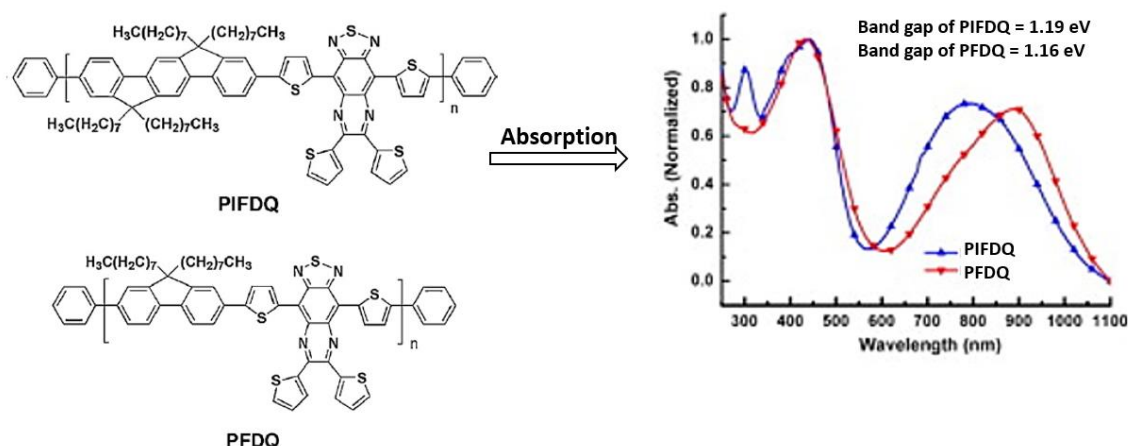


Figure I-26: The chemical structure of PIFDQ and PFDQ copolymers and their corresponding UV-vis-NIR absorption spectra.⁸²

3. Diketopyrrolopyrrole-containing copolymers

Diketopyrrolopyrrole (DPP) based-copolymers were previously studied and widely used as building blocks. They are characterized with good morphology for electron conductivity, low-bandgaps and near-IR absorption. The chemical structures of some diketopyrrolopyrrole-based copolymers are shown in **Figure I-27**. The first reported DPP-based copolymer is poly(diketopyrrolopyrrole-terthiophene) (**PDPP3T**)⁸³ with a bandgap of 1.31 eV and an absorption up to 930 nm. In 2012, DPP was combined with thienyl-substituted BDT (BDTT) yielding poly(2,6'-4,8-di(5-ethylhexylthienyl)benzo[1,2-b;3,4-b]dithiophene-*alt*-5,5'-dibutylotyl-3,6-bis(5-thiophen-2-yl)pyrrolo [3,4-c]pyrrole-1,4-dione) (**PBDTT-DPP**) that has a low-bandgap of 1.44 eV.⁸⁴ The analogue copolymer of the latter, (**PBDTT-SeDPP**), is obtained by replacing the sulfur atom in DPP by selenium. This copolymer is characterized by a red-shift in the absorption spectrum.⁸⁵

PFDPPSe is another NIR-absorbing copolymer with a bandgap of 1.34 eV. Such copolymer comprises diketopyrrolopyrrole-based acceptor and a simple furan donor. The optimized inverted device structure using PFDPPSe:PC₇₀BM showed a maximum PCE of 6.16% *via* solvent additive (diphenyl ether, DPE).⁸⁶

Recently, 1,4-bis(5-bromothiophen-2-yl)-3,6-bis-(ethylhexylthio) pyrrolo[3,4-c]pyrrole (DPP-EH-Br₂) or 1,4-bis(5-bromothiophen-2-yl)-3,6-bis(ethylhexylthio)- pyrrolo [3,-4-c]pyrrole (DAP-EH-Br₂) monomers, derived from DPP chromophore, were used by our group in the D-A strategy with 4,4'-bis(2-ethyl-hexyl)-5,5'- bis(trimethyltin)-dithieno[3,2-b:2',3'-d]silol (DTS), electron rich unit (donor moiety). This copolymerization yielded **P(DTS-DPP)** and **P(DTS-DAP)**, respectively. The synthesized copolymers possess low-bandgap around 1.5 eV and 1.3 eV, respectively.⁸⁷ In general, silicon containing aromatic compounds (siloles) have unique electronic structures that eventually lead to low-lying LUMO energy levels. The interaction between silicon σ^* orbitals and π^* orbitals of the butadiene moiety is responsible to the relatively small bandgaps.⁸⁸ HOMO and LUMO energy levels were found to be -5.4 eV and -4.1, respectively for **P(DTS-DAP)** while -5.5 eV and -4.0 eV, respectively for **P(DTS-DPP)**.⁸⁷

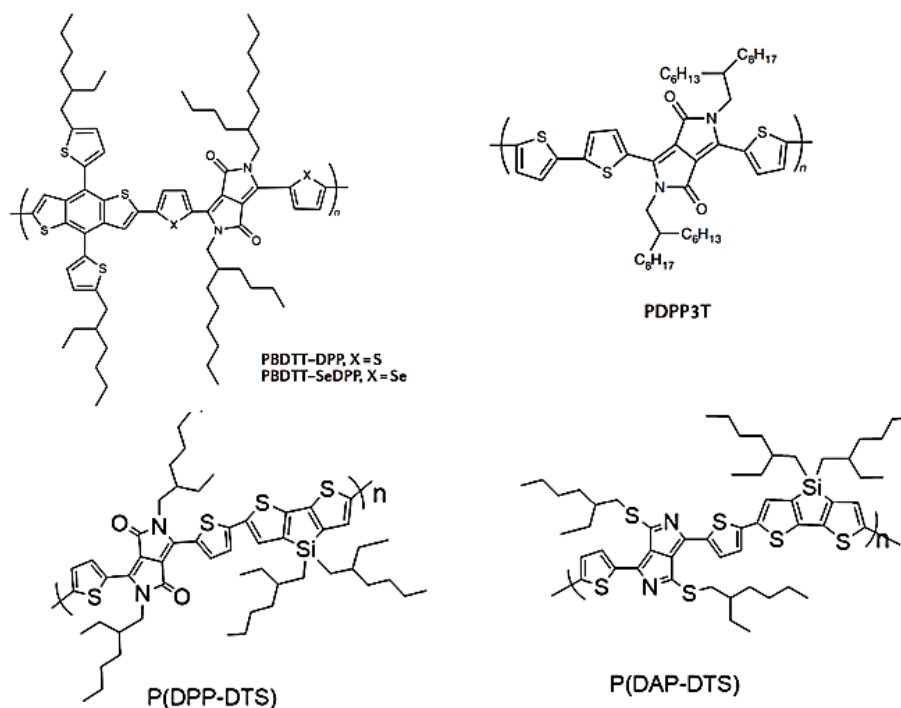


Figure I-27: The chemical structures of diketopyrrolopyrrole and its analogue-based copolymers.

The synthesized copolymers showed promising absorption properties that extend to the near-IR region for both films and solutions. As shown in **Figure I-28**, the λ_{onset} in films is located at 1010 nm and 1120 nm for **P(DTS-DPP)** and **P(DTS-DAP)**, respectively, *i.e.* in the second near-IR window. A property that makes them potential materials to be used in optoelectronic applications such as organic photovoltaics and photodetectors.⁸⁷ In general, substitution of DPP by DAP units in the donor-acceptor copolymers led to a red-shift of the maximum absorption by around 100 nm.⁸⁹ This red-shifting was attributed to the better π -electron conjugation between the donor and the acceptor moieties.

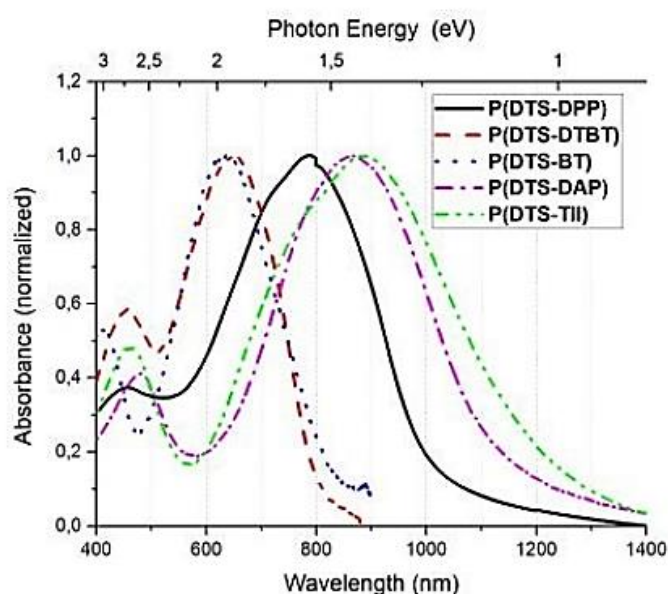


Figure I-28: Normalized UV-vis-NIR absorption spectra of DTS-based copolymers in films.⁸⁷

4. Isoindigo-derivatives-based copolymers

Thienyl-derived isoindigo units were also taken into consideration in the synthesis of low-bandgap copolymers absorbing in the near-IR. These units are characterized with a very strong electron-withdrawing property due to the internal lactam ring. In 2013, the first thienyl-derived isoindigo (TBII)-based copolymer with one benzene and one thiophene fused (**Figure I-29a**), was reported with a low-bandgap (1.4 eV).⁹⁰ A lower bandgap (1.15 eV) copolymer (**PTII2T-HD**) was obtained when a fully thiophene-based isoindigo was used (TII). It was proven that in polymers containing more thienyl substituent units, a greater backbone coplanarity is displayed and red-shifted absorption profiles with narrower optoelectronic bandgaps are observed.⁹⁰ The bandgap could be even lowered to 1 eV when the TII unit was copolymerized with different donor materials than thiophene including BDT and CPDT.⁹¹ The obtained copolymers are represented as P1 and P2, respectively as shown in **Figure I-29b**.

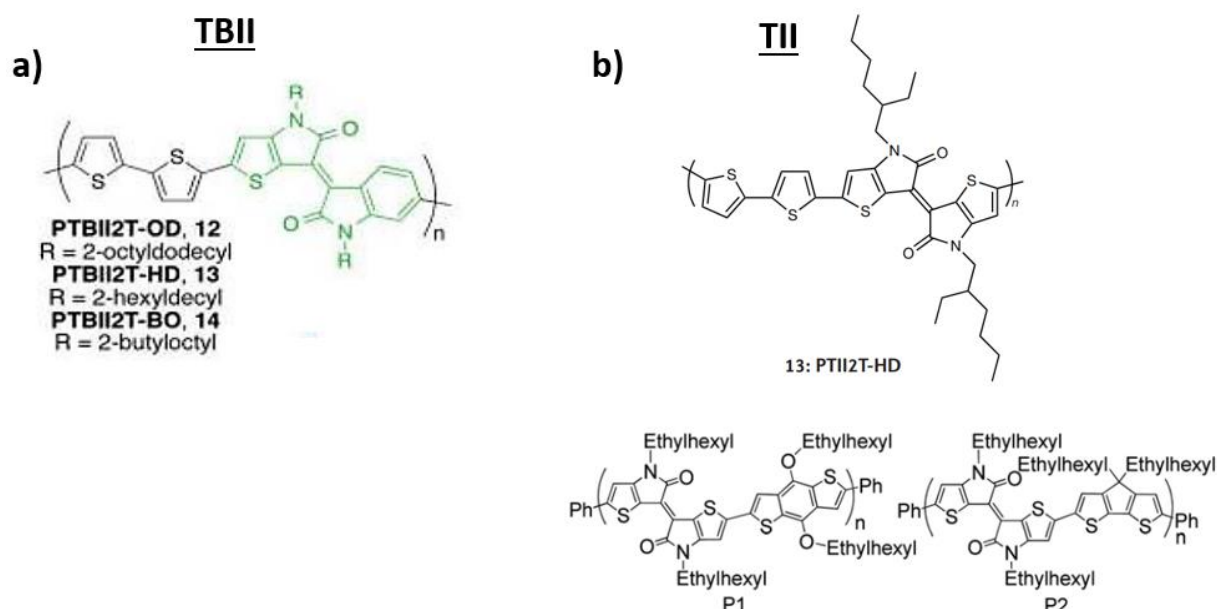
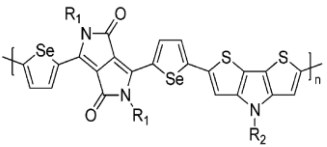
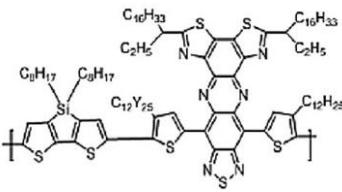
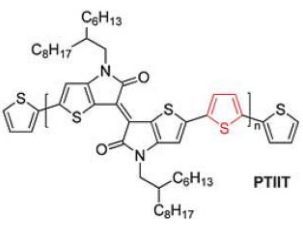
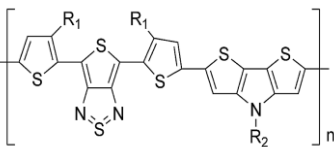
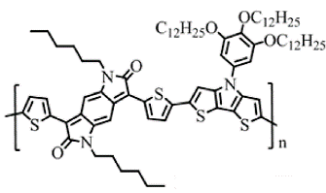
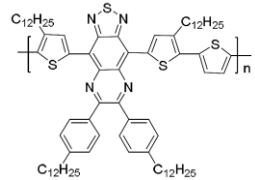
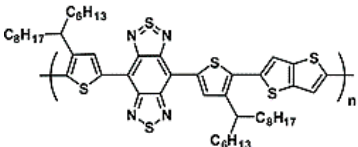


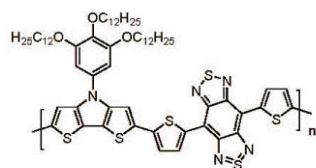
Figure I-29: Chemical structures of thienyl-derived isoindigo-based copolymers.⁹¹

Our recent work extended this family by designing a copolymer alternating the electron rich unit (donor moiety) DTS with thienoisoindigo (TII) acceptor yielding **P(DTS-TII)** copolymer which was compared to those copolymers incorporating BT, DPP and DAP accepting units. It has been proved that this new copolymer exhibited an improved near-infrared light harvesting in both solution and thin films with a λ_{onset} of 1120 and 1220 nm, respectively.⁸⁷

Examples of other studied near-IR absorbing copolymers are summarized in **Table I-1** with their optical properties, electrochemical properties and their potential applications.

Table I-1: Examples of some near-IR absorbing copolymers with their properties and applications.

Chemical structures	λ_{\max} film (nm) ^a	HOMO (eV) ^b	LUMO (eV) ^b	E_g^{optical} (eV) ^a	Application	Ref
	910	-5.17	-3.75	1.13	Solar cell	92
	1022	-5.34	-3.94	1.08	Solar cell	93
	1006	-4.82	-3.78	0.92	Transistor	94
	941	-4.9	-3.6	0.90	Solar cell	95
	1006	-4.57	-3.78	0.79	—	96
	1165	-4.95	-3.92	0.75	Transistor	97
	1225	-4.36	-3.40	0.56	Transistor	98



1208

0.50

Transistor

99

^a measured by UV-vis spectrophotometry and ^b measured by cyclic voltammetry

V. Synthesis of low-bandgap D-A copolymers

a. Techniques of polymerization

When it comes to polymerization, it is important to distinguish between two different classes: chain-growth and step-growth polymerization as illustrated in **Figure I-30**. Chain-growth polymerization is characterized by a chain extension due to the reaction of a monomer with the active site of a polymer chain while regenerating the active site spontaneously. On the other hand, step-growth polymerization involves one or more monomers with at least two reactive functional groups where the polymer chain proceeds either by addition or condensation.

Therefore, chain-growth and step-growth polymerization possess different mechanisms. During chain-growth, an initiation step leads to the formation of a reactive intermediate that could be radical, anion, cation. A propagation step then follows where the reactive intermediate reacts with monomers until the reactive center is transferred to the end of the chain in which termination takes place as shown in **Figure I-30**. On the other hand, in step-growth polymerization, the molar mass of the chain builds up slowly in which only one reaction mechanism for the polymer formation exists. In this case, the mechanism starts when two different bi-functional monomers, A-A and B-B, react together (or one A-B monomer) through their functional groups forming dimers which then increase their size to form x-mers. Reactive end-groups lead to the coupling of chains having different lengths and eventually achieving high molar mass polymers at the end of polymerization.¹⁰⁰

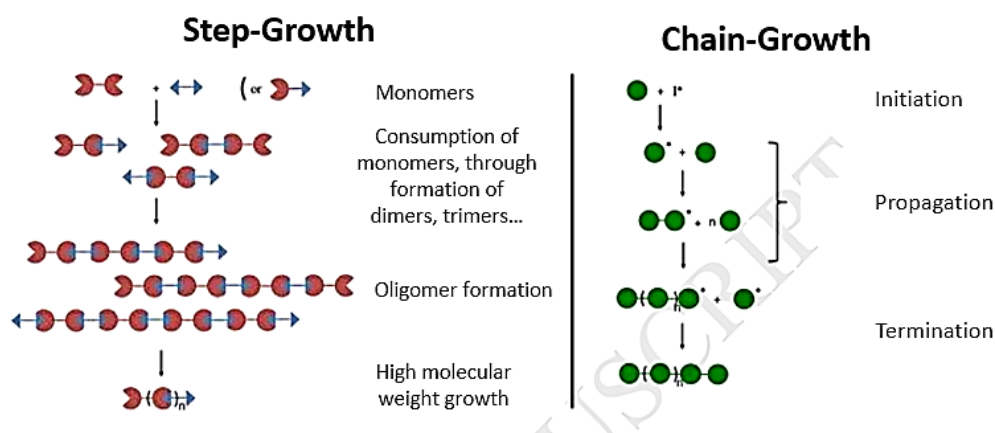


Figure I-30: An illustration of the mechanistic difference between step-growth and chain-growth polymerization.¹⁰⁰

As previously mentioned, the polymer chain in step-growth polymerization proceeds either by addition or condensation, leading to two different categories: polyaddition and polycondensation. The latter proceeds by eliminating small molecules (H₂O, HCl, etc.). While polyaddition represents the reaction in which monomers combine to each other without any elimination of small molecules. This includes polymers such as polyester, polyamides, polyurethanes and polycarbonates.

In 1930, Carothers developed a polycondensation reaction for the synthesis of polyesters. Later in 1935, he developed a mathematical theory to calculate the degree of average polymerization in number, (\bar{X}_n or DP_n) based on the conversion (p) and the average functionality (f) as shown in **Equation 4**.¹⁰¹

In the simplest case, a linear polymer is formed from the polycondensation between two bifunctional monomers.

$$\bar{X}_n = \frac{2}{2 - pf} \quad \text{Equation 4}$$

The conversion p is expressed as shown in **Equation 5**.

$$p = \frac{N_0 - N_t}{N_0} \quad \text{Equation 5}$$

Where N_0 is the number of molecules at $t=0$ and N_t is the number of moles at time t .

Thus, for high molar mass polymers, step-growth polymerization should address some criteria including:

- High reaction conversions (>99.9%)
- Monomer functionality (f) equal to 2
- Stoichiometry of functional groups equivalent to 1

In general, it was stated that the extension of the molar mass does not disturb the reactivity of the chain's end-groups.

In the case of stoichiometric deviation, the average degree of polymerization is described in **Equation 6**.¹⁰²

$$\bar{X}_n = \frac{1+r}{1+r-2rp} \quad \text{Equation 6}$$

Where r is the stoichiometric ratio of monomers. For an equal stoichiometry, r is equal to 1. In this case, this equation is reduced to **Equation 4** (with $f = 2$). However, in the case of non-stoichiometry and by assuming that the excess monomer is in the denominator, then $r < 1$.

Accordingly, for the limiting reactive monomer, total conversion p tends to be 1. In this case, \bar{X}_n tends to be as shown in **Equation 7**.

$$\bar{X}_n \rightarrow \frac{1+r}{1-r} \quad \text{Equation 7}$$

This thesis work involves the development of low-bandgap π -conjugated copolymers absorbing in the near-infrared region. The applied synthetic procedures must be robust, reproducible and give high yields. In the next section, some important synthetic routes are discussed but before a brief summary of the evolution in the synthetic methods is presented.

b. Evolution in the synthetic procedures for conjugated polymers

Since researchers discovered polyacetylene's conductivity and as a great interest was shown for other semiconducting polymers, chemical research was then oriented toward the development of new versatile synthetic methods. The first studied polyacetylene was synthesized *via* a Ziegler-Natta polymerization of acetylene developed by Shirakawa and co-workers.¹⁰³ Durham route is an alternative but indirect method to produce polyacetylene. The reaction is summarized by the polymerization of an appropriate monomer using ring opening metathesis polymerization and then followed by thermal elimination to give the desired polyacetylene.¹⁰⁴ However, this method shows incomplete conversion causing defects in the conjugation.

On the other hand, oxidative polymerization was considered as a straightforward method for the preparation of semiconductive polymers. Gilch method was also studied in the synthesis of poly(p-phenylene vinylene) (PPV) which has certain limitations leading to an incomplete conjugation.¹⁰⁵ Thus, for an improved synthesis, Wessling-Zimmermann method was studied and proved the synthesis of well-defined products with less defects.¹⁰⁶ Later, polycondensation reactions involving metal-catalyzed couplings were considered as the most commonly employed reactions for the synthesis of conjugated copolymers. Mizoroki-Heck, Stille, Suzuki-Miyaura, Sonogashira, Kumada and Negishi are categorized as polycondensation reactions involving two different bi-functionalized aromatic co-monomers (Ar and Ar') as shown in **Figure I-31**.

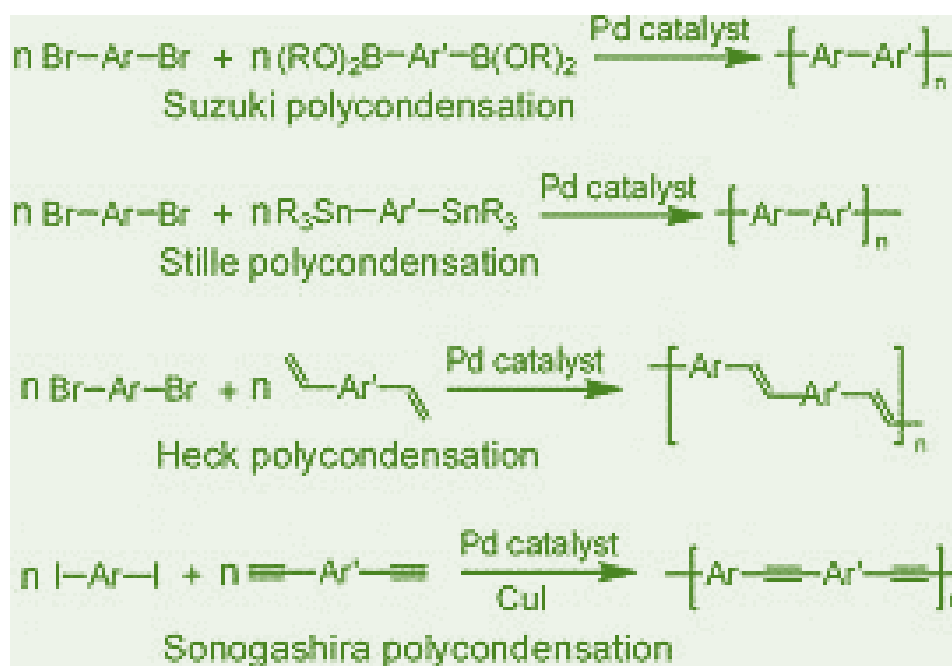


Figure I-31: Examples of metal-catalyzed couplings used for the synthesis of conjugated copolymers.¹⁰⁷

Heck polycondensation reaction is limited for the synthesis of poly(arylene-vinylene). In such reactions, organic halides and vinylbenzene compounds are coupled to generate a carbon-carbon bond. In comparison with other approaches, Heck reaction offers an easier and faster way to prepare processible poly(phenylenevinylene)s. The reaction takes place in the presence of a palladium(II) acetate ($\text{Pd}(\text{OAc})_2$) catalyst with tertiary amine and triarylphosphine under nitrogen atmosphere.¹⁰⁸ On the other hand, Sonogashira coupling is limited for the synthesis of poly(arylene-ethynylene).¹⁰⁹

A promising development was then demonstrated by Kumada¹¹⁰ and Negishi¹¹¹ *via* nickel-catalyzed transformations using organomagnesium and organozinc starting materials, respectively yielding regioregular polymers. However, the Kumada catalyst-transfer polycondensation which is also known as Grignard Metathesis (GRIM) is of great interest due to its quasi-living character, and is widely used for the synthesis of conjugated block copolymers. This technique is developed in the last part of this bibliography.

Since regularly alternating block copolymers cannot be obtained using such method, Stille and Suzuki polycondensations are preferred. Palladium-catalyzed Suzuki-Miyaura coupling is among the most efficient methods for the formation of C-C bonds in which the reaction can take place under mild conditions. It is characterized by certain advantages over Stille polycondensations since organoboranes are air and moisture stable. Moreover, boron-containing by-products can be easily separated during purification in large-scale productions. Features that simplify the synthesis and make it easier to be handled. In general, wide range of functionalities can be tolerated. In addition to the non-toxic starting materials, Suzuki polycondensation possess the characteristics of other cross-coupling reactions including stereospecificity and regioselectivity which made it applicable in industrial sectors. Although this coupling reaction is a good choice among other polycondensation reactions, but certain limitations must be taken into account. Some monomers are considered to be unstable in basic mediums and they require more complex protection and de-protection methodologies. Additionally, some polymers may show solubility limitations in the presence of the biphasic mixtures. Thus, low-molecular weight polymers are formed limiting their use in photovoltaic applications.¹¹²

As it is out of scope to discuss all the polycondensation reactions in details, only Stille cross-coupling are highlighted in the following section since it was used for the synthesis of the block copolymers in this thesis.

c. Stille coupling polycondensation

In 1976-1977, Eaborn¹¹³ and Kosugi¹¹⁴ were the first to work on the cross-coupling between organostannanes and electrophilic compounds. While the first publication on Stille cross-coupling appeared in 1978 by John K. Stille.¹¹⁵ This was a synthesis of ketones from a reaction between acyl chloride and organostannane using palladium catalyst. After this period, Stille coupling reaction became one of the versatile synthetic methodologies useful for the formation of sp^2 carbon-carbon bonds and it is the most promising technique for the synthesis of conjugated poly-aromatic systems. Interestingly, it was extensively employed for the construction of π -conjugated donor-acceptor (D-A) copolymers.

Generally speaking, Stille reaction is based on Pd(0)-mediated cross-coupling of an organostannane with organohalides (aryl, allyl or alkenyl halides), triflates or acyl halides under mild conditions with a wide choice of solvents.^{113,114}

The cyclic mechanism of Stille coupling is shown in **Figure I-32** as proposed by Stille in 1986.¹¹⁶ As presented, it involves three main steps. Starting from the oxidative addition of the low valent metal catalyst Pd(0) into the organic halide (R^1-X) forming the *trans* Pd(II) complex as an intermediate. This is followed by a transmetalation step during which the nucleophilic organostannane reacts with the *trans*-metal complex. Then, the halide (X group) coordinates with the tin *via* an associative addition leading to a palladium complex with R^1 and R^2 while leaving behind R_3Sn-X . The *trans*-metal complex then affords the *cis* complex which undergoes a reductive elimination step giving the final product R^1-R^2 in which the palladium catalyst is regenerated.

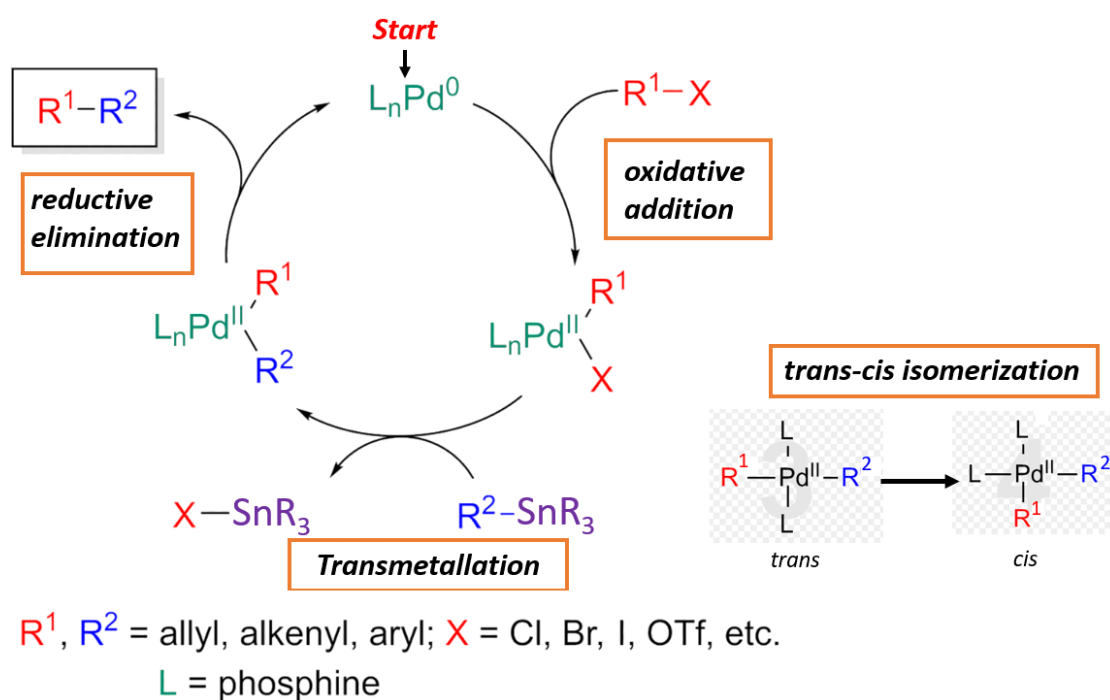


Figure I-32: General cyclic mechanism of Stille cross-coupling.

i. Monomers

As previously mentioned, Stille coupling polycondensation of conjugated copolymers generally involves two types of monomers, aryl halide or aryl triflate and an organostannane. It was proven that iodo-based monomers are more reactive than bromo ones which are in turn more reactive than chloro-based monomers. This is related to their reactivity in the oxidative addition step. In general, the oxidative addition step can be facilitated by electron-withdrawing groups while the transmetallation step is favored by electron-rich organostannanes. Therefore, for an efficient high molecular weight polymer synthesis, the reaction is preferred between electron-rich organotin compounds and unsaturated organohalides (or triflate).¹¹⁷

ii. Solvents

The solvent used in Stille coupling polycondensation plays an essential role during the reaction. In addition to dissolving starting monomers, the solvent must be suitable for maintaining the growth of polymer in solution to obtain high molar mass. Various solvents can be used during Stille coupling including chlorobenzene, toluene, chloroform and many others.

It is important to take into consideration that the used solvent must sustain the high temperature needed to proceed such reactions. Therefore, the solvent must possess a high boiling point. Although the usage of highly polar solvents such as dimethylformamide (DMF) can help by acting as coordinating ligands to the palladium center, some conjugated polymers have limited solubility in such solvents. Other solvents may help in the catalyst stabilization such as tetrahydrofuran (THF). Mixed solvent systems such as toluene/DMF are proved to be applicable in maintaining high molar mass polymers.¹¹⁷

iii. Catalyst and ligands

Various palladium compounds that can provide a Pd(II) catalytic center such as dichlorobis(triphenylphosphine)-palladium(II) $[\text{PdCl}_2(\text{PPh}_3)_2]$ and palladium(II) acetate $[\text{Pd}(\text{OAc})_2]$ can be used for Stille coupling polycondensation. But since Pd(0) complex is the active species in the catalytic cycle, a reducing agent such as triphenylphosphine (PPh_3) is needed. Thus, Pd(0) sources such as tetrakis(triphenylphosphine)palladium(0) $[\text{Pd}(\text{PPh}_3)_4]$ and tris(dibenzylideneacetonyl) dipalladium(0) $[\text{Pd}_2(\text{dba})_3]$ are the most commonly used in polymerization reactions. Although $\text{Pd}(\text{PPh}_3)_4$ is known to be reactive but it is not stable neither in air nor under moisture.

In addition to the catalyst, the choice of ligand is also important in such polymerization reactions. Phosphine ligands are the most widely used ones due to their suitable size and bulkiness, in addition to their electron-donating ability.¹¹⁸

iv. Advantages and disadvantages of Stille coupling polycondensation

Stille coupling polycondensation presents various advantages. The combination of palladium catalyst with various phosphine ligands can eventually lead to high yields, with the capability to tolerate many functional groups. Moreover, the organometallic compounds are far less oxygen and moisture sensitive in comparison with other organometallics.¹¹⁵

Despite the several advantages of such synthetic strategy, some drawbacks should be taken into consideration. The most important includes the undesirable properties of the organostannane monomers that could be toxic, difficult to purify and possess relatively poor stability over time. In addition, the use of palladium catalysts is expensive.¹¹⁸

v. Example of a low-bandgap D-A copolymer prepared using Stille coupling

Stille polycondensation was studied for synthesizing poly[4,8-bis[(2-ethylhexyl)oxy]benzo[1,2-b:4,5-b']dithiophene-2,6-diyl-*alt*-3-fluoro-2-[(2-ethylhexyl)carbonyl]thieno[3,4-b]thiophene-4,6-diyl] (**PTB7**) having donor-acceptor repetitive units used for OPV applications. Accordingly, the polycondensation reaction conditions were optimized including catalyst, reaction time, temperature, solvent and concentration. The utilization of more air-stable catalyst, Pd₂(dba)₃, with tri(*o*-tolyl)phosphine (P(*o*-tolyl)₃) ligand leads to slightly lower molar mass polymers than the ones obtained using Pd(PPh₃)₄. Therefore, Pd(PPh₃)₄ was chosen as the most suitable catalyst for this polymerization reaction that shows a complete conversion in less than 12 hours. A stepwise heating protocol for Stille polycondensation was performed yielding a very narrow distribution ($\mathcal{D} = 1.21$) of higher molecular weight polymers in comparison to the conventional Stille polymerization processed with steady heating procedure (**Figure I-33**).¹¹⁹

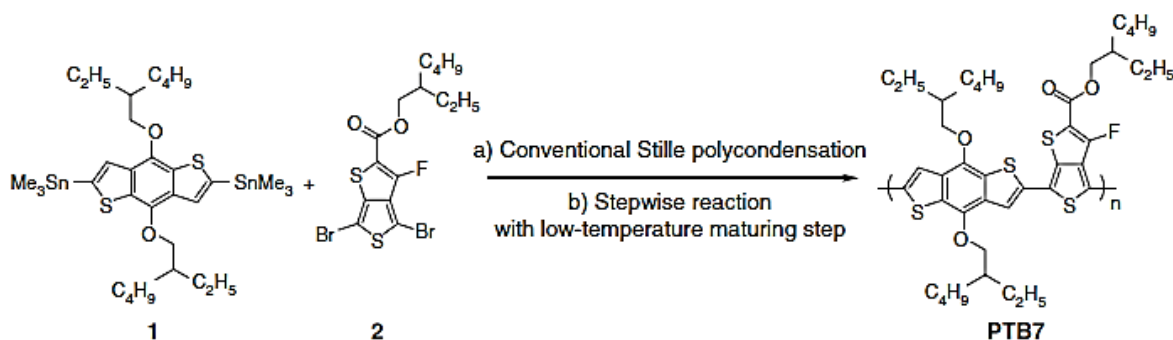


Figure I-33: Synthesis of PTB7 using either conventional or stepwise Stille polycondensation.¹¹⁹

Although the strategy of D-A copolymers shows promising results in organic solar cells, the morphological instability of blends leads to aggregation of donor and acceptor domains. This causes disruption of the nanoscale morphology through the formation of microscopic (and even macroscopic) domains of acceptor and donor materials. This eventually reduces the interfacial area between donor and acceptor, increasing the pathway length an exciton must travel before charge separation can occur. One option to stabilize the morphology of the photoactive layer is to incorporate block copolymers that are supposed to help overcome these obstacles. The separated microphases of block copolymers can be formed in the range of nanometric scale length (5-100 nm) which is comparable to the exciton diffusion length (5-20 nm).¹²⁰ This could enhance charge separation, collection and transfer to electrodes.¹²¹ Accordingly, block copolymers with their long term structural stability and morphology could provide ideal nanostructures in OPV helping in the steps of the energy conversion processes.^{122,123}

The main challenges that a researcher may face is how to design block copolymers consisting of donor and acceptor blocks to be used in OPV applications. Therefore, certain criteria must be taken into consideration including sufficient solubility for solution processing and high charge carrier mobility to facilitate charge transfer. Additionally, a broad and intense absorption profile across the solar spectrum must be achieved.

VI. Rod-Rod block copolymers: interest and synthesis

Block copolymers (BCP) represent a specific class of copolymers in which chemically distinct macromolecular sequences (called “blocks”) are covalently linked together. In the last decades, block copolymer science was strongly developed thanks to the progress in the controlled and living polymerization processes that allowed the synthesis of well-defined macromolecules.¹²⁴ Some of the typical block copolymer architectures are shown in **Figure I-34** including linear and branched structures. Among the diverse architectures, the simplest one is the linear diblock copolymer as a result of the covalently bonded distinct homopolymers. This section focuses on linear diblock copolymers.

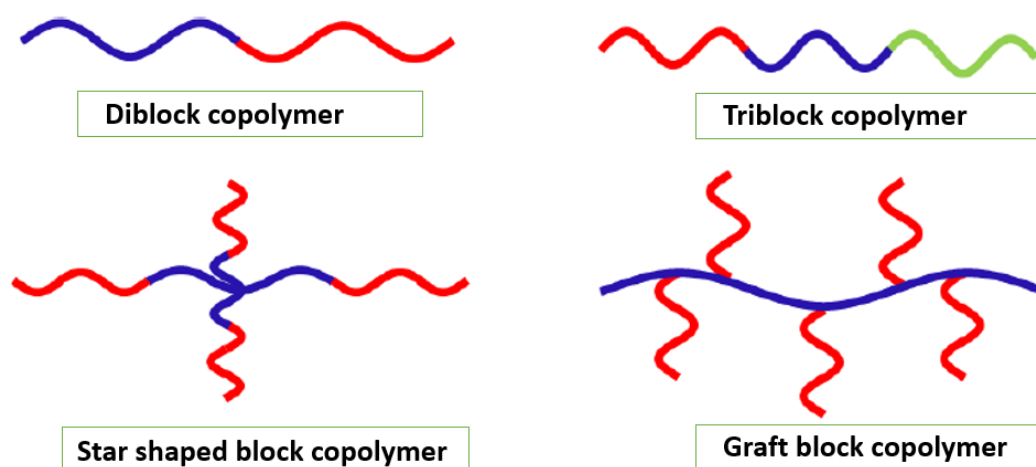


Figure I-34: Representative drawing for various architectures of block copolymers.

By observing the evolution in the number of publications regarding block copolymers from the early beginning in 1952¹²⁵ until 2019, four periods were recognized (**Figure I-35**). In the initial period, only 13 publications were infrequent in 1967. The number was then tremendously increased up to 350 publications *per year* in the second period. This early development period was followed by a fast growth period, with more than 2300 publications *per year*. The number of publications was then fluctuating in the last period from 2012 up to date suggesting the maturity level of the achievement. In addition to the progress achieved in the academic interest in the BCP, the scope of applications for BCPs is as well expanding including optoelectronic devices, drug delivery and many others.¹²⁶

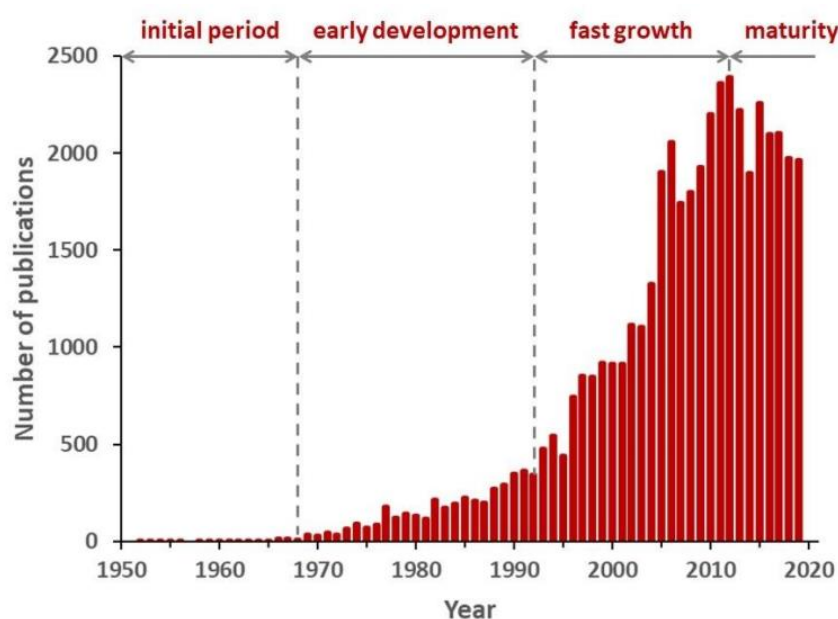


Figure I-35: Number of publications related to block copolymers infrequent between 1950 and 2019.¹²⁷

In general, blocks in block copolymers are characterized by different degree of flexibility. Depending on this degree, block copolymers may contain coil and/or rod segments. A coil block describes a flexible aliphatic polymer chain while the rod block describes a rigid block that can originate from a conjugated structure caused by the overlapping of π -orbitals.¹²¹ Accordingly, block copolymers can be categorized as rod-coil, rod-rod or coil-coil copolymers. The coil block in the coil-based copolymers is important as it can facilitate the controlled microphase separation but its insulating property limits their use in many applications especially photovoltaic devices. Therefore, in the last decades, researches were oriented toward the synthesis of all-conjugated rod-rod block copolymers that provide comprehensive opportunities for developing high-performance organic electronics. Rod-rod block copolymers have drawn attention due to their promising properties including self-assembly and electronic properties (such as tunable bandgaps) needed for variety of applications.¹²⁸ The enhanced electronic properties are caused by the continuous conjugation along the polymer chain.

Thus, in this part, only rod-rod block copolymers are discussed. And in general, most of the synthesized rod-rod block copolymers are based on P3HT as one of the conjugated blocks. Thus, the synthesis of P3HT is discussed in details by the end of this chapter.

a. Interest of rod-rod block copolymers in OPV

i. Morphology obtained upon self-assembly

Strong repulsion *i.e.* incompatibility between distinct polymers is the most characteristic feature of block copolymers, causing their segregation. However, since these blocks are chemically bonded, they cannot separate on a macroscopic scale like in the case of physically mixed homopolymers even if the segregation is complete.¹²⁹ In such case, microphase separation occurs leading to the formation of polymer-rich nanodomains.

It is worth mentioning that the flexibility variation is among the reason behind the difference in the self-assembly behavior observed in the different forms of block copolymers. Previous studies have analyzed and predicted the preferred morphologies of block copolymers although rod-rod copolymer thermodynamics are less studied than the classical coil-coil ones.

Coil-coil BCPs are described in term of the temperature-dependent Flory–Huggins interaction parameter χ .^{130,131} More specifically, the product χN controls the microphase separation and it represents the strength of segregation between the blocks in which N is the degree of polymerization or the total number of repetitive units. In general, χ is an indication of the incompatibility between polymers in which its value increases for more incompatible polymers, and this depends mainly on the chosen monomers. Since different polymers are usually chemically incompatible, χ value tends to be positive and this results in demixing or phase separation among the components of BCPs.^{132,133} Moreover, χ is inversely proportional to temperature. Thus, upon lowering the temperature, microphase separation takes place as the repulsive interactions start to dominate and this leads to the formation of nanostructures. However, increasing the temperature, lowers the value of χ (χ become smaller or even negative). In this case, the block copolymer chains are in a disordered melt state indicating favorable mixing.¹³⁴

In general, as the product of χN exceeds the criteria value of order-disorder transition (10.5), then the microphase separation occurs, forming nanodomains. This microphase separation is referred as self-assembly.^{121,135} The various equilibrium morphologies formed during microphase separation of coil-coil BCPs have been summarized in a theoretical phase diagram^{136,137,138,139} (**Figure I-36**). This diagram predicts morphologies of BCPs as a function of the volume fraction (f) of one of the blocks. This means that when microphase separation occurs, the nanodomains are not randomly located but they may form regular arrangements and morphologies. Thus, block copolymers are thermodynamically driven to self-assemble into well-ordered nanostructured morphologies such as lamellars (L), hexagonal (H), cubic (C) or gyroid (G) (**Figure I-36**).¹³⁴ This depends on the volume fraction of each block. Several techniques (thermal annealing, solvent vapor annealing) could be used to help obtain such morphologies. Self-assembly of block copolymers has been tremendously studied and several reviews were published in this regard.^{140,141} However, Leibler was first to describe how diblock copolymers self-assemble into various nanostructures.¹³³

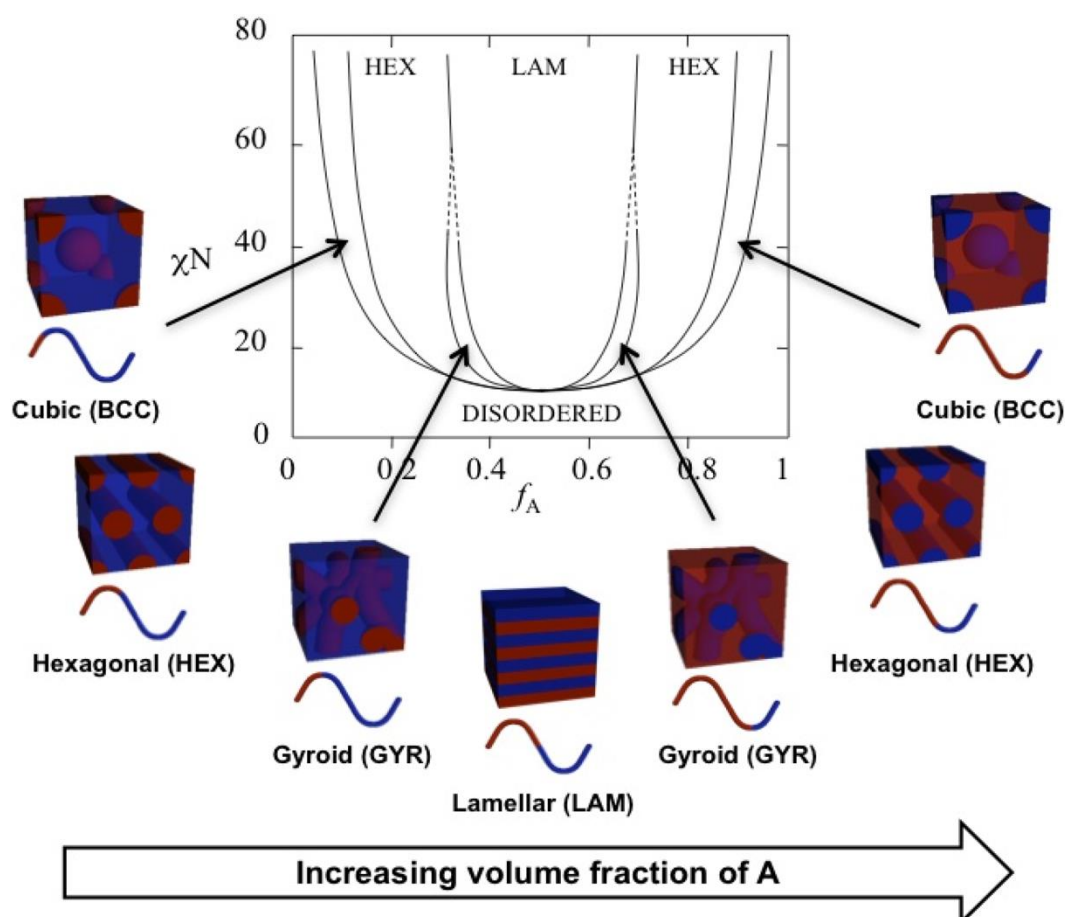


Figure I-36: Theoretical phase diagram and corresponding morphologies for coil-coil diblock copolymers. The phases are indicated as follows: body centred cubic (BCC), hexagonal cylinders (HEX), gyroid (GYR) and lamellar (LAM). f_A is the volume fraction of polymer block A.¹⁴²

As previously mentioned, the phase behavior of all-conjugated block copolymers is less studied than coil-coil ones. This could be attributed to the lack in the controlled polymerization techniques used to investigate such materials. As those polymers show high persistence length of each conjugated block, in addition to the extended π -electrons along the second block,¹⁴³ rod-rod block copolymers organize into large-area ordered lamellar nanostructures that originate from high rod-rod interactions.¹⁴⁴ The increase in interchains π - π stacking in such materials can eventually lead to an interplay between crystallinity and microphase separation. This plays an essential role in determining film morphologies. Accordingly, there exists three dominant classes of interactions that are recognized between microphase separation and crystallization.¹⁴⁵

The segregation strength of such block copolymers can be determined by comparing the Flory-Huggins parameter at the crystallization temperature (χ_c) and the one at the order-disorder temperature (χ_{ODT}). As a guideline, when the ratio of χ_c/χ_{ODT} is less than 3, a break-out crystallization behavior occurs. This break-out crystallization is observed when the microphase separation is only slightly favored. In this case, the segregation is weak while the crystallization dominates and destroys the entire microphase separated domains.¹⁴⁶

On the other hand, when χ_c/χ_{ODT} ratio is greater than 3, microphase separation is dominating. If the temperature of the order-disorder (T_{ODT}) is lower than the crystallization temperature (T_c), crystallization occurs first, driving phase separation into lamella or fibrillar structures. However, if T_c is lower than T_{ODT} , segregation limits crystallization. This behavior is known as confined crystallization.¹⁴⁷

The last behavior is the template crystallization that takes place at an intermediate segregation strength when χ_c/χ_{ODT} value is between 1 and 3 in which the volume fraction of the crystalline segment becomes larger. In this case, the microphase separation guides but does not entirely contain crystallization.^{145,146}

Recently, several all-conjugated block copolymers have been synthesized in which their self-assembly behavior has been investigated.^{147,148} For instance, Ge *et al.*¹⁴⁹ studied the synthesis of rod-rod block copolymer composed of poly-(3-butylthiophene) (P3BT) and poly[(3-hexylthiophene) (P3HT). The resultant crystalline-crystalline **P3BT-*b*-P3HT** block copolymer is characterized by a well-controlled molar mass and block ratios. It was observed that this diblock co-crystallized into uniform crystal domains with the interpenetration of the different side chains of the two crystalline blocks into a common lamellar stack.

Hashimoto *et al.*¹²⁸ previously reported the self-assembly behavior of poly[(3-hexylthiophene)-block-(3-(2-ethylhexyl)thiophene)] (**P3HT-*b*-P3EHT**) block copolymer. Their study demonstrated that the introduction of the amorphous P3EHT block induced the formation of microphase-separated nanodomains and enhanced the crystallization of the P3HT segments.

An all-conjugated block copolymer, poly(2,5-dihexyloxy-phenylene)-*block*-poly(3-hexylthiophene) (**PPP-*b*-P3HT**), having different block ratios has been synthesized and presented an interesting self-assembling behavior. The various nanostructures obtained due to self-assembly behavior are a result of the immiscibility and the different crystallinity of each block. Accordingly, it was proven that for a P3HT weight fraction (f_{P3HT}) of 0.28, the block copolymer shows a nanofibrillar structure. This indicates that the block copolymer self-assembled into a predominant PPP fiber-like structure or PPP nanowire morphology. As f_{P3HT} is increased to 0.53, a highly ordered lamellar structure was observed as a result of the rod-rod interactions inducing a competition between microphase separation and crystallization. By further increasing f_{P3HT} to 0.61, a broken lamellar structure having a less ordered morphology is obtained due to avoid the excessive chain stretching of P3HT block. For a higher value of P3HT weight fraction ($f_{P3HT} = 0.72$), the P3HT block is dominating the self-crystallization in the block copolymer forming P3HT fibril structure and thus, the self-assembly of the block was driven by the crystallization of P3HT block. Upon heating, the rod-rod interaction of P3HT blocks decreases and the crystals of the corresponding π -conjugated blocks melt. This eventually leads to random orientation of P3HT chains resulting in the transformation to a disordered phase (isotropic state) as shown in **Figure I-37**.¹⁵⁰

The synthesized block copolymer having the highest P3HT weight fractions (PPHT83) was used as a donor material for organic solar cells in the presence of a fullerene acceptor. This caused a significant improvement of the photovoltaic performances giving a higher PCE of 2.85% as compared to only 1.66% for the conventional P3HT-based devices. The enhancement could be attributed to the self-assembly of the block copolymer and the enhanced self-organization of P3HT block due to the presence of the PPP. This resulted in a higher crystallized nanochannels than that of the P3HT homopolymer, thus providing efficient transport pathways for charge transportation.¹⁵⁰

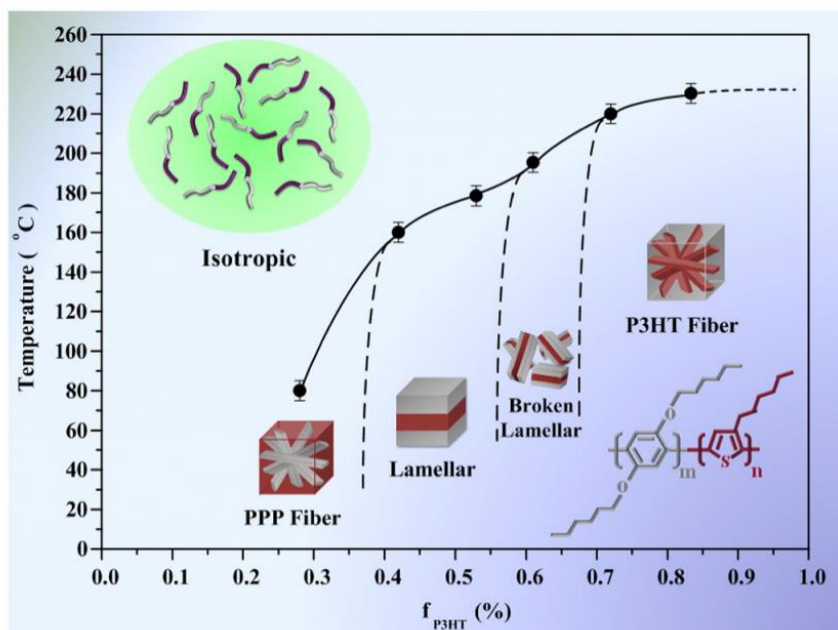


Figure I-37: Schematic representation describing self-assembly and phase transformations of PPP-*b*-P3HT block copolymer as function of composition and temperature.¹⁵⁰

ii. Donor-Acceptor behavior

What is really promising in such type of block copolymers is not only their self-assembly characteristics, but also the ability to design covalently linked donor and acceptor blocks. In the majority of OPV studies, the needed morphology for charge transport is maintained by combining p-type and n-type semiconductors in a bulk heterojunction (BHJ) active layer (**Figure I-38a**). Thereby, under the effect of thermal annealing or solvent vapor annealing, phase separation occurs. The phase separation gives rise to the formation of nanometer-scaled interpenetrating domains of pure donor material (often polymer), pure acceptor (often fullerene), and mixed phases needed for optimized performances.¹⁵¹ In some cases, although the appropriate morphology is optimized, the BHJ can be only metastable. With time, the films show further phase separation leading to an increase in the domain sizes. Thus, nanomorphological degradation of the photoactive layer can occur. This strongly influences the photovoltaic characteristics of polymer solar cells as the morphology plays a key role in how light is converted into electrical power.¹⁵²

On the other hand, although fullerene acceptors possess high electron mobility, they have negligible light absorption in the visible-near-IR regions, low compatibility with donor polymeric materials, and high cost for synthesis and purification.

From here, researches focused on the idea of incorporating both, donor and acceptor materials together into a single block copolymer. This favors the self-assembly into domains and limits the microphase separation on one hand while improves open circuit voltage and light absorption due to the acceptor polymer on the other hand.

Although D-A block copolymers can be considered to be ideal for use as OPV materials, the number of D-A block copolymers is still limited, because of their synthetic difficulties. However, academic interest in the synthetic methodology of D-A block copolymers is tremendously increasing.

In this section, the recent advancements in D-A block copolymer behavior are highlighted. In the first stage, block copolymers based on donor-acceptor were studied using a P3HT donor block (rigid rod) and an acceptor block made up of a flexible polyacrylate backbone with pendant side chains of crystalline perylene bisimides (coil).¹⁵³ However, the usage of such non-conjugated insulating block can prohibit the charge transport as previously reported.¹⁵⁴ Therefore, an improved charge transport was investigated by synthesizing fully conjugated donor-acceptor blocks characterized by dominated lamellar structures with maximized donor and acceptor interphases¹⁵⁵ as shown in **Figure I-38b**. Interestingly, an efficient direct charge path is expected. Thus, rod-rod block copolymers can be engineered to perform semiconductor p-n junctions with well-defined nanostructures.¹⁵⁶

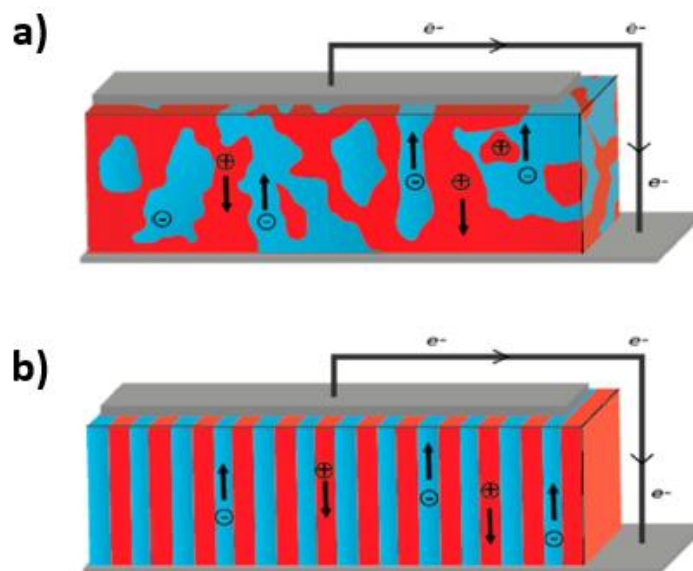


Figure I-38: Comparison between (a) bulk heterojunction morphology and (b) vertically aligned block copolymer morphology.¹⁵⁵

In this regard, poly(3-hexylthiophene)-*block*-poly((9,9-dioctylfluorene)-2,7-diyl-*alt*-[4,7-bis(thiophen-5-yl)-2,1,3-benzothiadiazole]-2',2''-diyl) (**P3HT-*b*-PFTBT**) was designed and studied as a sole active layer in normal-based structures of organic solar cells. The chemical structure of P3HT-*b*-PFTBT is shown in **Figure I-39a**. The block copolymer-based devices showed an efficient photoconversion (3%) which was well beyond devices composed of P3HT:PFTBT blend (1.1%). This was attributed to the fact that the block copolymer proved to self-assemble into mesoscale lamellar morphologies characterized by a primarily face-on crystallite orientations. In other words, the block copolymer caused an enhancement in the performances attributed to providing better exciton pathway by controlling the donor-acceptor interfaces.¹⁵⁷

Another work demonstrated the synthesis of all-conjugated donor-acceptor block copolymer shown in **Figure I-39b**. This **P3HT-*b*-PNDIT2** was synthesized from the copolymerization of P3HT with A-A (N,N'-bis(2-decyl-1-tetradecyl)-2,6-dibromonaphthalene-1,4,5,8-tetracarboxylic acid bisimide, NDI) and B-B (5,5'-bis(trimethylstannyl)-2,2'-bithiophene) type monomers with different donor and acceptor block chain lengths. This fully conjugated D-A block copolymer was proved to have fine film structures with smooth film morphology. Interestingly, **P3HT-*b*-PNDIT2** was used as a sole active layer in normal device structures of organic solar cells showing an enhanced power conversion efficiency (0.55%) than those based on P3HT:PNDIT2 polymer blend (0.05%) with a maximum efficiency obtained by increasing the P3HT block content to 26 kg.mol⁻¹ while maintaining the acceptor block content at 40-50 kg.mol⁻¹.¹⁵⁸

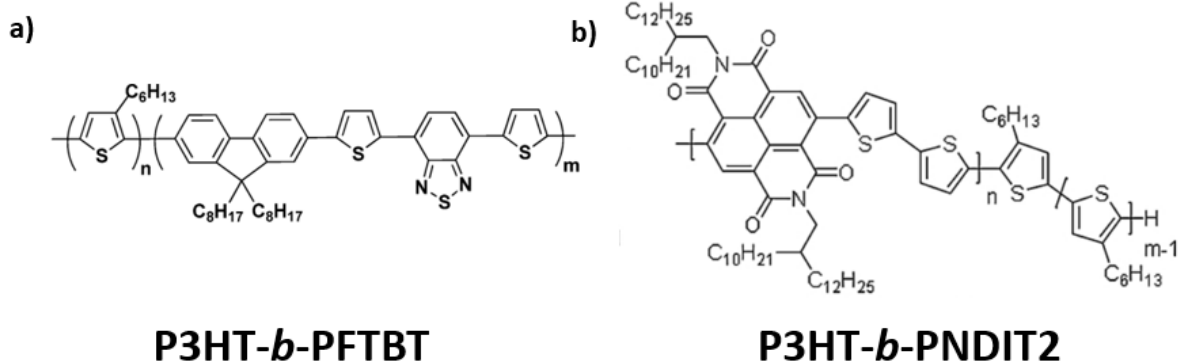


Figure I-39: Chemical structures of two different rod-rod diblock copolymers used as sole active materials in organic solar cells.

Studying the morphology of the D-A block and the D:A blend, a smoother film was obtained for the block copolymer with a lower root mean square roughness of 1.51 nm. A fine structure and phase separation having distinct domains was observed when compared to the blend film having an amorphous and featureless morphology with a high root mean square roughness of 8.18 nm as shown in **Figure I- 40**.¹⁵⁸

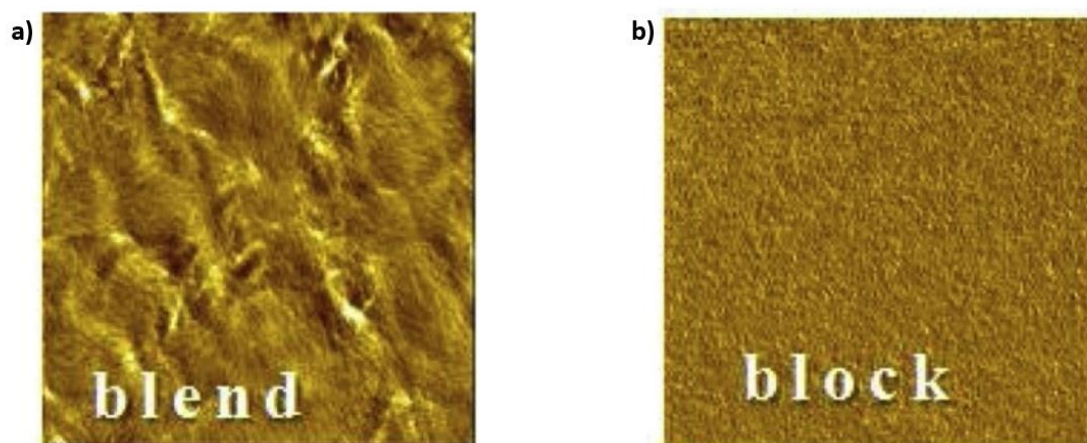


Figure I- 40 : AFM phase images of (a) P3HT:PNDIT2 polymer blend and (b) P3HT-b-PNDIT2 block copolymer.¹⁵⁸

iii. Complementary absorption

While synthesizing all-conjugated block copolymers, it is possible to copolymerize either one donor with an acceptor block or two donor units. However, in order to meet the requirements for OPV applications such as strong and broad optical absorption properties, a block copolymer should likely possess complementary light absorption between the corresponding blocks. This eventually maximizes light absorption in the solar spectrum.

As an example, a block copolymer comprised of P3HT and poly[4,8-bis(5-(2-ethylhexyl)thiophen-2-yl)benzo[1,2-b;4,5-b']dithiophene-2,6-diyl-*alt*-(4-(2-ethylhexyl)-3-fluorothieno[3,4-b]thiophene-)-2-carboxylate-2,6-diyl)] (PTB7-Th) was previously synthesized with different block ratios. The spectrophotometry of **P3HT-b-PTB7-Th** shown in **Figure I-41** revealed that the absorption of the diblock was extended to the near-IR region upon the incorporation of the low-bandgap PTB7-Th. The absorption spectra are characterized by two complementary broad absorption bands in the 320-570 and 500-800 nm ranges assigned to P3HT and PTB7-Th blocks, respectively. Moreover, the absorption profile is block composition dependent in which the % wt. of P3HT in P1 (93%) > P2 (42%) > P3 (26%). The block copolymer with 93 % wt. P3HT possesses a good hole mobility comparable to that of P3HT. Interestingly, P3HT-*b*-PTB7-Th:PC₇₀BM-based devices showed an enhanced PCE (3.6%) compared to P3HT:PC₇₀BM inverted-based devices (2.25%). This efficiency was obtained by even decreasing the processing temperature of the photoactive layer from 120 °C (for P3HT-based devices) to 60 °C which should have a significant impact on the manufacturing cost.¹⁵⁹

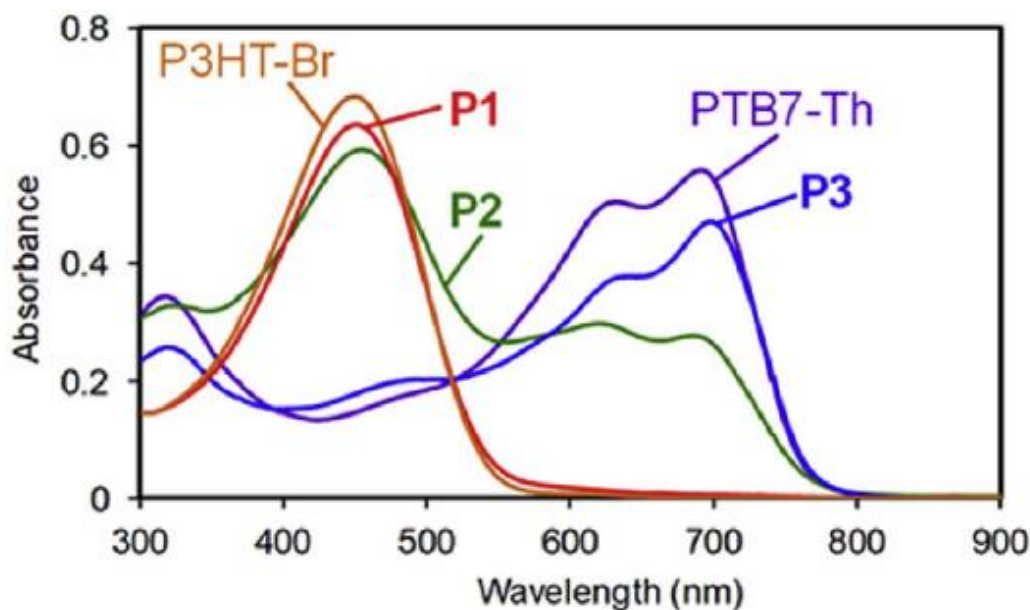


Figure I- 41: UV-vis absorption spectra of the different copolymers (P1,P2 and P3) with the corresponding homopolymers.¹⁵⁹

b. Synthesis of rod-rod block copolymers

Several block copolymers including rod and coil-based block copolymers having different morphologies and applications have already been synthesized. However, in order to achieve such a variety in morphology and applications, different synthetic strategies were explored. These strategies include grafting-to, end-functional polymer copolymerization, grafting-from, and sequential monomer addition (**Figure I-42**).

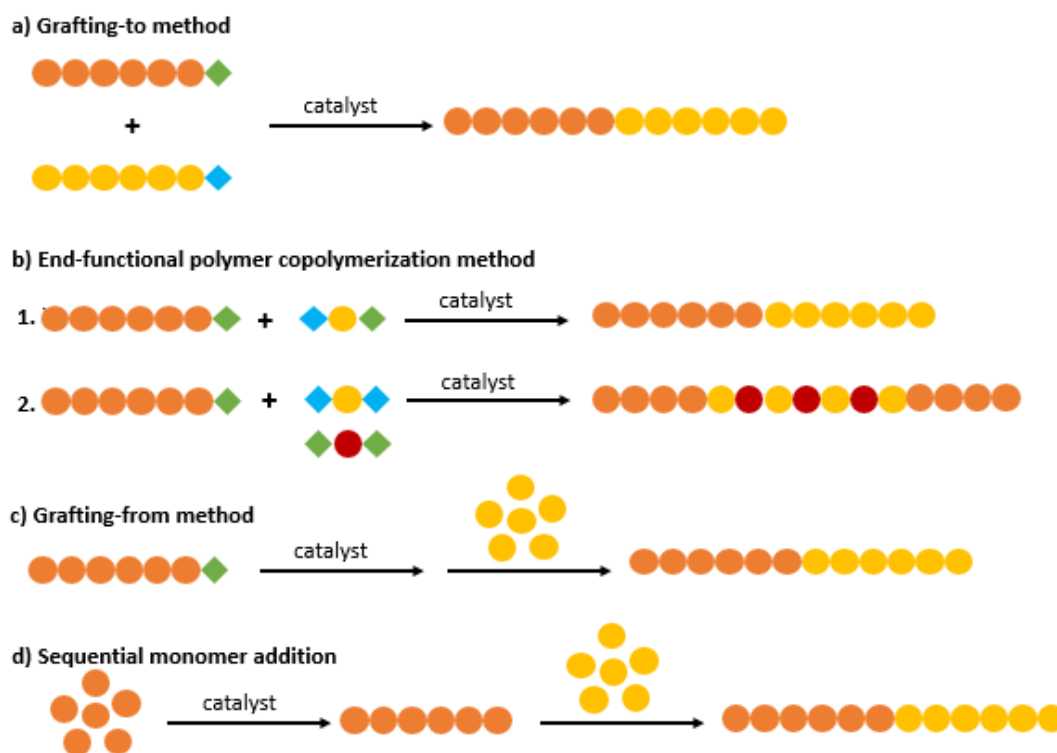


Figure I-42: Different methods to obtain block copolymers.¹⁶⁰

i. Grafting-to method

The grafting-to method, also known as the end-functional polymer coupling method, is based on the coupling of two macromolecules bearing functional groups at their end-chains, able to react with each other (**Figure I-42a**). For this, each block is synthesized through an optimal polymerization technique or catalytic system, then purified and characterized separately prior to coupling. The main difficulty with this route is reaching a high overall yield due to the multiple steps and the non-complete functionalization of the parent homopolymers. This issue can be overcome by using excess amount of one of the two polymers. However, this necessitates further purification steps, which is difficult in case of high molar mass polymers.¹⁶¹ Thus, in general, the efficiency of such synthetic route depends on the reaction between the two chain ends. An example of such strategy is the Cu-catalyzed click azide-alkyne cycloaddition.¹⁶² The azide or acetylene end-functionalized polymers can be obtained in two ways. In the first way, an initiator bearing a functional group that can be converted to an azide¹⁶² or acetylene¹⁶³ functionality is used. The second possibility is the utilization of functionalized Grignard reagents that can be used as end-capper to introduce the needed functionalities.¹⁶⁴ Moreover, Pd-catalyzed Suzuki coupling was also studied and summarized by the coupling between a polymer having a boronic ester and another one with a halogen end-group.¹⁶⁵ Block copolymers can be also formed from noncovalent interactions such as hydrogen bonds or ionic interactions. In this regard, a post-polymerization reaction can be performed to convert the functional groups on the polymers into matching H-donor and H-acceptor entities¹⁶⁶ or ionic functional groups as well.¹⁶⁷

As an example of such strategy, Mulherin *et al.*¹⁶⁸ studied the synthesis of all-conjugated D-A block copolymer, **P3HT-*b*-PFTBTT**, according to the synthetic procedure shown in **Figure I-43**. In this strategy, well defined P3HT with one terminal bromine end was synthesized by GRIM polymerization. On the other hand, the acceptor block, PFTBTT, was synthesized *via* Stille coupling reaction using monomers-type with α -stannyl and ω -bromo end-groups. After PFTBTT polymerization, P3HT-Br block was added to the reaction as a macromolecular end-capper. It was stated that the final product was a mixture of around 53% diblock copolymer, 42% PFTBTT homopolymer and 5% P3HT homopolymer.

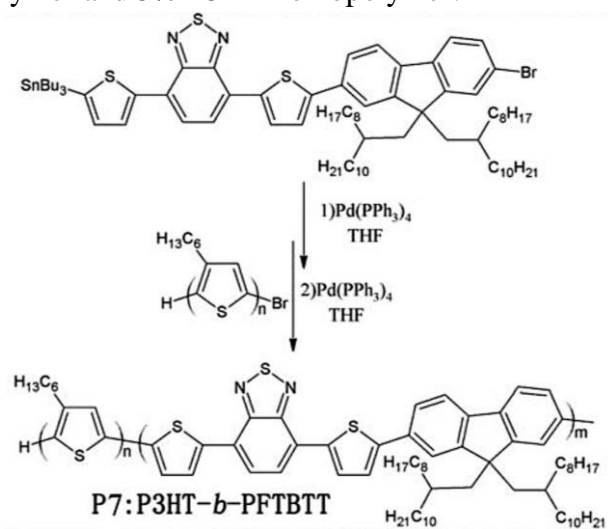


Figure I-43: Synthetic approach of P3HT-*b*-PFTBTT.¹⁶⁸

ii. End-functional polymer copolymerization method

End-functional polymer copolymerization is another method used for the synthesis of block copolymers. It necessitates the usage of an end-functionalized polymer, similar to the grafting-to method, however, the synthetic process is different and relatively simplistic. In this case, the end-functionalized block polymer is able to react as a monofunctional monomer in a step-growth polycondensation.¹⁶⁹ In this regard, the end-functionalized polymer and the monomers are added at the same time and copolymerized in a one-pot process.

The end-functionalized conjugated polymers that were used until now, typically P3HT-Br,¹⁶⁰ were synthesized *via* Kumada catalyst-transfer polycondensation (KCTP) using a functionalized initiator or end-capper. The needed functional group in the end-functionalized polymer depends on the type of copolymerization reaction used. It is well-known from Carothers studies that the block length of the second block is affected by the ratio of the amount of monomer and the end-capper. In general, this strategy is only a two-steps procedure allowing the combination of different mechanistic polymerizations which implies a large choice of monomers.

Two different protocols can be distinguished in the end-functional polymer copolymerization method, namely with A-B type monomers and with A-A type monomers. When A-B type monomers are used in the copolymerization, only diblock copolymers can be obtained (**Figure I-42b1**). To perform such copolymerization, Stille¹⁶⁸ and Suzuki–Miyaura¹⁷⁰ cross-coupling reactions were previously investigated. However, when A-A type monomers are used (if necessary, with B-B type monomers), diblock and even triblock copolymers can be obtained (**Figure I-42b2**). For this protocol, different types of reactions were used, such as Yamamoto,¹⁷¹ Suzuki–Miyaura,¹⁷² and Stille¹⁷³ cross-coupling reactions.

Following the end-functionalized strategy, various fully conjugated block copolymers were synthesized. For instance, poly(3-hexylthiophene)-*b*-poly{[N,N-9-bis(2-octyldodecyl)-naphthalene-1,4,5,7-bis(dicarboximide)-2,6-diyl]-*alt*-5,59-(2,29-bithiophene)}, **P3HT-*b*-P(ND I2OD-T2)** was synthesized using Stille coupling polymerization in the presence of Pd₂(dba)₃ and P(*o*-tolyl)₃. The mono-brominated P3HT functioning as a monofunctional monomer was reacted with 2,5-bis-(trimethylstannyl)bithiophene and dibrominated naphthalene-diimide (NDI) monomers that are covalently bonded together to form the conjugated BCP as shown in **Figure I-44**.¹⁷⁴

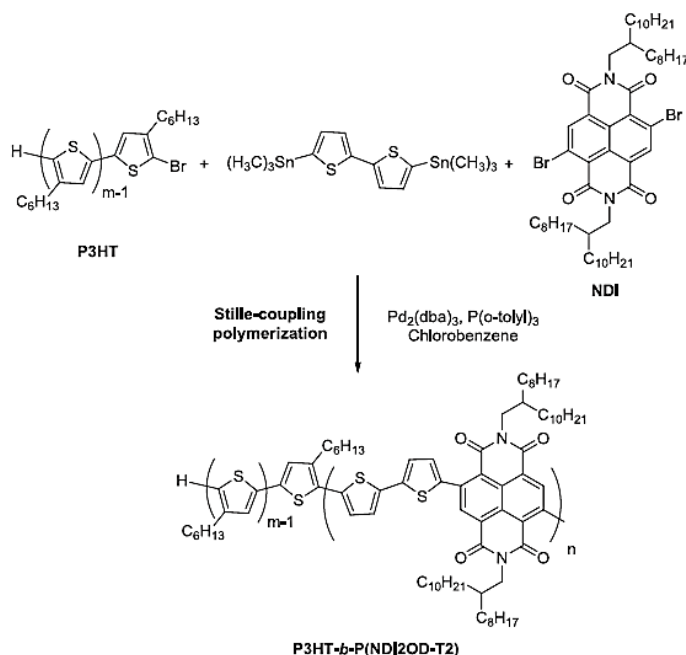


Figure I-44: Synthesis of P3HT-*b*-P(NDI2OD-T2) using end-functional polymer copolymerization strategy.¹⁷⁴

The previously mentioned diblock copolymer **P3HT-*b*-PTB7-Th** was also synthesized using Stille coupling polycondensation. In the same manner, the mono-brominated P3HT was reacted with distannyl BDT-T and dibromo TT-F monomers in the presence of $\text{Pd}(\text{PPh}_3)_4$ catalyst (**Figure I-45**). By adjusting the ratio of P3HT-Br to both monomers, P3HT-*b*-PTB7-Th with different block lengths were obtained in which the polymerization performed with larger BDT-T and TT-F amounts led to higher molecular weight block copolymers.¹⁵⁹

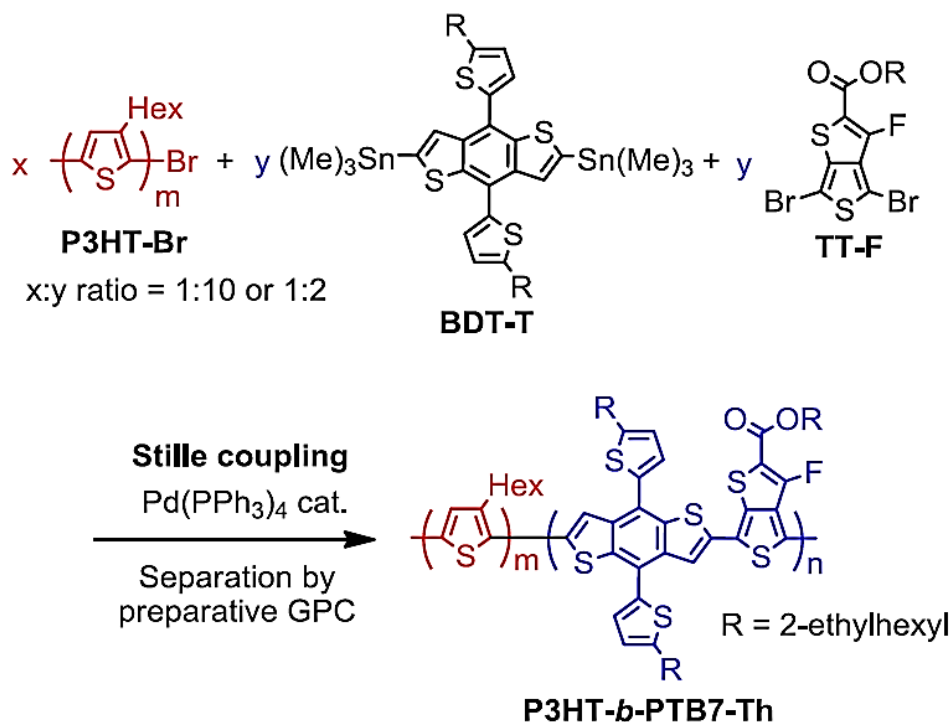


Figure I-45: Synthesis of P3HT-*b*-PTB7-Th using the end-functional polymer copolymerization strategy.¹⁵⁹

iii. Grafting-from method

In the grafting-from method, which is also known as the macroinitiator method, an end-functionalized polymer is used as a macroinitiator for the polymerization of the second monomer (**Figure I-42c**). In this strategy, two different polymerization techniques can be combined. Often, multiple post-polymerization reactions should be performed on the first block in order to install the initiator for the second block.

For example, as shown in **Figure I-46**, the n-type block, poly(N,N'-bis(2-decyltetradecyl)-1,4,5,8-naphthalene diimide-co-thiophene) (PNDITH-Br₂), was first prepared by Stille coupling reaction. In the second step, PNDITH-Br₂ was transformed into a macroinitiator with a Ni(COD) terminal, followed by an in situ ligand exchange to afford the Ni(dppp) terminal. Then, P3HT block was emanated from both ends of PNDITH-Br₂ via KCTP to form an all-conjugated triblock with both donor and acceptor segments. Such facile and reliable synthetic route showed a facility in tailoring the weight ratio of the two blocks by varying the feed molar ratio of thiophene monomers to PNDITH-Br₂.¹⁶⁹

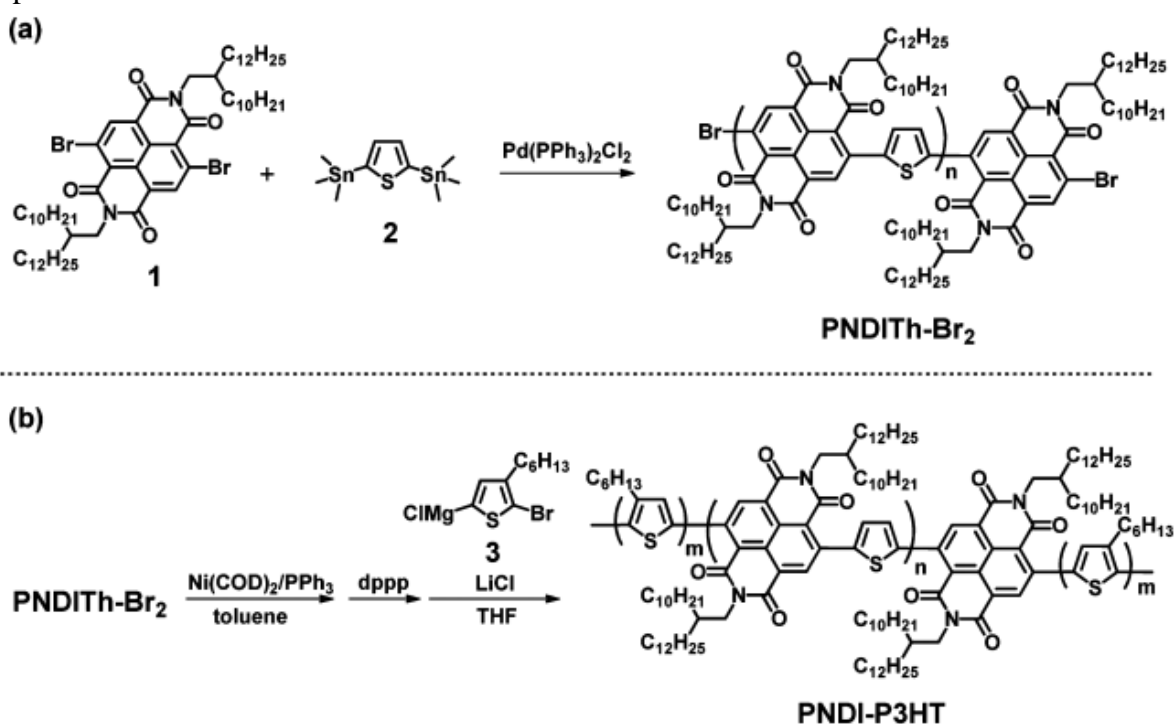


Figure I-46: Synthetic Routes for (a) PNDITH-Br₂ and (b) all-conjugated ABA-type triblock copolymer via KCTP.¹⁶⁹

iv. Sequential monomer addition

In this last strategy, the second monomer is directly added to the reaction mixture after the consumption of the first monomer (**Figure I-42d**).¹⁷⁵ Thus, it is a one-pot process in contrast to the other three techniques described above. This method is used for producing well-defined polymers with controlled molar mass and low dispersity.

The main polymerization mechanism for sequential monomer addition is KCTP. Using this strategy, block copolymers with different aromatic moieties or with the same aromatic moiety but different side chains can be synthesized. In case where both monomers are electronically different, the order of addition becomes important. For this, the strength of the complexation of the catalyst with the second monomer must always increase or remain the same as the first monomer to prevent that the catalyst sticks to the first block, thus preventing the growth of the second block.¹⁷⁶ However, when both blocks are electronically similar, there is possibility that the catalyst walks back to the first block during the polymerization of the second block. Consequently, BAB block copolymers are formed instead of AB block copolymers. On the contrary, the “random catalyst walking” is not an issue when the complexation of the catalyst with the second monomer is much stronger than with the first monomer, as in this case the catalyst remains favorably complexed to the growing second block.¹⁷⁷

Although the sequential monomer addition method shines by its simplicity, it implies full conversion of the first monomer before introducing the second one and limits the range of monomers polymerizable with the same coupling reaction.

Previous work on rod-rod diblock copolymers was investigated for synthesizing poly(3-hexylthiophene)-*b*-poly(quinoxaline-2,3-diyl) copolymer *via* sequential monomer addition in the presence of Ni(II) complex as a single catalyst (**Figure I-47**). It was proven that the block copolymerization proceeded in a living/controlled chain-extension manner.¹⁷⁸

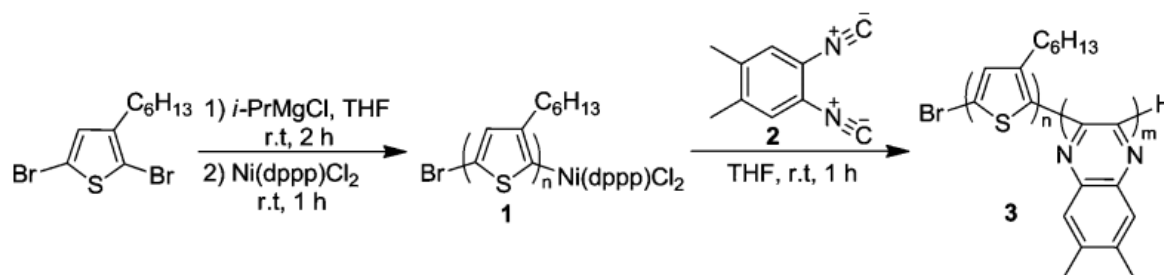


Figure I-47: Synthesis of P3HT-*b*-poly(quinoxaline-2,3-diyl) in one-pot process via sequential monomer addition.¹⁷⁸

Since most of the synthesized rod-rod block copolymers described in this chapter are involving P3HT as one of the conjugated blocks, the synthetic methods for P3HT are presented in the last part of this bibliography. Moreover, this chemistry was used during my PhD thesis.

VII. Poly(3-hexylthiophene) P3HT

a. Properties of P3HT

Among the regioregular poly(3-alkylthiophene)s P3ATs, P3HT is well-known for synthesizing all-conjugated block copolymers since it shows promising behavior in organic electronics such as photovoltaic applications.⁵⁴ This regioregular P3HT is widely studied for its promising properties including high hole mobility, high solubility in common solvents, high conductivity and good chemical stability. Moreover, P3HT can be ordered in three dimensions: conformational ordering along the backbone, π -stacking of flat polymer chains, and lamellar stacking between chains. These features are attractive for excellent electrical properties. Thus, P3HT is an important class of π -conjugated polymers.¹⁷⁹

After being coupled with different types of conjugated polymers, the resulting block copolymer revealed a nanometric-scale morphology with tunable optoelectronic properties. For this, the several synthetic strategies of P3HT are highlighted in details. But before, it is important to define the regioregularity behavior of P3ATs in general since the interesting properties of such polymers are dependent on the regiochemical couplings along the synthesized chain.

b. Regioregularity of P3ATs

3AT monomer is an asymmetric molecule, therefore, during polymerization, random couplings can be created. Accordingly, three possible couplings can take place. Those couplings are head-tail (HT or 2-5'), head-head (HH or 2-2') or tail-tail (TT or 5-5') as shown in **Figure I-48**.

In the HH manner, regio-irregular P3AT is formed from the twisting out of conjugation resulting from the steric repulsion between alkyl chains. As a result, the electrical conductivity of the polymer is reduced. However, when thiophene rings are coupled in consecutive HT manner, the polymerization leads to regio-regular P3AT characterized with a coplanar conformation resulting in lower energy. In this case, the polymerization results in a highly conjugated lower-bandgap polymer. Therefore, the regioregularity is then defined as the percentage of head-tail sequences of 3-alkylthiophene and can eventually affect the electronic properties of the polymer. In other words, it is proven that for a good crystal packing and electrical transport properties, the polymer should be regioregular where almost all the repetitive units are of the same conformation which is usually head-to-tail. On the other hand, the loss in regioregularity is caused by multiple head-to-head and tail-to-tail coupling in the polymer backbone. Thus, π -conjugation is reduced leading to destruction of high conductivity and other desired properties.¹⁷⁹

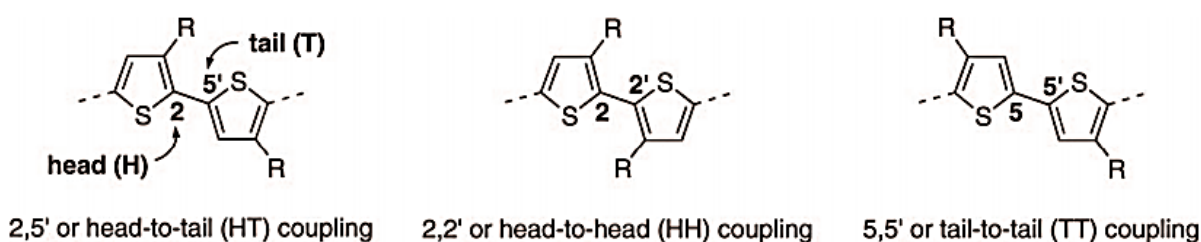


Figure I-48: Regioisomeric couplings of 3-alkylthiophenes.¹⁷⁹

c. Synthesis of poly(3-alkylthiophene) (P3AT)

Based on the properties of the regioregular P3ATs, variety of works were then investigated to synthesize them. Initially, McCullough *et al.*¹¹⁰ proposed McCullough method for the synthesis of regioregular P3AT in which 2-bromo-5-bromomagnesio-3-alkylthiophene monomer is cross-coupled thanks to 1,3-bis(diphenylphosphino)propane nickel (II) chloride ($\text{Ni}(\text{dppp})\text{Cl}_2$) as shown in **Figure I-49a**. This was the first reported synthesis for the regioregular P3ATs with 90% head-to-tail regioselectivity. In the meantime, Rieke method (**Figure I-49b**) was also studied in the presence of Rieke zinc (activated and highly reactive zinc) to generate the substituted thiophene monomer that couples with the nickel catalyst ($\text{Ni}(\text{dppp})\text{Cl}_2$).¹⁸⁰ In both methods, cryogenic temperatures and high reactive metals are needed, thus, limiting their usage in large-scale production.

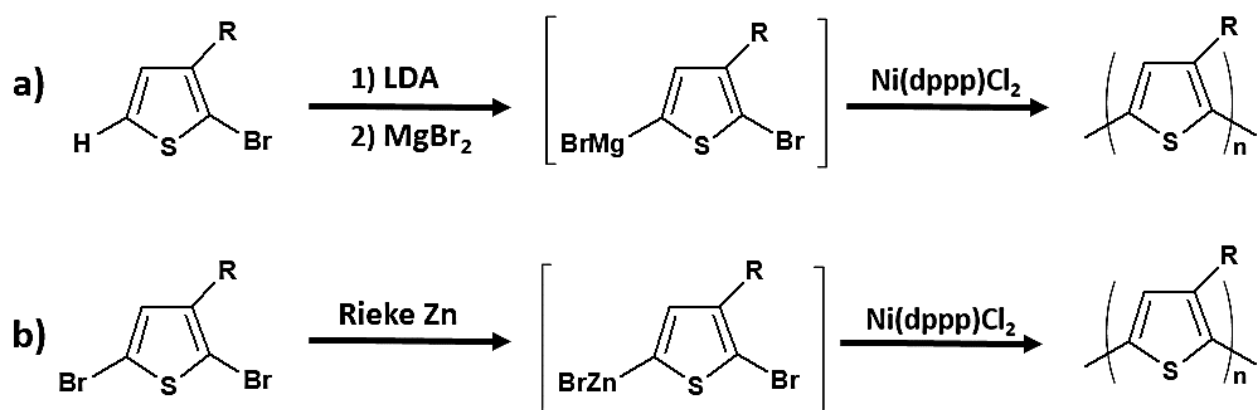


Figure I-49: Synthesis of P3ATs following (a) McCullough method and (b) Rieke method.^{110,180}

Thus, Grignard Metathesis polymerization (GRIM) which is also referred as Kumada catalyst-transfer polycondensation (KCTP) is the most studied and applicable for the synthesis of highly regioregular P3ATs. GRIM was discovered by McCullough and coworkers in 1999.¹⁸¹ This synthetic method is prevalently used due to its simplicity and possibility for large-scale manufacturing with wide range of applications.¹⁸² The advantage of GRIM over the other methods is the utilization of more amenable temperature¹⁸³ *i.e.* room temperature processing. The general synthesis of P3HT using GRIM polymerization is shown in **Figure I-50**.

It is based on the reaction between 2,5-dibromo-3-hexylthiophene with alkyl Grignard reagent.¹⁸⁴ This reaction generates two metallated regioisomers (A and B) in different proportions by a magnesium exchange reaction. The addition of Ni(dppp)Cl₂ to the medium produces P3HT with a high regioregularity. It was stated that after the addition of Ni(dppp)Cl₂, only isomer A is considered in the polymerization while isomer B is not consumed.

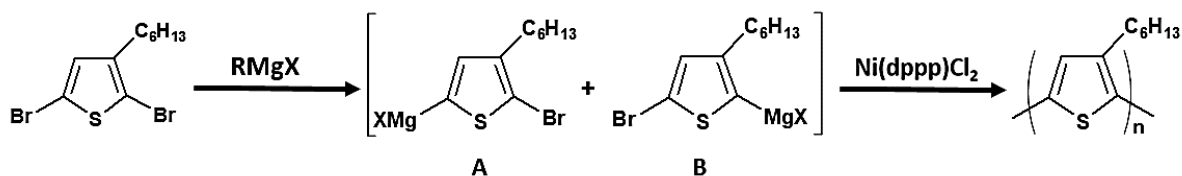


Figure I-50: Synthesis of P3HT by Grignard metathesis (GRIM) polymerization.¹⁸⁴

The molar mass of the synthesized P3HT can be monitored by controlling the ratio of the added monomer to the catalyst (quasi-living polymerization). Thus, polymerizations proceeded at room temperature with the same amount of Grignard reagent while varying the [monomer]/[Ni catalyst] ratio yield different molecular weight P3HT with low dispersity.¹⁸⁵

McCullough and Yokozawa independently demonstrated that the Grignard metathesis polymerization/Kumada catalyst-transfer polycondensation of P3HT proceeds by a living chain-growth mechanism instead of the traditionally accepted step-growth polycondensation.²⁰ The mechanism is illustrated in **Figure I-51**.¹⁸⁶

Ni(dppp)Cl₂ reacts first with two equivalents of the monomer M2a to form a dimer of M2a. This dimer is considered to be the chain initiator with zero-valent Ni(0) complex that is able to “walk” across the molecule and insert at the intramolecular C-Br bond by reductive elimination involving C-C bond formation. Following, another monomer M2a reacts with this Ni in which a coupling reaction and transfer of the Ni catalyst to the next C-Br bond takes place.¹⁸⁷ Accordingly, the chain growth continues with the Ni catalyst.

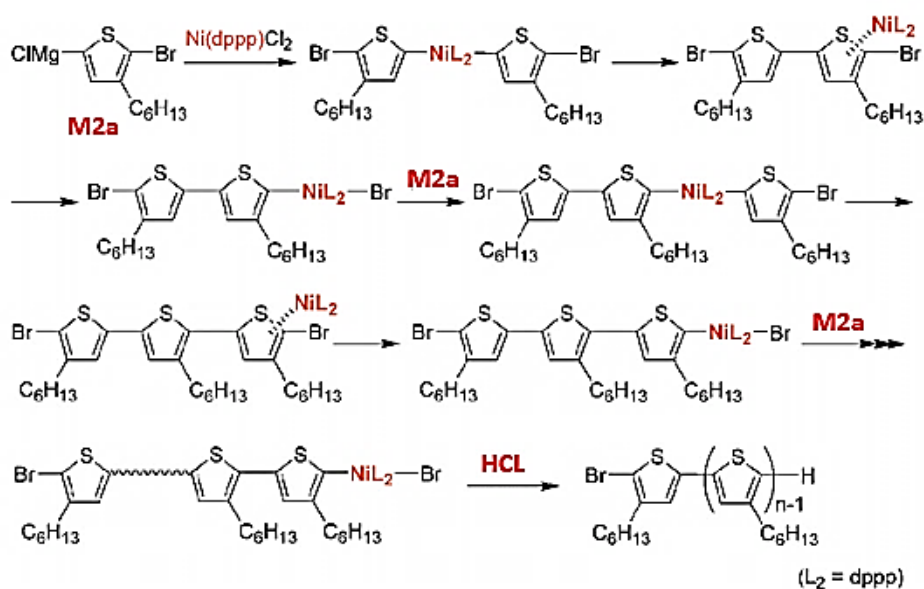


Figure I-51: Kumada catalyst-transfer polycondensation mechanism proposed by Yokozawa and coworkers.¹⁸⁶

VIII. Aim and strategy of this thesis

Based on this bibliographical overview, it is revealed that π -conjugated polymers are of great interest as they form a major multidisciplinary field of research and are used particularly in optoelectronic applications such as OPVs, OPDs, OFETs and others. The incorporation of conjugated polymers as active materials in such applications is coupled with several advantages including low cost, flexibility and solution processability suitable for large-area fabrication. More interestingly, conjugated polymers have tunable electronic and optical properties. Several studies were investigated for tuning such properties to meet the requirements of the targeted application. For instance, donor polymers in BHJ solar cells must fulfill some criteria as the intense and broad absorption into the near-infrared region. In other words, as the donor is the main solar light absorber in a device made with fullerene acceptors, a wide optical absorption range and large extinction coefficients are needed. Unfortunately, high-bandgap polymers as the regioregular P3HT ($E_g = 2.1$ eV) cannot effectively harvest photons and are capable of absorbing only around 46% of the solar spectrum. Thus, one of the effective strategies to narrow the bandgap of p-type materials is to develop donor-acceptor alternating copolymers. This method allows to target the required absorption properties of the desired materials.

In this work, an efficient and simple method for synthesizing all-conjugated diblock copolymers using Stille polycondensation of a ternary monomer blend are discussed in details in **Chapter II**. As discussed, due to morphological issues, designing donor-acceptor block copolymers has been one of the successful options to stabilize the active layers due to the ability of such polymers to form well-defined self-organized nanostructures. The incorporation of a donor and acceptor into single block copolymer favors the self-assembly into domains with various shapes which is affected by polymer's length and flexibility. Interestingly, besides being well-stabilized, the obtained morphology is suitable to create direct percolation pathways for charge transport and collection. Accordingly, numerous rod-rod block copolymers containing donor blocks (such as regioregular P3HT) have been synthesized and classified as third-generation polymers. These are characterized with their extended absorption, low cost and good carrier mobility. Thus, according to the various available methods for their preparation, block copolymers can probably, in some fashion or other, be a major class to study for the future development of viable OPVs.

Regioregular P3HT is a widely studied electron donor material in OPVs due to its easy preparation and capability of being end-functionalized for further diblock synthesis. Thus, in our study, a macro-monofunctional P3HT reagent serving as an electron donor has been synthesized *via* Grignard metathesis (GRIM) reaction and used in the initial feed of step-growth copolymerization of A-A (dithienosilole, DTS) and B-B (diketopyrrolopyrrole, DPP) or (diazapentalene, DAP) for the development of low-bandgap polymeric materials absorbing in the near-infrared region.

In its turn, DTS is a π -donor substructure that has been considered as an interesting building block in conjugated polymers for several reasons including its high stability at ambient atmosphere and good solubility due to its alkyl chain (ethyl-hexyl side chains) bounded onto a silicon atom. Moreover, it is attractive for being an end-functionalized reactive material in the synthesis of copolymers and block copolymers *via* different polycondensation reactions previously mentioned. Additionally, DPP acceptor unit has been also used for the synthesis of several conjugated polymers and showed promising absorption that is extended to the near-IR region. This absorption range could be further enhanced by using DAP, which is a DPP analogue. Thus, this subunit can be considered as an interesting building block for the development of variety of low-bandgap conjugated polymers with promising properties. After synthesis, different structural, optical, thermal and electrochemical characterization methods were employed to determine the properties of the synthesized block copolymers.

These conjugated polymers have been tested as active materials in inverted device structures of organic solar cells in which the photovoltaic performances are presented in **Chapter III**. In general, the study of the synthesized block copolymers enables to understand the relationship between molecular structure, morphology and photovoltaic performances in all-conjugated block copolymer systems.

Meanwhile, as P3HT is known for its hydrophobicity, its incorporation as a hole transport layer in normal-based organic solar cells can prevent water penetration into the devices. Thus, the methodology for synthesizing end-functionalized polymers was investigated. In this regard, triethoxysilane-terminated P3HT (P3HT-Si) has been prepared *via* modified Grignard metathesis (GRIM) reaction for the aim of anchoring on top of ITO substrates. However, the low ITO work function generated upon grafting necessitates the combination of P3HT-Si with a fluorinated organosilane surface modifier, namely 1H,1H,2H,2H-perfluorooctyltriethoxysilane (PTES), that increases the ITO work function. These modified grafted substrates have been prepared and used as PEDOT:PSS alternatives in normal-based solar cells as discussed in **Chapter IV**.

On the other hand, in **Chapter V**, novel hybrid block copolymers constituting of a conjugated low-bandgap block absorbing in the NIR region, P(DTS-DAP), and a polypeptide segment have been synthesized. For this aim, aniline-terminated P(DTS-DAP) having a primary amine end were prepared *via* Stille polycondensation to serve as a macroinitiator in the ring opening polymerization of N-carboxyanhydrides (NCA) of the peptide monomer. The self-assembled nanostructures of polypeptides and the extended absorbance in the NIR region of these hybrid block copolymers makes them efficient for photothermal applications.

References

- (1) Hirsch, R. L.; Bezdek, R.; Wendling, R. Peaking of World Oil Production: Impacts, Mitigation, & Risk Management; *National Energy Technology Laboratory (NETL), Pittsburgh, PA, Morgantown, WV, and Albany, OR*, **2005**.
- (2) Stoppato, A. Life Cycle Assessment of Photovoltaic Electricity Generation. *Energy Oxf.* **2008**, *33* (2), 224–232.
- (3) Badawy, W. A. A Review on Solar Cells from Si-Single Crystals to Porous Materials and Quantum Dots. *J. Adv. Res.* **2015**, *6* (2), 123–132.
- (4) Brown, G. F.; Wu, J. Third Generation Photovoltaics. *Laser Photonics Rev.* **2009**, *3* (4), 394–405.
- (5) Dennler, G.; Scharber, M. C.; Brabec, C. J. Polymer-Fullerene Bulk-Heterojunction Solar Cells. *Adv. Mater.* **2009**, *21* (13), 1323–1338.
- (6) Kaltenbrunner, M.; White, M. S.; Głowacki, E. D.; Sekitani, T.; Someya, T.; Sariciftci, N. S.; Bauer, S. Ultrathin and Lightweight Organic Solar Cells with High Flexibility. *Nat. Commun.* **2012**, *3*, 770.
- (7) He, Y.; Hong, W.; Li, Y. New Building Blocks for π -Conjugated Polymer Semiconductors for Organic Thin Film Transistors and Photovoltaics. *J. Mater. Chem. C* **2014**, *2* (41), 8651–8661.
- (8) Dou, L.; You, J.; Hong, Z.; Xu, Z.; Li, G.; Street, R. A.; Yang, Y. 25th Anniversary Article: A Decade of Organic/Polymeric Photovoltaic Research. *Adv. Mater.* **2013**, *25* (46), 6642–6671.
- (9) Malapaka, C.; Sharma, G.; Marri, A.; Daggupati, R. A Novel Carbazole-Phenothiazine Dyad Small Molecule as Non-Fullerene Electron Acceptor for Polymer Bulk Heterojunction Solar Cells. *RSC Adv* **2014**, *4*.
- (10) Jenkins, T. A Brief History of ... Semiconductors. *Phys. Educ.* **2005**, *40* (5), 430–439.
- (11) Chen, Z.; Debije, M. G.; Debaerdemaeker, T.; Osswald, P.; Würthner, F. Tetrachloro-Substituted Perylene Bisimide Dyes as Promising n-Type Organic Semiconductors: Studies on Structural, Electrochemical and Charge Transport Properties. *ChemPhysChem* **2004**, *5* (1),
- (12) Naarmann, H. Polymers, Electrically Conducting. In *Ullmann's Encyclopedia of Industrial Chemistry*; American Cancer Society, **2000**.
- (13) Marc Loudon, Organic Chemistry, *Subsequent edition.*; Benjamin-Cummings Pub Co: Redwood City, Calif, **1995**.
- (14) Salaneck, W. R.; Friend, R. H.; Brédas, J. L. Electronic Structure of Conjugated Polymers: Consequences of Electron–Lattice Coupling. *Phys. Rep.* **1999**, *319* (6), 231–251.
- (15) Heeger, A. J. Nobel Lecture: Semiconducting and Metallic Polymers: The Fourth Generation of Polymeric Materials. *Rev. Mod. Phys.* **2001**, *73* (3), 681–700.
- (16) Hoffmann, R.; Janiak, C.; Kollmar, C. A Chemical Approach to the Orbitals of Organic Polymers. *Macromolecules* **1991**, *24* (13), 3725–3746.
- (17) Pron, A.; Rannou, P. Processible Conjugated Polymers: From Organic Semiconductors to Organic Metals and Superconductors. *Prog. Polym. Sci.* **2002**, *27* (1), 135–190.
- (18) Wang, Y. J.; Yu, G. Conjugated Polymers: From Synthesis, Transport Properties, to Device Applications. *J. Polym. Sci. Part B Polym. Phys.* **2019**, *57* (23), 1557–1558.
- (19) Cheng, Y.-J.; Yang, S.-H.; Hsu, C.-S. Synthesis of Conjugated Polymers for Organic Solar Cell Applications. *Chem. Rev.* **2009**, *109* (11), 5868–5923.
- (20) Wudl, F.; Angus, R. O.; Lu, F. L.; Allemand, P. M.; Vachon, D.; Nowak, M.; Liu, Z. X.; Schaffer, H.; Heeger, A. J. Poly-p-Phenyleneamineimine: Synthesis and Comparison to Polyaniline. *J. Am. Chem. Soc.* **1987**, *109* (12), 3677–3684.
- (21) Letheby, H. XXIX.—On the Production of a Blue Substance by the Electrolysis of Sulphate of Aniline. *J. Chem. Soc.* **1862**, *15* (0), 161–163.
- (22) Saxman, A. M.; Liepins, R.; Aldissi, M. Polyacetylene: Its Synthesis, Doping and Structure. *Prog. Polym. Sci.* **1985**, *11* (1), 57–89.
- (23) Bolto, B. A.; McNeill, R.; Weiss, D. E. Electronic conduction in polymers 111. Electronic properties of polypyrrole. 14.
- (24) Shirakawa, H. The Discovery of Polyacetylene Film: The Dawning of an Era of Conducting Polymers (Nobel Lecture). *Angew. Chem. Int. Ed.* **2001**, *40* (14), 2574–2580.
- (25) Wen, Y.; Xu, J. Scientific Importance of Water-Processable PEDOT–PSS and Preparation, Challenge and New Application in Sensors of Its Film Electrode: A Review. *J. Polym. Sci. Part Polym. Chem.* **2017**, *55* (7), 1121–1150.
- (26) Heeger, A. J. Semiconducting and Metallic Polymers: The Fourth Generation of Polymeric Materials. *J. Phys. Chem. B* **2001**, *105* (36), 8475–8491.
- (27) Ates, M.; Karazehira, T.; Sarac, A. Conducting Polymers and Their Applications. *Curr. Phys. Chem.* **2012**, *2*, 224–240.

- (28) Li, R.; Mo, Y.; Shi, R.; Li, P.; Li, C.; Wang, Z.; Wang, X.; Li, S. Synthesis and Properties of Poly(p-Phenylene Vinylene) Derivatives with Hyperbranched Structure and Containing a Nitro Substituent. *Monatshefte Chem.* **2014**, *145* (1), 85–90.
- (29) Kaynak, A.; Foitzik, R. Synthesis and Characterization of Soluble Conducting Polymers. *Res. J. Text. Appar.* **2010**, *14* (2), 45–52.
- (30) Andersson, M. R.; Thomas, O.; Mammo, W.; Svensson, M.; Theander, M.; Inganäs, O. Substituted Polythiophenes Designed for Optoelectronic Devices and Conductors. *J. Mater. Chem.* **1999**, *9* (9), 1933–1940.
- (31) Park, S. H.; Roy, A.; Beaupré, S.; Cho, S.; Coates, N.; Moon, J. S.; Moses, D.; Leclerc, M.; Lee, K.; Heeger, A. J. Bulk Heterojunction Solar Cells with Internal Quantum Efficiency Approaching 100%. *Nat. Photonics* **2009**, *3* (5), 297–302.
- (32) Heeger, A. J. Semiconducting Polymers: The Third Generation. *Chem. Soc. Rev.* **2010**, *39* (7), 2354–2371.
- (33) Li, H.; Kim, F. S.; Ren, G.; Jenekhe, S. A. High-Mobility n-Type Conjugated Polymers Based on Electron-Deficient Tetraazabenzodifluoranthene Diimide for Organic Electronics. *J. Am. Chem. Soc.* **2013**, *135* (40), 14920–14923.
- (34) Bourass, M.; Touimi Benjelloun, A.; Hamidi, M.; Benzakour, M.; Mcharfi, M.; Sfaira, M.; Serein-Spirau, F.; Lère-Porte, J.-P.; Sotiropoulos, J.-M.; Bouzzine, S. M.; Bouachrine, M. DFT Theoretical Investigations of π -Conjugated Molecules Based on Thienopyrazine and Different Acceptor Moieties for Organic Photovoltaic Cells. *J. Saudi Chem. Soc.* **2016**, *20*, S415–S425.
- (35) Salzner, U.; Lagowski, J. B.; Pickup, P. G.; Poirier, R. A. Comparison of Geometries and Electronic Structures of Polyacetylene, Polyborole, Polycyclopentadiene, Polypyrrole, Polyfuran, Polysilole, Polyphosphole, Polythiophene, Polyselenophene and Polytellurophene. *Synth. Met.* **1998**, *96* (3), 177–189.
- (36) Tauc, J. Optical Properties and Electronic Structure of Amorphous Ge and Si. *Mater. Res. Bull.* **1968**, *3* (1), 37–46.
- (37) Davis, E. A.; Mott, N. F. Conduction in Non-Crystalline Systems V. Conductivity, Optical Absorption and Photoconductivity in Amorphous Semiconductors. *Philos. Mag. J. Theor. Exp. Appl. Phys.* **1970**, *22* (179), 0903–0922.
- (38) Lee, T. J.; Ko, Y.-G.; Yen, H.-J.; Kim, K.; Kim, D. M.; Kwon, W.; Hahm, S. G.; Liou, G.-S.; Ree, M. Programmable Digital Nonvolatile Memory Behaviors of Donor–Acceptor Polyimides Bearing Triphenylamine Derivatives: Effects of Substituents. *Polym. Chem.* **2012**, *3* (5), 1276–1283.
- (39) Bredas, J.-L. Mind the Gap! *Mater. Horiz.* **2013**, *1* (1), 17–19.
- (40) Rajagopal, A.; Wu, C. I.; Kahn, A. Energy Level Offset at Organic Semiconductor Heterojunctions. *J. Appl. Phys.* **1998**, *83* (5), 2649–2655.
- (41) Murakami, T.; Masuda, T.; Inoue, S.; Yano, H.; Iwamuro, N.; Shimoda, T. Photoelectron Yield Spectroscopy and Inverse Photoemission Spectroscopy Evaluations of P-Type Amorphous Silicon Carbide Films Prepared Using Liquid Materials. *AIP Adv.* **2016**, *6* (5), 055021.
- (42) Furukawa, Y. Electronic Absorption and Vibrational Spectroscopies of Conjugated Conducting Polymers. *J. Phys. Chem.* **1996**, *100* (39), 15644–15653.
- (43) McCulloch, I.; Heeney, M.; Bailey, C.; Genevicius, K.; Macdonald, I.; Shkunov, M.; Sparrowe, D.; Tierney, S.; Wagner, R.; Zhang, W.; Chabynyc, M. L.; Kline, R. J.; McGehee, M. D.; Toney, M. F. Liquid-Crystalline Semiconducting Polymers with High Charge-Carrier Mobility. *Nat. Mater.* **2006**, *5* (4), 328–333.
- (44) Sirringhaus, H.; Brown, P. J.; Friend, R. H.; Nielsen, M. M.; Bechgaard, K.; Langeveld-Voss, B. M. W.; Spiering, A. J. H.; Janssen, R. A. J.; Meijer, E. W.; Herwig, P.; de Leeuw, D. M. Two-Dimensional Charge Transport in Self-Organized, High-Mobility Conjugated Polymers. *Nature* **1999**, *401*, 685–688.
- (45) Coropceanu, V.; Cornil, J.; da Silva Filho, D. A.; Olivier, Y.; Silbey, R.; Brédas, J.-L. Charge Transport in Organic Semiconductors. *Chem. Rev.* **2007**, *107* (4), 926–952.
- (46) Zaumseil, J.; Sirringhaus, H. Electron and Ambipolar Transport in Organic Field-Effect Transistors. *Chem. Rev.* **2007**, *107* (4), 1296–1323.
- (47) Zhang, L.; Colella, N. S.; Liu, F.; Trahan, S.; Baral, J. K.; Winter, H. H.; Mannsfeld, S. C. B.; Briseno, A. L. Synthesis, Electronic Structure, Molecular Packing/Morphology Evolution, and Carrier Mobilities of Pure Oligo-/Poly(Alkylthiophenes). *J. Am. Chem. Soc.* **2013**, *135* (2), 844–854.
- (48) Karsten, B. P.; Janssen, R. A. J. Chain Length Dependence in Diketopyrrolopyrrole/Thiophene Oligomers. *Macromol. Chem. Phys.* **2011**, *212* (5), 515–520.
- (49) Roncali, J. Synthetic Principles for Bandgap Control in Linear π -Conjugated Systems. *Chem. Rev.* **1997**, *97* (1), 173–206.
- (50) Brédas, J. L. Relationship between Band Gap and Bond Length Alternation in Organic Conjugated Polymers. *J. Chem. Phys.* **1985**, *82* (8), 3808–3811.

- (51) Moliton, A.; Hiorns, R. C. Review of Electronic and Optical Properties of Semiconducting π -Conjugated Polymers: Applications in Optoelectronics. *Polym. Int.* **2004**, *53* (10), 1397–1412.
- (52) Grover, G.; Peters, G. M.; Tovar, J. D.; Kertesz, M. Quinonoid vs. Aromatic Structures of Heteroconjugated Polymers from Oligomer Calculations. *Phys. Chem. Chem. Phys.* **2020**, *22* (20), 11431–11439.
- (53) Kim, J.; Kwon, Y. S.; Shin, W. S.; Moon, S.-J.; Park, T. Carbazole-Based Copolymers: Effects of Conjugation Breaks and Steric Hindrance. *Macromolecules* **2011**, *44* (7), 1909–1919.
- (54) McCullough, R. D. The Chemistry of Conducting Polythiophenes. *Adv. Mater.* **1998**, *10* (2), 93–116.
- (55) Grimsdale, A. C.; Müllen, K. Oligomers and Polymers Based on Bridged Phenylenes as Electronic Materials. *Macromol. Rapid Commun.* **2007**, *28* (17), 1676–1702.
- (56) Shacklette, L. W.; Chance, R. R.; Ivory, D. M.; Miller, G. G.; Baughman, R. H. Electrical and Optical Properties of Highly Conducting Charge-Transfer Complexes of Poly(p-Phenylene). *Synth. Met.* **1980**, *1* (3), 307–320.
- (57) Roncali, J. Molecular Engineering of the Band Gap of π -Conjugated Systems: Facing Technological Applications. *Macromol. Rapid Commun.* **2007**, *28* (17), 1761–1775.
- (58) Grant, P. M.; Batra, I. P. Band Structure of Polyacetylene, (CH)_x. *Solid State Commun.* **1979**, *29* (3), 225–229.
- (59) Zhang, X.; Johnson, J. P.; Kampf, J. W.; Matzger, A. J. Ring Fusion Effects on the Solid-State Properties of α -Oligothiophenes. *Chem. Mater.* **2006**, *18* (15), 3470–3476.
- (60) Sandstedt, C. A.; Rieke, R. D.; Eckhardt, C. J. Solid-State and Solvatochromic Spectra of a Highly Regular Polythiophene. *Chem. Mater.* **1995**, *7* (6), 1057–1059.
- (61) Tremel, K.; Ludwigs, S. Morphology of P3HT in Thin Films in Relation to Optical and Electrical Properties. In *Advances in Polymer Science*; 2014; Vol. 265, pp 39–82.
- (62) Ghosh, R.; Luscombe, C. K.; Hamsch, M.; Mannsfeld, S. C. B.; Salleo, A.; Spano, F. C. Anisotropic Polaron Delocalization in Conjugated Homopolymers and Donor–Acceptor Copolymers. *Chem. Mater.* **2019**, *31* (17), 7033–7045.
- (63) Brocks, G.; Tol, A. Small Band Gap Semiconducting Polymers Made from Dye Molecules: Polysquaraines. *J. Phys. Chem.* **1996**, *100* (5), 1838–1846.
- (64) Li, G.; Chang, W.-H.; Yang, Y. Low-Bandgap Conjugated Polymers Enabling Solution-Processable Tandem Solar Cells. *Nat. Rev. Mater.* **2017**, *2* (8), 1–13.
- (65) Zhou, Z.-H.; Maruyama, T.; Kanbara, T.; Ikeda, T.; Ichimura, K.; Yamamoto, T.; Tokuda, K. Unique Optical and Electrochemical Properties of π -Conjugated Electrically Conducting Copolymers Consisting of Electron-Withdrawing Pyridine Units and Electron-Donating Thiophene Units. *J. Chem. Soc. Chem. Commun.* **1991**, No. 17, 1210–1212.
- (66) Havinga, E. E.; ten Hoeve, W.; Wynberg, H. Alternate Donor-Acceptor Small-Band-Gap Semiconducting Polymers; Polysquaraines and Polycroconaines. *Synth. Met.* **1993**, *55* (1), 299–306.
- (67) Kitamura, C.; Tanaka, S.; Yamashita, Y. Design of Narrow-Bandgap Polymers. Syntheses and Properties of Monomers and Polymers Containing Aromatic-Donor and o-Quinoid-Acceptor Units. *Chem. Mater.* **1996**, *8* (2), 570–578.
- (68) Zhang, Z.-G.; Wang, J. Structures and Properties of Conjugated Donor–Acceptor Copolymers for Solar Cell Applications. *J. Mater. Chem.* **2012**, *22* (10), 4178–4187.
- (69) Zhao, W.; Li, S.; Yao, H.; Zhang, S.; Zhang, Y.; Yang, B.; Hou, J. Molecular Optimization Enables over 13% Efficiency in Organic Solar Cells. *J. Am. Chem. Soc.* **2017**, *139* (21), 7148–7151.
- (70) Yuan, M.-C.; Chou, Y.-J.; Chen, C.-M.; Hsu, C.-L.; Wei, K.-H. A Crystalline Low-Bandgap Polymer Comprising Dithienosilole and Thieno[3,4-c]Pyrrole-4,6-Dione Units for Bulk Heterojunction Solar Cells. *Polymer* **2011**, *52* (13), 2792–2798.
- (71) Katsouras, A.; Gasparini, N.; Koulogiannis, C.; Spanos, M.; Ameri, T.; Brabec, C. J.; Chochos, C. L.; Avgeropoulos, A. Systematic Analysis of Polymer Molecular Weight Influence on the Organic Photovoltaic Performance. *Macromol. Rapid Commun.* **2015**, *36* (20), 1778–1797.
- (72) Liu, Y.; Zhao, J.; Li, Z.; Mu, C.; Ma, W.; Hu, H.; Jiang, K.; Lin, H.; Ade, H.; Yan, H. Aggregation and Morphology Control Enables Multiple Cases of High-Efficiency Polymer Solar Cells. *Nat. Commun.* **2014**, *5* (1), 5293.
- (73) Zhao, J.; Li, Y.; Yang, G.; Jiang, K.; Lin, H.; Ade, H.; Ma, W.; Yan, H. Efficient Organic Solar Cells Processed from Hydrocarbon Solvents. *Nat. Energy* **2016**, *1* (2), 1–7.
- (74) He, Z.; Zhong, C.; Su, S.; Xu, M.; Wu, H.; Cao, Y. Enhanced Power-Conversion Efficiency in Polymer Solar Cells Using an Inverted Device Structure. *Nat. Photonics* **2012**, *6* (9), 591–595.
- (75) Dkhil, S. B.; Pfannmöller, M.; Bals, S.; Koganezawa, T.; Yoshimoto, N.; Hannani, D.; Gaceur, M.; Videlot-Ackermann, C.; Margeat, O.; Ackermann, J. Square-Centimeter-Sized High-Efficiency Polymer Solar Cells: How the Processing Atmosphere and Film Quality Influence Performance at Large Scale. *Adv. Energy Mater.* **2016**, *6* (13), 1600290.

- (76) Chen, J.; Li, G.; Zhu, Q.; Guo, X.; Fan, Q.; Ma, W.; Zhang, M. Highly Efficient Near-Infrared and Semitransparent Polymer Solar Cells Based on an Ultra-Narrow Bandgap Nonfullerene Acceptor. *J. Mater. Chem. A* **2019**, *7* (8), 3745–3751.
- (77) Graham, K. R.; Cabanetos, C.; Jahnke, J. P.; Idso, M. N.; El Labban, A.; Ngongang Ndjawa, G. O.; Heumueller, T.; Vandewal, K.; Salleo, A.; Chmelka, B. F.; Amassian, A.; Beaujuge, P. M.; McGehee, M. D. Importance of the Donor:Fullerene Intermolecular Arrangement for High-Efficiency Organic Photovoltaics. *J. Am. Chem. Soc.* **2014**, *136* (27), 9608–9618.
- (78) Daehne, S., Resch-Genger, U., Wolfbeis, O. S., Eds.; Near-Infrared Dyes for High Technology Applications; *Nato Science Partnership Subseries: 3; Springer Netherlands*, **1998**.
- (79) Chen, H.-Y.; Hou, J.; Zhang, S.; Liang, Y.; Yang, G.; Yang, Y.; Yu, L.; Wu, Y.; Li, G. Polymer Solar Cells with Enhanced Open-Circuit Voltage and Efficiency. *Nat. Photonics* **2009**, *3* (11), 649–653.
- (80) Qian, G.; Qi, J.; Wang, Z. Y. Synthesis and Study of Low-Bandgap Polymers Containing the Diazapentalene and Diketopyrrolopyrrole Chromophores for Potential Use in Solar Cells and near-Infrared Photodetectors. *J. Mater. Chem.* **2012**, *22* (25), 12867–12873.
- (81) Dou, L.; Chen, C.-C.; Yoshimura, K.; Ohya, K.; Chang, W.-H.; Gao, J.; Liu, Y.; Richard, E.; Yang, Y. Synthesis of 5H-Dithieno[3,2-b:2',3'-d]Pyran as an Electron-Rich Building Block for Donor–Acceptor Type Low-Bandgap Polymers. *Macromolecules* **2013**, *46* (9), 3384–3390.
- (82) Tamilavan, V.; Song, M.; Jin, S.-H.; Park, H. J.; Yoon, U. C.; Hyun, M. H. Synthesis of New near Infrared Absorption Polymers Based on Thiadiazoloquinoxaline and Their Solar Cell Applications. *Synth. Met.* **2012**, *162* (13), 1184–1189.
- (83) Hendriks, K. H.; Heintges, G. H. L.; Gevaerts, V. S.; Wienk, M. M.; Janssen, R. A. J. High-Molecular-Weight Regular Alternating Diketopyrrolopyrrole-Based Terpolymers for Efficient Organic Solar Cells. *Angew. Chem. Int. Ed Engl.* **2013**, *52* (32), 8341–8344.
- (84) Dou, L.; You, J.; Yang, J.; Chen, C.-C.; He, Y.; Murase, S.; Moriarty, T.; Emery, K.; Li, G.; Yang, Y. Tandem Polymer Solar Cells Featuring a Spectrally Matched Low-Bandgap Polymer. *Nat. Photonics* **2012**, *6* (3), 180–185.
- (85) Dou, L.; Chang, W.-H.; Gao, J.; Chen, C.-C.; You, J.; Yang, Y. A Selenium-Substituted Low-Bandgap Polymer with Versatile Photovoltaic Applications. *Adv. Mater.* **2013**, *25* (6), 825–831.
- (86) Oklem, G.; Song, X.; Toppare, L.; Baran, D.; Gunbas, G. A New NIR Absorbing DPP-Based Polymer for Thick Organic Solar Cells. *J. Mater. Chem. C* **2018**, *6* (12), 2957–2961.
- (87) Brymora, K.; Khelifi, W.; Awada, H.; Blanc, S.; Hirsch, L.; Bousquet, A.; Lartigau-Dagron, C.; Castet, F. Comprehensive Theoretical and Experimental Study of near Infrared Absorbing Copolymers Based on Dithienosilole. *Polym. Chem.* **2020**.
- (88) Song, J.; Du, C.; Li, C.; Bo, Z. Silole-Containing Polymers for High-Efficiency Polymer Solar Cells. *J. Polym. Sci. Part Polym. Chem.* **2011**, *49* (19), 4267–4274.
- (89) Khelifi, W.; Awada, H.; Brymora, K.; Blanc, S.; Hirsch, L.; Castet, F.; Bousquet, A.; Lartigau-Dagron, C. Halochromic Switch from the 1st to 2nd Near-Infrared Window of Diazapentalene–Dithienosilole Copolymers. *Macromolecules* **2019**, *52* (13), 4820–4827.
- (90) Chen, M. S.; Niskala, J. R.; Unruh, D. A.; Chu, C. K.; Lee, O. P.; Fréchet, J. M. J. Control of Polymer-Packing Orientation in Thin Films through Synthetic Tailoring of Backbone Coplanarity. *Chem. Mater.* **2013**, *25* (20), 4088–4096.
- (91) Koizumi, Y.; Ide, M.; Saeki, A.; Vijayakumar, C.; Balan, B.; Kawamoto, M.; Seki, S. Thienoisindigo-Based Low-Band Gap Polymers for Organic Electronic Devices. *Polym. Chem.* **2013**, *4* (3), 484–494.
- (92) Hendriks, K. H.; Li, W.; Wienk, M. M.; Janssen, R. A. J. Small-Bandgap Semiconducting Polymers with High Near-Infrared Photoresponse. *J. Am. Chem. Soc.* **2014**, *136* (34), 12130–12136.
- (93) Keshtov, M. L.; Kuklin, S. A.; Radychev, N. A.; Nikolaev, A. Y.; Ostapov, I. E.; Krayushkin, M. M.; Konstantinov, I. O.; Koukaras, E. N.; Sharma, A.; Sharma, G. D. New Low Bandgap Near-IR Conjugated D–A Copolymers for BHJ Polymer Solar Cell Applications. *Phys. Chem. Chem. Phys.* **2016**, *18* (12), 8389–8400.
- (94) Pruisen, G. W. P. V.; Gholamrezaie, F.; Wienk, M. M.; Janssen, R. A. J. Synthesis and Properties of Small Band Gap Thienoisindigo Based Conjugated Polymers. *J. Mater. Chem.* **2012**, *22* (38), 20387–20393.
- (95) Zhou, E.; Hashimoto, K.; Tajima, K. Low Band Gap Polymers for Photovoltaic Device with Photocurrent Response Wavelengths over 1000nm. *Polymer* **2013**, *54* (24), 6501–6509.
- (96) Cui, W.; Wudl, F. Dithienylbenzodipyrrolidone: New Acceptor for Donor–Acceptor Low Band Gap Polymers. *Macromolecules* **2013**, *46* (18), 7232–7238.
- (97) An, C.; Li, M.; Marszalek, T.; Guo, X.; Pisula, W.; Baumgarten, M. Investigation of the Structure–Property Relationship of Thiadiazoloquinoxaline-Based Copolymer Semiconductors via Molecular Engineering. *J. Mater. Chem. C* **2015**, *3* (16), 3876–3881.

- (98) Fan, J.; Yuen, J. D.; Wang, M.; Seifert, J.; Seo, J.-H.; Mohebbi, A. R.; Zakhidov, D.; Heeger, A.; Wudl, F. High-Performance Ambipolar Transistors and Inverters from an Ultralow Bandgap Polymer. *Adv. Mater.* **2012**, *24* (16), 2186–2190.
- (99) Steckler, T. T.; Zhang, X.; Hwang, J.; Honeyager, R.; Ohira, S.; Zhang, X.-H.; Grant, A.; Ellinger, S.; Odom, S. A.; Sweat, D.; Tanner, D. B.; Rinzler, A. G.; Barlow, S.; Brédas, J.-L.; Kippelen, B.; Marder, S. R.; Reynolds, J. R. A Spray-Processable, Low Bandgap, and Ambipolar Donor-Acceptor Conjugated Polymer. *J. Am. Chem. Soc.* **2009**, *131* (8), 2824–2826.
- (100) Bossion, A.; Heifferon, K. V.; Meabe, L.; Zivic, N.; Taton, D.; Hedrick, J. L.; Long, T. E.; Sardon, H. Opportunities for Organocatalysis in Polymer Synthesis via Step-Growth Methods. *Prog. Polym. Sci.* **2019**, *90*, 164–210.
- (101) Carothers, W. H. Polymers and Polyfunctionality. *Trans. Faraday Soc.* **1936**, *32* (0), 39–49.
- (102) Knoester, H. Theoretical Derivation of the Molecular Weight Distribution of End-Capped Linear Condensation Polymers. *Macromol. Theory Simul.* **2009**, *18* (1), 61–69.
- (103) Ito, T.; Shirakawa, H.; Ikeda, S. Simultaneous Polymerization and Formation of Polyacetylene Film on the Surface of Concentrated Soluble Ziegler-Type Catalyst Solution. *J. Polym. Sci. Polym. Chem. Ed.* **1974**, *12* (1), 11–20.
- (104) Swager, T. M.; McDonald, B. R. Heat On, Heat Off: A Synthesis of Polyacetylene Revisited. **2019**.
- (105) Gilch, H. G.; Wheelwright, W. L. Polymerization of α -Halogenated p-Xylenes with Base. *J. Polym. Sci. [A1]* **1966**, *4* (6), 1337–1349.
- (106) Wessling, R. A. The Polymerization of Xylylene Bisdialkyl Sulfonium Salts. *J. Polym. Sci. Polym. Symp.* **1985**, *72* (1), 55–66.
- (107) Suzuka, T.; Kimura, K.; Nagamine, T. Reusable Polymer-Supported Terpyridine Palladium Complex for Suzuki-Miyaura, Mizoroki-Heck, Sonogashira, and Tsuji-Trost Reaction in Water. *Polymers* **2011**, *3* (1), 621–639.
- (108) Bao, Z.; Chen, Y.; Cai, R.; Yu, L. Conjugated Liquid-Crystalline Polymers - Soluble and Fusible Poly(Phenylenevinylene) by the Heck Coupling Reaction. *Macromolecules* **1993**, *26* (20), 5281–5286.
- (109) Fiesel, R.; Scherf, U. A Chiral Poly(Para-Phenyleneethynylene) (PPE) Derivative. *Macromol. Rapid Commun.* **1998**, *19* (8), 427–431.
- (110) McCullough, R. D.; Lowe, R. D. Enhanced Electrical Conductivity in Regioselectively Synthesized Poly(3-Alkylthiophenes). *J. Chem. Soc. Chem. Commun.* **1992**, No. 1, 70–72.
- (111) Chen, T.-A.; Wu, X.; Rieke, R. D. Regiocontrolled Synthesis of Poly(3-Alkylthiophenes) Mediated by Rieke Zinc: Their Characterization and Solid-State Properties. *J. Am. Chem. Soc.* **1995**, *117* (1), 233–244.
- (112) Huang, F.; Yip, H.-L.; Cao, Y. Polymer Photovoltaics: Materials, Physics and Device Engineering; *Royal Society of Chemistry*, **2016**.
- (113) Azarian, D.; Dua, S. S.; Eaborn, C.; Walton, D. R. M. Reactions of Organic Halides with R₃MMR₃ Compounds (M = Si, Ge, Sn) in the Presence of Tetrakis(Triarylphosphine)Palladium. *J. Organomet. Chem.* **1976**, *117* (3), C55–C57.
- (114) Kosugi, M.; Arai, H.; Yoshino, A.; Migita, T. Reaction of α -chloro ketones with allyltri-n-butyltin. control of reaction site by the variation of reaction conditions. *Chem. Lett.* **1978**, *7* (7), 795–796.
- (115) Milstein, D.; Stille, J. K. A General, Selective, and Facile Method for Ketone Synthesis from Acid Chlorides and Organotin Compounds Catalyzed by Palladium. *J. Am. Chem. Soc.* **1978**, *100* (11), 3636–3638.
- (116) Stille, J. K. The Palladium-Catalyzed Cross-Coupling Reactions of Organotin Reagents with Organic Electrophiles[New Synthetic Methods(58)]. *Angew. Chem. Int. Ed. Engl.* **1986**.
- (117) Carsten, B.; He, F.; Son, H. J.; Xu, T.; Yu, L. Stille Polycondensation for Synthesis of Functional Materials. *Chem. Rev.* **2011**, *111* (3), 1493–1528.
- (118) Zheng, T.; Schneider, A. M.; Yu, L. Stille Polycondensation: A Versatile Synthetic Approach to Functional Polymers. In *Synthetic Methods for Conjugated Polymers and Carbon Materials*; John Wiley & Sons, Ltd, **2017**; pp 1–58.
- (119) Lee, S.; Park, K.; Jung, S.; Park, H.; Yang, C. Stepwise Heating in Stille Polycondensation toward No Batch-to-Batch Variations in Polymer Solar Cell Performance. *Nat. Commun.* **2018**, *9*.
- (120) Stübinger, T.; Brütting, W. Exciton Diffusion and Optical Interference in Organic Donor-Acceptor Photovoltaic Cells. *J. Appl. Phys.* **2001**, *90* (7), 3632–3641.
- (121) Topham, P. D.; Parnell, A. J.; Hiorns, R. C. Block Copolymer Strategies for Solar Cell Technology. *J. Polym. Sci. Part B Polym. Phys.* **2011**, *49* (16), 1131–1156.
- (122) Lee, J. I.; Cho, S. H.; Park, S.-M.; Kim, J. K.; Kim, J. K.; Yu, J.-W.; Kim, Y. C.; Russell, T. P. Highly Aligned Ultrahigh Density Arrays of Conducting Polymer Nanorods Using Block Copolymer Templates. *Nano Lett.* **2008**, *8* (8), 2315–2320.

- (123) Rider, D. A.; Cavicchi, K. A.; Vanderark, L.; Russell, T. P.; Manners, I. Orientationally Controlled Nanoporous Cylindrical Domains in Polystyrene-*b*-Poly(Ferrocenylethylmethylsilane) Block Copolymer Films. *Macromolecules* **2007**, *40* (10), 3790–3796.
- (124) Liu, C.-L.; Lin, C.-H.; Kuo, C.-C.; Lin, S.-T.; Chen, W.-C. Conjugated Rod–Coil Block Copolymers: Synthesis, Morphology, Photophysical Properties, and Stimuli-Responsive Applications. *Prog. Polym. Sci.* **2011**, *36* (5), 603–637.
- (125) Dunn, A. S.; Melville, H. W. Synthesis of ‘Block’ Copolymers. *Nature* **1952**, *169* (4304), 699–700.
- (126) Kim, H.-C.; Park, S.-M.; Hinsberg, W. D. Block Copolymer Based Nanostructures: Materials, Processes, and Applications to Electronics. *Chem. Rev.* **2010**, *110* (1), 146–177.
- (127) Lazzari, M.; Torneiro, M. A Global View on Block Copolymers. *Polymers* **2020**, *12* (4).
- (128) Zhang, Y.; Tajima, K.; Hirota, K.; Hashimoto, K. Synthesis of All-Conjugated Diblock Copolymers by Quasi-Living Polymerization and Observation of Their Microphase Separation. *J. Am. Chem. Soc.* **2008**, *130* (25), 7812–7813. =
- (129) Bates, F. S.; Fredrickson, G. H. Block Copolymers—Designer Soft Materials. *Physics Today* **1999**, *52* (2), 32–38.
- (130) Fredrickson, G. H.; Liu, A. J.; Bates, F. S. Entropic Corrections to the Flory-Huggins Theory of Polymer Blends: Architectural and Conformational Effects. *Macromolecules* **1994**, *27* (9), 2503–2511.
- (131) Flory, P. J. Thermodynamics of High Polymer Solutions. *J. Chem. Phys.* **1942**, *10* (1), 51–61.
- (132) Bower, D. I. An Introduction to Polymer Physics. *Am. J. Phys.* **2003**, *71* (3), 285–286.
- (133) Leibler, L. Theory of Microphase Separation in Block Copolymers. *Macromolecules* **1980**, *13* (6), 1602–1617.
- (134) Matsen, M. W.; Bates, F. S. Conformationally Asymmetric Block Copolymers. *J. Polym. Sci. Part B Polym. Phys.* **1997**, *35* (6), 945–952.
- (135) Yassar, A.; Miozzo, L.; Girona, R.; Horowitz, G. Rod-Coil and All-Conjugated Block Copolymers for Photovoltaic Applications. *Prog. Polym. Sci.* **2013**, *38* (5), 791.
- (136) Han, C. D.; Kim, J.; Kim, J. K. Determination of the Order-Disorder Transition Temperature of Block Copolymers. *Macromolecules* **1989**, *22* (1), 383–394.
- (137) Han, C. D.; Baek, D. M.; Kim, J. K. Effect of Microdomain Structure on the Order-Disorder Transition Temperature of Polystyrene-Block-Polyisoprene-Block-Polystyrene Copolymers. *Macromolecules* **1990**, *23* (2), 561–570.
- (138) Kim, D.-C.; Lee, H.-K.; Sohn, B.-H.; Zin, W.-C. Order–Disorder Transition Temperature Depression of a Diblock Copolymer Induced by the Addition of a Random Copolymer. *Macromolecules* **2001**, *34* (22), 7767–7772.
- (139) Khandpur, A. K.; Foerster, S.; Bates, F. S.; Hamley, I. W.; Ryan, A. J.; Bras, W.; Almdal, K.; Mortensen, K. Polyisoprene-Polystyrene Diblock Copolymer Phase Diagram near the Order-Disorder Transition. *Macromolecules* **1995**, *28* (26), 8796–8806.
- (140) Orilall, M. C.; Wiesner, U. Block Copolymer Based Composition and Morphology Control in Nanostructured Hybrid Materials for Energy Conversion and Storage: Solar Cells, Batteries, and Fuel Cells. *Chem. Soc. Rev.* **2011**, *40* (2), 520–535.
- (141) Kim, J. K.; Yang, S. Y.; Lee, Y.; Kim, Y. Functional Nanomaterials Based on Block Copolymer Self-Assembly. *Prog. Polym. Sci.* **2010**, *35* (11), 1325–1349.
- (142) Matsen, M. W.; Bates, F. S. Unifying Weak- and Strong-Segregation Block Copolymer Theories. *Macromolecules* **1996**, *29* (4), 1091–1098.
- (143) Sun, Y.-S.; Chung, T.-M.; Li, Y.-J.; Ho, R.-M.; Ko, B.-T.; Jeng, U.-S.; Lotz, B. Crystalline Polymers in Nanoscale 1D Spatial Confinement. *Macromolecules* **2006**, *39* (17), 5782–5788.
- (144) Wu, P.-T.; Ren, G.; Li, C.; Mezzenga, R.; Jenekhe, S. A. Crystalline Diblock Conjugated Copolymers: Synthesis, Self-Assembly, and Microphase Separation of Poly(3-Butylthiophene)-*b*-Poly(3-Octylthiophene). *Macromolecules* **2009**, *42* (7), 2317–2320.
- (145) Loo, Y.-L.; Register, R. A.; Ryan, A. J. Modes of Crystallization in Block Copolymer Microdomains: Breakout, Templated, and Confined. *Macromolecules* **2002**, *35* (6), 2365–2374.
- (146) Mitchell, V. D.; Jones, D. J. Advances toward the Effective Use of Block Copolymers as Organic Photovoltaic Active Layers. *Polym. Chem.* **2018**, *9* (7), 795–814..
- (147) Yu, X.; Yang, H.; Wu, S.; Geng, Y.; Han, Y. Microphase Separation and Crystallization of All-Conjugated Phenylene–Thiophene Diblock Copolymers. *Macromolecules* **2012**, *45* (1), 266–274.
- (148) Ho, C.-C.; Liu, Y.-C.; Lin, S.-H.; Su, W.-F. Synthesis, Morphology, and Optical and Electrochemical Properties of Poly(3-Hexylthiophene)-*b*-Poly(3-Thiophene Hexylacetate). *Macromolecules* **2012**, *45* (2), 813–820.
- (149) Ge, J.; He, M.; Qiu, F.; Yang, Y. Synthesis, Cocrystallization, and Microphase Separation of All-Conjugated Diblock Copoly(3-Alkylthiophene)s. *Macromolecules* **2010**, *43* (15), 6422–6428.

- (150) Shen, C.; Lee, Y.-H.; Lee, Y.-P.; Chiang, C.-J.; Wei, F.-K.; Wu, C.-H.; Kau, K.-C.; Liu, H.-W.; Hsieh, C.-C.; Wang, L.; Dai, C.-A. Self-Organization and Phase Transformation of All π -Conjugated Diblock Copolymers and Its Applications in Organic Solar Cells. *React. Funct. Polym.* **2016**, *108*, 94–102.
- (151) Verploegen, E.; Mondal, R.; Bettinger, C. J.; Sok, S.; Toney, M. F.; Bao, Z. Effects of Thermal Annealing Upon the Morphology of Polymer–Fullerene Blends. *Adv. Funct. Mater.* **2010**, *20* (20), 3519–3529.
- (152) Schaffer, C. J.; Palumbiny, C. M.; Niedermeier, M. A.; Jendrzewski, C.; Santoro, G.; Roth, S. V.; Müller-Buschbaum, P. A Direct Evidence of Morphological Degradation on a Nanometer Scale in Polymer Solar Cells. *Adv. Mater.* **2013**, *25* (46), 6760–6764.
- (153) Sommer, M.; Lang, A. S.; Thelakkat, M. Crystalline–Crystalline Donor–Acceptor Block Copolymers. *Angew. Chem. Int. Ed.* **2008**, *47* (41), 7901–7904.
- (154) Hufnagel, M.; Fischer, M.; Thurn-Albrecht, T.; Thelakkat, M. Influence of Fullerene Grafting Density on Structure, Dynamics, and Charge Transport in P3HT-b-PPC61BM Block Copolymers. *Macromolecules* **2016**, *49* (5), 1637–1647.
- (155) Mitchell, V. D.; Gann, E.; Huettner, S.; Singh, C. R.; Subbiah, J.; Thomsen, L.; McNeill, C. R.; Thelakkat, M.; Jones, D. J. Morphological and Device Evaluation of an Amphiphilic Block Copolymer for Organic Photovoltaic Applications. *Macromolecules* **2017**, *50* (13), 4942–4951.
- (156) Liang, Y.; Wang, H.; Yuan, S.; Lee, Y.; Gan, L.; Yu, L. Conjugated Block Copolymers and Co-Oligomers: From Supramolecular Assembly to Molecular Electronics. *J. Mater. Chem.* **2007**, *17* (21), 2183–2194.
- (157) Guo, C.; Lin, Y.-H.; Witman, M. D.; Smith, K. A.; Wang, C.; Hexemer, A.; Strzalka, J.; Gomez, E. D.; Verduzco, R. Conjugated Block Copolymer Photovoltaics with near 3% Efficiency through Microphase Separation. *Nano Lett.* **2013**, *13* (6), 2957–2963.
- (158) Wang, S.; Jin, X.; Yao, B.; Du, X.; Dong, L.; Wang, X.; Huang, W. Influence of the Molecular Weight in P3HT Block on Fully Conjugated Block Copolymers. *Synth. Met.* **2019**, *253*, 20–25.
- (159) Tyagi, P.; Hua, S.-C.; Amorim, D. R.; Faria, R. M.; Kettle, J.; Horie, M. All-Conjugated Block Copolymers for Efficient and Stable Organic Solar Cells with Low Temperature Processing. *Org. Electron.* **2018**, *55*, 146–156.
- (160) Wang, J.; Higashihara, T. Synthesis of All-Conjugated Donor–Acceptor Block Copolymers and Their Application in All-Polymer Solar Cells. *Polym. Chem.* **2013**, *4* (22), 5518–5526.
- (161) Woody, K. B.; Leever, B. J.; Durstock, M. F.; Collard, D. M. Synthesis and Characterization of Fully Conjugated Donor–Acceptor–Donor Triblock Copolymers. *Macromolecules* **2011**, *44* (12), 4690–4698.
- (162) Van den Bergh, K.; Willot, P.; Cornelis, D.; Verbiest, T.; Koeckelberghs, G. Influence of the Presence and Length of an Alkyl Spacer on the Supramolecular Chirality of Block Copoly(Thiophene)s. *Macromolecules* **2011**, *44* (4), 728–735.
- (163) Bergh, K. V. den; Winter, J. D.; Gerbaux, P.; Verbiest, T.; Koeckelberghs, G. Ni-Catalyzed Polymerization of Poly(3-Alkoxythiophene)s. *Macromol. Chem. Phys.* **2011**, *212* (4), 328–335.
- (164) Jeffries-El, M.; Sauvé, G.; McCullough, R. D. Facile Synthesis of End-Functionalized Regioregular Poly(3-Alkylthiophene)s via Modified Grignard Metathesis Reaction. *Macromolecules* **2005**, *38* (25), 10346–10352.
- (165) Gu, Z.; Kanto, T.; Tsuchiya, K.; Ogino, K. Synthesis of Poly(3-Hexylthiophene)-b-Poly(Ethylene Oxide) for Application to Photovoltaic Device. *J. Photopolym. Sci. Technol. - J PHOTOPOLYM SCI TECHNOL* **2010**, *23*, 405–406.
- (166) Lin, Y.-H.; Darling, S. B.; Nikiforov, M. P.; Strzalka, J.; Verduzco, R. Supramolecular Conjugated Block Copolymers. *Macromolecules* **2012**, *45* (16), 6571–6579.
- (167) Takahashi, A.; Rho, Y.; Higashihara, T.; Ahn, B.; Ree, M.; Ueda, M. Preparation of Nanoporous Poly(3-Hexylthiophene) Films Based on a Template System of Block Copolymers via Ionic Interaction. *Macromolecules* **2010**, *43* (11), 4843–4852.
- (168) Mulherin, R. C.; Jung, S.; Huettner, S.; Johnson, K.; Kohn, P.; Sommer, M.; Allard, S.; Scherf, U.; Greenham, N. C. Ternary Photovoltaic Blends Incorporating an All-Conjugated Donor-Acceptor Diblock Copolymer. *Nano Lett.* **2011**, *11* (11), 4846–4851.
- (169) Wang, J.; Ueda, M.; Higashihara, T. Synthesis of All-Conjugated Donor–Acceptor–Donor ABA-Type Triblock Copolymers via Kumada Catalyst-Transfer Polycondensation. *ACS Macro Lett.* **2013**, *2* (6), 506–510.
- (170) Tu, G.; Li, H.; Forster, M.; Heiderhoff, R.; Balk, L. J.; Sigel, R.; Scherf, U. Amphiphilic Conjugated Block Copolymers: Synthesis and Solvent-Selective Photoluminescence Quenching. *Small Weinh. Bergstr. Ger.* **2007**, *3* (6), 1001–1006.
- (171) Tu, G.; Li, H.; Forster, M.; Heiderhoff, R.; Balk, L. J.; Scherf, U. Conjugated Triblock Copolymers Containing Both Electron-Donor and Electron-Acceptor Blocks. *Macromolecules* **2006**, *39* (13), 4327–4331.

- (172) Verduzco, R.; DiMasi, E.; Botiz, I.; Pickel, D. L.; Kilbey, I. I.; Hong, K.; Darling, S. B. Polythiophene-Block-Polyfluorene and Polythiophene-Blockpoly(Fluorene-Co-Benzothiadiazole): Insights into the Self-Assembly of All-Conjugated Block Copolymers. *Macromolecules* **2010**, *44* (3).
- (173) Ku, S.-Y.; Brady, M. A.; Treat, N. D.; Cochran, J. E.; Robb, M. J.; Kramer, E. J.; Chabinyk, M. L.; Hawker, C. J. A Modular Strategy for Fully Conjugated Donor–Acceptor Block Copolymers. *J. Am. Chem. Soc.* **2012**, *134* (38), 16040–16046.
- (174) Kim, J.-S.; Ku, S.-Y.; Economou, N. J.; Jang, W.; Wang, D. H. Selective Doping of Conjugated Block Copolymer for Organic Thermoelectric Applications. *Nanoscale Microscale Thermophys. Eng.* **2019**, *23* (3), 222–234.
- (175) Chan, S.-H.; Lai, C.-S.; Chen, H.-L.; Ting, C.; Chen, C.-P. Highly Efficient P3HT: C60 Solar Cell Free of Annealing Process. *Macromolecules* **2011**, *44* (22), 8886–8891.
- (176) Miyakoshi, R.; Yokoyama, A.; Yokozawa, T. Importance of the Order of Successive Catalyst-Transfer Condensation Polymerization in the Synthesis of Block Copolymers of Polythiophene and Poly(p-Phenylene). *Chem. Lett. - CHEM LETT* **2008**, *37*, 1022–1023.
- (177) Leclerc, M.; Morin, J.-F. Synthetic Methods for Conjugated Polymer and Carbon Materials; *John Wiley & Sons*, **2017**.
- (178) Wu, Z.-Q.; Liu, D.-F.; Wang, Y.; Liu, N.; Yin, J.; Zhu, Y.-Y.; Qiu, L.-Z.; Ding, Y.-S. One Pot Synthesis of a Poly(3-Hexylthiophene)-b-Poly(Quinoxaline-2,3-Diyl) Rod–Rod Diblock Copolymer and Its Tunable Light Emission Properties. *Polym. Chem.* **2013**, *4* (17), 4588–4595.
- (179) Osaka, I.; McCullough, R. D. Advances in Molecular Design and Synthesis of Regioregular Polythiophenes. *Acc. Chem. Res.* **2008**, *41* (9), 1202–1214.
- (180) Chen, T. A.; Rieke, R. D. The First Regioregular Head-to-Tail Poly(3-Hexylthiophene-2,5-Diyl) and a Reginandom Isopolymer: Nickel versus Palladium Catalysis of 2(5)-Bromo-5(2)-(Bromozincio)-3-Hexylthiophene Polymerization. *J. Am. Chem. Soc.* **1992**, *114* (25), 10087–10088.
- (181) Iovu, M. C.; Sheina, E. E.; Gil, R. R.; McCullough, R. D. Experimental Evidence for the Quasi-“Living” Nature of the Grignard Metathesis Method for the Synthesis of Regioregular Poly(3-Alkylthiophenes). *Macromolecules* **2005**, *38* (21), 8649–8656.
- (182) Kiriy, A.; Senkovskyy, V.; Sommer, M. Kumada Catalyst-Transfer Polycondensation: Mechanism, Opportunities, and Challenges. *Macromol. Rapid Commun.* **2011**, *32* (19), 1503–1517.
- (183) Geoghegan, M.; Hadziioannou, G. Polymer Electronics; *Oxford Master Series in Physics*; *Oxford University Press: Oxford, New York*, **2013**.
- (184) Loewe, R. S.; Khersonsky, S. M.; McCullough, R. D. A Simple Method to Prepare Head-to-Tail Coupled, Regioregular Poly(3-Alkylthiophenes) Using Grignard Metathesis. *Adv. Mater.* **1999**, *11* (3), 250–253.
- (185) Yokoyama, A.; Miyakoshi, R.; Yokozawa, T. Chain-Growth Polymerization for Poly(3-Hexylthiophene) with a Defined Molecular Weight and a Low Polydispersity. *Macromolecules* **2004**, *37* (4), 1169–1171.
- (186) Yokozawa, T.; Yokoyama, A. Chain-Growth Condensation Polymerization for the Synthesis of Well-Defined Condensation Polymers and π -Conjugated Polymers. *Chem. Rev.* **2009**, *109* (11), 5595–5619.
- (187) Miyakoshi, R.; Yokoyama, A.; Yokozawa, T. Catalyst-Transfer Polycondensation. Mechanism of Ni-Catalyzed Chain-Growth Polymerization Leading to Well-Defined Poly(3-Hexylthiophene). *J. Am. Chem. Soc.* **2005**, *127* (49), 17542–17547.

Chapter II:
Synthesis and Characterization
of All-Conjugated Diblock
Copolymers based on DPP and
DAP Acceptor Monomers

I. Introduction

All-conjugated block copolymers have been of great interest for organic photovoltaic (OPV) applications because of their promising unique and attractive combination of nanomorphology and electronic activity.

In the past decades, researches were oriented toward the development of new conjugated block copolymers (CBCPs), especially donor-acceptor (D-A) type polymers due to the possibility of using a single material in the active layer and to have a morphology corresponding to the ideal structure with 20 nm channels of donor and acceptor domains oriented perpendicularly to the electrodes. Interestingly, block copolymers have also shown the potential to present complementary absorption in a single macromolecule. Recently, different new materials have been developed for this aim.

In its turn, poly(3-hexylthiophene) (P3HT) is the most widely used conjugated polymer donor for organic optoelectronic applications. It is still interesting due to its easy and versatile synthetic procedure, high solubility in organic solvents, high mobility, high crystallinity and good thermal stability.¹

Low-bandgap polymers are made up of an alternated sequence of electron deficient monomers (donors) and electron rich ones (acceptors). Among the well-known acceptors, diketopyrrolopyrrole (DPP) gained a lot of attention and has been widely used as a co-monomer in a variety of polymer synthesis showing excellent performances in OPV.^{2,3,4} The DPP lactam can be further modified by N-alkylation to prevent solubility problems.⁵ On the other hand, 2,5-diazapentalene (DAP), is a stronger acceptor than DPP. DAP is derived from DPP by thionation and after the conversion of the DPP lactam to lactim.⁶ DPP and DAP-based copolymers have previously shown promising optical properties due to their extended absorption to the NIR region. According to computational calculations performed on both DPP and DAP, it was proved that DAP exhibits a lower lying HOMO level which in its turn decreases the bandgap as shown in **Figure II-1**. The lack of the donation from the lone pair electrons on the nitrogen π -orbit of the diene moiety in DAP is responsible for this decrease in the HOMO energy level than DPP.⁷

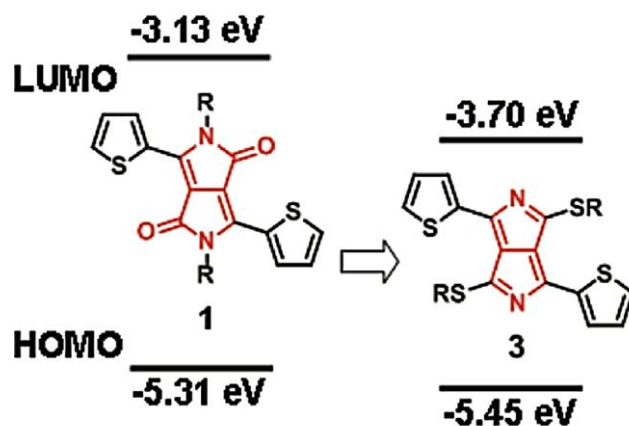


Figure II-1: Energy level orbitals of DPP and its DAP derivative.⁷

Among the most known electron donors, dithieno[3,2-b:2',3'-d]silole (DTS) is extensively used as a silicon-containing π -conjugated building block which is characterized by its good stability at ambient atmosphere.⁸ The use of the silole-containing polymers or in other words, the replacement of the carbon atom by silicon atom, is considered an important step to control the film morphology and improve the efficiency of organic solar cells.⁹ Being longer than the C-C bond, the Si-C bond can change the geometry of the thiophene unit. This improves the ordering of the polymer chain and thus enhances the hole transport properties and lowers HOMO energy level than that of the carbon-bridged counterpart.¹⁰ Many studies revealed that DTS-based alternated copolymers can exhibit better optoelectronic properties than the corresponding carbon-bridged cyclopentadithiophene (CPDT) based-polymers.¹¹

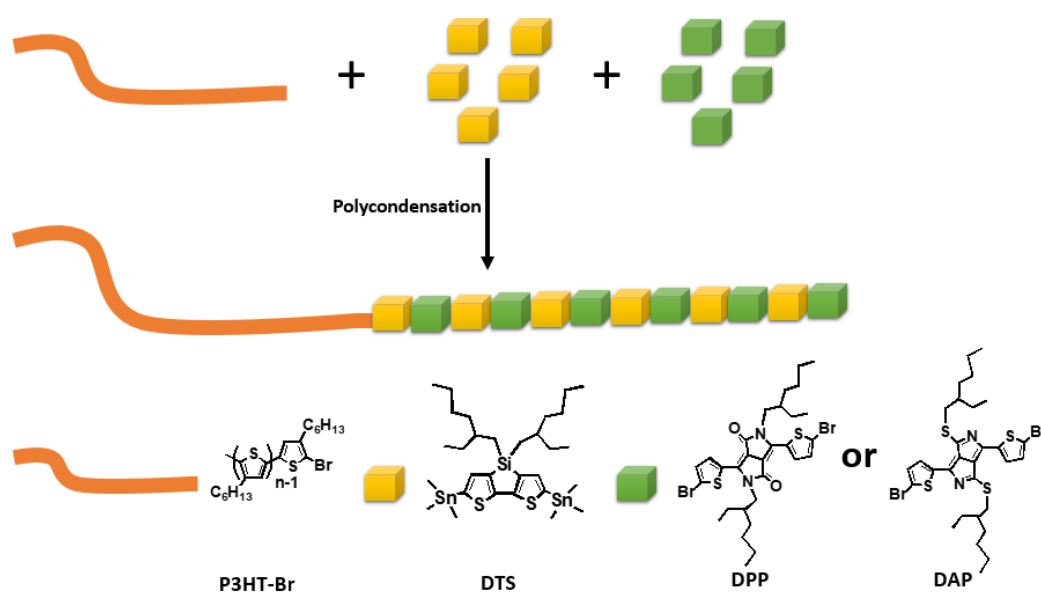
All-conjugated block copolymers that constitute two or more chemically different monomer units can be synthesized using condensation polymerization procedures.¹² Several studies, discussed in the bibliographic part of this manuscript, showed the possibility of synthesizing different conjugated block copolymers composed of an electron donating P3HT block and an electron accepting block. For instance, a CBCP was synthesized based on P3HT as the electron donating block and poly-(diketopyrrolopyrrole-terthiophene) as the electron accepting block using Stille coupling polymerization.¹³ The Stille coupling polymerization involves coupling reactions between organic tin compounds and organic halides, catalyzed by palladium for carbon-carbon bond formation.¹⁴

One important parameter during the synthesis of CBCPs is the choice of the linker between the two blocks. Lee *et al.*¹⁵ recently showed that the introduction of a flexible and non-conjugated spacer between block improved the photovoltaic performances by increasing the degree of crystallization for both blocks. On the contrary, Hu *et al.*¹⁶ found out that the insertion of a flexible spacer reduced quenching between donor and acceptor blocks and as a consequence decreased photovoltaic performances compared to an analogue copolymer presenting a rigid linker.¹⁷ They reported that the flexible spacer allowed the block to rotate to a non-planar orientation leading to a significant loss of overlap. Consequently, this reduces charge separation and increases recombination rates.

Thus, we based our study on rigid linkers, mainly DTS as it was previously demonstrated that this repetitive unit has been successfully used for synthesizing fully conjugated block copolymers with P3HT block using Negishi catalyst-transfer polycondensation.¹⁸ From here, it was of great interest to focus on P(DTS-DPP) and P(DTS-DAP) blocks while taking into consideration the importance of P3HT for developing photoactive materials for OPVs and the complementary absorption between the latter and the two mentioned blocks.

II. Objectives

This chapter focuses on the chemical synthesis of different monomers and copolymers. A synthetic strategy to create rod-rod conjugated block copolymers has been followed starting from bromine terminated P3HT and difunctional monomers DTS and DPP or DTS and DAP as shown in **Scheme II-1** via Stille coupling polycondensation. The synthesized diblock copolymers are low-bandgap blocks with a complementary absorption ranging from the visible range up to the near-infrared (NIR) region, *i.e.* from 400 to 900 nm. Moreover, in such a material, P3HT could serve as an electron donating block while the second block serves as an electron accepting one. Another attractive feature of such a synthetic strategy is the possibility to tune the molar mass and so the volume ratio of each block. The influence of the P3HT length and the feed amount in the polycondensation to prepare the second block on the final dimension of the chains will be discussed from Nuclear Magnetic Resonance (NMR) and Size Exclusion Chromatography (SEC) results. Indeed, different block lengths have been obtained and their influence on optoelectronic properties, as UV-vis-NIR absorption and cyclic voltammetry have been studied.

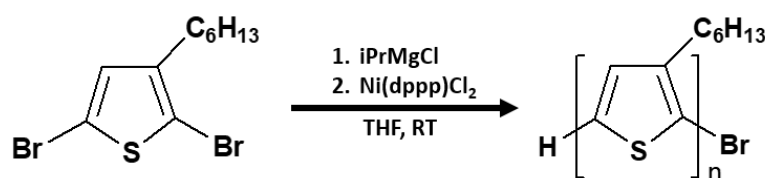


Scheme II-1: Representative Scheme for the synthesis of the diblock copolymers.

III. Synthesis of molecular and macromolecular precursors

a. Synthesis and characterization of poly(3-hexylthiophene) (P3HT)

Bromine-terminated P3HT (P3HT-Br) was prepared by a Grignard metathesis polymerization as shown in **Scheme II-2** following a procedure described by McCullough *et al.*¹⁹ 2,5-dibromo-3-hexyl-thiophene monomer was added with isopropyl magnesium chloride (iPrMgCl₂) in dry tetrahydrofuran (THF). The reaction mixture was stirred before the addition of the dichloro[1,3bis(diphenylphosphino)propane] nickel (Ni(dppp)Cl₂). The latter plays the role of an initiator/catalyst in which the Ni(dppp) moiety is incorporated in the growing polymers as a propagating end-group. After agitation, the polymer was quenched with methanol, precipitated in cold methanol and then purified. Soxhlet extraction was used to purify the polymer from the excess catalyst and the low molecular chains. After purification, a yield of 50 to 60% of P3HT-Br was obtained in the chloroform fraction.



Scheme II-2: Synthesis of the bromine-terminated P3HT.

It is important to mention that the number average molar mass (M_n) of the polymer is based on the molar ratio of the monomer to the Ni(dppp)Cl₂ initiator/catalyst. Accordingly, different molar masses can be obtained by varying the ratio of the monomer:catalyst that were initially added to the reaction mixture. Kumada Catalyst-Transfer Polycondensation (KCTP) is a controlled chain growth polymerization, thus, the theoretical degree of polymerization (DP_n) can be estimated by **Equation 1** shown below.

$$DP_n = \frac{n \text{ Monomer}}{n \text{ Catalyst}} \times \text{conversion} \quad \text{Equation 1}$$

P3HT-Br presenting different molar masses were prepared by simply changing this ratio, as shown in **Table II-1**. P3HT₂₅, P3HT₃₇ and P3HT₉₆ were synthesized with DP_n of 25, 37 and 96, respectively. The theoretical DP_n was calculated from **Equation 1** assuming that conversion equal 1. The experimental DP_n was determined from proton nuclear magnetic resonance spectra (¹H NMR).

Table II-1: The theoretical DP_n values of the synthesized P3HT-Br.

Synthesized polymer	n Ni(dppp)Cl ₂ (mmol)	Theoretical DP_n^a	Experimental DP_n^b
P3HT ₂₅	0.075	40	25
P3HT ₃₇	0.06	50	37
P3HT ₉₆	0.03	100	96

^a calculated based on Equation 1 and ^b calculated from ¹H NMR

All the synthesized P3HT-Br polymers were characterized by different techniques. The successful polymerization was proved using size exclusion chromatography (SEC) having a UV-detector. The UV detection wavelength was set at 450 nm which corresponds to the maximum absorption of the P3HT polymer. The normalized SEC traces of P3HT₂₅, P3HT₃₇, P3HT₉₆ and P3HT₂₄₀ (this one provided by Solaris Chem.) are plotted in **Figure II-2**. SEC was also used to determine the number average molar mass and the dispersity (\bar{D}) for each polymer. These data are summarized in **Table II-2**. It is worth mentioning that SEC calibrated against polystyrene standards overestimates the molar masses by a factor between 1.5 and 2.^{20,21}

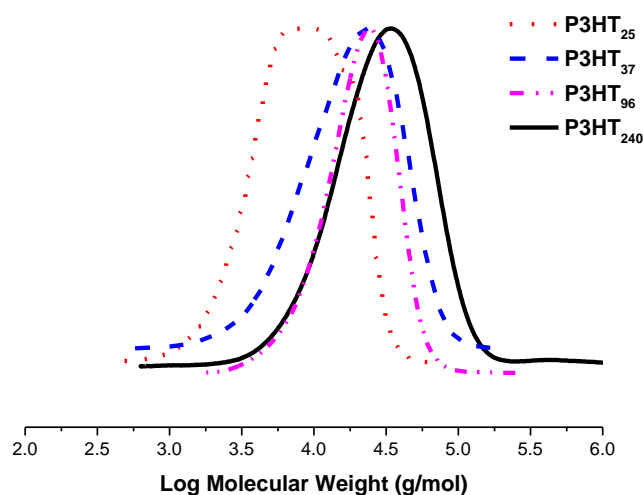


Figure II-2: Normalized size exclusion chromatograms of different P3HTs using a UV detector at $\lambda = 450$ nm.

The SEC traces showed a monomodal peak distribution for all P3HT polymers with dispersities ranging from 1.3 to 2 (**Table II-2**). It should be noted that a narrow peak distribution with symmetrical shape was observed in P3HT₃₇, P3HT₉₆ and P3HT₂₄₀, while a wider peak distribution was observed in the P3HT₂₅ chromatogram.

The quenching of nickel terminated poly(3-alkylthiophene) with methanol has been demonstrated to result in the formation of H/Br terminated polymers.²² Thus, to identify the end-groups of the synthesized polymers, Matrix Assisted Laser Desorption Ionization/Time of Flight (MALDI-TOF) analysis was performed. It was reported that very high molar mass polymers are difficult to be identified due to the low efficiency of desorption/ionization.²¹ Thus, in our study, it was possible to determine the molar mass of the synthesized P3HT by MALDI-TOF. By considering 166.23 is the molecular weight of one thiophene unit, the molar mass of the polymer was calculated according to **Equation 2**.

$$\mathbf{Mn = (166.23)n + MwX + MwY} \quad \mathbf{Equation\ 2}$$

Where n is the number of the repetitive units of thiophene, MwX and MwY represent the molecular weight of the terminated end-groups. For the analyzed polymer (P3HT₂₅), this equation was used to identify the peaks shown in the spectrum of **Figure II-3**.

For example, the peaks at 2907 Da and 2986 Da and based on **Equation 2**, revealed the existence of H, Br and Br, Br end-groups, respectively, for P3HT₂₅.

$$\mathbf{Mn = (166.23) \times 17 + 80 + 1 = 2907}$$

$$\mathbf{Mn = (166.23) \times 17 + 80 + 80 = 2986}$$

The difference between the two peaks is 80 which corresponds to the molecular weight of one bromine atom. The calculations revealed that the polymer samples were composed of 85 molar % of mono-brominated P3HT and 15% of α - ω -dibrominated chains, thus achieving the goal in synthesizing Br-terminated P3HT polymers.

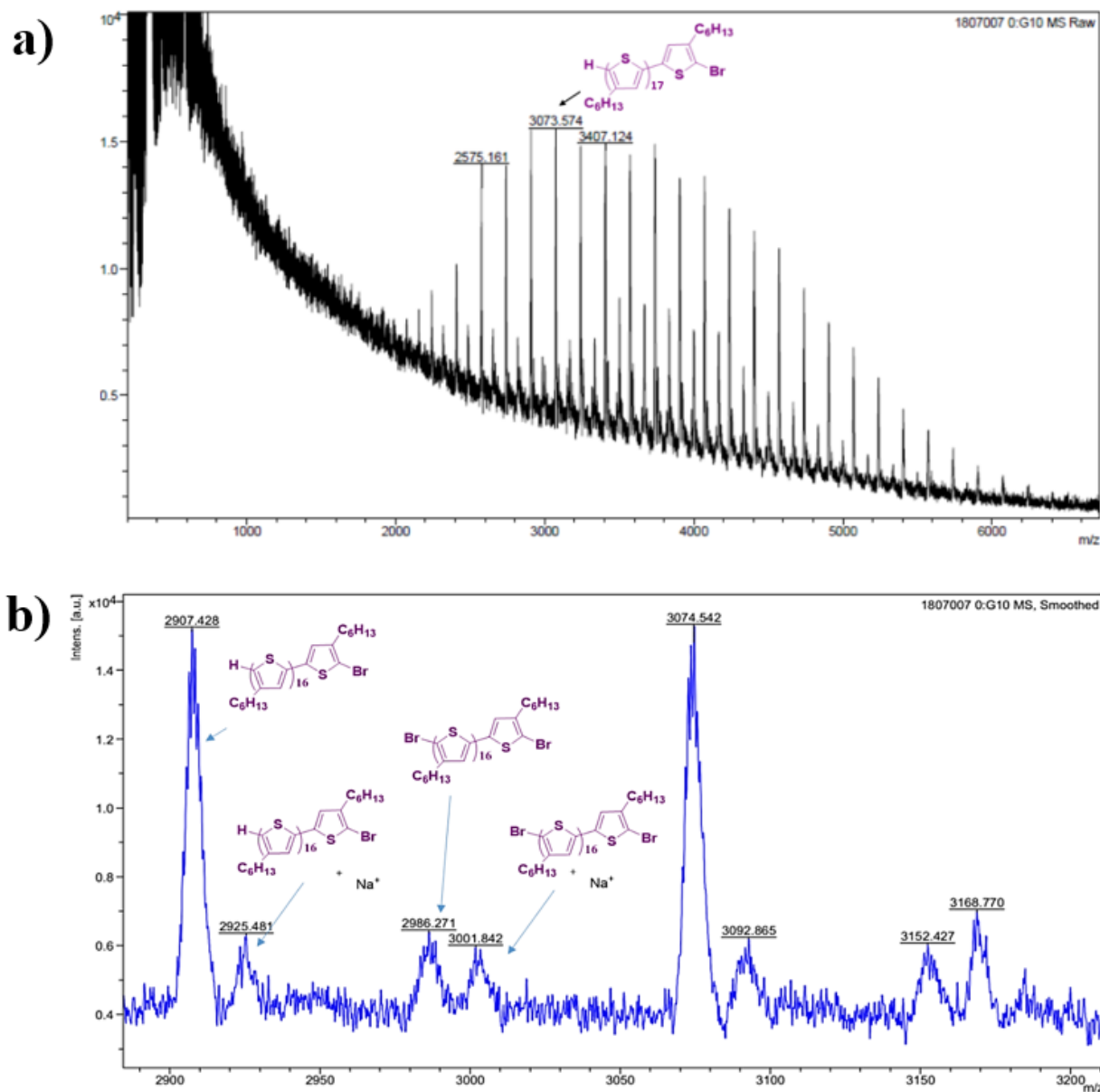


Figure II-3: (a) Full spectrum MALDI-TOF of P3HT₂₅ and (b) zoom in spectrum.

¹H NMR analysis has been also used for characterizing the synthesized P3HT polymers. This characterization allows the calculation of the molar mass and regioregularity. Usually, the synthesis of poly(3-alkylthiophenes) using Grignard metathesis method yields regioregular polymers (~98% head-to-tail).

According to McCullough, the mechanism behind the KCTP consists of the reduction of Ni(II) catalyst into Ni(0) through the tail-to-tail coupling as a first step in the polymerization.²³ The catalyst randomly moves to the last monomer unit in the growing polymer chain after each step of reduction/elimination, thus the regio-defects can be created anywhere in the growing chain. Moreover, the quenching of polymerization with methanol leaves randomly one bromine and one hydrogen at the chain ends (H/Br terminated P3HT). This makes the interpretation of ¹H NMR more difficult.²⁴ The ¹H NMR spectra of P3HT₂₅ and P3HT₃₇ are shown in **Figure II-4**. The head-to-tail (HT) and the tail-to-tail (TT) arrangements of the synthesized polymers can be determined from the characteristic peaks of the α-methylene protons. The shift in the peaks between H d' to d at 2.6 to 2.78 ppm, respectively is caused by the head-to-head (HH) arrangements. It is important to mention that the percentage of the HH and the HT can be calculated by referring to the integrals of the corresponding peaks. Regioregularity was determined by considering the integration of these peaks using **Equation 3**.

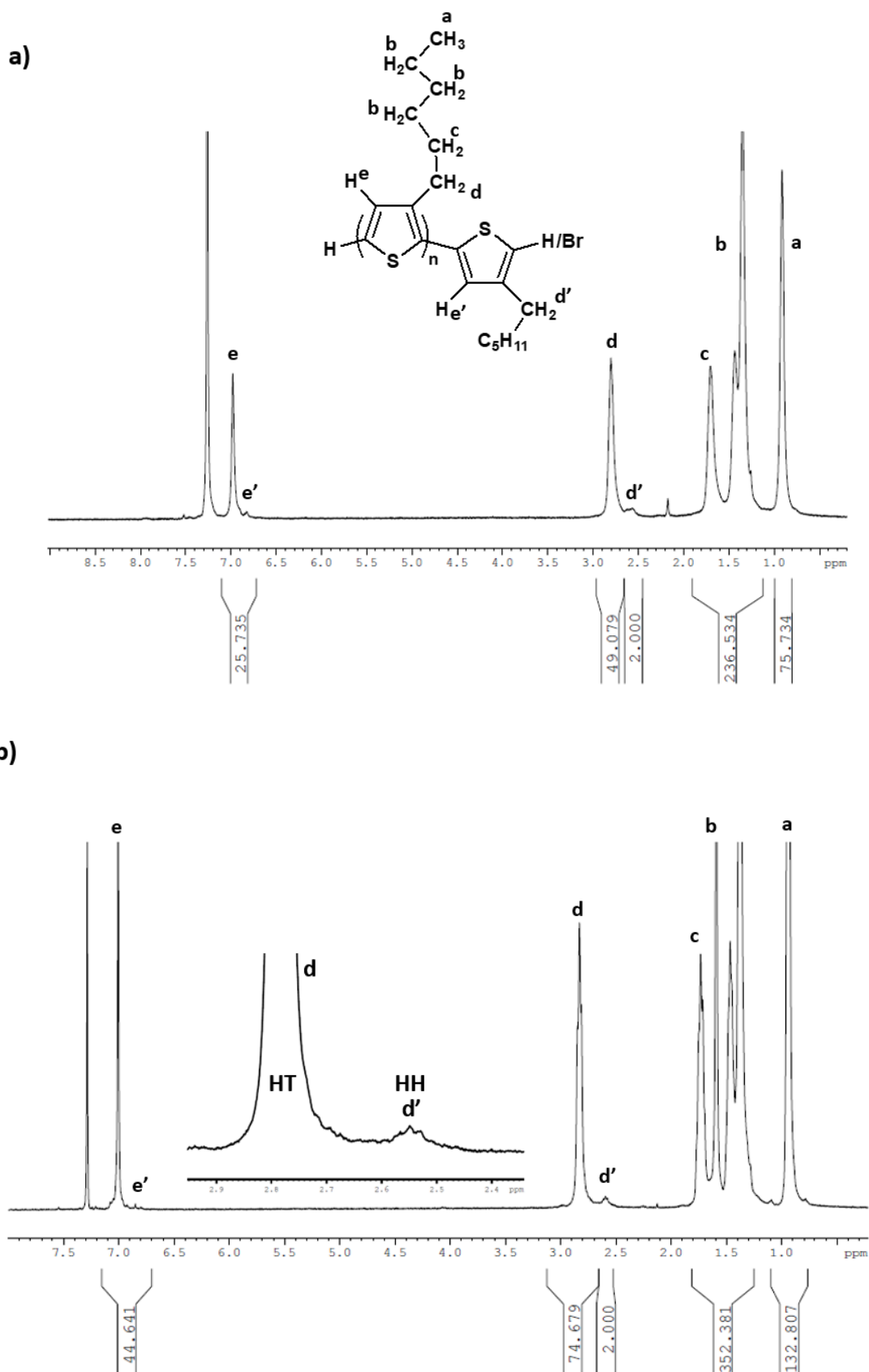
$$\% \text{ Regioregularity} = \frac{I_d}{I_d + I_{d'}} \times 100 \quad \text{Equation 3}$$

In our case, the regioregularity of the synthesized P3HT₂₅ was calculated to be 96%. **Table II-2** summarizes the calculated regioregularity from the ¹H NMR for the different P3HT polymers synthesized in this study. ¹H NMR allows the relative determination of the average molar mass. Thus, by integrating the α-methyl proton (**d**) of the hexylthiophene, it is possible to determine the DP_n (repetitive unit) by considering the ratio of the integration between the peaks **d** and **d'** divided by 2; (d+d')/2. DP_n of 25 and 37 were calculated for P3HT₂₅ and P3HT₃₇, respectively. From these values, it was possible to determine the number average molar mass of the characterized polymers as it is summarized in **Table II-2**.

Table II-2: Characteristics of the synthesized P3HT polymers.

Polymer	M _n ^a (g.mol ⁻¹)	M _n ^b (g.mol ⁻¹)	DP _n ^a	Đ ^b	% RR ^{a2} Regioregularity
P3HT ₂₅	4150	4500	25	1.4	96
P3HT ₃₇	6150	13,000	37	1.7	97.5
P3HT ₉₆	16,000	16,000	96	1.4	99
P3HT ₂₄₀	40,000	19,000	240	2.1	94

^a calculated from ¹H NMR and ^b measured by SEC-THF



Finally, the absorbance of the synthesized P3HT polymers was measured in solution (**Figure II-5a**) and in films (**Figure II-5b**). In this regard, polymers were solubilized in chloroform (CHCl_3). All spectra measured in solution show a broad absorption peak between 350 and 570 nm which is a classical absorption of P3HT²⁵ with a slight bathochromic shift of λ_{max} due to the increase in the π - π conjugation length. This could be related to the increase in the molar mass. By contrast, film spectra of P3HT (prepared by spin-coating $10 \text{ mg}\cdot\text{mL}^{-1}$ P3HT solution onto glass substrates) are significantly red-shifted with well-defined vibronic features at high wavelengths. Thus, films of P3HT₃₇, P3HT₉₆ and P3HT₂₄₀ revealed two peaks between 500 nm and 555 nm in addition to a shoulder at 600 nm (**Figure II-5b**). These three bands are related to the π - π^* transitions and referred as vibronic absorption of the crystalline intermolecular π - π stacking. The vibronic shoulders are related to the order and stacking of P3HT.¹ On the contrary, the characteristics of P3HT₂₅ were limited by finite confinement of the π - π conjugation length, in agreement with results found in literature.²⁶

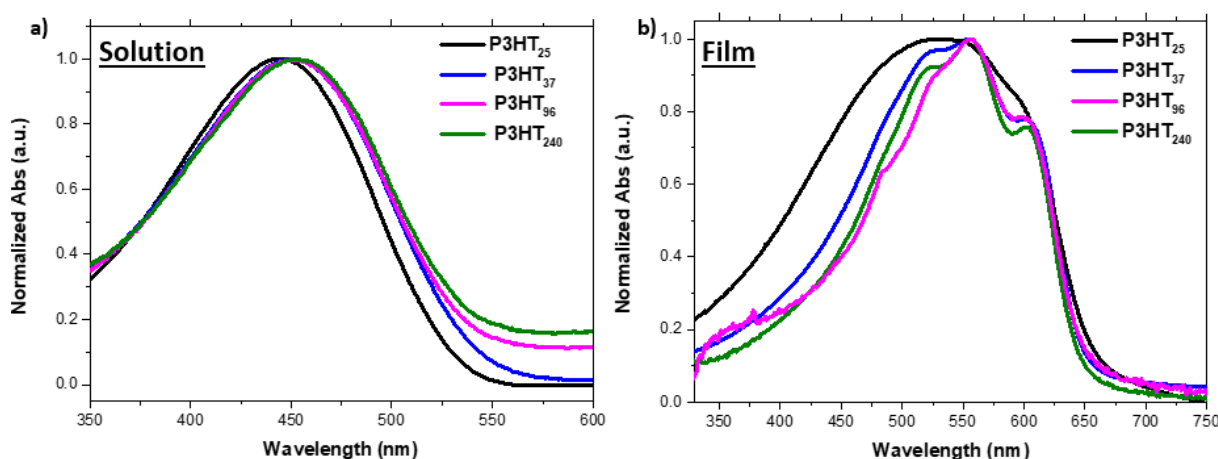


Figure II-5: UV-vis absorption spectra of different P3HTs in (a) CHCl_3 solution and (b) film.

Based on the absorption spectra it is then possible to determine the optical bandgap ($E_g^{(\text{opt})}$) of the synthesized polymers depending on the Planck's equation (**Equation 4**).

$$E_g(\text{opt}) = \frac{hc}{\lambda_{\text{onset}}} = \frac{1240}{\lambda_{\text{onset}}} \quad \text{Equation 4}$$

The optical bandgaps for P3HT polymers were calculated and summarized in **Table II-3**. These data show that optical bandgaps calculated from solutions (around 2.2 eV) are higher than that calculated from films (around 1.8 eV). It is worth mentioning that the typical optical bandgap of P3HT film is 1.9 eV. This energy gap value is dependent on the film crystal structure and the distribution of the atoms in the crystal lattice.¹

Table II-3: Optical properties of the P3HT polymers in solution vs. in film.

Polymer	λ_{onset} (nm) ^a	$E_g^{(\text{opt})}$ (± 0.05 eV) ^a	λ_{onset} (nm) ^b	$E_g^{(\text{opt})}$ (± 0.05 eV) ^b
P3HT ₂₅	550	2.25	671	1.84
P3HT ₃₇	562	2.20	665	1.86
P3HT ₉₆	568	2.18	665	1.86
P3HT ₂₄₀	572	2.16	660	1.87

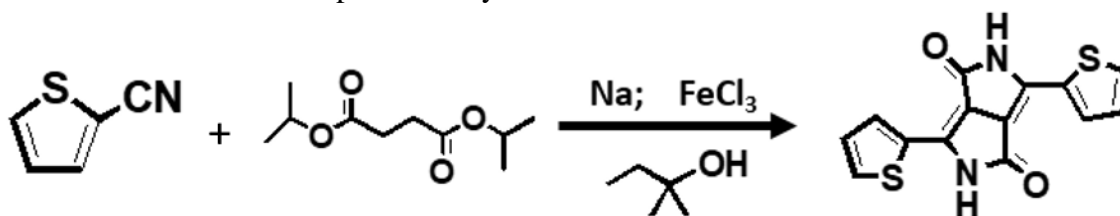
^a calculated from solutions and ^b calculated from films

b. Synthesis of diketopyrrolopyrrole (DPP) monomer

3,6-diphenyl-substituted diketopyrrolopyrrole (DPP) was first synthesized by Farnum *et al.*²⁷ in 1974 with a very low percentage yield (5-20%). In 1983, Iqbal *et al.*²⁸ reported an efficient synthetic procedure for the synthesis of DPP derivatives. The DPP core is usually substituted in the 3 and 6 positions with different groups such as phenyl. Changing the phenyl substituent to 2-cyanofuran²⁹ or 2-cyanothiophene³⁰ in the reaction with succinic acid ester gives the corresponding DPPs with higher yields. Moreover, replacing the phenyl groups in the 3,6-diphenyl DPP by a thiophene group can result in the formation of a thieno-DPP (DPP chromophore core unit with thiophene units on the 3 and 6 positions). This change can cause a red-shift in the absorption by a value of 50 nm. Thus, the synthesized polymers based on dithieno-DPP exhibit a better absorption towards the near-IR region characterized by lower bandgaps and higher charge carrier mobilities.^{31,32} In addition, the smaller 5 membered heterocyclic rings lead to a smaller dihedral angle between the DPP core and the substituent. This results in a greater planarity of the molecular backbone and thus increases the π -delocalization and the intermolecular π - π interactions.³³ This is in addition to the fact that thiophenes are stronger electron donors than phenyl groups, due to the intermolecular charge transfer enhancement. For all the reasons mentioned above, dithieno-DPP monomer was synthesized in a high yield according to the procedure followed by Iqbal *et al.*²⁸ This monomer has been synthesized in three steps including the formation of the DPP chromophore as a core unit with the thiophenes. Then, N,N-alkylation was performed to overcome the solubility problems, followed by a bromination to obtain the final brominated-DPP monomer (DPP-Br₂).

i. Synthesis of 3,6-Dithiophene-2-yl-2,5-dihydropyrrolo[3,4-c]pyrrole-1,4-dione (DPP)

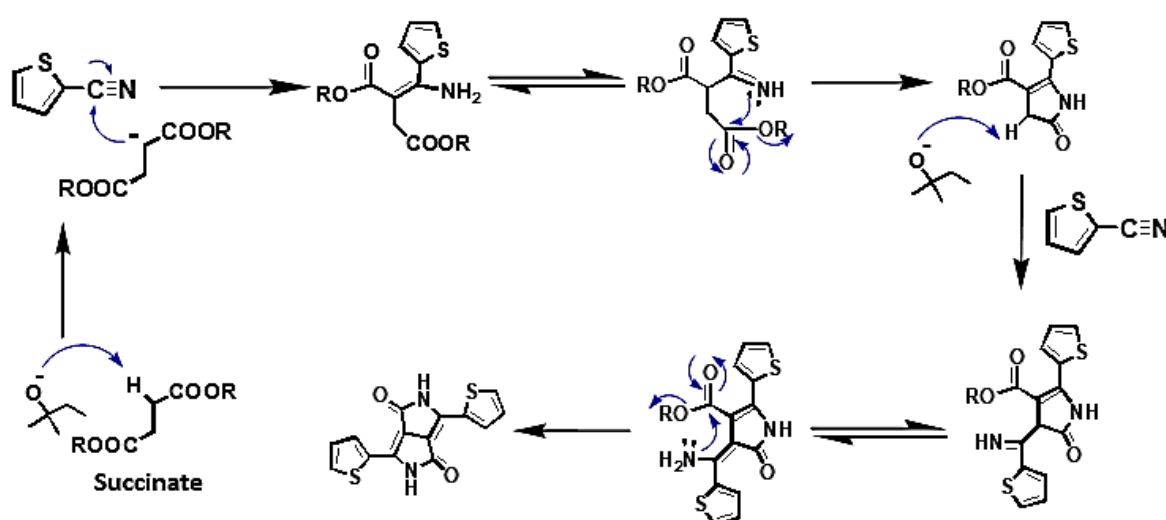
The synthesis of the DPP core is a one-step reaction between thiophene nitrile and succinic acid diester derivative.²⁸ This synthesis is described in **Scheme II-3** in which 2-thiophene-carbonitrile was reacted with di-isopropyl succinate in a basic medium in the presence of sodium (Na) in t-amyl alcohol and anhydrous iron(III) chloride (FeCl₃). Concerning the basic medium used in this synthetic procedure, the best choice was the tertiary alkoxide that is known to be strong enough for deprotonating the succinic acid esters but a weak nucleophile to attack the cyano group of the used nitriles.²⁸ The final product was then collected by filtration using Buchner funnel. The brown-red solid filtrate was washed several times with warm deionized water and methanol. The experimental yield of the DPP was 80%.



Scheme II-3: Synthesis of diketopyrrolopyrrole (DPP).

The use of the reactive succinic acid ester in the solvent *t*-amyl alcohol is to minimize the dimerization reaction by the Claisen condensation mechanism that may lead to the formation of cyclic-diester.³⁴ Thus, succinic acid must be added dropwise into the medium to keep its concentration low. Moreover, it is important to keep the temperature of the medium high (80 °C) during the reaction, since the nitrile is a weak electrophile, thus it may prevent the nucleophilic addition of the anion generated by the ester succinate in a low temperature reaction.³⁵ Thus, the reaction's rate is directly proportional to the reaction's temperature and the concentration of the succinic acid.

The general mechanism for the DPP synthesis is described in **Scheme II-4**. In the presence of the strong base, succinate is deprotonated and stabilized by resonance. The enolate undergoes a nucleophilic attack on carbonitrile forming the secondary imine. Schiff's base then attacks the ester's carbonyl to form the iminium ion that undergoes hydrolysis to form lactam. The α -proton of the lactam is then attacked by the base, followed by a nucleophilic attack on a second carbonitrile to form the imine. This results in the formation of a second lactam. Finally, the conjugated bicyclic structure is formed. As previously mentioned, the usage of thiophene as spacers reduces the steric hindrance and improves the mobility in the polymer chain. The lactam groups formed have electron-withdrawing effects, thus increasing the electronic affinity of the chromophore.



Scheme II-4: The general mechanism for the synthesis of diketopyrrolopyrrole (DPP).

¹H NMR was performed for the first step DPP product. The spectrum in **Figure II-6** shows a singlet at 11.22 ppm which is assigned to the proton (**a**) of the lactam. In addition to two doublets at 8.19 and 7.94 ppm and a doublet of doublet at 7.28 ppm corresponding to the aromatic protons (**b**), (**d**) and (**c**), respectively of the thiophene group.

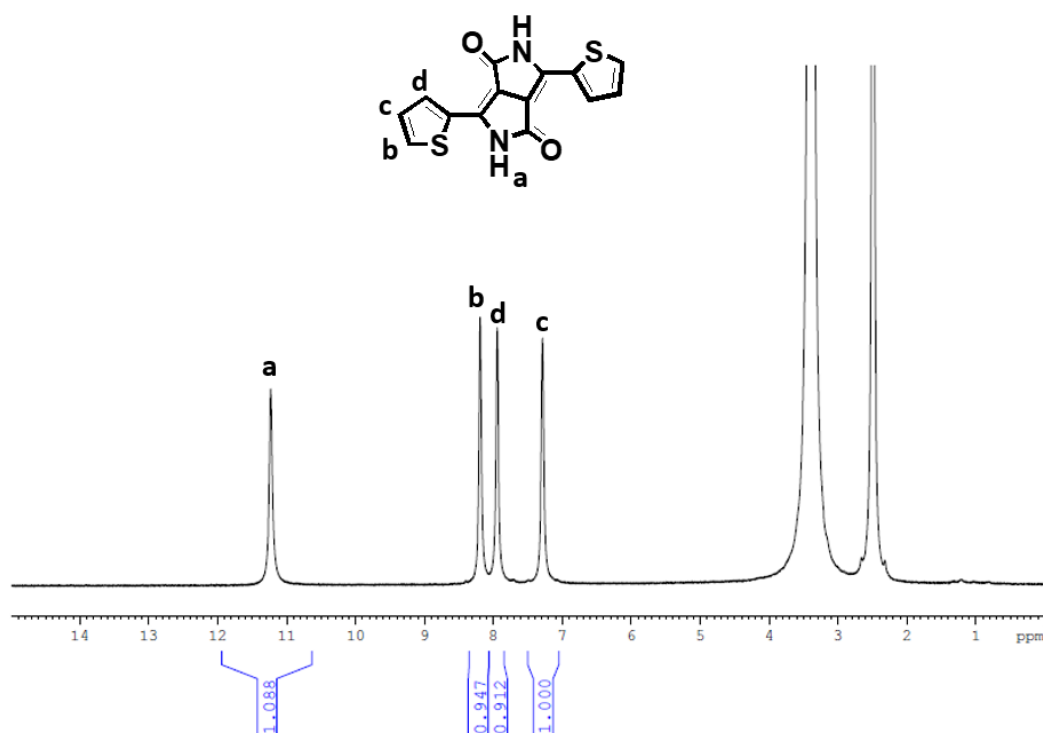


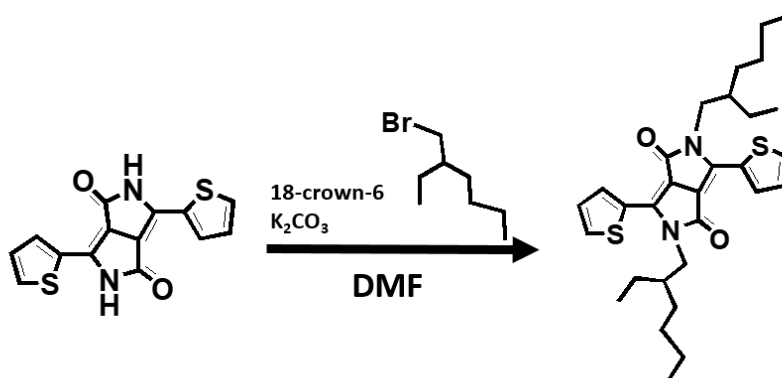
Figure II-6: ^1H NMR spectrum of the diketopyrrolopyrrole (DPP) (d_6 -DMSO, 400 MHz).

ii. Synthesis of 2,5-bis-(2-ethyl-hexyl)-3,6-dithiophen-2-ylpyrrolo[3,4-c]pyrrole-1,4-dione (DPP-eH)

The synthesized DPP in step 1 has a planar rigid structure that may induce hydrogen bonding and other intramolecular interactions. These interactions actually make the core insoluble in the most commonly used solvents. Thus, for the aim of increasing the solubility of the DPP, the lactam unit should be N-functionalized (alkylated) in order to prevent the formation of such interactions and hydrogen bonds between the DPP units.⁵ Therefore, for the majority of the applications that require good solubility, the alkylation step is necessary. Being with different reactive heteroatoms (nitrogen and oxygen), the DPP monomer can be alkylated on either side depending on the reaction conditions and may lead to secondary products. Thus, controlling the alkylation position is directly related to several conditions including the solvent, the temperature and the medium pH.³⁶ In neutral media, the O-alkylation is the kinetically stable product. While under thermodynamic control, the N-alkylated product is favored. An excess in the alkylating reagents or increasing the reaction time, can sometimes yield to the observation of both N- and O-alkylation. In some cases, the alkylation occurs solely on oxygen atom instead of nitrogen in which the driving force in this case is the aromatization.^{37,38} However, it was proved that the relative reactivity of N-alkylation is superior than O-alkylation, thus, the N-alkylation is chemically preferred.⁷ Both N-alkylated and O-alkylated polymers were studied as photovoltaics materials and are of great interest.^{39,40}

In the common alkylation methods, aprotic solvents such as N,N-dimethylformamide (DMF) are widely used in the presence of potassium carbonate (K_2CO_3). The latter is an effective base used for the deprotonation of the amide-NH. A mixture of 18-crown-6 and K_2CO_3 improves the yield and can prevent the proton catalyzed ring-opening to occur. The 18-crown-6 coordinates the metal cations in the central cavity, makes the inorganic salts more nucleophilic and helps in reducing the reaction's time and increasing the yield. It is worth mentioning that the yield of the reaction is dependent on the nature of the alkylating reagent (branched or linear) and its leaving group.⁴¹ Moreover, it was stated that the yield of the alkylated product increases with the increase in the alkylated chain length which is related to the better solubility in the used organic solvent.⁴² Additionally, the branched side chains improve the solubility when compared to the linear side chains.⁴³

In our case, the functionalization (N-alkylation) of the DPP was carried out as a one pot reaction (**Scheme II-5**) in the presence of K_2CO_3 to reach basic conditions. In such a medium, the proton of the nitrogen atom is deprotonated and the formed anion is stabilized by resonance. The 18-crown-6 is used as a catalytic transfer agent in the presence of the DMF solvent.⁷ To achieve the main goal behind the alkylation which is to improve the solubility of the corresponding monomer, the chosen alkyl chain was the 2-ethylhexyl bromide. The final product was filtered, washed, and purified using a classical column chromatography. The product was then collected as a dark red solid with a yield of 80%.



Scheme II-5: Synthesis of diethylhexyl diketopyrrolopyrrole (DPP-eH).

The structure was confirmed by 1H NMR. The spectrum shown in **Figure II-7** revealed three distinct peaks in the aromatic region at 8.88, 7.62 and 7.27 ppm. These are assigned for the aromatic protons of thiophene (**a**, **c** and **b**, respectively). In addition, a peak at 4.02 ppm corresponding to the alkyl (CH_2 , proton **d**) in the α -nitrogen position.

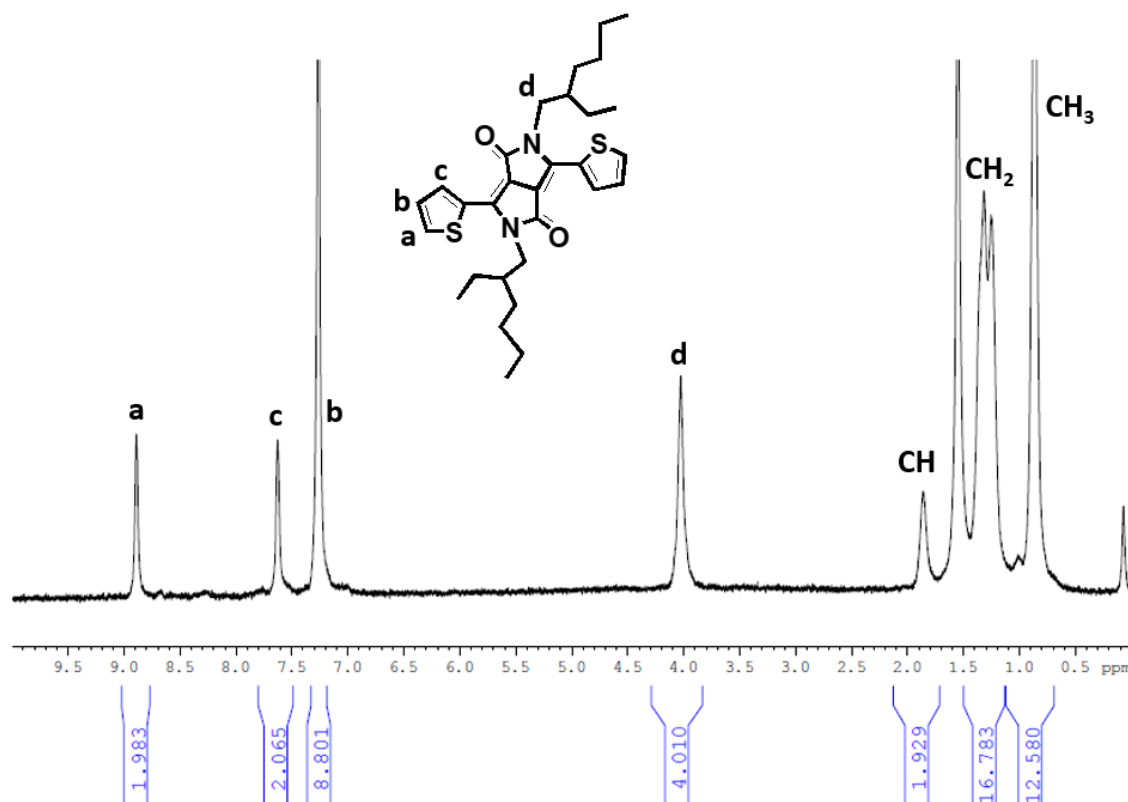
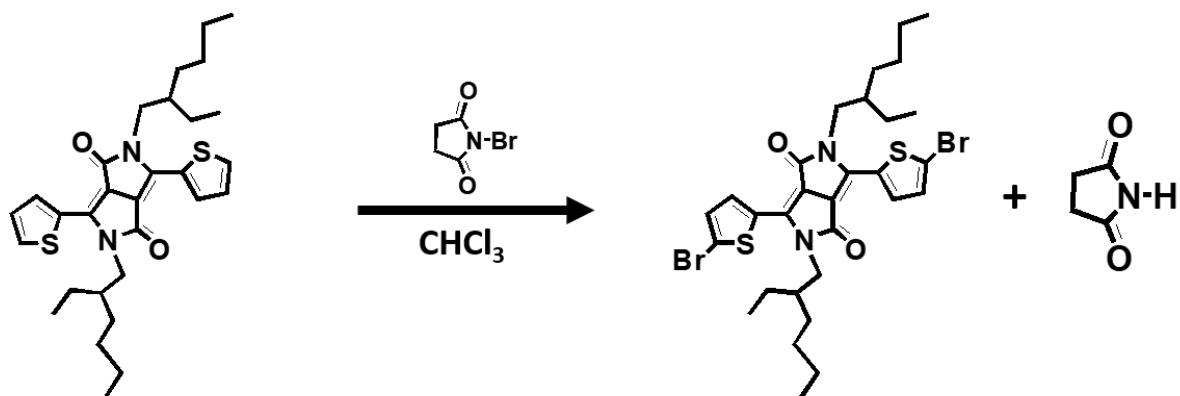


Figure II-7: ^1H NMR spectrum of the diethylhexyl diketopyrrolopyrrole (DPP-eH) (CDCl_3 , 400 MHz).

iii. Synthesis of 1,4-bis(5-bromothiophen-2-yl)-3,6-bis(Ethylhexylthio)pyrrolo[3,4-c]pyrrole (DPP- Br_2)

The synthesized DPP unit was further functionalized to be polymerized *via* Stille coupling. Different polarizable groups can be used including halogen atoms especially bromine.⁴² In the case where thiophene is the aryl unit in DPP, a direct bromination with N-bromosuccinimide (NBS) is efficient for the bromine functionalization of DPP. In this type of bromination reactions, the concentration of bromine in the medium must be low to avoid multiple bromination or other side reactions from taking place. Therefore, NBS is preferred over Br_2 and HBr mixtures as it can provide the medium with a low concentration of Br_2 during the reaction.⁴⁴

Thus, in our case, NBS was used as the brominating agent to brominate the thiophene by radical substitution (**Scheme II-6**). The reaction was performed in dry chloroform, protected from light and followed by Thin Layer Chromatography (TLC) until the starting material (DPP-eH) was totally consumed and transformed into the dibrominated-DPP. The latter was then precipitated in cold methanol and purified by column chromatography using a 2:1 ratio of hexane and dichloromethane as an eluent to give 70% yield of DPP- Br_2 .



Scheme II-6: Synthesis of dibromo-diketopyrrolopyrrole (DPP- Br_2).

The final product was dried and then characterized by ^1H NMR. The spectrum in **Figure II-8** revealed the disappearance of one of the peaks related to the aromatic protons of the thiophene which was observed before at $\delta = 7.62$ ppm, in which only two distinct peaks assigned for the two aromatic protons of the thiophene group appeared at 8.62 and 7.22 ppm (**a** and **b**, respectively). This was a proof for the complete dibromination of the corresponding DPP. Another peak appeared at 3.92 ppm was assigned to the alkyl (CH_2 , proton **c**) substituent in the α -nitrogen position.

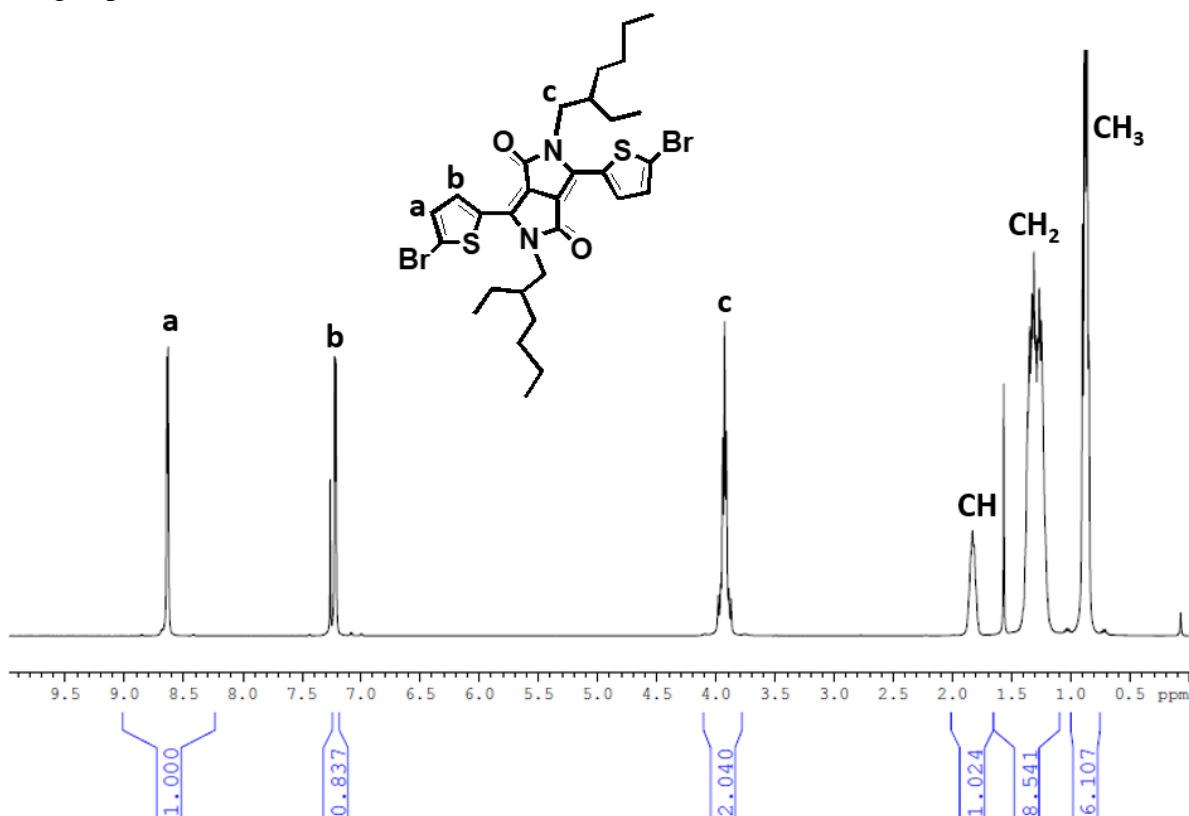


Figure II-8: ^1H NMR spectrum of the dibromo-diketopyrrolopyrrole (DPP- Br_2) (CDCl_3 , 400 MHz).

^{13}C NMR was also performed on the final product and the spectrum is shown in **Figure II-9**.

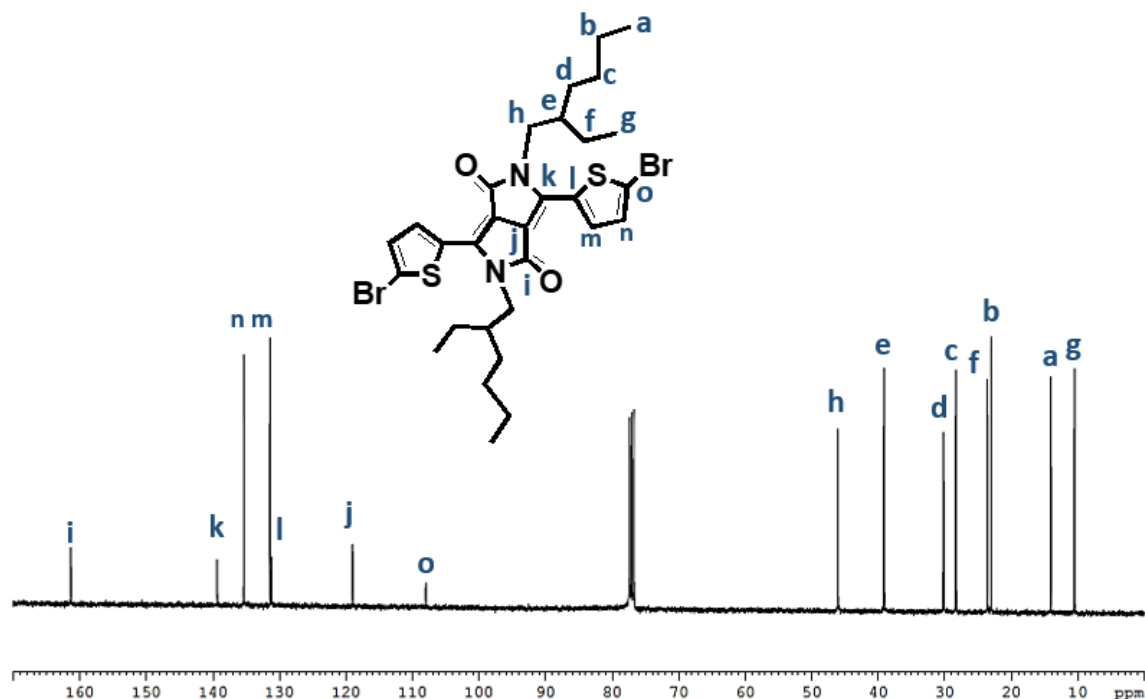


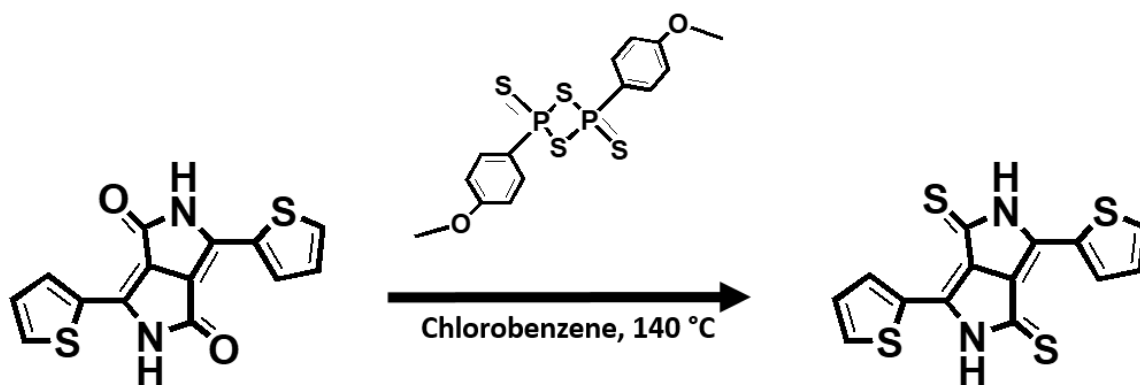
Figure II-9: ^{13}C NMR spectrum of the dibromo-diketopyrrolopyrrole (DPP-Br₂) (CDCl₃, 100 MHz).

c. Synthesis of 2,5-diazapentalene (DAP) monomer

After the synthesis of the DPP monomer, it was then possible to synthesize the 2,5-diazapentalene chromophores monomers (DAP). The latter was synthesized by substituting the oxygen atom in DPP molecule by a sulfur atom, a procedure known as thionation. The thionated-DPP (DTPP) possesses a better solubility than DPP monomer in most organic solvents. The reaction strategy is summarized by starting from the core DPP and converting the oxygen atom into sulfur atom, followed by the thio-alkylation to improve the solubility. The final step is the bromide functionalization that leads to the creation of a polymerizable monomer.⁴⁵

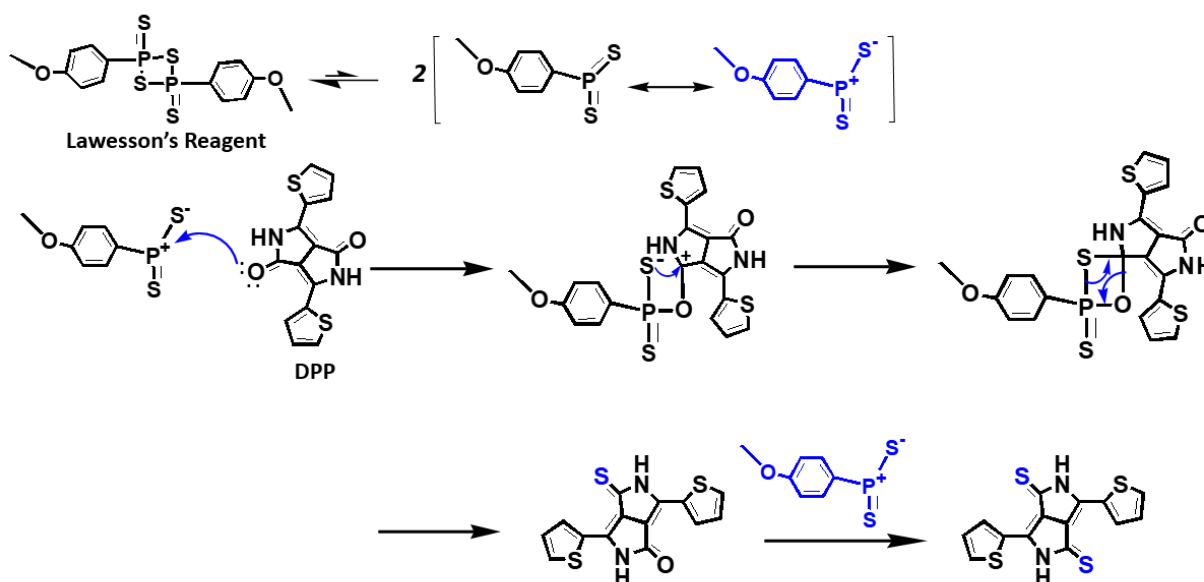
i. Synthesis of 3,6-di(thiophen-2-yl)-2,5-dihydropyrrolo[3,4-c]pyrrole-1,4-dithione (DTPP)

The DPP core was transformed into DTPP by thionation according to a reported procedure.^{6,7} This reaction was performed in the presence of Lawesson's reagent in chlorobenzene and heated-up at 140 °C under inert atmosphere (**Scheme II-7**). The reaction was stopped after the color turned dark green. The product was quickly purified using a Soxhlet extraction in ethanol to remove the phosphorous that may degrade the desired product over time. The final product was then collected with a yield of 85%.



Scheme II-7: Synthesis of dithiodiketopyrrolopyrrole DTPP.

The **Scheme II-8** describes the mechanism occurring between the Lawesson's reagent and the DPP core to form DTPP.



Scheme II-8: Mechanism of the reaction occurring between DPP and the Lawesson's reagent.

The ^1H NMR spectrum of DTPP shown in **Figure II-10** revealed the existence of 3 hydrogen peaks corresponding to the aromatic region of the thiophene group. Two doublets of doublet appeared at 7.52 and 8.18 ppm correspond to protons (**c**) and (**d**), respectively and a doublet at 9.12 ppm corresponding to proton (**b**). Additionally, a singlet at 12.90 ppm is assigned to proton (**a**) located on the nitrogen atom. The assigned peaks revealed the successful thionation of the DPP monomer to form the DTPP molecule.

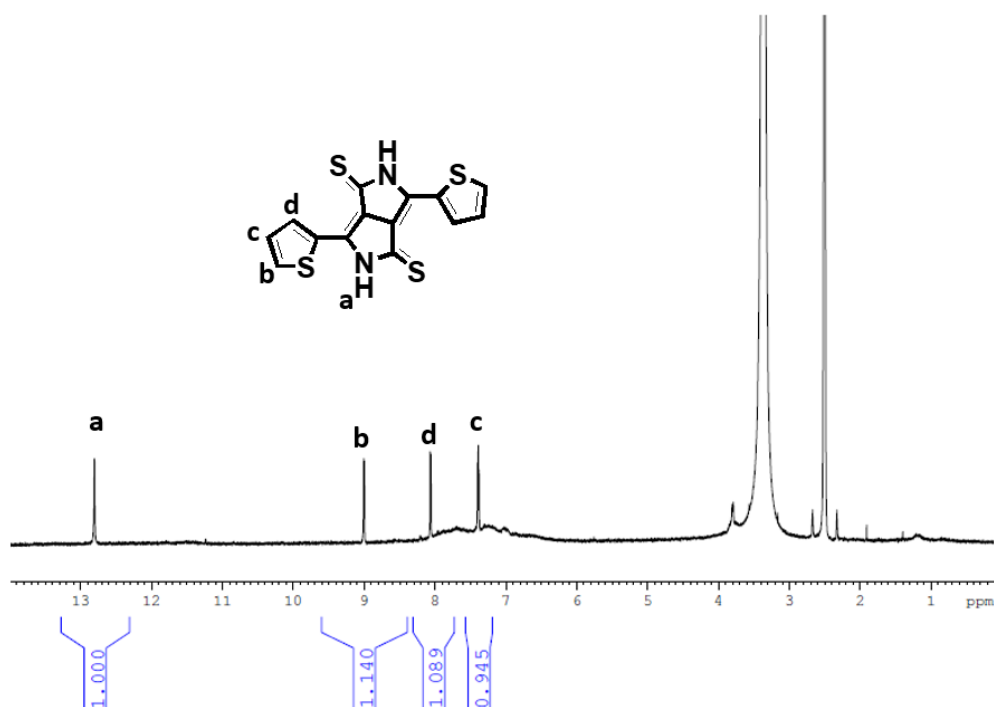
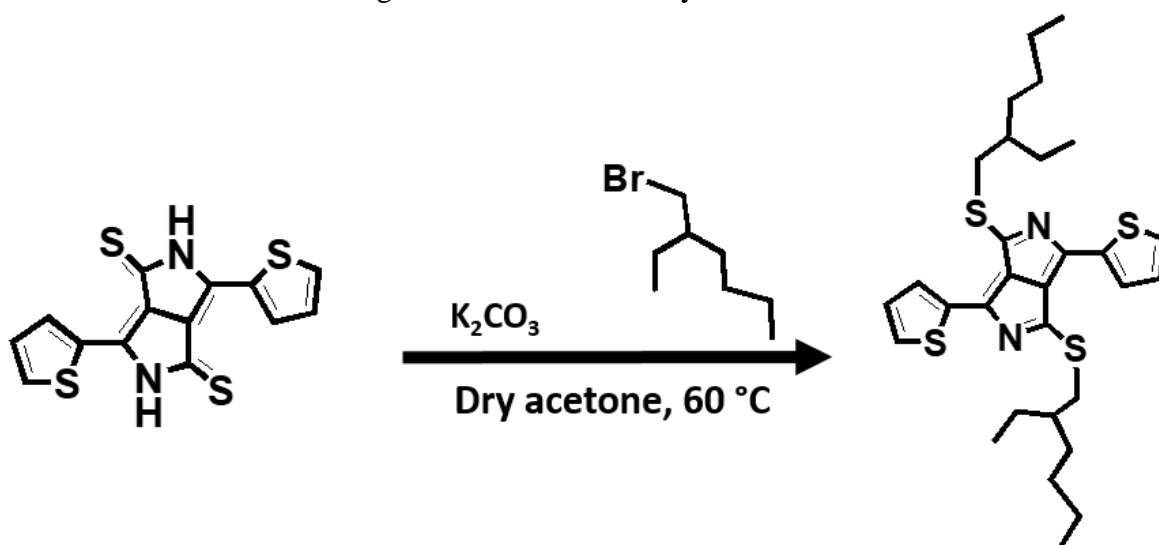


Figure II-10: ^1H NMR spectrum of the dithiodiketopyrrolopyrrole (DTPP) (d_6 -DMSO, 400 MHz).

ii. Synthesis of 1,4-bis ((2-ethylhexyl)thio)-3,6-di(thiophen-2-yl) pyrrolo[3,4-c]pyrrole (DAP-eH)

To solve the solubility issue of DPP, DTPP was alkylated to form the thioalkylated DTPP. Although the DTPP molecule bears two reactive atoms (S and N), the relative reactivity of S-alkylation is higher than that of the N-alkylation, thus the thio-alkylation is preferred.⁷ This alkylation reaction was done in dry acetone in the presence of potassium carbonate as a base and using 2-ethylhexyl bromide as the alkyl chain (**Scheme II-9**). Then, the product was purified and collected as a dark green solid with a 45% yield.



Scheme II-9: Synthesis of diethylhexyl diazapentalene DAP-eH.

The ^1H NMR spectrum of DAP-eH is given in **Figure II-11**. This spectrum shows three types of aromatic protons (**a**), (**c**) and (**b**) located at 8.10, 7.62 and 7.27 ppm, respectively. In addition, a peak assigned to proton (**d**) at 3.51 ppm corresponds to CH_2 that is deshielded due to its α -sulfur position.

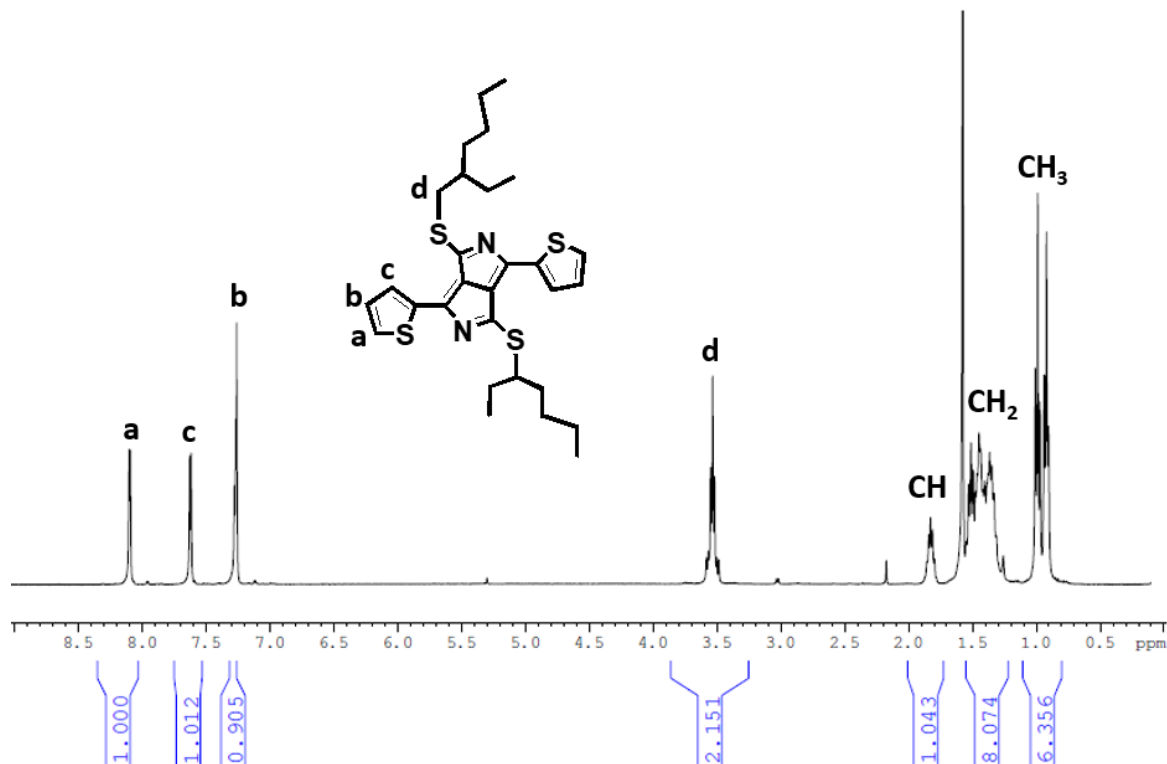
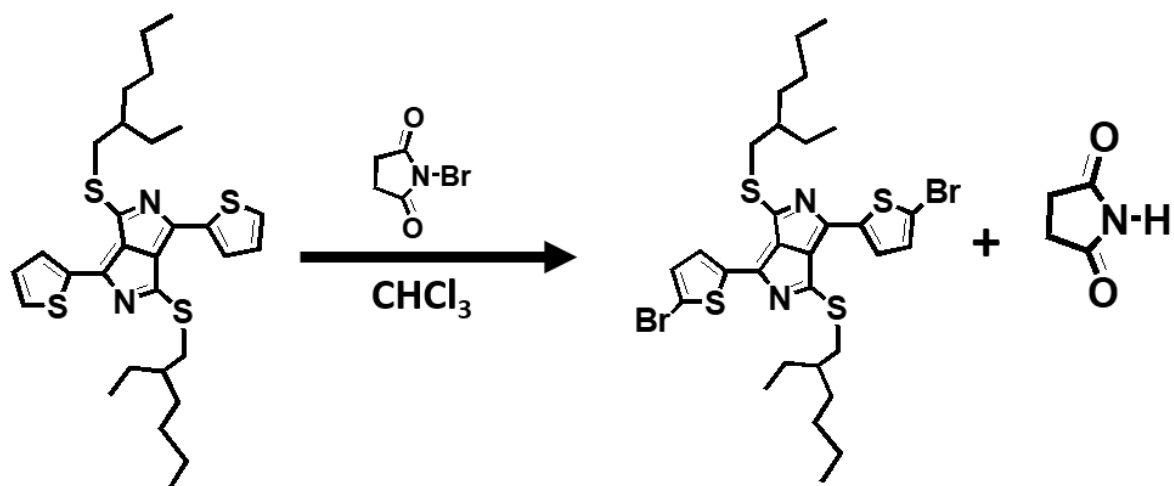


Figure II-11: ^1H NMR spectrum of the diethylhexyl diazapentalene DAP-eH (CDCl_3 , 400 MHz).

iii. Synthesis of 1,4-bis(5-bromothiophen-2-yl)-3,6-bis(Ethylhexylthio) pyrrolo [3,4c] pyrrole (DAP- Br_2)

Similar to the DPP monomer, DAP was dibrominated for further polycondensation. The reaction is shown in **Scheme II-10**. NBS was used as the brominating agent in dry chloroform. The reaction was carried out at room temperature in dark and followed by TLC until the complete conversion. Once completed, the reaction was quenched with distilled water and extracted with dichloromethane (CH_2Cl_2). The final product was purified by the classical column chromatography. The dry DAP- Br_2 was obtained with an 82% yield.



Scheme II-10: Synthesis of dibromo diazapentalene (DAP-Br₂).

Figure II-12 represents the ¹H NMR spectrum of the dibrominated DAP monomer. In this case, only two protons (**a** and **b**) appeared at 7.79 and 7.21 ppm, respectively, assigned to the aromatic ones of the thiophene group. The disappearance of one of the aromatic peaks of the alkylated DAP (DAP-eH) was enough to confirm the successful bromination at both ends of DAP. Another signal appeared at 3.50 ppm which corresponds to proton (**c**) of the alkyl (CH₂) substituent in the α-sulfur position.

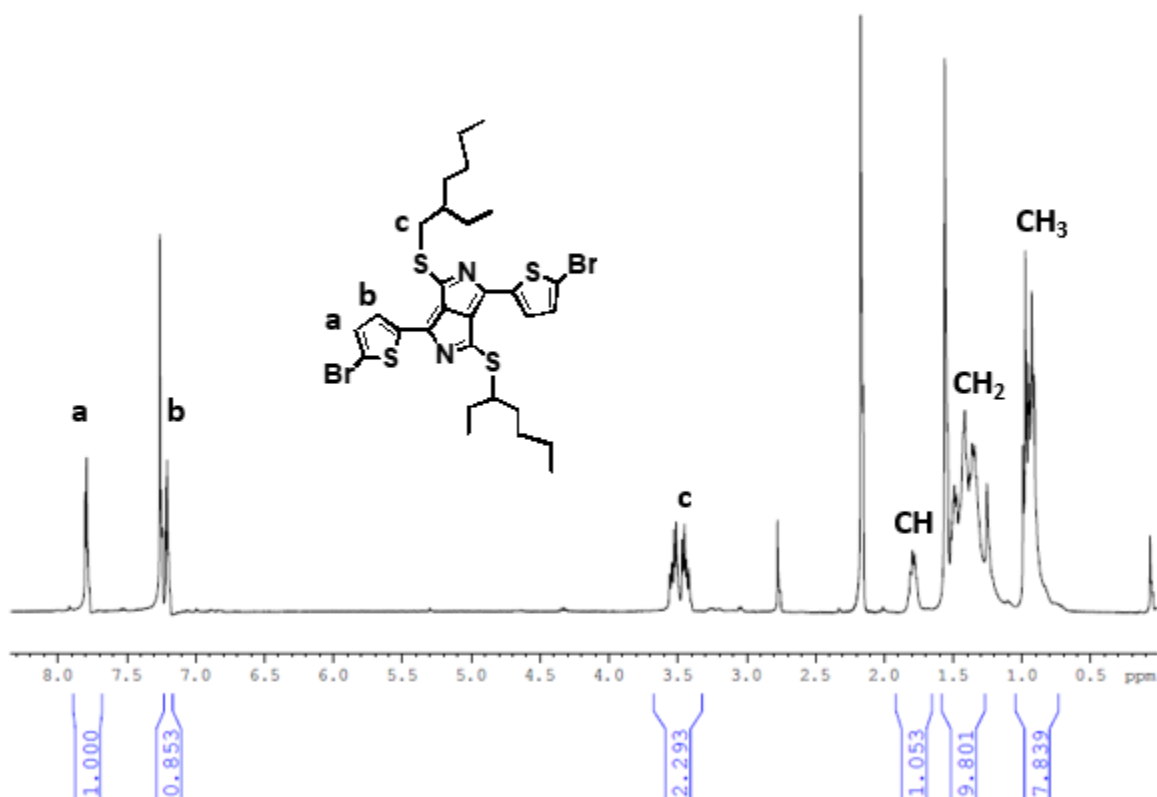


Figure II-12: ¹H NMR spectrum of the dibromo diazapentalene (DAP-Br₂) (CDCl₃, 400 MHz).

^{13}C NMR was also performed and the spectrum is shown below in **Figure II-13**. It is worth mentioning that although carbon (**h**) should be more deshielded than carbon (**e**) due to sulfur, DEPT 135 proved that the carbon at 40 ppm corresponds to CH and not CH_2 .

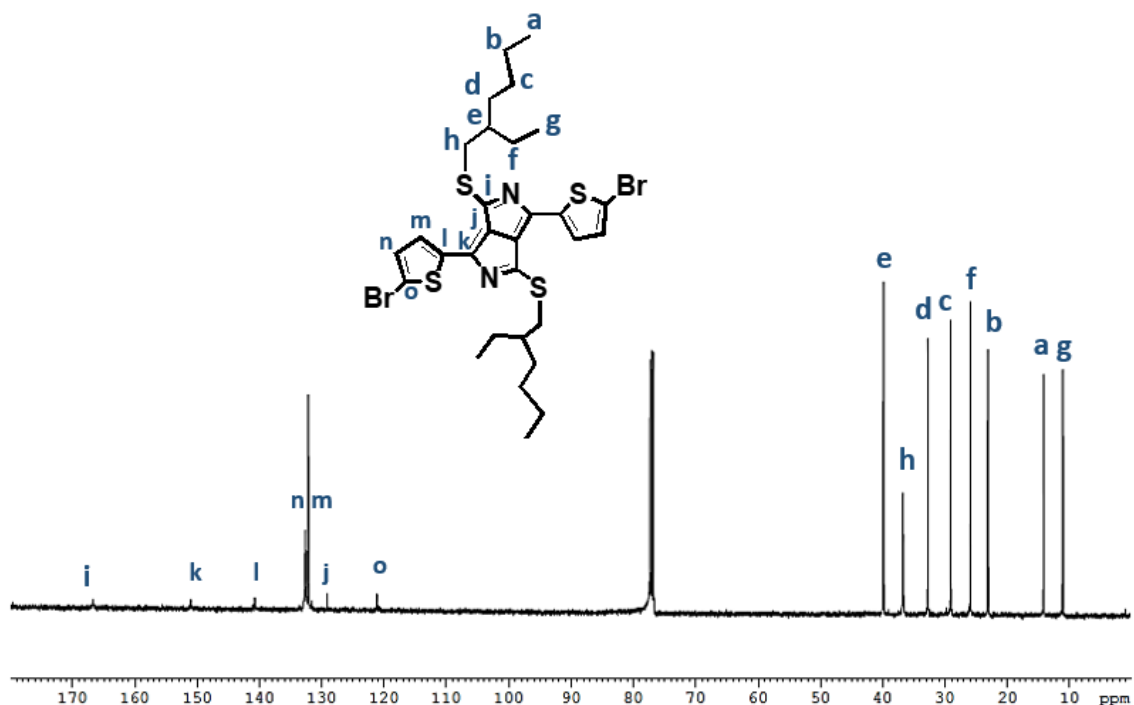


Figure II-13: ^{13}C NMR spectrum of the dibromo diazapentalene (DAP-Br_2) (CDCl_3 , 100 MHz).

d. Optical properties of DPP and DAP monomers

The optical properties of dibrominated DPP and DAP monomers were studied in CHCl_3 solution at room temperature. The UV-vis spectra are shown in **Figure II-14**. The synthesized DPP monomer presents an absorption band between 420 and 582 nm with a maximum absorbance at $\lambda_{\text{max}} = 547$ nm which is due to the transfer of the charges from the thiophene group to the DPP core chromophore. Concerning the DAP monomer, two absorption bands were observed. The first one between 399 and 459 nm corresponds to the $\pi\text{-}\pi^*$ transition and the second one between 491 and 700 nm with a maximum at $\lambda_{\text{max}} = 563$ nm (red-shifted 16 nm in comparison with DPP) corresponds to the intramolecular charge transfer from the thiophene group to the core of the DAP.⁷ The λ_{onset} of DAP monomer is found to be 650 nm which is red-shifted in a value of 65 nm when compared to that of DPP ($\lambda_{\text{onset}} = 585$ nm). It is then possible to calculate the optical bandgap $E_g^{(\text{opt})}$ of each molecule to get 2.1 eV and 1.9 eV for DPP and DAP monomers, respectively. The strongest acceptor characteristic of the DAP monomer is literally responsible for lowering the HOMO level of the molecule which in its turn narrows the bandgap. In other words, the lack in the donation from the lone-pair electrons of the nitrogen in DAP when compared to the DPP monomer is the main contribution behind the HOMO level lowering.⁷

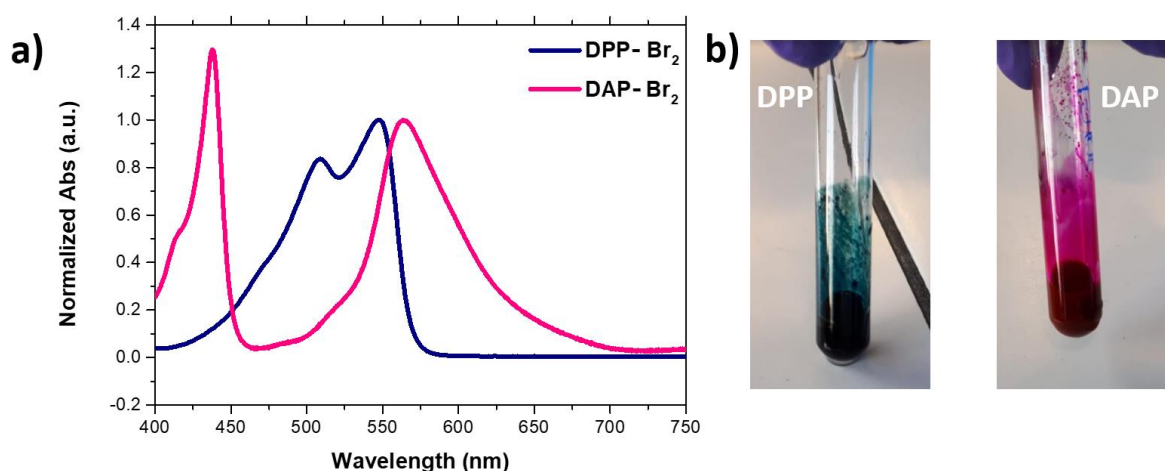


Figure II-14: (a) UV-vis absorption spectra and (b) the images of the synthesized DPP and DAP chloroform-based solutions.

e. The donor monomer 4,4'-bis(2-ethyl-hexyl)-5,5'-bis(trimethyltin)-dithieno[3,2b:2',3'-d]silole (DTS)

As mentioned elsewhere, DTS is an electron donor that is extensively used as a silicon-containing π -conjugated building block.⁸ Although DTS with a di-(trimethylstannyl) groups was previously synthesized,¹¹ our choice was to buy it commercially to save time. The chemical structure and the absorption of DTS is shown in **Figure II-15**.

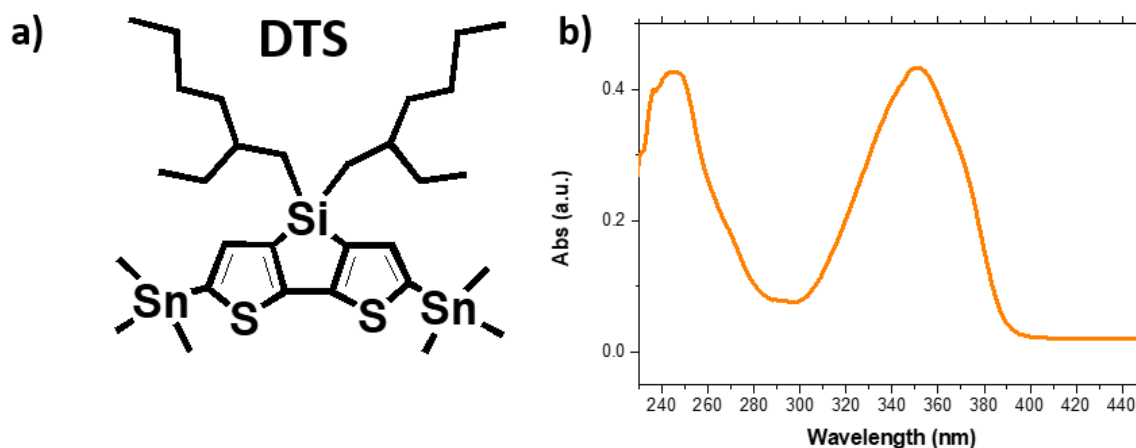


Figure II-15: (a) Chemical structure and (b) UV-vis absorption spectrum in CHCl₃ of the di-stannyl DTS monomer.

IV. Synthesis and characterization of rod-rod block copolymers

a. Preliminary Stille coupling: P3HT-DPP

One of the objectives of this work is to prepare a conjugated diblock copolymer using the Stille coupling by reacting the aromatic halide (Br) of the synthesized P3HT-Br. Thus, the reactivity of the Br group in the synthesized P3HT was first tested with a commercially available stannylated monomer which was a diketopyrrolopyrrole with ethyl-hexyl alkyl chain and a tin (Sn) ends (DPPeH-Sn). The chemical structure and the ^1H NMR spectrum of the DPPeH-Sn monomer is shown in **Figure II-16** and this reagent was used as received without any modifications.

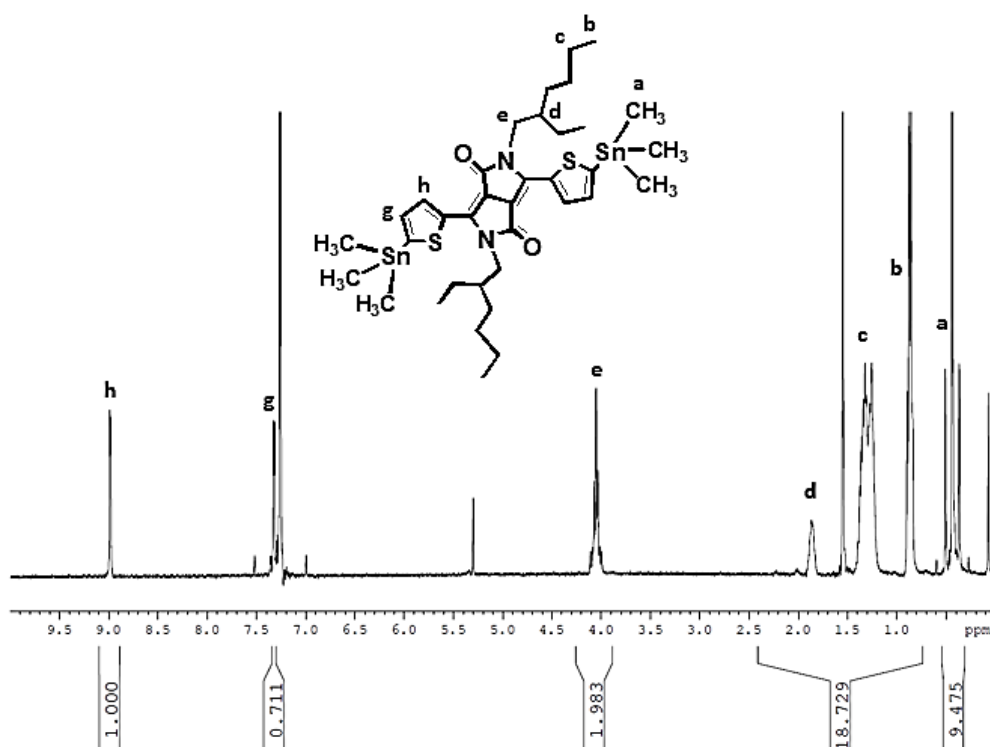
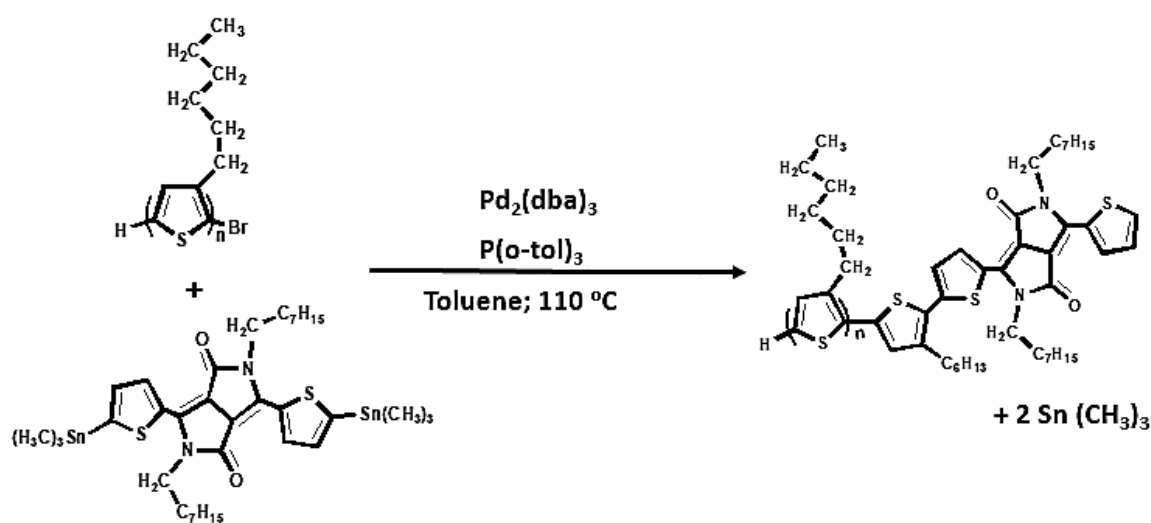


Figure II-16: ^1H NMR spectrum of the commercially available DPPeH-Sn (CDCl_3 , 400 MHz).

First, the bromine-terminated P3HT₂₅ was coupled with DPPeH-Sn monomer *via* a Stille coupling based on a 1:2 ratio. The reaction took place in the presence of tris(dibenzylideneacetone) dipalladium(0) (Pd_2dba_3) catalyst and tri(*o*-tolyl) phosphine $\text{P}(\text{o-tolyl})_3$ ligand in an anhydrous toluene solution as shown in **Scheme II-11**. The combination of palladium catalyst with various phosphine ligands results in an excellent yield. The coupling was carried out at 110 °C under nitrogen atmosphere and kept under agitation for 3 hours. The obtained product was then precipitated in methanol (MeOH). After filtration, the product was purified using Soxhlet successive extractions in acetone and methanol to remove the unreacted monomer then the polymer was recovered in chloroform. The coupling product was dried under vacuum and characterized by different techniques.



Scheme II-11: Coupling between P3HT-Br and DPPeH-Sn monomer.

Since only 1 equivalent of P3HT₂₅ was added with 2 equivalents of DPPeH-Sn, it was expected that the polymer's molar mass will not be intensively changed since a di-system structure composed of (P3HT)_n-DPP is probably formed and not a tri-system structure (P3HT)_n-DPP-(P3HT)_n. This was clearly proved by SEC-THF in which the number average molar mass (M_n) value was increased only from 4500 to 6100 $\text{g}\cdot\text{mol}^{-1}$ due to the monomer coupling. The dispersity was increased from 1.4 to 1.58.

UV-vis spectrometry was used to determine whether there is any change in the absorption behavior of chloroform-based P3HT₂₅ solution before and after coupling. As shown in **Figure II-17**, the spectrum of P3HT₂₅-DPP shows a broad absorption band between 350 and 550 nm similar to that of the starting P3HT₂₅ polymer. Moreover, a new broad absorption band appears between 550 and 800 nm, coming from the coupled DPPeH-Sn monomer.

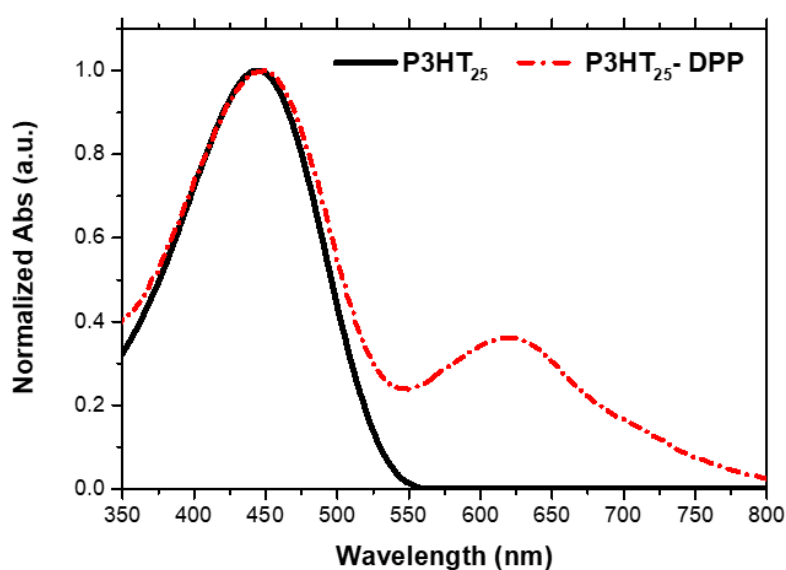


Figure II-17: Normalized UV-vis absorption spectra of the starting P3HT₂₅ and P3HT₂₅-DPP.

^1H NMR was studied for P3HT₂₅-DPP. It was easy to identify the peaks related to each of the P3HT₂₅ and DPP-Sn monomers since DPP-Sn was added in 2 equivalents with respect to the polymer. Thus, as shown in the ^1H NMR spectrum of **Figure II-18**, we could identify the aromatic peaks of the thiophene unit of DPP (proton **c**), in addition to proton (**b**) which is assigned to the CH₂ alkyl chain in the α -N position.

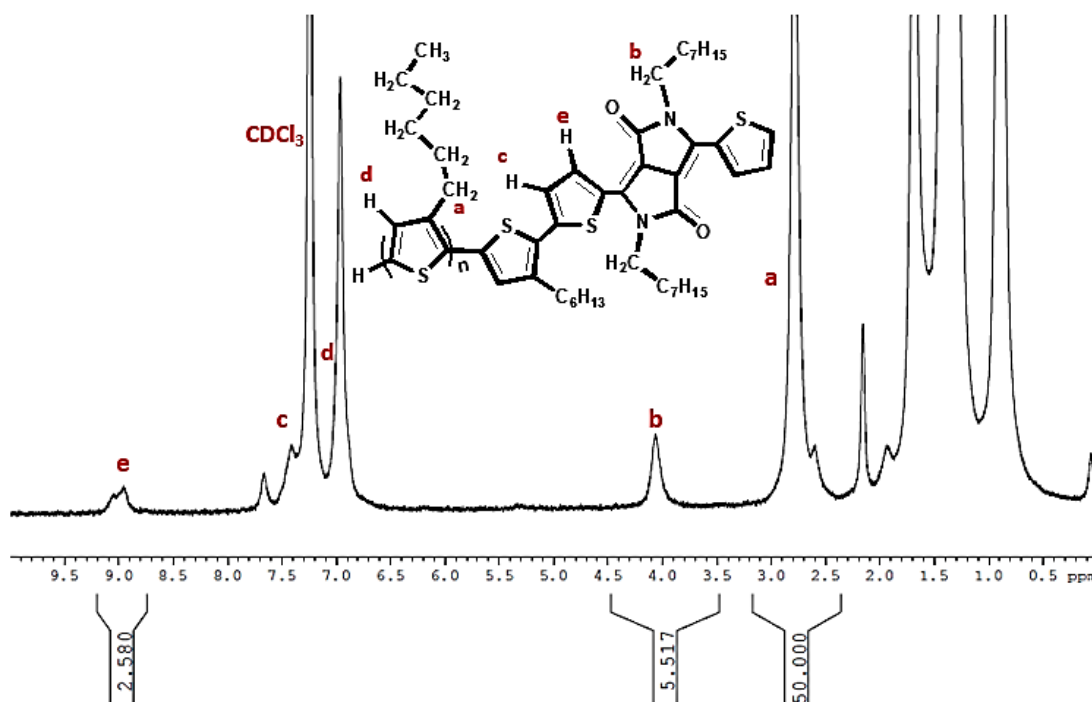


Figure II-18: ^1H NMR spectrum of P3HT₂₅-DPP (CDCl_3 , 400 MHz).

On the contrary, 2:1 ratio of P3HT₃₇ and DPPeH-Sn monomer was also tested to be compared with the 1:2 ratio. The same reaction conditions were followed in which the final product was collected after Soxhlet successive extractions.

In this case, the incorporation of 2 equivalents of P3HT₃₇ should facilitate the formation of the tri-system structure ((P3HT)_n-DPP-(P3HT)_n). This was proved by the clear shift in the elution volume of the coupling product to a lower value as shown in the size exclusion chromatograms of **Figure II-19a**. A higher number average molar mass for the coupling product ($M_n=19,000 \text{ g}\cdot\text{mol}^{-1}$) was obtained when compared to the starting P3HT₃₇ ($M_n=13,000 \text{ g}\cdot\text{mol}^{-1}$) with an increase of dispersity from 1.7 to 2.04. The large increase in the dispersity and the small increase in the average molar mass of the sample could be attributed to the synthesis of a mixture of (P3HT)_n-DPP-(P3HT)_n and (P3HT)_n-DPP.

Additionally, P3HT₃₇-DPP reveals an absorption band related to P3HT₃₇ between 350 and 550 nm and a very slight absorption peak between 550 and 750 nm originated from the absorption of DPP-Sn (**Figure II-19b**). The intensity of this additional peak is not as high as in the case of P3HT₂₅-DPP.

This could be attributed to the higher contribution of P3HT₃₇ which was added in a double amount than that of DPP-Sn (2:1 ratio), unlike in the case of P3HT₂₅-DPP in which the DPP-Sn was added in 2 equivalents (1:2 ratio).

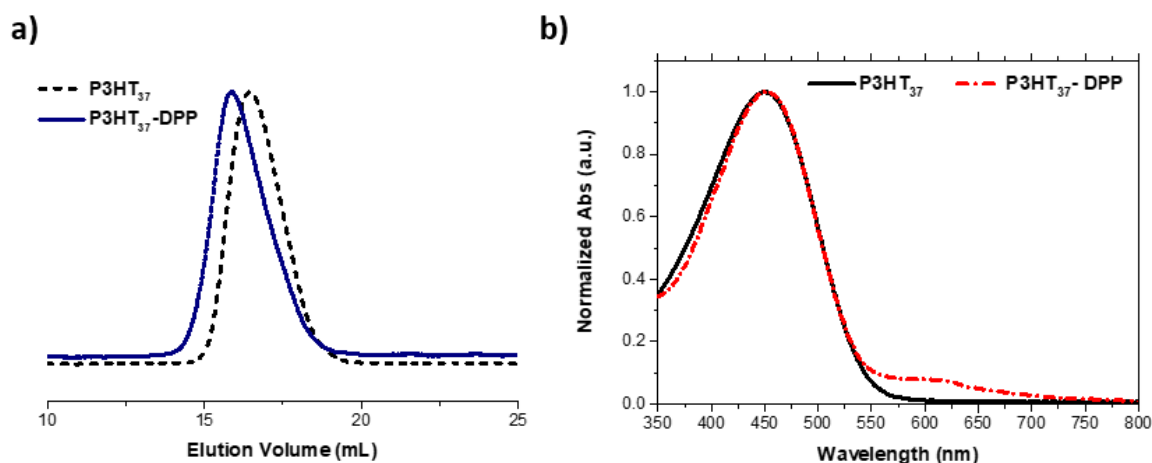


Figure II-19: (a) Normalized size exclusion chromatograms using UV detector at $\lambda=450$ nm and (b) normalized UV-vis absorption spectra of the starting P3HT₃₇ and P3HT₃₇-DPP.

In ¹H NMR spectrum, it was difficult to identify the peaks related to the ending DPP probably due to the higher amount of P3HT in the medium.

As a conclusion and depending on the characterization data of the coupling products, we could approve that coupling was successful in which the bromine end of the synthesized P3HT reacted with the Sn group of the DPP-Sn monomer *via* a Stille coupling reaction to form a new C-C bond between P3HT and DPP. Based on these results, additional polymerization experiments were settled.

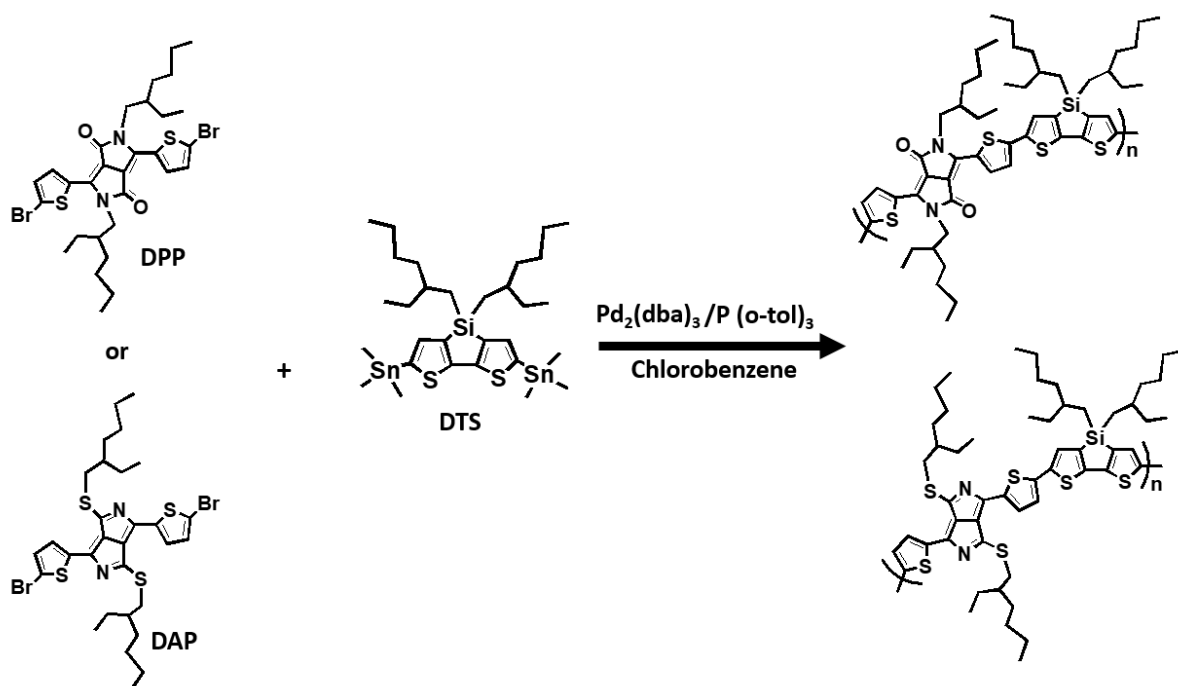
b. Synthesis of P(DTS-DPP) and P(DTS-DAP) alternated copolymers

Since the main objective of this work is to synthesize diblock copolymers based on ternary monomer blend consisting of P3HT, DTS and DPP or DAP, control P(DTS-DPP) and P(DTS-DAP) polymers were synthesized in the absence of P3HT end-capping agent for the comparison with the synthesized diblock copolymers.

In this regard, DPP-Br₂ and DAP-Br₂ monomers were polymerized *via* Stille polycondensation with stanilated DTS following the procedure of Khelifi *et al.*⁴⁵ It was catalyzed by a palladium complex, the dipalladium (dibenzylideneacetone) (Pd₂(dba)₃) and tri(*o*-tolyl) phosphine (P(*o*-tolyl)₃) ligand in chlorobenzene and under nitrogen atmosphere (**Scheme II-12**). It is worth mentioning that this polymerization may yield to high molar mass polymers that may face solubility problems in commonly used organic solvents. Thus, it is important to synthesize moderate molar mass chains to be solution processable. To a certain extent, this can be done by controlling the viscosity of the polymerization medium and stop the reaction when desired.

The final viscous solution was precipitated in cold methanol and then filtered. It is important to purify the polymer to get rid of the metallic by-products that can be formed, the remaining catalyst and ligand, the unreacted monomers in addition to the small chain polymers like oligomers. The purification step was performed using Soxhlet successive extractions in different solvents including acetone, methanol and cyclohexane.

The product was finally recovered in chloroform, then the solvent was evaporated to obtain the final dark black polymer with a high yield ranging between 75 and 82%.



Scheme II-12: Stille coupling polycondensation for the synthesis of P(DTS-DPP) and P(DTS-DAP).

The synthesized P(DTS-DPP) and P(DTS-DAP) were characterized by ^1H NMR in $\text{C}_2\text{D}_2\text{Cl}_4$ at a high temperature (80 °C) because of the difficulty to observe the aromatic peaks at room temperature due to lack of solubility. **Figure II-20** shows the ^1H NMR spectrum of the synthesized P(DTS-DPP). This spectrum reveals distinct peaks for protons **b** (8.92 ppm) and **a, c** (7.49-7.15 ppm). These peaks correspond to the aromatic protons of the thiophene units. The spectrum shows as well a peak at 4.11 ppm, assigned to the alkyl (CH_2) substituent in the α -nitrogen position (proton **d**). The aliphatic protons in the alkyl chain (CH , CH_2 and CH_3) appear between 2.00 and 0.90 ppm.

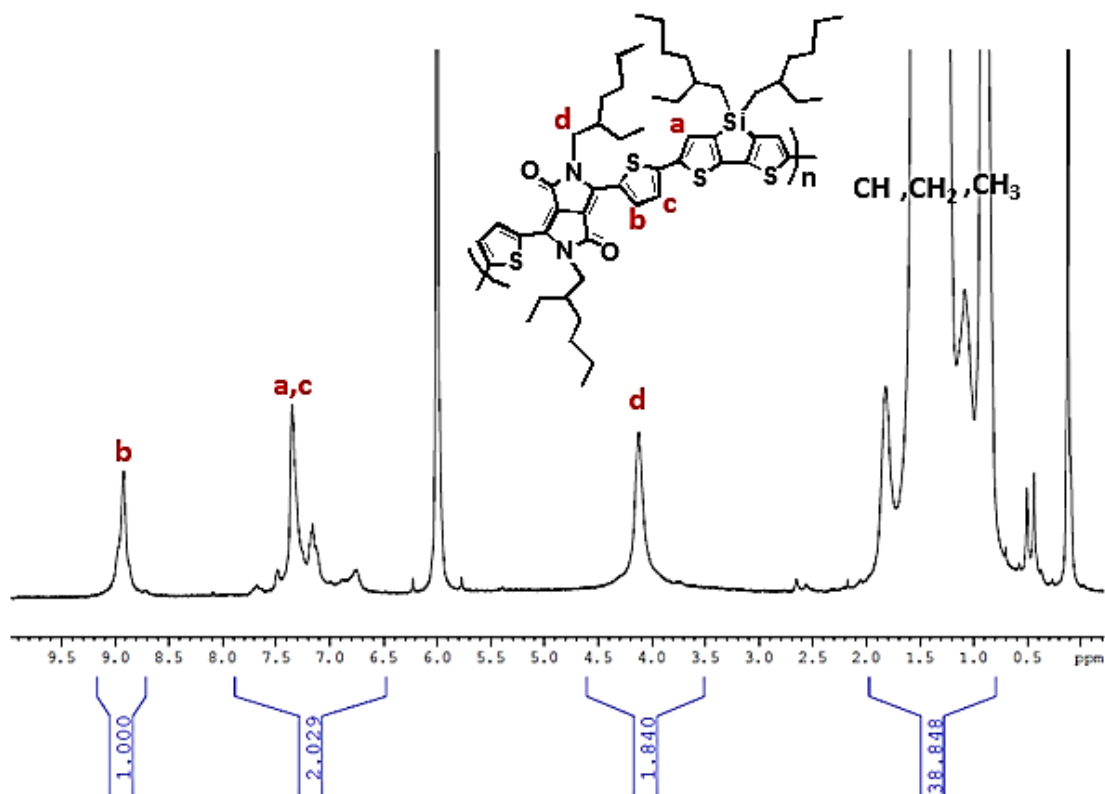


Figure II- 20: ^1H NMR spectrum of the synthesized P(DTS-DPP) ($\text{C}_2\text{D}_2\text{Cl}_4$, 400 MHz).

P(DTS-DAP) was also analyzed by ^1H NMR in $\text{C}_2\text{D}_2\text{Cl}_4$ at $80\text{ }^\circ\text{C}$ and the ^1H NMR spectrum is shown in **Figure II-21**. The same peaks were assigned to the aromatic protons of the thiophene unit, **b** (8.08 ppm) and **a, c** (between 7.39 and 7.2 ppm). The peak between 3.61 and 3.59 ppm can be assigned to the alkyl (CH_2) substituent in the α -sulfur position (proton **d**). Additionally, the aliphatic protons in the alkyl chain (CH , CH_2 and CH_3) appear between 2.59 and 0.72 ppm. According to the assigned peaks from the ^1H NMR spectra of both P(DTS-DPP) and P(DTS-DAP), we could conclude that the polymerization reactions were successfully performed.

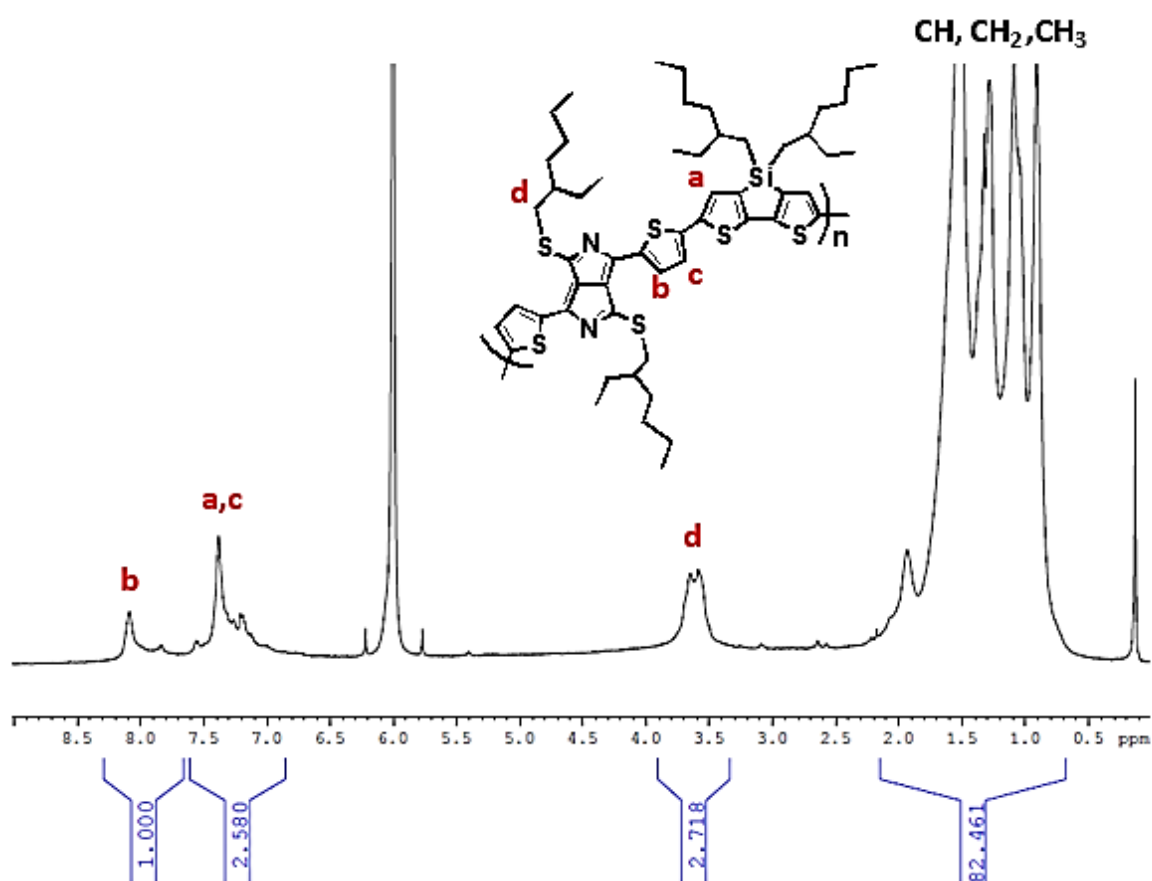


Figure II-21: ¹H NMR spectrum of the synthesized P(DTS-DAP) (C₂D₂Cl₄, 400 MHz).

The optical properties of the synthesized copolymers P(DTS-DPP) and P(DTS-DAP) were investigated in chloroform. The absorption spectra shown in **Figure II-22** revealed for both copolymers a broad absorption in the near-IR region extending from 400 nm to 900 nm in the case of P(DTS-DPP) and to 1080 nm in the case of P(DTS-DAP). This absorption is characterized by two bands. The first one is at low wavelength (between 400 to 600 nm) and corresponds to the π - π^* transition while the other peak found at higher wavelength is due to the intramolecular charge transfer from the donor unit to the acceptor moieties. These two distinct absorption bands are referred as high energy and low energy absorption bands, respectively.⁴⁶ Concerning P(DTS-DPP), the maximum absorption is at $\lambda_{\text{max}}=800$ nm, while for P(DTS-DAP) it is red-shifted to a higher wavelength (850 nm). The substitution of the DPP by the DAP monomer which exhibits a more electron deficient nature in the copolymer structure is the reason behind this shift to a higher wavelength in the near-IR region.⁴⁷

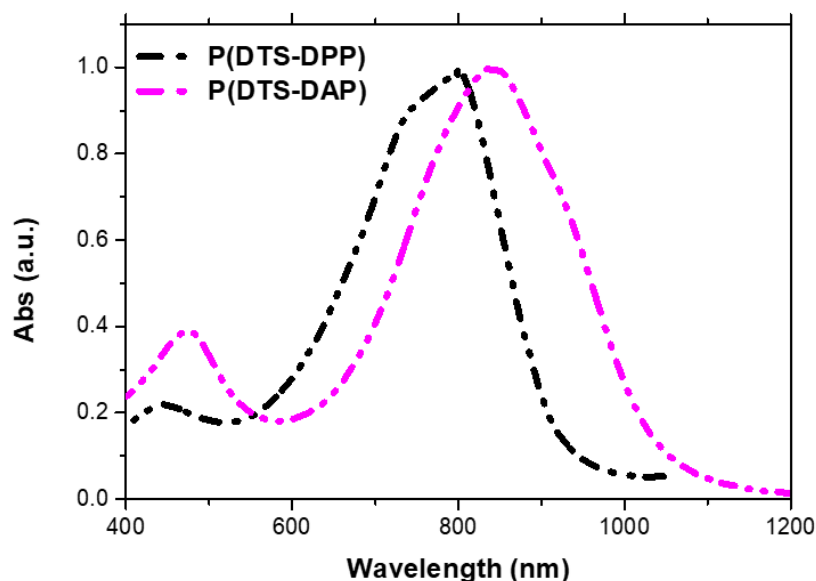


Figure II-22: Normalized UV-vis-NIR absorption spectra of P(DTS-DPP) and P(DTS-DAP) copolymers in $CHCl_3$.

The optical properties of the synthesized copolymers are summarized in **Table II-4**.

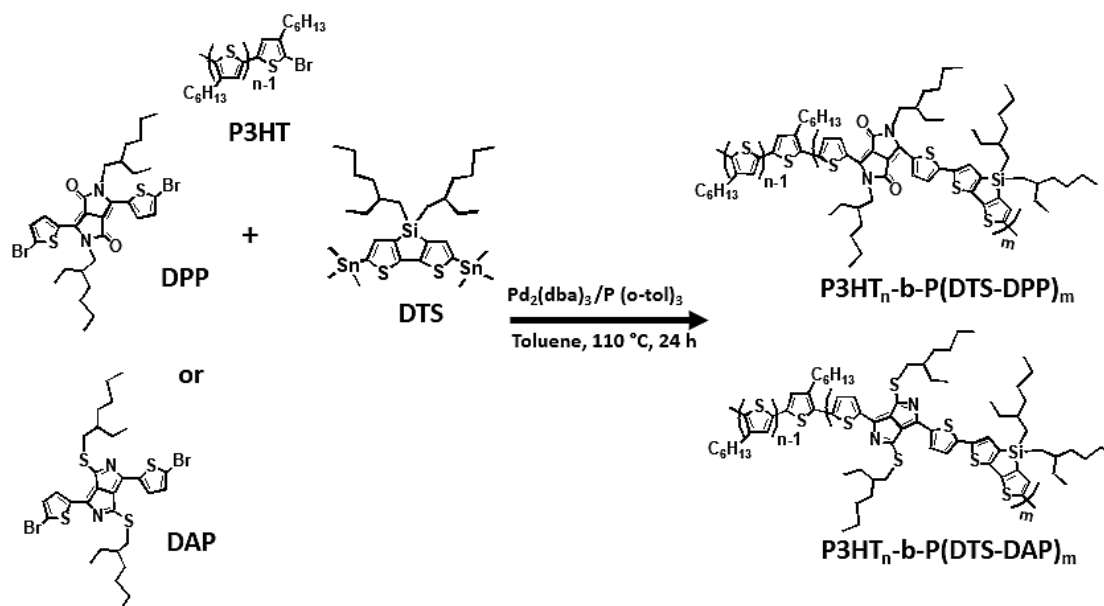
Table II-4: Optical properties of the synthesized P(DTS-DPP) and P(DTS-DAP) solutions.

Polymer	λ_{\max} (nm)	λ_{onset} (nm)	$E_g^{(\text{opt})}$ (eV)
DPP	547	585	2.1
DAP	563	650	1.9
P(DTS-DPP)	800	975	1.27
P(DTS-DAP)	850	1080	1.14

Further characterization techniques were performed with the synthesized alternated copolymers but these are discussed in the next section of this chapter for comparison with the synthesized conjugated diblock copolymers.

c. Synthesis of conjugated diblock copolymers (CBCPs)

The general objective of this chapter is to use the “end-functional coupling method” for designing novel diblock copolymers based on the complementary absorption and the donor-acceptor relationship. Block copolymers could lead to an ordered morphology that is interesting for OPV applications.⁴⁸ In such kind of systems, P3HT serves as an electron donor while the second block constituting of two monomers; di-stannilated dithienosilole (DTS) and dibromodiketopyrrolopyrrole (DPP) or DTS and diazapentalene (DAP) serves as an electron acceptor.⁴⁹ The bromo end-functionalized P3HT is used as a monobrominated end-capping agent in the Stille polycondensation of a mixture of DTS with DPP or DTS with DAP. The reaction mixture was heated at 110 °C in anhydrous toluene using $Pd_2(dba)_3/P(o\text{-tolyl})_3$ catalyst system for 24 hours under inert atmosphere as shown in **Scheme II-13**. Pd(0) catalyst was generated in situ from $[Pd_2(dba)_3]$ and $P(o\text{-tolyl})_3$ ligand.



Scheme II-13: Stille Coupling Polymerization for the synthesis of $P3HT_n\text{-}b\text{-}P(\text{DTS-DPP})_m$ and $P3HT_n\text{-}b\text{-}P(\text{DTS-DAP})_m$.

This polycondensation led to the synthesis of poly(3-hexylthiophene)-*block*-poly(dithienosilole-diketopyrrolopyrrole), $P3HT\text{-}b\text{-}P(\text{DTS-DPP})$ or poly(3-hexylthiophene)-*block*-poly(dithienosilole-diazapentalene), $P3HT\text{-}b\text{-}P(\text{DTS-DAP})$.

The stoichiometry of monomers and end-capping agent in this reaction is a key factor that predetermines the length of the low-bandgap block. In this regard, the stoichiometry of the species was maintained according to **Equation 5**.



In which N_A , N_B , $N_{B'}$ represent the mole number of stannate functions and bromide groups pertaining to the DPP or DAP monomer and to the end-capping agent (P3HT), respectively. N_{DTS} , N_{DXP} and N_{P3HT} represent the number of DTS, DPP or DAP monomers and P3HT end-capper, respectively. By following this stoichiometry, the total number of aryl bromides is equal to the total number of aryl stannanes and the formation of chains containing P3HT is promoted.

The number average degree of polymerization (\overline{DP}_n) of polymers obtained in the case of A-A and B-B polycondensation, like DTS and DPP or DAP, with an end-capping agent, can be predicted thanks to the Carothers equation (**Equation 6**).^{50,51,52}

$$\overline{DP}_n = \frac{1+r}{1+r-2rp} \quad \text{Equation 6}$$

In which r is the ratio of monomer groups, and p is the conversion. It should be noted that in this equation, the calculated \overline{DP}_n counts the number of DTS + DPP or DAP units, so it is twice the number of repeat units n used in the calculation of the number average molecular weight M_n . Therefore, M_n can be determined based on **Equation 7**.

$$\overline{M}_n = M_0 \frac{\overline{DP}_n}{2} + x M_{\text{P3HT}} = \frac{M_0}{2} \frac{1+r}{1+r-2rp} + x M_{\text{P3HT}} \quad \text{Equation 7}$$

where M_0 and M_{P3HT} are the molecular weight of the repeating unit and the end-group, respectively. x is the number of P3HT chains incorporated in the final material, and can be equal to 0, 1 or 2. When a monofunctional reagent (as the end-capping agent) is introduced, the monomer group ratio is defined by **Equation 8**.⁵¹

$$r = \frac{N_A}{N_B + 2N_{B'}} = \frac{2N_{DTS}}{2N_{DXP} + 2N_{P3HT}} = \frac{N_{DTS}}{N_{DXP} + N_{P3HT}} \quad \text{Equation 8}$$

Where the factor 2 relative to $N_{B'}$ enters in the equation because the end-capping agent has the same effect on the degree of polymerization as the difunctional monomer therefore is two times more effective.

At the end of all polymerization reactions, the media were first precipitated in cold methanol and subsequently fractionated by Soxhlet successive extraction in acetone, methanol, cyclohexane and the polymer of interest was finally recovered from chloroform.

During purification, the acetone and cyclohexane fractions were analyzed by UV-visible spectroscopy and size exclusion chromatography (**Figure II-23a and b**) and compared to pure P3HT and block copolymer final fractions (chloroform fraction). From these data, it was easy to identify that acetone removed unbound short P3HT chains, having an absorbance at 450 nm and a chromatogram peak corresponding to the P3HT homopolymer, and a small fraction of oligomers of P(DTS-DPP) with a secondary absorbance peak at 665 nm. Cyclohexane fraction was mainly constituted of P(DTS-DPP) low molar mass homopolymers, with a large SEC peak finishing after P3HT reference elution volume. The low absorbance at 450 nm reveals the absence of P3HT while the large absorbance band from 550 to 850 nm is attributed to the low-bandgap sequence. The cyclohexane fraction containing low molar mass polymers, means that during the reaction some DPP and DTS monomers reacted with each other but were not attached to a P3HT chain. The same observation was realized for the DAP-based block copolymers. For all synthesized diblock copolymers the percentage of removed homopolymer from acetone and cyclohexane Soxhlet extraction was around 10 w%. Another conclusion of this washing procedure that removes homopolymers is that the conversion must be below 1 for all the synthesized copolymers.

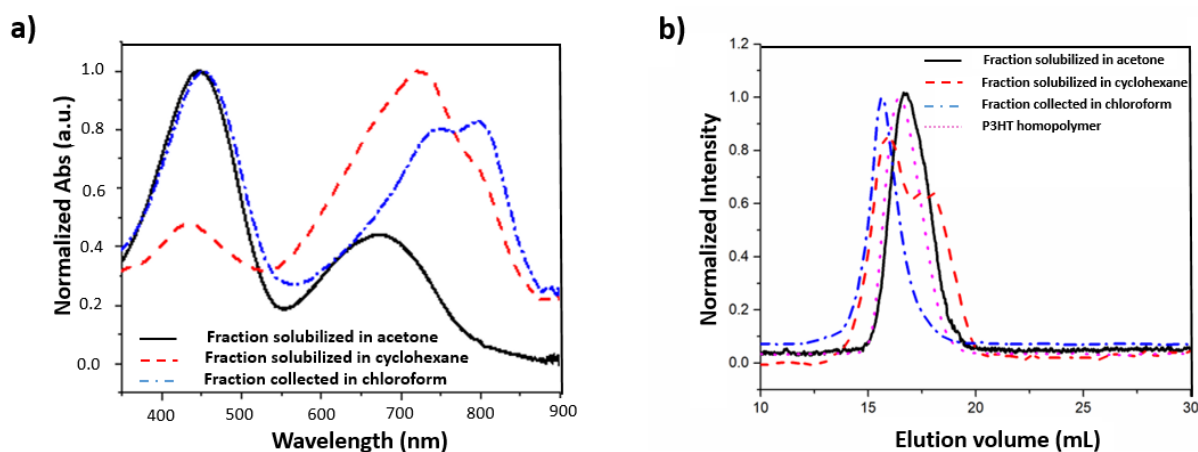


Figure II-23: (a) UV-vis absorption spectra of the fractions extracted from Soxhlet purification of DPP-based copolymer and (b) the SEC chromatograms of the fractions.

i. DPP-based block copolymers

Several DPP-based block copolymers having different degree of polymerization were synthesized with general yield between 70 and 85% by simply varying the ratios of the starting materials according to the Carothers equations (**Table II-5**).

Table II-5: Theoretical molecular characteristics of the synthesized DPP-based CBCPs.

Entry	Polymer	N ^a A	N ^a B	N ^a C	DP _n P3HT-	M _n th ^b
		DTS	DPP	P3HT-Br	DP _n A-B th ^b	
1	P3HT ₂₅	-	-	-	25-0	-
2	P3HT _{25-b} -P(DTS-DPP) ₈	1	0.96	0.08	25-12	15,500
3	P3HT ₃₇	-	-	-	37-0	-
4	P3HT _{37-b} -P(DTS-DPP) ₁₉	1	0.98	0.04	37-25	29,300
5	P3HT _{37-b} -P(DTS-DPP) ₄	1	0.92	0.16	37-6	11,750
6	P3HT ₉₆	-	-	-	96-0	-
7	P3HT _{96-b} -P(DTS-DPP) ₁₃	1	0.98	0.04	96-25	39,500
8	P3HT ₂₄₀	-	-	-	240-0	-
9	P3HT _{240-b} -P(DTS-DPP) ₁₁	1	0.98	0.04	240-25	63,000

^a feed ratio calculated according to Equation 5 and ^b calculated from the Carothers equation

The first block copolymer to be discussed is reported in **Table II-5, entry 4**. This copolymer was synthesized from P3HT₃₇ using DPP and DTS monomers with a feed molar composition of 1/0.98/0.04 equivalent of DTS/DPP/P3HT, satisfying **Equation 5**. It was recovered from chloroform Soxhlet fraction and analyzed by SEC. **Figure II-24** shows the superposition of the pure P3HT₃₇ and the P3HT_{37-b}-P(DTS-DPP)₁₉ chromatograms using UV detector at two wavelengths; 450 nm to screen mainly the presence of the P3HT block and 720 nm to reveal the low-bandgap block.

Comparing both chromatograms (P3HT₃₇ and the diblock) registered at 450 nm, a clear shift towards a low elution volume is observed in the case of diblock, meaning an increase of the molar mass. The dispersity was increased from 1.7 to 3.4 because of the step-growth mechanism of the polycondensation. When the UV detector was set at 720 nm, the chromatogram perfectly matches the one at 450 nm meaning that the low-bandgap block has the same retention time as that of the P3HT block, proving their attachment.

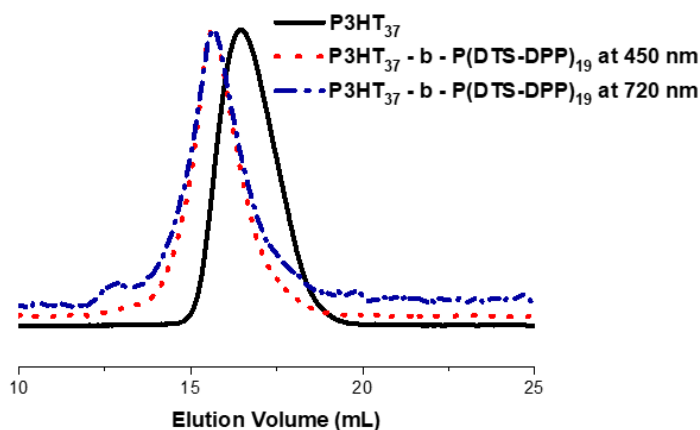


Figure II-24: Size exclusion chromatograms using UV detector at 450 and 720 nm of the synthesized $P3HT_{37}$ - b - $P(DTS-DPP)_{19}$ in comparison with the starting $P3HT_{37}$ -Br at 450 nm.

The molar masses M_n obtained by SEC were $13,000 \text{ g}\cdot\text{mol}^{-1}$ for $P3HT_{37}$ and $26,000 \text{ g}\cdot\text{mol}^{-1}$ for the copolymer as calculated from conventional calibration using polystyrene samples (**Table II-6, entry 4**).

To obtain more accurate values, ^1H NMR was performed to estimate the ratio between the $P(DTS-DPP)$ repetitive unit and the $P3HT$ ($N_{DTS-DPP}/N_{P3HT}$). **Figure II-25** shows the spectrum of $P3HT_{37}$ - b - $P(DTS-DPP)_{19}$ in $\text{C}_2\text{D}_2\text{Cl}_4$. The comparison of the signal integral at 2.9 ppm pertaining to the CH_2 proton in the alpha position of the thiophene cycle of $P3HT$ (2 protons *per* monomer unit) with the one at 4.2 ppm attributed to the CH_2 in the alpha position of the nitrogen in the DPP alkyl chains (4 protons *per* monomer unit) allowed to calculate a $N_{DTS-DPP}/N_{P3HT}$ ratio of 19.

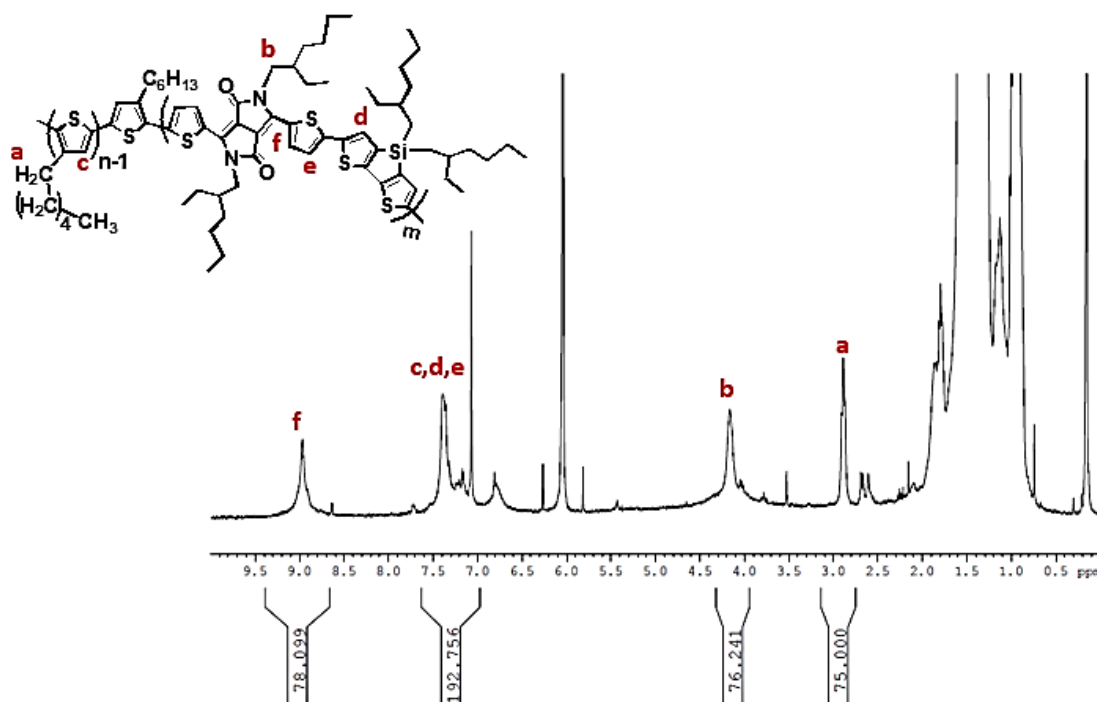


Figure II-25: ^1H NMR spectrum of the synthesized $P3HT_{37}$ - b - $P(DTS-DPP)_{19}$ ($\text{C}_2\text{D}_2\text{Cl}_4$, 400MHz).

Following the Carothers equation (**Equation 6**), at 100% conversion, the theoretical DP_n of the low-bandgap block should be 100, corresponding to 50 DTS-DPP repetitive units. Since P3HT has been included in the stoichiometry, P3HT chains should be present at both ends of the low-bandgap macromolecules to produce a triblock. Therefore, for this theoretical polymer, the $N_{DTS-DPP}/N_{P3HT}$ ratio is 50/2 or 25 (reported in **Table II-5**). The difference between the theory and the experiment (25 to 19) was low and may be due to an incomplete conversion, since unbound homopolymers have been found and extracted from the copolymer by Soxhlet extraction. Now, with an incomplete conversion, there may be a mixture of diblock $P3HT_{37}-b-P(DTS-DPP)_{19}$ and triblock $P3HT_{37}-b-P(DTS-DPP)_{38}-b-P3HT_{37}$ copolymers. Since the dispersity of the copolymer is high, chromatograms could not completely rule out the presence of triblock even though no shoulder in the high molar masses was detected. Thus, NMR was used for diffusion ordered spectroscopy (DOSY) to determine the diffusion coefficient of the species in the copolymer sample. Samples of P3HT macroinitiator and diblock copolymer were prepared under the same conditions regarding concentration and were analyzed under the same temperature for comparison. As shown in **Figure II-26**, the diffusion coefficient of $P3HT_{37}-b-P(DTS-DPP)_{19}$ shows lower value ($2.45 \times 10^{-11} \text{ m}^2 \cdot \text{s}^{-1}$) than that of $P3HT_{37}$ macroinitiator ($4.55 \times 10^{-11} \text{ m}^2 \cdot \text{s}^{-1}$). This can at least prove the presence of copolymer products having different hydrodynamic radii from those of the macroinitiator. Moreover, the diblock shows only one diffusion coefficient with all the protons pertaining to $P3HT_{37}$ (at $\delta = 3$ and 7 ppm) and the $P(DTS-DPP)$ (at $\delta = 9$ and 7.5 ppm) blocks aligned. This is a clear indication that only one kind of macromolecules has been synthesized, and since the conversion is incomplete, the formation of triblock is excluded.

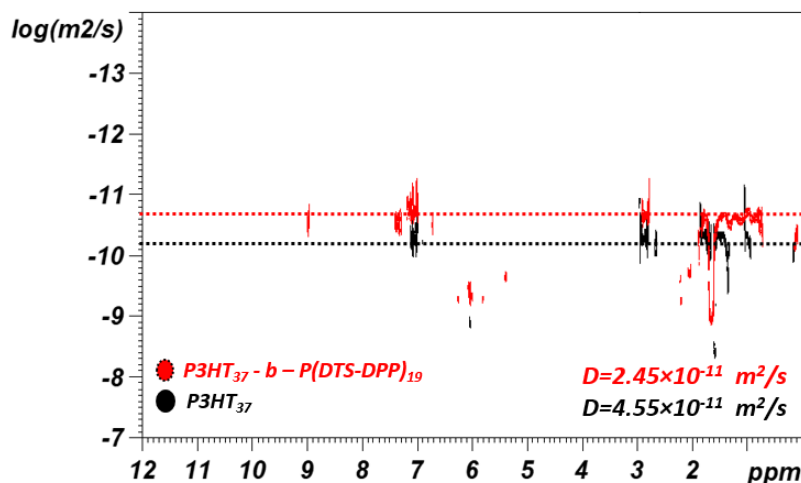


Figure II-26: DOSY NMR of $P3HT_{37}-b-P(DTS-DPP)_{19}$ in red superimposed with the one of $P3HT_{37}$ reference in black ($C_2D_2Cl_4$, 400 MHz).

Therefore, the degree of polymerization and molar masses calculated from 1H NMR based on $N_{DTS-DPP}/N_{P3HT}$ ratio while considering the formation of diblock copolymers are shown in **Table II-6**. The different synthesized CBCPs were named in this report based on these DP_n values.

Table II-6: Experimental molecular characteristics of the synthesized DPP-based CBCPs.

Entry	Polymer	DP _n P3HT-	DP _n P3HT-	M _n th ^a	M _n ^b	M _n ^c	Đ ^c
		DP _n A-B th ^a	DP _n A-B ^b				
1	P3HT ₂₅	25-0	25-0	-	4150	4500	1.4
2	P3HT ₂₅ -b-P(DTS-DPP) ₈	25-12	25-8	15,500	11,600	22,750	2.8
3	P3HT ₃₇	37-0	37-0	-	6150	13,000	1.7
4	P3HT ₃₇ -b-P(DTS-DPP) ₁₉	37-25	37-19	29,300	24,000	26,000	3.4
5	P3HT ₃₇ -b-P(DTS-DPP) ₄	37-6	37-4	11,750	9,900	24,000	7.3
6	P3HT ₉₆	96-0	96-0	-	16,000	16,000	1.4
7	P3HT ₉₆ -b-P(DTS-DPP) ₁₃	96-25	96-13	39,500	28,160	26,300	2.1
8	P3HT ₂₄₀	240-0	240-0	-	40,000	19,000	2.1
9	P3HT ₂₄₀ -b-P(DTS-DPP) ₁₁	240-25	240-11	63,000	50,200	26,700	2.1

^a calculated from the Carothers equation, ^b calculated from ¹H NMR and ^c measured by SEC-THF using polystyrene calibration

Following the same procedure, another block copolymer was synthesized from 0.16 eq of P3HT₃₇ with 1 eq of DTS and 0.92 eq of DPP, named P3HT₃₇-b-P(DTS-DPP)₄ (Table II-5, entry 5). According to the Carothers equation, a theoretical DP_n of 26 should be found at complete conversion, *i.e.* N_{DTS-DPP}/N_{P3HT} ratio of 6.

This time, size exclusion chromatography (Figure II-27) showed, in addition to the shift of the P3HT signal due to the formation of the diblock copolymer (elution volume around 16 mL), a shoulder corresponding to higher molar masses (elution volume of 13 mL), probably due to the presence of a non-negligible fraction of triblock copolymer. Since the equivalent of P3HT macromonomer was 4 times higher than in the previous polymerization, the introduction of P3HT monofunctional reagent must also be higher leading to the formation of a certain amount of P3HT₃₇-b-P(DTS-DPP)₈-b-P3HT₃₇. As a consequence of this blend of copolymers, the dispersity of the sample was quite high, Đ = 7.3.

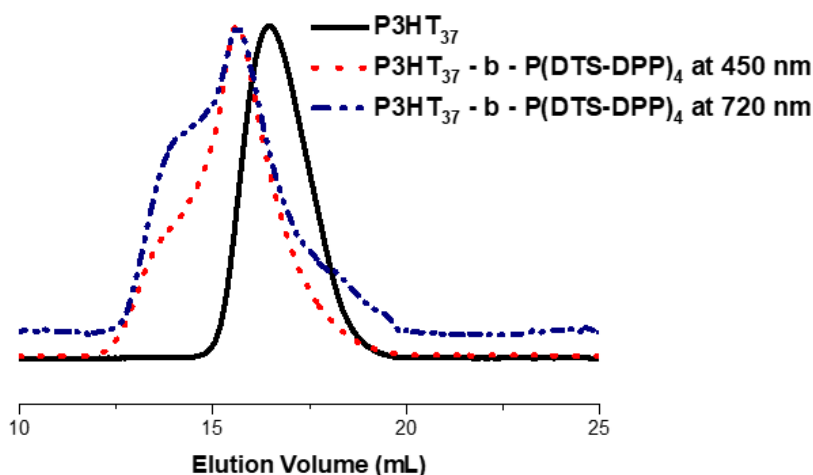


Figure II-27: Size exclusion chromatograms using UV detector at 450 and 720 nm of the synthesized P3HT₃₇-b-P(DTS-DPP)₄ in comparison with the starting P3HT₃₇-Br at 450 nm.

The purified polymer was characterized by ^1H NMR (**Figure II-28**) and the experimental $N_{\text{DTS-DPP}}/N_{\text{P3HT}}$ was 4, in close agreement with the theoretical one. M_n calculated from this value was $9900 \text{ g}\cdot\text{mol}^{-1}$ (**Table II-6, entry 5**).

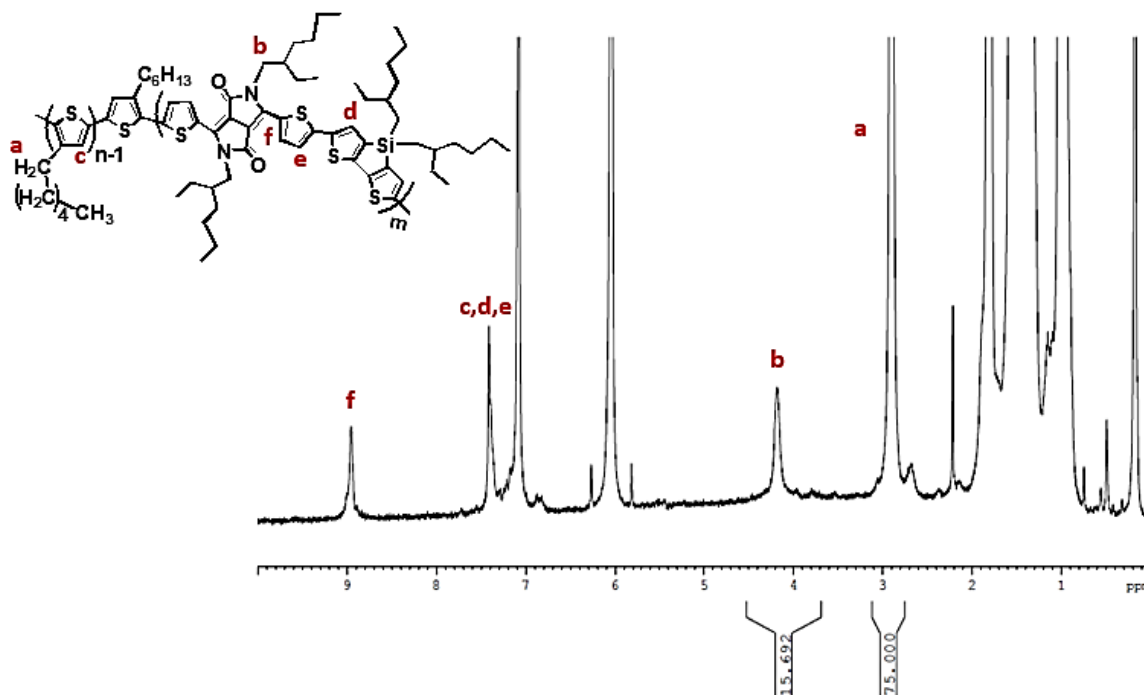


Figure II-28: ^1H NMR spectrum of the synthesized P3HT₃₇-b-P(DTS-DPP)₄ ($\text{C}_2\text{D}_2\text{Cl}_4$, 400 MHz).

To gain more information regarding the synthesized diblock copolymers, SEC using toluene as elution solvent was also performed using diode array detector (DAD) recording the chromatograms sequentially from 400 to 800 nm. **Figure II-29a** shows the superposition of P3HT₃₇-b-P(DTS-DPP)₄ chromatograms collected at 500 and 700 nm, with that of P3HT₃₇ at 500 nm. **Figure II-29b** is a 3-dimensional (3D) image of the P3HT₃₇-b-P(DTS-DPP)₄ chromatogram describing the relation between the eluted material and its absorbance and showing the difference in intensity according to the corresponding wavelength. The diblock copolymer was eluted at a lower elution time than P3HT₃₇ revealing its higher molar mass. However, the presence of multiple peaks and shoulders is an indication of its impurity. From an elution time of 16 to 18 min, the presence of low molar mass homo P(DTS-DPP) can be observed with an absorption spectrum characteristic of this polymer. Also, homo P3HT can be seen at 13 min. From 10.5 to 13 min, higher molar mass macromolecules are shown with an absorbance spectrum presenting two large bands around 500 nm and 800 nm. This is in agreement with the synthesis of a block copolymer. A weak shoulder can also be observed exactly at 10.7 min that we attribute to the elution of the triblock copolymer. We believe that the elution of the diblock and triblock are almost merged in this chromatography. Indeed, the SEC system in THF is constituted of 4 columns while SEC toluene has only two, therefore the macromolecules separation is less efficient in the latter case.

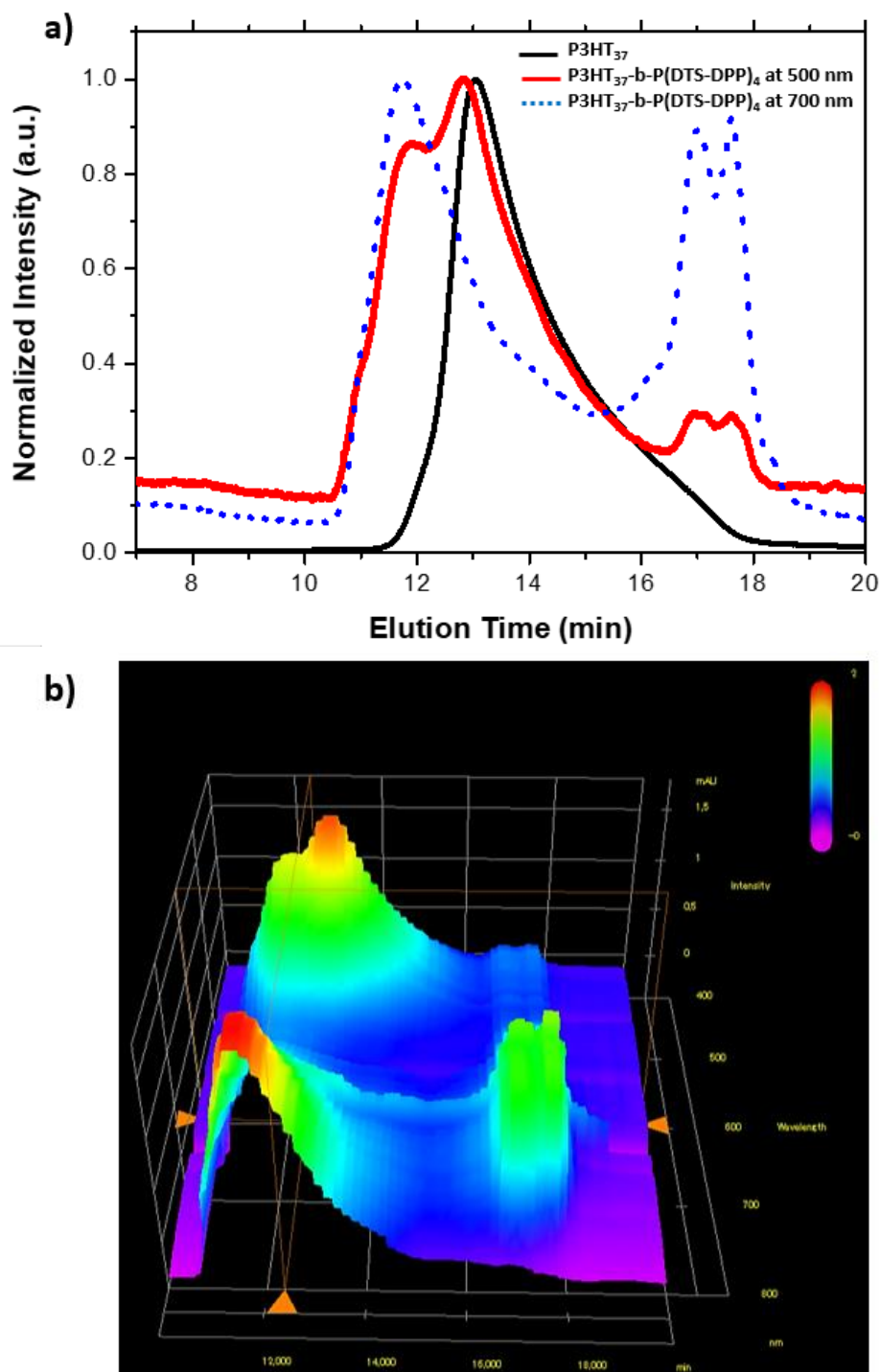


Figure II-29: (a) SEC chromatogram of P3HT₃₇-b-P(DTS-DPP)₄ in toluene and (b) a 3-D plot.

The third block copolymer to be discussed was synthesized from a commercial P3HT with a high molar mass ($40,000 \text{ g}\cdot\text{mol}^{-1}$) which is commonly used to prepare solar cells. P3HT₂₄₀ bearing a bromide end-terminal group, was introduced as a monofunctional reagent (0.04 eq) in the Stille copolymerization with DTS (1 eq) and DPP (0.98 eq) (**Table II-5, entry 9**). ¹H NMR spectrum of P3HT₂₄₀-b-P(DTS-DPP)₁₁ was performed and the $N_{\text{DTS-DPP}}/N_{\text{P3HT}}$ ratio was calculated to be 11 (**Figure II-30**).

This is lower than the expected value of 25 but can be explained by the high molar mass of P3HT, rendering a difficult coupling to form the low-bandgap sequences.

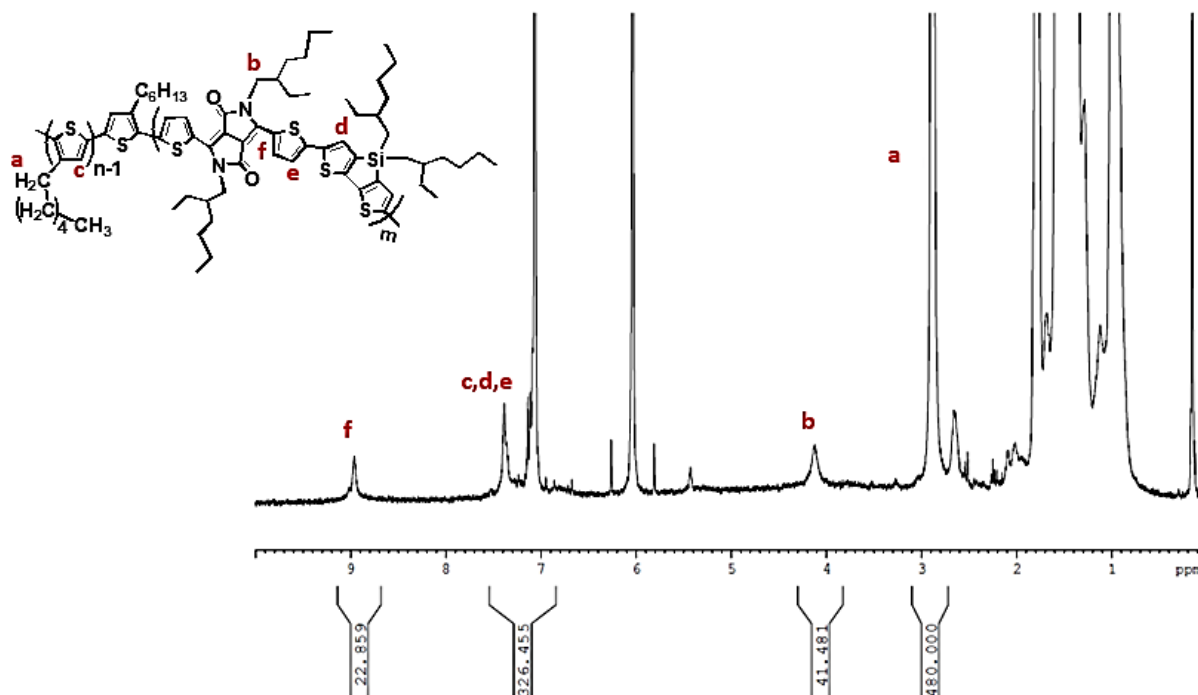


Figure II-30: ^1H NMR spectrum of the synthesized $\text{P3HT}_{240}\text{-}b\text{-P(DTS-DPP)}_{11}$ ($\text{C}_2\text{D}_2\text{Cl}_4$, 400 MHz).

This is in agreement with the SEC analysis (Figure II-31) in which no shoulder pertaining to a hypothetical triblock was observed. The only shift from the P3HT reagent to the high molar mass was attributed to the elaboration of a diblock copolymer as discussed before.

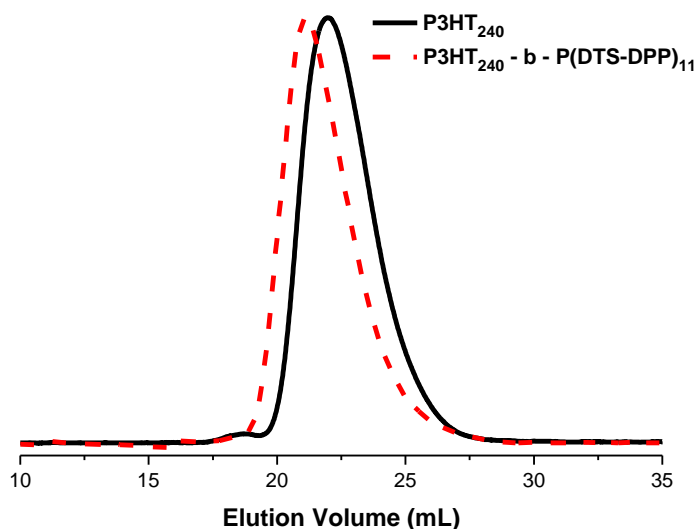


Figure II-31: Size exclusion chromatograms using UV-vis detector at 450 nm of the synthesized $\text{P3HT}_{240}\text{-}b\text{-P(DTS-DPP)}_{11}$ in comparison with the starting P3HT_{240} .

As can be seen in Table II-5 (entries 2 and 7), two other DPP-based block copolymers, $\text{P3HT}_{25}\text{-}b\text{-P(DTS-DPP)}_8$ and $\text{P3HT}_{96}\text{-}b\text{-P(DTS-DPP)}_{13}$ were synthesized and characterized by ^1H NMR and SEC to be used also in our studies. The molecular characteristics are summarized in Table II-6.

ii. DAP-based block copolymers

As previously mentioned, several DAP-based block copolymers having different degree of polymerization were also synthesized in a similar way to DPP-based ones by simply varying the ratios of the starting materials according to the Carothers equations.

Among them, P3HT₃₇-*b*-P(DTS-DAP)₄ and P3HT₃₇-*b*-P(DTS-DAP)₁₁ were synthesized with a feed molar composition of 1/0.92/0.16 and 1/0.98/0.04 equivalent of DTS/DAP/P3HT₃₇, respectively (**Table II-7, entry 4 and 5**, respectively).

Figure II-32 shows a representative ¹H NMR spectrum of this series of block copolymers with the P3HT₃₇-*b*-P(DTS-DAP)₁₁ one. All polymers present the same spectrum with only a difference in terms of proton integration, due to the respective composition of the blocks.

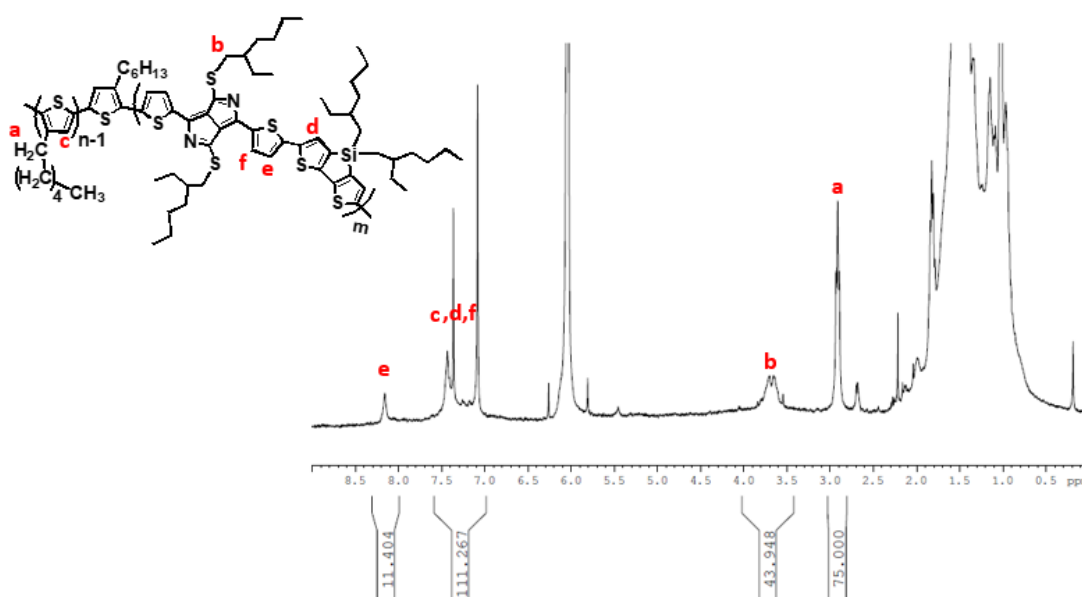


Figure II-32: ¹H NMR spectrum of P3HT₃₇-*b*-P(DTS-DAP)₁₁ (C₂D₂Cl₄, 400 MHz).

The experimental degree of polymerization for the synthesized CBCPs was estimated by comparing the signal integral at 2.9 ppm pertaining to the CH₂ proton in the alpha position of the thiophene cycle of P3HT (2 protons *per* monomer unit; protons **a**) with the signal at 4.2 ppm attributed to the CH₂ in the alpha position of the sulfur in DAP alkyl chains (4 protons *per* monomer unit; protons **b**). Thus, the degree of polymerization and molar masses calculated from ¹H NMR (based on N_{DTS-DPP}/N_{P3HT} ratio) and SEC-THF for the synthesized block copolymers are summarized in **Table II-7**.

Table II-7: Molecular characteristics of the synthesized DAP-based CBCPs.

Polymer	N ^a A	N ^a B	N ^a C	DP _n P3HT-	DP _n P3HT-	M _n th ^b	M _n ^c	M _n ^d	D ^d
	DTS	DAP	P3HT-Br	DP _n A-B th ^b	DP _n A-B ^c				
P3HT ₂₅	-	-	-	25-0	25-0	-	4150	4500	1.4
P3HT ₂₅ - <i>b</i> -P(DTS-DAP) ₉	1	0.96	0.08	25-12	25-9	16,000	13,000	14,000	2.2
P3HT ₃₇	-	-	-	37-0	37-0	-	6150	13,000	1.7
P3HT ₃₇ - <i>b</i> -P(DTS-DAP) ₄	1	0.92	0.16	37-6	37-4	12,000	10,000	13,000	1.8
P3HT ₃₇ - <i>b</i> -P(DTS-DAP) ₁₁	1	0.98	0.04	37-25	37-11	30,000	17,000	16,000	12.5

^a feed ratio calculated according to Equation 5, ^b calculated from the Carothers equation, ^c calculated from ¹H NMR and ^d measured by SEC-THF using polystyrene calibration

The chromatograms of **Figure II-33** (detected at 450 nm) verifies the different molar masses of P3HT₃₇-*b*-P(DTS-DAP)_m obtained. The clear shift towards low elution volumes in the case of P3HT₃₇-*b*-P(DTS-DAP)₁₁ is an indication of the increase in molar mass compared to P3HT₃₇-*b*-P(DTS-DAP)₄.

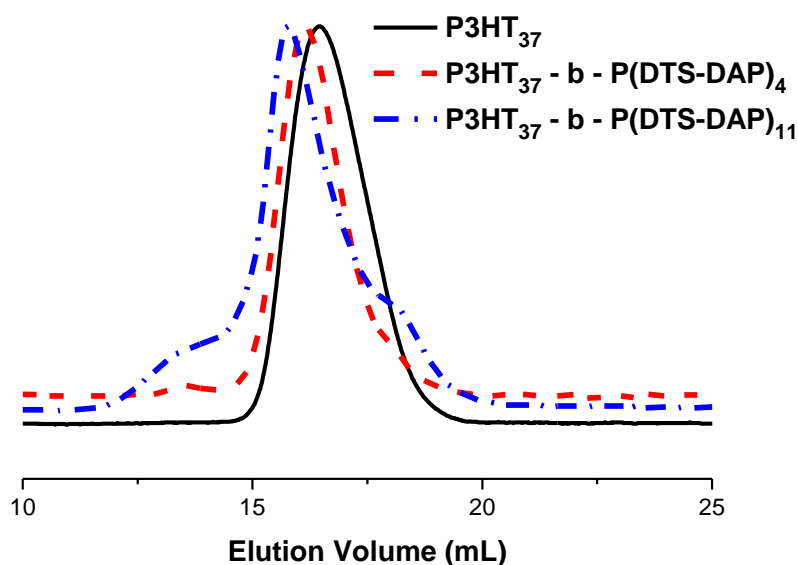


Figure II-33: Size exclusion chromatograms using UV-vis detector at 450 nm of the synthesized P3HT₃₇-*b*-P(DTS-DPP)₄ and P3HT₃₇-*b*-P(DTS-DPP)₁₁ in comparison with the starting P3HT₃₇.

Analysis in SEC-toluene was also performed for P3HT₃₇-*b*-P(DTS-DAP)₄. The chromatograms were collected at 500 and 700 nm and compared with that of P3HT₃₇ at 500 nm (**Figure II-34a**). **Figure II-34b** is a 3-dimensional (3D) image of the diblock chromatogram.

In general, the diblock copolymer was eluted at a lower elution time than P3HT₃₇ revealing its higher molar mass. At both detection wavelengths, P3HT₃₇-*b*-P(DTS-DAP)₄ was eluted at the same time with matching chromatograms. However, the one at 700 nm reveals the existence of some free chains represented by a small shoulder appearing at higher elution time (16-18 min). This can be attributed to the low molar mass of free P(DTS-DPP) absorbing at this wavelength. Another slight shoulder can also be observed (around 11 min) that could be related to the presence of higher molar mass species, probably a triblock copolymer.

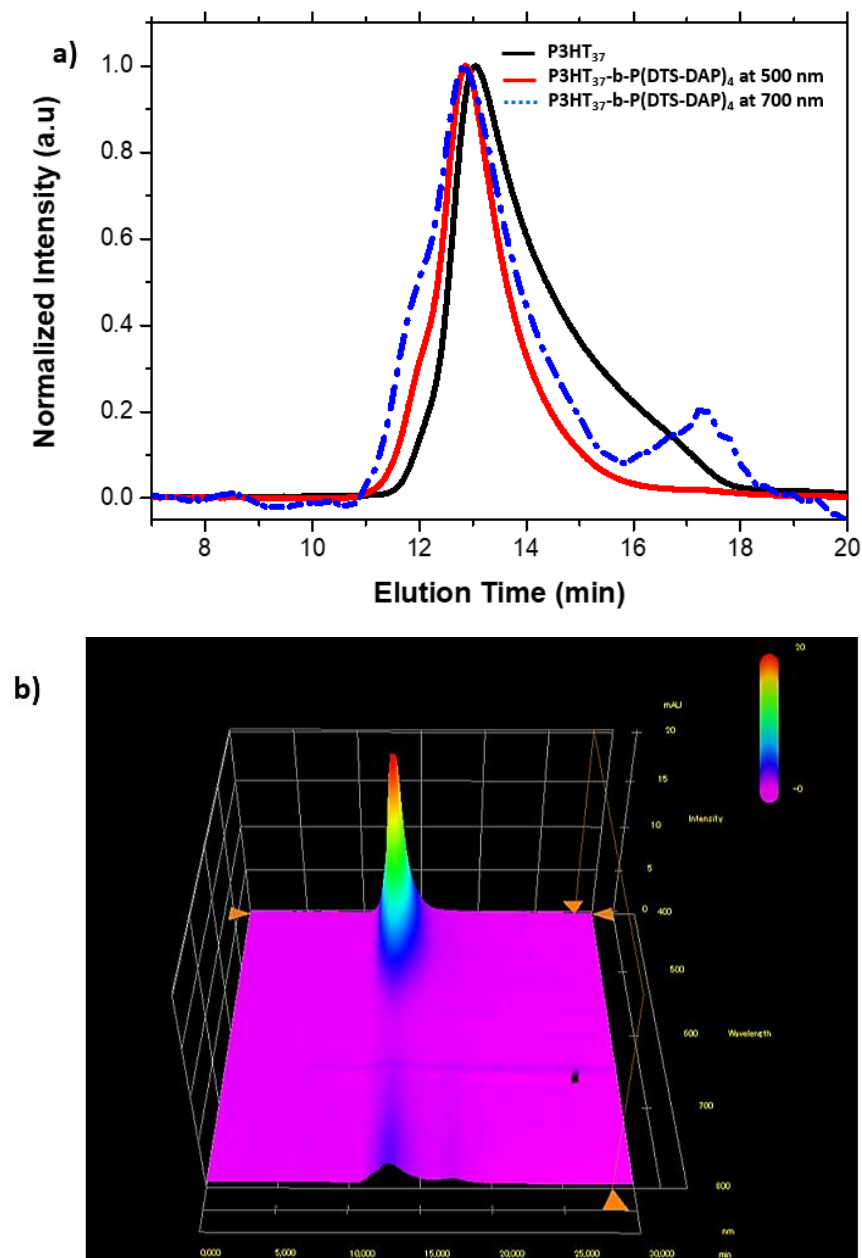


Figure II-34: (a) SEC chromatogram of P3HT₃₇-*b*-P(DTS-DAP)₄ in toluene and (b) a 3-D chromatogram plot.

The same procedure was followed to synthesize P3HT₂₅-*b*-P(DTS-DAP)₉ with a feed molar composition of 1/0.96/0.08 equivalent of DTS/DAP/P3HT₂₅, respectively. The molecular characteristics based on ¹H NMR and SEC are summarized in **Table II-7, entry 2**.

V. Optical properties of diblock copolymers

a. Optical behavior

The goal beyond synthesizing conjugated block copolymers is to incorporate them in organic solar cells. Thus, a broad optical absorbance is highly desired for such application. UV-visible-near-IR spectrophotometry was performed on the synthesized diblocks to detect their absorption. For $P3HT_n-b-P(DTS-DPP)_m$ copolymers, spectra in **Figure II-35a** (solution in chloroform) showed two broad absorption bands. The first one with a λ_{max} of 445 nm is mainly attributed to P3HT absorption but also in a lesser extent to the P(DTS-DPP) block. Indeed, the spectrum of P(DTS-DPP) homopolymer exhibited a small absorption peak at 450 nm attributed to the $\pi-\pi^*$ transition. A wide absorption band from 550 to 900 nm is also present corresponding to the charge transfer interaction. The vibronic shoulder at 800 nm suggests a strong interchain interaction in chloroform. Moreover, the second band in the diblock copolymers' spectra has two λ_{max} at 745 and 800 nm pertaining to the P(DTS-DPP) block.

The $P3HT_n-b-P(DTS-DPP)_m$ spectra reflect the composition in the copolymers. Indeed, the absorbance ratio at $\lambda = 445$ nm and $\lambda = 800$ nm, A_{445}/A_{800} , is higher for the $P3HT_{240}-b-P(DTS-DPP)_{11}$ than $P3HT_{37}-b-P(DTS-DPP)_4$ and finally for $P3HT_{37}-b-P(DTS-DPP)_{19}$, 1.89, 1.02 and 0.33, respectively in agreement with the block composition. Two optical bandgaps were calculated from the onset of the absorption wavelength at 550 and 920 nm for all copolymers with a value around 2.2 and 1.3 eV, respectively.

In the case of $P3HT_n-b-P(DTS-DAP)_m$, the near-IR peak was shifted to a higher wavelength (900 to 950 nm) as shown in **Figure II-35b**. As explained before, the replacement of DPP by DAP having a more electron deficient nature is the reason behind this red-shift. The intensity of each absorption peak was also in agreement with the initial ratio of the starting materials. In the CBCPs containing a larger amount of P3HT, such as $P3HT_{37}-b-P(DTS-DAP)_4$ compared to $P3HT_{37}-b-P(DTS-DAP)_{11}$, the absorption peak at 445 nm corresponding to the P3HT block appears with a higher intensity. Also, there is a bathochromic shift for the low-bandgap block absorption peak from 850 to 950 nm when the size of the P(DTS-DAP) block was bigger which correspond to an increase of the conjugation length.

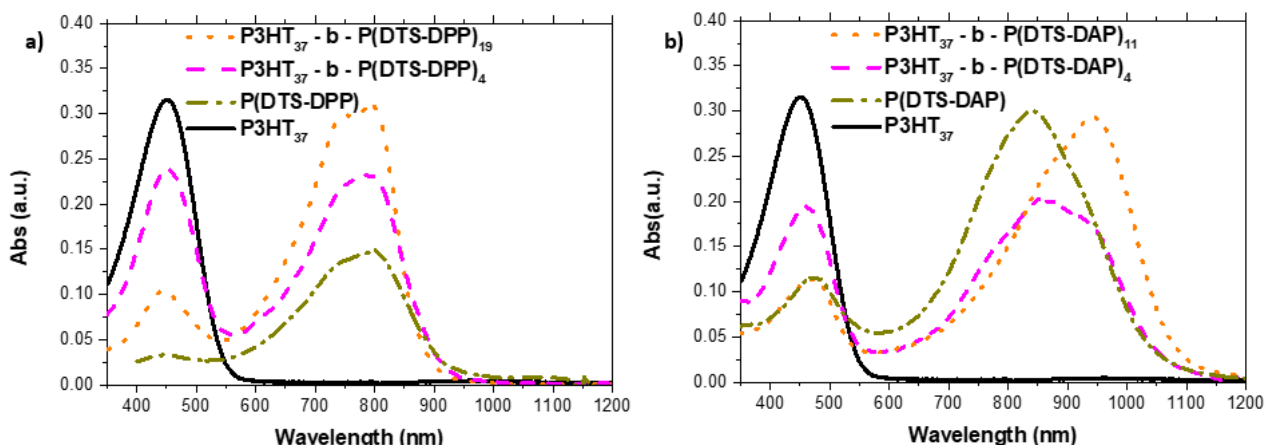


Figure II-35: UV-vis-NIR absorption spectra of the conjugated block copolymers based on either (a) DPP or (b) DAP repetitive units (chloroform solutions).

The absorption of thin films was also studied. For the film preparation, a 10 mg.mL⁻¹ solution of the copolymer in chloroform was spin-coated on glass substrates. Spectra shown in **Figure II-36** present the superposition of the solid state behavior of the copolymers in comparison with solutions. Wide absorption bands were observed for the copolymers in films. Concerning P3HT₃₇-*b*-P(DTS-DPP)₁₉, its spectrum in **Figure II-36a** shows a bathochromic shift to the near-IR region from λ_{max} =800 nm (in solution) to 900 nm (in film). The observation of a vibronic structure (around 500 nm) that is characteristic in P3HT film is an indication that the P3HT block in the diblock polymer is able to form π -stacking.¹² On the other hand, the spectrum of P3HT₃₇-*b*-P(DTS-DAP)₁₁ film presents a broader absorption peak when compared to the spectrum in solution but with the same λ_{max} , 950 nm.

Similar behaviors were obtained for the copolymers in **Figure II-36b** and **c**. For instance, a slight red-shift was observed in the case of P3HT₂₅-*b*-P(DTS-DAP)₉ film in which the maximum absorbance was found around 1000 nm. In general, the wide absorption in the solid state can be explained by the strong intermolecular interactions defined by strong π -stacking interactions as a result of the assembly of the macromolecular chains in the solid state.⁴⁷ Additionally, red-shifting is an indication for the enhanced chain ordering during casting.¹³

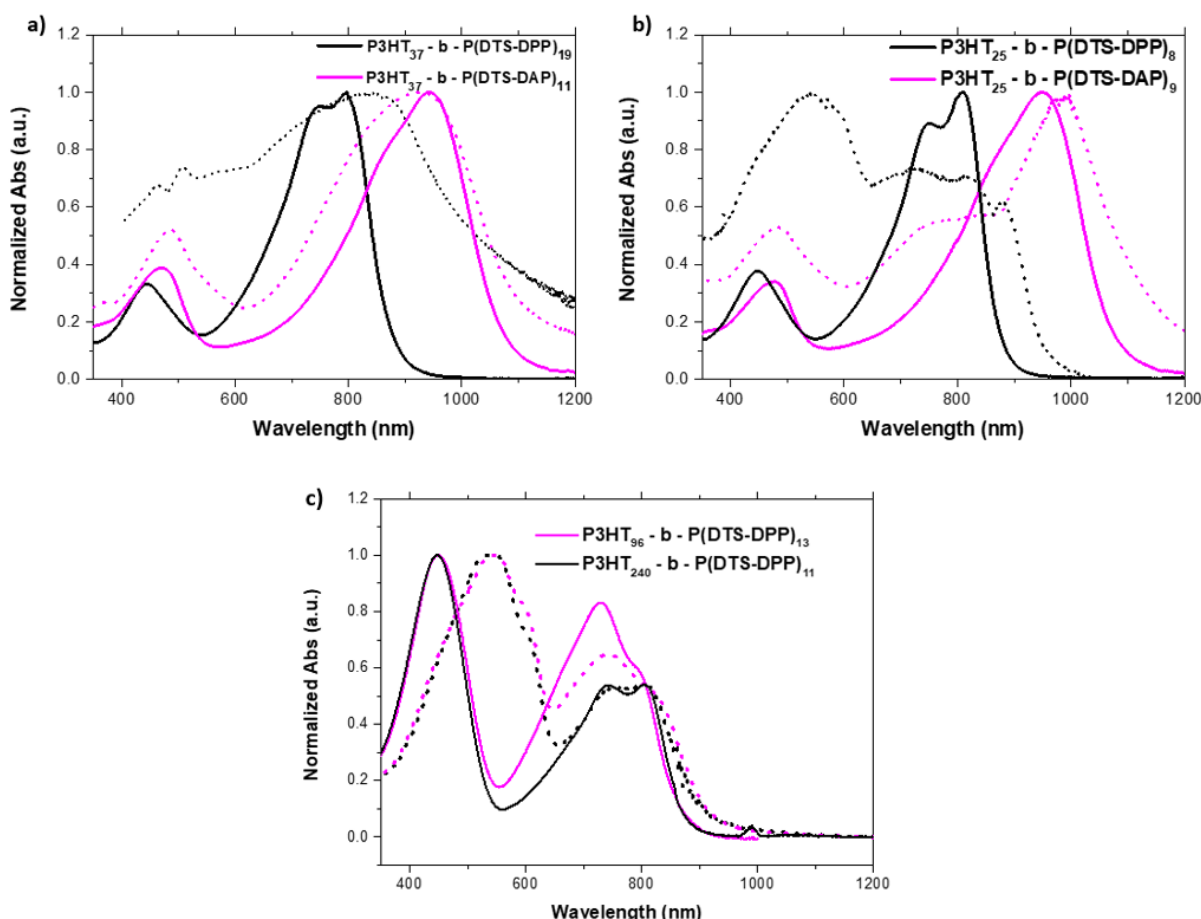


Figure II-36: UV-vis-NIR absorption spectra of some diblock copolymers in films (dotted) and in solution (solid).

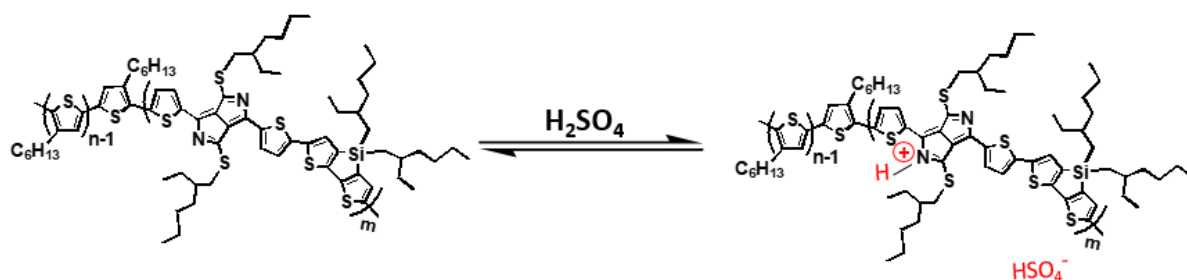
The red-shift behavior affects the optical bandgap by changing the onset of absorption (λ_{onset}) to a higher wavelength. The λ_{onset} and the calculated optical bandgaps are summarized in **Table II-8**. The results revealed lower optical bandgaps for DAP-based diblock copolymers when compared to DPP-based ones. For example, in films, the optical bandgaps of P3HT₃₇-*b*-P(DTS-DAP)₁₁ is around 1.0 eV while that of P3HT₃₇-*b*-P(DTS-DPP)₁₉ is around 1.24 eV.

Table II-8: Optical properties of the synthesized P3HT_{*n*}-*b*-P(DTS-DPP)_{*m*} and P3HT_{*n*}-*b*-P(DTS-DAP)_{*m*} in solution vs. solid state.

Spectra	Polymer	λ_{max} (nm)	λ_{onset} (nm)	$E_g^{\text{(opt)}}$ (eV)
Solution	P3HT ₂₅ - <i>b</i> -P(DTS-DPP) ₈	815	915	1.36
	P3HT ₃₇ - <i>b</i> -P(DTS-DPP) ₁₉	800	925	1.40
	P3HT ₃₇ - <i>b</i> -P(DTS-DPP) ₄	800	975	1.27
	P3HT ₉₆ - <i>b</i> -P(DTS-DPP) ₁₃	810	930	1.33
	P3HT ₂₄₀ - <i>b</i> -P(DTS-DPP) ₁₁	810	930	1.33
	P3HT ₂₅ - <i>b</i> -P(DTS-DAP) ₉	950	1115	1.12
	P3HT ₃₇ - <i>b</i> -P(DTS-DAP) ₁₁	950	1125	1.10
	P3HT ₃₇ - <i>b</i> -P(DTS-DAP) ₄	850	1080	1.14
Film	P3HT ₃₇ - <i>b</i> -P(DTS-DPP) ₁₉	900	1000	1.24
	P3HT ₃₇ - <i>b</i> -P(DTS-DAP) ₁₁	950	1250	1.00
	P3HT ₂₄₀ - <i>b</i> -P(DTS-DPP) ₁₁	810	975	1.27

b. Chromism

An additional optical property for the DAP-based diblocks was studied. Interestingly, several approaches can be used to tune the optical and electronic properties of diblocks.⁵³ These include protonation in the presence of acids,⁵⁴ chemical doping⁵⁵ or metal ion complexation.⁵⁶ Different conjugated polymers were synthesized with heteroatoms bearing lone pair electrons which can be protonated in the presence of acid.⁵⁷ Since lactim nitrogen in the DAP monomer is more basic than the lactam nitrogen in DPP, acid-base reactions can be undergoing. These reactions can alter the absorption properties of DAP. Thus, as shown in **Scheme II-14**, DAP monomer in P3HT_{*n*}-*b*-P(DTS-DAP)_{*m*} diblock can be readily protonated in the presence of an acid, in which the absorption is red-shifted to the near-IR region. This is caused by lowering the HOMO and LUMO levels due to the decrease of the electron density of the entire π -conjugated system which decreases the corresponding bandgap.⁵⁸



Scheme II-14: Acid-base reaction of the DAP chromophore in $P3HT_n$ - b - $P(DTS-DAP)_m$ copolymer.

A chromism behavior denotes the reversible variation of the electronic absorption properties of a material that changes its color. It can be observed in conjugated polymers⁴⁵ under the influence of external conditions; pH variation (halochromism) or temperature (thermochromism).⁵⁹ Chromism can be attributed to intramolecular conformational changes, as a twist in the main chain resulting in a reduction of the conjugation length.⁶⁰ Or can be induced by creations and destructions of intermolecular interactions such as π - π stacking between the aromatic repeat units.⁶¹ Previously, Khelifi *et al.*⁴⁵ reported a halochromic effect for DAP-based copolymers P(DTS-DAP) by either being protonated with a Brønsted acid or coordinated with a Lewis acid.

In our study, halochromism has been performed with different synthesized diblock copolymers having the DAP repetitive unit in two different organic solvents; chloroform and chlorobenzene, in which different behaviors were observed. The halochromic behavior of $P3HT_{25}$ - b - $P(DTS-DAP)_9$ was studied in chloroform in the presence of sulfuric acid (H_2SO_4) and the polymer's optical properties were studied using UV-visible-NIR spectroscopy. The amount of H_2SO_4 to be added was calculated based on one repetitive unit of P(DTS-DAP) block by considering that 1 equivalent of H_2SO_4 , as a diacid, protonates 2 equivalents of the repetitive units in the conjugated block copolymer.

In chloroform (**Figure II-37a**), by increasing the amount of sulfuric acid added, the intensity of the absorption band at λ_{max} (950 nm) is slightly decreased, until the band is suddenly totally shifted with a bathochromic shift of 220 nm with λ_{max} around 1175 nm after adding 250 equivalents of H_2SO_4 . At this protonation level, λ_{onset} was at 1500 nm, thus the optical bandgap was decreased from 1.12 eV for the neutral diblock copolymer to 0.82 eV for the cationic one. The decrease in the bandgap is caused by the modification of the HOMO-LUMO energy levels alignment due to the less delocalization across the π -conjugated backbone.⁵⁸ After adding an excess of acid, the maximum peak was slightly shifted to around 1200 nm. Adding more acid did not change the absorption spectrum which is an indication that the maximum protonation has been reached. On the other hand, halochromism in chloroform using acetic acid which is a weaker acid than sulfuric acid with a higher pKa, did not ensure the complete protonation even after its large excess addition (**Figure II-37b**).

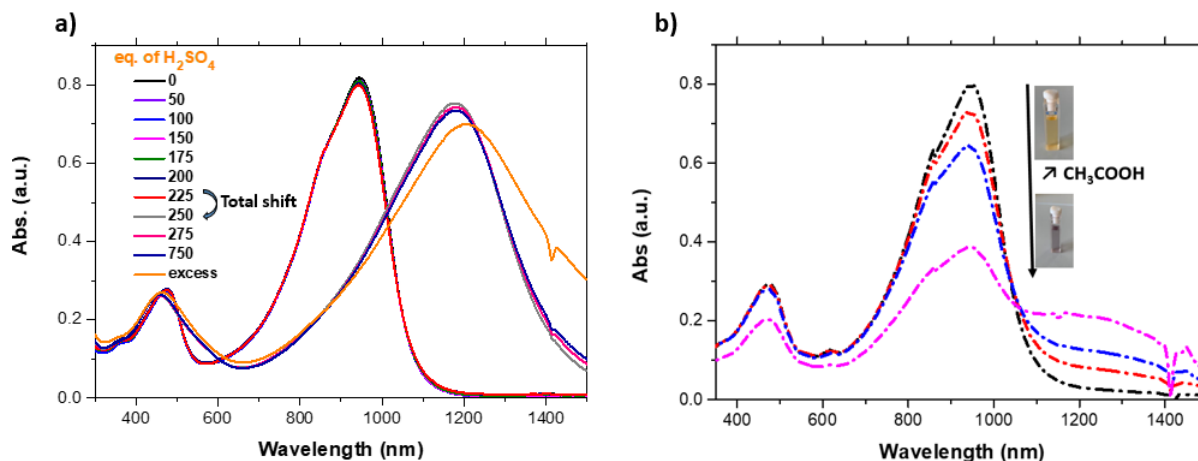


Figure II-37: UV-vis-NIR absorption spectra of P3HT₂₅-b-P(DTS-DAP)₉ in chloroform after adding (a) sulfuric acid and (b) acetic acid.

The behavior of the same DAP-based copolymer in chlorobenzene was different, since the change in absorption is occurring gradually with the addition of H₂SO₄. As shown in **Figure II-38**, again, by increasing the amount of sulfuric acid added (from 0 eq to 48 eq), the intensity of the absorption band at λ_{max} (950 nm) decreased, and a broad absorption band raised at 1175 nm after the addition of 56 eq of H₂SO₄. By adding more acid, the first peak completely disappeared and a new absorption peak was observed with a λ_{onset} of 1500 nm. The behavior of the DAP-based diblock copolymer was not the same than in the case of chloroform, maybe due to the difference in the copolymer's organization in each solvent. For instance, in chloroform, P(DTS-DAP) chains were organized in a way that they were not exposed to the acid-containing medium, until the addition of a certain amount of H₂SO₄ that can change such organization. However, in the case of chlorobenzene, P(DTS-DAP) chains could be exposed directly to the medium. Sadly, by lack of time, the experiments to confirm this hypothesis have not been performed.

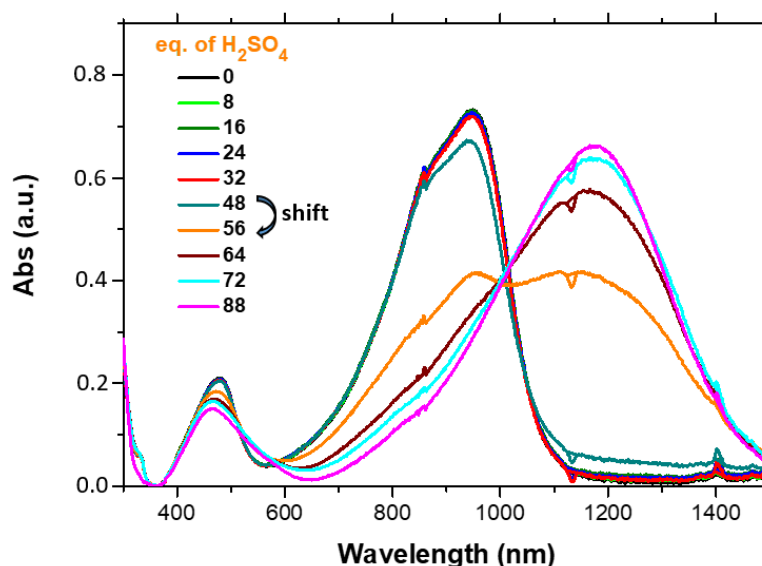
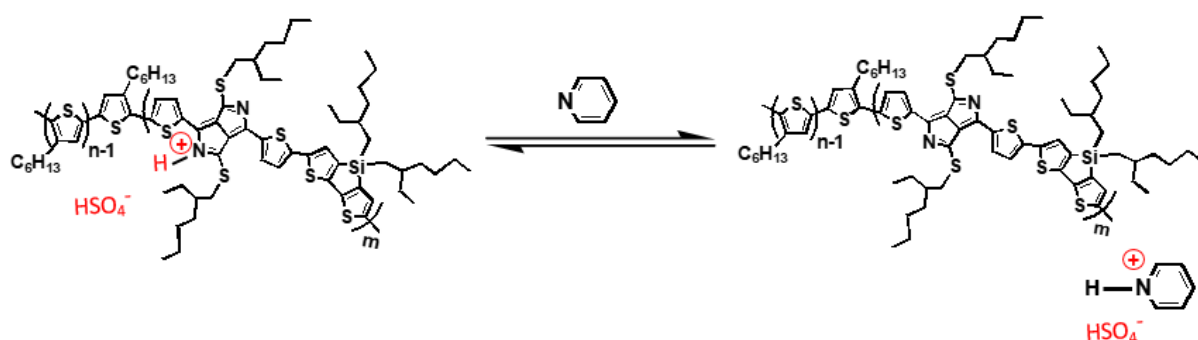


Figure II-38: UV-vis-NIR absorption spectra of P3HT₂₅-b-P(DTS-DAP)₉ in chlorobenzene upon the addition of sulfuric acid.

The effect of a base on the protonated copolymer was then studied. For this, we have chosen pyridine which is a stronger base than the lactim nitrogen of the DAP monomer. After the addition of 65 eq of pyridine, the peak at 1175 nm disappeared and a new peak was formed which corresponds to the peak of the neutral state with a maximum absorption at 950 nm (**Figure II-39a**). Thus, this shows that the protonation of the DAP monomer in the diblock copolymer is reversible with the possibility of deprotonation in the presence of a strong base such as pyridine as shown in **Scheme II-15**.



Scheme II-15: The reaction of the DAP chromophore in $P3HT_n$ - b - $P(DTS-DAP)_m$ copolymer with pyridine.

The halochromic behavior of DAP monomer in the diblock copolymer can be detected from the color change shown in **Figure II-39b**.

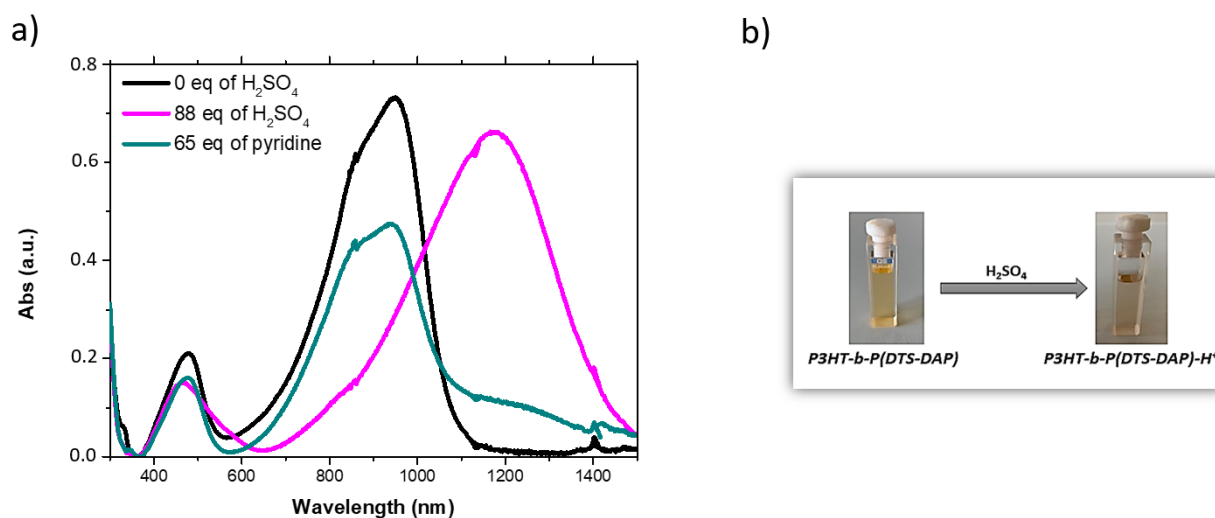


Figure II-39: (a) UV-vis-NIR absorption spectra of $P3HT_{25}$ - b - $P(DTS-DAP)_9$ in chlorobenzene upon the addition of H_2SO_4 followed by pyridine. (b) Image showing the change in color of $P3HT_{25}$ - b - $P(DTS-DAP)_9$ upon the addition of H_2SO_4 .

VI. Electrochemical characterizations

Electrochemical properties of the synthesized conjugated block copolymers were determined by Cyclic Voltammetry (CV). Polymer solutions in chloroform were prepared and deposited on a platinum (Pt) working electrode by drop-casting. This study was performed in acetonitrile containing 0.1 M of tetrabutylammonium hexafluorophosphate (NBu₄PF₆) that acts as a supporting electrolyte in the presence of Ag/AgCl reference electrode. The analysis has been performed under inert atmosphere with a scanning rate of 0.1 V/s. All the calculated potentials were calibrated versus the formal potential E° of the used standard redox couple ferrocene/ferrocenium Fc/Fc⁺ as proposed by previous reports.⁶² All solutions were purged with nitrogen (N₂) prior to use. The measurements allowed the detection of the oxidation and reduction potentials of the materials and therefore calculating the HOMO and LUMO energy levels according to previously reported equations.⁶³

HOMO energy level is calculated according to **Equation 9**.

$$E_{\text{HOMO}} \text{ (eV)} = -(E_{\text{onset}}^{\text{ox}} + 4.70) \quad \text{Equation 9}$$

where $E_{\text{onset}}^{\text{ox}}$ corresponds to the oxidation potential threshold of the polymer in comparison with the reference electrode. The 4.70 eV corresponds to the reduction of Hg₂Cl₂/Hg in vacuum.⁶⁴

LUMO energy level is calculated according to **Equation 10**.

$$E_{\text{LUMO}} \text{ (eV)} = -(E_{\text{onset}}^{\text{red}} + 4.70) \quad \text{Equation 10}$$

where $E_{\text{onset}}^{\text{red}}$ corresponds to the reduction potential threshold of the polymer. The estimations of the potential onsets are described below.

The electrochemical bandgap ($E_{\text{g}}^{(\text{cv})}$) is then calculated using **Equation 11**.

$$E_{\text{g}}^{(\text{cv})} = E_{\text{HOMO}} - E_{\text{LUMO}} \quad \text{Equation 11}$$

After measuring the oxidation/reduction of homopolymers P3HT, P(DTS-DPP) and P(DTS-DAP), it was then possible to deduce the oxidation/reduction waves pertaining to each block of the conjugated copolymer. Concerning P3HT₃₇ homopolymer film, HOMO and LUMO positions were measured from the $E_{\text{onset}}^{\text{ox}}$ of the first anodic signal and $E_{\text{onset}}^{\text{red}}$ of the first cathodic signal, respectively. As shown in **Figure II-40**, $E_{\text{onset}}^{\text{ox}}$ and $E_{\text{onset}}^{\text{red}}$ were estimated to be 0.7 eV and -1.8 eV, respectively versus Ag/AgCl. These values were estimated by the tangent method illustrated by the violet lines shown in the figure below. The arrows in the plot represent the scan directions. Based on the previously mentioned equations, the HOMO and LUMO energy levels of P3HT₃₇ were estimated to be -5.3 eV and -2.9 eV, respectively. The electrochemical bandgap was then calculated to be 2.4 eV while the optical bandgap derived from UV-vis absorption spectrum was calculated to be 2.2 eV. The difference between the value of the optical and electrochemical bandgap is due to the different approaches used by each technique. Optical bandgap is based on optical excitation of an electron from the ground state to the first excited state, whereas electrochemical bandgap is calculated from oxidation/reduction processes that lead to the formation of cations or anions in the polymer film morphology.⁶⁵

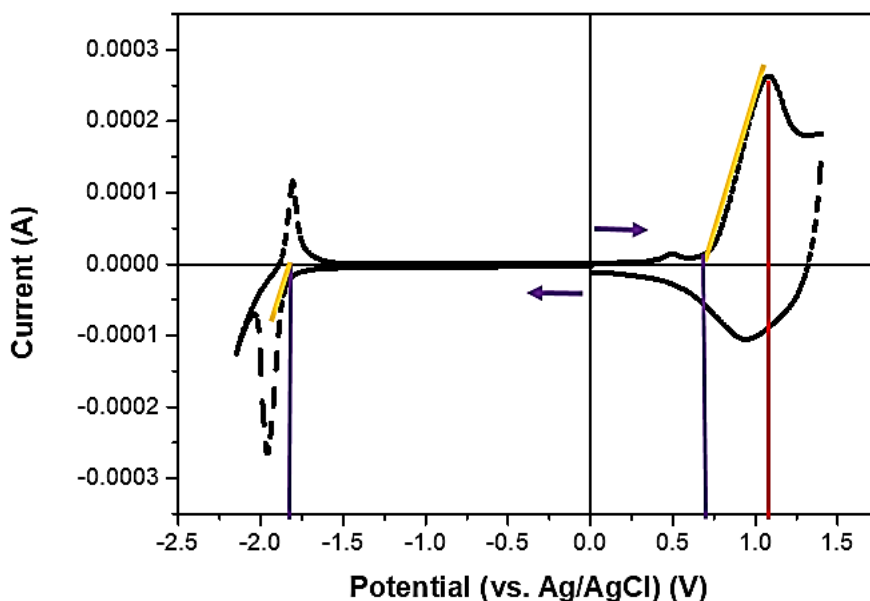


Figure II-40: Cyclic voltammograms of the drop-casted film of P3HT₃₇ with a scanning rate of 0.1 V/s.

Regarding P(DTS-DPP) and P(DTS-DAP) copolymers, a lower LUMO energy was observed when compared to the P3HT homopolymer. For P(DTS-DAP), a lower LUMO (-4.2 eV) than that of P(DTS-DPP) (-3.8 eV) was obtained with a slightly higher HOMO energy level (Figure II-41), thus lowering the electrochemical bandgap. This lower bandgap when compared to P(DTS-DPP) is explained by the incorporation of the strong electron donor (DAP) which effectively decreases the gap.⁷ In general, the optical bandgap was lower than the electrochemical bandgap calculated by cyclic voltammetry. This difference can be attributed to the interface barrier between the polymer film and the electrode surface. It was reported that the electrochemical bandgap is the combination of the optical bandgap with this injection barrier.⁶⁶

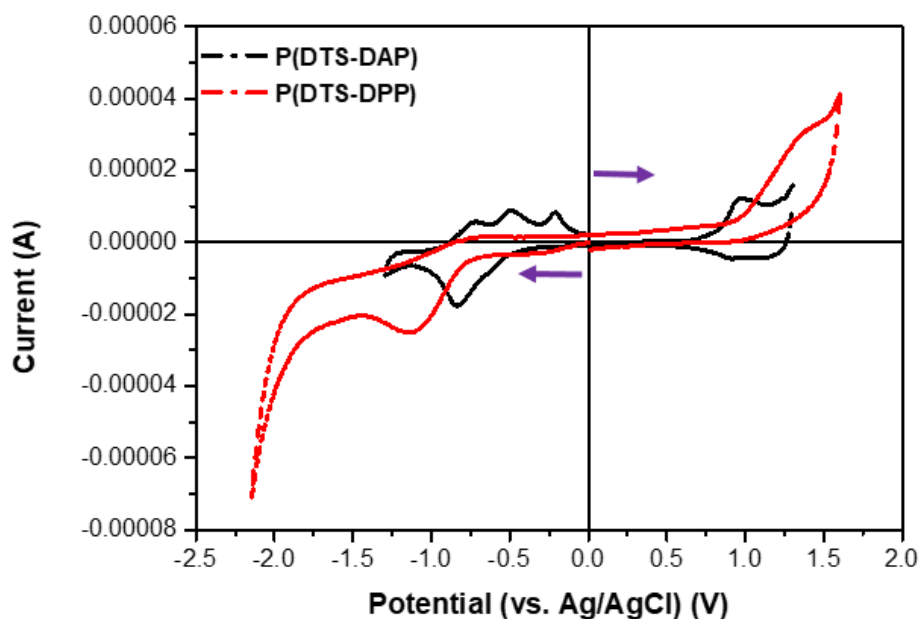


Figure II-41: Cyclic voltammograms of the drop-casted film of P(DTS-DPP) and P(DTS-DAP) in 0.1 M acetonitrile solution with a scanning rate of 0.1 V/s.

The diblock copolymers show different behaviors in which two oxidations and two reductions were observed in the redox reactions as shown in **Figure II-42**. Each oxidation and reduction wave is compared to the corresponding oxidation and reduction of the separated blocks. For example, in the case of $P3HT_n$ - b - $P(DTS-DPP)_m$ (**Figure II-42a**), the first oxidation wave around 0.6 eV pertains to the P3HT block and the second wave around 0.7 eV is driven by the low-bandgap block P(DTS-DPP). Similarly, for the reduction, the wave around -0.8 eV is attributed to the low-bandgap block whereas the second wave around -1.8 eV corresponds to that of P3HT block. Thus, each diblock copolymer is characterized by having two HOMO/LUMO energy levels. In some cases, the voltammogram shows only one reduction that can be assigned to P3HT block (**Figure II-42b**) while the reduction of the second block P(DTS-DAP), was only observed in the first running cycle as shown in **Figure II-42c**.

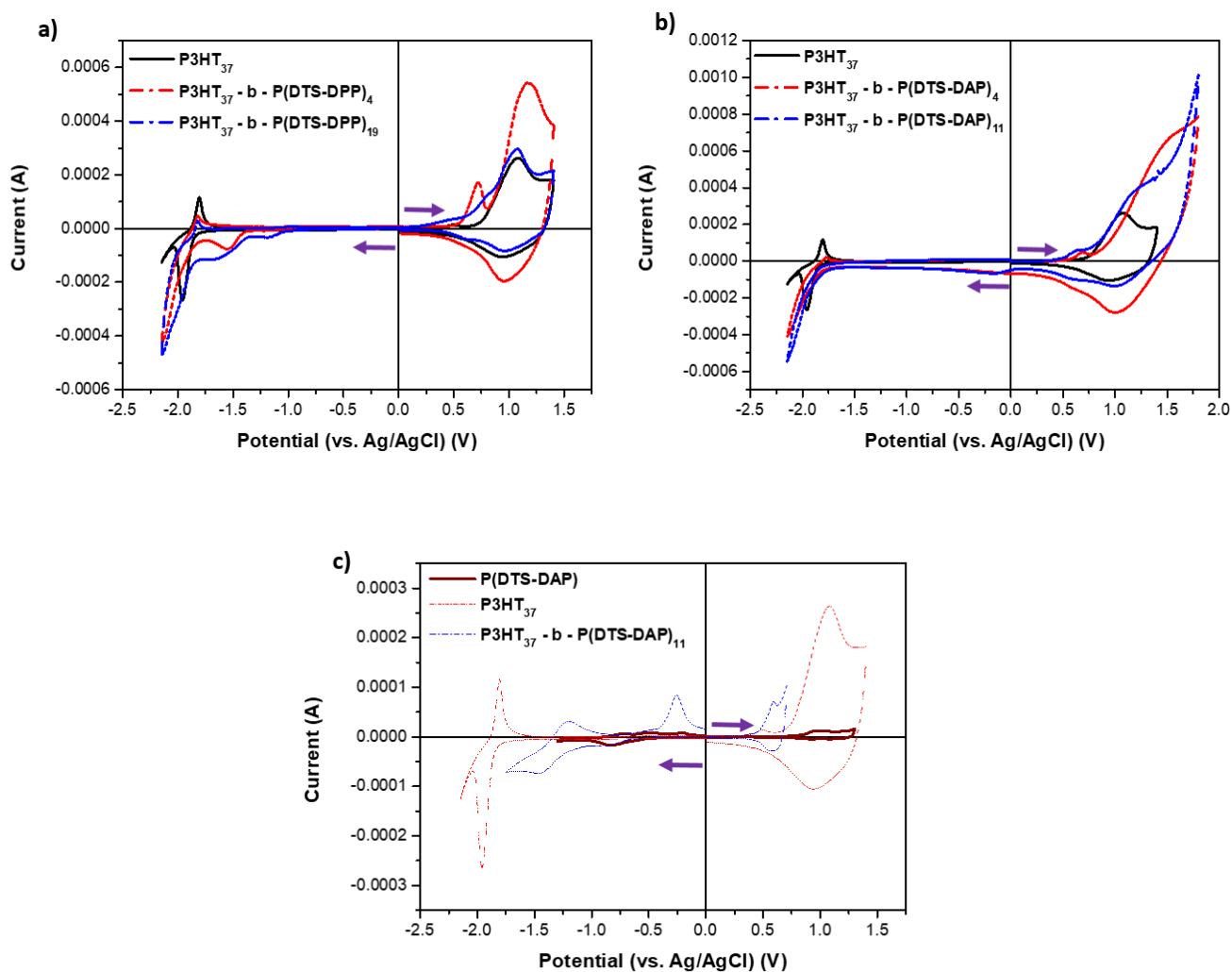


Figure II-42: Cyclic voltammograms of the drop-casted films of P3HT₃₇ and the corresponding (a) DPP, (b) and (c) DAP-based copolymers in 0.1 M acetonitrile solution with a scanning rate of 0.1 V/s.

The calculated HOMO and LUMO energy levels as well as the electrochemical bandgap of each diblock are reported in **Table II-9**.

In general, the results show that the P3HT LUMO is higher than the P(DTS-DPP) and P(DTS-DAP) ones, showing the possible donor-acceptor electron transfer.

P3HT block in the diblock copolymer exhibits a bandgap of 2.5 ± 0.1 eV in all copolymers. The second block exhibits a bandgap of 1.5 ± 0.1 eV in DPP-based diblock copolymers which is higher than that obtained for the DAP-based diblocks (1.2 ± 0.1 eV) due to the strong donor character of DAP when compared to DPP.

Table II-9: Electronic properties of the synthesized block copolymers.

Polymer	E_{HOMO} P3HT	E_{LUMO} P3HT	$E_{\text{g}}^{(\text{cv})}$ ^a P3HT	E_{HOMO} P(DTS- DXP)	E_{LUMO} P(DTS- DXP)	$E_{\text{g}}^{(\text{cv})}$ ^a P(DTS- DXP)	$E_{\text{g}}^{(\text{opt})}$ ^b
P3HT ₃₇	-5.3 eV	-2.9 eV	2.4 eV	-	-	-	2.20 eV
P3HT ₂₄₀	-5.3 eV	-2.9 eV	2.4 eV	-	-	-	2.10 eV
P(DTS-DPP)	-	-	-	-5.7 eV	-3.8 eV	1.9 eV	1.30 eV
P3HT ₃₇ - <i>b</i> -P(DTS-DPP) ₁₉	-5.3 eV	-2.9 eV	2.4 eV	-5.4 eV	-3.8 eV	1.6 eV	1.40 eV
P3HT ₃₇ - <i>b</i> -P(DTS-DPP) ₄	-5.3 eV	-2.9 eV	2.4 eV	-5.4 eV	-3.8 eV	1.6 eV	1.27 eV
P3HT ₂₄₀ - <i>b</i> -P(DTS-DPP) ₁₁	-5.3 eV	-3 eV	2.3 eV	-5.6 eV	-3.9 eV	1.7 eV	1.33 eV
P(DTS-DAP)	-	-	-	-5.4 eV	-4.2 eV	1.2 eV	1.14 eV
P3HT ₃₇ - <i>b</i> -P(DTS-DAP) ₁₁	-5.5 eV	-2.9 eV	2.6 eV	-5.3 eV	-4.1 eV	1.2 eV	1.10 eV
P3HT ₃₇ - <i>b</i> -P(DTS-DAP) ₄	-5.5 eV	-2.9 eV	2.6 eV	-5.2 eV	-4.0 eV	1.2 eV	1.14 eV

^a calculated from cyclic voltammetry and ^b calculated from UV-vis spectrometry

The energy level alignments of the homopolymer P3HT₃₇, P(DTS-DAP), P(DTS-DPP) and the corresponding diblock copolymers are shown in **Figure II-43**. It could be recognized that the HOMO and LUMO energy levels of the homopolymers are approximately the same as the diblocks except for P(DTS-DPP) having its HOMO level lower in comparison with its corresponding diblock.

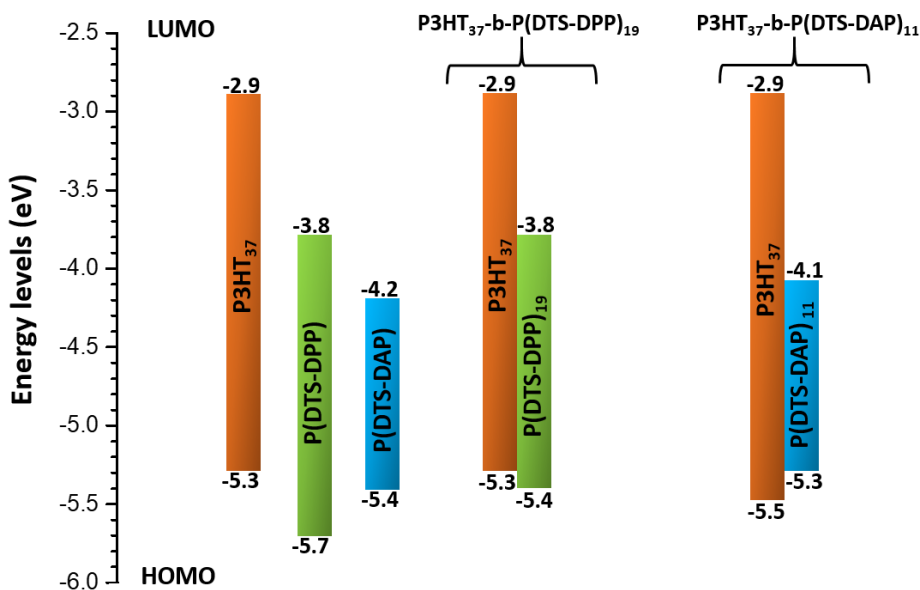


Figure II-43: Energy diagram showing HOMO and LUMO energy level alignments for P3HT₃₇, P(DTS-DPP), P(DTS-DAP) and the corresponding diblocks.

VII. Thermal characterizations

Thermal stability is an important parameter for organic materials that are aimed for optoelectronic applications. Thermogravimetric Analysis (TGA) was conducted to investigate the thermal stability of the synthesized diblock copolymers. The study was carried out under nitrogen atmosphere starting from 50 to 600 °C with a ramp of 10 °C/min. **Figure II-44** shows typical thermograms of the synthesized diblock copolymers based on either P3HT₃₇ or P3HT₂₅ macroinitiators.

As shown in **Figure II-44a and b**, the thermal decomposition of P3HT₃₇ homopolymer is a one-step decomposition with around 60% loss starting from 400 °C to 530 °C with a maximum rate of degradation at 460 °C. The residual mass after degradation was found to be 40%. Similarly, P3HT₂₅ had an onset of degradation observed between 440 °C to 550 °C with a residual mass of 30% (**Figure II-44c**). The P3HT degradation is mainly due to cleavage of the alkyl chain attached to the thiophene unit.⁶⁷ Concerning copolymers, it was observed that P(DTS-DPP) is also quite stable with a degradation temperature starting from 370 °C. The degradation continues in a one-step until reaching 500 °C while keeping a residual mass of 48%. On the other hand, P(DTS-DAP) is less stable showing 50% loss starting as early as 230 °C with two-stages degradation, the first between 230 and 335 °C with a residual mass of 80%, and a second between 335 and 507 °C with a residual mass of 50%. The degradation of both alternated copolymers is due to the decomposition of the alkyl chain attached to the dithienosilole unit.⁶⁸ Regarding P3HT₃₇-b-P(DTS-DPP)_m diblocks (**Figure II-44a**), the same one-stage degradation behavior was observed by analyzing all polymers and this was not dependent of the ratio between the two blocks. The decomposition started around 400 °C with a residual mass of 50%. Similarly, P3HT₂₅-b-P(DTS-DPP)₈ is thermally decomposed starting from 370 °C until 510 °C with a residual mass of 50% (**Figure II-44c**).

However, $P3HT_n-b-P(DTS-DAP)_m$ diblocks showed a different behavior than the P3HT homopolymer indicating different decomposition features, and the behavior differs by changing the ratio of each block. For example, $P3HT_{37}-b-P(DTS-DAP)_4$ (Figure II-44b) reveals a degradation behavior quite similar to P3HT₃₇ with a 50% residual mass as it contains a high P3HT content. For $P3HT_{37}-b-P(DTS-DAP)_{11}$, the same degradation behavior as P(DTS-DAP) was observed with a multi-stages degradation that ends at 540 °C with a residual mass of 45%. The low stability of this diblock could be related to the higher weight fraction content of the less stable P(DTS-DAP). $P3HT_{25}-b-P(DTS-DAP)_9$ have an intermediate stability when compared to the other two DAP-based diblocks as it was synthesized using an intermediate weight fraction of P(DTS-DAP). Its decomposition is a two-steps process starting from 280 °C to 440 °C, then until 525 °C with a residual mass of 55%.

Although the DPP-based block copolymers show a higher thermal stability than the DAP-based ones, TGA analysis proves that a thermal annealing up to 200 °C is possible for all the synthesized block copolymers which is essential for their use as photovoltaic materials in OPVs.

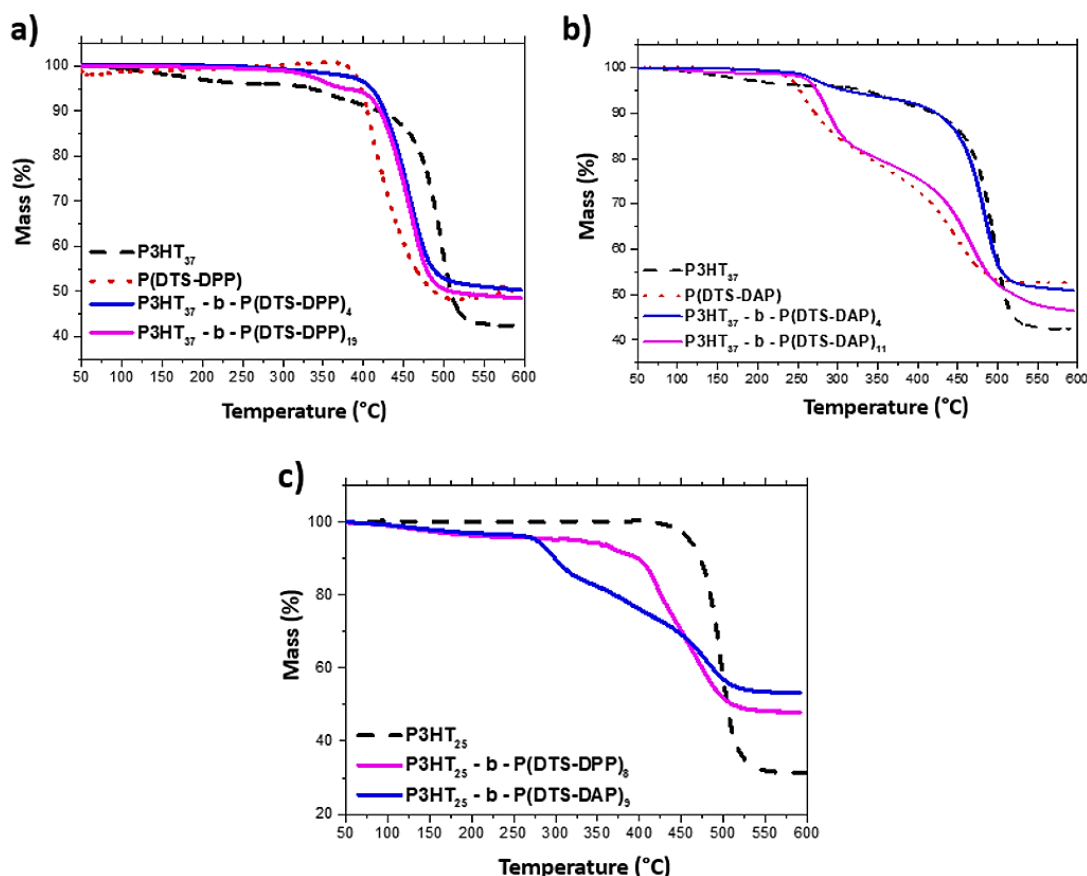


Figure II-44: Thermograms of the synthesized conjugated block copolymers.

Then, the thermal properties including the crystalline behavior of the synthesized copolymers were investigated using Differential Scanning Calorimetry (DSC) analysis. This analysis can help to better understand the phase transitions of the synthesized homopolymers and the conjugated diblock copolymers by determining the glass transitions (T_g), the melting and crystallization transitions.

All samples were prepared by drop-casting 20 mg.mL⁻¹ chloroform-based solutions on an aluminum plate to form films that were analyzed after drying as shown in **Figure II-45**. It is worth mentioning that in this analysis we consider the first cycle in which the study was performed using a temperature ramp of 10 °C/min under nitrogen.



Figure II-45: Sample preparation for DSC.

Concerning the synthesized solid copolymers, P(DTS-DPP) and P(DTS-DAP), no thermal transition was visible during the analyzed temperature interval (up to 300 °C) as shown in **Figure II-46**. Thus, no melting or recrystallization temperature was observed. The absence of such transitions could be attributed to the low crystallinity of the two copolymers caused by the inhibited π -stacking interactions. Additionally, the rigidity of the conjugate skeleton and the strong interchain interactions can lead to a melting temperature above the analyzed range.⁶⁹

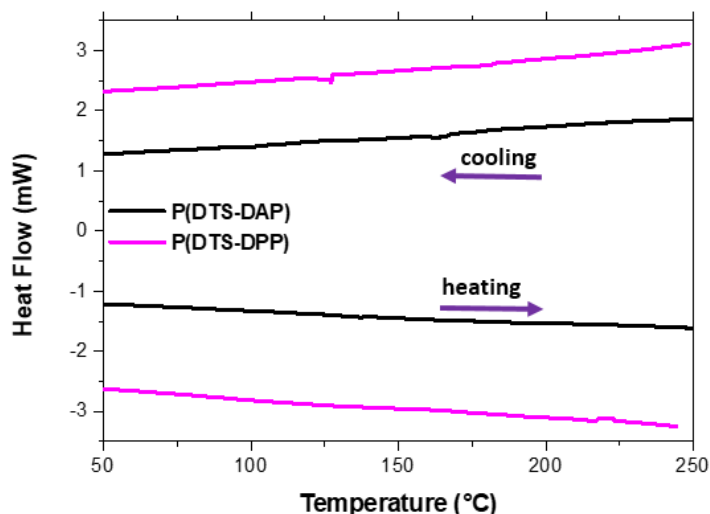


Figure II-46: DSC thermograms of P(DTS-DAP) and P(DTS-DPP).

P3HT and the conjugated diblock copolymers have also been studied by DSC between 50 and 300 °C. Thermograms are shown in **Figure II-47**. Regarding P3HT₃₇, a melting temperature was observed around 242 °C upon heating followed by a crystallization temperature around 203 °C upon cooling. Thus, P3HT is semi-crystalline.

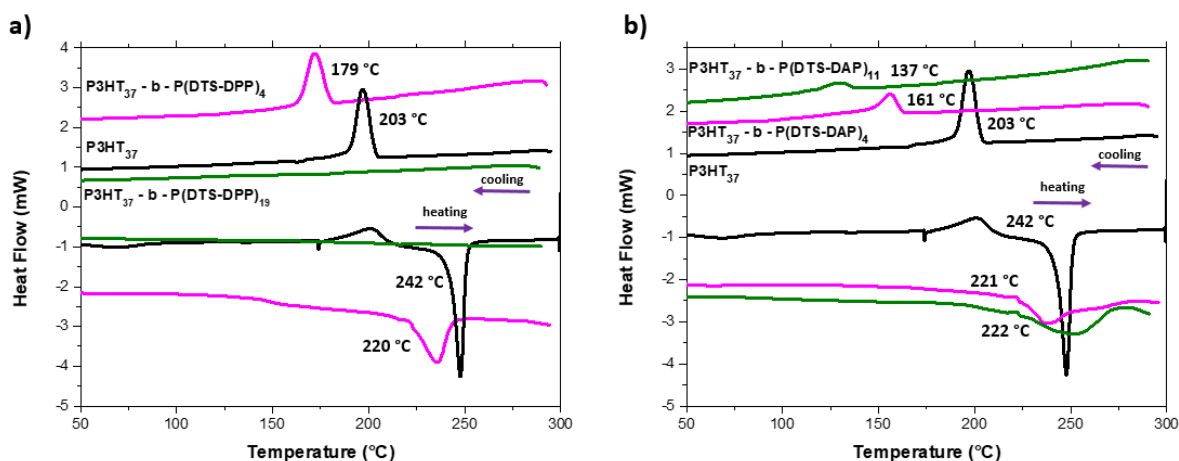


Figure II-47: DSC thermograms of P3HT₃₇ and the synthesized CBCPs based on P3HT₃₇ macroinitiator.

Although thermal transition behaviors were not detected for P(DTS-DPP) and P(DTS-DAP) copolymers, the synthesized diblock copolymers show thermal and phase transitions which are contributed to the P3HT block.

In general, the DSC results revealed that for these synthesized CBCPs, the melting temperature of P3HT was either suppressed or widened compared to that of the homopolymer due to the presence of the second block. P3HT₃₇-b-P(DTS-DPP)₁₉ has no melting endothermic peak. However, for P3HT₃₇-b-P(DTS-DPP)₄, the melting temperature was found around 220 °C (**Figure II-47a**). While in the case of P3HT₃₇-b-P(DTS-DAP)₄ and P3HT₃₇-b-P(DTS-DAP)₁₁, a single endothermic peak appears as a small enthalpy at 221 °C at 222 °C, respectively (**Figure II-47b**).

After cooling, a recrystallization behavior was detected by a single exothermic peak. The crystallization is a result of the P3HT block crystallization and is found to be at a lower temperature in copolymer than that of the P3HT macroinitiator. This lower crystallization is due to the presence of low-bandgap blocks that can disturb this process since they might be considered as impurities to be excluded. This exclusion leads to a slower crystallization than that of pure P3HT-Br, thus lowering the crystallization temperature. It is expected that this crystallization disturbance is more pronounced in block copolymers having lower P3HT block ratio.⁴¹ The lower the P3HT content in the diblock, the higher will be the content of the low-bandgap block, thus the lower the crystalline degree for P3HT block. In the case of DPP-based diblocks, a recrystallization transition temperature was observed at 179 °C for P3HT₃₇-b-P(DTS-DPP)₄ while no recrystallization was observed for P3HT₃₇-b-P(DTS-DPP)₁₉. The complete disappearance of transition temperatures for P3HT₃₇-b-P(DTS-DPP)₁₉ can be explained by the fact that the amount of P3HT by weight in this diblock is low (with respect to the calculations based on ¹H NMR). While P3HT₃₇-b-P(DTS-DAP)₄ and P3HT₃₇-b-P(DTS-DAP)₁₁ show a recrystallization transition around 161 °C and 137 °C, respectively. Melting and recrystallization temperatures were also missed in copolymers such as P3HT₂₅-b-P(DTS-DAP)₉ that also have low P3HT content around 30% (as calculated from ¹H NMR). These results are in agreement with some previous studies.¹²

To study the effect of the P3HT block on the crystallization of the diblock, DSC thermal analysis was performed on three diblock copolymers having different P3HT molar masses; P3HT₃₇-*b*-P(DTS-DPP)₄, P3HT₉₆-*b*-P(DTS-DPP)₁₃ and P3HT₂₄₀-*b*-P(DTS-DPP)₁₁. The thermograms are shown in **Figure II-48**.

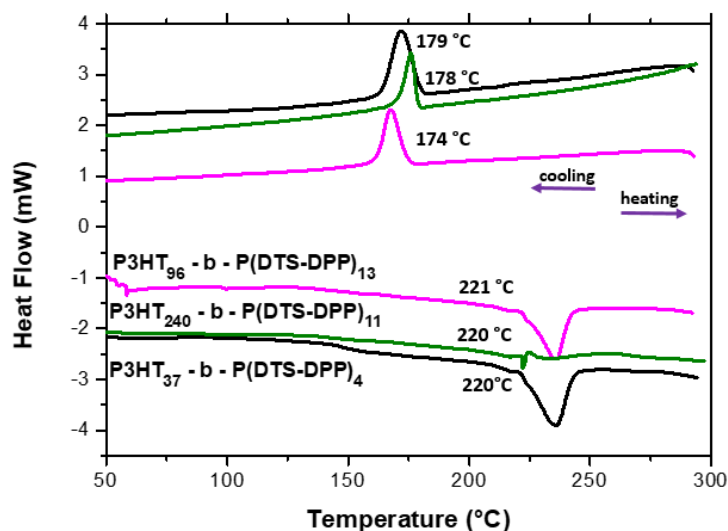


Figure II-48: DSC thermograms of CBCPs synthesized starting from different P3HT macroinitiators.

By increasing the molar mass of P3HT macroinitiator in the diblock from 37 repetitive units to 96, endothermic peaks did not change effectively. However, at very high molar mass of P3HT in the diblock (240 repetitive units), the endothermic peak could be hardly detected. It is worth noting that this peak was clearly seen in the second cycle. Regarding the exothermic peaks, that reveal the crystallization temperature, there was a slight increase in the temperature for P3HT₃₇-*b*-P(DTS-DPP)₄ (179 °C) when compared to that for P3HT₂₄₀-*b*-P(DTS-DPP)₁₁ and P3HT₉₆-*b*-P(DTS-DPP)₁₃ (178 °C and 174 °C, respectively). **Table II-10** summarizes the thermal properties of the synthesized polymers.

Table II-10: Thermal melting (T_m) and crystallization (T_c) temperatures of the synthesized polymers.

Polymer	T_m^a (°C)	T_m^b (°C)	T_c^a (°C)	% P3HT ^c
P3HT ₂₅	188	188	178	100
P3HT ₂₅ - <i>b</i> -P(DTS-DAP) ₉	----	----	----	32
P3HT ₂₅ - <i>b</i> -P(DTS-DPP) ₈	227	220	185	36
P3HT ₃₇	242	226	203	100
P3HT ₃₇ - <i>b</i> -P(DTS-DPP) ₄	220	220	179	62
P3HT ₃₇ - <i>b</i> -P(DTS-DPP) ₁₉	----	----	----	25
P3HT ₃₇ - <i>b</i> -P(DTS-DAP) ₄	221	198	161	61
P3HT ₃₇ - <i>b</i> -P(DTS-DAP) ₁₁	222	----	137	54
P3HT ₉₆	232	208	189	100
P3HT ₉₆ - <i>b</i> -P(DTS-DPP) ₁₃	221	213	174	56
P3HT ₂₄₀	216	220	197	100
P3HT ₂₄₀ - <i>b</i> -P(DTS-DPP) ₁₁	220	202	178	79

^a first cycle heating, ^b second cycle heating and ^c calculated from ¹H NMR ratios

VIII. Morphological characterizations

The morphology of the conjugated diblock copolymers was studied by Atomic Force Microscopy (AFM) in the tapping mode. The films were prepared by either spin-coating or dip-coating on hydrophilic SiO₂/Si (silicon wafer) substrates from 20 mg.mL⁻¹ solutions, then dried by thermal annealing.

For P3HT₃₇, films were prepared from chloroform-based solutions by both methods and annealed at 200 °C for 10 minutes then cooled under controlled cooling procedure. Annealing was done to ensure a high degree of crystallinity by decreasing the disorder of P3HT phase. **Figure II-49a and b** represent height images of samples prepared by dip-coating and spin-coating, respectively. The images reveal nano-meter scale fibrillar crystalline domains. This originates from π - π stacking interactions. Crystallinity and crystalline domain regions are dependent on different criteria including the film deposition process. Films casted by dip-coating show well-developed spherulites which are less clear by spin-coating. This can be explained by the slow drying process using dip-coating which offers an opportunity for P3HT to grow in a well-developed way by facilitating its self-assembly into a nanofibrillar lamellar structure after solvent evaporation.⁷⁰

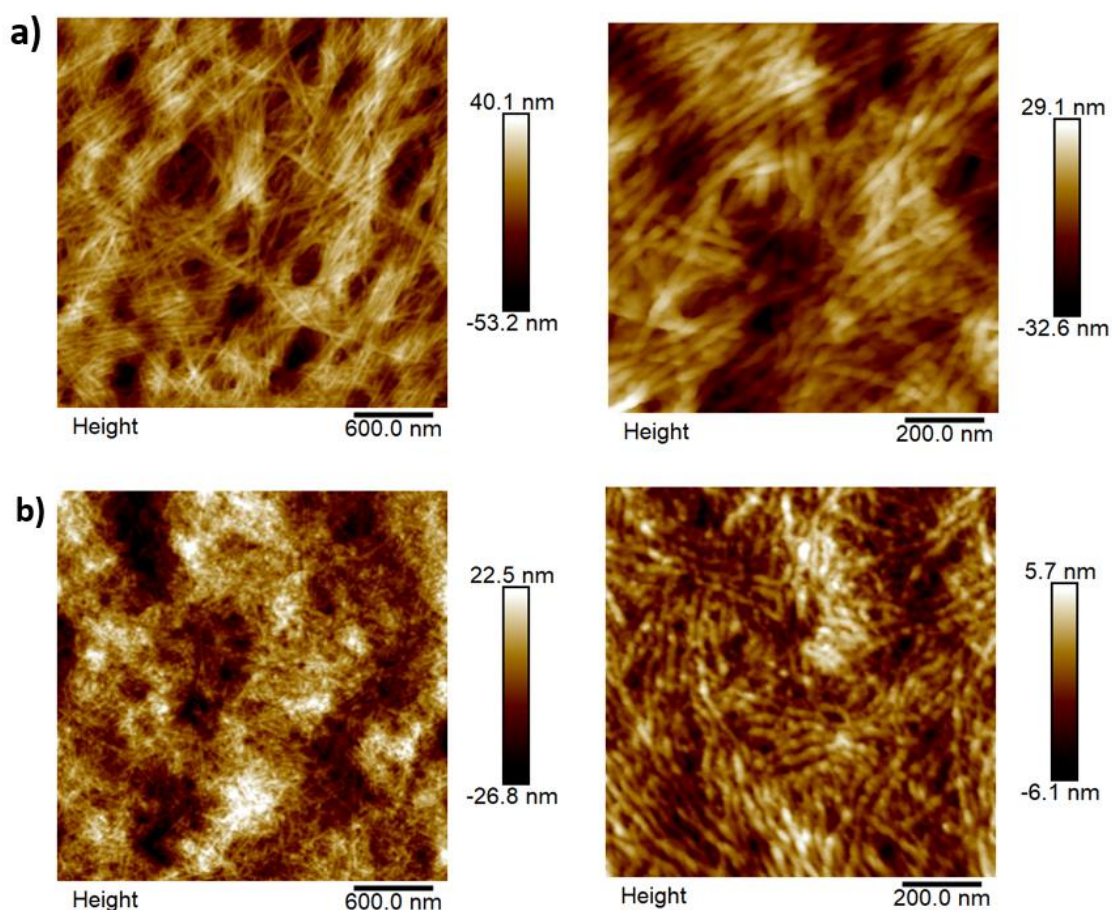


Figure II-49: Height AFM images of P3HT₃₇ films casted by (a) dip-coating and (b) spin-coating from chloroform.

P3HT₃₇-*b*-P(DTS-DPP)₄ and P3HT₂₄₀-*b*-P(DTS-DPP)₁₁ thin films were prepared by spin-coating 20 mg.mL⁻¹ chloroform-based solutions on SiO₂/Si substrates, then annealed at 150 °C for 10 min. From the AFM images of **Figure II-50**, it was evidenced that the highly semi-crystalline character of P3HT block seems to become weaker in the diblock copolymer. The well-defined nanowires probably correspond to the polythiophene block. This is an indication that the morphology of the diblock was governed by the molecular packing of the conjugated P3HT block. P3HT₃₇-*b*-P(DTS-DPP)₄ shows finer fibrillar structured crystallinity when compared to P3HT₂₄₀-*b*-P(DTS-DPP)₁₁ which constitutes a higher molar mass of P3HT block. Since the crystallinity of the diblock copolymer is originated from the P3HT block, the lower molar mass P3HT chains can find a better equilibrium between the amorphous and the polycrystalline domains. This allows P3HT to form ordered structures more easier than the high molar mass chains that are characterized by low crystallization kinetics.⁷¹

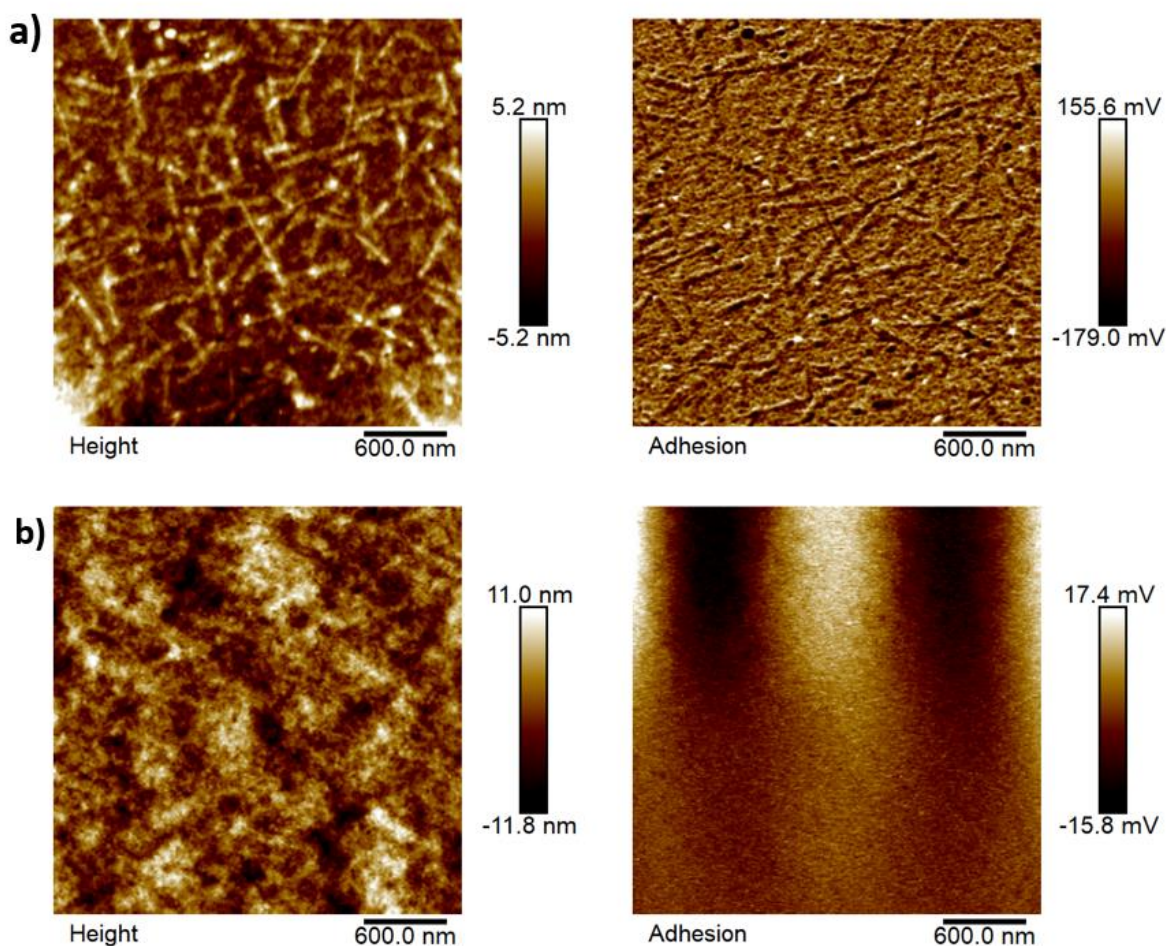


Figure II-50: Height and adhesion AFM images of (a) P3HT₃₇-*b*-P(DTS-DPP)₄ and (b) P3HT₂₄₀-*b*-P(DTS-DPP)₁₁ films casted by spin-coating from chloroform.

Interestingly, the morphological behavior differs by changing the casting solvent from chloroform to *o*-xylene under the same conditions. The films contain more elongated P3HT fiber-like nanodomains over the entire area for both P3HT₃₇-*b*-P(DTS-DPP)₄ and P3HT₂₄₀-*b*-P(DTS-DPP)₁₁ as shown in **Figure II-51**. This can be attributed to the higher boiling point of *o*-xylene when compared to chloroform. Thus, the drying process is slow, which renders a better film organization.⁷²

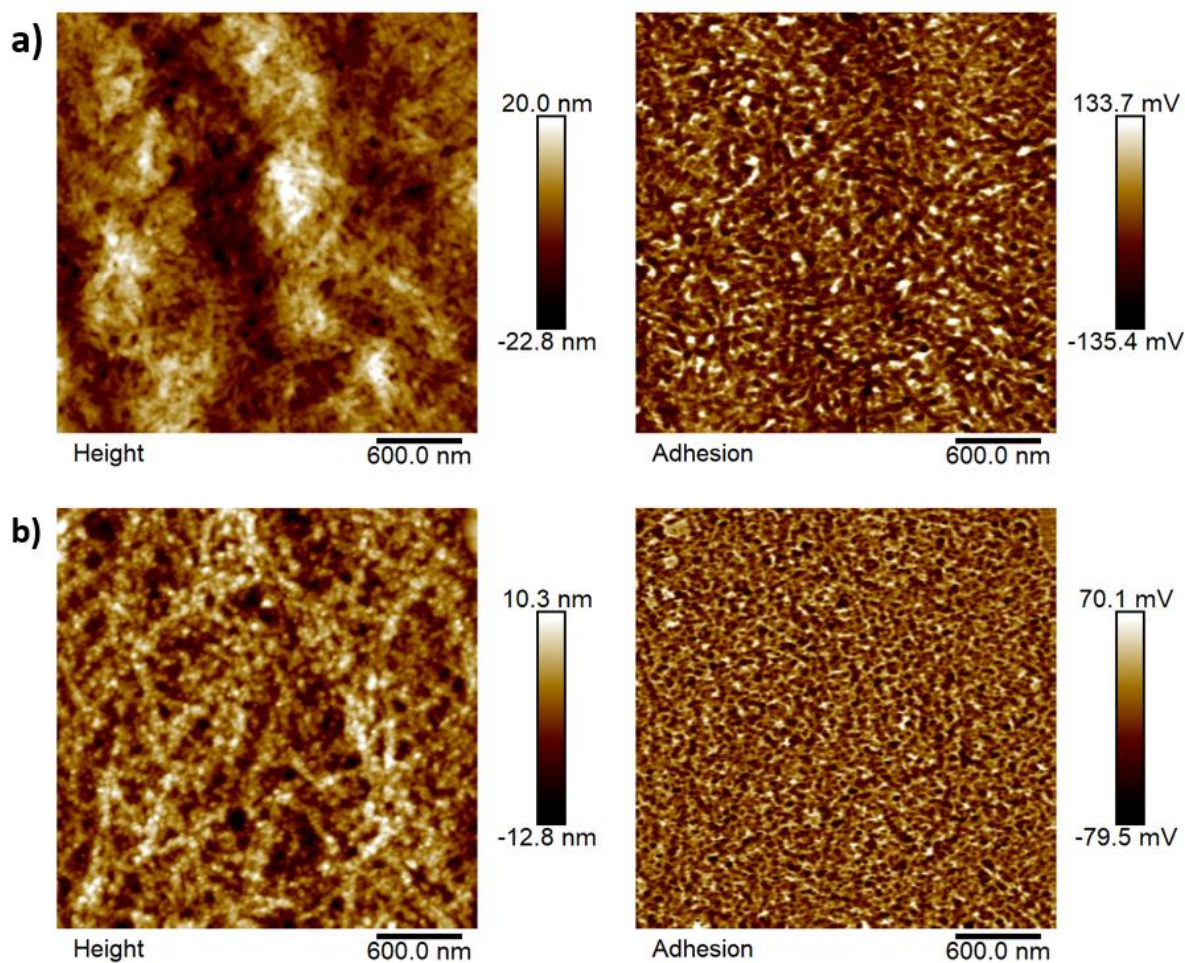


Figure II-51: Height and adhesion AFM images of (a) $P3HT_{37}\text{-}b\text{-}P(\text{DTS-DPP})_4$ and (b) $P3HT_{240}\text{-}b\text{-}P(\text{DTS-DPP})_{11}$ films casted by spin-coating from *o*-xylene.

Morphology of $P3HT_{37}\text{-}b\text{-}P(\text{DTS-DAP})_4$ thin films was also studied by AFM. These layers were prepared in a similar way to that of the DPP-based diblocks by spin-coating from chloroform solution and annealed at 150 °C. As revealed by **Figure II-52a**, the nanostructured morphology of this diblock copolymer is well governed by the self-assembly of the P3HT block as the obtained crystalline elongated fibers look like those obtained for P3HT homopolymer. However, unlike $P3HT_{37}\text{-}b\text{-}P(\text{DTS-DPP})_4$, the surface was not completely covered. Thus, films were prepared again by dip-coating to see the effect on the surface coverage but as can be seen on **Figure II-52b**, the same morphology was obtained.

Thus, in general, $P3HT_{37}\text{-}b\text{-}P(\text{DTS-DAP})_4$ shows a highly heterogeneous structure characterized by relatively dense network of fibers but not enough to ensure the full coverage of the surface. Thus, the substrate can be observed in some places.

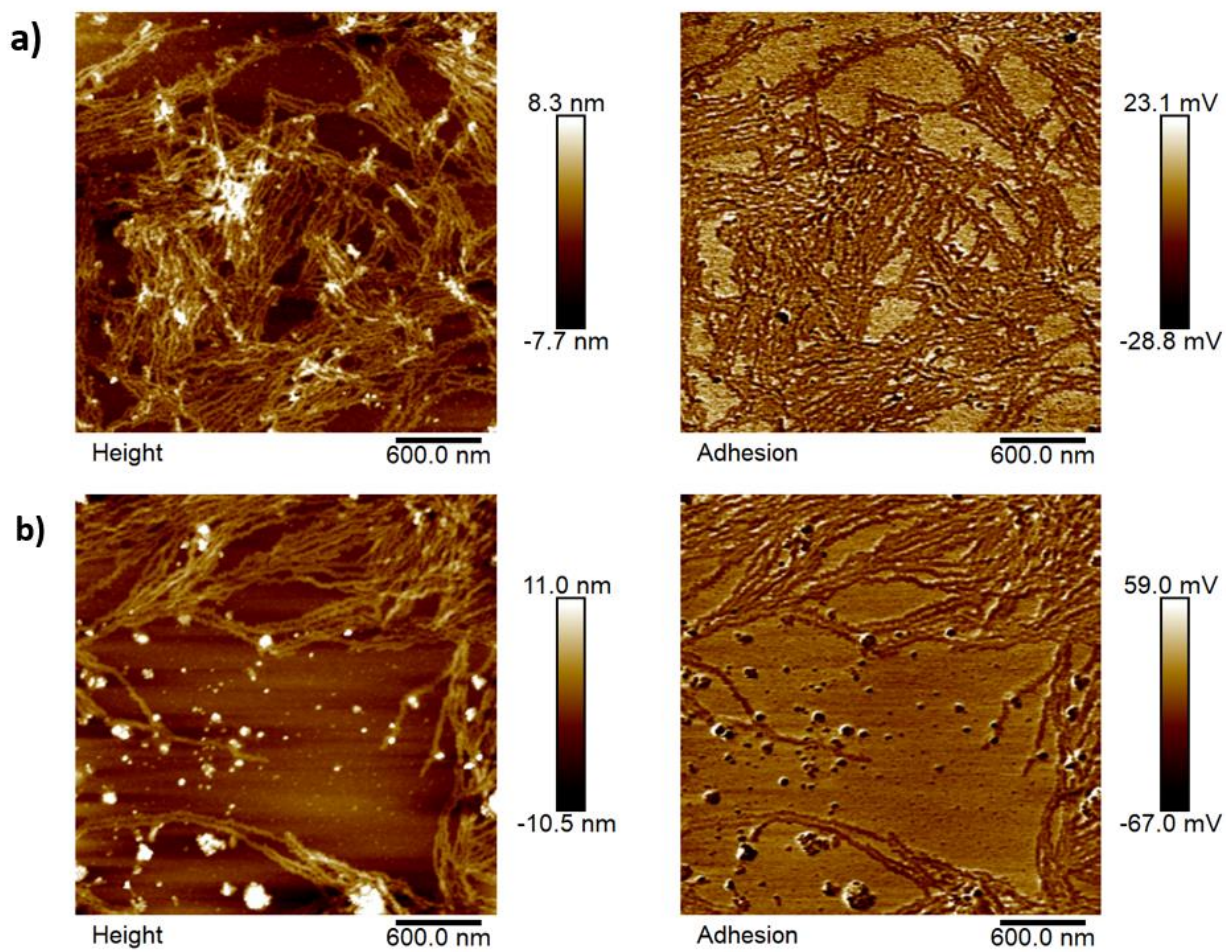


Figure II-52: Height and adhesion AFM images of $P3HT_{37}\text{-}b\text{-}P(\text{DTS-DAP})_4$ films casted from chloroform solution by (a) spin-coating and (b) dip-coating.

IX. Conclusion

DPP and DAP acceptor monomers were prepared and characterized after optimizing their synthetic procedures. Well-defined P3HT polymers having different molar masses and dispersities were also synthesized and characterized by several methods. After proving the single bromo chain-end of P3HT by MALDI-TOF, Stille coupling polymerization has been used to create rod-rod conjugated block copolymers with either DPP or DAP building blocks. The synthesized CBCPs were based on P3HT that serves as electron donor block and DTS-DPP or DTS-DAP serving as electron acceptor blocks. The synthesized diblock copolymers were purified by Soxhlet successive extractions in different solvents and finally collected in chloroform. An attractive feature of such a modular strategy is the high degree of flexibility afforded over the structure and chemical composition of the resulting CBCPs. Molar mass and the resulting relative block lengths of the CBCPs were tailored by varying the amount of starting materials using the Carothers equation, thus different molar mass CBCPs were obtained and characterized. Structural analysis revealed the formation of the desired block copolymers such as ^1H NMR, DOSY NMR and SEC in THF and in Toluene.

Optoelectronic properties of the diblocks were studied. Interestingly, both kinds absorb in the near-IR region in which P3HT contributes to one peak at low wavelength (around 445 nm), while the second absorption peak was shifted to a higher wavelength (around 900 nm or more) in the case of $\text{P3HT}_n\text{-}b\text{-P(DTS-DAP)}_m$ when compared to $\text{P3HT}_n\text{-}b\text{-P(DTS-DPP)}_m$ (around 810 nm). Due to the strong donor character of DAP monomer since it is more electron deficient than DPP, optical bandgap calculations revealed lower bandgaps for DAP-based diblocks when compared to DPP-based ones which was also proved after calculating the electrochemical bandgaps by cyclic voltammetry.

Thermal characterizations using TGA revealed high decomposition temperatures for diblocks which is an indication for their high thermal stability. Although, DAP-based blocks were less stable than DPP-based blocks, in general, this high stability is an important property that allow them to be used as photovoltaic materials in organic solar cells. DSC analysis revealed thermal and phase transitions for the synthesized diblock copolymers which were contributed from the P3HT block and impacted by the weight content of the P3HT block.

The crystallinity of $\text{P3HT}_n\text{-}b\text{-P(DTS-DPP)}_m$ and $\text{P3HT}_n\text{-}b\text{-P(DTS-DAP)}_m$ was also revealed by AFM. Thin films for both polymer types in chloroform and *o*-xylene support the periodic P3HT nanofibrillar structure which resembles the same morphology encountered in regioregular P3HT homopolymers. Thus, the organization of the synthesized diblocks is governed by the self-assembly of P3HT block.

Based on the obtained results, it was then interesting to evaluate the photovoltaic properties of the synthesized diblock copolymers under different conditions in organic solar cells.

References

- (1) Hussein, A. A.; Sultan, A. A.; Obeid, M. T.; Abdulnabi, A. T.; Ali, M. T. Synthesis and Characterization of Poly(3-Hexylthiophene). *IJSEAS* **2015**, *1* (7), 6.
- (2) Bronstein, H.; Chen, Z.; Ashraf, R. S.; Zhang, W.; Du, J.; Durrant, J. R.; Shakya Tuladhar, P.; Song, K.; Watkins, S. E.; Geerts, Y.; Wienk, M. M.; Janssen, R. A. J.; Anthopoulos, T.; Sirringhaus, H.; Heeney, M.; McCulloch, I. Thieno[3,2-b]Thiophene–Diketopyrrolopyrrole-Containing Polymers for High-Performance Organic Field-Effect Transistors and Organic Photovoltaic Devices. *J. Am. Chem. Soc.* **2011**, *133* (10), 3272–3275.
- (3) Bijleveld, J. C.; Zoombelt, A. P.; Mathijssen, S. G. J.; Wienk, M. M.; Turbiez, M.; de Leeuw, D. M.; Janssen, R. A. J. Poly(Diketopyrrolopyrrole-Terthiophene) for Ambipolar Logic and Photovoltaics. *J. Am. Chem. Soc.* **2009**, *131* (46), 16616–16617.
- (4) Oh, J. Y.; Rondeau-Gagné, S.; Chiu, Y.-C.; Chortos, A.; Lissel, F.; Wang, G.-J. N.; Schroeder, B. C.; Kurosawa, T.; Lopez, J.; Katsumata, T.; Xu, J.; Zhu, C.; Gu, X.; Bae, W.-G.; Kim, Y.; Jin, L.; Chung, J. W.; Tok, J. B.-H.; Bao, Z. Intrinsically Stretchable and Healable Semiconducting Polymer for Organic Transistors. *Nature* **2016**, *539* (7629), 411–415.
- (5) Pop, F.; Humphreys, J.; Schwarz, J.; Brown, L.; Berg, A. van den; Amabilino, D. B. Towards More Sustainable Synthesis of Diketopyrrolopyrroles. *New J. Chem.* **2019**, *43* (15), 5783–5790.
- (6) Closs, F.; Gompper, R. 2,5-Diazapentalenes. *Angew. Chem. Int. Ed. Engl.* **1987**, *26* (6), 552–554.
- (7) Qian, G.; Qi, J.; Davey, J. A.; Wright, J. S.; Wang, Z. Y. Family of Diazapentalene Chromophores and Narrow-Band-Gap Polymers: Synthesis, Halochromism, Halofluorism, and Visible–Near Infrared Photodetectivity. *Chem. Mater.* **2012**, *24* (12), 2364–2372.
- (8) Chu, T.-Y.; Lu, J.; Beaupré, S.; Zhang, Y.; Pouliot, J.-R.; Wakim, S.; Zhou, J.; Leclerc, M.; Li, Z.; Ding, J.; Tao, Y. Bulk Heterojunction Solar Cells Using Thieno[3,4-c]Pyrrole-4,6-Dione and Dithieno[3,2-b:2',3'-d]Silole Copolymer with a Power Conversion Efficiency of 7.3%. *J. Am. Chem. Soc.* **2011**, *133* (12), 4250–4253.
- (9) Zhang, M.; Fan, H.; Guo, X.; He, Y.; Zhang, Z.; Min, J.; Zhang, J.; Zhao, G.; Zhan, X.; Li, Y. Synthesis and Photovoltaic Properties of Bithiazole-Based Donor–Acceptor Copolymers. *Macromolecules* **2010**, *43* (13), 5706–5712.
- (10) Chen, H.-Y.; Hou, J.; Hayden, A. E.; Yang, H.; Houk, K. N.; Yang, Y. Silicon Atom Substitution Enhances Interchain Packing in a Thiophene-Based Polymer System. *Adv. Mater.* **2010**, *22* (3), 371–375.
- (11) Huang, J.-H.; Teng, C.-M.; Hsiao, Y.-S.; Yen, F.-W.; Chen, P.; Chang, F.-C.; Chu, C.-W. Nanoscale Correlation between Exciton Dissociation and Carrier Transport in Silole-Containing Cyclopentadithiophene-Based Bulk Heterojunction Films. *J. Phys. Chem. C* **2011**, *115* (5), 2398–2405.
- (12) Sommer, M.; Komber, H.; Huettner, S.; Mulherin, R.; Kohn, P.; Greenham, N. C.; Huck, W. T. S. Synthesis, Purification, and Characterization of Well-Defined All-Conjugated Diblock Copolymers PF8TBT-b-P3HT. *Macromolecules* **2012**, *45* (10), 4142–4151.
- (13) Ku, S.-Y.; Brady, M. A.; Treat, N. D.; Cochran, J. E.; Robb, M. J.; Kramer, E. J.; Chabinc, M. L.; Hawker, C. J. A Modular Strategy for Fully Conjugated Donor–Acceptor Block Copolymers. *J. Am. Chem. Soc.* **2012**, *134* (38), 16040–16046.
- (14) Carsten, B.; He, F.; Son, H. J.; Xu, T.; Yu, L. Stille Polycondensation for Synthesis of Functional Materials. *Chem. Rev.* **2011**, *111* (3), 1493–1528.
- (15) Lee, D. H.; Lee, J. H.; Kim, H. J.; Choi, S.; Park, G. E.; Cho, M. J.; Choi, D. H. (D)n-σ-(A)m Type Partially Conjugated Block Copolymer and Its Performance in Single-Component Polymer Solar Cells. *J. Mater. Chem. A* **2017**, *5* (20), 9745–9751.
- (16) Hu, Z.; Jakowski, J.; Zheng, C.; Collison, C. J.; Strzalka, J.; Sumpter, B. G.; Verduzco, R. An Experimental and Computational Study of Donor-Linker-Acceptor Block Copolymers for Organic Photovoltaics. *J. Polym. Sci. Part B Polym. Phys.* **2018**, *56* (16), 1135–1143.
- (17) Mok, J. W.; Lin, Y.-H.; Yager, K. G.; Mohite, A. D.; Nie, W.; Darling, S. B.; Lee, Y.; Gomez, E.; Gosztola, D.; Schaller, R. D.; Verduzco, R. Conjugated Polymers: Linking Group Influences Charge Separation and Recombination in All-Conjugated Block Copolymer Photovoltaics. *Adv. Funct. Mater.* **2015**, *25* (35), 5569–5569.
- (18) Erdmann, T.; Back, J.; Tkachov, R.; Ruff, A.; Voit, B.; Ludwigs, S.; Kiriy, A. Dithienosilole-Based All-Conjugated Block Copolymers Synthesized by a Combination of Quasi-Living Kumada and Negishi Catalyst-Transfer Polycondensations. *Polym. Chem.* **2014**, *5* (18), 5383–5390.
- (19) Iovu, M. C.; Sheina, E. E.; Gil, R. R.; McCullough, R. D. Experimental Evidence for the Quasi-“Living” Nature of the Grignard Metathesis Method for the Synthesis of Regioregular Poly(3-Alkylthiophenes). *Macromolecules* **2005**, *38* (21), 8649–8656.

- (20) Langeveld-Voss, B. M. W.; Janssen, R. A. J.; Spiering, A. J. H.; Dongen, J. L. J. van; Vonk, E. C.; Claessens, H. A. End-Group Modification of Regioregular Poly(3-Alkylthiophene)s. *Chem. Commun.* **2000**, No. 1, 81–82.
- (21) Liu, J.; Loewe, R. S.; McCullough, R. D. Employing MALDI-MS on Poly(Alkylthiophenes): Analysis of Molecular Weights, Molecular Weight Distributions, End-Group Structures, and End-Group Modifications. *Macromolecules* **1999**, *32* (18), 5777–5785.
- (22) Bannock, J. H.; Treat, N. D.; Chabiny, M.; Stingelin, N.; Heeney, M.; de Mello, J. C. The Influence of Polymer Purification on the Efficiency of Poly(3-Hexylthiophene):Fullerene Organic Solar Cells. *Sci. Rep.* **2016**, *6*.
- (23) Sheina, E. E.; Liu, J.; Iovu, M. C.; Laird, D. W.; McCullough, R. D. Chain Growth Mechanism for Regioregular Nickel-Initiated Cross-Coupling Polymerizations. *Macromolecules* **2004**, *37* (10), 3526–3528.
- (24) Delbos, N.; De Winter, J.; Moins, S.; Persoons, A.; Dubois, P.; Coulembier, O. Macrocyclic P3HT Obtained by Intramolecular McMurry Coupling of Linear Bis-Aldehyde Polymer: A Direct Comparison with Linear Homologue. *Macromolecules* **2017**, *50* (5), 1939–1949.
- (25) Cruz, R. A.; Catunda, T.; Facchinatto, W. M.; Balogh, D. T.; Faria, R. M. Absolute Photoluminescence Quantum Efficiency of P3HT/CHCl₃ Solution by Thermal Lens Spectrometry. *Synth. Met.* **2013**, *163*, 38–41.
- (26) Hiorns, R. C.; de Bettignies, R.; Leroy, J.; Bailly, S.; Firon, M.; Sentein, C.; Khoukh, A.; Preud'homme, H.; Dagron-Lartigau, C. High Molecular Weights, Polydispersities, and Annealing Temperatures in the Optimization of Bulk-Heterojunction Photovoltaic Cells Based on Poly(3-Hexylthiophene) or Poly(3-Butylthiophene). *Adv. Funct. Mater.* **2006**, *16* (17), 2263–2273.
- (27) Farnum, D. G.; Mehta, G.; Moore, G. G. I.; Siegal, F. P. Attempted Reformatskii Reaction of Benzonitrile, 1,4-Diketo-3,6-Diphenylpyrrolo[3,4-C]Pyrrole. A Lactam Analogue of Pentalene. *Tetrahedron Lett.* **1974**, *15* (29), 2549–2552.
- (28) Iqbal, A.; Jost, M.; Kirchmayr, R.; Pfenninger, J.; Rochat, A.; Wallquist, O. The Synthesis and Properties of 1,4-Diketo-Pyrrolo[3,4-C]Pyrroles. *Bull. Sociétés Chim. Belg.* **1988**, *97* (8–9), 615–644.
- (29) Bijleveld, J. C.; Karsten, B. P.; Mathijssen, S. G. J.; Wienk, M. M.; Leeuw, D. M. de; Janssen, R. A. J. Small Band Gap Copolymers Based on Furan and Diketopyrrolopyrrole for Field-Effect Transistors and Photovoltaic Cells. *J. Mater. Chem.* **2011**, *21* (5), 1600–1606.
- (30) Huo, L.; Hou, J.; Chen, H.-Y.; Zhang, S.; Jiang, Y.; Chen, T. L.; Yang, Y. Bandgap and Molecular Level Control of the Low-Bandgap Polymers Based on 3,6-Dithiophen-2-Yl-2,5-Dihydropyrrolo[3,4-c]Pyrrole-1,4-Dione toward Highly Efficient Polymer Solar Cells. *Macromolecules* **2009**, *42* (17), 6564–6571.
- (31) Zou, Y.; Gendron, D.; Neagu-Plesu, R.; Leclerc, M. Synthesis and Characterization of New Low-Bandgap Diketopyrrolopyrrole-Based Copolymers. *Macromolecules* **2009**, *42* (17), 6361–6365.
- (32) Stas, S.; Balandier, J.-Y.; Lemaire, V.; Fenwick, O.; Tregnago, G.; Quist, F.; Cacialli, F.; Cornil, J.; Geerts, Y. H. Straightforward Access to Diketopyrrolopyrrole (DPP) Dimers. *Dyes Pigments* **2013**, *97* (1), 198–208.
- (33) Hendsbee, A. D.; Sun, J.-P.; Rutledge, L. R.; Hill, I. G.; Welch, G. C. Electron Deficient Diketopyrrolopyrrole Dyes for Organic Electronics: Synthesis by Direct Arylation, Optoelectronic Characterization, and Charge Carrier Mobility. *J. Mater. Chem. A* **2014**, *2* (12), 4198–4207.
- (34) Grzybowski, M.; Gryko, D. T. Diketopyrrolopyrroles: Synthesis, Reactivity, and Optical Properties. *Adv. Opt. Mater.* **2015**, *3* (3), 280–320.
- (35) Chandran, D.; Lee, K.-S. Diketopyrrolopyrrole: A Versatile Building Block for Organic Photovoltaic Materials. *Macromol. Res.* **2013**, *21* (3), 272–283.
- (36) Sana, A. e.; Khan, S. W.; Zaidi, J. H.; Ambreen, N.; Khan, K. M.; Perveen, S. Syntheses and Antimicrobial Activities of Amide Derivatives of 4-[(2-Isopropyl-5-Methylcyclohexyl)Oxo]-4-Oxobutanoic Acid. *Nat. Sci.* **2011**, *3* (10), 855–861.
- (37) Kroon, R.; Diaz de Zerio Mendaza, A.; Himmelberger, S.; Bergqvist, J.; Bäcke, O.; Faria, G. C.; Gao, F.; Obaid, A.; Zhuang, W.; Gedefaw, D.; Olsson, E.; Inganäs, O.; Salleo, A.; Müller, C.; Andersson, M. R. A New Tetracyclic Lactam Building Block for Thick, Broad-Bandgap Photovoltaics. *J. Am. Chem. Soc.* **2014**, *136* (33), 11578–11581.
- (38) Breugst, M.; Mayr, H. Ambident Reactivities of Pyridone Anions. *J. Am. Chem. Soc.* **2010**, *132* (43), 15380–15389.
- (39) He, B.; Pun, A. B.; Klivansky, L. M.; McGough, A. M.; Ye, Y.; Zhu, J.; Guo, J.; Teat, S. J.; Liu, Y. Thiophene Fused Azacoronenes: Regioselective Synthesis, Self-Organization, Charge Transport and Its Incorporation in Conjugated Polymers. *Chem. Mater.* **2014**, *26* (13), 3920–3927.

- (40) Guérette, M.; Najari, A.; Maltais, J.; Pouliot, J.-R.; Dufresne, S.; Simoneau, M.; Besner, S.; Charest, P.; Leclerc, M. New Processable Phenanthridinone-Based Polymers for Organic Solar Cell Applications. *Adv. Energy Mater.* **2016**, *6* (9), 1502094.
- (41) Kirkus, M.; Wang, L.; Mothy, S.; Beljonne, D.; Cornil, J.; Janssen, R. A. J.; Meskers, S. C. J. Optical Properties of Oligothiophene Substituted Diketopyrrolopyrrole Derivatives in the Solid Phase: Joint J- and H-Type Aggregation. *J. Phys. Chem. A* **2012**, *116* (30), 7927–7936.
- (42) Mishra, S. P.; Palai, A. K.; Patri, M. Synthesis and Characterization of Soluble Narrow Band Gap Conducting Polymers Based on Diketopyrrolopyrrole and Propylenedioxythiophenes. *Synth. Met.* **2010**, *160* (23), 2422–2429.
- (43) Matthews, J. R.; Niu, W.; Tandia, A.; Wallace, A. L.; Hu, J.; Lee, W.-Y.; Giri, G.; Mannsfeld, S. C. B.; Xie, Y.; Cai, S.; Fong, H. H.; Bao, Z.; He, M. Scalable Synthesis of Fused Thiophene-Diketopyrrolopyrrole Semiconducting Polymers Processed from Nonchlorinated Solvents into High Performance Thin Film Transistors. *Chem. Mater.* **2013**, *25* (5), 782–789.
- (44) Fu, B.; Baltazar, J.; Sankar, A. R.; Chu, P.-H.; Zhang, S.; Collard, D. M.; Reichmanis, E. Enhancing Field-Effect Mobility of Conjugated Polymers Through Rational Design of Branched Side Chains. *Adv. Funct. Mater.* **2014**, *24* (24), 3734–3744.
- (45) Khelifi, W.; Awada, H.; Brymora, K.; Blanc, S.; Hirsch, L.; Castet, F.; Bousquet, A.; Lartigau-Dagron, C. Halochromic Switch from the 1st to 2nd Near-Infrared Window of Diazapentalene–Dithienosilole Copolymers. *Macromolecules* **2019**, *52* (13), 4820–4827.
- (46) Wood, S.; Wade, J.; Shahid, M.; Collado-Fregoso, E.; Bradley, D. D. C.; Durrant, J. R.; Heeney, M.; Kim, J.-S. Natures of Optical Absorption Transitions and Excitation Energy Dependent Photostability of Diketopyrrolopyrrole (DPP)-Based Photovoltaic Copolymers. *Energy Environ. Sci.* **2015**, *8* (11), 3222–3232.
- (47) Qian, G.; Qi, J.; Wang, Z. Y. Synthesis and Study of Low-Bandgap Polymers Containing the Diazapentalene and Diketopyrrolopyrrole Chromophores for Potential Use in Solar Cells and near-Infrared Photodetectors. *J. Mater. Chem.* **2012**, *22* (25), 12867–12873.
- (48) Hedley, G. J.; Ward, A. J.; Alekseev, A.; Howells, C. T.; Martins, E. R.; Serrano, L. A.; Cooke, G.; Ruseckas, A.; Samuel, I. D. W. Determining the Optimum Morphology in High-Performance Polymer-Fullerene Organic Photovoltaic Cells. *Nat. Commun.* **2013**, *4* (1), 1–10.
- (49) Zhang, X.; Richter, L. J.; DeLongchamp, D. M.; Kline, R. J.; Hammond, M. R.; McCulloch, I.; Heeney, M.; Ashraf, R. S.; Smith, J. N.; Anthopoulos, T. D.; Schroeder, B.; Geerts, Y. H.; Fischer, D. A.; Toney, M. F. Molecular Packing of High-Mobility Diketo Pyrrolo-Pyrrole Polymer Semiconductors with Branched Alkyl Side Chains. *J. Am. Chem. Soc.* **2011**, *133* (38), 15073–15084.
- (50) Carothers, W. H. Polymers and Polyfunctionality. *Trans. Faraday Soc.* **1936**, *32* (0), 39–49.
- (51) Knoester, H. Theoretical Derivation of the Molecular Weight Distribution of End-Capped Linear Condensation Polymers. *Macromol. Theory Simul.* **2009**, *18* (1), 61–69.
- (52) Flory, P. J. Molecular Size Distribution in Linear Condensation Polymers. *J. Am. Chem. Soc.* **1936**, *58* (10), 1877–1885.
- (53) Qian, G.; Wang, Z. Y. Design, Synthesis, and Properties of Benzobisthiadiazole-Based Donor– π –Acceptor– π –Donor Type of Low-Band-Gap Chromophores and Polymers. *Can. J. Chem.* **2010**, *88* (3), 192–201.
- (54) Romero-Nieto, C.; Durben, S.; Kormos, I. M.; Baumgartner, T. Simple and Efficient Generation of White Light Emission From Organophosphorus Building Blocks. *Adv. Funct. Mater.* **2009**, *19* (22), 3625–3631.
- (55) Moliton, A.; Hiorns, R. C. Review of Electronic and Optical Properties of Semiconducting π -Conjugated Polymers: Applications in Optoelectronics. *Polym. Int.* **2004**, *53* (10), 1397–1412.
- (56) Lamare, S.; Aly, S. M.; Fortin, D.; Harvey, P. D. Incorporation of Zinc(II) Porphyrins in Polyaniline in Its Perigraniline Form Leading to Polymers with the Lowest Band Gap. *Chem. Commun.* **2011**, *47* (39), 10942–10944.
- (57) Cheng, Y.-J.; Yang, S.-H.; Hsu, C.-S. Synthesis of Conjugated Polymers for Organic Solar Cell Applications. *Chem. Rev.* **2009**, *109* (11), 5868–5923.
- (58) Welch, G. C.; Coffin, R.; Peet, J.; Bazan, G. C. Band Gap Control in Conjugated Oligomers via Lewis Acids. *J. Am. Chem. Soc.* **2009**, *131* (31), 10802–10803.
- (59) Rughoputh, S. D. D. V.; Hotta, S.; Heeger, A. J.; Wudl, F. Chromism of Soluble Polythienylenes. *J. Polym. Sci. Part B Polym. Phys.* **1987**, *25* (5), 1071–1078.
- (60) Lévesque, I.; Leclerc, M. Ionochromic and Thermochromic Phenomena in a Regioregular Polythiophene Derivative Bearing Oligo(Oxyethylene) Side Chains. *Chem. Mater.* **1996**, *8* (12), 2843–2849.
- (61) Lee, Y.-H.; Yen, W.-C.; Su, W.-F.; Dai, C.-A. Self-Assembly and Phase Transformations of π -Conjugated Block Copolymers That Bend and Twist: From Rigid-Rod Nanowires to Highly Curvaceous Gyroids. *Soft Matter* **2011**, *7* (21), 10429–10442.

- (62) Gritzner, G.; Kuta, J. Recommendations on Reporting Electrode Potentials in Nonaqueous Solvents (Recommendations 1983). *Pure Appl. Chem.* **1984**, *56* (4), 461–466.
- (63) Alfassi, Z. General aspects of the chemistry of radicals, **1999**.
- (64) Bredas, J. L.; Silbey, R.; Boudreaux, D. S.; Chance, R. R. Chain-Length Dependence of Electronic and Electrochemical Properties of Conjugated Systems: Polyacetylene, Polyphenylene, Polythiophene, and Polypyrrole. *J. Am. Chem. Soc.* **1983**, *105* (22), 6555–6559.
- (65) Tremel, K.; Ludwigs, S. Morphology of P3HT in Thin Films in Relation to Optical and Electrical Properties. In *Advances in Polymer Science*; 2014; Vol. 265, pp 39–82.
- (66) Misra, A.; Kumar, P.; Srivastava, R.; Dhawan, S. K.; Kamalasanan, M. N.; Chandra, S. Electrochemical and Optical Studies of Conjugated Polymers for Three Primary Colours. *APPL PHYS* **2005**, *43*, 5.
- (67) Ramani, R.; Srivastava, J.; Alam, S. Application of Model-Free Kinetics to the Thermal and Thermo-Oxidative Degradation of Poly(3-Hexyl Thiophene). *Thermochim. Acta* **2010**, *499* (1), 34–39.
- (68) David, J.; Weiter, M.; Vala, M.; Vyňuchal, J.; Kučerík, J. Stability and Structural Aspects of Diketopyrrolopyrrole Pigment and Its N-Alkyl Derivatives. *Dyes Pigments* **2011**, *89* (2), 137–143.
- (69) Yuan, M.-C.; Chou, Y.-J.; Chen, C.-M.; Hsu, C.-L.; Wei, K.-H. A Crystalline Low-Bandgap Polymer Comprising Dithienosilole and Thieno[3,4-c]Pyrrole-4,6-Dione Units for Bulk Heterojunction Solar Cells. *Polymer* **2011**, *52* (13), 2792–2798.
- (70) Hu, Z.; Zhang, J.; Xiong, S.; Zhao, Y. Performance of Polymer Solar Cells Fabricated by Dip Coating Process. *Sol. Energy Mater. Sol. Cells* **2012**, *99*, 221–225.
- (71) Kline, R. J.; McGehee, M. D.; Kadnikova, E. N.; Liu, J.; Fréchet, J. M. J.; Toney, M. F. Dependence of Regioregular Poly(3-Hexylthiophene) Film Morphology and Field-Effect Mobility on Molecular Weight. *Macromolecules* **2005**, *38* (8), 3312–3319.
- (72) Shin, P.-K.; Kumar, P.; Kumar, A.; Kannappan, S.; Ochiai, S. Effects of Organic Solvents for Composite Active Layer of PCDTBT/PC₇₁ BM on Characteristics of Organic Solar Cell Devices. *Int. J. Photoenergy* **2014**, *2014*, 1–8.

Chapter III:
Performances of Diblock
Copolymer-Based Organic Solar
Cells

I. Introduction

In a world of ever-increasing energy demands caused by technological advancement in mass communication and economy, the need for renewable energy sources is becoming important for energy production.¹ The majority of the produced energy worldwide (80%) is based on non-renewable fossil fuels energy sources including coal, natural gas and petroleum as shown in **Figure III-1a**. They are formed from plants buried underground, thus these sources require costly explorations and potentially dangerous mining and drilling. Moreover, they are expensive as supplies are limited and take long time to be formed. However, the true cost of these fossil fuels are not always obvious, but their impacts can be disastrous. Paying money to get such energy source is a direct cost. However, the main harmful issue behind fossil fuel burning, is generation of the greenhouse gas, carbon dioxide CO₂, which is increasing tremendously as shown in **Figure III-1b**.² This causes air pollution and global warming that eventually increase public health risk such as respiratory illness and death.³

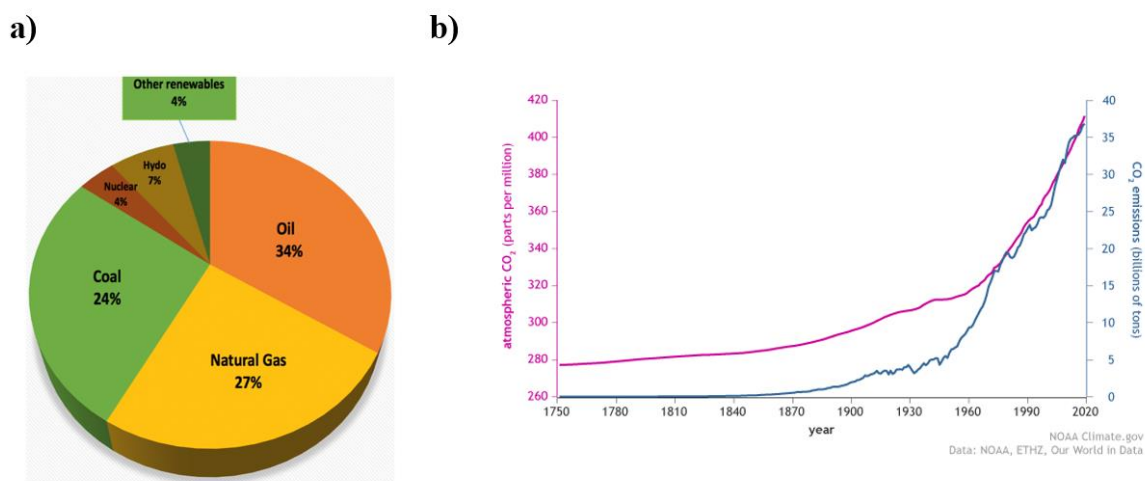


Figure III-1: (a) Pie-chart of global energy consumption in 2018 and (b) atmospheric and annual emission of CO₂.²

Looking for better permanent alternatives, renewable energy sources are the best choices to replace non-renewable ones. These sources are naturally available with unlimited supplies. They include biomass, hydrothermal, geothermal, wind and solar energy.

The International Renewable Energy Agency (IRENA) published that the global renewable generation capacity increased tremendously including solar energy in which the world revealed the great importance of fresh photovoltaic capacity.⁴ Other studies showed that solar energy contributed to less than 1% of the total energy related global warming emissions.⁵ Thus, solar energy is of great interest in our work.

II. Organic photovoltaic cells

a. Concept of organic solar cells

Solar cells, also known as photovoltaic cells are important source of renewable energy that convert solar energy (sunlight or artificial light) directly into electric energy using the photovoltaic effect.⁶

Three different generations of solar cells were recognized and classified based on their fabrication methods and materials used. Among the third generation, organic solar cells (OSC) or organic photovoltaics (OPV) are considered as promising emerging generation of photovoltaics.

Organic solar cells are characterized by their semi-transparency, low weight, flexibility, solution processability, use of abundant elements, low temperature processing and rapid energy payback time. They are environmentally friendly with less environmental impact during manufacturing and operation.⁷ Interestingly, they meet the requirements for low-cost large-scale production.⁸ This is in addition to their efficiency enhancement reaching up to 18% which demonstrates that OPV can compete with mature technologies (silicon-based solar cells).⁹ However, organic solar cells still suffer from weak stability which is caused by the metastable bulk-heterojunction morphology which is sensitive to oxygen and moisture, the diffusion of the electrodes and the interfacial layers sandwiching the photoactive layers.¹⁰

b. Architecture of organic photovoltaic cells

Organic solar cell is a stack of multi-layers as shown in **Figure III-2**. It is built on a transparent substrate covered with a semi-transparent electrode such as indium tin oxide (ITO) that helps light to pass through. A photoactive layer made up of organic semiconductor molecules is sandwiched between two interfacial layers, a hole transport layer (HTL) and an electron transport layer (ETL). On top, there is a metal electrode used for charge collection.⁷

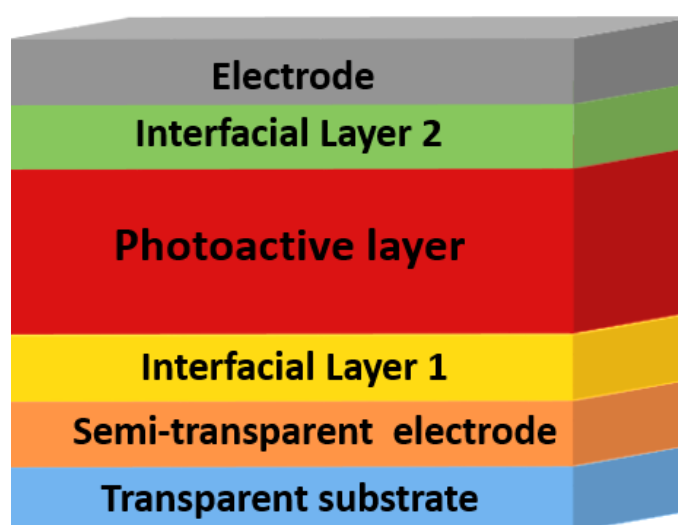


Figure III-2: Basic structure of an organic solar cell.

The polarity of the devices differs based on the used device architecture. In this regard, there is normal and inverted device structures. In normal device structures, the high work function electrode (ITO), with a hole transport layer on top of it, is where positive charge carriers (holes) are collected. For such device structures, poly(3,4-ethylenedioxythiophene)-poly(styrenesulfonate) (PEDOT:PSS) is a commonly used HTL. A non-transparent electrode with a low work function such as aluminum (Al) is used for collecting negative charge carriers (electrons).

In inverted device structures, the polarity of the electrodes is reversed in which ITO, with an electron transport layer on top of it such as zinc oxide (ZnO) or titanium oxide (TiO_x), is used for electron collection. Since, in principle, ITO is able to collect both holes and electrons, as its work function matches the highest occupied molecular orbital (HOMO) of donors and the lowest unoccupied molecular orbital (LUMO) of acceptors.¹¹ High work function air-stable metals such as silver (Ag) or gold (Au) serve as hole collecting electrodes.¹² Both the normal and the inverted device structures are illustrated in **Figure III-3**.

It is worth mentioning that in both cases, the work functions of the two electrodes should be in a well matching alignment with HOMO of the donor and LUMO of the acceptor.¹³



Figure III-3: Typical normal (left) and inverted (right) device structure of OSC.

c. Constituents of the photoactive blend

The photoactive layer in organic solar cell is the light harvesting layer and is made up of a well-mixed blend of donor and acceptor molecules.

Donors are usually π -conjugated small molecules or polymers with a typical molecular structure of alternating electron-donating and electron-accepting blocks resulting in a semiconducting material. An ideal donor should possess specific criteria including high hole mobility and affinity with an enhanced absorption spectrum in the visible and near-IR region.¹⁴ One more important criterion is its crystallinity. Briefly, the generated exciton in the photoactive layer must diffuse into the donor/acceptor interface and eventually separates into free charges that are transported into the corresponding electrode.

The exciton diffusion length and the charge carrier mobility drive the optimal dimension of the donor:acceptor domains. Typically, a highly crystalline polymer can increase charge mobility by reducing the interchain spaces. Also, highly crystalline material can generate large domain size (>100 nm). This is efficient for charge transport but it limits exciton diffusion due to the limited lifetime of exciton. On the other hand, amorphous polymers form highly mixed layers, that facilitate exciton diffusion into the interface, but are detrimental for charge transport into the electrode due to charge recombination. Therefore, it is important to control the crystallinity of the conjugated polymers for a suitable micro-phase separation.¹⁵ Poly(3-hexylthiophene) (**P3HT**) and poly([2,6'-4,8-di(5-ethylhexylthienyl) benzo [1,2-b;3,3-b] dithiophene]{3-fluoro-2[(2-ethylhexyl) carbonyl] thieno[3,4-b]thiophenediyl}) (**PTB7-Th**) are typical examples of donor polymers.

Acceptors could be either fullerene derivatives like [6,6]-Phenyl C₆₁ butyric acid methyl ester (**PC₆₀BM**) and [6,6]-Phenyl C₇₁ butyric acid methyl ester (**PC₇₀BM**) or non-fullerene acceptors that can be small molecules as 2,2'-[[6,6,12,12-Tetrakis(4-hexylphenyl)-6,12-dihydrodithieno[2,3-d:2',3'-d']-s-indaceno[1,2-b:5,6b']dithiophene-2,8-diyl] bis [methylidyne(3-oxo-1H-indene-2,1(3H)-diylidene)]]bis[propanedi nitrile] (**ITIC**) and its derivatives. An ideal acceptor is the one with high electron affinity and good electron transport property in film. A sufficient solubility with an intense visible to near-IR light absorption are also desired. In a photoactive blend, acceptors should have energy levels that match the corresponding donor and they must possess large nonplanar structures that promote nanoscale phase separation, charge separation and charge transport in films.¹⁶ The chemical structures of few donors and acceptors are shown in **Figure III-4**.

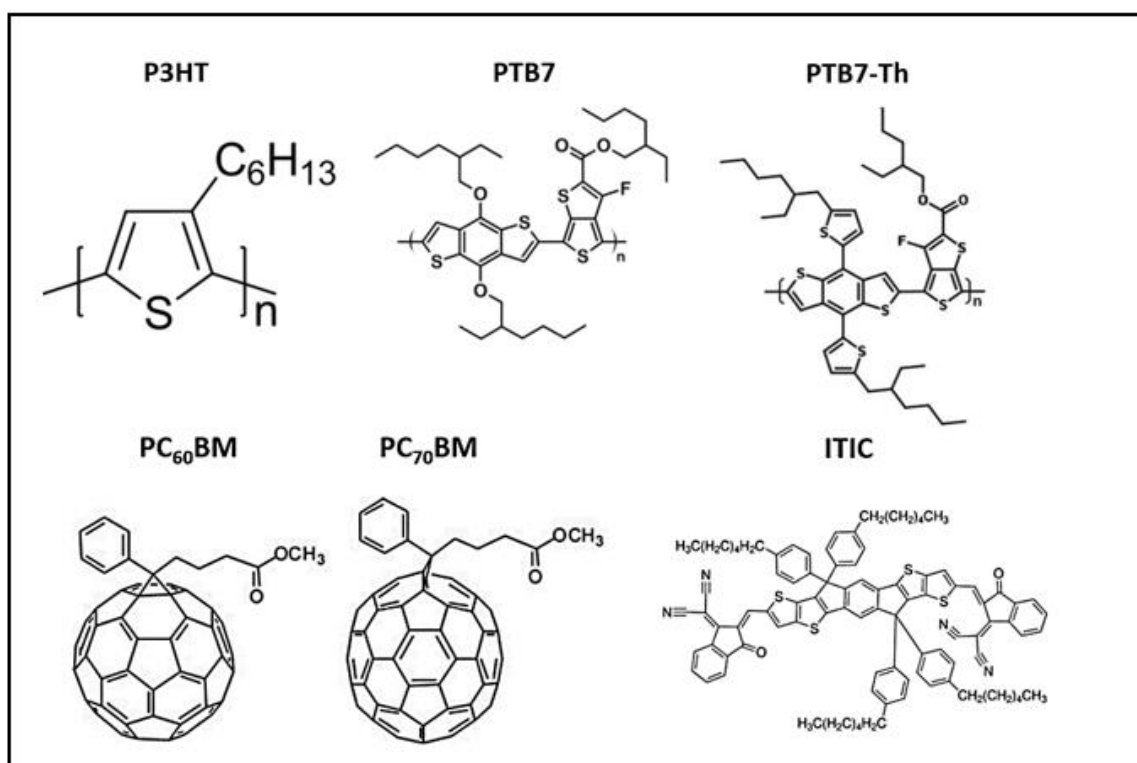


Figure III-4: Chemical structures of some commonly used donors and acceptors in OSCs.

d. Blend morphology

As the photoactive blend consists of donor and acceptor molecules, both should possess good solubility in the same organic solvent. The ratio between both components must be optimized in a way to maintain a balance between donors and acceptors as they have different charge mobilities, but sufficient enough to obtain nanoscale morphology with appropriate domain sizes.¹⁷ However, in some cases, processing a blend from a single solvent results in films with poor morphology. Thus, thermal annealing,¹⁸ solvent vapor annealing¹⁹ or additives were used to adjust film morphology. It was observed that adding solvent additives such as 1,8-diiiodooctane (DIO)²⁰ having higher boiling points than the primary host solvent can improve the device performance. The increase in efficiency can be due to the effect of additives in reducing the aggregate size of fullerenes, which enhances intercalation of fullerene in the polymer chain, leading to a better donor-acceptor intermixing.²⁰ Naphthalene derivatives were also used for P3HT:PC₆₀BM blends in which they improve the donor-acceptor phase separation, leading to the formation of nanoscale domains as well as enhance the degree of crystallinity and photon absorption property of the BHJ film.²¹ It is worth mentioning that several studies demonstrated that the incorporation of a solvent additive as a third component affects the thermal stability of the devices.²⁰ For instance, PTB7:PC₇₀BM-based devices processed in the presence of DIO show strong losses in efficiency after annealing at 80-100 °C.²² However, in the absence of DIO, the devices maintain good thermal stability up to 140 °C.²³

e. General working principle of organic photovoltaic devices

The overall process occurring in organic solar cells can be summarized in five successive steps illustrated in **Figure III-5** and constitutes of:

i. Light absorption and exciton generation

Upon irradiation, the photoactive materials absorb light energy (photons) to generate excitons which are tightly bound electron-hole pairs. Donors (D) usually donate electrons and are responsible for hole transportation while acceptors (A) withdraw and transport electrons. Due to the energy of the absorbed light, electrons are excited from the HOMO of donor to its LUMO energy level, leaving behind a positive charge (hole) in the HOMO level.

ii. Exciton diffusion

After exciton generation, they diffuse to the donor/acceptor interface. These photo-generated excitons can diffuse during their short lifetime (few picoseconds) with limited diffusion length in the range of 5 to 20 nm in conjugated polymers.²⁴ If the excitons are generated far from the interface, exciton decay or charge carrier recombination can occur.

iii. Exciton dissociation

The exciton undergoes a charge transfer from the LUMO of the donor to the LUMO level of the acceptor, where there is creation of a charge-transfer state (CT). In this state, charges reside on different molecules but are still bound by coulombic attraction. When the difference between the LUMO of the donor and that of the acceptor is higher than the exciton binding energy, an efficient exciton dissociation takes place at the donor/acceptor interface. At this level, the CT state dissociates into free charge carriers; electrons and holes.²⁵

iv. Charge extraction and transport

Free holes and electrons are transported through p-type donors and n-type acceptors toward the corresponding electrodes. The direction of the transported charges is actually affected by the work function difference between the metallic electrodes, while efficiency of charge transportation is affected by the conductivity of donors and acceptors.

v. Charge collection

After their transportation, holes and electrons are collected at hole and electron collecting electrodes, respectively. The charge collection generates photocurrent by either short circuiting or by applying voltage to an external circuit.^{26,27}

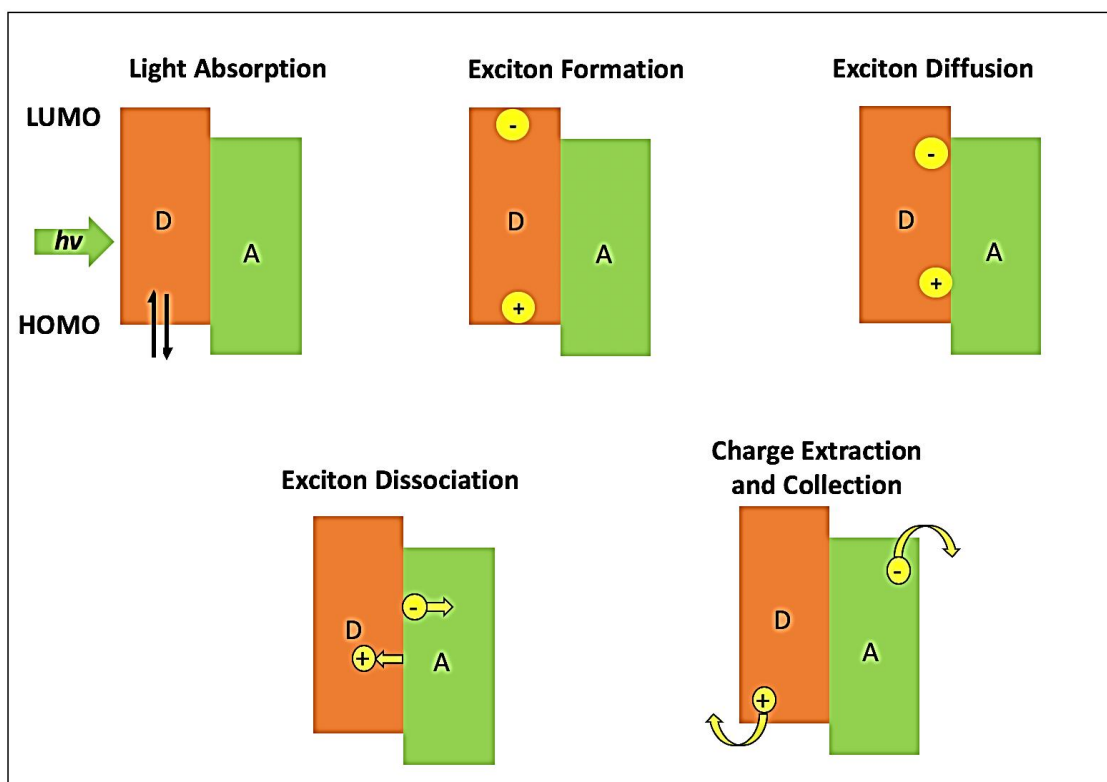


Figure III-5: Working principle of OSCs.

f. Device characteristics

When it comes to device characterization, it is important to shed light on the photovoltaic parameters that describe the performance of fabricated devices. These include short-circuit current density (J_{SC}), open-circuit voltage (V_{OC}), fill factor (FF), series resistance (R_S), shunt resistance (R_{Sh}), power conversion efficiency (PCE) and quantum efficiency (QE). The defined parameters can be deduced from a current density-voltage (J-V) curve of a working device in dark and under illumination as shown in **Figure III-6**. For standard test conditions, a spectral light distribution of 1.5 (air mass AM 1.5 global) and a radiation intensity of $100 \text{ mW}\cdot\text{cm}^{-2}$ are used.²⁸

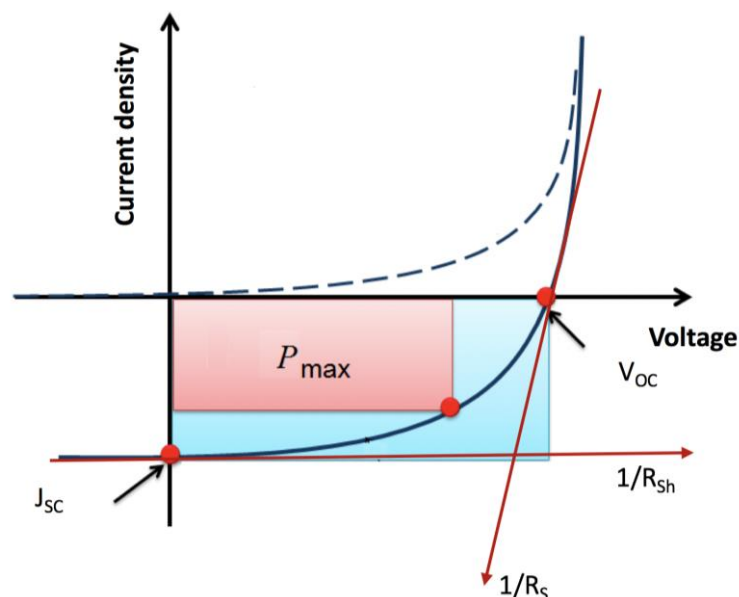


Figure III-6: J-V characteristics of a solar cell in dark and under illumination.

i. Short-circuit current density (J_{SC})

J_{SC} (mA/cm^2) is the current density which flows in a device under illumination when no voltage is applied ($V=0$). J_{SC} is highly affected by several parameters including light intensity, number of absorbed photons, optical properties of photoactive layers, recombination mechanism and charge carrier mobility.²⁹

ii. Open-circuit voltage (V_{OC})

V_{OC} (V) is the maximum voltage across the terminals of a device when no current flows through the external circuit. It is found to be the difference between the highest-occupied molecular orbital (HOMO) of electron donor material and the lowest unoccupied molecular orbital (LUMO) of the electron acceptor material which is equivalent to the ionization potential and the electron affinity of the respective materials.³⁰ V_{OC} is affected by several parameters such as temperature, intensity of the irradiated light, morphology, defect states and crystallinity of the photoactive layer.³¹

iii. Fill factor (FF)

FF measures the quality of a solar cell. In other words, FF can give an information about how “difficult” or “easy” the photo-generated carriers are extracted out of a photovoltaic device. As shown in **Equation 1**, FF is the ratio between the maximum power output of the studied device ($P_{max} = J_{max} \times V_{max}$) and the theoretical power output which can be achieved if the device is ideal diode ($V_{OC} \times J_{SC}$).

$$FF = \frac{P_{max}}{P_{theo}} = \frac{J_{max} V_{max}}{V_{oc} J_{sc}} \quad \text{Equation 1}$$

High FF can be obtained with low series resistance (R_S) and high shunt resistance (R_{Sh}).

iv. Series resistance (R_S)

R_S is also one of the parameters that affects device performances. It results from the low conductivity of the active layer, resistance of the electrodes and interfacial contact resistance of every interface in the device. A low series resistance can improve FF and J_{SC} but has no impact on V_{OC} . A commonly used method to calculate R_S is to consider the inverse of the slope of a J-V curve at V_{OC} .

v. Shunt resistance (R_{Sh})

R_{Sh} describes the leakage current in the cells. These losses could be due to morphology of the casted film (pinholes) or recombination induced by trap states and impurities. R_{Sh} has a direct effect on V_{OC} ; a decrease in R_{Sh} can lower the V_{OC} . The inverse of the slope of a J-V curve at J_{SC} represents R_{Sh} .

vi. Power conversion efficiency (PCE)

PCE is an essential parameter to evaluate the performance of a solar cell. As defined, it is the percentage of the maximum generated electrical power (P_{max}) in comparison with the incident light power (P_{in}) (**Equation 2**).²⁸

$$PCE = \frac{P_{max}}{P_{in}} = \frac{J_{max} V_{max}}{P_{in}} = \frac{J_{sc} V_{oc} FF}{P_{in}} \times 100 \quad \text{Equation 2}$$

vii. External quantum efficiency (EQE)

The quantum efficiency (QE) measurement is related to the responsivity of the device measured in the range of different wavelengths and gives information about the efficiency of the device at each wavelength. The usage of monochromatic light in such measurements helps in observing and identifying solar cell's characteristics in a particular range of wavelength. There are two types of QE: External Quantum Efficiency (EQE) and Internal Quantum Efficiency (IQE).

EQE is an important parameter used in the characterization of solar devices. As defined, EQE is the number of electrons extracted in an external circuit divided by the number of incident photons at a certain wavelength. The measured value includes the losses due to reflection at the surface and the transmission through device. EQE can be calculated according to **Equation 3**.

$$\text{EQE}(\lambda) = \frac{\text{Electrons out}}{\text{Incident photons}} = \frac{\text{JSC}}{q\Phi} = \frac{hc}{q\lambda} \frac{\text{JSC}}{\text{Pin}} = 1240 \cdot \frac{\text{JSC}}{\lambda \cdot \text{Pin}} \quad \text{Equation 3}$$

Where Φ is the photon flux, Pin is the light intensity at a certain wavelength λ , q is the elementary charge, and h and c are Planck's constant and speed of light, respectively.

On the other hand, the internal quantum efficiency is only concerned with the absorbed photons by the photoactive layer. This can explain why the value of IQE is always higher than EQE. The IQE is calculated according to **Equation 4** in which the $\text{Ref}(\lambda)$ and $\text{Trans}(\lambda)$ represents the reflected and transmitted light, respectively.³²

$$\text{IQE}(\lambda) = \frac{\text{number of charges generated}}{\text{number of photons absorbed}} = \frac{\text{EQE}(\lambda)}{1 - \text{Ref}(\lambda) - \text{Trans}(\lambda)} \quad \text{Equation 4}$$

III. State of art

Being responsible for photons absorption in solar cells, the photoactive layer is essential to be studied. When the efficiency of OSCs was not exceeding 1% for bilayer junctions, a bulk heterojunction structure was first fabricated using a conjugated polymer poly(2-methoxy-5-(2'-ethyl-hexyloxy)-1,4-phenylene vinylene) (**MEH-PPV**) and PC_{60}BM to show an efficiency of 2.9%.³³ From then on, BHJ organic solar cells have attracted lots of attention. However, MEH-PPV and other polymers as poly[2-methoxy-5-(3',7'-dimethyloctyloxy)-1,4-phenylenevinyl-ene] (**MDMO-PPV**) have optical absorption between 400 and 600 nm which limit device performances.³⁴ Thus, to overcome this problem, P3HT with an optical absorption extending up to 650 nm was used with fullerene acceptors (PC_{60}BM). However, the efficiency of P3HT: PC_{60}BM normal-based devices was limited to an average of 5%^{18,35,36} due to the poor overlap between P3HT absorption spectrum and the solar emission.^{37,38} For this, several strategies were followed to optimize the efficiency of organic solar cells.

a. Optimizing the PCE of BHJ OPVs

To improve the performance of OSCs, several strategies were followed. These include processing of new device architectures (inverted device structures and tandem cells), replacing fullerene acceptors by non-fullerene ones, incorporating interfacial layers and using low-bandgap polymers.

i. Processing of new device architectures

1. Inverted device structures

Due to the ITO corrosion caused by acidic PEDOT:PSS and the oxidation of the low work function (WF) electrodes (Al) used in normal device structures, inverted device structures were fabricated to overcome such problems and to enhance device stability.^{39,40,41} The highest efficiency recorded for an inverted device structure using a non-fullerene acceptor was 16.5%.⁴²

2. Tandem device structures

A tandem device is made up of a multi-junction solar cell configuration where two or more sub-cells with complementary absorption spectrum are stacked and connected in series or parallel. These devices show enhancement in performances.⁴³

ii. Non-fullerene acceptors

Although fullerenes were proved to be good choice acceptors in certain devices, they are still facing some challenges such as low absorption in the visible/near-IR region, large V_{OC} loss, poor electronic tunability, tendency to crystallize and form aggregates.^{44,45,46} These limit their efficiency to 10-12%. Thus, non-fullerene acceptors having high absorption spectra, structural flexibility, bandgap tunability, controlled crystallinity and high V_{OC} are highly recommended.^{44,47} A previous work revealed that normal and inverted-based structures using P3HT and a non-fullerene acceptor O-IDTBR (rhodanine-endcapped indacenodithiophene) showed efficiency of 6.5% and 6.6%, respectively.⁴⁸ Additionally, P3HT:O-IDTBR inverted-based modules of 60 cm² delivered 5% power conversion efficiency.⁴⁹

Recently, a new non-fullerene acceptor, 2,2'-((12,13-bis(2-butyldecyl)-3,9-diundecyl-12,13-dihydro-[1,2,5]-thiadiazolo[3,4-e]thieno[2",3":4',5']thieno[2',3':4,5]pyrrolo[3, 2-g]thieno[2',3':4,5]thieno[3,2-b]indole-2,10-diyl)bis(methanelylidene))bis(5,6-dichloro-1H-indene-1,3(2H)-dione) (**ZY-4Cl**) was synthesized. Interestingly, P3HT:ZY-4Cl normal-based OSC exhibited a significantly improved PCE of ~9.5%, which is a new record for the P3HT-based OSCs.⁵⁰

A wide bandgap (2.24 eV) copolymer named poly[4,8-bis(4-fluoro-5-(2-butylhexylthio)thiophen-2-yl)Benzo[1,2-b:4,5-b']dithiophene-2,6-diyl-*alt*-TZNT] (**PBDTSF-TZNT**) was blended with a non-fullerene acceptor (**IT-4F**) to show 13.25% efficiency for an inverted device structure.⁵¹

Up to date, the highest efficiency obtained for a normal device structure is 18% using a non-fullerene acceptor, (2,20 -((2Z,20 Z)- ((12, 13-bis(2-ethylhexyl)-3,9-diundecyl-12,13-dihydro-[1,2,5]thiadiazolo[3,4-e]thieno[200,300:40,50]thieno[20,30:4,5]pyrrolo[3,2-g] thieno[20,30:4,5]thieno[3,2-b]indole-2,10-diyl)bis(-metha nylylidene))bis(5,6-difluoro-3-oxo-2,3-dihydro-1H-indene2,1-diyliidene))dimalononitrile) (**Y6** or **BTP-4F**) and ditheino[3',2':3,4;2'',3'':5,6] benzo[1,2 -c][1,2,5]thiadia-zole (**D18**) donor.⁹

iii. Interfacial layers

The power conversion efficiency of an OSC can be further enhanced by incorporating suitable interfacial layers.^{52,53} Both HTLs and ETLs improve charge extraction and collection, which eventually enhance device performances.⁵⁴

The majority of high efficiency solar cells are fabricated with PEDOT:PSS HTLs. PEDOT:PSS improves hole selectivity⁵⁵ and decreases the roughness of electrodes while increasing their work function.⁵⁶ Previous work showed that the efficiency of P3HT:PC₆₀BM normal-based devices was increased from 1.8 to 3.81% upon inserting a PEDOT:PSS layer.⁵⁷ Graphene oxide and thermally evaporated or solution-processed transition metal oxides as molybdenum oxide (MoO₃), nickel oxide (NiO_x) and tungsten oxide (WO_x) are also used as HTLs.⁵⁴ For example, the efficiency of P3HT:PC₆₀BM inverted-based devices was improved from 2.30 to 3.09% after evaporating a MoO₃ layer.⁵⁸

Regarding ETLs, zinc oxide (ZnO) is one of the widely used transport materials in OSCs as it possesses a low WF (≈ 4.30 eV) that perfectly matches the LUMO levels of various acceptors, in addition to its hole blocking property.⁵⁹ Other than ZnO, titanium oxide, n-type neutral polymers such as polyethylenimine (PEI) and polyethylenimine ethoxylated (PEIE), organic-inorganic hybrids, graphene oxides and others can be used as ETLs.⁵⁴

iv. Usage of low-bandgap polymers

For an efficient light absorption at around 700 nm, the HOMO energy levels of donors should reside at approximately 5.4 eV.⁶⁰ Thus, high-bandgap polymers such as P3HT ($E_g = 2.1$ eV) are not efficient enough for photon harvesting as they have limited absorption in the near-IR region. This eventually affects device performances.

In this regard, low-bandgap polymers ($E_g < 1.8$ eV) are considered as good candidates for OSCs as they possess higher absorption in the visible and near-IR region, high charge carrier mobilities and excellent power conversion efficiencies because of the controlled intramolecular charge transfer from donor to acceptor unit.⁶¹ In other words, the small bandgap allows an easy charge injection of the electrons into the LUMO where the strong molecular polarity enables an effective charge transport of both charges. Thus, narrowing the bandgap and tuning the energy levels of conjugated polymers have been a major task for polymer chemists in the last decades. For this, larger π -conjugation length and fusing more aromatic rings in the used polymers can eventually narrow the bandgap.⁶²

Conceptually, novel strategies were developed to have a better control over the bandgap of conjugated polymers including the utilization of donor-acceptor design as previously discussed in **Chapter I**.⁶³ In addition to the low-bandgap D-A copolymers mentioned in **Chapter I** that yield high power conversion efficiencies, we can find other low-bandgap copolymers showing low efficiencies even if they absorb in the near-IR region.

For example, a donor-acceptor-based copolymer consisting of phenanthro[1,2-b:8,7-b']dithiophene (PDT) donor and benzothiadiazole (BT) derivative acceptor formed an appropriate phase separation when blended with PC₆₀BM in an inverted-based OSC, but yielded low PCE which was not exceeding 3.8% due to the low J_{SC} obtained. They demonstrated that this low performance is attributed to the molecular orientation of the polymer forming well-ordered crystallites in a predominantly edge-on manner. This orientation is not suitable for high-performance devices as it prevents efficient carrier transport and reduces charge collection resulting in low J_{SC} and PCE.⁶⁴

Another example of two new near-IR-absorbing alternating polymers, namely **P(BTz-FQ)** and **P(BTz-DTFQ)** with a lowest bandgap (1.41 eV) among quinoxaline-based polymers were used with PC₇₀BM in normal-based OSCs. Low efficiencies of 0.51% and 0.71% were obtained for P(BTz-FQ) and P(BTz-DTFQ)-based devices, respectively.⁶⁵

However, introducing a low-bandgap D-A copolymer such as **HTh6BT** ($E_g=1.65$ eV) as an additive donor for P3HT:PC₆₀BM blends in the normal device structures enhances all photovoltaic parameters including the efficiency. The photoluminescence (PL) spectra shown in **Figure III-7** revealed that with the addition of PC₆₀BM to the P3HT system, a quenched electron-hole was observed. This increase in quenching is an indication of the increase in the dissociation efficiency of the electron-hole.⁶⁶ Moreover, the quenching ratio was enhanced by 54.3% when HTh6BT was added. This proves that more excitons are formed in the polymer thin film after HTh6BT addition and that both P3HT/PC₆₀BM and HTh6BT/PC₆₀BM interfaces create efficient charge dissociation.⁶⁷

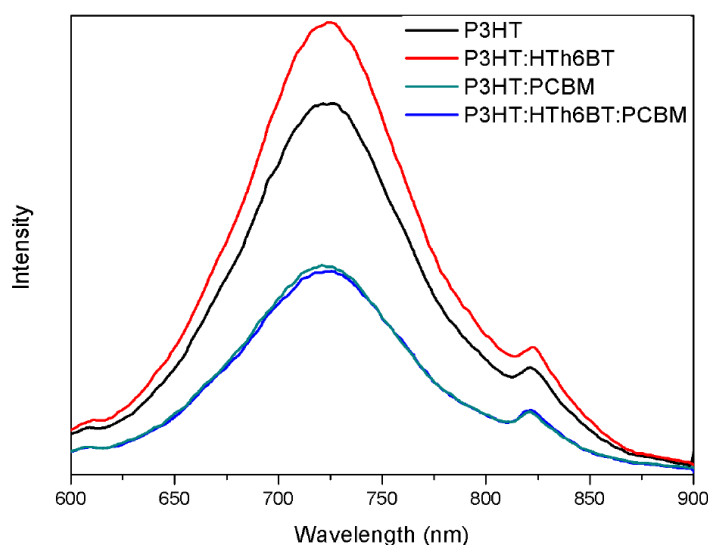


Figure III-7: PL spectra of P3HT, P3HT:PC₆₀BM, P3HT:HTh6BT and P3HT:HTh6BT:PC₆₀BM films.⁶⁷

IV. Objectives

Based on what was discussed in **Chapter I** regarding the morphological instability of the photoactive blends incorporating D-A copolymers,⁶⁸ in addition to the importance of adding low-bandgap D-A copolymers to the main polymer block,⁶⁷ we focused in **Chapter II** on synthesizing low-bandgap block copolymers including the main polymer block covalently linked to a low-bandgap block.

Although block copolymers are widely used in OSCs, in general, they still show efficiencies less than 4% due to many problems associated during synthesis such as difficulties in purification methods (presence of trace impurities as residual catalyst).^{69,70} However, the promising electronic and optical properties of the synthesized block copolymers, including broad absorption in the near-IR region and matching energy levels, make it worth to study their photovoltaic behaviors in organic solar cells. Despite the fact that DPP-containing copolymers showed better preliminary photovoltaic properties in OSCs than the DAP-based ones,⁷¹ both P3HT_n-*b*-P(DTS-DPP)_m and P3HT_n-*b*-P(DTS-DAP)_m were examined in our study.

V. Results and discussion

a. Architecture and constituents of the fabricated devices

In order to evaluate the newly synthesized block copolymers as photoactive layers in organic solar cells, we fabricated inverted device structures consisting of ITO/ZnO/PEIE/photoactive layer/MoO₃/Ag as shown in **Figure III-8**.

Different conditions regarding annealing temperature, solvent, donor:acceptor ratio, and additives were conducted for the aim of optimizing device performances. It is worth noting that the mentioned performances in this chapter correspond to the champion cell of each system.

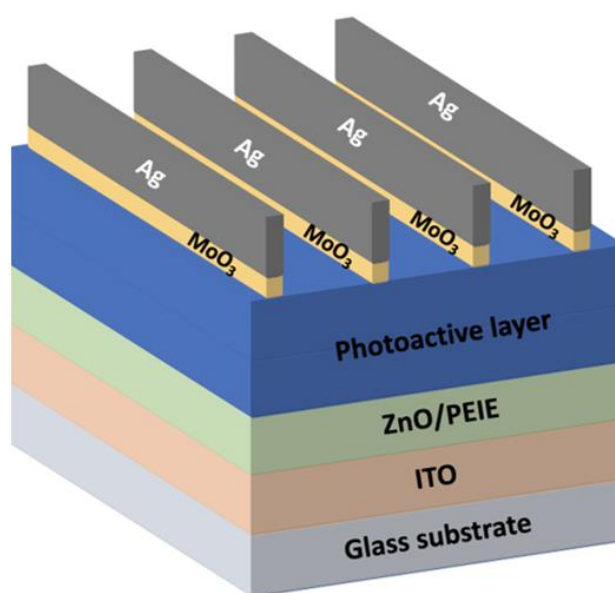


Figure III-8: The fabricated inverted device structure.

In such a device structure, ITO serves as an electron collecting electrode covered by an electron transport layer, which is a bilayer of ZnO and aqueous-based PEIE. ZnO solution was prepared by mixing zinc acetate in absolute ethanol and ethanolamine. The solution was stirred at 55 °C for 30 min before it was cooled down.

It is worth mentioning that the pre-cleaned ITO substrates should be exposed to UV-ozone treatment right before depositing the ETL on top of them. Besides removing any trace of organic contamination, this treatment passivates the ITO surface so that a better interface is created with the material deposited on top of them. It also increases the surfaces' hydrophilicity and the ITO work function to 4.7 eV.⁷²

The choice of the electron transport layer (ZnO/PEIE) was in accordance to previous studies showing an enhanced power conversion efficiency using both materials in comparison with other devices fabricated with only PEIE or ZnO.⁷³ PEIE can accelerate charge transfer and reduce recombination at the interface between the active layer and ZnO by reducing defects that are caused by adsorbed oxygen. This eventually provides a better contact with the photoactive layer.⁷³

Additionally, it was demonstrated that the enhanced PCE upon inserting a neutral polymer can be attributed to the lowered conduction band energy of ZnO layer *via* the formation of an interfacial dipole layer at the interface between ZnO layer and the neutral polymer layer. In general, incorporating a neutral polymer layer could minimize the surface roughness of ZnO, thus decreasing the series resistance of the device.⁷⁴

Evaporated MoO₃ was proved to be one of the excellent metal oxides used as hole transport materials in inverted device structures to replace the water-based PEDOT:PSS solution that faces wettability problems when deposited on hydrophobic photoactive layers. A sufficient thickness of MoO₃ buffer layer (10 nm) is required to prevent damaging the photoactive layer during the electrode deposition.⁷⁵ A 70 nm-thick high work function Ag serves as a hole collecting electrode.

In a bulk heterojunction, a larger interfacial area could be obtained by mixing donor and acceptor materials in a homogenous way. Thus, choosing an acceptor for the corresponding donor is of great importance to achieve a successful blending. At first, the synthesized diblock copolymers have been employed as sole active layers in the devices and compared to those incorporating an additional acceptor.

As previously mentioned, PC₆₀BM fullerene acceptors are widely used due to their high electron affinity, electron mobility, isotropic charge transport and their ability to form appropriate phase separation.⁷⁶ Thus, to check whether electronic levels of PC₆₀BM are compatible with the ones of the synthesized block copolymers, cyclic voltammetry measurement was performed. The experiments were conducted as explained in **Chapter II**, and the HOMO/LUMO energy levels of PC₆₀BM were calculated according to the previously reported equations⁷⁷ after estimating oxidation and reduction onsets of the cyclic voltammograms shown in **Figure III-9**. Based on this, the LUMO and HOMO energy levels of PC₆₀BM were estimated to be -3.9 and -6.1 eV, respectively with an $E_g^{(cv)}$ of 2.2 eV.

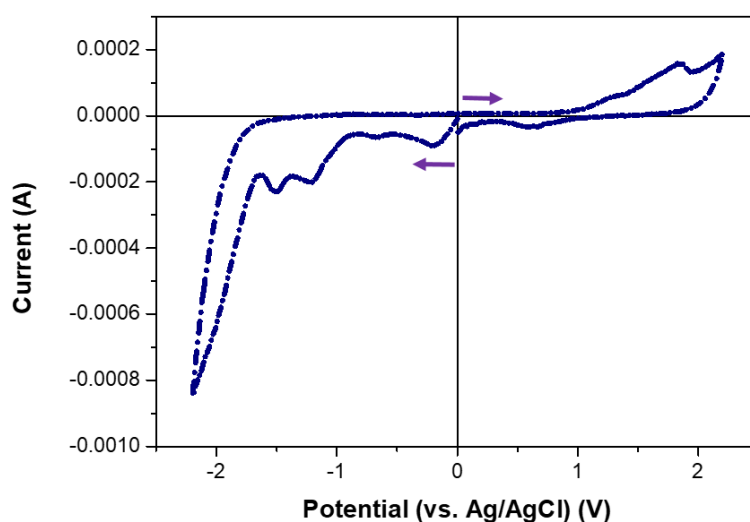


Figure III-9: Cyclic voltammogram of the drop-casted PC₆₀BM film in 0.1 M acetonitrile solution with a scanning rate 0.1 V/s.

In this regard, we referred to the electrochemical studies of the synthesized block copolymers discussed in **Chapter II** to compare them with that of PC₆₀BM. The chemical structures of the different materials used in the device fabrication are shown in **Figure III-10** and their energy levels with the corresponding electrodes are illustrated in **Figure III-11**.

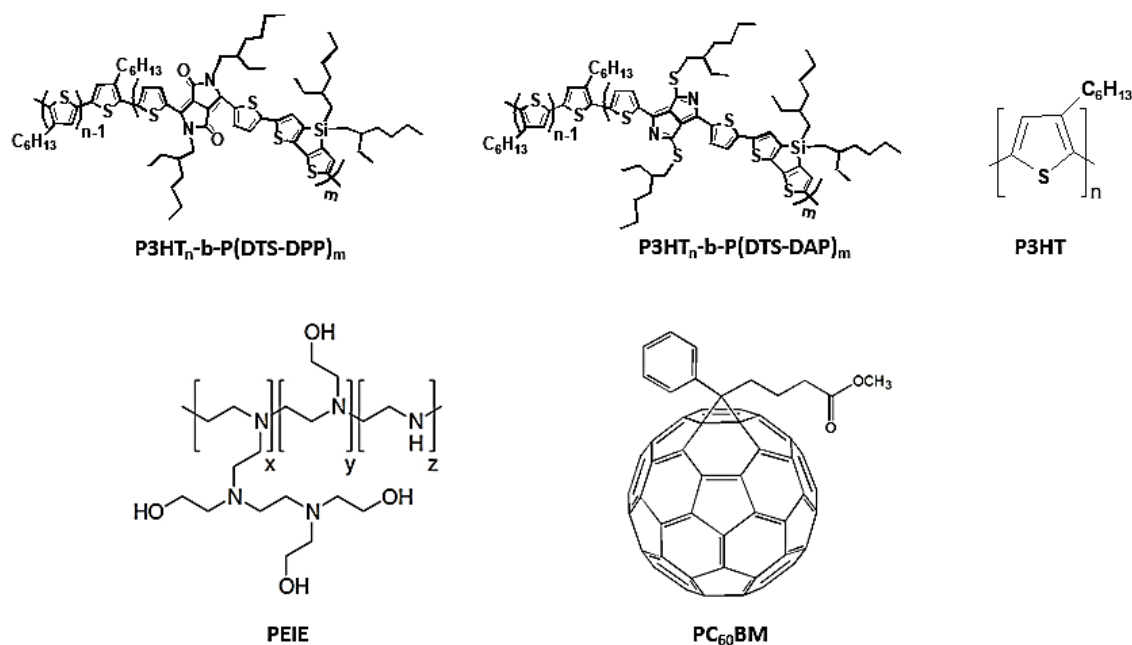


Figure III-10: Chemical structures of different materials used in the fabricated OSCs.

In general, the energy level alignment between donors and acceptors is a key parameter for an efficient charge separation and transfer. In other words, the LUMO energy level of the acceptor must be slightly lower than the LUMO of the donor (low energy offset).⁷⁸ As can be seen from the figure below, the LUMO of PC₆₀BM energetically matches the LUMO of the DPP-based copolymers more than DAP-based ones. Such an energy band alignment is expected to lead to an efficient charge separation of the generated excitons at the donor/acceptor interfaces.

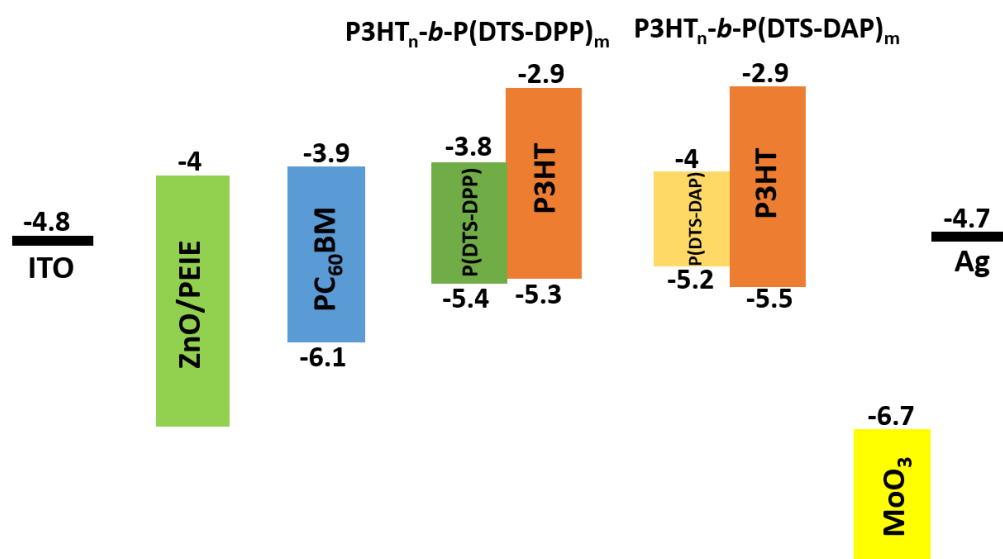


Figure III-11: Energy level alignment diagram of the components of the fabricated OSCs.

b. Device performances using DPP-based block copolymers

i. P3HT₃₇-*b*-P(DTS-DPP)₄

P3HT₃₇-*b*-P(DTS-DPP)₄ copolymer was first used as a single component in the photoactive layer given its donor-*b*-acceptor structure and the compatible HOMO/LUMO energy levels measured by cyclic voltammetry.

A 10 mg.mL⁻¹ chlorobenzene-based solution was spin-coated at 800 rpm/50 seconds followed by 1000 rpm/3 seconds and led to an 80 nm-thick photoactive layer (measured by profilometry). In this configuration, the efficiency was very low ($\approx 0\%$) with a FF of 0.27 and V_{OC} of 0.29 V. The generated photocurrent was 0.01 mA/cm² (**Figure III-12**). As shown in linear J-V curves (**Figure III-12a**), almost the same behavior was observed in dark and light, while by plotting the semi-log curves (**Figure III-12b**), a slight deviation in the generated photocurrent and voltage was detected under illumination.

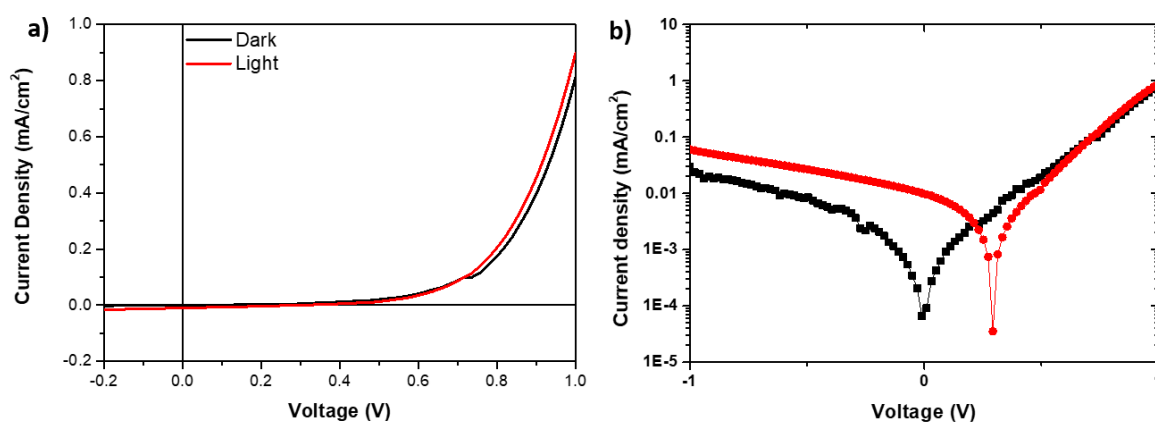


Figure III-12: J-V curves of P3HT₃₇-*b*-P(DTS-DPP)₄-based devices using (a) linear and (b) semi-log plots.

The low performance obtained could be explained by either a weak charge transfer between the P3HT block and the P(DTS-DPP) block and/or low electron and hole mobilities on the block copolymer layer. Thus, Photoluminescence Spectroscopy (PL) was performed on P3HT₃₇-*b*-P(DTS-DPP)₄ copolymer with an excitation at 445 nm in the absorption band of P3HT and compared with the P3HT homopolymer (**Figure III-13**). A slight decrease of the photoluminescence intensity was observed in the copolymer sample compared to the homopolymer, which we did not attribute to an electron transfer from one block to another. Indeed, this slight difference was rather assigned to (i) the slightly lower absorption of the copolymer sample at the excitation wavelength of 450 nm and (ii) the probable reabsorption of the P3HT emission from 550 to 650 nm by the P(DTS-DPP) block.

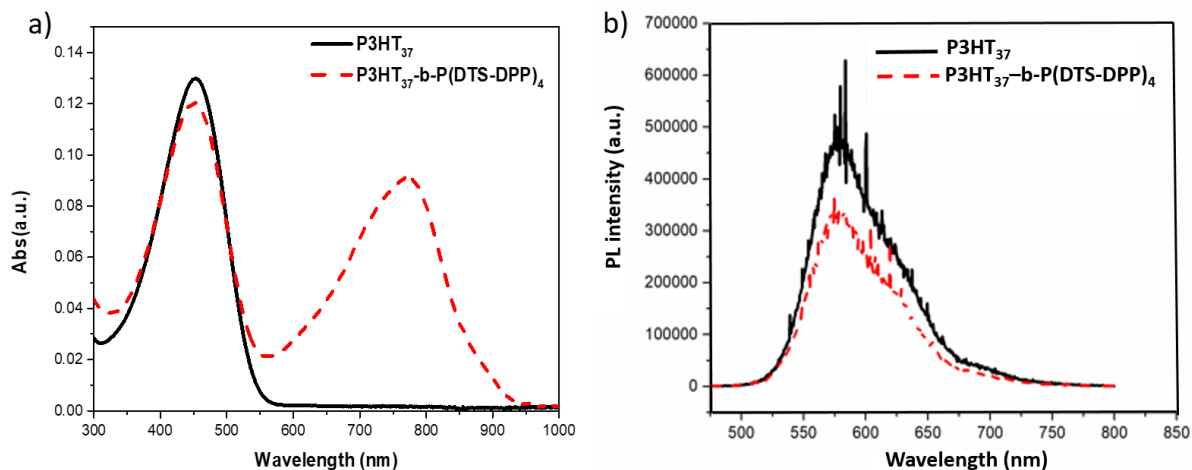


Figure III-13: (a) Absorption spectra and (b) photoluminescence spectra of P3HT₃₇ and P3HT₃₇-b-P(DTS-DPP)₄.

Thus, as electron transfer is not efficient between the two blocks of the copolymers, PC₆₀BM was added to the photoactive layer in order to enhance exciton dissociation and possibly electron mobility. Once the block copolymer was mixed with the fullerene acceptor in a 1:1 weight ratio (total of 20 mg.mL⁻¹/140 nm-thick layer), a slight increase in performance from \approx 0% to 0.29% was observed, with an increase in all photovoltaic parameters. The corresponding J-V curves are shown in **Figure III-14** and the photovoltaic parameters are summarized in **Table III-1**.

This increase in the power conversion efficiency can be attributed to the presence of the acceptor that facilitates electron mobility and charge transport by the formation of appropriate phase domains. In other words, PC₆₀BM was necessary for the creation of more interfacial areas or donor-acceptor contacts for better exciton dissociation, transfer and transport.⁷⁹

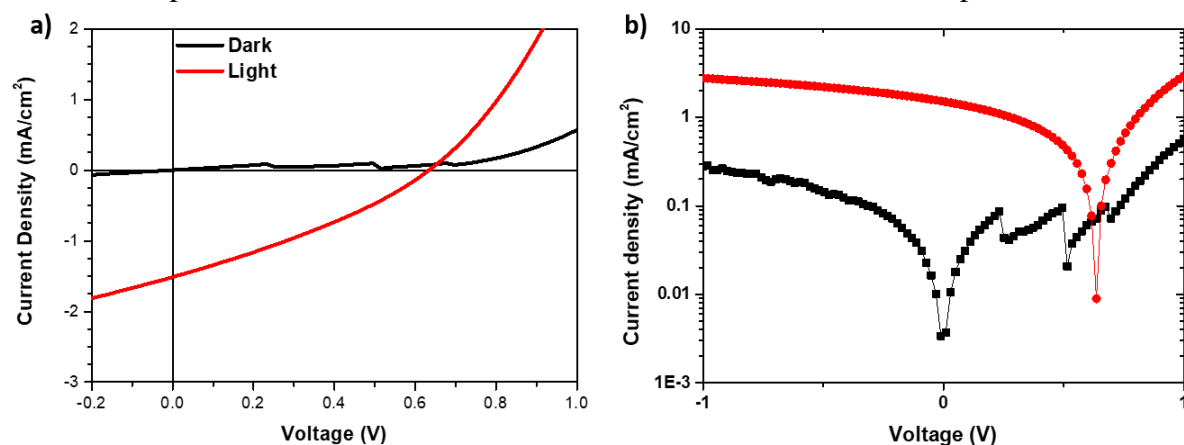


Figure III-14: J-V curves of P3HT₃₇-b-P(DTS-DPP)₄:PC₆₀BM-based devices with 1:1 weight ratio in (a) linear and (b) semi-log plots.

Table III-1: Photovoltaic parameters of P3HT₃₇-b-P(DTS-DPP)₄-based devices.

Photoactive layer	Photoactive layer thickness (nm)	FF	V _{oc} (V)	J _{sc} (mA/cm ²)	PCE (%)
P3HT ₃₇ -b-P(DTS-DPP) ₄	80	0.27	0.29	0.01	\approx 0
P3HT ₃₇ -b-P(DTS-DPP) ₄ :PC ₆₀ BM	140	0.31	0.63	1.51	0.29

As a result, incorporating materials having different electron affinities and ionization potentials in the photoactive layer is important as the resulting electron field across the donor/acceptor interface is the driving force for the exciton dissociation.

External quantum efficiency (EQE) measurements were conducted for both devices; with and without PC₆₀BM. The spectra shown in **Figure III-15a** revealed some difficulties in charge collection in the case of devices fabricated with polymers as sole active materials, in which a small contribution from the P3HT block was observed (0.075%) with less contribution from the low-bandgap block. After the addition of PC₆₀BM to the photoactive layer, an increase in EQE to 7.5% in the range corresponding to P3HT absorption was observed with a better contribution from the low-bandgap block. In general, the lower ΔE of the LUMO for P(DTS-DPP)/PC₆₀BM than for P3HT/PC₆₀BM decreases the efficiency of the electron transfer rate at P(DTS-DPP):PC₆₀BM interface.

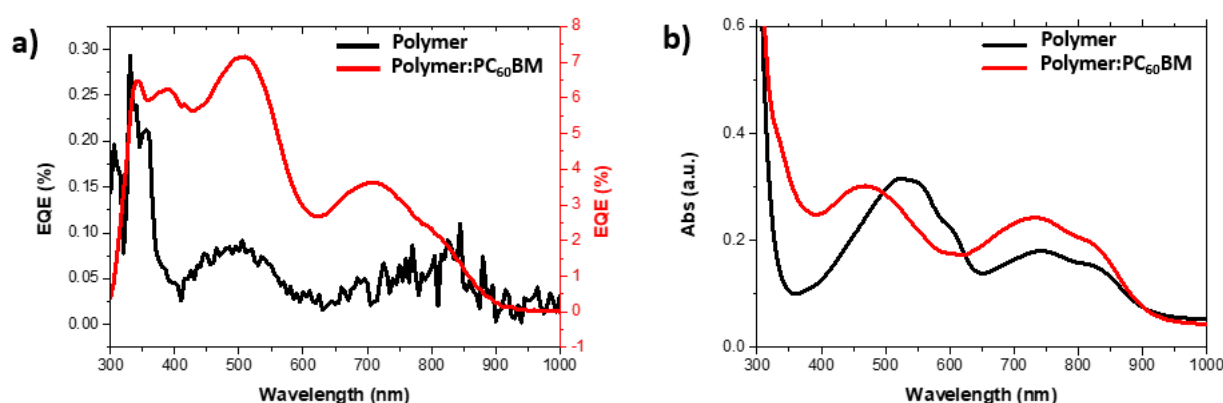


Figure III-15: (a) EQE of P3HT_{37-b}-P(DTS-DPP)₄ and P3HT_{37-b}-P(DTS-DPP)₄:PC₆₀BM-based devices. (b) UV-vis absorption spectra of the corresponding photoactive layers.

The absorption spectra of thin films were studied (**Figure III-15b**) to better understand the PC₆₀BM effect on the organization and absorption properties of P3HT_{37-b}-P(DTS-DPP)₄. Thin films were prepared by spin-coating chlorobenzene-based solutions without any further thermal treatment. In both cases, a wide absorption was observed between 350 and 900 nm consisting of two absorption bands characteristic of the synthesized diblock copolymer as discussed in **Chapter II**. The spectrum revealed a slight blue-shifting in the P3HT absorption region (400-650 nm) upon the addition of PC₆₀BM which could be attributed to the destruction of the ordering of the P3HT chains as a result of PC₆₀BM incorporation.⁸⁰ On the contrary, the blend exhibits a slight broader and more defined absorption profile in the region of the spectrum between 600 nm and 900 nm.

To investigate the morphological changes at a smaller scale, atomic force microscopy experiments were carried out. AFM images were taken for as-casted films of P3HT_{37-b}-P(DTS-DPP)₄ (**Figure III-16a** and **b**) and P3HT_{37-b}-P(DTS-DPP)₄:PC₆₀BM (**Figure III-16c** and **d**). The layers were deposited from chlorobenzene solutions on top of glass substrates.

The images shown below revealed that before mixing the block copolymer with PC₆₀BM, slight fiber-like structures appeared due to the P3HT block in the block copolymer. This morphology is a feature describing P3HT rich domains. Once PC₆₀BM was added, the blend morphology was changed in which the fiber-like structures were less apparent. Accordingly, the corresponding morphology became less defined. Thus, the self-assembly behavior is affected by loading the fullerene acceptor. The effect of PC₆₀BM could be summarized by different phenomena described in literature. For instance, PC₆₀BM could disturb the structure by slowing down P3HT aggregation/crystallization in which it confines the P3HT assembly.⁸¹ No clear phase separation was observed in this case yet. In both cases, the films were relatively smooth with a root mean square roughness (Rq) of 0.8 nm and 1.5 nm, without and with PC₆₀BM, respectively.

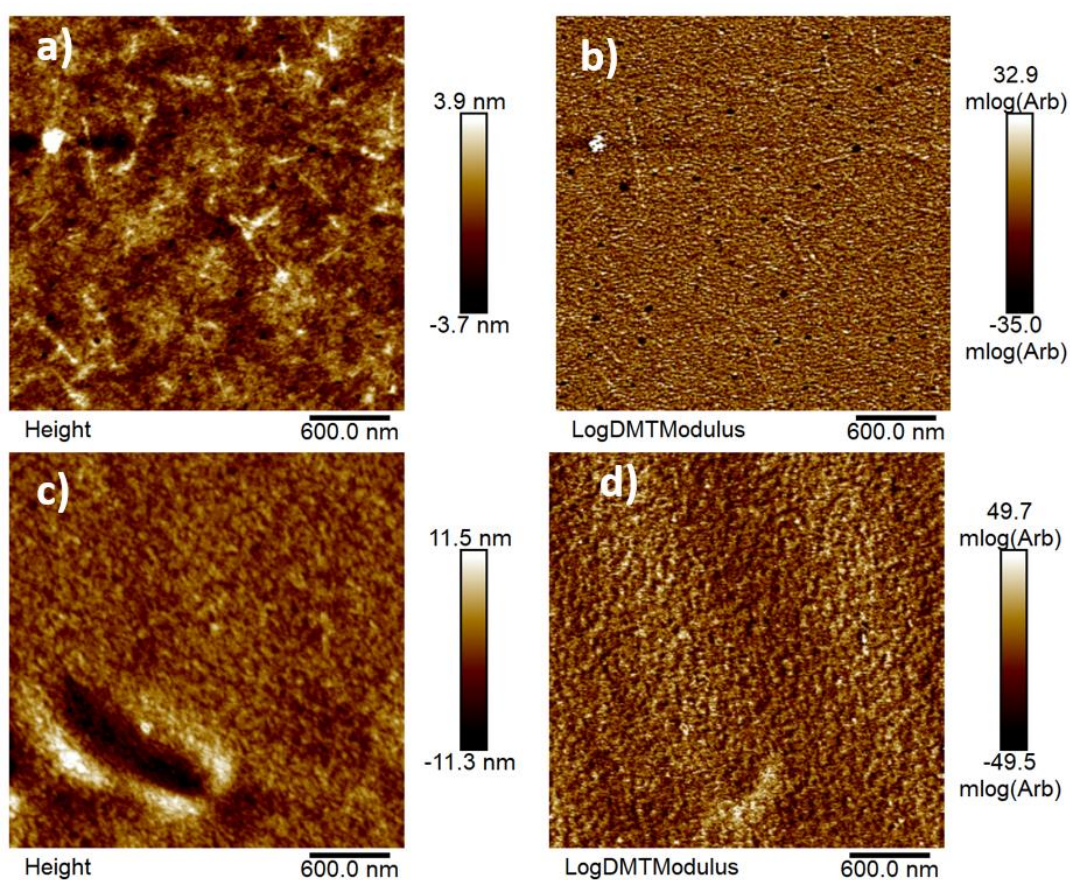


Figure III-16: AFM images for as-casted films of (a), (b) P3HT₃₇-b-P(DTS-DPP)₄ and (c), (d) P3HT₃₇-b-P(DTS-DPP)₄:PC₆₀BM deposited on glass substrates.

ii. Optimizing the processing conditions of P3HT₃₇-*b*-P(DTS-DPP)₄: PC₆₀BM

1. Effect of pre-annealing temperatures

In order to study the influence of the annealing temperature before evaporating MoO₃/Ag on device performance (pre-annealing), the photoactive blend (20 mg.mL⁻¹ of P3HT₃₇-*b*-P(DTS-DPP)₄:PC₆₀BM) was deposited on top of PEIE and annealed at different temperatures 80, 120 and 150 °C for 10 minutes. The thermal annealing is well-known to better rearrange the polymer and fullerene acceptors, thus optimizing blend morphology.⁸²

Figure III-17 represents the J-V curves of the fabricated inverted device structures showing the effect of the pre-annealing temperature of the photoactive layer on the device performance. The photovoltaic parameters of the corresponding devices are summarized in **Table III-2**. The results revealed that after pre-annealing the photoactive layer at 80 °C, the PCE was increased from 0.29% to 0.78% with an increase in J_{SC} from 1.51 to 4.76 mA/cm². Further increase in the pre-annealing temperature up to 120 °C, resulted in enhancing the PCE to a maximum value of 1.38%. This increase in PCE was coupled with an increase in both FF (0.48) and J_{SC} (6.71 mA/cm²).

The reported optimum annealing temperature of P3HT-based blends in literature is in the range of 120 °C-140 °C. Thus, in our case, the enhancement can be related to an improvement of the morphology and phase separation which increases the exciton dissociation rate and/or lead to the formation of collection pathways for the separated charges.⁸³ The crystallinity of the P3HT chains could also be increased upon annealing. This improves hole mobility,⁸⁴ enhances the light harvest of the device⁸⁵ and therefore facilitates charge transport to the corresponding electrodes.⁸⁶ Thus, this improvement in morphology and interfaces eventually improve FF and J_{SC}. The lower V_{OC} could be attributed to the higher recombination rate upon annealing due to the presence of isolated domains that prevent charge collection at electrodes.

Above 120 °C, the PCE was decreased to 1.04% with a drop in V_{OC}, J_{SC} and FF to 0.38 V, 6.3 mA/cm² and 0.44, respectively. This drop in performance could be explained by the formation of even larger PC₆₀BM clusters as previously described in literature.⁸⁵

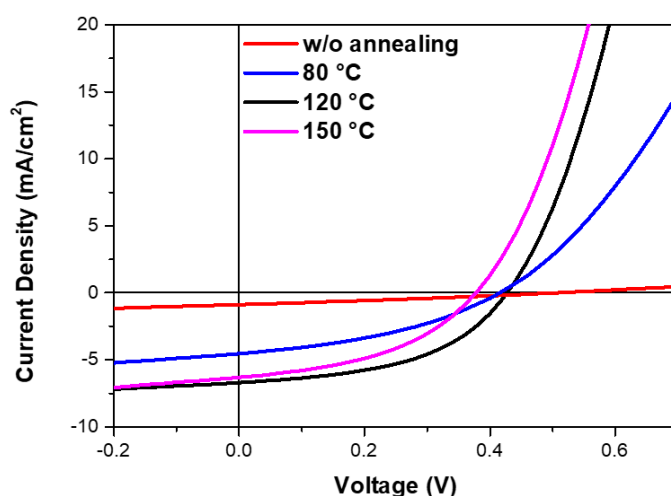


Figure III-17: J-V curves of P3HT₃₇-*b*-P(DTS-DPP)₄:PC₆₀BM-based devices pre-annealed at different temperatures.

Table III-2: Photovoltaic parameters of P3HT₃₇-b-P(DTS-DPP)₄:PC₆₀BM-based devices pre-annealed at different temperatures.

Pre-annealing temperature	FF	V _{oc} (V)	J _{sc} (mA/cm ²)	PCE (%)
w/o annealing	0.31	0.63	1.51	0.29
80 °C	0.38	0.43	4.76	0.78
120 °C	0.48	0.43	6.71	1.38
150 °C	0.44	0.38	6.30	1.05

External quantum efficiencies agreed with those obtained from J-V curves and UV-vis spectroscopy in which the charge collection was proportional to the generated photocurrent and the absorption of the corresponding active layer. As shown in **Figure III-18a**, devices fabricated without any thermal treatment showed the lowest EQE (around 7%). This EQE value was increased by annealing. The highest percentage obtained (27%) was for the pre-annealed device at 120 °C corresponding to the relative absorption maxima of the blend. These results revealed that the efficiency of photon to electron conversion is increasing by pre-annealing the photoactive layer at an optimum temperature (120 °C). As previously mentioned, annealing at 150 °C could lead to some recognizable defects and deformations due to PC₆₀BM aggregation. Thus, the important contribution to EQE comes from an easier transport of charge carriers in optimally annealed devices due to the presence of less traps resulting in an increase in the number of charge carriers.⁸⁷

Figure III-18b represents the UV-vis absorption spectra of the corresponding photoactive layers. Two broad absorption peaks appeared, attributed to P3HT absorption between 400-625 nm and low-bandgap block, P(DTS-DPP) (625-900 nm). After annealing the photoactive layer, an absorption behavior of the well-organized P3HT block was observed with an enhanced π - π interchain interactions in this P3HT block and a slight red-shift by gradually increasing the annealing temperature from 0 to 120 °C. These π - π interchain interactions appeared as vibronic peaks in the range of 500 to 650 nm. This is a good indication for the enhanced P3HT crystallinity and chain ordering in the active layer upon annealing that probably improve charge transport properties as previously explained. The absence of the vibronic peaks in case of non-annealed films explains the amorphous fraction which is dominant in the morphologic structure of these layers. Importantly, no optical changes were observed in the near-IR region upon annealing.

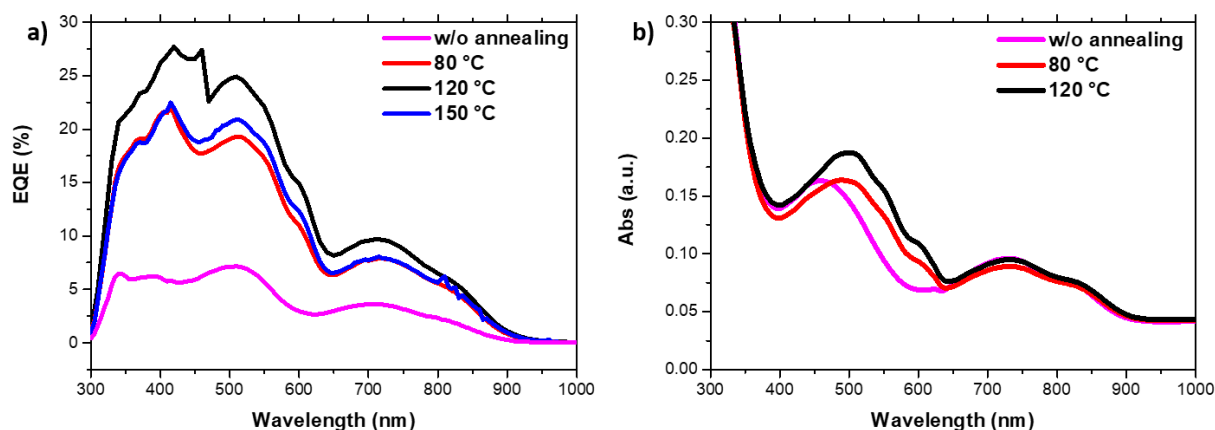


Figure III-18: (a) EQE of $P3HT_{37}$ - b - $P(DTS-DPP)_4$: $PC_{60}BM$ -based devices and (b) UV-vis absorption spectra of the photoactive layers pre-annealed at different temperatures.

Since film morphology and crystallinity are key parameters for device performance, it is interesting to study the morphology of the photoactive layers (diblock: $PC_{60}BM$) upon annealing by AFM. No obvious phase separation was observed in the blend that was studied as-casted (without thermal annealing) as shown in **Figure III-19a**. Once the films were annealed, phase separation was promoted and fullerenes were better segregated. This can be explained by the increased crystallinity and reorganization of the diblock copolymer into thermodynamically favored conformation and the increased interchain interactions of the fullerene molecules after thermal annealing.^{88,89}

As shown in **Figure III-19b, c** and **d**, $PC_{60}BM$ aggregates were increased upon annealing which leads to its better intercalation with the block copolymer. These results are consistent with what was explained in literature, in which increasing the temperature up to 120 °C led to the segregation of $PC_{60}BM$ out of the donor, thereby forming phase segregated donor and acceptor structures, and reordering the polymer chain structure. Thus, charge transfer is enhanced and PCE is eventually improved.⁸²

Above 120 °C, the performance was dropped to a lower value. This could be explained by the presence of more serious aggregations of $PC_{60}BM$ that affect exciton dissociation and transport.⁹⁰

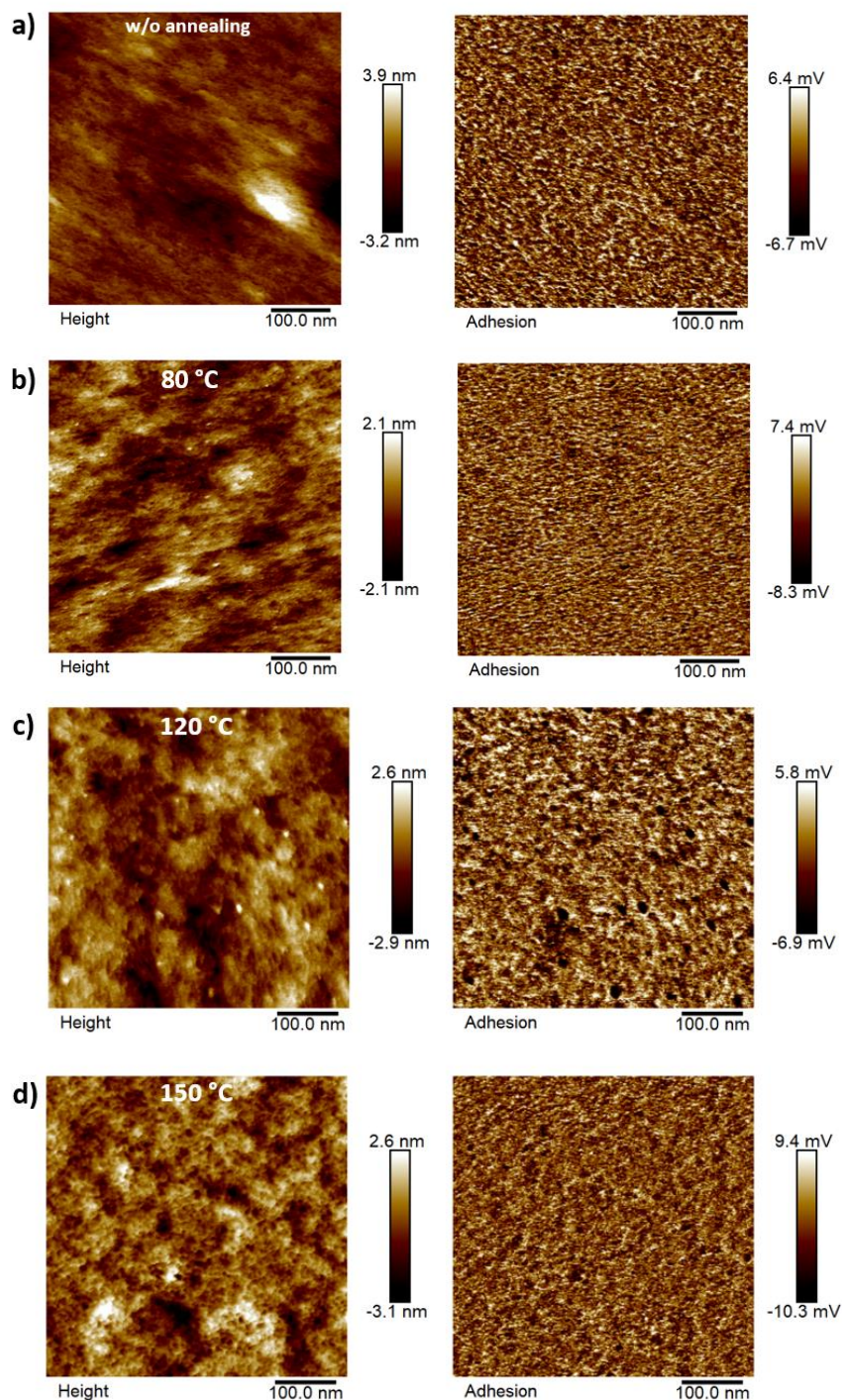


Figure III-19: AFM images for $P3HT_{37}\text{-}b\text{-}P(\text{DTS-DPP})_4\text{:}PC_{60}BM$ nanocomposite films (a) as casted, (b) annealed at 80 °C, (c) annealed at 120 °C and (d) annealed at 150 °C.

Therefore, pre-annealing the photoactive layer (ratio 1:1) at an optimum temperature of 120 °C enhances the ordered structure formation as indicated by the vibronic peaks in the absorption spectrum and improves the interpenetrating network between polymer and $PC_{60}BM$. Thus, the higher absorption and the enhanced morphology that affect carrier mobility and charge collection are most likely the reasons for the efficiency enhancement.

2. Effect of blend ratio

The donor:acceptor blend ratio significantly influences the device performance of the BHJ solar cells. Indeed, it has been shown that it strongly affects the crystalline order, phase separation, and morphology of the thin films.⁹¹ To obtain the best percolation pathways with maximal interfacial areas, the optimal D:A ratio (by weight) depends on the choice of the materials used. For the aim of optimizing the blend morphology and determining the effect of the amount of PC₆₀BM, several experiments were performed with different weight ratios of P3HT₃₇-*b*-P(DTS-DPP)₄:PC₆₀BM including 1:1, 1:1.5, 1:2 with 10 mg.mL⁻¹ for the block copolymer. J-V curves in **Figure III-20** represents the performances of devices fabricated using different blend ratios and pre-annealed at 120 °C for 10 minutes.

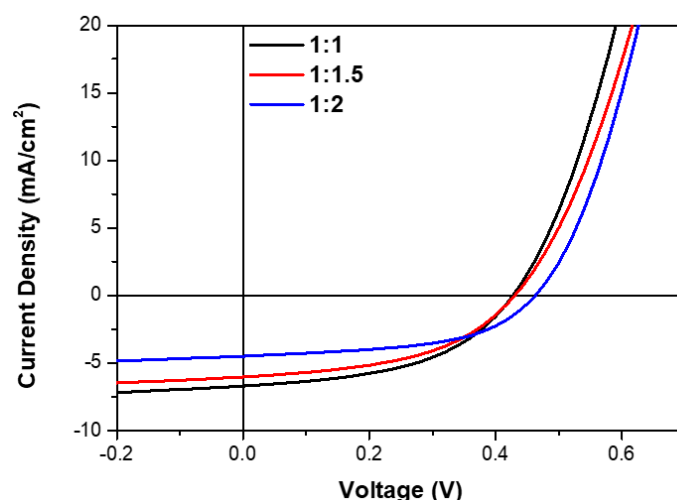


Figure III-20: J-V curves of P3HT₃₇-*b*-P(DTS-DPP)₄:PC₆₀BM-based devices using different blend ratios.

Table III-3 summarizes the photovoltaic parameters of the corresponding devices fabricated using different donor:acceptor ratios. It was observed that by increasing the amount of PC₆₀BM, PCE was decreased with a drop in J_{SC} from 6.71 mA/cm² to 6.03 mA/cm² and then to 4.50 mA/cm² for 1:1, 1:1.5 and 1:2, respectively. However, V_{OC} and FF values were increased with the amount of PC₆₀BM added to the blend. The drop in PCE could be correlated to the interruption of interactions between P3HT polymer chains by PC₆₀BM molecules, thus impeding P3HT crystallization. This could reduce the charge carrier mobility, thereby decreasing the efficiency of OSCs as revealed by previous studies.^{91,92} Additionally, Kywa *et al.*⁹³ suggested that hole and electron mobilities are balanced at a specific composition which is 1:1 in our case.

Table III-3: Photovoltaic parameters of P3HT₃₇-*b*-P(DTS-DPP)₄:PC₆₀BM-based devices using different blend ratios.

Blend ratio	Photoactive layer thickness (nm)	FF	V _{OC} (V)	J _{SC} (mA/cm ²)	PCE (%)
1:1	140	0.48	0.43	6.71	1.38
1:1.5	190	0.48	0.43	6.03	1.24
1:2	200	0.53	0.46	4.50	1.10

Figure III-21a and **b** show EQE and UV-vis absorption spectra, respectively. The highest EQE (27%) corresponds to devices based on 1:1 blend ratio. Thus, photon to electron conversion was maximized using this blend ratio probably due to the presence of more donor/acceptor interfaces enhancing charge dissociation and transfer. The EQE spectra fit the relative absorption maxima of the blend. The more PC₆₀BM was added, the more blue-shifted absorption spectrum (hypsochromic shift) was observed with a slight decrease in the absorption intensity and a decrease in the EQE to around 22%. Interestingly, the P3HT impeded crystallization discussed before can be clearly observed in the absorption spectrum of the active blend. In which the blue-shifted vibronic bands could be attributed to the reduction of the interchain interactions between the P3HT chains, thus lowering the degree of order of P3HT framework.⁸⁰ Additionally, the decrease in the vibronic bands is another indication for further reduction in interactions and conjugation lengths⁹⁴ which could be a result of the isolation of the P3HT chains by PC₆₀BM.³⁶ It can also be noted that the absorption of the low-bandgap block is weakly affected by the incorporation of PC₆₀BM. This may suggest that PC₆₀BM has a stronger affinity for the P3HT block than for the P(DTS-DPP) one.

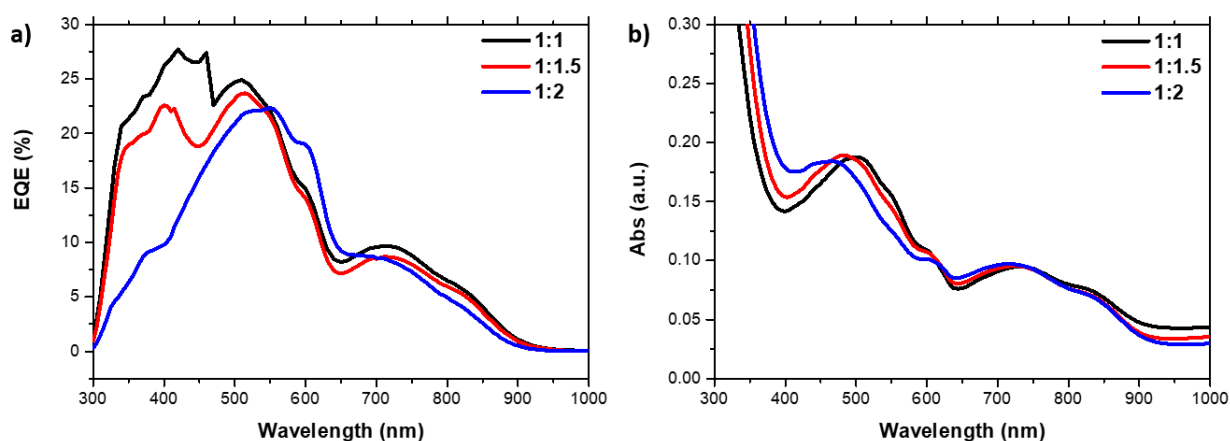


Figure III-21: (a) EQE of P3HT₃₇-b-P(DTS-DPP)₄:PC₆₀BM-based devices and (b) UV-vis absorption spectra of the corresponding photoactive layers having different blend ratios.

Thus, the optimized weight ratio needed for P3HT₃₇-b-P(DTS-DPP)₄:PC₆₀BM blend to achieve the highest power conversion efficiency is 1:1 with pre-annealing at 120 °C.

3. Effect of solvent additives

As discussed in the state of art, in some cases, a large scaled phase separation was observed when D:A blends are deposited from a single solvent. Thus, mixed solvents are used for the aim of changing the crystallization behavior of π -conjugated polymer and homogenizing the distribution of PC₆₀BM in thin films.^{20,21} This secondary additive solvent must be a good solvent for either donor or acceptor.

In this regard, the effect of 3 vol% acetophenone and diphenyl ether additives on the morphology of P3HT₃₇-b-P(DTS-DPP)₄:PC₆₀BM blend (1:1 weight ratio) has been studied using the same host solvent, chlorobenzene, and the same pre-annealing temperature (120 °C). **Figure III-22** and **Table III-4** represent the J-V curves and photovoltaic parameters of the corresponding devices, respectively.

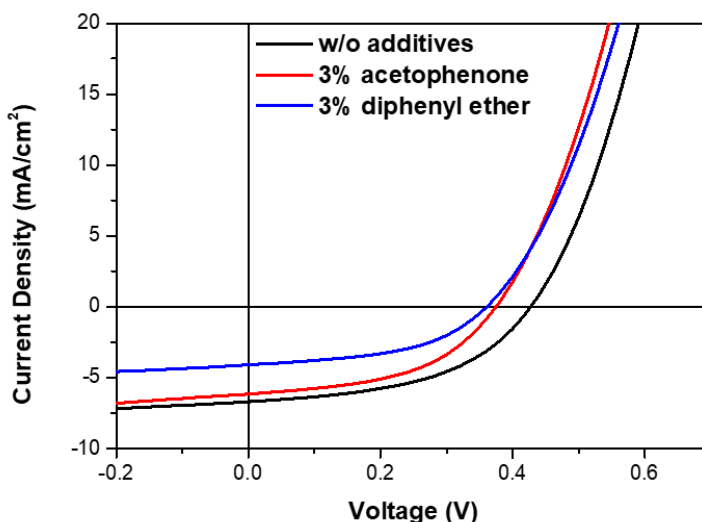


Figure III-22: J-V curves of P3HT₃₇-b-P(DTS-DPP)₄:PC₆₀BM-based devices using different additives.

In this study, none of the two additives improved the overall device performance probably because they have a negative impact on blend morphology. Slight decrease in power conversion efficiency from 1.38% to 1.12% and 0.71% was even observed after the addition of 3 vol% acetophenone and diphenyl ether additives, respectively. In particular, J_{SC} was strongly reduced from 6.71 mA/cm² with pure chlorobenzene to 6.16 and 4.1 mA/cm², respectively. The loss in V_{OC} in the presence of either additives might be attributed to a higher recombination rate due to the aggregation of polymers caused by its poor interaction with the additives.⁹⁵ Another reason could be a bad morphology driven by these additives although no effect on FF was recognized in both cases.

Table III-4: Photovoltaic parameters of P3HT₃₇-b-P(DTS-DPP)₄:PC₆₀BM-based devices processed using different additives.

Additive (3%)	FF	V_{OC} (V)	J_{SC} (mA/cm ²)	PCE (%)
w/o	0.48	0.43	6.71	1.38
acetophenone	0.48	0.38	6.16	1.12
diphenyl ether	0.48	0.36	4.10	0.71

To better understand the negative impact of the added additives on the performance of the fabricated devices, EQE measurements and optical properties were conducted as shown in **Figure III-23a** and **b**. The highest EQE obtained was for the device fabricated with a blend without any solvent additive. This EQE of 27% around 450 nm corresponds to the relative absorption maxima of the blend as shown in **Figure III-23b**. Although a higher intensity was observed for the blend with acetophenone in the absorption spectrum, the obtained EQE value was around 19% while a lower value was observed for the blend with diphenyl ether (15%). Therefore, the use of an additive gave a negative impact on the photon to electron conversion, resulting in a decreased EQE in the 300-900 nm range. A slight red-shifted absorption was observed with additives. This bathochromic shift could be attributed to the low solubility of the block polymer in the used additive, thus forming aggregation in thin film.⁹⁶

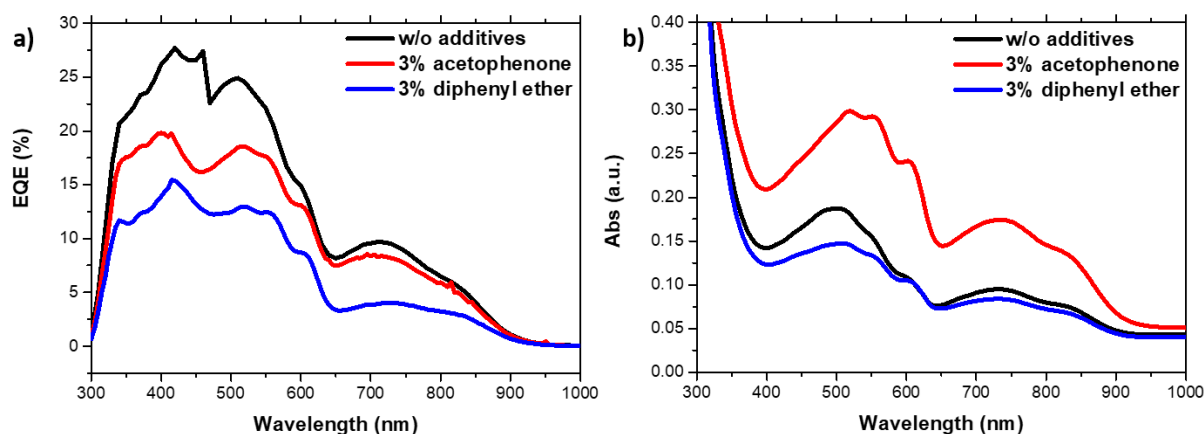


Figure III-23: (a) EQE of P3HT₃₇-b-P(DTS-DPP)₄:PC₆₀BM-based devices and (b) UV-vis absorption spectra of the corresponding photoactive layers processed with and without additives.

Although it is known that the addition of co-solvents improves device performance, in our case, the incorporation of 3 w% additives did not improve the efficiency.

4. Effect of blend solvent

On the basis of the encouraging results obtained for the fabricated devices and given that the morphology has such an important impact on the PV performances, the solvent of the donor:acceptor solution was changed from chlorobenzene to *o*-xylene and chloroform.

J-V curves of the fabricated devices are presented in **Figure III-24** and the photovoltaic parameters are summarized in **Table III-5**. The use of chloroform-based photoactive layers led to a strong decrease in the efficiency (0.12%) when compared to those fabricated using chlorobenzene-based photoactive layers (1.38%). This low PCE is due to drop in all photovoltaic parameters, especially J_{SC} that decreases from 6.71 to 0.9 mA/cm², probably due to the lower photoactive layer thickness (100 nm). On the contrary, by using *o*-xylene solvent, the power conversion efficiency was enhanced to 1.59%. This increase in PCE was coupled with an increase in both V_{OC} and FF while J_{SC} remained almost the same when compared to the chlorobenzene-based devices (6.70 mA/cm²).

The reason beyond this behavior could be the higher boiling point of the *o*-xylene solvent that stays a longer time than chlorobenzene and chloroform in the thin film before drying, giving more mobility to materials to self-organize. This generally leads to a better phase separation of the polymer and PC₆₀BM with the formation of bicontinuous networks, thus increasing charge transport.⁹⁷ Moreover, this substitution has another benefit, as *o*-xylene is a non-chlorinated and less toxic solvent, commonly used by OPV industry.

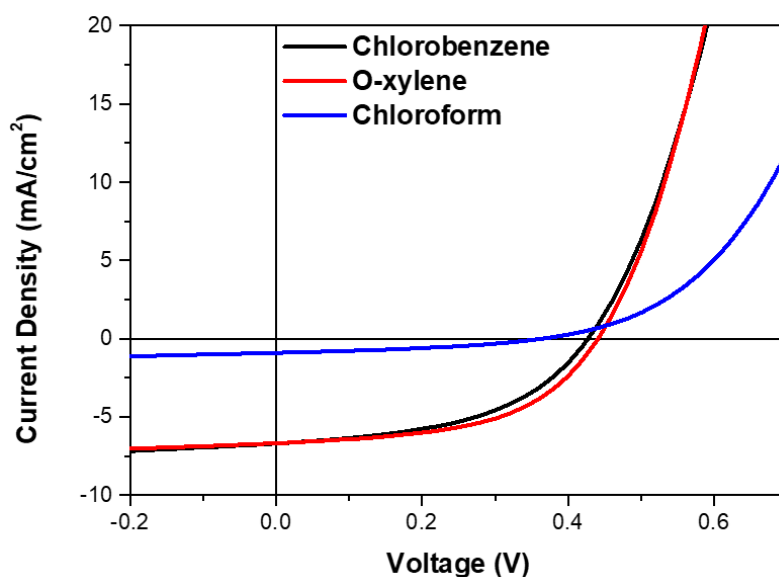


Figure III-24: J-V curves of P3HT₃₇-b-P(DTS-DPP)₄:PC₆₀BM-based devices using different blend solvents.

Table III-5: Photovoltaic parameters of P3HT₃₇-b-P(DTS-DPP)₄:PC₆₀BM-based devices using different blend solvents.

Solvent	Photoactive layer thickness (nm)	FF	V _{oc} (V)	J _{sc} (mA/cm ²)	PCE (%)
chloroform	100	0.37	0.36	0.9	0.12
chlorobenzene	140	0.48	0.43	6.71	1.38
o-xylene	140	0.53	0.45	6.70	1.59

EQE measurements and UV-vis absorption spectra of the corresponding devices are shown in **Figure III-25a** and **b**, respectively. As expected, the highest EQE (32%) was obtained for devices fabricated using o-xylene-based blends in comparison with those based on chlorobenzene showing an EQE value of 22%. The EQE spectra fit to the relative absorption maxima of the blend shown in **Figure III-25b**. The enhancement in EQE for o-xylene blends was observed for both blocks, P3HT and P(DTS-DPP). Therefore, processing blends in o-xylene increased photon to current conversion in all wavelength's region. However, EQE is much more efficient in the 500 nm region than in the 800 nm one due to the higher absorption of photons in the P3HT region. On the contrary, the chloroform-based blends showed very low EQE values (almost null) when compared to other devices, thus the EQE curve was not plotted. The UV-vis spectrum of chloroform-based photoactive layers showed a slightly narrower absorption in the near-IR region corresponding to the absorption of the low-bandgap block in comparison with the other blends having slight bathochromic shift. Additionally, a very slight red-shift was observed in the case of o-xylene which could be attributed to the improved ordering and crystallinity of P3HT in the block copolymer.⁹⁸

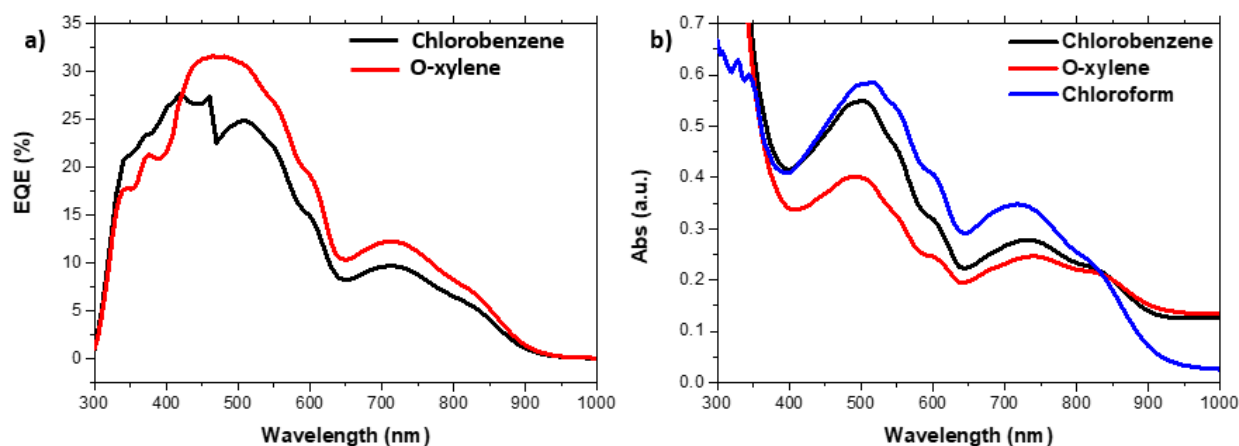


Figure III-25: (a) EQE of $P3HT_{37}$ - b - $P(DTS-DPP)_4:PC_{60}BM$ -based devices and (b) UV-vis absorption spectra of the corresponding photoactive layers deposited from different solvents.

To fully capture the nano-morphological structure of $P3HT_{37}$ - b - $P(DTS-DPP)_4:PC_{60}BM$ photoactive layer in two different solvents (chlorobenzene and o-xylene), AFM has been performed and the images are shown in **Figure III-26**. The films are deposited on glass substrates and annealed at 120 °C for 10 min. A homogeneously intermixed block with $PC_{60}BM$ is observed in both films. The relative R_q roughness for o-xylene and chlorobenzene-based films is 1.20 nm which is quite low. This smooth layer is needed for an efficient solar cell.

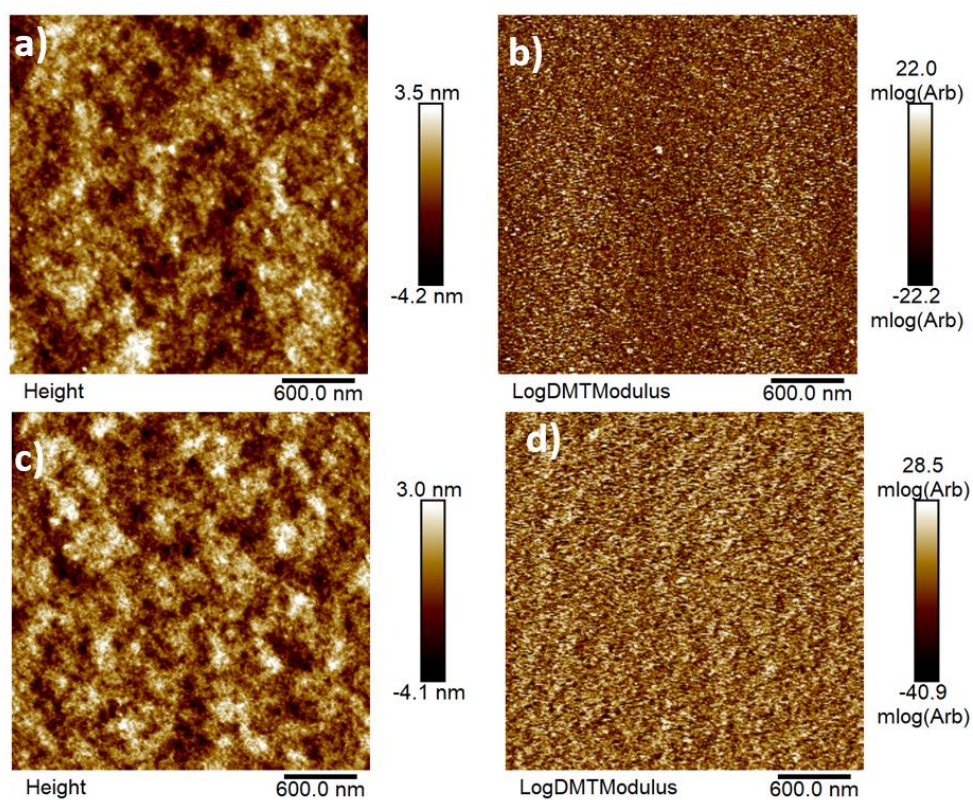


Figure III-26: AFM images for $P3HT_{37}$ - b - $P(DTS-DPP)_4:PC_{60}BM$ nanocomposite films (a), (b) in chlorobenzene and (c), (d) in o-xylene.

To conclude on this part, it was clearly proven that the performance of the fabricated inverted device structures and the photovoltaic parameters are strongly dependent on the processing conditions of the donor:acceptor blend. In summary, the champion devices based on P3HT₃₇-*b*-P(DTS-DPP)₄ were found to be optimized when **blended with PC₆₀BM at a 1:1 weight ratio** in *o*-xylene and **without the usage of any processing solvent additives**. The photoactive layers should be **pre-annealed at 120 °C for 10 minutes** before evaporating MoO₃ and Ag.

The J-V curves in dark and under illumination and the EQE of the optimized devices are shown in **Figure III-27a** and **b**, respectively. Although the efficiencies were increased with the different optimizations, the efficiency remains low for this block copolymer with a particularly low V_{OC} (below 0.5 V).

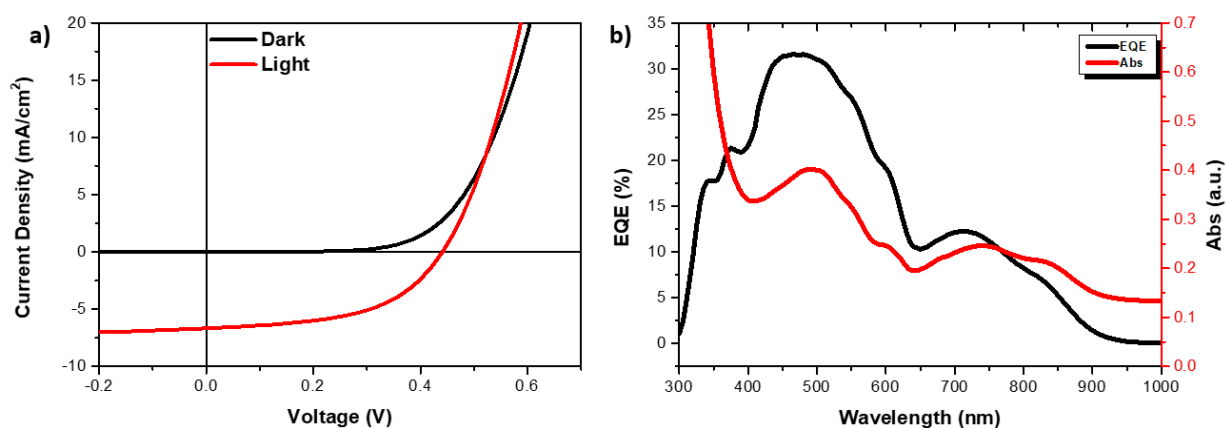


Figure III-27: (a) J-V curves and (b) EQE of the optimized device based on P3HT₃₇-*b*-P(DTS-DPP)₄:PC₆₀BM with an absorption spectrum of the corresponding photoactive layer.

For the aim of evaluating the performance of the synthesized block copolymer P3HT₃₇-*b*-P(DTS-DPP)₄, reference devices based on P3HT:PC₆₀BM were fabricated. The processing conditions were exactly the same optimized conditions for devices based on the block copolymer. A blend of P3HT:PC₆₀BM with 1:1 weight ratio in *o*-xylene was used. The 130 nm-thick photoactive layers were thermally annealed for 10 min at 120 °C. The J-V curve of the corresponding device is plotted and shown in **Figure III-28** against the J-V curve of the optimized device based on the block copolymer, P3HT₃₇-*b*-P(DTS-DPP)₄.

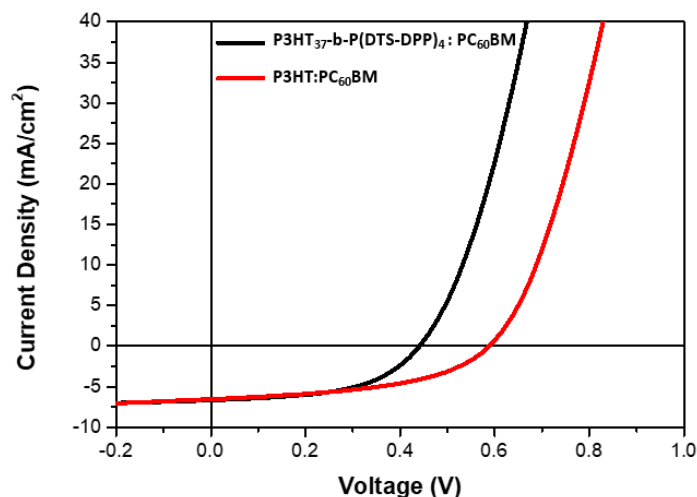


Figure III-28: J-V curves of P3HT₃₇-*b*-P(DTS-DPP)₄:PC₆₀BM and P3HT:PC₆₀BM-based devices.

The photovoltaic parameters summarized in **Table III-6** reveal the higher efficiencies of P3HT:PC₆₀BM-based devices (1.9%) when compared to P3HT_{37-b}-P(DTS-DPP)₄:PC₆₀BM-based ones (1.59%). The increase in efficiency is attributed to an improvement in V_{OC} from 0.45 to 0.6 V. Both FF and J_{SC} show a slight unexpected decrease for the P3HT:PC₆₀BM-based devices.

Table III-6: Photovoltaic parameters of P3HT_{37-b}-P(DTS-DPP)₄:PC₆₀BM and P3HT:PC₆₀BM-based devices.

Polymer donor	FF	V _{OC} (V)	J _{SC} (mA/cm ²)	PCE (%)
P3HT _{37-b} -P(DTS-DPP) ₄	0.53	0.45	6.70	1.59
P3HT	0.48	0.60	6.60	1.9

In general, the performance of the fabricated P3HT:PC₆₀BM devices was low in comparison to those shown in literature. To the best of our knowledge, the highest efficiency obtained in inverted device structures based on P3HT:PC₆₀BM was 3.6% (in *o*-xylene)⁹⁹ and around 4% (in 1,2-dichlorobenzene).¹⁰⁰ This could be related to the processing conditions including thermal treatment temperatures and additives.

On the other hand, the lower efficiency of devices based on the synthesized block copolymer when compared to devices based on the commercially available P3HT could be related to the fact that the molar mass and the dispersity of the polymer can have a great influence on the charge carrier mobility. In general, they claimed that by increasing the molar mass of the polymer, the charge mobility increases.^{101,102} Thus, in our case, the low molar mass of the P3HT polymer used in the block copolymer (6150 g.mol⁻¹ from the ¹H NMR) when compared to the commercial P3HT (up to 40,000 g.mol⁻¹) can affect device performance. Additionally, the presence of the low-bandgap block slightly impedes the crystallization of P3HT as previously shown in the DSC study of **Chapter II**.

iii. P3HT_{37-b}-P(DTS-DPP)₁₉

Based on the experiments performed above, it was interesting to study the effect of the low-bandgap block on the performance of the fabricated OSCs. In this regard, P3HT_{37-b}-P(DTS-DPP)₁₉ was used as the donor material and blended with PC₆₀BM in *o*-xylene with a 1:1 weight ratio. The photoactive layers were prepared based on the optimized conditions previously discussed, in which the 110 nm-thick active layers were pre-annealed at 120 °C for 10 min. Although, energy level alignments of P3HT_{37-b}-P(DTS-DPP)₁₉ were matching those of PC₆₀BM (based on cyclic voltammetry), the device efficiency was very low (0.24%) when compared to those obtained for the previously studied block copolymer. This low PCE is attributed to the low photovoltaic parameters with J_{SC} of 4.30 mA/cm², V_{OC} of 0.2 V and FF of 0.28 (**Figure III-29**).

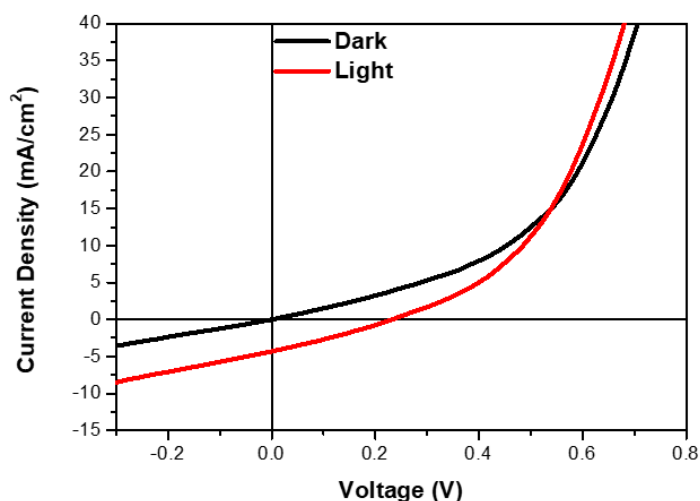


Figure III-29: *J-V* curves of inverted device structure based on 1:1 weight ratio of P3HT₃₇-*b*-P(DTS-DPP)₁₉:PC₆₀BM in *o*-xylene.

As proved from the DSC analysis discussed in **Chapter II (Figure II-47)**, this polymer did not show any thermal transition, meaning absence of melting and crystallization behavior. The crystallization of P3HT was impeded and prohibited due to the presence of the low-bandgap polymer in a higher amount. Additionally, non-crystalline P3HT₃₇-*b*-P(DTS-DPP)₁₉ formed highly mixed layer with PC₆₀BM, that facilitates exciton diffusion into the interface, but is detrimental for charge transport into the electrode due to the high rate of charge recombination.^{15,103}

In general, the studied devices showed lower J_{SC} values than the previous copolymers with and without pre-annealing. As shown in **Figure III-30**, the absorption of the photoactive layer was dominated by the low-bandgap block. Thus, as P3HT absorption is very low, exciton formation is limited at the P3HT interface, thereby affecting charge collection and lowering EQE (0.2%) and J_{SC} . All this probably explain why this polymer is not itself an efficient donor in solar cells.

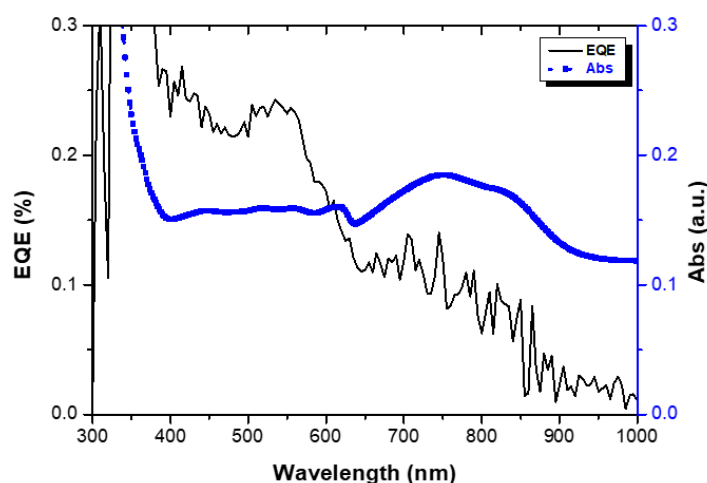


Figure III-30: EQE of the device based on P3HT₃₇-*b*-P(DTS-DPP)₁₉:PC₆₀BM with the absorption spectrum of the corresponding photoactive layer.

As a conclusion, the performance of solar cells incorporating copolymers was block composition dependent.

iv. P3HT₂₄₀-*b*-P(DTS-DPP)₁₁

In general, the polymer's molar mass influences the ratio of crystalline/amorphous phases, therefore plays a role on morphology and hole mobility. This eventually affects device performances.^{104,105} A previous study revealed that P3HT with molar mass up to 10,000 g.mol⁻¹ led to bad film morphology with low device performance in P3HT:PC₆₀BM normal device structures. While P3HT with molar mass up to 50,000 g.mol⁻¹ achieved high performances due to the appropriate chain length resulting in a better film morphology and donor/acceptor interface contact. More than 50,000 g.mol⁻¹ of P3HT can limit the film fabrication and negatively impact the performance.¹⁰² Another recent study showed that a longer P3HT block chain in the block copolymer is beneficial for the photovoltaic performance at a fixed acceptor block length.¹⁰⁶ This is attributed to the balanced donor and acceptor block lengths and appropriate degree of phase separation that can afford bicontinuous networks for hole and electron transport.

In this regard, P3HT₂₄₀-*b*-P(DTS-DPP)₁₁ diblock copolymer with a higher P3HT molar mass (40,000 g.mol⁻¹) was then used as the donor material with the idea to enhance the crystallization and increase charges mobility. Due to the higher molar mass of P3HT in P3HT₂₄₀-*b*-P(DTS-DPP)₁₁, different conditions were examined for the photoactive layer while taking into account the results obtained for P3HT₃₇-*b*-P(DTS-DPP)₄ block copolymer. The photovoltaic parameters of some fabricated devices are summarized in **Table III-7** and the corresponding J-V curves are shown in **Figure III-31a**.

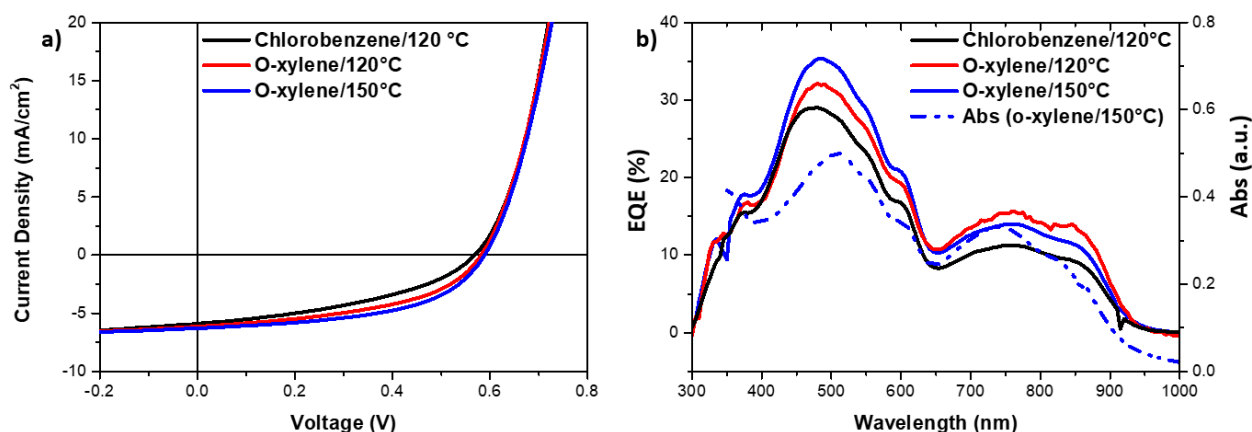
When a 1:1 weight ratio of P3HT₂₄₀-*b*-P(DTS-DPP)₁₁:PC₆₀BM blend was deposited from chlorobenzene followed by pre-annealing at 120 °C for 10 min, 1.38% efficiency was obtained which is similar to devices fabricated from P3HT₃₇-*b*-P(DTS-DPP)₄ under the same conditions. By using *o*-xylene, a higher power conversion efficiency was obtained (1.71%) with an increase in FF and J_{SC} from 0.41 to 0.48 and from 5.9 to 6.14 mA/cm², respectively. As previously explained, the higher boiling point of *o*-xylene contributes to the presence of better mixing and interpenetrating network between the polymer and PC₆₀BM, improving crystallinity, charge transportation and mobility.⁹⁷ Under the same processing conditions, this PCE was higher than that obtained for the devices using P3HT₃₇-*b*-P(DTS-DPP)₄:PC₆₀BM. Moreover, P3HT₂₄₀-*b*-P(DTS-DPP)₁₁-based devices showed higher V_{OC} values than those based on P3HT₃₇-*b*-P(DTS-DPP)₄.

Previously, it was demonstrated that the annealing temperature should be chosen regarding the molar mass of P3HT.⁸⁴ Therefore, it was necessary to consider the molar mass when optimizing the pre-annealing temperature and duration as it can impact the crystallization temperature of the P3HT block. Interestingly, by increasing the annealing temperature to 150 °C, the devices showed an enhanced power conversion efficiency of 1.93%. This increase in efficiency is attributed to an increase in FF (0.52) and J_{SC} (6.3 mA/cm²). Under the same conditions, adding acetophenone additive to the 1:1 blend ratio in *o*-xylene or increasing the amount of PC₆₀BM (1:1.5), has detrimental effect on the device performances. The photoactive layer thickness was measured to be around 120 nm in all cases, except for 1:1.5 blend, it was around 130 nm.

Table III-7: Photovoltaic parameters of P3HT₂₄₀-b-P(DTS-DPP)₁₁:PC₆₀BM-based devices processed under different conditions.

Blend ratio	Additives	pre-annealing Temp °C	Solvent	FF	V _{oc} (V)	J _{sc} (mA/cm ²)	PCE (%)
1:1	w/o	120	chlorobenzene	0.41	0.57	5.90	1.38
1:1	w/o	120	o-xylene	0.48	0.58	6.14	1.71
1:1	w/o	150	o-xylene	0.52	0.59	6.3	1.93
1:1	acetophenone	150	o-xylene	0.5	0.42	6.74	1.4
1:1.5	w/o	150	o-xylene	0.44	0.6	5.6	1.47

EQE measurements were conducted for the fabricated devices (**Figure III-31b**). For all devices, charge collection was taking place in the whole absorption range of the photoactive layer which is characterized by two broad absorption peaks, attributed to P3HT (400-650 nm) and the low-bandgap block which is P(DTS-DPP) (650-950 nm). The less efficient device (in chlorobenzene) shows the lowest EQE value (28% at 500 nm). Once again, the behavior in o-xylene shows a better performance due to the increased light to current conversion at all wavelengths. The highest efficient device, thermally pre-annealing at 150 °C, showed the highest EQE value around 35% at 500 nm while the photogeneration of charges from 700 to 900 nm was with an EQE around 12%. In this case, the conversion is higher in the region of P3HT absorption but not in that of the low-bandgap polymer. Thus, thermal annealing mainly impacts the P3HT block.

Figure III-31: (a) J-V curves and (b) EQE of P3HT₂₄₀-b-P(DTS-DPP)₁₁:PC₆₀BM-based devices processed under different conditions with the absorption spectrum of the corresponding photoactive layer.

The champion device based on P3HT₂₄₀-b-P(DTS-DPP)₁₁ showed the highest efficiency when blended with **1:1 weight ratio** of PC₆₀BM in **o-xylene**, and treated at **150 °C without the use of processing solvent additives**.

For the aim of evaluating the performance of the synthesized P3HT₂₄₀-b-P(DTS-DPP)₁₁, we compared its performance to the reference device based on P3HT:PC₆₀BM as previously discussed (see **Figure III-28**). The corresponding J-V curves are shown in **Figure III-32**. Interestingly, we could recognize that with P3HT₂₄₀-b-P(DTS-DPP)₁₁-based devices, a V_{oc} close to that of P3HT:PC₆₀BM-based ones can be reached. This could be related to the higher P3HT chain length in P3HT₂₄₀-b-P(DTS-DPP)₁₁ which is in the range of P3HT.

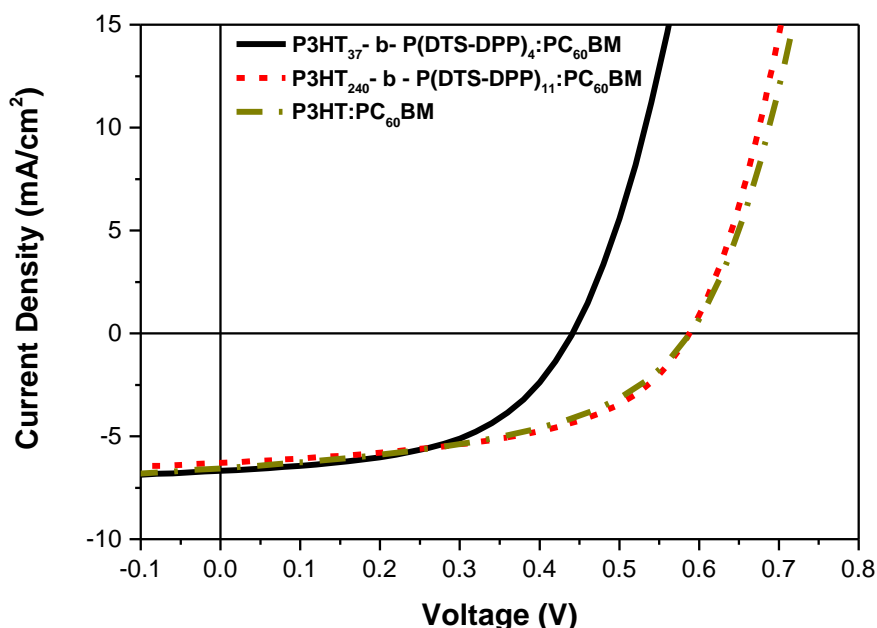


Figure III-32: J-V curves of $P3HT_n-b-P(DTS-DPP)_m:PC_{60}BM$ and $P3HT:PC_{60}BM$ -based devices in *o*-xylene.

For comparison, external quantum efficiency for the three best devices are plotted in **Figure III-33**. For $P3HT:PC_{60}BM$ -based devices, a maximum EQE of 40% was obtained at the typical maximum wavelength of P3HT, 500 nm. For $P3HT_{37}-b-P(DTS-DPP)_4$, a loss of EQE at 500 nm (to 32%) was balanced by the addition of the band, in the range 700 to 900 nm, due to the low-bandgap block. This proves that the charge dissociation is happening also at the $P(DTS:DPP):PC_{60}BM$ interface despite the difference of the LUMO energy levels. When $P3HT_{240}-b-P(DTS-DPP)_{11}$ was used, the EQE maximum at 500 nm was slightly higher (35%) and the photogeneration of charges from 700 to 900 nm was slightly shifted to the near-IR region with an EQE of 12%.

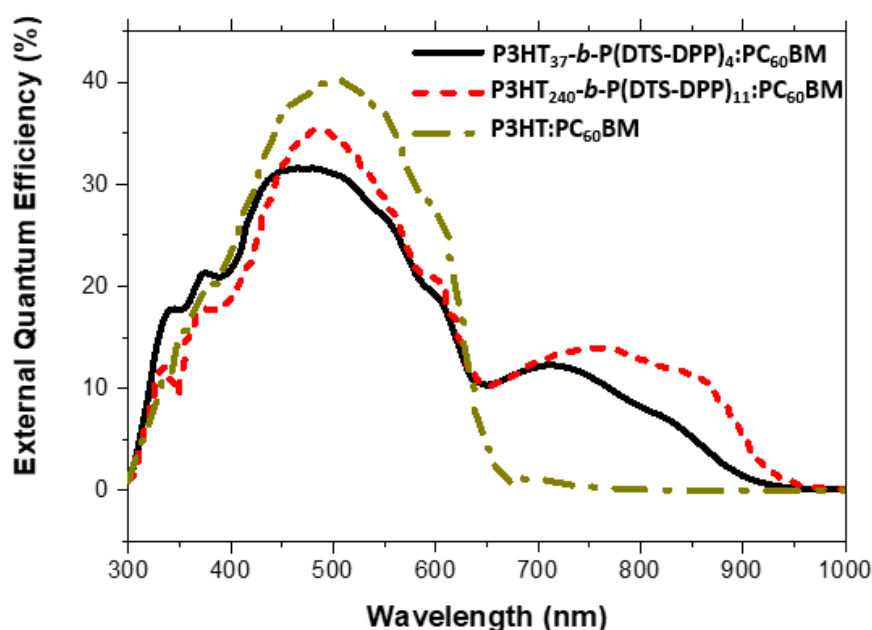


Figure III-33: EQE spectra of $P3HT_n-b-P(DTS-DPP)_m:PC_{60}BM$ and $P3HT:PC_{60}BM$ -based solar cells in *o*-xylene.

AFM of P3HT:PC₆₀BM (annealed at 120 °C) and P3HT₂₄₀-*b*-P(DTS-DPP)₁₁:PC₆₀BM (annealed at 150 °C) films were performed and compared to those of P3HT₃₇-*b*-P(DTS-DPP)₄:PC₆₀BM (annealed at 120 °C). This comparison was conducted to understand the variation in V_{OC} and the decrease in EQE at 500 nm when the diblock copolymers were used compared to P3HT homopolymer. As observed in **Figure III-34a** and **b**, the surface morphology of P3HT:PC₆₀BM revealed ordered fibrillar crystalline domains of P3HT (Rq of 3 nm), unlike the finer nodular morphology obtained for P3HT₃₇-*b*-P(DTS-DPP)₄ (**Figure III-34c** and **d**) in which the fibrils were much smaller. These structural changes were also observed in pure polymer films (*i.e.* with no PC₆₀BM). For P3HT₂₄₀-*b*-P(DTS-DPP)₁₁:PC₆₀BM films, slight fibrillar structures attributed to P3HT domains (Rq of 0.95 nm) were observed (**Figure III-34e** and **f**). Thus, the high molar mass of P3HT and P3HT₂₄₀-*b*-P(DTS-DPP)₁₁, results in a fibrillar nanomorphology which improves V_{OC} when compared to P3HT₃₇-*b*-P(DTS-DPP)₄:PC₆₀BM.¹⁰² However, the larger clusters observed for P3HT₂₄₀-*b*-P(DTS-DPP)₁₁ can lead to geminate recombination which could be beyond the decrease in EQE at 500 nm. On the other hand, the nodular morphology and the intermixed organization of P3HT₃₇-*b*-P(DTS-DPP)₄:PC₆₀BM could lead to an increase of non-geminate recombination as collection pathways are missing. This can also explain the drop of V_{OC} and the lower EQE value at 500 nm for this diblock copolymer.¹⁰⁷

In general, it has already been observed in previous studies that rod-*b*-rod block copolymers linked by a rigid unit, like thiophene in our case, could lead to a disruption of the crystallization of the individual blocks.^{70,108} Moreover, in the case of P3HT, high charge mobility is obtained when the crystallinity is strong.¹⁰⁷ Therefore, in both copolymer systems, what is won with the photons absorbed in the 700 to 900 nm region and converted into electrons is lost with the copolymer structuration which lowers the number of charges collected at the electrodes.

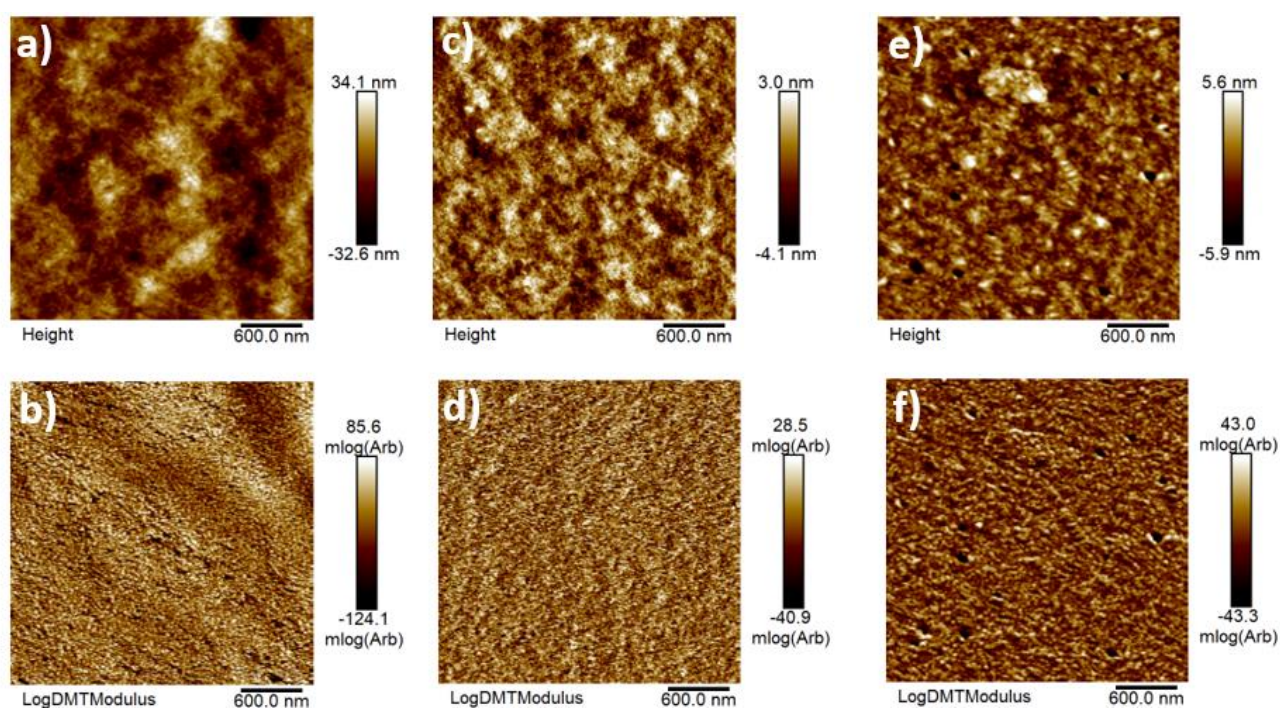


Figure III-34: AFM images of (a,b) P3HT:PC₆₀BM, (c,d) P3HT₃₇-*b*-P(DTS-DPP)₄:PC₆₀BM and (e,f) P3HT₂₄₀-*b*-P(DTS-DPP)₁₁:PC₆₀BM active layers deposited from *o*-xylene.

c. Device performances using DAP-based block copolymers

i. P3HT₃₇-b-P(DTS-DAP)₄

After achieving promising results using synthesized DPP-based polymers, it was interesting to study the behavior of DAP-based polymers in inverted device structures. Based on the previously discussed conditions, P3HT₃₇-b-P(DTS-DAP)₄ was blended with PC₆₀BM acceptor in chlorobenzene at 1:1 weight ratio. The 130 nm-thick photoactive layers were pre-annealed at 120 °C to yield an efficiency of 1.16%. A slightly higher efficiency was obtained (1.20%) when the photoactive blends were processed in the presence of 3 vol% acetophenone. This increase in PCE was attributed to a slight increase in FF to 0.49, which could be due to better blend morphology. The photovoltaic parameters of the fabricated devices are summarized in **Table III-8** and the corresponding J-V curves are plotted in **Figure III-35a**.

Table III-8: Photovoltaic parameters of P3HT₃₇-b-P(DTS-DAP)₄:PC₆₀BM-based devices processed with and without additives.

Additives	FF	V _{OC} (V)	J _{SC} (mA/cm ²)	PCE (%)
w/o	0.42	0.46	6.01	1.16
Acetophenone	0.49	0.45	5.43	1.2

Although both devices showed only slight difference in J_{SC} values, large difference in EQE percentage was observed (**Figure III-35b**). This could be attributed to the lower air stability of the DAP-based copolymers as EQE measurements have been conducted outside the glovebox. In general, EQE spectrum corresponds to the relative absorption of the photoactive layer as shown in the same figure in which two distinct bands were observed, one corresponding to P3HT block (400 to 660 nm) and another attributed to the low-bandgap block, P(DTS-DAP) absorbing between 660 to 1000 nm. But the common feature observed in the EQE of both cases is the low contribution of the low-bandgap block. Thus, the charge dissociation at P(DTS-DAP):PC₆₀BM interface was weak, lowering device performance.

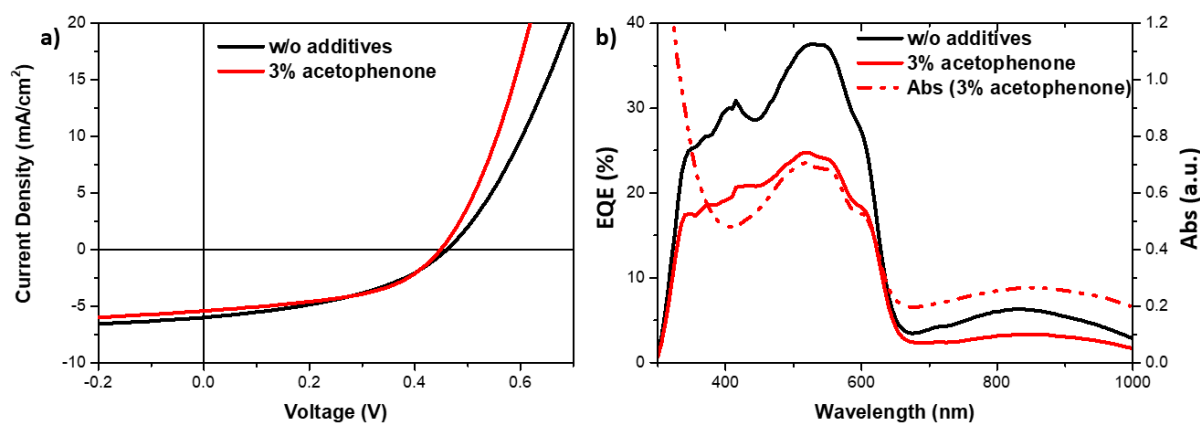


Figure III-35: (a) J-V curves and (b) EQE of P3HT₃₇-b-P(DTS-DAP)₄:PC₆₀BM-based devices processed with and without additives.

Although under the same processing conditions, P3HT₃₇-b-P(DTS-DAP)₄:PC₆₀BM-based devices showed slightly lower device performances (1.2%) than P3HT₃₇-b-P(DTS-DPP)₄:PC₆₀BM-based devices (1.38%), DAP-based photoactive blends were not optimized in terms of solvent (o-xylene) and P3HT molar mass.

ii. P3HT₃₇-b-P(DTS-DAP)₁₁

To check whether higher molecular weight of the low-bandgap block has the same effect on DAP-based polymers as DPP-based polymers, P3HT₃₇-b-P(DTS-DAP)₁₁ was tested in solar devices. The block copolymer was blended with PC₆₀BM in chlorobenzene with a 1:1 weight ratio. As before, the photoactive layers (130 nm-thick) were pre-annealed at 120 °C for 10 min. The fabricated devices showed lower PCE (0.39%) than those based on P3HT₃₇-b-P(DTS-DAP)₄ with V_{OC} of 0.4 V and very low J_{SC} value (3.5 mA/cm²). Additionally, the low FF (0.28) was accompanied with low shunt resistance and high series resistance as can be seen from the J-V curve of **Figure III-36a**.

The absorption spectrum of the photoactive layer, shown in **Figure III-36b**, revealed two distinct bands, one attributed to the P3HT block (400 to 600 nm) and a second broad one with a higher intensity attributed to the low-bandgap block P(DTS-DAP) (600 to 1000 nm). This absorption agrees with the polymer's absorption in solution.

Although in DSC analysis shown in **Chapter II**, it was possible to detect the melting and crystallization behavior of this block, the vibronic peaks attributed to the π - π interchain interactions characterizing the crystallization of the P3HT polymer were not observed. Thus, the crystallinity of P3HT in the block copolymer could be prohibited by the high volume of P(DTS-DAP), thus affecting the charge transport and collection.¹⁵ This contributes to the drop in efficiency. It is worth mentioning that the same efficiency losses were observed after increasing the length of the P(DTS-DPP) block. EQE measurements revealed low charge collection in the range of absorption of P3HT block with a maximum value of 9% and a slight contribution from the low-bandgap block (3%).

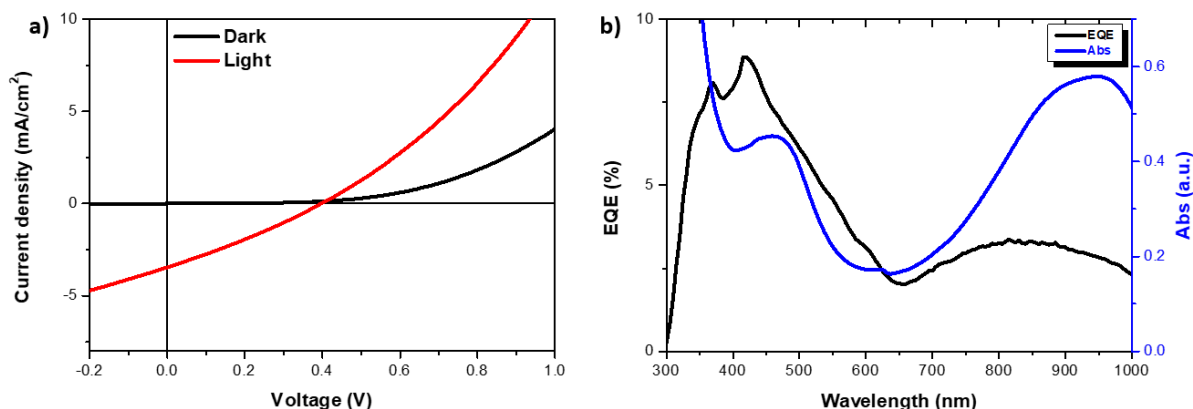


Figure III-36: (a) J-V curves and (b) EQE of P3HT₃₇-b-P(DTS-DAP)₁₁:PC₆₀BM-based devices with the absorption spectrum of the corresponding photoactive layer.

Besides the non-optimization, the low performances obtained using the DAP-based block copolymers could be due to the incorporation of PC₆₀BM which is probably not a suitable acceptor for DAP given their HOMO-LUMO levels.

VI. Conclusion

Synthesized block copolymers constituted of P3HT block and a low-bandgap block P(DTS-DPP) or P(DTS-DAP) in a donor-acceptor strategy showed promising absorption in the near-IR region. Although the energy levels of the two blocks calculated from cyclic voltammetry could mean a donor-acceptor behavior, single component active layer solar cells presented very poor performances. Instead, the addition of PC₆₀BM as an electron acceptor in the blend enhanced device efficiencies. To further optimize the device performance, active blends were prepared in *o*-xylene. Additionally, the photoactive layers were pre-annealed to improve the morphology.

In general, DPP-based block copolymers showed enhanced power conversion efficiencies when compared to DAP-based ones. However, the performances of these solar cells made from the copolymers were block composition dependent. In fact, long block of P(DTS-DPP) or P(DTS-DAP) impeded the crystallization of P3HT and lowered the short circuit current.

For DPP-based copolymers, the best devices were obtained with the copolymer presenting the highest molar mass (P3HT₂₄₀-*b*-P(DTS-DPP)₁₁) in which the morphology was optimized by the choice of *o*-xylene solvent and pre-thermal annealing at 150 °C. The highest PCE achieved was around 2%. In the fabricated solar cells, both P3HT and the low-bandgap block contributed to the charge collection mechanism extended in the absorption range as revealed by EQE measurements. When P3HT:PC₆₀BM-based devices were processed under the same optimized conditions, similar power conversion efficiencies were obtained. Interestingly, we could recognize that with P3HT₂₄₀-*b*-P(DTS-DPP)₁₁-based devices, a V_{OC} close to that of P3HT:PC₆₀BM-based ones can be reached. This could be related to the higher P3HT chain length in P3HT₂₄₀-*b*-P(DTS-DPP)₁₁ which is in the range of P3HT.

Regarding DAP-based copolymers, the highest PCE obtained was for P3HT₃₇-*b*-P(DTS-DAP)₄:PC₆₀BM-based devices processed in chlorobenzene (1.2%). For this, future work could be done for optimizing DAP-based solar cells by using *o*-xylene solvent which leads to better blend morphology, by increasing the molar mass of the P3HT block in the diblock copolymer and by using an acceptor with a lower LUMO than PC₆₀BM.

References

- (1) Shahzad, U. The Need For Renewable Energy Sources.
- (2) Lüthi, D.; Le Floch, M.; Bereiter, B.; Blunier, T.; Barnola, J.-M.; Siegenthaler, U.; Raynaud, D.; Jouzel, J.; Fischer, H.; Kawamura, K.; Stocker, T. F. High-Resolution Carbon Dioxide Concentration Record 650,000–800,000 Years before Present. *Nature* **2008**, *453* (7193), 379–382.
- (3) McMichael, A.; Woodruff, R. Climate Change and Risk to Health. *BMJ* **2004**, *329* (7480), 1416–1417.
- (4) IRENA – International Renewable Energy Agency.
- (5) U.S. Energy Information Administration (EIA) - Environment <https://www.eia.gov/environment>.
- (6) Kim, H.; Nam, S.; Jeong, J.; Lee, S.; Seo, J.; Han, H.; Kim, Y. Organic Solar Cells Based on Conjugated Polymers : History and Recent Advances. *Korean J. Chem. Eng.* **2014**, *31* (7), 1095–1104.
- (7) Scharber, M. C.; Sariciftci, N. S. Efficiency of Bulk-Heterojunction Organic Solar Cells. *Prog. Polym. Sci.* **2013**, *38* (12), 1929–1940.
- (8) Hösel, M.; Angmo, D.; Krebs, F. C. 17 - Organic Solar Cells (OSCs). In *Handbook of Organic Materials for Optical and (Opto)electronic Devices*; Ostroverkhova, O., Ed.; Woodhead Publishing Series in Electronic and Optical Materials; Woodhead Publishing, 2013; pp 473–507.
- (9) Liu, Q.; Jiang, Y.; Jin, K.; Qin, J.; Xu, J.; Li, W.; Xiong, J.; Liu, J.; Xiao, Z.; Sun, K.; Yang, S.; Zhang, X.; Ding, L. 18% Efficiency Organic Solar Cells. *Sci. Bull.* **2020**, *65* (4), 272–275.
- (10) Landerer, D.; Mertens, A.; Freis, D.; Droll, R.; Leonhard, T.; Schulz, A. D.; Bahro, D.; Colmann, A. Enhanced Thermal Stability of Organic Solar Cells Comprising Ternary D-D-A Bulk-Heterojunctions. *Npj Flex. Electron.* **2017**, *1* (1).
- (11) Po, R.; Carbonera, C.; Bernardi, A.; Camaioni, N. The Role of Buffer Layers in Polymer Solar Cells. *Energy Environ. Sci.* **2011**, *4* (2), 285–310.
- (12) You, H.; Dai, L.; Zhang, Q.; Chen, D.; Jiang, Q.; Zhang, C. Enhanced Performance of Inverted Non-Fullerene Organic Solar Cells by Using Metal Oxide Electron- and Hole-Selective Layers with Process Temperature ≤ 150 °C. *Polymers* **2018**, *10* (7), 725.
- (13) Zhang, F. J.; Zhao, D. W.; Zhuo, Z. L.; Wang, H.; Xu, Z.; Wang, Y. S. Inverted Small Molecule Organic Solar Cells with Ca Modified ITO as Cathode and MoO₃ Modified Ag as Anode. *Sol. Energy Mater. Sol. Cells* **2010**, *94* (12), 2416–2421.
- (14) Cao, W.; Xue, J. Recent Progress in Organic Photovoltaics: Device Architecture and Optical Design. *Energy Environ. Sci.* **2014**, *7* (7), 2123
- (15) Kouijzer, S.; Michels, J. J.; van den Berg, M.; Gevaerts, V. S.; Turbiez, M.; Wienk, M. M.; Janssen, R. A. J. Predicting Morphologies of Solution Processed Polymer:Fullerene Blends. *J. Am. Chem. Soc.* **2013**, *135* (32), 12057–12067.
- (16) Sauv e, G.; Fernando, R. Beyond Fullerenes: Designing Alternative Molecular Electron Acceptors for Solution-Processable Bulk Heterojunction Organic Photovoltaics. *J. Phys. Chem. Lett.* **2015**, *6* (18), 3770–3780.
- (17) Bi, S.; Ouyang, Z.; Shaik, S.; Li, D. Effect of Donor-Acceptor Vertical Composition Profile on Performance of Organic Bulk Heterojunction Solar Cells. *Sci. Rep.* **2018**, *8* (1), 9574.
- (18) Ma, W.; Yang, C.; Gong, X.; Lee, K.; Heeger, A. J. Thermally Stable, Efficient Polymer Solar Cells with Nanoscale Control of the Interpenetrating Network Morphology. *Adv. Funct. Mater.* **2005**, *15* (10), 1617–1622.
- (19) Li, G.; Shrotriya, V.; Huang, J.; Yao, Y.; Moriarty, T.; Emery, K.; Yang, Y. High-Efficiency Solution Processable Polymer Photovoltaic Cells by Self-Organization of Polymer Blends. *Nat. Mater.* **2005**, *4* (11), 864.
- (20) Dkhil, S. B.; Pfannm ller, M.; Saba, M. I.; Gaceur, M.; Heidari, H.; Videlot-Ackermann, C.; Margeat, O.; Guerrero, A.; Bisquert, J.; Garcia-Belmonte, G.; Mattoni, A.; Bals, S.; Ackermann, J. Toward High-Temperature Stability of PTB7-Based Bulk Heterojunction Solar Cells: Impact of Fullerene Size and Solvent Additive. *Adv. Energy Mater.* **2017**, *7* (4), 1601486.
- (21) Heo, S. W.; Kim, S. H.; Lee, E. J.; Moon, D. K. Enhanced Performance in Bulk Heterojunction Solar Cells by Introducing Naphthalene Derivatives as Processing Additives. *Sol. Energy Mater. Sol. Cells* **2013**, *111*, 16–22.
- (22) Tessarolo, M.; Guerrero, A.; Gedefaw, D.; Bolognesi, M.; Prosa, M.; Xu, X.; Mansour, M.; Wang, E.; Seri, M.; Andersson, M. R.; Muccini, M.; Garcia-Belmonte, G. Predicting Thermal Stability of Organic Solar Cells through an Easy and Fast Capacitance Measurement. *Sol. Energy Mater. Sol. Cells* **2015**, *141*, 240–247.
- (23) Tada, K. Thermally Robust Bulk Heterojunction Photocells Based on PTB7:C70 Composites. *Sol. Energy Mater. Sol. Cells* **2015**, *132*, 15–20.
- (24) Pettersson, L. A. A.; Roman, L. S.; Ingan s, O. Modeling Photocurrent Action Spectra of Photovoltaic Devices Based on Organic Thin Films. *J. Appl. Phys.* **1999**, *86* (1), 487–496.

- (25) Zhuang, T.; Wang, X.-F.; Sano, T.; Hong, Z.; Yang, Y.; Kido, J. Fullerene Derivatives as Electron Donor for Organic Photovoltaic Cells. *Appl. Phys. Lett.* **2013**, *103* (20), 203301.
- (26) Chiechi, R. C.; Havenith, R. W. A.; Hummelen, J. C.; Koster, L. J. A.; Loi, M. A. Modern Plastic Solar Cells: Materials, Mechanisms and Modeling. *Mater. Today* **2013**, *16* (7–8), 281–289.
- (27) V. K. A. Organic solar cells: principles, mechanism and recent developments. *Int. J. Res. Eng. Technol.* **2014**, *03* (09), 338–341.
- (28) Qi, B.; Wang, J. Fill Factor in Organic Solar Cells. *Phys. Chem. Chem. Phys.* **2013**, *15* (23), 8972–8982.
- (29) Brabec, C. J. Organic Photovoltaics: Technology and Market. *Sol. Energy Mater. Sol. Cells* **2004**, *83* (2), 273–292.
- (30) Thakur, A. K.; Wantz, G.; Garcia-Belmonte, G.; Bisquert, J.; Hirsch, L. Temperature Dependence of Open-Circuit Voltage and Recombination Processes in Polymer-Fullerene Based Solar Cells. *Sol. Energy Mater. Sol. Cells* **2011**, *95* (8), 2131–2135.
- (31) Elumalai, N. K.; Uddin, A. Open Circuit Voltage of Organic Solar Cells: An in-Depth Review. *Energy Environ. Sci.* **2016**, *9* (2), 391–410.
- (32) Ananda, W. External Quantum Efficiency Measurement of Solar Cell; 2017; pp 450–456.
- (33) Yu, G.; Gao, J.; Hummelen, J. C.; Wudl, F.; Heeger, A. J. Polymer Photovoltaic Cells: Enhanced Efficiencies via a Network of Internal Donor–Acceptor Heterojunctions. *Science* **1995**, 1789–1791.
- (34) Soylu, M. GaAs Heterojunction Devices with MDMO-PPV Thin Films. *Vacuum* **2014**, *106*, 33–38.
- (35) Lee, S.-H.; Kim, J.-H.; Shim, T.-H.; Park, J.-G. Effect of Interface Thickness on Power Conversion Efficiency of Polymer Photovoltaic Cells. *Electron. Mater. Lett.* **2009**, *5* (1), 47–50.
- (36) Dang, M. T.; Hirsch, L.; Wantz, G.; Wuest, J. D. Controlling the Morphology and Performance of Bulk Heterojunctions in Solar Cells. Lessons Learned from the Benchmark Poly(3-Hexylthiophene):[6,6]-Phenyl-C61-Butyric Acid Methyl Ester System. *Chem. Rev.* **2013**, *113* (5), 3734–3765.
- (37) Padinger, F.; Rittberger, R. S.; Sariciftci, N. S. Effects of Postproduction Treatment on Plastic Solar Cells. *Adv. Funct. Mater.* **2003**, *13* (1), 85–88.
- (38) Kim, Y.; Cook, S.; Tuladhar, S. M.; Choulis, S. A.; Nelson, J.; Durrant, J. R.; Bradley, D. D. C.; Giles, M.; McCulloch, I.; Ha, C.-S.; Ree, M. A Strong Regioregularity Effect in Self-Organizing Conjugated Polymer Films and High-Efficiency Polythiophene: Fullerene Solar Cells. In *Materials for Sustainable Energy*; Co-Published with Macmillan Publishers Ltd, UK, 2010; pp 63–69.
- (39) Savagatrup, S.; Printz, A. D.; O'Connor, T. F.; Zaretski, A. V.; Rodriguez, D.; Sawyer, E. J.; Rajan, K. M.; Acosta, R. I.; Root, S. E.; Lipomi, D. J. Mechanical Degradation and Stability of Organic Solar Cells: Molecular and Microstructural Determinants. *Energy Environ. Sci.* **2014**, *8* (1), 55–80.
- (40) Şahin, Y.; Alem, S.; de Bettignies, R.; Nunzi, J.-M. Development of Air Stable Polymer Solar Cells Using an Inverted Gold on Top Anode Structure. *Thin Solid Films* **2005**, *476* (2), 340–343.
- (41) Hau, S. K.; Yip, H.-L.; Baek, N. S.; Zou, J.; O'Malley, K.; Jen, A. K.-Y. Air-Stable Inverted Flexible Polymer Solar Cells Using Zinc Oxide Nanoparticles as an Electron Selective Layer. *Appl. Phys. Lett.* **2008**, *92* (25), 253301.
- (42) Cui, Y.; Yao, H.; Zhang, J.; Zhang, T.; Wang, Y.; Hong, L.; Xian, K.; Xu, B.; Zhang, S.; Peng, J.; Wei, Z.; Gao, F.; Hou, J. Over 16% Efficiency Organic Photovoltaic Cells Enabled by a Chlorinated Acceptor with Increased Open-Circuit Voltages. *Nat. Commun.* **2019**, *10*.
- (43) Liu, G.; Jia, J.; Zhang, K.; Jia, X.; Yin, Q.; Zhong, W.; Li, L.; Huang, F.; Cao, Y. 15% Efficiency Tandem Organic Solar Cell Based on a Novel Highly Efficient Wide-Bandgap Nonfullerene Acceptor with Low Energy Loss. *Adv. Energy Mater.* **2019**, *9* (11), 1803657.
- (44) Cheng, P.; Li, G.; Zhan, X.; Yang, Y. Next-Generation Organic Photovoltaics Based on Non-Fullerene Acceptors. *Nat. Photonics* **2018**, *12* (3), 131–142.
- (45) He, Y.; Li, Y. Fullerene Derivative Acceptors for High Performance Polymer Solar Cells. *Phys Chem Chem Phys* **2011**, *13* (6), 1970–1983.
- (46) Jørgensen, M.; Norrman, K.; Gevorgyan, S. A.; Tromholt, T.; Andreasen, B.; Krebs, F. C. Stability of Polymer Solar Cells. *Adv. Mater.* **2012**, *24* (5), 580–612.
- (47) Yan, C.; Barlow, S.; Wang, Z.; Yan, H.; Jen, A. K.-Y.; Marder, S. R.; Zhan, X. Non-Fullerene Acceptors for Organic Solar Cells. *Nat. Rev. Mater.* **2018**, *3*, 18003.
- (48) Khan, J. I.; Ashraf, R. S.; Alamoudi, M. A.; Nabi, M. N.; Mohammed, H. N.; Wadsworth, A.; Firdaus, Y.; Zhang, W.; Anthopoulos, T. D.; McCulloch, I.; Laquai, F. P3HT Molecular Weight Determines the Performance of P3HT:O-IDTBR Solar Cells. *Sol. RRL* **2019**, *3* (8), 1900023.
- (49) Strohm, S.; Machui, F.; Langner, S.; Kubis, P.; Gasparini, N.; Salvador, M.; McCulloch, I.; Egelhaaf, H.-J.; Brabec, C. J. P3HT: Non-Fullerene Acceptor Based Large Area, Semi-Transparent PV Modules with Power Conversion Efficiencies of 5%, Processed by Industrially Scalable Methods. *Energy Environ. Sci.* **2018**, *11* (8), 2225–2234.
- (50) Yang, C.; Zhang, S.; Ren, J.; Gao, M.; Bi, P.; Ye, L.; Hou, J. Molecular Design of a Non-Fullerene Acceptor Enables a P3HT-Based Organic Solar Cell with 9.46% Efficiency. *Energy Environ. Sci.* **2020**.

- (51) Feng, K.; Yuan, J.; Bi, Z.; Ma, W.; Xu, X.; Zhang, G.; Peng, Q. Low-Energy-Loss Polymer Solar Cells with 14.52% Efficiency Enabled by Wide-Band-Gap Copolymers. *iScience* **2019**, *12*, 1–12.
- (52) Dkhil, S. B.; Pfannmöller, M.; Bals, S.; Koganezawa, T.; Yoshimoto, N.; Hannani, D.; Gaceur, M.; Videlot-Ackermann, C.; Margeat, O.; Ackermann, J. Square-Centimeter-Sized High-Efficiency Polymer Solar Cells: How the Processing Atmosphere and Film Quality Influence Performance at Large Scale. *Adv. Energy Mater.* **2016**, *6* (13), 1600290.
- (53) Li, M.; Ni, W.; Kan, B.; Wan, X.; Zhang, L.; Zhang, Q.; Long, G.; Zuo, Y.; Chen, Y. Graphene Quantum Dots as the Hole Transport Layer Material for High-Performance Organic Solar Cells. *Phys. Chem. Chem. Phys.* **2013**, *15* (43), 18973–18978.
- (54) Chueh, C.-C.; Li, C.-Z.; Jen, A. K.-Y. Recent Progress and Perspective in Solution-Processed Interfacial Materials for Efficient and Stable Polymer and Organometal Perovskite Solar Cells. *Energy Environ. Sci.* **2015**, *8* (4), 1160–1189.
- (55) Khodabakhsh, S.; Sanderson, B. M.; Nelson, J.; Jones, T. S. Using Self-Assembling Dipole Molecules to Improve Charge Collection in Molecular Solar Cells. *Adv. Funct. Mater.* **2006**, *16* (1), 95–100.
- (56) Arias, A. C.; Granström, M.; Thomas, D. S.; Petritsch, K.; Friend, R. H. Doped Conducting-Polymer--Semiconducting-Polymer Interfaces: Their Use in Organic Photovoltaic Devices. *Phys. Rev. B* **1999**, *60* (3), 1854–1860.
- (57) Awada, H.; Mattana, G.; Tournebize, A.; Rodriguez, L.; Flahaut, D.; Vellutini, L.; Lartigau-Dagron, C.; Billon, L.; Bousquet, A.; Chambon, S. Surface Engineering of ITO Electrode with a Functional Polymer for PEDOT:PSS-Free Organic Solar Cells. *Org. Electron.* **2018**, *57*, 186–193.
- (58) Kyaw, A. K. K.; Sun, X. W.; Jiang, C. Y.; Lo, G. Q.; Zhao, D. W.; Kwong, D. L. An Inverted Organic Solar Cell Employing a Sol-Gel Derived ZnO Electron Selective Layer and Thermal Evaporated MoO₃ Hole Selective Layer. *Appl. Phys. Lett.* **2008**, *93* (22), 221107.
- (59) Yin, Z.; Wei, J.; Zheng, Q. Interfacial Materials for Organic Solar Cells: Recent Advances and Perspectives. *Adv. Sci.* **2016**, *3* (8), 1500362.
- (60) Soci, C.; Hwang, I.-W.; Moses, D.; Zhu, Z.; Waller, D.; Gaudiana, R.; Brabec, C. J.; Heeger, A. J. Photoconductivity of a Low-Bandgap Conjugated Polymer. *Adv. Funct. Mater.* **2007**, *17* (4), 632–636.
- (61) Sharma, G. D.; Reddy, M. A.; Ramana, D. V.; Chandrasekharam, M. A Novel Carbazole-Phenothiazine Dyad Small Molecule as a Non-Fullerene Electron Acceptor for Polymer Bulk Heterojunction Solar Cells. *RSC Adv.* **2014**, *4* (63), 33279–33285.
- (62) Grimsdale, A. C.; Leok Chan, K.; Martin, R. E.; Jokisz, P. G.; Holmes, A. B. Synthesis of Light-Emitting Conjugated Polymers for Applications in Electroluminescent Devices. *Chem. Rev.* **2009**, *109* (3), 897–1091.
- (63) Gibson, G. L.; McCormick, T. M.; Seferos, D. S. Atomistic Band Gap Engineering in Donor-Acceptor Polymers. *J. Am. Chem. Soc.* **2012**, *134* (1), 539–547.
- (64) Mori, H.; Nonobe, H.; Nishihara, Y. Highly Crystalline, Low Band-Gap Semiconducting Polymers Based on Phenanthrothiophene-Benzothiadiazole for Solar Cells and Transistors. *Polym. Chem.* **2016**, *7* (8), 1549–1558.
- (65) Agneeswari, R.; Kong, M.; Lee, J.; Tamilavan, V.; Lee, W.-K.; Park, S. H.; Jin, Y. Visible to Near-Infrared-Absorbing Polymers Containing Bithiazole and 2,3-Didodecyl-6,7-Difluoroquinoxaline Derivatives for Polymer Solar Cells. *Bull. Korean Chem. Soc.* **2019**, *40* (7), 686–690.
- (66) Heo, S.; Song, K.; Choi, M. H.; Oh, H.; Moon, D. Influence of Alkanediol Series as Processing Additives in Photo-Active Layer on the Power Conversion Efficiency of Polymer Solar Cells. *Sol. Energy Mater. Sol. Cells* **2013**, *114*, 82–88.
- (67) Lee, E. J.; Choi, M. H.; Moon, D. K. Enhanced Photovoltaic Properties of Bulk Heterojunction Organic Photovoltaic Devices by an Addition of a Low Band Gap Conjugated Polymer. *Materials* **2016**, *9* (12), 996.
- (68) Stübinger, T.; Brütting, W. Exciton Diffusion and Optical Interference in Organic Donor-Acceptor Photovoltaic Cells. *J. Appl. Phys.* **2001**, *90* (7), 3632–3641.
- (69) Mok, J. W.; Lin, Y.-H.; Yager, K. G.; Mohite, A. D.; Nie, W.; Darling, S. B.; Lee, Y.; Gomez, E.; Gosztola, D.; Schaller, R. D.; Verduzco, R. Linking Group Influences Charge Separation and Recombination in All-Conjugated Block Copolymer Photovoltaics. *Adv. Funct. Mater.* **2015**, *25* (35), 5578–5585.
- (70) Nikiforov, M. P.; Lai, B.; Chen, W.; Chen, S.; Schaller, R. D.; Strzalka, J.; Maser, J.; Darling, S. B. Detection and Role of Trace Impurities in High-Performance Organic Solar Cells. *Energy Environ. Sci.* **2013**, *6* (5), 1513–1520.
- (71) Qian, G.; Qi, J.; Wang, Z. Y. Synthesis and Study of Low-Bandgap Polymers Containing the Diazapentalene and Diketopyrrolopyrrole Chromophores for Potential Use in Solar Cells and near-Infrared Photodetectors. *J. Mater. Chem.* **2012**, *22* (25), 12867–12873.

- (72) Anagnostou, K.; Stylianakis, M. M.; Petridis, K.; Kymakis, E. Building an Organic Solar Cell: Fundamental Procedures for Device Fabrication. *Energies* **2019**, *12* (11), 2188.
- (73) Li, P.; Cai, L.; Wang, G.; Zhou, D. C.; Xiang, J.; Zhang, Y. J.; Ding, B. F.; Alameh, K.; Song, Q. L. PEIE Capped ZnO as Cathode Buffer Layer with Enhanced Charge Transfer Ability for High Efficiency Polymer Solar Cells. *Synth. Met.* **2015**, *203*, 243–248.
- (74) Woo, S.; Kim, W. H.; Kim, H.; Yi, Y.; Lyu, H.-K.; Kim, Y. 8.9% Single-Stack Inverted Polymer Solar Cells with Electron-Rich Polymer Nanolayer-Modified Inorganic Electron-Collecting Buffer Layers. *Adv. Energy Mater.* **2014**, *4* (7), 1301692.
- (75) Zang, Y.; Huang, J.; Li, H.; Yu, J.; Jiang, Y. Effect of Molybdenum Oxide Anode Buffer Layer on the Performance of Inverted Small Molecular Organic Solar Cells. *Energy Procedia* **2011**, *12*, 513–518.
- (76) Zhao, G.; He, Y.; Xu, Z.; Hou, J.; Zhang, M.; Min, J.; Chen, H.-Y.; Ye, M.; Hong, Z.; Yang, Y.; Li, Y. Effect of Carbon Chain Length in the Substituent of PCBM-like Molecules on Their Photovoltaic Properties. *Adv. Funct. Mater.* **2010**, *20* (9), 1480–1487.
- (77) Alfassi, Z. General aspects of the chemistry of radicals, **1999**.
- (78) Choy, W. C. H. *Organic Solar Cells: Materials and Device Physics*; Springer Science & Business Media, 2012.
- (79) Vandewal, K.; Himmelberger, S.; Salleo, A. Structural Factors That Affect the Performance of Organic Bulk Heterojunction Solar Cells. *Macromolecules* **2013**, *46* (16), 6379–6387.
- (80) Chirvase, D.; Parisi, J.; Hummelen, J. C.; Dyakonov, V. Influence of Nanomorphology on the Photovoltaic Action of Polymer–Fullerene Composites. *Nanotechnology* **2004**, *15* (9), 1317–1323.
- (81) Da Pian, M.; Maggini, M.; Vancso, G. J.; Causin, V.; Benetti, E. M. Assembly of Poly-3-(Hexylthiophene) Nanocrystals in Marginal Solvent: The Role of PCBM. *Eur. Polym. J.* **2018**, *109*, 222–228.
- (82) Singh, I. Effect of Thermal Annealing on the Efficiency of Poly (3-Hexylthiophene):[6,6]-Phenyl-C₆₁-Butyric Acid Methyl Ester Bulk Heterojunction Solar Cells. *J. Nanophotonics* **2011**, *5* (1), 053504.
- (83) Wadsworth, A.; Hamid, Z.; Bidwell, M.; Ashraf, R. S.; Khan, J. I.; Anjum, D. H.; Cendra, C.; Yan, J.; Rezasoltani, E.; Guilbert, A. A. Y.; Azzouzi, M.; Gasparini, N.; Bannock, J. H.; Baran, D.; Wu, H.; Mello, J. C. de; Brabec, C. J.; Salleo, A.; Nelson, J.; Laquai, F.; McCulloch, I. Progress in Poly (3-Hexylthiophene) Organic Solar Cells and the Influence of Its Molecular Weight on Device Performance. *Adv. Energy Mater.* **2018**, *8* (28), 1801001.
- (84) Hiorns, R. C.; de Bettignies, R.; Leroy, J.; Bailly, S.; Firon, M.; Sentein, C.; Khoukh, A.; Preud'homme, H.; Dagron-Lartigau, C. High Molecular Weights, Polydispersities, and Annealing Temperatures in the Optimization of Bulk-Heterojunction Photovoltaic Cells Based on Poly(3-Hexylthiophene) or Poly(3-Butylthiophene). *Adv. Funct. Mater.* **2006**, *16* (17), 2263–2273.
- (85) Lu, Y.; Wang, Y.; Feng, Z.; Ning, Y.; Liu, X.; Lü, Y.; Hou, Y. Temperature-Dependent Morphology Evolution of P3HT:PCBM Blend Solar Cells during Annealing Processes. *Synth. Met.* **2012**, *162* (23), 2039–2046.
- (86) Jo, J.; Kim, S.-S.; Na, S.-I.; Yu, B.-K.; Kim, D.-Y. Time-Dependent Morphology Evolution by Annealing Processes on Polymer:Fullerene Blend Solar Cells. *Adv. Funct. Mater.* **2009**, *19* (6), 866–874.
- (87) Güney, H. Y.; Avdan, Z.; Yetkin, H. Optimization of Annealing Temperature and the Annealing Effect on Life Time and Stability of P3HT:PCBM-Based Organic Solar Cells. *Mater. Res. Express* **2019**, *6* (4), 045103
- (88) Aloui, W.; Adhikari, T.; Nunzi, J.-M.; Bouazizi, A.; Khirouni, K. Effect of Thermal Annealing on the Electrical Properties of P3HT:PC70BM Nanocomposites. *Mater. Sci. Semicond. Process.* **2015**, *39*, 575–581.
- (89) Gao, H. L.; Zhang, X. W.; Meng, J. H.; Yin, Z. G.; Zhang, L. Q.; Wu, J. L.; Liu, X. Quantitative Characterization of Phase Separation in the Photoactive Layer of Polymer Solar Cells by the Phase Image of Atomic Force Microscopy. *Thin Solid Films* **2015**, *576*, 81–87.
- (90) Miyanishi, S.; Tajima, K.; Hashimoto, K. Morphological Stabilization of Polymer Photovoltaic Cells by Using Cross-Linkable Poly(3-(5-Hexenyl)Thiophene). *Macromolecules* **2009**, *42* (5), 1610–1618.
- (91) Chen, F.-C.; Ko, C.-J.; Wu, J.-L.; Chen, W.-C. Morphological Study of P3HT:PCBM Blend Films Prepared through Solvent Annealing for Solar Cell Applications. *Sol. Energy Mater. Sol. Cells - Sol. ENERG MATER Sol. CELLS* **2010**, *94*, 2426–2430.
- (92) Kadem, B.; Hassan, A. The Effect of Fullerene Derivatives Ratio on P3HT-Based Organic Solar Cells. *Energy Procedia* **2015**, *74*, 439–445.
- (93) Ko Ko Kyaw, A.; Hwan Wang, D.; Tseng, H.-R.; Zhang, J.; Bazan, G. C.; Heeger, A. J. Electron and Hole Mobility in Solution-Processed Small Molecule-Fullerene Blend: Dependence on the Fullerene Content. *Appl. Phys. Lett.* **2013**, *102* (16), 163308.
- (94) Herranz, M. Á.; Illescas, B.; Martín, N.; Luo, C.; Guldi, D. M. Donor/Acceptor Fulleropyrrolidine Triads. *J. Org. Chem.* **2000**, *65* (18), 5728–5738.

- (95) Solanki, A.; Wu, B.; Lam, Y. M.; Sum, T. C. Charge Dynamics in Alkanedithiols-Additives in P3HT:PCBM Bulk Heterojunction Solar Cells; 2014; p 91841W.
- (96) Liu, C.-M.; Su, Y.-W.; Jiang, J.-M.; Chen, H.-C.; Lin, S.-W.; Su, C.-J.; Jeng, U.-S.; Wei, K.-H. Complementary Solvent Additives Tune the Orientation of Polymer Lamellae, Reduce the Sizes of Aggregated Fullerene Domains, and Enhance the Performance of Bulk Heterojunction Solar Cells. *J. Mater. Chem. A* **2014**, 2 (48), 20760–20769.
- (97) Shin, P.-K.; Kumar, P.; Kumar, A.; Kannappan, S.; Ochiai, S. Effects of Organic Solvents for Composite Active Layer of PCDTBT/PC₇₁ BM on Characteristics of Organic Solar Cell Devices. *Int. J. Photoenergy* **2014**, 2014, 1–8.
- (98) Xie, Y.; Dutta, P.; Cengher, D.; Bommisetty, V.; Li, J.; Galipeau, D.; Qiao, Q. Solvent Effect on the Morphology of P3HT/PCBM Films. In *Organic Photovoltaics X*; International Society for Optics and Photonics, 2009; Vol. 7416, p 74161Q.
- (99) Steim, R.; Choulis, S. A.; Schilinsky, P.; Brabec, C. J. Interface Modification for Highly Efficient Organic Photovoltaics. *Appl. Phys. Lett.* **2008**, 92 (9), 093303.
- (100) Gholamkhash, B.; Kiasari, N. M.; Servati, P. An Efficient Inverted Organic Solar Cell with Improved ZnO and Gold Contact Layers. *Org. Electron.* **2012**, 13 (6), 945–953.
- (101) Usluer, Ö.; Abbas, M.; Wantz, G.; Vignau, L.; Hirsch, L.; Grana, E.; Brochon, C.; Cloutet, E.; Hadziioannou, G. Metal Residues in Semiconducting Polymers: Impact on the Performance of Organic Electronic Devices. *ACS Macro Lett.* **2014**, 3 (11), 1134–1138.
- (102) Junle, Y.; Jie, T.; Chao, W.; Yanqiong, Z.; Chihaya, A.; Chenghui, Z. Influence of P3HT Molecular Weight on Film Processing and Solar Cell Performance. In *2018 19th International Conference on Electronic Packaging Technology (ICEPT)*; 2018; pp 1602–1604.
- (103) Mitchell, V. D.; Gann, E.; Huettner, S.; Singh, C. R.; Subbiah, J.; Thomsen, L.; McNeill, C. R.; Thelakkat, M.; Jones, D. J. Morphological and Device Evaluation of an Amphiphilic Block Copolymer for Organic Photovoltaic Applications. *Macromolecules* **2017**, 50 (13), 4942–4951.
- (104) Koppe, M.; Brabec, C. J.; Heiml, S.; Schausberger, A.; Duffy, W.; Heeney, M.; McCulloch, I. Influence of Molecular Weight Distribution on the Gelation of P3HT and Its Impact on the Photovoltaic Performance. *Macromolecules* **2009**, 42 (13), 4661–4666.
- (105) Ballantyne, A. M.; Chen, L.; Dane, J.; Hammant, T.; Braun, F. M.; Heeney, M.; Duffy, W.; McCulloch, I.; Bradley, D. D. C.; Nelson, J. The Effect of Poly(3-Hexylthiophene) Molecular Weight on Charge Transport and the Performance of Polymer:Fullerene Solar Cells. *Adv. Funct. Mater.* **2008**, 18 (16), 2373–2380.
- (106) Wang, S.; Jin, X.; Yao, B.; Du, X.; Dong, L.; Wang, X.; Huang, W. Influence of the Molecular Weight in P3HT Block on Fully Conjugated Block Copolymers. *Synth. Met.* **2019**, 253, 20–25.
- (107) Kline, R. J.; McGehee, M. D.; Kadnikova, E. N.; Liu, J.; Fréchet, J. M. J.; Toney, M. F. Dependence of Regioregular Poly(3-Hexylthiophene) Film Morphology and Field-Effect Mobility on Molecular Weight. *Macromolecules* **2005**, 38 (8), 3312–3319.
- (108) Lee, D. H.; Lee, J. H.; Kim, H. J.; Choi, S.; Park, G. E.; Cho, M. J.; Choi, D. H. (D)_n-σ-(A)_m Type Partially Conjugated Block Copolymer and Its Performance in Single-Component Polymer Solar Cells. *J. Mater. Chem. A* **2017**, 5 (20), 9745–9751.

Chapter IV:
**Elaboration of Self-Assembled
Monolayers as Hole Transport
Materials for Organic Solar
Cells**

I. State of art

a. Hole transporting layers

i. PEDOT:PSS HTLs

For highly efficient organic solar cells, four critical factors shall be carefully considered: (1) light absorption, (2) energy levels, (3) charge mobilities and (4) active layer morphology.¹ Based on these factors, and as previously mentioned, several strategies were applied to increase the efficiency of solar cells such as the usage of low-bandgap polymers² or non-fullerene acceptors.³ The presence of suitable interfacial layers between the active layer and electrodes is also desired since by an adequate work function (WF), they can match the energetic levels of the donor and acceptor materials. This enhances the collection efficiency of holes and electrons to the respective electrodes, which eventually improves device performances. Besides the materials used, the device architecture is also important, normal or inverted, which may affect the final performance and the stability.

For normal-based devices, the main material used as a hole transport layer is poly(3,4-ethylenedioxythiophene)-poly(styrenesulfonate) (PEDOT:PSS).⁴ Its chemical structure is shown in **Figure IV-1**. In fact, PEDOT polymer is doped with PSS to improve both conductivity and dispersion in polar solvent, such as ethanol or water. PEDOT:PSS possesses a range of electrical conductivity that can be changed by the compositional ratio between PEDOT and PSS.⁵

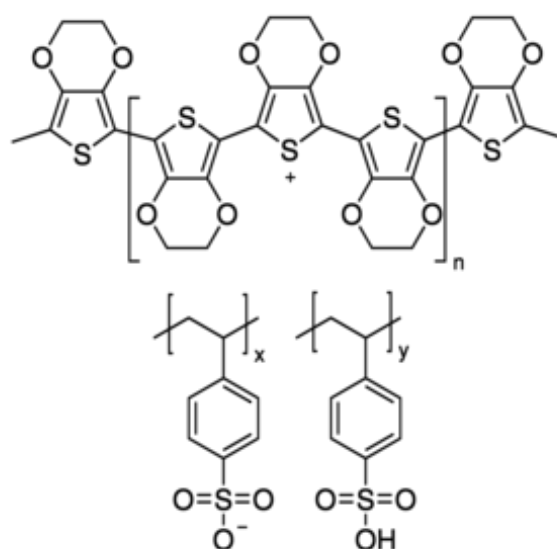


Figure IV-1: The chemical structure of the PEDOT:PSS.

PEDOT:PSS is characterized by a high work function between 4.8 and 5.2 eV. This promotes an ohmic contact with the HOMO levels of the most commonly used donor polymers.⁶

To date, the best efficiency obtained using PEDOT:PSS HTL is 18.2% in a normal device structure based on **D18:Y6 blends**.⁷ Despite these high efficiencies, PEDOT:PSS is hygroscopic and can cause corrosion of the indium tin oxide (ITO) electrode due to its extreme acidity (pH 1-2).⁸ Thus, PEDOT:PSS has an impact on the device degradation and results in poor stability of normal device structures of OSCs.⁹ Additionally, the top metal electrode with a low WF (Ca or Al) can be easily oxidized in air,¹⁰ and during its vacuum evaporation deposition, micropores can be formed causing oxygen and moisture to be diffused into the photoactive layer. This leads to a rapid degradation of the underlying polymer.¹¹ Thus, one of the solutions to circumvent the above problems and improve the stability of OSCs, is the usage of inverted device structures. In this device architecture, the polarity of charge collection is reversed. The ITO acts as the cathode to collect the electrons and the high work function, air-stable metals such as silver (Ag) or gold (Au), are used as the top anode to collect holes, thus eliminating the oxidation problem. The transparent electron conducting layer can be metal oxides, like zinc oxide (ZnO) or titanium oxide (TiO_x), eliminating the problem of the acidic PEDOT:PSS on ITO or FTO.¹² However, to keep on using a normal device structure, a substitution of PEDOT:PSS is needed.

ii. PEDOT:PSS replacement with self-assembled monolayers

ITO is the most commonly used transparent electrode for OSCs. However, in a normal device structure, the WF of this semi-transparent conducting electrode (4.8 eV) is not well-aligned with the HOMO levels of most common donor polymers, thus it cannot form an ohmic contact with them. This mismatch between the electrode WF and the energy level of the donor materials (non-ohmic contact) leads to a drop in V_{OC} .¹³

In order to effectively collect the holes at the electrode and to increase the open-circuit voltage, the contact barrier between the electrode and the active layer must be effectively reduced to form a good ohmic contact. To alleviate these energy barriers, the WF of the anode can be altered by UV-ozone treatment of ITO.¹⁴ This removes the surface carbon atoms and increases the surface oxygen concentration, yielding an increase in the ITO WF.¹⁵ Oxygen plasma can also be used for WF modification of ITO.¹⁶ Additionally, the insertion of a proper HTL between the BHJ layer and the electrode is effective to increase the WF and improve the collection and extraction efficiency of holes.

To date, many HTLs have been designed for both normal and inverted device structures. The commonly used ones include: graphene oxides and their derivatives,¹⁷ transition metal oxides,^{18,19} conducting polymers and their composites, metal sulfides,²⁰ and organic surface modifiers such as self-assembled monolayers (SAMs).^{21,22,23} Thus, in this chapter, we focus on SAM materials for the aim of modifying the ITO WF and improving the device stability.

In general, self-assembly is an efficient and versatile strategy for surface modification. Self-assembled monolayer (SAMs) can be generated on semiconductors and dielectric surfaces and they represent an autonomous organization of different components into patterns of specific structures.²⁴

Thus, a SAM is defined as a small molecule with a specific functional group that can be attached to the surface of metals or metal oxides in an organized manner. Through this, SAM is capable of altering the electrical properties of metal oxides' surface. The interactions behind the SAMs-substrate grafting could be covalent bonds, hydrogen bonding, electrostatic interactions, hydrophobic interactions or Van der Waals forces.²⁵

As previously mentioned, these organic surface modifiers (SAMs) can be considered as alternatives to PEDOT:PSS HTLs in both organic and perovskite solar cells. Insertion of SAMs molecules in the semiconductor polymer/electrode interface can minimize the energy barrier between the HOMO of the donor and the electrode^{26,27} by simply altering the work function of ITO leading to an ohmic contact between the active layer and the electrode.^{28,14} The WF modification is made possible through altering the permanent dipole moment of the ITO surface with the SAM, thus improving device performances. However, the effect of the SAM insertion is not only on the device performance but also on the device stability.²⁹

SAMs can be formed from molecules that can be either dissolved in solution or condensed on the surface from a gas phase.³⁰ Although the majority of SAMs' examples were formed on the solid (poly-)crystalline surfaces, they can also be formed on liquid surfaces such as mercury drops.³¹ Regarding the solid surfaces, they include rigid substrates (ITO, TiO₂, ZnO, Au, Ag) and flexible substrates (polyethylene terephthalate, PET) since SAMs require only low-temperature solution processing. Different methods were used for the preparation of the self-assembled monolayers on ITO substrates. This can be done by either immersion,³² spin-coating³³ or soft imprinting methods.³⁴

iii. Use of SAM materials in OPV

1. Carboxylic acid-based SAM molecules

Organic surface modifiers can include those that end with carboxylic acid functional groups. Choi *et al.*³⁵ demonstrated that PTB7:PC₇₀BM normal-based devices having their ITO modified with chlorobenzoic acid (CBA) by simple spin-coating achieved higher PCE (8.5%) than those fabricated using PEDOT:PSS HTLs (7.5%). This improvement is mainly related to the increased WF of ITO caused by the chlorine atom pointing out of the surface (**Figure IV-2**). This leads to a more efficient hole extraction from the active layer. The second benefit was the increased transparency of the HTL (when compared to PEDOT:PSS) in the 500-800 nm region, increasing light absorption within the active layer. Finally, the contact resistance at the ITO/active layer interface was reduced.

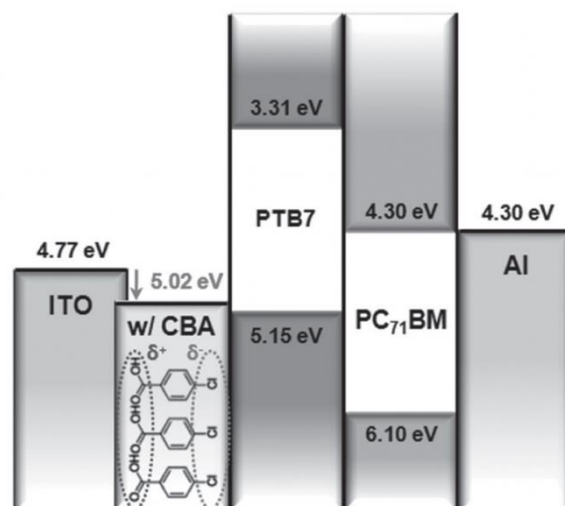


Figure IV-2: The energy-band diagram of devices incorporating CBA layer between ITO and the active layer.³⁵

Two other distinct SAM molecules having also carboxylic acid functional groups were grafted to form coated ITO substrates. These are TPA (12-*O*-Tetradecanoylphorbol-13-acetate) and the MC-43 (40-[bis(20,40-dimethoxybiphenyl-4-yl)amino]-biphenyl-4-carboxylic acid). The chemical structures of the corresponding molecules are shown in **Figure IV-3**.³²

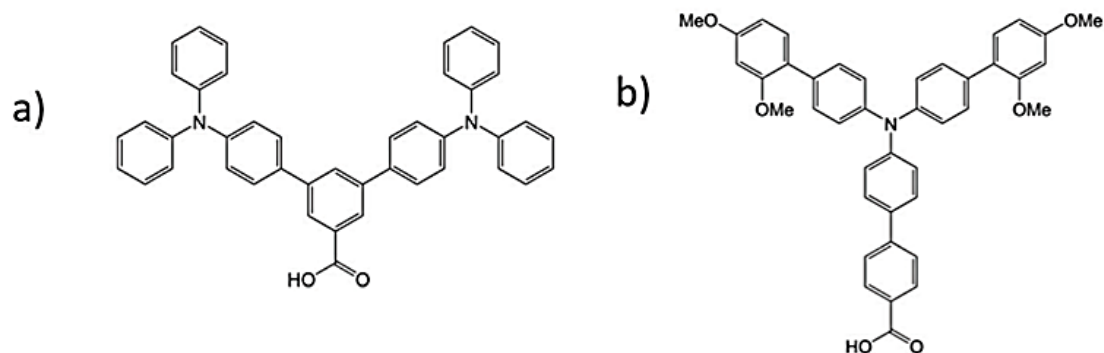


Figure IV-3: The chemical structures of (a) TPA and (b) MC-43 molecules.³²

These tertiary amines have a very low LUMO level (around -2.6 eV) acting as an electron blocking layer.³⁶ In this study, Yalcin *et al.*³² proposed to dip the ITO substrates in SAMs solution for a specific time enough for their attachment on the ITO surface as shown in **Figure IV-4**.



Figure IV-4: Schematic representation for the preparation of the SAMs-coated ITO by immersion.³²

To prove the presence of the SAM, the wettability of the ITO surfaces was studied by contact angle measurement using a water drop. This experiment revealed the hydrophobic character of the coated substrates (85° and 90° for TPA-coated ITO and MC-43 coated ITO, respectively) in comparison to the hydrophilic bare ITO surface (53°) as shown in **Figure IV-5**.³²

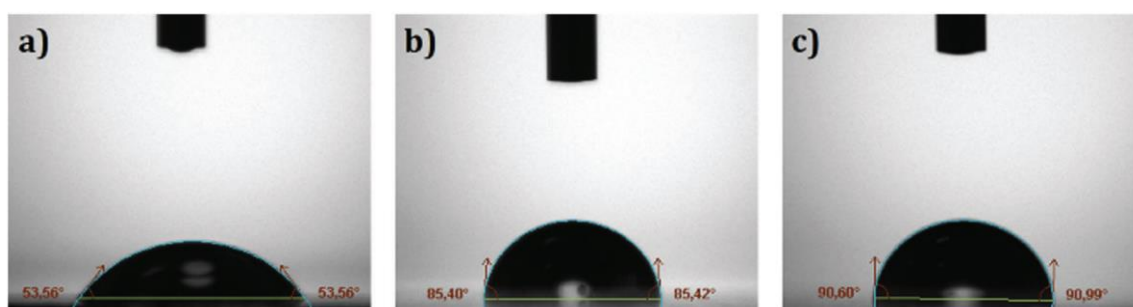


Figure IV-5: Contact angle measurements of (a) bare ITO, (b) TPA-coated ITO and (c) MC-43-coated ITO.³²

These SAM organic molecules were used as WF modifiers to replace PEDOT:PSS in the inverted-based methyl ammonium lead iodide perovskite solar cells. Compared to PEDOT:PSS-based devices (PCE of 13%), the SAM-based cells perform much better with the best cells showing 15.9% and 17.3% for TPA and the MC-43, respectively.³²

2. Phosphonic acid-based SAM molecules

Organo-phosphonates having both aliphatic or aromatic chains have been used as SAMs on the oxide surface of Si, ITO and others.²⁵ A dimethoxydiphenylamine substituted carbazole (V1036 in **Figure IV-6**), bearing a hole transporting fragment and functionalized with phosphonic acid was used to prepare SAMs on ITO substrates by immersion. This SAM molecule was used as a HTL in inverted-based perovskite solar cells. It was demonstrated that the addition of a small insulating molecule known as butylphosphonic acid (C4, **Figure IV-6**) reduces the direct contact of the photoactive layer with the ITO by filling the gaps left by the larger V1036 molecule.

This improves the quality of the formed monolayers and reduces the interfacial recombination, enhancing the device performance. Despite the decreased wettability of the perovskite solution on top of ITO in the presence of C4 molecule, the film morphology was improved.³⁷ After studying the impact of the ratio between the charge transporting V1036 and the electrically inactive filler molecule C4 on the device performance, it was deduced that the optimized PCE obtained (17.8%) was using a 1:9 ratio of V1036:C4 SAM. The reason beyond this is the better wettability of the perovskite solution by using the 1:9 ratio when compared to the other ratios. Moreover, the presence of C4 slightly increases the ionization potential (I_p) of the SAM making it closer to the perovskite valence band, this gives a higher V_{OC} . In this study, the highest V_{OC} is obtained by the SAM mixture (1:9) with the highest I_p .³⁷

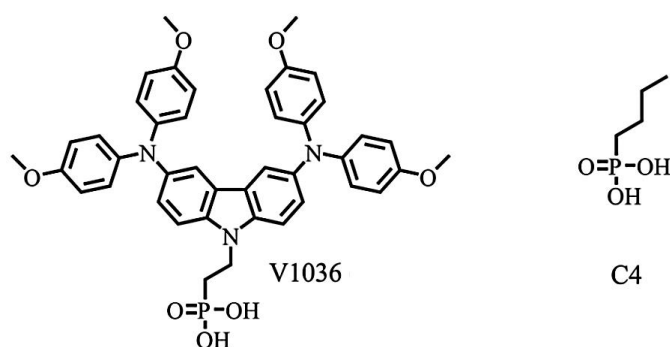


Figure IV-6: The chemical structures of the synthesized V1036 and C4 molecules used in the mixed self-assembled hole transport layer.³⁷

In another study, Sharma *et al.*¹⁶ investigated the effects of the surface modification of ITO on the performance of devices based on pentacene/ C_{60} bi-layer. As shown in **Figure IV-7**, the unmodified ITO exhibits a work function of 4.50 eV. The incorporation of F5BPA (pentafluorobenzyl phosphonic acid) increased the work function to 4.90 eV. A further increase to 5.30 eV was observed when FOPA (3,3,4,4,5,5, 6,6,7,7,8,8,8-tridecafluorooctylphosphonic acid) was used. The variation in the WF is related to the modification of the dipole moment at the ITO surface due to the different terminal functional groups on the phosphonic acids of the SAM molecules. Despite the WF modifications of ITO, the performances of the solar cells were found to be nearly insensitive with a constant V_{OC} value around 0.4 V. The reason beyond this is that the energy barrier between the modified ITO electrodes and the pentacene was constant when the work function of ITO was changed. This observation was attributed to Fermi level pinning effect.

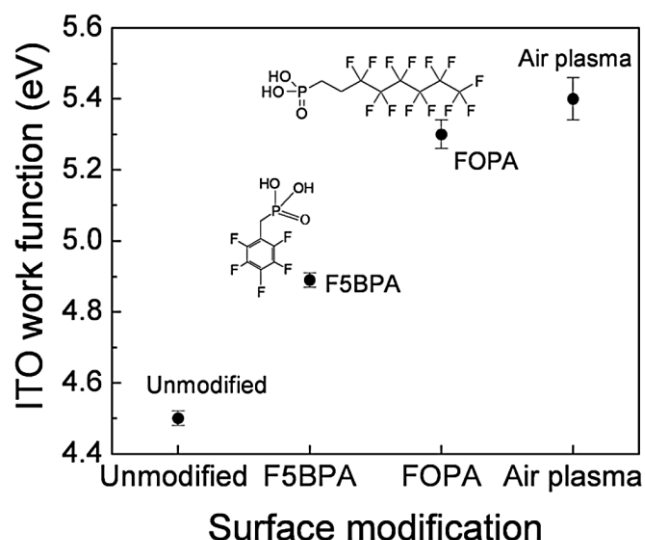


Figure IV-7: The range of the measured work functions of ITO treated with various surface modifiers.¹⁶

Fluoro-alkyl and hydrogenated-alkyl phosphonic acid derivatives (F_m SAM and H_m SAM) were utilized to form SAMs on ITO substrates. The P3HT:PC₆₀BM-based devices using the modified-ITO showed higher V_{OC} than those fabricated using PEDOT:PSS HTLs. The studies proved that V_{OC} variations were not due to WF modification of ITO since the Fermi level of ITO was constant with respect to the hole transport level in the polymer active layer. Rather, the adsorption of SAMs materials induced a barrier for the minority carrier transport to ITO as shown in **Figure IV-8**. This improved the hole selectivity and increased the V_{OC} .³⁸

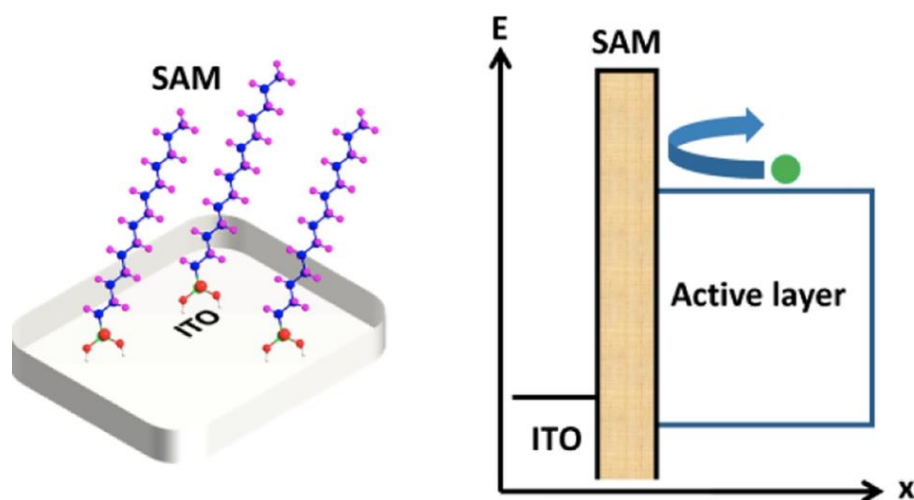


Figure IV-8: Scheme representing the adsorption of SAMs on the ITO substrate with the induced barrier.³⁸

Yang *et al.*³⁹ introduced surface-bound poly(3-methylthiophene) P3MT interfacial layers, grown *via* surface-initiated Kumada catalyst-transfer polycondensation (SI-KCTP).³⁹ The P3MT has been covalently bound to ITO as shown in **Figure IV-9a** and has been successfully incorporated as HTLs for P3HT:PC₆₀BM-based devices.

Using a doped P3MT layer (9 nm), the devices showed comparable efficiencies (2.5%) with those obtained from PEDOT:PSS-based devices (3%) (**Figure IV-9b**). More importantly, the surface-bound P3MT interfacial layers offer superior stability in air, water, and organic solvents more than that of PEDOT:PSS. This study shed the light on the possibility of using conjugated polymers brushes as self-assembled hole transport layers in OPVs.

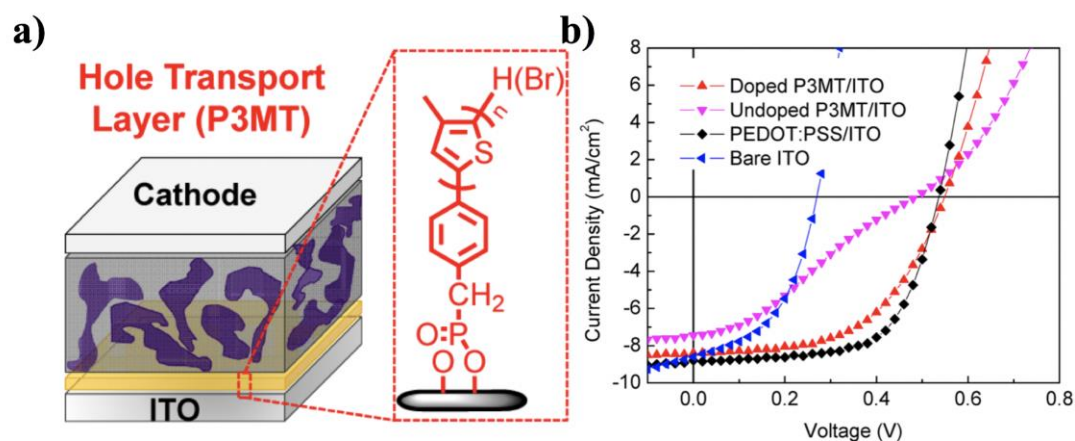


Figure IV-9: (a) Device structure of BHJ polymer solar cells based on the P3MT interfacial layer and (b) the J - V curves of P3HT:PC₆₀BM-based devices using different HTLs.³⁹

3. Silane-based SAM molecules

In addition to the organo-phosphonates, organo-silicon monolayers can also be used. These monolayers are formed by condensation on substrates exposing surface hydroxyl groups of metal oxides. This kind of molecule, capable of creating three bonds, is known for its irreversible grafting to the surface and to the neighbor SAM molecule by siloxane Si–O–Si.²⁵

For the aim of improving the work function and increasing the hydrophobic characteristics of the ITO surface, Soo Won Heo *et al.*³³ introduced triethoxy(1H,1H,2H,2H-perfluoro-1-octyl) silane (FOTES) as a SAM material by spin-coating. Transmittance measurements were studied on bare ITO and FOTES-modified ITO substrates. The results shown in **Figure IV-10a** revealed that no change in transmittance has been observed between both substrates.³³ This minimizes the optical losses by absorption and concentrates the absorption only by the photoactive layer.⁴⁰ P3HT:PC₆₀BM-based organic solar cells were fabricated in which the PCE of FOTES-based devices was increased from 3% to 3.4% when compared to PEDOT:PSS-based devices (**Figure IV-10b**). Moreover, the presence of the grafted FOTES results in a better air stability than those based on the PEDOT:PSS as shown in **Figure IV-10c**.³³

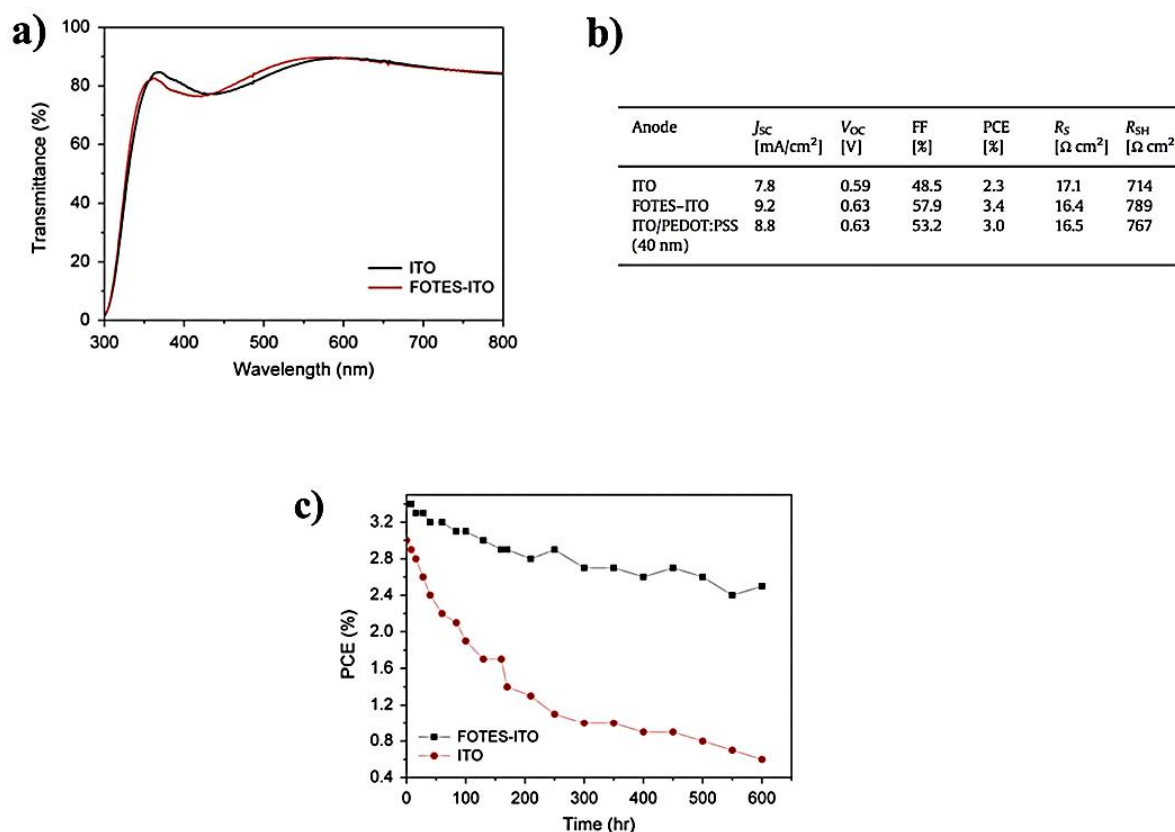


Figure IV-10: (a) Transmittance data of the ITO and FOTES-ITO substrates. (b) Photovoltaic parameters of P3HT:PC₆₀BM-based devices fabricated using bare ITO, PEDOT:PSS and FOTES-ITO and (c) PCE as a function of storage time in air for the PEDOT:PSS and the FOTES-ITO-based devices.³³

Other organo-silane SAM molecules terminated with different functional groups like NH₂, CH₃ and CF₃ were also used to control the hole injection barrier of ITO. A study done by Kim *et al.*⁴¹ showed that a trichloro(3,3,3-trifluoropropylsilane) SAM prepared by conventional immersion method increased the WF of ITO to 5.16 eV. This WF matches well the HOMO level of P3HT causing an increase in efficiency for P3HT:PC₆₀BM-based normal devices from 0.75% (unmodified ITO) to 3.15% (CF₃-modified ITO).

Soft-imprinting is another method which was employed for the preparation of organo-silane SAM materials when they cannot be easily fabricated using the existing techniques such as the conventional immersion methods. Soft-imprinting provides good conditions for a fast and simple surface modification, it also allows patterning. The overall steps of such a method are shown in **Figure IV-11**. In the presented example, the ITO surface was treated with CF₃-silane. At first, the CF₃-silane solution has been deposited on the surface of a PDMS film stamp. This PDMS film was inversely attached onto the ITO surface and then was peeled off to obtain the final CF₃ modified-ITO substrate.³⁴

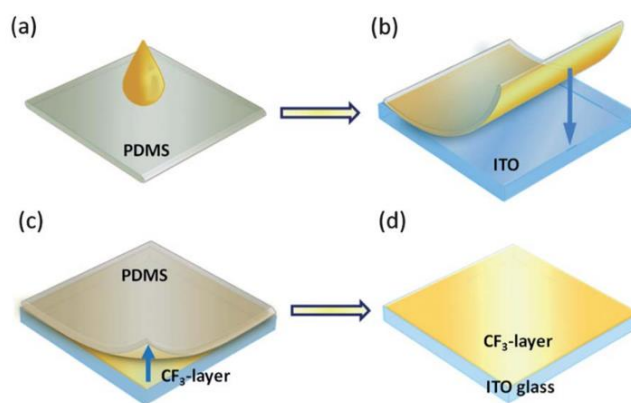


Figure IV-11: Schematic representation of CF_3 self-assembled multilayer by the soft-imprinting method.³⁴

These SAM molecules were used as PEDOT:PSS alternatives in P3HT:PC₆₀BM-based devices. In this study, the obtained PCE using the CF_3 -silane treated ITO surface was 3.42% which was higher than the corresponding PCE (3.18%) using PEDOT:PSS HTL. It was observed that using CF_3 -silane modification, both J_{SC} and FF were enhanced whereas the series resistance was decreased when compared to PEDOT:PSS-based devices.³⁴

As previously mentioned, Yang *et al.*³⁹ showed for the first time the potentiality of replacing the commonly used PEDOT:PSS HTL by a grafted polymer on ITO surface. However, in their case, the ITO surface modification with a phosphonic acid-terminated P3MT was a three-steps synthetic procedure *via* a surface initiating polymerization. This made it hardly viable at the industrial scale. Additionally, the authors did not study the stability of the solar devices over time. Our group reported a “grafting onto” one-step method to replace PEDOT:PSS with triethoxysilane terminated poly(3-hexylthiophene) (P3HT-Si) (**Figure IV-12a**). The surface modification was performed by spin-coating the silane-terminated P3HT solution onto ITO. Different characterization techniques were used to prove the successful grafting of P3HT-Si on the ITO surface such as UV-vis spectroscopy, contact angle and XPS surface measurements. P3HT:PC₆₀BM-based devices showed lower efficiencies using the modified ITO (3.18%) when compared to PEDOT:PSS (3.8%) HTLs. Moreover, as shown in **Figure IV-12b**, the hydrophobic P3HT HTL prevented the penetration of water into the device and thus improved the lifetime in comparison with the PEDOT:PSS-based normal devices.²⁹



Figure IV-12: (a) Chemical structure of P3HT-Si and (b) normalized evolutions of PCE of P3HT:PC₆₀BM-based devices with PEDOT:PSS (brown) or modified ITO (pink) under air storage without encapsulation.²⁹

II. Objectives

Based on this previous study done by Awada *et al.*²⁹, the work function generated after P3HT modification of ITO revealed a decrease to 4.5 eV compared to bare ITO (4.8 eV) or PEDOT:PSS (5.1 eV). This behavior leads to a non-ohmic contact with the active layer and loss in performances. Therefore, the main objective of the work presented below was to improve the efficiency of organic solar cells through modifying the ITO surface by grafting two molecules; silinated poly(3-hexylthiophene) (P3HT-Si) and 1H,1H,2H,2H-perfluorooctyltriethoxysilane (PTES) which is a fluorinated molecule.

P3HT is a conjugated polymer known for its hydrophobicity, preventing the penetration of water molecules into the devices when used as a HTL. In its turn, PTES, being an organosilane, is a surface modifier that increases the work function of ITO when deposited onto it. **Figure IV-13** is a schematic representation of a mixed SAM layer including grafted P3HT-Si and PTES on ITO substrate.

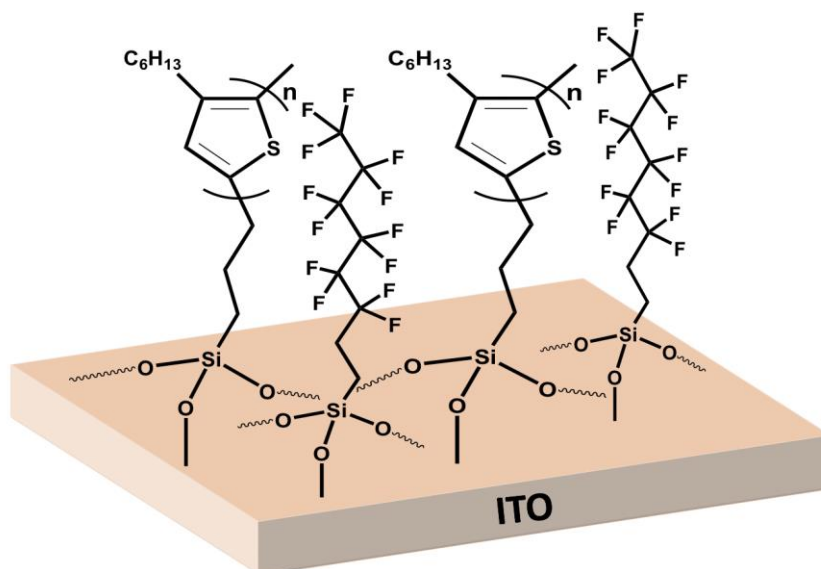


Figure IV-13: Schematic representation of the grafted P3HT-Si and PTES on ITO substrate.

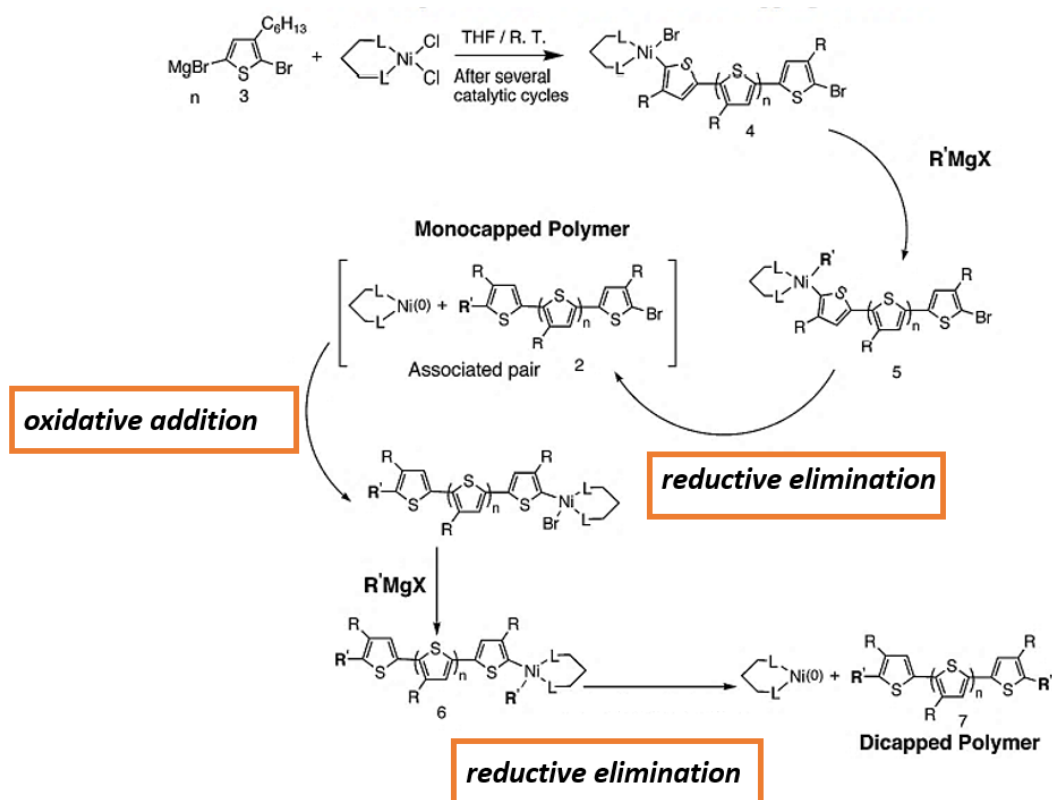
In the first section of this part, triethoxysilane-terminated P3HT has been synthesized and characterized with the aim of anchoring it on top of ITO substrates *via* hydrolysis/condensation reactions. Mono grafting experiments for either P3HT-Si or PTES have been performed separately to optimize the grafting conditions for each molecule. Then, a mixed solution of P3HT-Si and PTES has been used for grafting on ITO substrates. All these modified grafted substrates have been used as PEDOT:PSS alternatives in P3HT:PC₆₀BM normal-based solar cells.

III. Elaboration of SAMs on ITO substrates

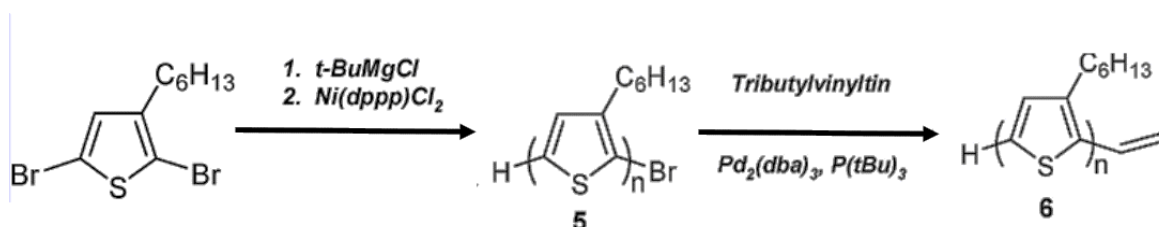
a. End-functionalization of P3HT to be grafted on ITO

For the aim of grafting P3HT on several surfaces such as ITO, end-functionalization is widely used to introduce specific groups that can help the polymer to bind on the surface.²⁹ Thus, different methodologies were previously performed to end-functionalize P3HT polymer. One of these strategies is based on the addition of a functionalized molecule at the end of polymerization. In this regard, in-situ synthetic procedures were investigated for synthesizing end-functionalized P3AT such as trimethylsilyl-terminated regioregular rr-P3ATs⁴² and rr-P3ATs bearing amino or hydroxyl groups.⁴³ Among the used in-situ methods, modified Grignard metathesis (GRIM) reaction was demonstrated. This method is based on a facile one-step procedure through the addition of a second Grignard reagent to produce P3AT having different end-functional groups.⁴⁴ Generally, and as previously explained, a reaction between 2,5-dibromo-3-hexylthiophene and tert-butylmagnesium chloride yields 2-bromo-5-magnesiobromo-3-hexylthiophene as an intermediate product. In the case of modified GRIM, a second monofunctional Grignard reagent was introduced after the addition of the nickel catalyst. As the polymerization generally follows the chain growth mechanism, the addition of a second Grignard reagent causes the termination of the reaction, resulting in the formation of an end-functionalized polymer. In this regard, allyl-terminated P3HT polymer can be synthesized using an allyl magnesium bromide. Additionally, aryl, alkyl, vinyl and other Grignard reagents can be also utilized. It was stated that depending on the reagent's reactivity, the polymer can be either functionalized from one end or from both ends. It was reported that allyl, ethynyl, and vinyl groups produce mono-functionalized polymers.

The mechanism of the corresponding reaction is shown in **Scheme IV-1**. First, and as explained in **Chapter I**, the polymer is extended by the reaction of thienyl Grignard intermediate (3) with catalytic amounts of Ni(dppp)Cl₂. After the polymerization proceeded, the species (4) which remains in solution reacts with the second Grignard reagent (R'MgX) to give the polymer (5). This polymer then undergoes a reductive-elimination step yielding the monocapped polymer (2). Again the Ni(0) catalyst reacts with the bromine end of the polymer (2) producing the polymer (6) after a reaction with another R'MgX. The reductive elimination of polymer (6) yields a dicapped polymer (7). The chance of mono or dicapped polymer is dependent on the reactivity of the Grignard reagent *i.e.* in the case of unsaturated Grignard reagent (such as allyl and vinyl), it reacts with Ni(0) to form a stable π -complex thus preventing dicapping to occur.⁴⁴



Another strategy was also studied for synthesizing functionalized P3HT based on post-functionalizing the reactive H and Br terminal groups of P3HT. For instance, vinyl-terminated P3HT was previously synthesized starting by the conventional GRIM polymerization to prepare P3HT. Then, the Br-termination was used for a Stille coupling reaction between P3HT-Br and vinyl tri-*n*-butyltin yielding the desired vinyl-terminated polythiophene as shown in **Scheme IV-2**. This reaction was proved to be effective for the preparation of different end-functionalized P3HT.⁴⁵



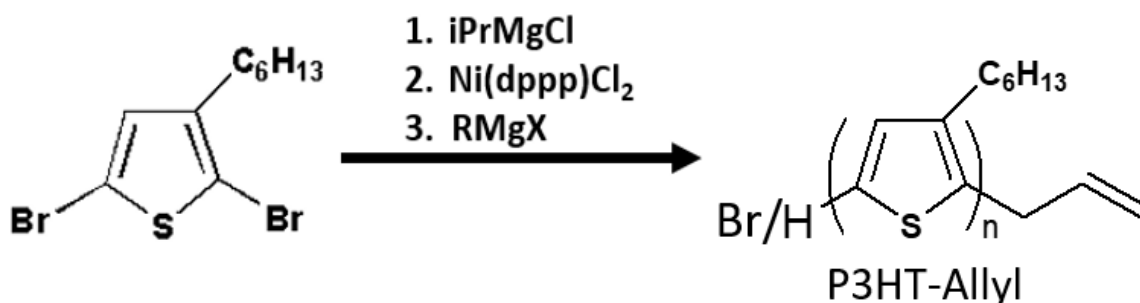
b. Synthesis and characterization of triethoxysilane-terminated P3HT

i. Synthesis of allyl-terminated P3HT

Allyl-terminated poly(3-hexylthiophene) was prepared using Kumada catalyst-transfer polycondensation (KCTP) known as Grignard metathesis polymerization.⁴⁶ The ratio of monomer to catalyst can determine the approximate desired degree of polymerization (DP_n) according to **Equation 1**, and considering that conversion=1. In our case, the monomer to catalyst ratio was calculated to target a DP_n of 30.

$$DP_n = \frac{n_{\text{Monomer}}}{n_{\text{Catalyst}}} \times \text{Conversion} \quad \text{Equation 1}$$

As shown in **Scheme IV-3**, 2,5-dibromo-3-hexylthiophene monomer was mixed with isopropylmagnesium chloride at room temperature to produce 2-bromo-5-chloromagnesio-3-hexylthiophene. The quasi-living chain of the polymer was formed after the addition of 1,3-bis(diphenylphosphino)propane nickel(II) chloride ($\text{Ni}(\text{dppp})\text{Cl}_2$) catalyst. To proceed in the functionalization process, the Grignard allyl magnesium bromide was added after 10 minutes of polymerization and the reaction was kept under stirring for 30 minutes. The final P3HT polymer was then precipitated in cold methanol and further purified using Soxhlet extraction in ethanol, acetone and finally collected using chloroform extraction with a yield of 55%.



Scheme IV-3: Synthesis of the allyl-terminated P3HT polymer.

The allyl-terminated P3HT has been characterized by different techniques starting with ^1H NMR. The efficiency of the functionalization can be proved by three peaks (**b**, **c** and **d**) as shown in the spectrum of **Figure IV-14**. Allylic signals are represented by proton **c** (CH_2 , $\delta=5.12$ ppm, multiplet), **b** (CH , $\delta=5.96$ ppm, multiplet) and **d** (CH_2 , $\delta=3.50$ ppm, doublet). Signal **e** (CH_2 from the regioregular units, $\delta=2.801$ ppm, triplet) and **a** (CH aromatics, $\delta=6.97$ ppm, singlet) are the characteristic signals of the repetitive 3-hexyl thiophene unit. The signal **f** (CH_2 , $\delta=2.511$ ppm) was set as 4 protons (it corresponds to two units, the regioirregular ones from GRIM process) from which the integrals of the spectrum were calibrated. It was then possible to determine the number of the repetitive units by adding the integral of the signals **e** and **f** corresponding to the regioregular and regioirregular units, respectively.

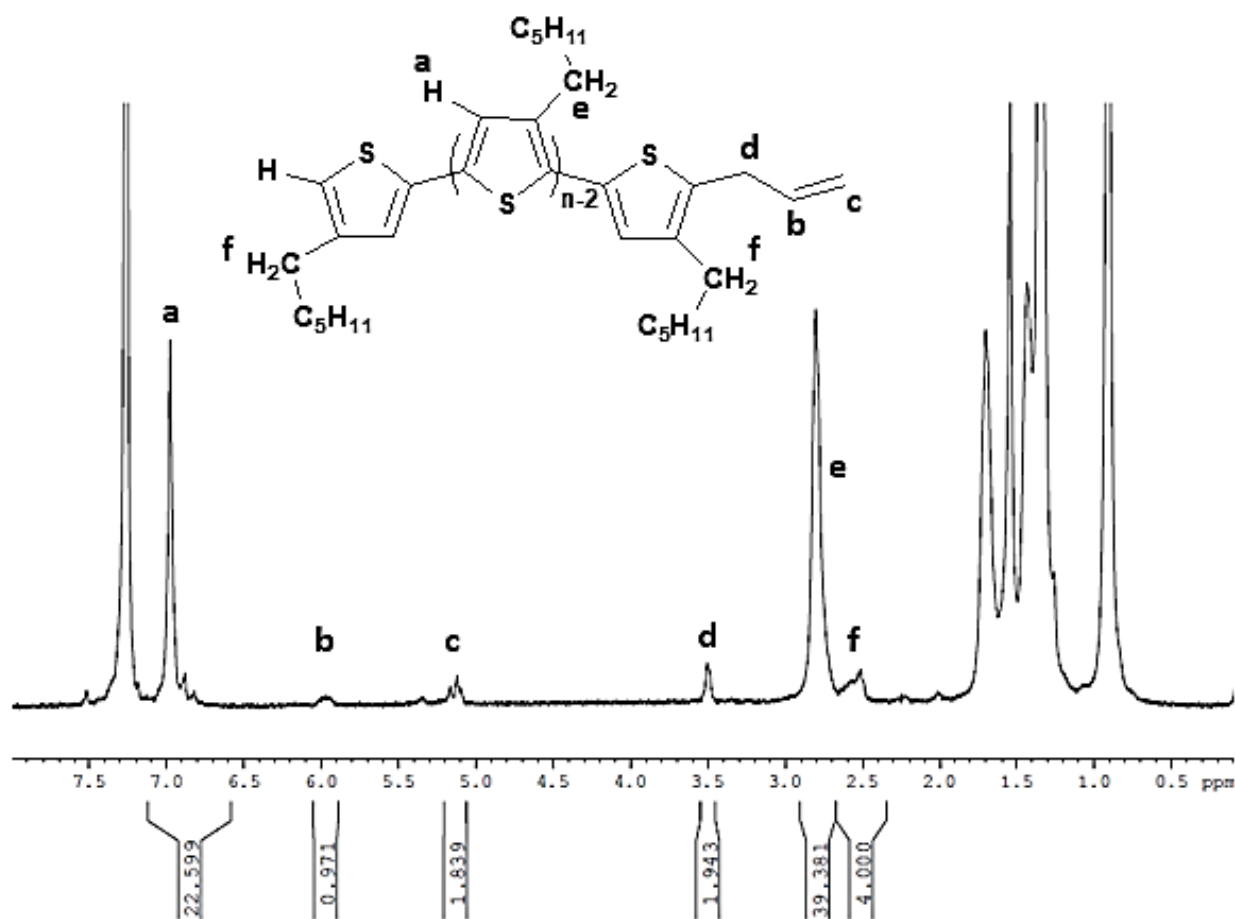


Figure IV-14: ^1H NMR spectrum of the allyl-terminated P3HT (400 MHz, CDCl_3).

Although the desired degree of polymerization was 30, the experimental degree of polymerization was calculated to be 22 according to **Equation 2** based on the integration (I) of the corresponding peaks. Thus, for a total repetitive unit of 22, it was then possible to estimate the total molar mass of the polymer by considering the molecular weight of one hexyl-thiophene unit (M_0) to be $166.23 \text{ g}\cdot\text{mol}^{-1}$. The number average molar mass (M_n) was estimated to be $3700 \text{ g}\cdot\text{mol}^{-1}$.

$$\text{DP}_n = \frac{I_e + I_f}{2} \quad \text{Equation 2}$$

From **Equation 3**, regioregularity was calculated to be 90% also based on the integration of signals **f** and **e**. As previously mentioned, the **f** signal was calibrated to 4 protons.

$$\% \text{ Regioregularity} = \frac{I_e}{(I_e + I_f)} \times 100 \quad \text{Equation 3}$$

$$\% \text{ Regioregularity} = \frac{39.38}{43.38} \times 100 = 90\%$$

To calculate the percentage of the end-group functionalization, the integration of protons (**b**) or (**c**) or (**d**) which corresponds to the allyl group was compared to the referenced 4 protons (**f**) as shown in **Equation 4**. Thus, in this case, a functionalization between 91 and 97% has been obtained.

$$\% \text{ Functionalization} = \frac{\text{Integration of b or } \left(\frac{c}{2}\right) \text{ or } \left(\frac{d}{2}\right)}{\text{Integration of f/4}} \times 100 \quad \text{Equation 4}$$

The number average molar mass of the synthesized polymer was estimated by size exclusion chromatography (SEC) performed in THF using a UV detector (set at 450 nm) with a conventional polystyrene calibration. A narrow peak distribution was observed on the SEC chromatogram of **Figure IV-15** with a symmetrical shape where M_n was $3700 \text{ g}\cdot\text{mol}^{-1}$ with a dispersity (\mathcal{D}) of 1.2. The obtained results were in agreement with the number average molar mass calculated by ^1H NMR.

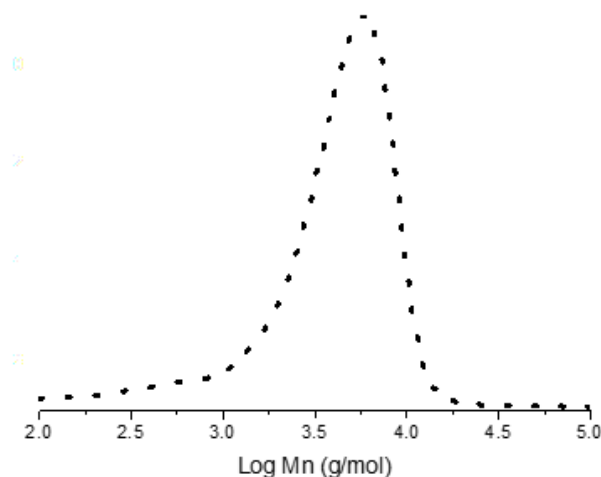
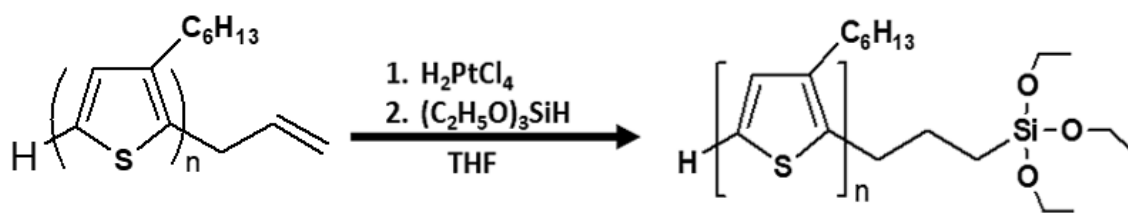


Figure IV-15: Normalized SEC chromatogram of the allyl-terminated P3HT based on polystyrene calibration.

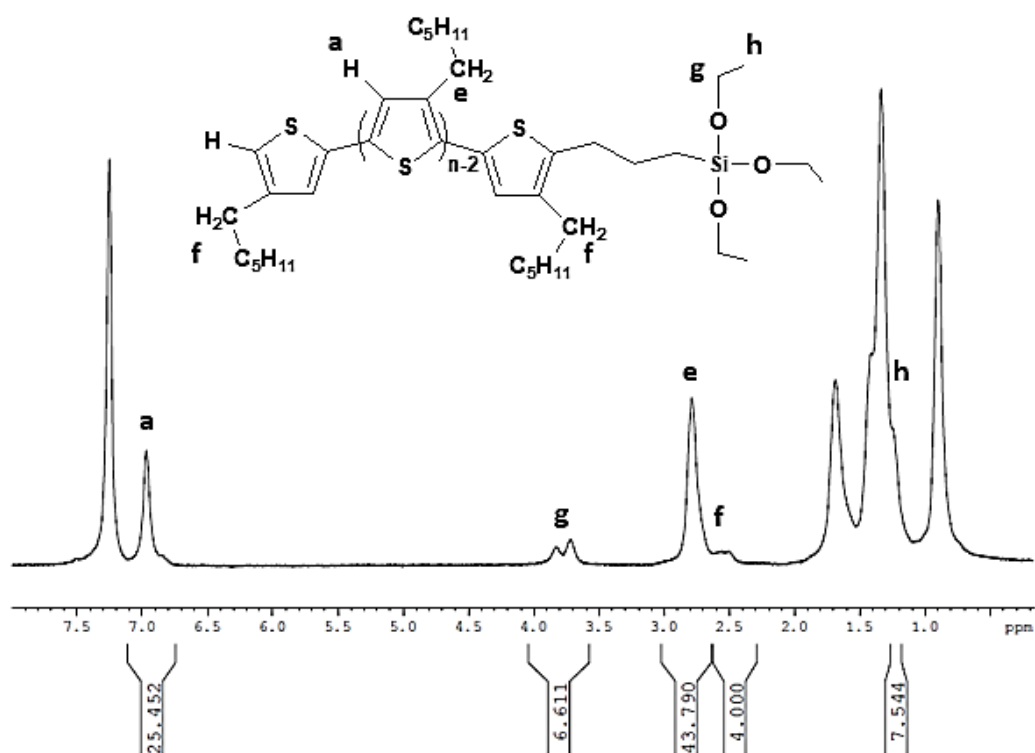
ii. Synthesis of triethoxysilane-terminated P3HT

To graft P3HT on ITO substrates, further functionalization of the terminal double bond was needed. For this, hydrosilation reaction was used to transform the alkene group into a triethoxysilane. The reaction was performed according to previous literature works^{47,48} under dry conditions. The synthesized allyl-terminated P3HT was mixed with chloroplatinic acid (H_2PtCl_6) catalyst at room temperature in THF. The mixture was degassed for 20 minutes to eliminate air from the medium. Triethoxysilane was then added dropwise and the mixture was stirred for 30 minutes before increasing the temperature to $55 \text{ }^\circ\text{C}$. After 5 hours, the resulted triethoxy-terminated P3HT polymer was precipitated twice in ethanol and filtrated under nitrogen to avoid the hydrolysis of the Si functional group (Yield=90%). **Scheme IV-4** resumes the synthetic route of P3HT-Si.



Scheme IV-4: Synthesis of triethoxysilane-terminated P3HT.

The ^1H NMR spectrum of P3HT-Si shown in **Figure IV-16** revealed the complete disappearance of the allylic protons and the appearance of two new signals related to CH_2 and CH_3 of the Si-O ethyl group; **g** (CH_2 ; $\delta=3.72$ ppm) and **h** (CH_3 ; $\delta=1.22$ ppm).

Figure IV-16: ^1H NMR spectrum of triethoxysilane-terminated P3HT (400 MHz, CDCl_3).

The synthesized triethoxysilane-terminated P3HT was grafted on ITO surface and then annealed at a specific temperature. So, it was important to previously study the thermal characteristics of the synthesized polymer to avoid its degradation during grafting. The thermogravimetric analysis has been performed under nitrogen and the thermogram is shown in **Figure IV-17**. The polymer exhibited a very stable behavior when heated up to 410 $^\circ\text{C}$. Beyond this temperature, it started to degrade losing 70% of its mass above 550 $^\circ\text{C}$. Then, a stable behavior appeared again above 600 $^\circ\text{C}$.

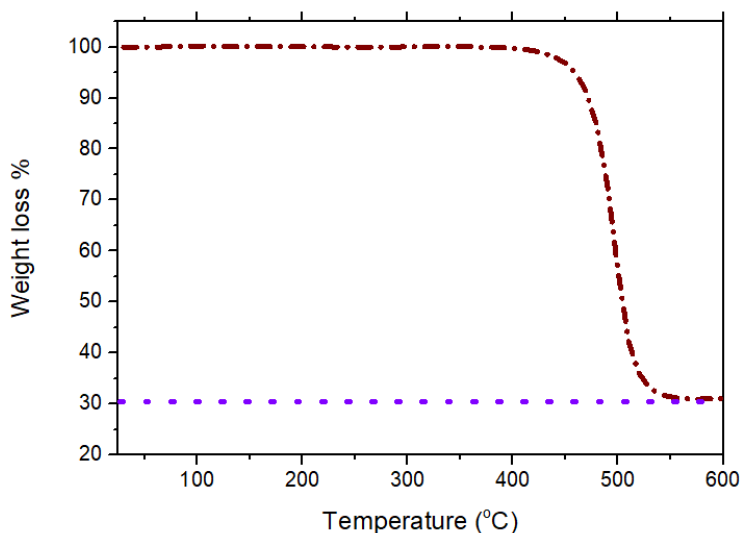


Figure IV-17: Thermogravimetric diagram of triethoxysilane-terminated P3HT.

c. Grafting of SAM molecules on ITO substrates

i. Preparation and characterization of bare ITO

Prior to use, ITO substrates should be cleaned properly with deionized water and alcohols to remove any residual dusts or organic contaminants. It is worth mentioning that the pre-cleaned ITO substrates should be exposed to UV-ozone treatment right before depositing the HTL on top of them. Besides removing any traces of organic contamination, this process increases the surfaces' hydrophilicity by increasing the surface oxygen concentration. This technique also increases the ITO work function to 4.8 eV. It should be pointed out that this treatment must be done just before grafting the HTL since organic contamination may occur within 4 hours.⁴⁹

To confirm the grafting of the polymer on ITO substrates, bare ITO was first characterized by several techniques to compare the data with the modified-ITO substrates. X-ray Photoelectron Spectroscopy (XPS) has been used to indicate the composition of the ITO surface. In general, ITO is a mixture of 90% by weight indium oxide (In_2O_3) and 10% by weight tin oxide (SnO_2).⁵⁰ According to the XPS spectrum of the bare ITO shown in **Figure IV-18**, only oxygen, indium, tin and carbon elements were detected. This indicates the absence of impurities on the surface of ITO after cleaning except for some surface contamination proved by the presence of a small peak of carbon signal.

The high-resolution spectrum helped to identify and quantify the chemical components of each element. By comparing the peaks of In 3d and Sn 3d, it was recognized that the spectra are divided in two parts: $3d_{5/2}$ and $3d_{3/2}$, with a ratio of 2:1 due to the phenomenon of spin-orbit coupling. In $3d_{3/2}$ and In $3d_{5/2}$ peaks are located to 451.6 eV and 444.2 eV, respectively with $\Delta = 7.4$ eV. The Sn 3d peaks also exist as Sn $3d_{3/2}$ and Sn $3d_{5/2}$ at 494.7 and 486.32 eV, respectively with $\Delta = 8.4$ eV. These results were in agreement with a previous work reported in literature.⁵¹ The chemical shifts of In 3d and Sn 3d correspond to oxidation states of +III and +IV for both indium and tin, respectively.

Concerning oxygen, three distinct components were observed. A component at 529.7 eV corresponds to O²⁻ state found in the ITO structure and two other components at 530.9 and 532.2 eV that originate from the oxygen atoms on the surface of the ITO due to the adsorbed OH groups.

By integrating the peaks of 3d_{5/2} states of In and Sn and the peak of O 1s at 529.7 eV, it is possible to approximately estimate the chemical composition of the studied ITO with respect to In by ignoring the peaks of contamination of oxygen at 530.9 and 532.2 eV. Thus, the chemical composition of a bare ITO substrate is InSn_{0.1}O_{0.9} (**Table IV-1**).

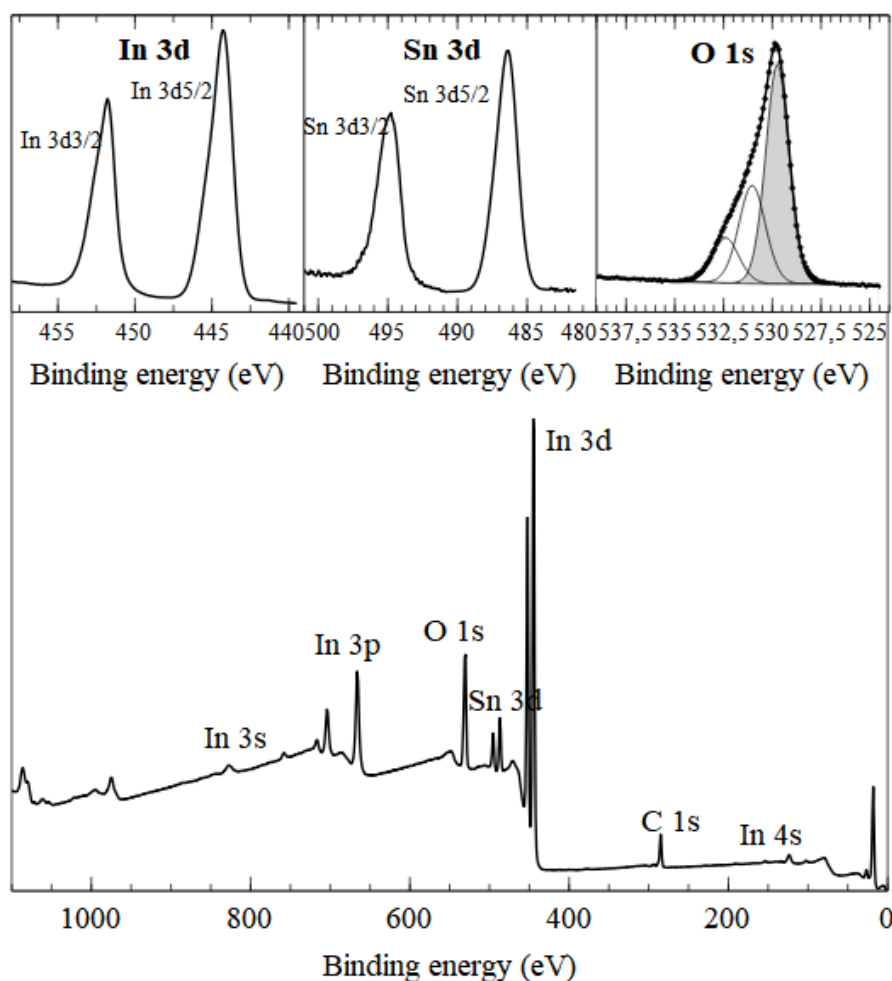


Figure IV-18: XPS spectrum of a bare ITO showing In 3d, Sn 3d and O 1s orbitals.

Table IV-9: Atomic percentage and binding energy of the elements of a bare ITO substrate given by XPS measurements.

Elements	In 3d _{5/2}	Sn 3d _{5/2}	O 1s	O 1s (contamination)	C 1s	K 2p
Binding Energy (eV)	444.2	486.32	529.7	530.9 & 532.2	285	292.7
Atomic %	29.5	3.2	25.3	28.4	5.8	8

The contact angle measurements have been performed to determine the surface characteristics of bare ITO substrates. These measurements depend on the pre-cleaning procedure of ITO, since the contact angles and the surface energies of ITO films may change by the different solvents used during the cleaning processes and plasma treatments. For the measurement, a drop of distilled water was casted on top of the ITO substrate. This revealed the hydrophilic characteristic of the UV-ozone treated-bare ITO substrates with an angle of 53° .

Topographic images of the surface of a bare ITO were taken using AFM. The average root mean square (RMS) roughness was measured (1.5 nm) to compare it with that obtained after grafting. 3D and 1D topographic images are shown in **Figure IV-19a** and **b**, respectively.

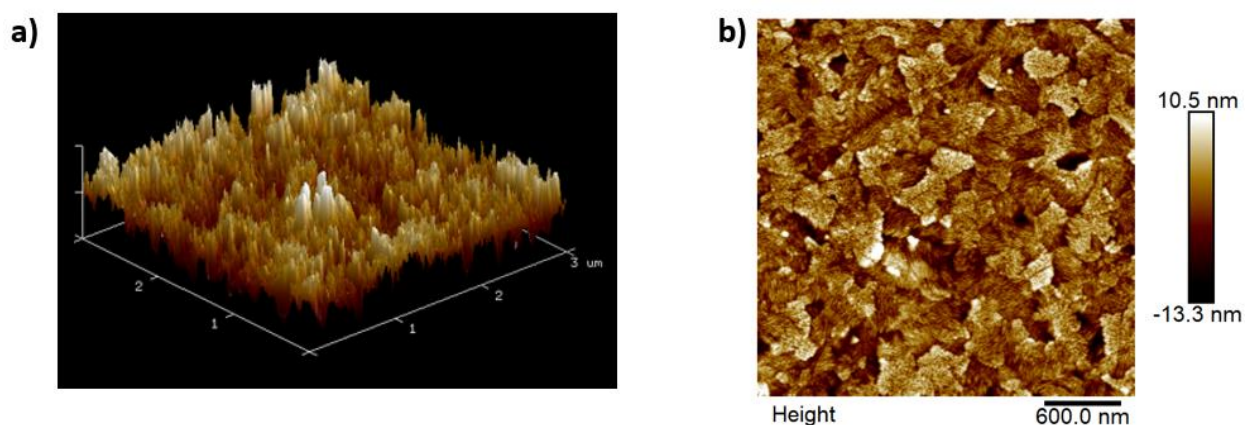


Figure IV-19: (a) 3D and (b) 1D topographic images of the surface of a bare ITO substrate.

ii. Grafting of 1H,1H,2H,2H-Perfluorooctyltriethoxysilane (PTES)

Before grafting the mixed self-assembled layers of PTES and P3HT-Si, it was worth trying each SAM molecule separately for the aim of optimizing the grafting conditions. The chosen fluorinated molecule was PTES which is terminated with a triethoxysilane group. Before proceeding, the pre-cleaned ITO substrates must be treated with UV-ozone to promote the formation of the OH groups on the surface. The PTES SAMs were grafted using three different protocols as inspired by some literature works:

- immersion of ITO substrates in 1 w% PTES **toluene-based solution** for 30 minutes then annealing at 150°C for 2 hours⁵²
- immersion of ITO substrates in 1 w% PTES **methanol-based solution** for 1 hour then annealing at 140°C for 1 hour⁵³
- spin-coating a $5\text{ mg}\cdot\text{mL}^{-1}$ PTES **toluene-based solution** at 1200 rpm/90 seconds after which the ITO substrates were annealed at 150°C for 3 hours on a hot plate²⁹

In all cases, the substrates must be washed in the good solvent several times under ultrasonication to remove the un-grafted molecules.

As mentioned before, this PTES is grafted on ITO surface *via* hydrolysis/condensation mechanism. Initially, the triethoxysilane groups undergo hydrolysis, then these OH-terminated silanes were grafted on the ITO surface *via* condensation reaction as illustrated in **Figure IV-20**.

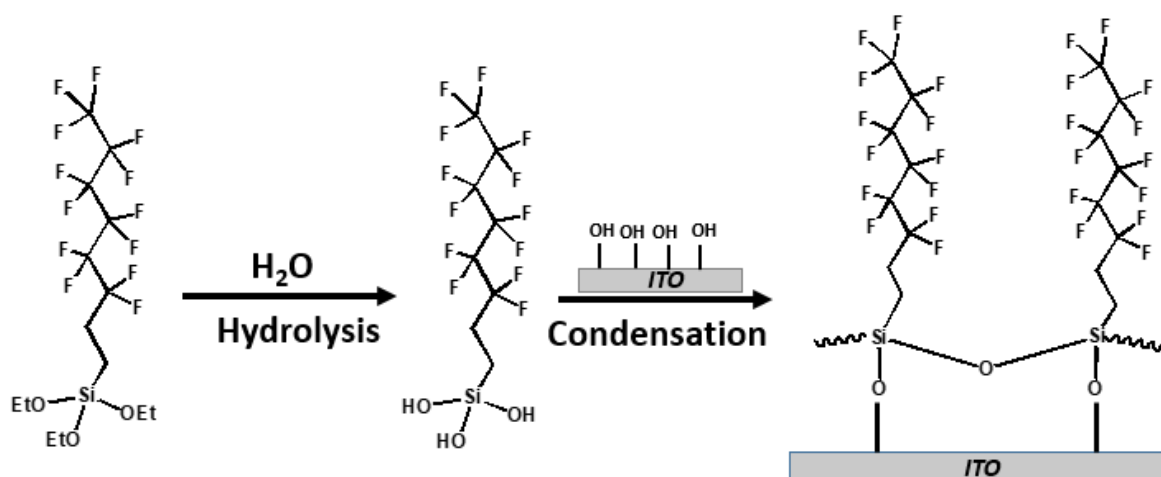
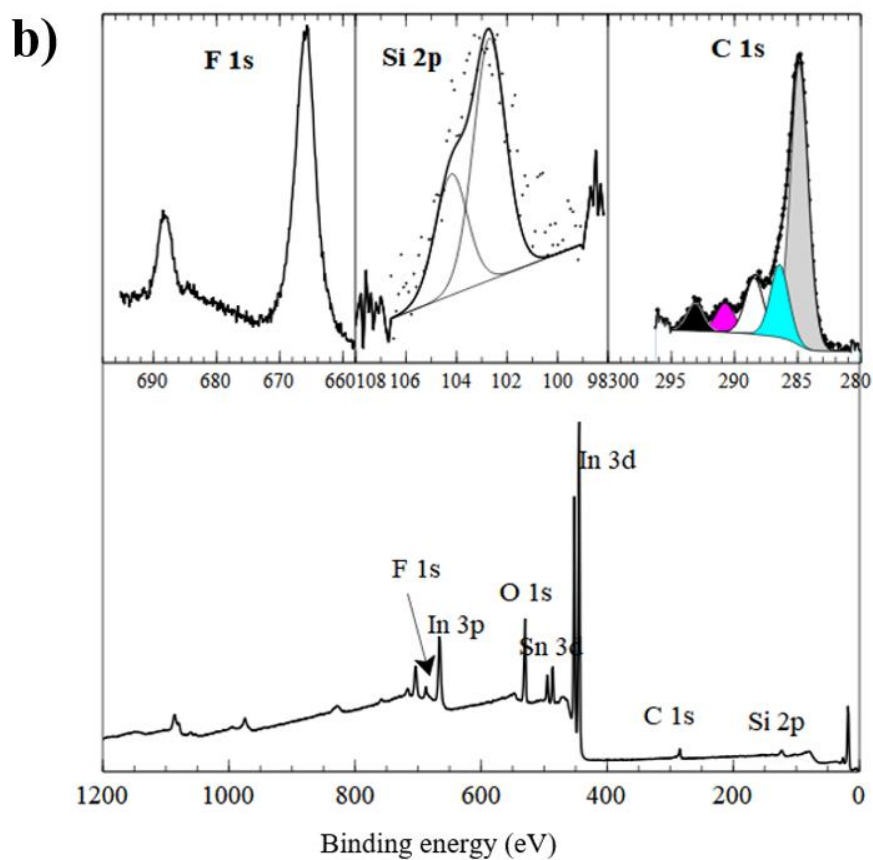
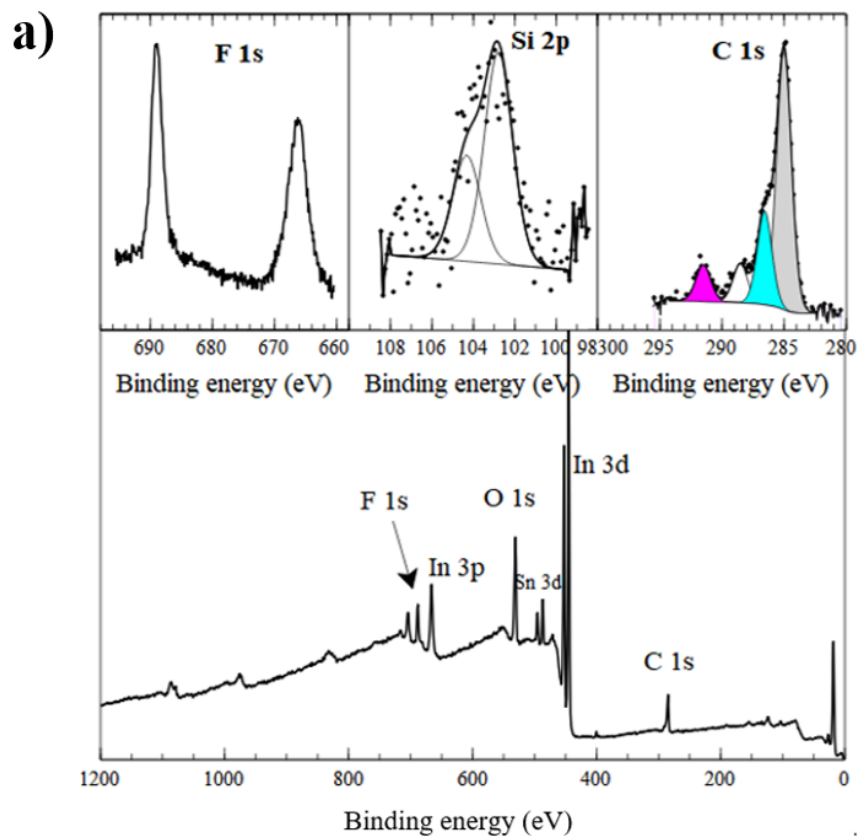


Figure IV-20: Grafting of PTES on ITO substrates via hydrolysis/condensation mechanism.

The XPS spectra from toluene by immersion (**Figure IV-21a**) shows the characteristic peaks of bare ITO (In, Sn, O) in addition to peaks revealing the successful grafting of PTES: peaks related to silicon and fluorine in addition to a more intense carbon peak generated from the grafted PTES on ITO. The C 1s core peak is made up of several components. The most intensive component at 285 eV is attributed to aliphatic carbons (C-C, C-H). The full spectrum was calibrated based on this component. The components located at 286.6 eV and 288.5 eV represent the carbons coupled to oxygen (C-O, C=O).⁵⁴ The peak at 291.5 eV is assigned to carbon atoms in a fluorinated environment (C-F). This peak along with the one corresponding to F 1s orbital (688.9 eV) confirm the presence of fluorine on ITO surface.⁵³ The doublet peak of the 2p orbital of Si observed at 102.7 eV is the characteristic peak of the silane function in PTES molecule.⁵⁴

One can note slight differences between the spectra from toluene and that from methanol (**Figure IV-21b**). By comparing survey spectra and more precisely the relative intensity ratio of C 1s, F 1s and In 3d, it is clear that the grafting with methanol is less efficient than with toluene. For C 1s core peak, the component associated to carbon atoms in a fluorinated environment C-F appears at 290.8 eV. The F 1s peak is shifted to lower binding energy (688.4 eV) due to the lower fluorine content. Indeed, by comparing the ratio of the atomic percentages of F or Si to In (by integrating the peaks of the XPS spectra shown in **Figure IV-21a and b**), F/In and Si/In ratios were higher for toluene-based grafting when compared to methanol-based ones as presented in **Table IV-2**. This proved that more fluorinated PTES were grafted when toluene solution was used for immersion. Thus, grafting was more efficient by using toluene-based PTES solutions. The other important reason for using toluene is that it is considered a good solvent to dissolve P3HT.

On the other hand, by comparing the atomic percentage ratios of the toluene-based solutions by immersion and spin-coating (**Figure IV-21c, Table IV-2**), it was confusing to choose the most efficient protocol for grafting. This could be due to the fact that XPS measurements were performed on a small spot of 50 microns, then the outcome might be affected by the non-homogeneity of the grafting of the PTES on the ITO surface.



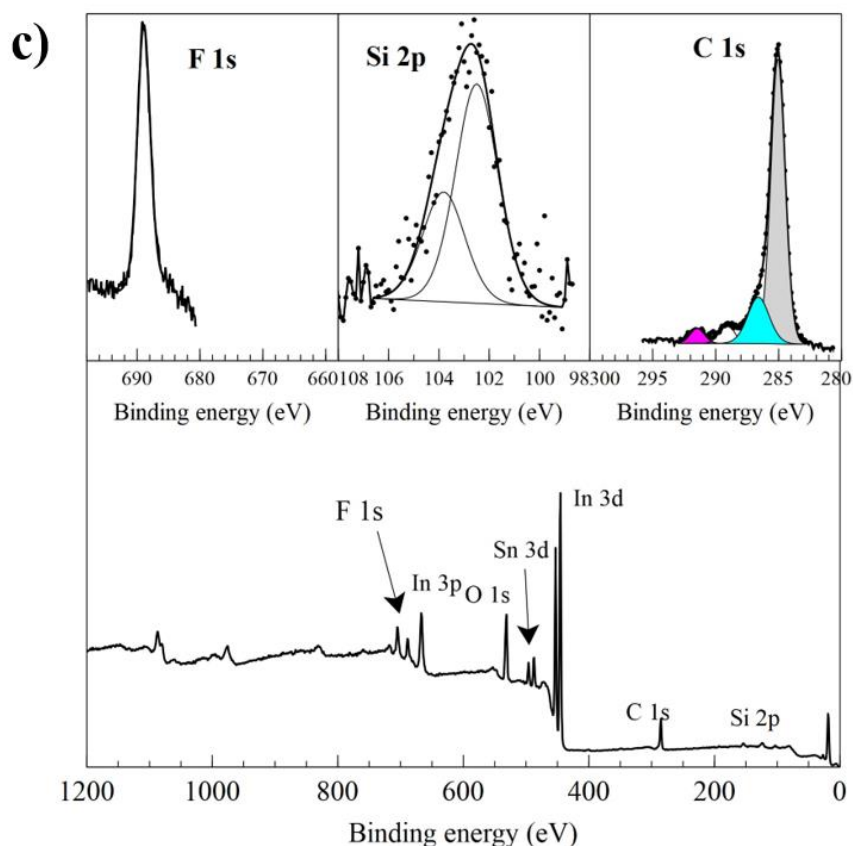


Figure IV-21: XPS spectra of PTES-modified ITO by immersion from (a) toluene, (b) methanol-based solutions and (c) by spin-coating from toluene-based solution.

Table IV-10: Atomic percentage ratios obtained from the XPS measurements.

	F/In	Si/In
Toluene-based grafting (immersion)	0.68	0.17
Methanol-based grafting (immersion)	0.43	0.08
Toluene-based grafting (spin-coating)	0.4	0.2

Thus, contact angle measurements have been used as a qualitative method to determine the most efficient grafting procedure. Eventually, by grafting a hydrophobic fluorinated molecule onto the ITO surface, the contact angle must increase. Therefore, the values of the angles can give an estimation of the quality of the grafting carried out. As previously mentioned, the un-grafted ITO is a hydrophilic oxide surface with a contact angle of 53° (**Figure IV-22a**). The grafting by immersion in toluene-based solution gave a contact angle of 94° (**Figure IV-22b**) which is greater than that obtained by immersion in methanol-based solution (71°). This result is in agreement with what was obtained by XPS.

However, the contact angle of the ITO surface after spin-coating the toluene-based PTES solution was 97° (**Figure IV-22c**). Thus, it can be estimated that the protocol and the annealing temperature used influenced the quantity of molecules grafted on the ITO surface.

For this, spin-coating seems to be more efficient for the grafting process and this protocol was followed for further studies.

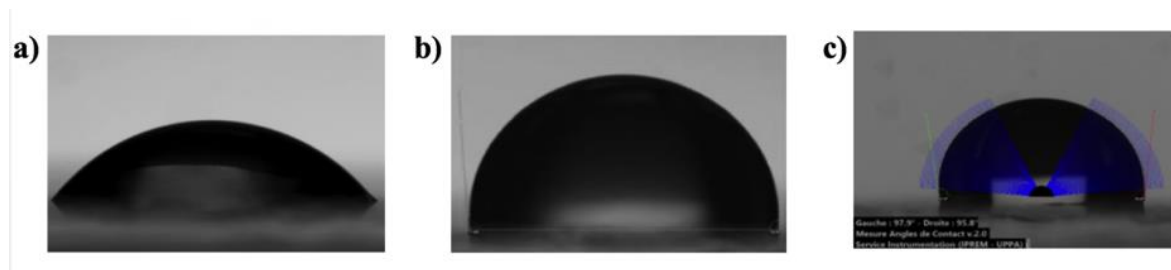


Figure IV-22: Contact angle measurements for (a) bare ITO and grafted-ITO substrates by (b) immersion from toluene and (c) spin-coating from toluene-based solutions.

Topographic images were taken for the PTES-modified ITO substrates by spin-coating to determine the morphological effect of the grafted material in terms of the corresponding roughness. The measured RMS roughness was 1.7 nm which is approximately the same as that of the bare ITO. This revealed that the PTES SAM is a homogeneous layer which is a good candidate to be used as an interfacial material. 3D and 1D topographic images are shown in **Figure IV-23a** and **b**, respectively.

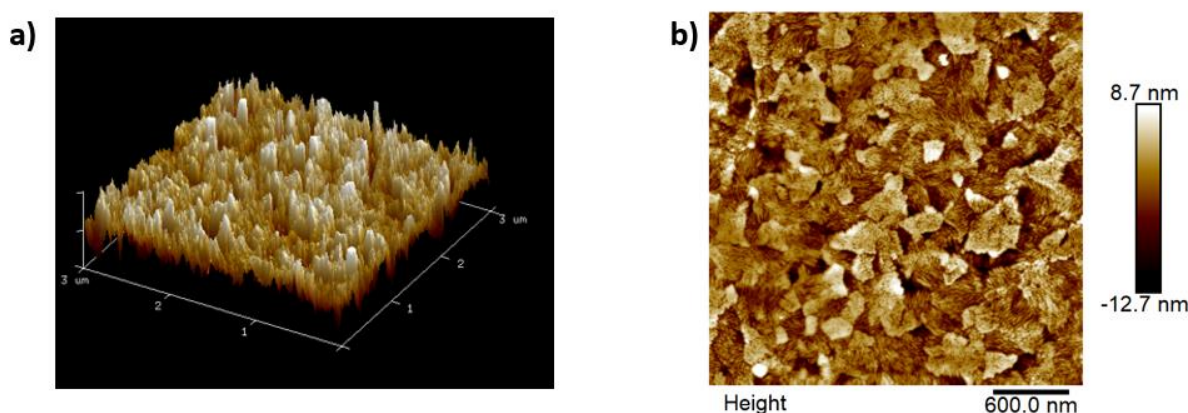


Figure IV-23: (a) 3D and (b) 1D topographic images of the PTES-ITO surface.

iii. Grafting of triethoxysilane-terminated P3HT (P3HT-Si)

The procedure followed for grafting P3HT-Si was already reported in literature.²⁹ A P3HT-Si solution of $5 \text{ mg}\cdot\text{mL}^{-1}$ in toluene has been used. The grafting conditions have been optimized in which spin-coating under inert atmosphere was used to deposit these SAM molecules. Substrates were then annealed at either 120°C or 150°C on a hot plate for 3 hours in the glovebox. Finally, the grafted-ITO substrates were washed in chloroform three times under ultrasonication for 10 minutes to eliminate the un-grafted polymer.

P3HT-Si was grafted *via* hydrolysis/condensation mechanism as shown in **Figure IV-24** in a way similar to the fluorinated PTES SAM.

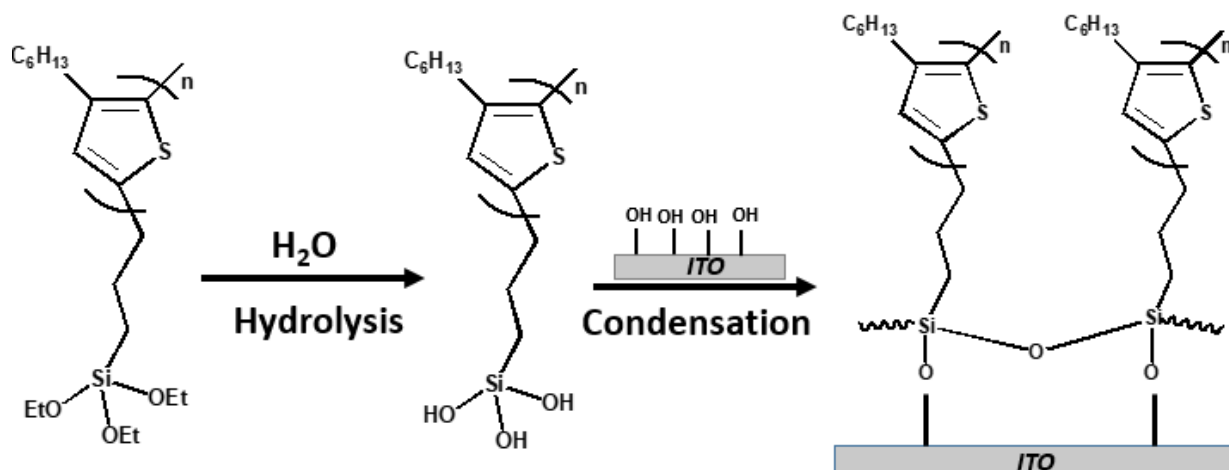


Figure IV-24: Grafting of P3HT-Si on the ITO substrates via hydrolysis/condensation mechanism.

The P3HT-Si grafted ITO substrates were first characterized by XPS to determine the elemental composition of their surfaces. The spectra in **Figure IV-25** are slightly the same whatever the annealing temperature is (120 °C or 150 °C). These spectra revealed the existence of peaks for sulfur (S) and silicon (Si). The orbital peak of S 2p constitutes S 2p_{1/2} and S 2p_{3/2} with a spacing energy of 1.2 eV and a binding energy of 164.2 eV for S 2p_{3/2} component. The peak identifying the orbital S 2p is the characteristic peak of the thiophene in P3HT.¹⁰ Also, the Si 2p peak is a doublet with a spacing energy of 0.7 eV in which Si 2p_{3/2} is located at a binding energy of 103.0 eV. This Si 2p peak is the characteristic peak for silane. Thus, these peaks proved the successful grafting of P3HT-Si on ITO. In addition, the characteristic peaks for ITO (In, Sn, and O) appeared on both XPS spectra. An intense peak identifying carbon (C) was also observed which originated from the carbon chain of the grafted polymer. The higher intensity of the C 1s peak at 285 eV and the decrease in the intensity of the In 3d peak when compared to the bare ITO revealed as well the grafting of the P3HT-Si.

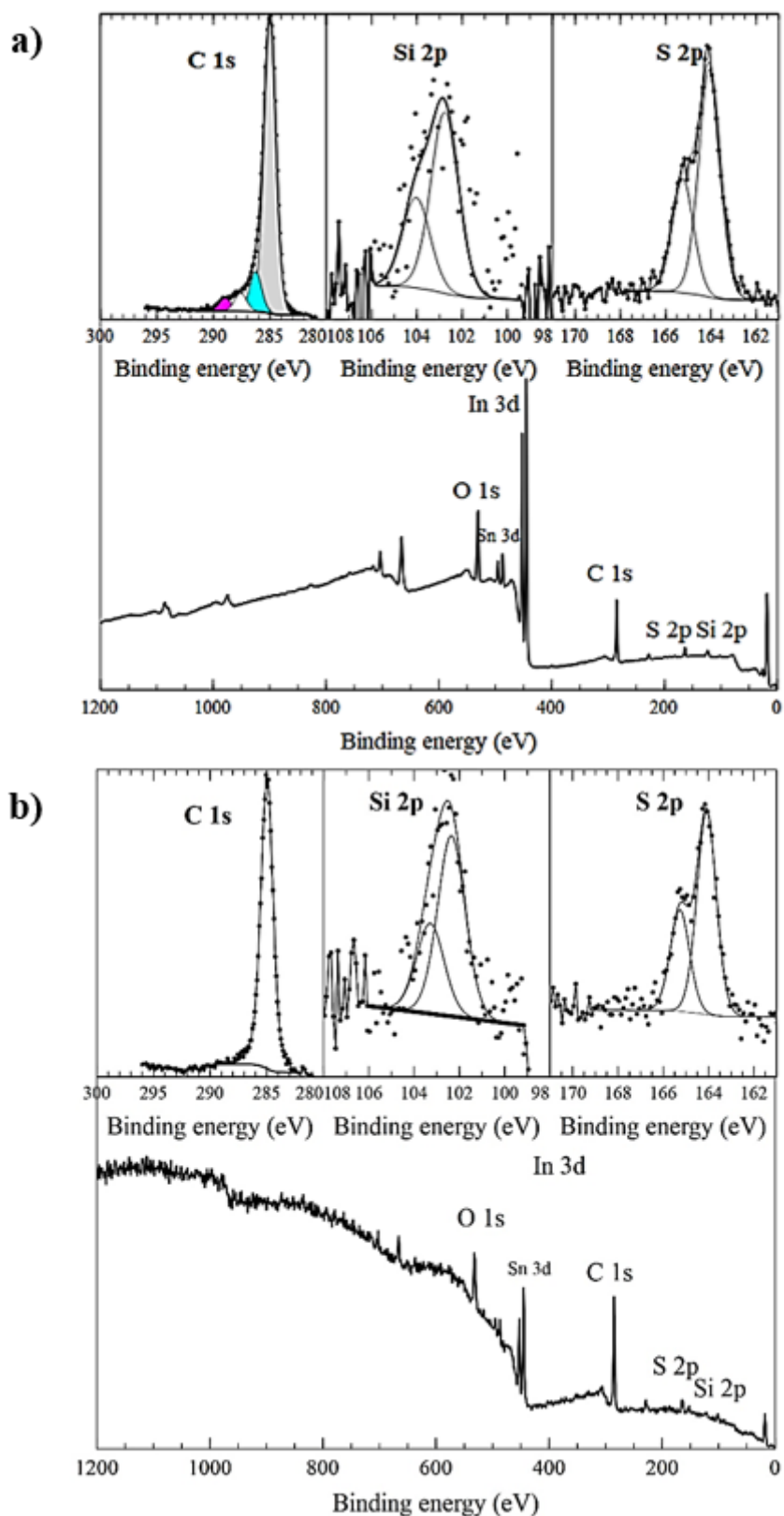


Figure IV-25: XPS spectra of the P3HT-Si grafted ITO substrates (a) annealed at 120 °C and (b) annealed at 150 °C.

The atomic percentage of each element was calculated by integrating the peaks of the XPS spectra of both modified ITO substrates that were annealed at either 120 °C or 150 °C. The results are summarized in **Table IV-3**.

Table IV-11: Atomic percentage of the elements of P3HT-Si grafted ITO substrates annealed at two different temperatures.

	Bare ITO	Substrates annealed at 120 °C	Substrates annealed at 150 °C
atomic % by XPS	In	29.5	19.5
	Sn	3.2	2.1
	O	53.7	25.0
	C	5.8	48.2
	Si	----	1.2
	S	----	3.9

These atomic percentages were used to compare the degree of grafting on ITO substrates based on the annealing temperature. The aim behind this analysis is to determine the role of the annealing temperature on the amount of the grafted P3HT-Si. By comparing the data, there was an increase in the carbon content after annealing the layers at 150 °C (63.3%) when compared to those annealed at 120 °C (48.2%) (**Table IV-3**). These carbons represent the hydrocarbon chain of P3HT. Additionally, the elemental ratios of S/In and Si/In are slightly higher with the substrates annealed at 150 °C as shown in **Table IV-4**. This may indicate that by annealing at 150 °C, more P3HT-Si were grafted on ITO substrates.

Table IV-12: Atomic percentage ratios obtained from the XPS measurements.

	Atomic % ratio		
	S/In	Si/In	Sn/In
ITO annealed at 120 °C	0.20	0.06	0.1
ITO annealed at 150 °C	0.9	0.72	0.13

The contact angles of the modified ITO substrates after different annealing temperatures were also measured. The angle increased from 53° for a bare ITO to 79° for the substrates annealed at 120 °C (**Figure IV-26a**) then to 95° upon annealing at 150 °C (**Figure IV-26b**). The higher contact angle between the water droplet and the surface of the modified ITO indicated the successful grafting of the hydrophobic polymer on the hydrophilic ITO. Moreover, the highest contact angle obtained at the highest annealing temperature (150 °C) seems to indicate that more P3HT-Si were grafted leading to a higher hydrophobicity. Interestingly, these results were in agreement with the data obtained by XPS measurements. However, UV-vis spectroscopy could also help to confirm the best annealing temperature.

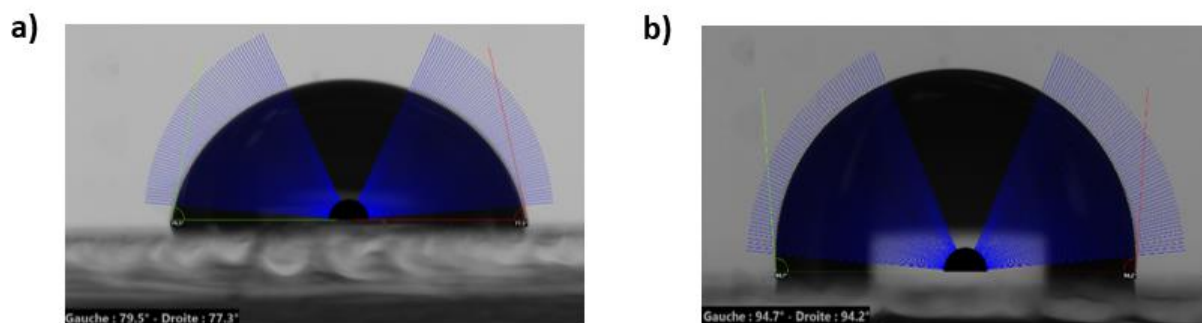


Figure IV-26: Contact angle measurements for P3HT-Si grafted ITO substrates (a) annealed at 120 °C and (b) annealed at 150 °C.

Indeed, P3HT exhibits a single broad absorption peak at a short visible wavelength (455 to 600 nm).⁵⁵ Thus, on an ITO substrate, the intensity of the absorption is dependent on the amount of P3HT-Si adsorbed on the surface. The spectra shown in **Figure IV-27** revealed an absorption band between 455 and 650 nm with a maximum at 520 nm. By comparing the absorption intensity of the substrates annealed at 120 °C and 150 °C, we could recognize that the ITO annealed at the higher temperature (150 °C) showed a higher intensity maximum peak. This indicates that more P3HT-Si were grafted on the ITO surface as deduced from the previous results. This increase in the P3HT absorbance with the annealing temperature can be attributed to the increased thickness of the grafted P3HT film by silane multi-layer or extended monolayer formation or due to the increased P3HT grafting density.²⁹ Thus, in general, we can deduce that by increasing the annealing temperature of the modified ITO substrate, the self-assembled monolayer become denser (or maybe thicker). For this, 150 °C was used as the annealing temperature for the mixed SAM.

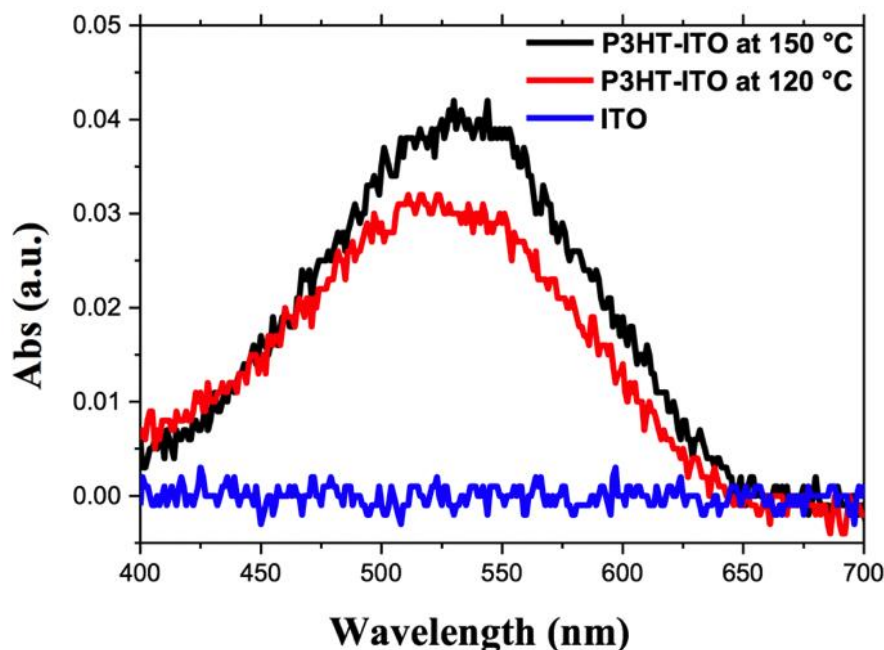


Figure IV-27: UV-vis absorption spectra of the bare and the grafted-ITO substrates annealed at different temperatures.

3D and 1D topographic images for the P3HT-Si grafted ITO surface are shown in **Figure IV-28**. RMS roughness of approximately 1.78 nm was measured which is close to that of the bare ITO substrate. This proves the smoothness of this SAM grafted layer and the possibility to be used as an interfacial layer in solar cells.

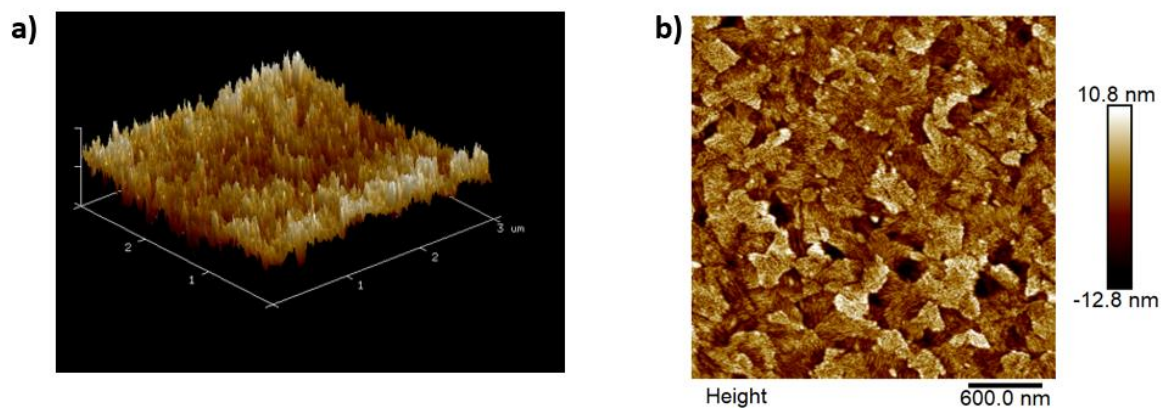


Figure IV-28: (a) 3D and (b) 1D topographic images of the P3HT-Si ITO surface.

To conclude, **spin-coating** was used for the deposition of the SAM **toluene-based solutions** on top of ITO substrates followed by an annealing **at 150 °C** for 3 hours on a hot plate.

iv. Grafting of the mixed SAM, P3HT-Si/PTES

As previously mentioned, the aim of this work is to modify the ITO surface with a mixed layer of P3HT-Si polymer and PTES molecule. Thus, after the successful grafting of each of the P3HT-Si and PTES, separately, we can study the grafting of the mixed layers. The binding of the mixed self-assembled monolayer on ITO substrate is based on the same hydrolysis/condensation mechanism as illustrated in **Figure IV-29**.

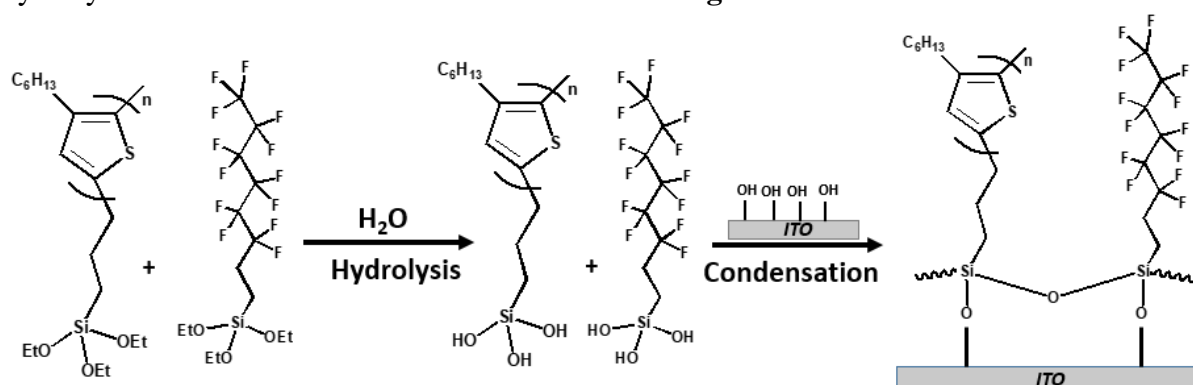


Figure IV-29: Grafting of the mixed SAM on the ITO surface via hydrolysis/condensation mechanism.

For this purpose, solutions having different P3HT-Si/PTES ratios were prepared and referred as solutions 1 to 7 as shown in **Table IV-5** while the detailed preparation is presented in the **Experimental Part of Chapter VI**.

Table IV-13: The prepared solutions having different mole fraction of P3HT-Si and PTES.

Solution	Mol f P3HT-Si	Mol f PTES	P3HT-Si/PTES
1	1	0	1/0
2	0.75	0.25	1/0.33
3	0.5	0.5	1/1
4	0.25	0.75	1/3
5	0.1	0.9	1/10
6	0.05	0.95	1/20
7	0	1	0/1

The grafting of solutions (1 to 7) was performed using spin-coating deposition process under the optimized conditions previously identified in terms of solvent, annealing temperature and time. Thus, the layers were spin-coated from toluene onto the pre-cleaned ITO substrates at 1200 rpm/90 seconds and subsequently annealed at 150 °C for 3 hours under inert atmosphere. After annealing, the grafted substrates were subjected to ultrasonic agitation in chloroform 3 times for 10 minutes to remove the free silanes (un-grafted molecules).

For the aim of detecting the elements and their atomic percentages on the grafted-ITO surfaces with different SAM solutions, XPS measurements were performed and the spectra are shown in **Figure IV-30**. The presence of Si 2p, S 2p and F 1s orbitals for solutions 2 to 6 proves the existence of both P3HT and PTES on the ITO surface. Thus, this is an indication for the successful grafting of the mixed SAM on the surface. As summarized in **Table IV-6**, the atomic percentages of the characteristic peaks for ITO, In 3d and Sn 3d, were decreased upon depositing the SAM layers. While those of Si 2p, S 2p and F 1s were increased. This is another indication for the successful grafting. More specifically, the atomic percentage of F 1s was gradually increased while that of S 2p was decreased upon increasing the PTES amount in the mixed solutions. As a result of the grafting, the atomic percentage of C 1s was also increased due to the carbon chain of P3HT and PTES.

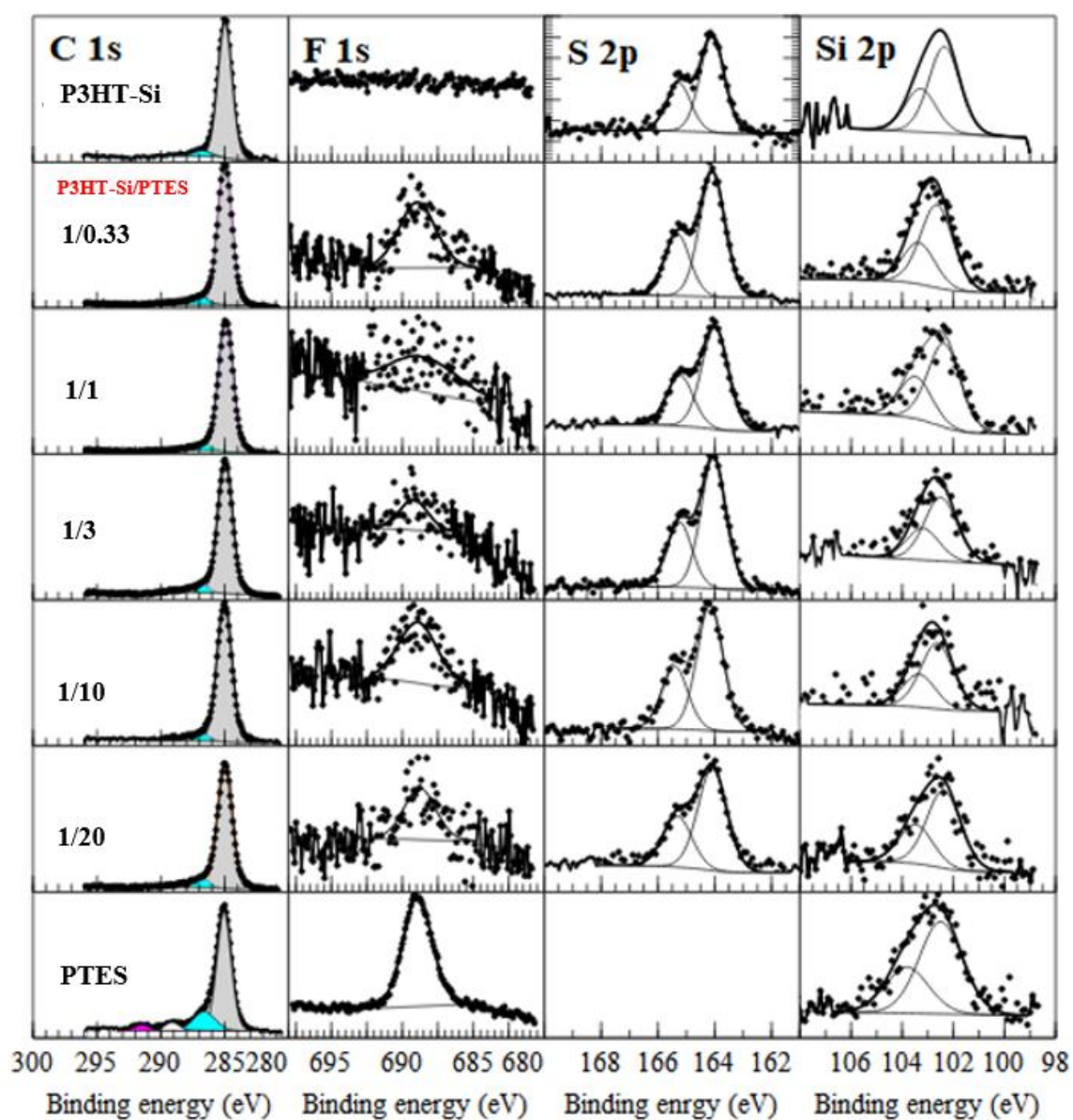


Figure IV-30: XPS spectra of ITO surfaces grafted with different SAMs solutions (1 to 7).

Table IV-14: Atomic percentages estimated by XPS for bare and grafted ITO substrates with different SAMs solutions (1 to 7).

	Elements	Bare ITO	P3HT-Si	1/0.33	1/1	1/3	1/10	1/20	PTES
atomic %	In	29.5	6.5	5.0	6.2	5.1	12.3	8.8	19.3
	Sn	3.2	0.9	0.5	0.7	0.5	1.3	0.9	2.2
	O	53.7	18.7	13.6	14.7	15.8	20.3	18.6	31.6
	C	5.8	63.3	69.9	67.4	68.1	55.8	61.7	35.1
	Si	----	4.7	3.5	2.8	3.8	4.9	3.9	3.8
	S	----	6	6.8	7.5	6.4	5.9	5.1	----
	F	----	----	0.9	0.8	0.8	1.5	1.0	8
	%F/S	----	----	0.13	0.11	0.13	0.25	0.2	----

Contact angles have been measured for the grafted ITO substrates and compared to those obtained for the bare ITO (53°). After grafting with different solutions (2 to 6), the measured angles were in the range of 90° to 99° . The hydrophobic characteristics of the grafted ITO substrates revealed the successful grafting of the SAM.

UV-vis absorption spectroscopy was also used to verify the grafting of SAMs on ITO (**Figure IV-31**). As previously explained, the intensity of absorption should be proportional to the amount of P3HT-Si grafted on the ITO substrate. In general, the intensity of absorption was increased with the increased amount of P3HT-Si initially added to the solution (from solution 7 to solution 1), except for solution 4.

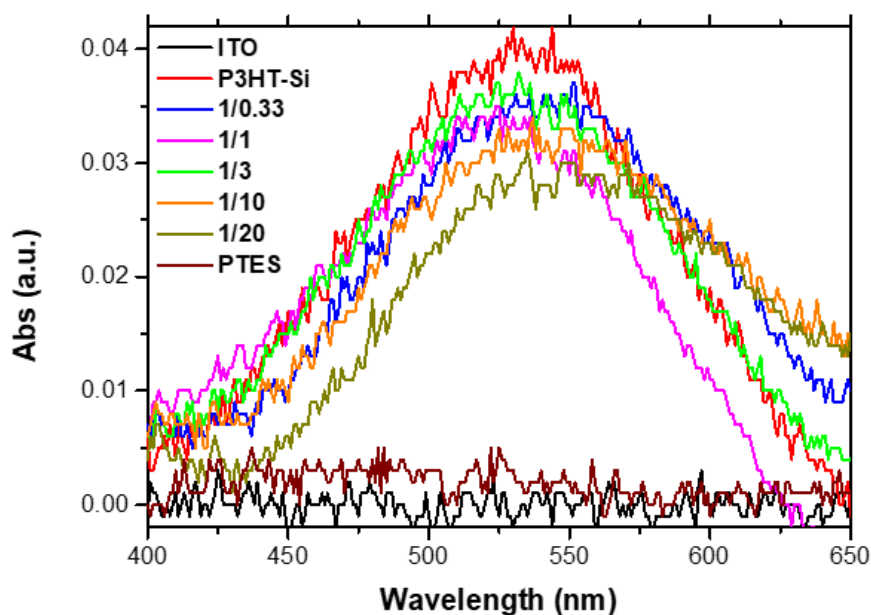


Figure IV-31: UV-vis absorption spectra of the grafted ITO substrates with different SAMs.

Figure IV-32 represents the 3D and the 1D topographic images of the ITO surface grafted with a 1:1 ratio of P3HT-Si:PTES (solution 3). The measured roughness was 1.78 nm. All the other layers grafted with different solution ratios showed the same average roughness, which is low enough for fabricating a smooth HTL.

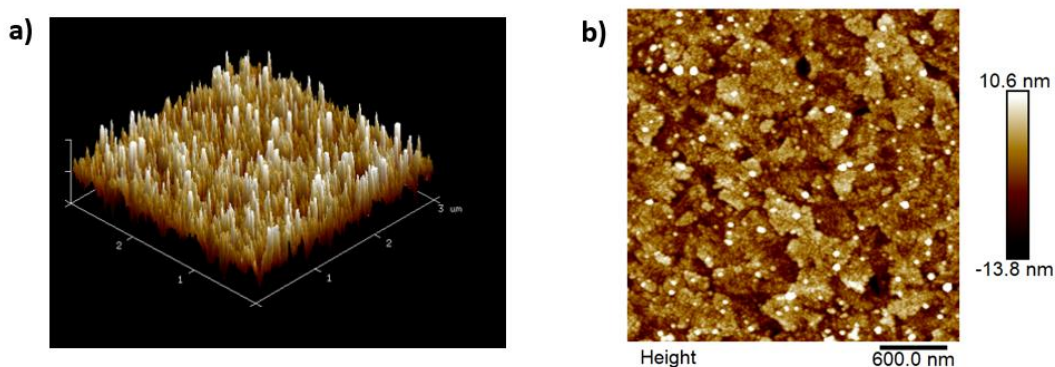


Figure IV-32: (a) 3D and (b) 1D topographic images of the ITO surface grafted with 1:1 ratio of P3HT-Si/PTES.

One of the main features for a successful HTL is its transparency to minimize the optical losses by absorption. **Figure IV-33** shows the optical transmittance spectra of bare ITO, PTES-grafted ITO and P3HT-Si grafted ITO. The transparency of the PTES-grafted ITO was similar to that of the bare ITO. However, P3HT-ITO substrate exhibited a slightly lower transparency in the visible region between 450 and 600 nm, but still acceptable to function as a HTL.

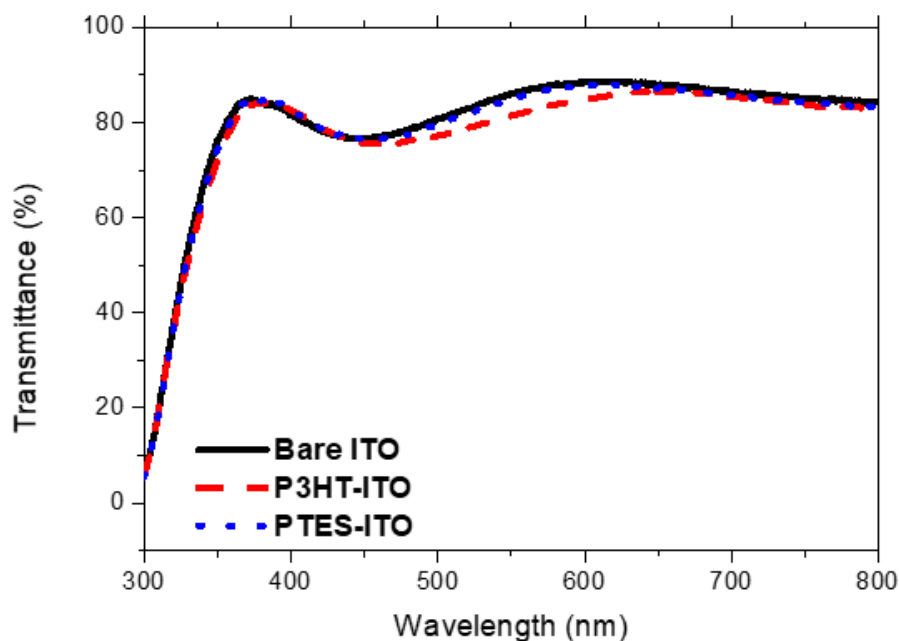


Figure IV-33: Transmission spectra of bare, PTES-grafted and P3HT-Si grafted ITO substrates.

IV. Organic solar cells

a. Device architecture and fabrication

To examine the influence of SAMs HTLs between the photoactive layer and ITO, organic solar cells using the normal device architecture were tested. The device as shown in **Figure IV-34** is consisting of ITO/grafted layer/P3HT:PC₆₀BM/Ca/Al.

In this regard, the HTLs (PTES, P3HT-Si or mixed P3HT-Si/PTES) were grafted based on the methodology previously described. Then, the modified ITO substrates have been stored in glovebox under nitrogen to avoid degradation. 180 nm-thick photoactive layers were deposited from 40 mg.mL⁻¹ P3HT:PC₆₀BM blends (1:1 weight ratio) in 1,2-dichlorobenzene, then solvent vapor annealing has been performed as previously reported.²⁹ After drying the substrates, 30 nm-thick Ca and 100 nm-thick Al were thermally evaporated on top of the photoactive layers.

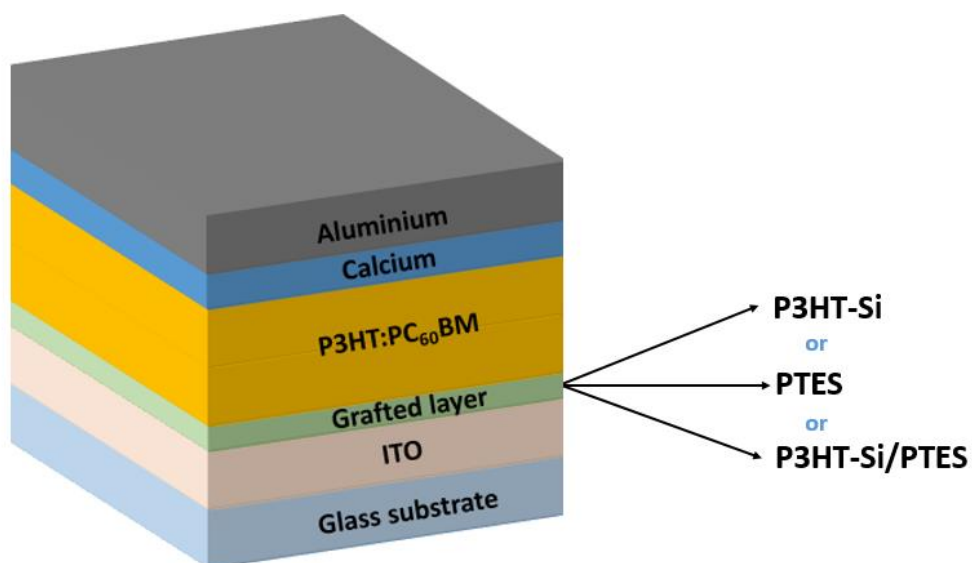


Figure IV-34: Normal device architecture of an OSC using different grafted HTLs.

In order to evaluate the efficiency of the newly used SAMs, control devices using either bare ITO or 45 nm-thick PEDOT:PSS HTL were fabricated. The thicknesses of the photoactive layers and the HTLs (PEDOT:PSS and SAMs) were measured using profilometry.

It is worth mentioning that spin-coating the photoactive blend at 800 rpm on top of the grafted ITO with mixed SAMs led to heterogeneous layers having bad compatibility with the underlying layers as shown in **Figure IV-35a**. Indeed, the fluorine coating decreases the water wettability but also the organic solvent (here 1,2 dichlorobenzene) wettability. Nevertheless, using two-steps spin-coating procedure (the first at 1000 rpm/50 seconds then at 3000 rpm/3 seconds) rendered the photoactive layers more homogenous and allowed to fully cover the grafted-ITO surfaces (**Figure IV-35b**).

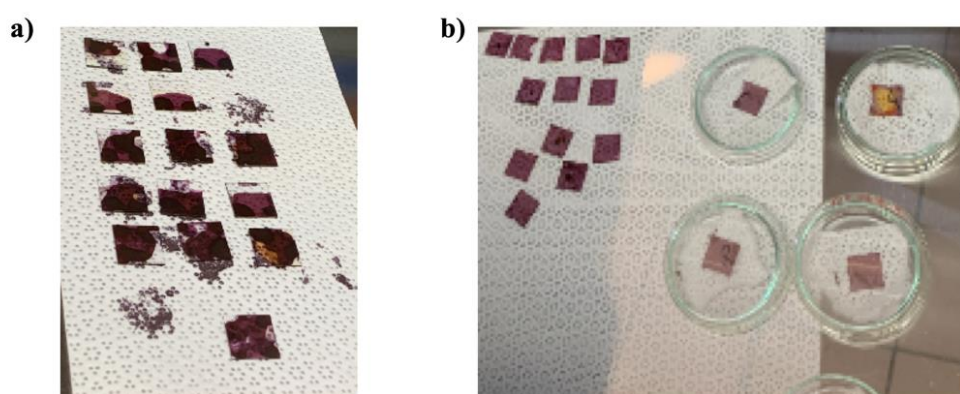


Figure IV-35: Photos of the casted photoactive layers on top of the grafted-ITO substrates (a) at 800 rpm and (b) using the two-steps process.

b. Photovoltaic performances

The efficiency of the PEDOT:PSS-based devices were first measured. In this case, PEDOT:PSS was casted on ITO substrate (4000 rpm, 60 s) and the resulting layers were annealed at 100 °C for 30 minutes. J-V curves of the reference cell are shown in **Figure IV-36a**. A maximum PCE of 2.7% was obtained, with a J_{SC} of 6.24 mA/cm², a V_{OC} of 0.64 V and a FF of 0.66. The reason beyond this low efficiency when compared to literature (3.8%)²⁹ is the low J_{SC} which could be related to the thinner photoactive layer minimizing the light absorption and thus decreasing the PCE. However, this obtained PCE is still higher than that obtained using a bare ITO (1.34%) represented by the J-V curve in **Figure IV-36b**. This low PCE was accompanied with a low V_{OC} (0.53 V) and FF (0.4) which could be attributed to the low WF of the bare ITO (4.7 eV) when compared to that with PEDOT:PSS (5.1 eV) as determined by Kelvin probe measurements. This low WF along with the absence of a selective hole transport material were responsible for the formation of a charge barrier in the interface of the ITO/photoactive layer, thus limiting the hole extraction efficiency.¹³

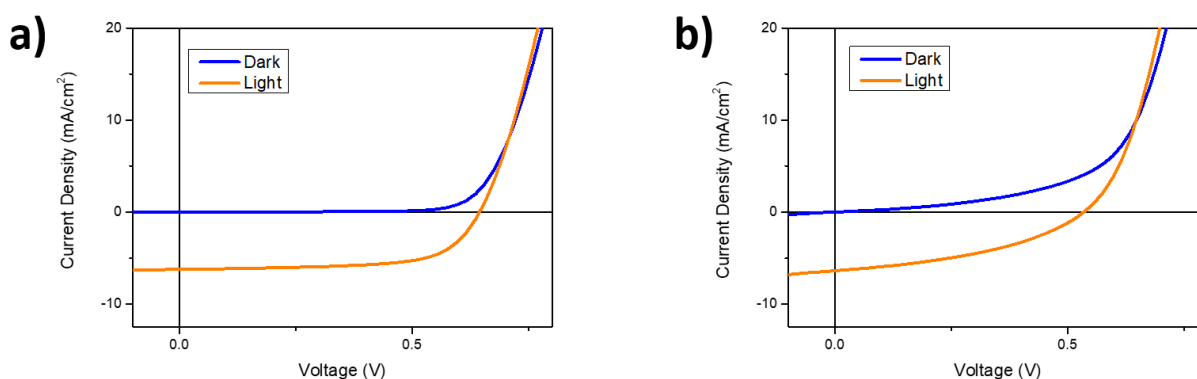


Figure IV-36: J-V curves of the P3HT:PC₆₀BM-based normal devices using (a) PEDOT:PSS HTL or (b) bare ITO.

PEDOT:PSS HTL has been replaced by the different SAM solutions that include P3HT-Si (solution 1), PTES (solution 7) and the mixed solutions having different ratios of P3HT-Si/PTES (solutions 2 to 6). The J-V curves of the fabricated normal device structures are shown in **Figure IV-37** and the photovoltaic parameters are summarized in **Table IV-7**.

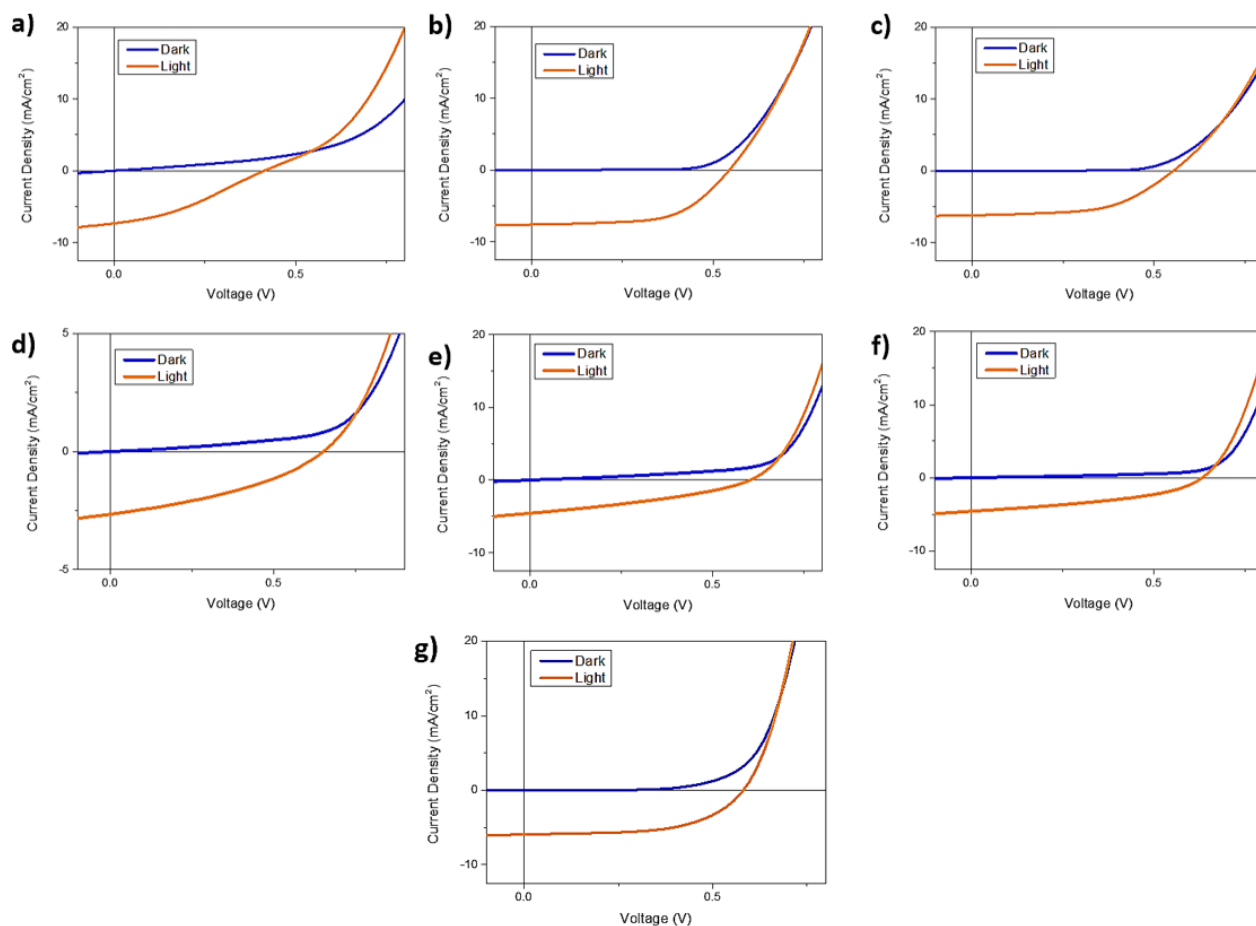


Figure IV-37: J-V curves of the P3HT:PC₆₀BM-based normal devices using P3HT-Si (a), P3HT-Si/PTES= (b) 1/0.33, (c) 1/1, (d) 1/3, (e) 1/10, (f) 1/20 and PTES (g) as hole transport materials.

Table IV-15: Thicknesses and WF of the different HTLs with a summary of photovoltaic parameters of the P3HT:PC₆₀BM-based normal devices using the corresponding HTLs.

HTL	HTL thickness (nm)	WF (eV)	J _{sc} (mA/cm ²)	V _{oc} (V)	FF	PCE (%)	R _{sh} (Kohm)	R _s (ohm)
Sln 1: 1/0	20	4.55	7.3	0.41	0.39	1.17	9.1x10 ⁻¹	1.7x10 ³
Sln 2: 1/0.33	18	4.81	7.5	0.54	0.37	1.50	2.8x10 ⁻¹	4.5x10 ⁴
Sln 3: 1/1	20	4.85	6.19	0.55	0.30	1.02	4.7x10 ⁻¹	2x10 ⁵
Sln 4: 1/3	20	5.02	2.6	0.65	0.36	0.60	7.61	2x10 ²
Sln 5: 1/10	22	4.9	4.55	0.60	0.34	0.93	3.1	5.2x10 ¹
Sln 6: 1/20	20	4.92	4.5	0.63	0.41	1.16	7.02	4.7 x10 ¹
Sln 7: 0/1	15	4.85	5.96	0.58	0.57	2	2.1x10 ¹	2.4x10 ¹
ITO	-----	4.7	6.3	0.53	0.4	1.34	5.7x10 ⁻¹	2.6x10 ¹
PEDOT:PSS	45	5.1	6.24	0.64	0.66	2.7	1.8x10 ¹	3.6x10 ¹

A large dispersion of the device performances was observed and rendered the impact of ITO functionalization complicated. We attributed it to poor wetting of the solution onto the substrates and the formation of pinholes. This leads to a lot of variations and problems in the devices (defects, leakage currents...) that will probably lower device performances. In general, the surface modification by SAM can lead to some changes in the morphology of the photoactive layers which will eventually modify the J_{SC} generated. Nevertheless, it can be deduced from the photovoltaic parameters that the more PTES was added to the SAM mixture, the higher is the V_{OC} until reaching a maximum value of 0.65 V using solution 4 (1/3 P3HT-Si/PTES). This V_{OC} is close to that obtained using PEDOT:PSS HTLs. In general, PTES was added for the aim of increasing the WF of ITO. The results show that the WF of ITO was increased by increasing the PTES content in the SAM mixture, causing this V_{OC} change, until reaching a maximum WF of 5.02 eV using solution 4 which is close to that obtained using PEDOT:PSS (5.1 eV). Thus, the change in V_{OC} can be correlated to the ITO WF modification. The more suitable WF, the easier is the charge extraction, the higher the V_{OC} . On the contrary, the lower V_{OC} observed could be attributed to the energy level mismatch between the grafted-ITO WF (which is lower than that of ITO-PEDOT:PSS) and the HOMO level of P3HT.

In some cases, the devices with SAM molecules out-performed the devices with bare ITO, however still lower than that obtained using PEDOT:PSS. The highest PCE obtained was 2% corresponding to a simple 15 nm-thick PTES-grafted layer. This low PCE is due to lower photovoltaic parameters when compared to PEDOT:PSS-based devices. The losses in FF could be attributed to the low conductivity of the SAM HTLs, caused by their high layer thickness (around 20 nm).

When mixing PTES with P3HT-Si, the highest efficiency obtained was 1.50% using an 18 nm-thick HTL of solution 2 (1/0.33 P3HT-Si/PTES). It was observed that the FF was higher for the PTES-based devices. This could be attributed to the better series and shunt resistances as can be seen from the J-V curves in **Figure IV-37g** and the values in **Table IV-7**. Another probable reason is the better layer morphology of the PTES when compared to the mixed SAM layers that could contain pinholes and some aggregates. Thus, in general, the low conductivity and the thickness of the mixed grafted layers prevent its optimization to reach the high performance observed with PEDOT:PSS HTLs.

V. Conclusion

SAM molecules have been used to modify the ITO work function and hydrophobicity. PTES, P3HT-Si or P3HT-Si/PTES modified-ITO substrates were prepared. These modified surfaces were characterized by several techniques that prove the successful grafting of these SAM molecules on top of ITO. From the XPS measurements, elements corresponding to the grafted molecules have been found. Although low roughness was maintained upon grafting (< 2 nm), the surfaces become more hydrophobic upon the attachment of SAM molecules. Despite the successful grafting, using these SAMs as PEDOT:PSS alternatives in P3HT:PC₆₀BM-based normal device structures did not bring any improvement in terms of efficiency as the highest PCE obtained was with PTES solution (2%). This PCE was lower than that obtained using PEDOT:PSS (2.7%) but higher than that using bare ITO (1.34%). In general, the low conductivity and the thickness of the mixed grafted layers limited the device performances. Thus, as a perspective, the low mobility and poor charge transport in the mixed SAM layers could be addressed *via* doping such interfacial layers as previously reported by Yang et al.³⁹ In addition, the photoactive layers faced wettability problems when deposited onto the SAMs layers in which they were not fully optimized due to the time shortage. Future work will be dedicated to optimize the SAMs layers and to modify the parameters for depositing the photoactive layers in order to improve their morphology and enhance device performances.

References

- (1) Sun, H.; Chen, F.; Chen, Z.-K. Recent Progress on Non-Fullerene Acceptors for Organic Photovoltaics. *Mater. Today* **2019**, *24*, 94–118.
- (2) Dkhil, S. B.; Pfannmöller, M.; Bals, S.; Koganezawa, T.; Yoshimoto, N.; Hannani, D.; Gaceur, M.; Videlot-Ackermann, C.; Margeat, O.; Ackermann, J. Square-Centimeter-Sized High-Efficiency Polymer Solar Cells: How the Processing Atmosphere and Film Quality Influence Performance at Large Scale. *Adv. Energy Mater.* **2016**, *6* (13), 1600290.
- (3) Zhang, H.; Yao, H.; Hou, J.; Zhu, J.; Zhang, J.; Li, W.; Yu, R.; Gao, B.; Zhang, S.; Hou, J. Over 14% Efficiency in Organic Solar Cells Enabled by Chlorinated Nonfullerene Small-Molecule Acceptors. *Adv. Mater. Deerfield Beach Fla* **2018**, *30* (28), e1800613.
- (4) Chueh, C.-C.; Li, C.-Z.; Jen, A. K.-Y. Recent Progress and Perspective in Solution-Processed Interfacial Materials for Efficient and Stable Polymer and Organometal Perovskite Solar Cells. *Energy Environ. Sci.* **2015**, *8* (4), 1160–1189.
- (5) Yip, H.-L.; Jen, A. K.-Y. Recent Advances in Solution-Processed Interfacial Materials for Efficient and Stable Polymer Solar Cells. *Energy Environ. Sci.* **2012**, *5* (3), 5994–6011.
- (6) Po, R.; Carbonera, C.; Bernardi, A.; Camaioni, N. The Role of Buffer Layers in Polymer Solar Cells. *Energy Environ. Sci.* **2011**, *4* (2), 285–310.
- (7) Liu, Q.; Jiang, Y.; Jin, K.; Qin, J.; Xu, J.; Li, W.; Xiong, J.; Liu, J.; Xiao, Z.; Sun, K.; Yang, S.; Zhang, X.; Ding, L. 18% Efficiency Organic Solar Cells. *Sci. Bull.* **2020**, *65* (4), 272–275.
- (8) Kawano, K.; Pacios, R.; Poplavskyy, D.; Al-Hashimi, M.; Bradley, D.; Durrant, J. Degradation of Organic Solar Cells Due to Air Exposure. *Sol. Energy Mater. Sol. Cells - Sol. ENERG MATER Sol. CELLS* **2006**, *90*, 3520–3530.
- (9) Savagatrup, S.; Printz, A. D.; O'Connor, T. F.; Zaretski, A. V.; Rodriguez, D.; Sawyer, E. J.; Rajan, K. M.; Acosta, R. I.; Root, S. E.; Lipomi, D. J. Mechanical Degradation and Stability of Organic Solar Cells: Molecular and Microstructural Determinants. *Energy Environ. Sci.* **2014**, *8* (1), 55–80.
- (10) Voroshazi, E.; Verreet, B.; Buri, A.; Müller, R.; Di Nuzzo, D.; Heremans, P. Influence of Cathode Oxidation via the Hole Extraction Layer in Polymer:Fullerene Solar Cells. *Org. Electron.* **2011**, *12* (5), 736–744.
- (11) Lloyd, M. T.; Olson, D. C.; Lu, P.; Fang, E.; Moore, D. L.; White, M. S.; Reese, M. O.; Ginley, D. S.; Hsu, J. W. P. Impact of Contact Evolution on the Shelf Life of Organic Solar Cells. *J. Mater. Chem.* **2009**, *19* (41), 7638–7642.
- (12) You, H.; Dai, L.; Zhang, Q.; Chen, D.; Jiang, Q.; Zhang, C. Enhanced Performance of Inverted Non-Fullerene Organic Solar Cells by Using Metal Oxide Electron- and Hole-Selective Layers with Process Temperature ≤ 150 °C. *Polymers* **2018**, *10* (7), 725.
- (13) Mihalechi, V. D.; Blom, P. W. M.; Hummelen, J. C.; Rispen, M. T. Cathode Dependence of the Open-Circuit Voltage of Polymer:Fullerene Bulk Heterojunction Solar Cells. *J. Appl. Phys.* **2003**, *94* (10), 6849–6854.
- (14) Miozzo, L.; Yassar, A.; Horowitz, G. Surface Engineering for High Performance Organic Electronic Devices: The Chemical Approach. *J. Mater. Chem.* **2010**, *20* (13), 2513–2538.
- (15) Hu, T.; Zhang, F.; Xu, Z.; Zhao, S.; Yue, X.; Yuan, G. Effect of UV–Ozone Treatment on ITO and Post-Annealing on the Performance of Organic Solar Cells. *Synth. Met.* **2009**, *159* (7–8), 754–756.
- (16) Sharma, A.; Haldi, A.; Jr, W. J. P.; Hotchkiss, P. J.; Marder, S. R.; Kippelen, B. Effects of Surface Modification of Indium Tin Oxide Electrodes on the Performance of Molecular Multilayer Organic Photovoltaic Devices. *J. Mater. Chem.* **2009**, *19* (30), 5298–5302.
- (17) Tu, K.-H.; Li, S.-S.; Li, W.-C.; Wang, D.-Y.; Yang, J.-R.; Chen, C.-W. Solution Processable Nanocarbon Platform for Polymer Solar Cells. *Energy Environ. Sci.* **2011**, *4* (9), 3521–3526.
- (18) Zilberberg, K.; Trost, S.; Schmidt, H.; Riedl, T. Solution Processed Vanadium Pentoxide as Charge Extraction Layer for Organic Solar Cells. *Adv. Energy Mater.* **2011**, *1* (3), 377–381.
- (19) Zilberberg, K.; Gharbi, H.; Behrendt, A.; Trost, S.; Riedl, T. Low-Temperature, Solution-Processed MoO_x for Efficient and Stable Organic Solar Cells. *ACS Appl. Mater. Interfaces* **2012**, *4* (3), 1164–1168.
- (20) Yin, Z.; Wei, J.; Zheng, Q. Interfacial Materials for Organic Solar Cells: Recent Advances and Perspectives. *Adv. Sci.* **2016**, *3* (8), 1500362.
- (21) Ma, H.; Yip, H.-L.; Huang, F.; Jen, A. K.-Y. Interface Engineering for Organic Electronics. *Adv. Funct. Mater.* **2010**, *20* (9), 1371–1388.
- (22) Knesting, K. M.; Ju, H.; Schlenker, C. W.; Giordano, A. J.; Garcia, A.; Smith, O. L.; Olson, D. C.; Marder, S. R.; Ginger, D. S. ITO Interface Modifiers Can Improve VOC in Polymer Solar Cells and Suppress Surface Recombination. *J. Phys. Chem. Lett.* **2013**, *4* (23), 4038–4044.

- (23) Vaynzof, Y.; Kabra, D.; Zhao, L.; Ho, P. K. H.; Wee, A. T.-S.; Friend, R. H. Improved Photoinduced Charge Carriers Separation in Organic-Inorganic Hybrid Photovoltaic Devices. *Appl. Phys. Lett.* **2010**, *97* (3), 033309.
- (24) Whitesides, G. M.; Grzybowski, B. Self-Assembly at All Scales. *Science* **2002**, *295* (5564), 2418–2421.
- (25) Casalini, S.; Bortolotti, C. A.; Leonardi, F.; Biscarini, F. Self-Assembled Monolayers in Organic Electronics. *Chem. Soc. Rev.* **2017**, *46* (1), 40–71.
- (26) Koch, N. Energy Levels at Interfaces between Metals and Conjugated Organic Molecules. *J. Phys. Condens. Matter* **2008**, *20* (18), 184008.
- (27) de Boer, B.; Hadipour, A.; Mandoc, M. M.; van Woudenberg, T.; Blom, P. W. M. Tuning of Metal Work Functions with Self-Assembled Monolayers. *Adv. Mater.* **2005**, *17* (5), 621–625.
- (28) Tada, A.; Geng, Y.; Nakamura, M.; Wei, Q.; Hashimoto, K.; Tajima, K. Interfacial Modification of Organic Photovoltaic Devices by Molecular Self-Organization. *Phys. Chem. Chem. Phys.* **2012**, *14* (11), 3713–3724.
- (29) Awada, H.; Mattana, G.; Tournebize, A.; Rodriguez, L.; Flahaut, D.; Vellutini, L.; Lartigau-Dagron, C.; Billon, L.; Bousquet, A.; Chambon, S. Surface Engineering of ITO Electrode with a Functional Polymer for PEDOT:PSS-Free Organic Solar Cells. *Org. Electron.* **2018**, *57*, 186–193.
- (30) Tran, E.; Duati, M.; Ferri, V.; Müllen, K.; Zharnikov, M.; Whitesides, G. M.; Rampi, M. A. Experimental Approaches for Controlling Current Flowing through Metal–Molecule–Metal Junctions. *Adv. Mater.* **2006**, *18* (10), 1323–1328.
- (31) Ulman, A. Formation and Structure of Self-Assembled Monolayers. *Chem. Rev.* **1996**, *96* (4), 1533–1554.
- (32) Yalcin, E.; Can, M.; Rodriguez-Seco, C.; Aktas, E.; Pudi, R.; Cambarau, W.; Demic, S.; Palomares, E. Semiconductor Self-Assembled Monolayers as Selective Contacts for Efficient PiN Perovskite Solar Cells. *Energy Environ. Sci.* **2019**, *12* (1), 230–237.
- (33) Heo, S. W.; Lee, E. J.; Seong, K. W.; Moon, D. K. Enhanced Stability in Polymer Solar Cells by Controlling the Electrode Work Function via Modification of Indium Tin Oxide. *Sol. Energy Mater. Sol. Cells* **2013**, *115*, 123–128.
- (34) Huang, L.-C.; Liu, H.-W.; Liang, C.-W.; Chou, T.-R.; Wang, L.; Chao, C.-Y. Self-Assembled Multilayers of Modified ITO in Polymer Solar Cells by Soft-Imprinting. *Soft Matter* **2012**, *8* (5), 1467–1472.
- (35) Choi, H.; Kim, H.-B.; Ko, S.-J.; Kim, J. Y.; Heeger, A. J. An Organic Surface Modifier to Produce a High Work Function Transparent Electrode for High Performance Polymer Solar Cells. *Adv. Mater.* **2015**, *27* (5), 892–896.
- (36) Panneerselvam, M.; Kathiravan, A.; Solomon, R. V.; Jaccob, M. The Role of π -Linkers in Tuning the Optoelectronic Properties of Triphenylamine Derivatives for Solar Cell Applications – A DFT/TDDFT Study. *Phys. Chem. Chem. Phys.* **2017**, *19* (8), 6153–6163.
- (37) Magomedov, A.; Al-Ashouri, A.; Kasparavičius, E.; Strazdaite, S.; Niaura, G.; Jošt, M.; Malinauskas, T.; Albrecht, S.; Getautis, V. Self-Assembled Hole Transporting Monolayer for Highly Efficient Perovskite Solar Cells. *Adv. Energy Mater.* **2018**, *8* (32), 1801892.
- (38) Wang, H.; Gomez, E. D.; Guan, Z.; Jaye, C.; Toney, M. F.; Fischer, D. A.; Kahn, A.; Loo, Y.-L. Tuning Contact Recombination and Open-Circuit Voltage in Polymer Solar Cells via Self-Assembled Monolayer Adsorption at the Organic–Metal Oxide Interface. *J. Phys. Chem. C* **2013**, *117* (40), 20474–20484.
- (39) Yang, L.; Sontag, S. K.; LaJoie, T. W.; Li, W.; Huddleston, N. E.; Locklin, J.; You, W. Surface-Initiated Poly(3-Methylthiophene) as a Hole-Transport Layer for Polymer Solar Cells with High Performance. *ACS Appl. Mater. Interfaces* **2012**, *4* (10), 5069–5073.
- (40) Lattante, S. Electron and Hole Transport Layers: Their Use in Inverted Bulk Heterojunction Polymer Solar Cells. *Electronics* **2014**, *3* (1), 132–164.
- (41) Kim, J. S.; Park, J. H.; Lee, J. H.; Jo, J.; Kim, D.-Y.; Cho, K. Control of the Electrode Work Function and Active Layer Morphology via Surface Modification of Indium Tin Oxide for High Efficiency Organic Photovoltaics. *Appl. Phys. Lett.* **2007**, *91* (11), 112111.
- (42) Langeveld-Voss, B. M. W.; Janssen, R. A. J.; Spiering, A. J. H.; Dongen, J. L. J. van; Vonk, E. C.; Claessens, H. A. End-Group Modification of Regioregular Poly(3-Alkylthiophene)s. *Chem. Commun.* **2000**, No. 1, 81–82.
- (43) Liu, J.; McCullough, R. D. End Group Modification of Regioregular Polythiophene through Postpolymerization Functionalization. *Macromolecules* **2002**, *35* (27), 9882–9889.
- (44) Jeffries-El, M.; Sauvé, G.; McCullough, R. D. Facile Synthesis of End-Functionalized Regioregular Poly(3-Alkylthiophene)s via Modified Grignard Metathesis Reaction. *Macromolecules* **2005**, *38* (25), 10346–10352.
- (45) Zhang, Q.; Russell, T. P.; Emrick, T. Synthesis and Characterization of CdSe Nanorods Functionalized with Regioregular Poly(3-Hexylthiophene). *Chem. Mater.* **2007**, *19* (15), 3712–3716.

- (46) Osaka, I.; McCullough, R. D. Advances in Molecular Design and Synthesis of Regioregular Polythiophenes. *Acc. Chem. Res.* **2008**, *41* (9), 1202–1214.
- (47) Marciniak, B. *Comprehensive Handbook on Hydrosilylation*; Elsevier, 2013.
- (48) Awada, H.; Medlej, H.; Blanc, S.; Delville, M.-H.; Hiorns, R. C.; Bousquet, A.; Dagon-Lartigau, C.; Billon, L. Versatile Functional Poly(3-Hexylthiophene) for Hybrid Particles Synthesis by the Grafting onto Technique: Core@shell ZnO Nanorods. *J. Polym. Sci. Part Polym. Chem.* **2014**, *52* (1), 30–38.
- (49) Anagnostou, K.; Stylianakis, M. M.; Petridis, K.; Kymakis, E. Building an Organic Solar Cell: Fundamental Procedures for Device Fabrication. *Energies* **2019**, *12* (11), 2188.
- (50) Hines, C. J.; Roberts, J. L.; Andrews, R. N.; Jackson, M. V.; Daddens, J. A. Use of and Occupational Exposure to Indium in the United States. *J. Occup. Environ. Hyg.* **2013**, *10* (12), 723–733.
- (51) Pujilaksono, B.; Klement, U.; Nyborg, L.; Jelvestam, U.; Hill, S.; Burgard, D. X-Ray Photoelectron Spectroscopy Studies of Indium Tin Oxide Nanocrystalline Powder. *Mater. Charact.* **2005**, *54* (1), 1–7.
- (52) Wu, L.; Cai, L.; Liu, A.; Wang, W.; Yuan, Y.; Li, Z. Self-Assembled Monolayers of Perfluoroalkylsilane on Plasma-Hydroxylated Silicon Substrates. *Appl. Surf. Sci.* **2015**, *349*, 683–694.
- (53) Zhang, F.; Chen, S.; Dong, L.; Lei, Y.; Liu, T.; Yin, Y. Preparation of Superhydrophobic Films on Titanium as Effective Corrosion Barriers. *Appl. Surf. Sci.* **2011**, *257* (7), 2587–2591.
- (54) Moulder, J. F. *Handbook of X-Ray Photoelectron Spectroscopy: A Reference Book of Standard Spectra for Identification and Interpretation of XPS Data*; Physical Electronics Division, Perkin-Elmer Corporation, 1992.
- (55) Rahimi, K.; Botiz, I.; O. Agumba, J.; Motamen, S.; Stingelin, N.; Reiter, G. Light Absorption of Poly(3-Hexylthiophene) Single Crystals. *RSC Adv.* **2014**, *4* (22), 11121–11123.

Chapter V:
**Synthesis of Hybrid Block
Copolymers Based on
Polypeptide Segment**

I. Introduction

As previously mentioned, conjugated polymers have been widely experienced in the recent years due to their wide range of advanced applications including OPVs.¹ The main challenge is still the ability to control the organization of the active materials on length scales needed for charge separation. Therefore, efforts were oriented toward merging homopolymers into block copolymers while combining the desired self-assembly properties with the useful electronic properties, thus affording controlled and highly ordered morphologies.² Accordingly, several rod-coil block copolymers were synthesized consisting of a conjugated polymer block with another block used in guiding self-assembly.³ However, the analogue rod-rod block copolymers were less studied due to their synthetic challenges and the unclear effect of replacing the flexible segment with a rigid segment on self-assembly.⁴ In this regard, it was reported that the tendency of a rigid-rod segment to self-organize eventually leads to distinct morphologies than the one obtained from rod-coil block copolymers.⁵

Among the interesting topics in the last decades is the investigation of polypeptide hybrid copolymers that contain polypeptide segment and another π -conjugated polymer.^{6,7} Generally, polypeptides are chains of amino acids and essential portions of proteins in cells. The novel hybrid block copolymer architecture can exhibit both, rod-rod or rod-coil conformations by the transformation of the helix rod-to-coil transition of polypeptides. As it was stated in the literature, these hybrid block copolymers are expected to improve the interaction between the electro and photoactive block (π -conjugated polymer) and biomolecules (thanks to the polypeptide blocks) while facilitating dispersion and self-assembly in water.⁸

This opened the way to attractive possible applications of these hybrid block copolymers in different domains including drug and gene delivery,⁹ tissue engineering,¹⁰ biosensing¹¹ and nanoelectronics.

In general, polypeptides are known for their ability to fold into well-ordered secondary structures as rod-like α -helices or β -sheets as shown in **Figure V-1**.¹² The secondary structure formation corresponds to local organization of amino acids, creating structured segments along the peptide backbone. As defined, an α -helix is a rod-like structure in which a tightly coiled main chain formed its inner section. In such a structure, the side chains extend outward in a helical array. On the other hand, the main chain of a β -sheet is fully extended rather than tightly coiled, in which the side chains of the adjacent amino acids point in opposite directions. Previously, several studies showed that the tendency of amino acids to form one of the secondary structures is dependent on the combination of the influence of their lateral chain function and some environmental factors (solvent, pH, temperature...¹²

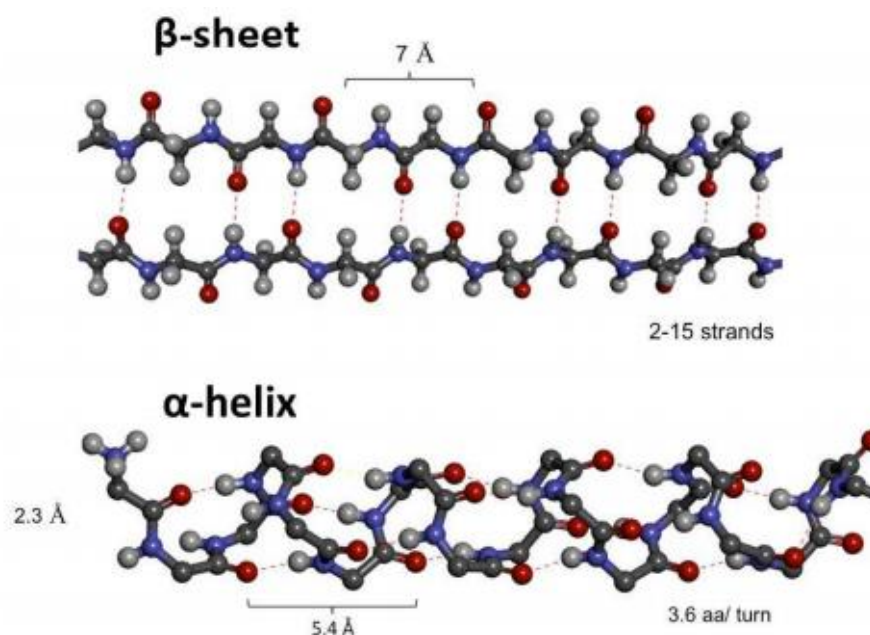


Figure V-1: Molecular modelling of the two main secondary structures found within polypeptides.¹²

It is worth mentioning that polypeptides synthesized by ring-opening polymerization (ROP) can maintain in certain cases an amino group at the end of the polymeric chain which could give a possibility for further functionalizations.¹³

Poly(γ -benzyl-*L*-glutamate) (PBLG) is one of the widely studied polypeptides which could be easily synthesized by ROP of *N*-carboxyanhydrides (NCA) derived from γ -benzyl-*L*-glutamate (**Figure V-2**). The design of block copolymers incorporating a PBLG segment is generally done using amino-functionalized macroinitiator.¹⁴ It is well known that the PBLG can form a rigid-rod like conformation at a specific degree of polymerization in which it is stabilized by intramolecular hydrogen bonds.¹⁵ Indeed, PBLG generally gives rise to a rigid rod-like α -helical conformation in both water and organic solvents and that has often been employed as a model system to drive lamellar morphologies.¹⁶ Moreover, PBLG can go from α -helix to coil conformation transition by the effect of external stimuli such as heat, solvent... These transitions being employed in smart materials for biomedical applications.¹⁷

Several studies already showed the possibility of incorporating PBLG as a directing component in block copolymers. PBLG-based block copolymers are known to self-assemble forming micellar or vesicular aggregates.¹⁸ As defined, micelles are nanoparticles made up of a hydrophobic core and a hydrophilic shell. In this regard, series of hybrid triblock copolymers consisting of poly(9,9-dihexylfluorene-2,7-diyl) (PHF) as a middle block and two poly(γ -benzyl-*L*-glutamate) (PBLG) end blocks with different block ratios were previously designed and investigated.^{8,19} It was stated that the α -helical secondary structure of the PBLG block may be either maintained or suppressed based on the solvent casting history. Thus, the hybrid triblock copolymers exhibit two different conformations: a rod-rod-rod or coil-rod-coil configuration, respectively as a result of a rod-to-coil transition of the polypeptide helices.¹⁹ Since these triblock copolymers are expected to enhance the interaction between the electro and photoactive blocks with biomolecules, applications including biosensors²⁰ or wires for delivering electrical stimuli to influence cell growth and morphology²¹ can be targeted.

In addition to polypeptides made of γ -benzyl-*L*-glutamate (BLG) units, polypeptides made of trifluoroacetyl-*L*-lysine (TFA-Lys) (**Figure V-2**) were also widely used for the preparation of "rod"-like polypeptides *via* NCA ring-opening polymerization.

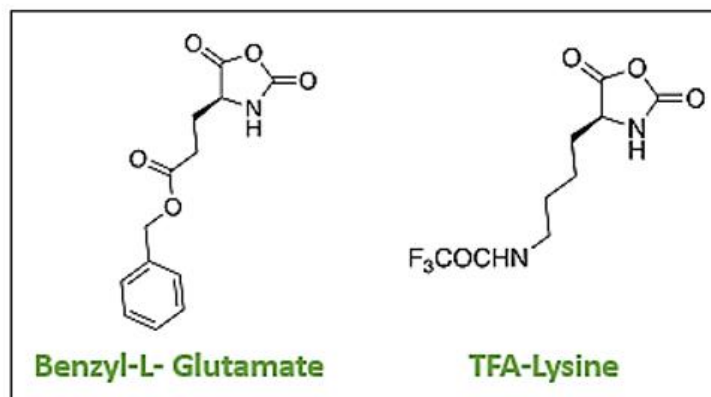


Figure V-2: Chemical structures of BLG and TFA-Lys-based monomers.

It is important to note that the trifluoroacetyl-*L*-lysine side chains or the γ -benzyl-*L*-glutamate side chains are both functional groups that can be hydrolyzed using orthogonal conditions (either *via* hydrogenation, under acidic and/or basic conditions) to afford poly(*L*-Lysine) (**P(Lys)**) and poly(*L*-glutamic acid) (**P(GA)**), respectively. Such polypeptides are interesting in a way that they are water soluble and are used to enable a structuring switch upon biologically relevant stimuli changes including metal coordination and pH (metal and pH responsiveness).²² In general, the design of hybrid materials incorporating unprotected side-chains should take into consideration these reaction conditions that may pose some restrictions on the choice of the non-biological segment.²³

a. Traditional methods for NCA polymerizations

NCA is a simple C-activated α -amino acid derivative that provides high electrophilic reactivity at the carbonyl group of the α -amino acid as shown in **Figure V-3**. In general, this cyclic anhydride group gives the NCA a high reactivity with various nucleophiles.

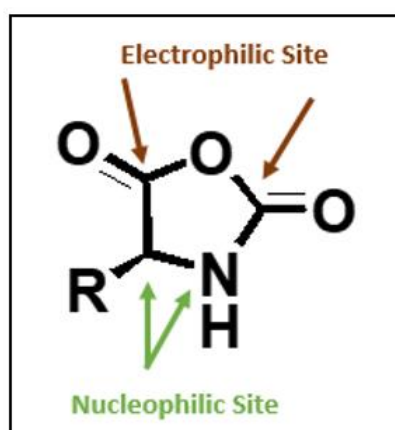
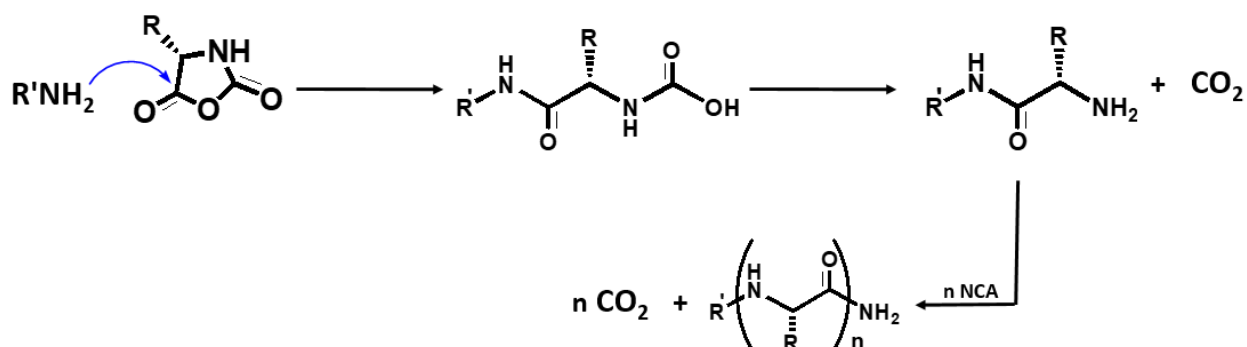


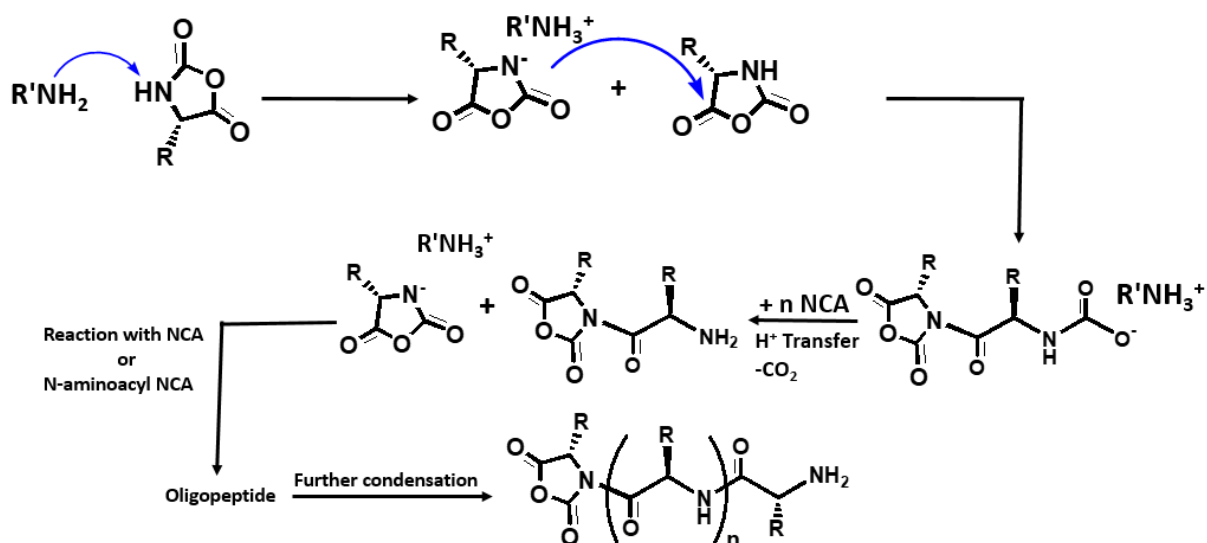
Figure V-3: The chemical structure of a NCA α -amino acid.

The initiation of NCA polymerizations can be performed using different nucleophiles and bases. As primary amines are more nucleophilic than basic, they are widely used as good initiators for NCA polymerizations. In general, NCA reaction with nucleophiles is considered to be clean and leads to only carbon dioxide as a byproduct. Regarding this amine promoted pathway, it is considered as a nucleophilic ring opening chain growth polymerization in which the polymer can eventually grow linearly with the monomer conversion if there are no side reactions. After the ring opens, carbon dioxide molecule is cleaved and a monomer unit is formed. This monomer is capable of propagating the corresponding polymerization through its amine function. The general mechanism of the ring opening polymerization was previously reported and illustrated in **Scheme V-1**.²⁴



*Scheme V-1: The amine nucleophilic ring opening mechanism; NCA polymerization.*²⁴

On another hand, tertiary amines, alkoxides and other initiators that are more basic than nucleophilic can be also used and are in some cases able to prepare very high molar mass polymers which primary amine initiators cannot do. In this second mechanism, called the activated monomer mechanism, the polymerization is initiated by the deprotonation of the first NCA monomer which in its turn becomes the nucleophile that initiates the chain growth (**Scheme V-2**).²⁴



*Scheme V-2: The activated monomer mechanism; NCA polymerization.*²⁴

It is worth mentioning that for a studied system, the polymerization can switch between amine and activated monomer mechanism many times during the polymerization. Thus, a propagation step for one type mechanism is the side reaction of the other type. A major problem in such traditional NCA polymerization arises from the lack of control over the reactivity of the growing polymer chain-ends, resulting in side products.²⁴ Generally, there is no universal initiators or conditions that have been stated for an optimal polymerization. Rather, optimization is related to the different properties of individual NCAs and the corresponding polymers such as solubility. It is also related to the side reactions that may take place during polymerization.²⁴ So far, to build hybrid diblock copolymers, the most likely pathway for NCA polymerization is the amine (nucleophilic) monomer mechanism.^{25,26}

b. Polypeptide-based block copolymers

It was previously denoted the possibility of synthesizing block copolymers by using macroinitiators functionalized with primary amine. For example, PBLG-*b*-PHF-*b*-PBLG block copolymer was the first hybrid diblock published containing a π -conjugated polymer, poly(9,9-dihexylfluorene-2,7-diyl) (PHF) and a PBLG polypeptide chain.⁸ It was synthesized by ring-opening polymerization of the γ -Benzyl-*L*-glutamate *N*-carboxyanhydride (BLG-NCA) using benzylamine end-functionalized polyfluorene macroinitiators as shown in **Figure V-4**. It has been shown that different assemblies made of these block copolymers were obtained with morphologies influenced by the block copolymer composition and the secondary structure (helix or coil) of the polypeptide blocks.⁸

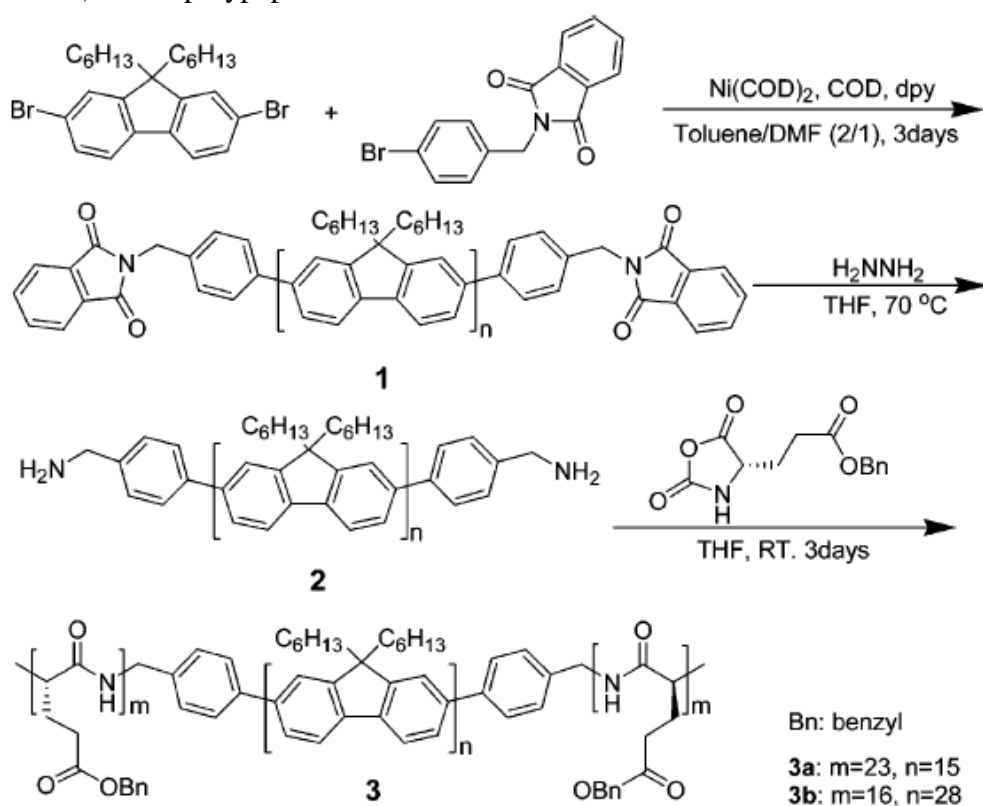


Figure V-4: Synthetic route of the hybrid block copolymer PBLG-*b*-PHF-*b*-PBLG.⁸

A series of polythiophene-polypeptide rod-rod diblock copolymers (P3HT-*b*-PBLG) have also been investigated.^{27,25} One of the synthetic strategies to prepare P3HT-*b*-PBLG was based on Huisgen cycloaddition to graft ethynyl-terminated P3HT with an azide-terminated PBLG (prepared separately using 1-azido-3-aminopropane as the initiator) as shown in **Figure V-5a**. In this study, the self-assembly behavior of the hybrid block copolymer P3HT-*b*-PBLG was investigated in solution and in solid state. In this framework, the slow addition of DMF into a THF solution of the diblock polymer induced a color change indicating P3HT aggregation. The Transmission Electron Microscopic (TEM) analysis of the resulting aggregation revealed the formation of spherical particles (nanostructures) with an average size of 287 ± 52 nm (**Figure V-5b**). Thus, it was suggested that in solution, aggregates containing a P3HT core and PBLG shell were formed. On the other hand, the solid state morphology of the diblock polymer was studied by tapping mode AFM in which they exhibited a nanofibrillar morphology with persistent lengths > 200 nm (**Figure V-5c**). Moreover, the analysis revealed that the desirable properties of each of the homopolymers were successfully integrated into a single block copolymer material including the electronic properties of P3HT and the α -helical secondary structure of PBLG block.²⁷ As stated, the synthesized P3HT-*b*-PBLG can be potentially used in OPV and related applications.

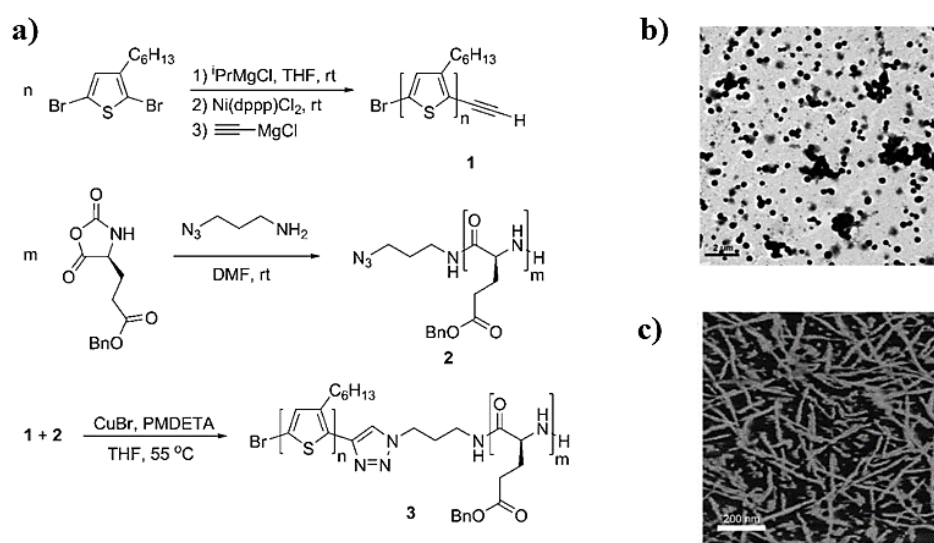


Figure V-5: (a) Synthesis of (1) ethynyl functionalized P3HT, (2) PBLG-N3 and (3) their corresponding block copolymer P3HT-*b*-PBLG, (b) TEM image of the nanoparticles and (c) Tapping mode AFM phase image of the diblock copolymer spin-coated from CHCl₃ solution onto a Si wafer.²⁷

P3HT-*b*-PBLG was also synthesized by a ring-opening polymerization of BLG-NCA from a benzylamine-terminated regioregular P3HT macroinitiator (**Figure V-6a**).²⁵ Upon polymerization, the diblock copolymer maintains the semiconducting properties of P3HT as demonstrated by the relatively similar optoelectronic properties in solution and solid state. Interestingly, P3HT-*b*-PBLG displayed solvatochromic behavior in different solvents as the choice of the solvent is known to affect the helical twist of PBLG.

For instance, these block copolymers showed elongated granular features when deposited from the low boiling point chloroform solvent (**Figure V-6b**) while they displayed a ribbon-like nanostructure distributed on top of the granular features when deposited from high boiling point trichlorobenzene solvent (**Figure V-6c**).

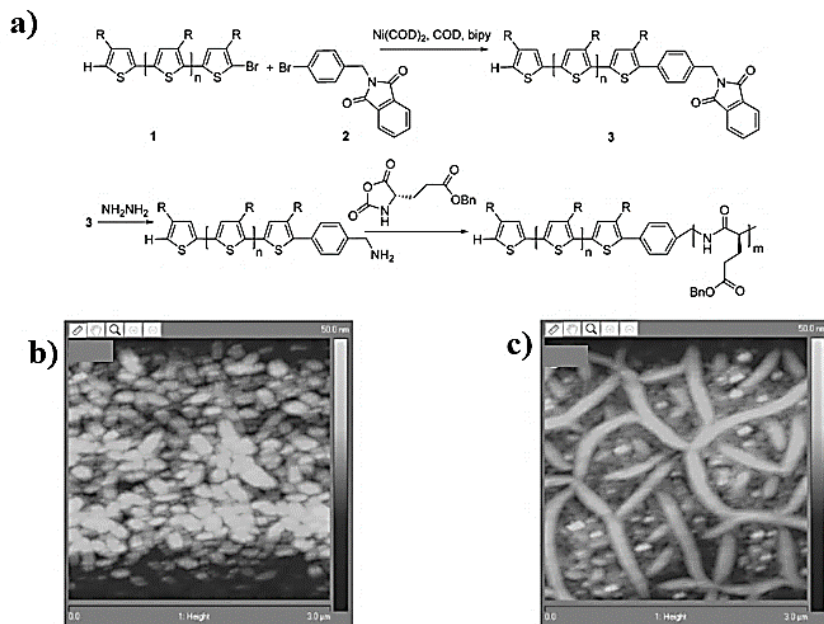


Figure V-6: (a) Synthesis of P3HT-*b*-PBLG using benzylamine-terminated P3HT macroinitiator. Height AFM images of copolymer film deposited from (b) chloroform and (c) trichlorobenzene.²⁵

II. Objectives

The photothermal effect is defined when light absorption is followed by a non-radiative relaxation in the form of heat energy (conversion of light into heat energy). Photothermal materials can be used in a variety of biomedical applications (biosensing, bioimaging, drug delivery, therapy....) as well as non-biomedical ones (energy, nanocatalysis...) which all require and utilize specific and localized heat energy.²⁸ In fact, the biological origin/compatibility of polypeptides makes their self-assembled nanostructures excellent candidates for biological integrations.²⁹ Moreover, excellent photothermal agents should possess the characteristic features of high light-to-heat conversion yield and strong absorbance in the NIR region. Infrared light is interesting as it does not cause any damage to human's skin like the ultraviolet light and it deeply penetrates into the skin where it can reach the body tissues.³⁰ Thus, incorporating a near-IR absorbing polymer, P(DTS-DAP), into the polypeptide segment could be an efficient strategy for such biological applications.

In this chapter, novel hybrid block copolymers have been synthesized by combining a low-bandgap block absorbing in the NIR region, P(DTS-DAP), with a polypeptide segment (either PBLG or P(TFA-Lys)). The choice of the amino acid monomers was made in order to have two different families of polypeptides that present different groups after deprotection, either carboxylic acid or amine functional group for P(GA) and P(Lys), respectively. Generally, for the self-assembly of diblock copolymers, the rigidity due to secondary structures provides an opportunity to direct nanoscale structures formation, such as lamellar structures and others.¹² Thus, the rod behavior plays a dominant role in driving such self-assembly.³¹

The first step in this work includes the preparation of an aniline-terminated P(DTS-DAP) having a primary amine end. After proving a successful end-functionalization using different characterization techniques, the aniline-terminated P(DTS-DAP) has been used as a macroinitiator in the ring opening polymerization of N-carboxyanhydrides (NCA). The resulting hybrid block copolymer has been deprotected to form the corresponding acid which was water soluble to be used as a photothermal material.

III. Synthesis of aniline-terminated P(DTS-DAP)

As previously mentioned, the general objective of this chapter is to use the “end-functional coupling method” for designing NH₂-terminated P(DTS-DAP). This aniline-terminated copolymer was used as a macroinitiator in the ring opening polymerization of the N-carboxyanhydride (NCA) of the corresponding peptide monomer to form a diblock copolymer.

Tour and co-workers³² have already shown that nitro, ketone, amine, and quinone groups³³ are all compatible with Stille polycondensation conditions. Thus, 4-bromoaniline was chosen as the end-functional capper agent (monofunctional) to provide NH₂ end-group in the Stille polycondensation of a mixture of dibrominated DAP (A-A) and distannylated DTS (B-B).

As previously developed in **Chapter II**, the stoichiometry of monomers and end-capping agent (4-bromoaniline in this case) is a key factor that predetermines the length of the low-bandgap block. Thus, the stoichiometry of the species was maintained according to **Equation 1**.



In which N_A , N_B , $N_{B'}$ represent the mole number of stannate functions and bromide groups pertaining to the DAP monomer and the end-capping agent, respectively. In other words, N_{DTS} , N_{DAP} and $N_{\text{end-capper}}$ represent the number of DTS, DAP monomers and 4-bromoaniline end-capper, respectively. By following this stoichiometry, the total number of aryl bromides is equal to the total number of aryl stannanes and the formation of chains containing the end-capper is promoted. Thus, aniline-terminated P(DTS-DAP) was synthesized using the molar equivalents mentioned in **Table V-1**.

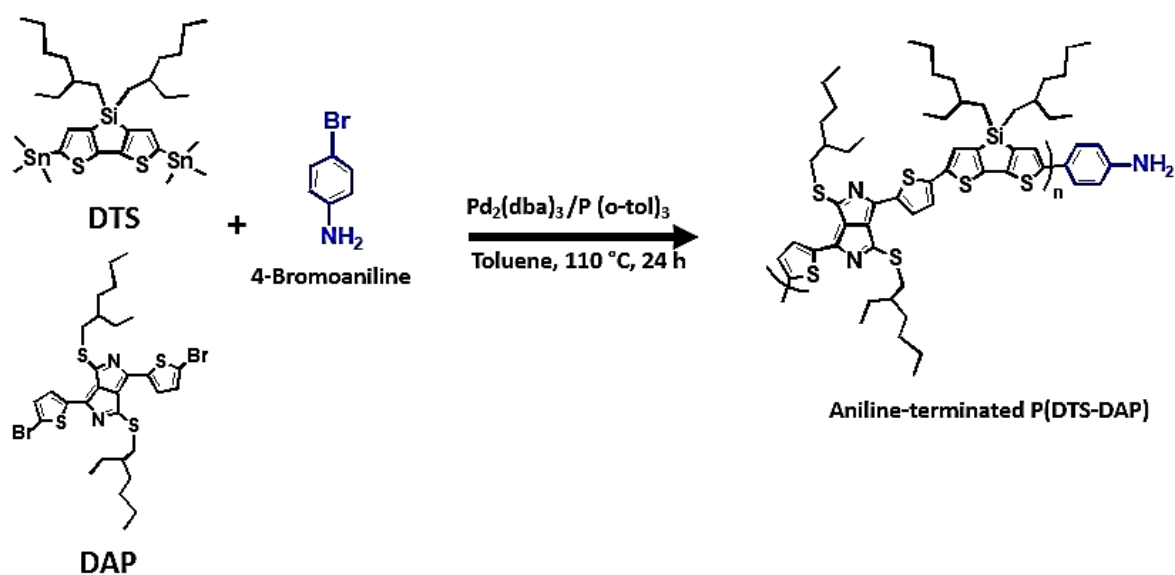
Table V-1: Theoretical and experimental molecular characteristics of the aniline-terminated P(DTS-DAP).

Polymer	N_{DTS}^a	N_{DAP}^a	N_{EC}^a	$N_{DTS-DAP}/N_{EC}^b$	M_n th ^b	$N_{DTS-DAP}/N_{EC}^c$	M_n ^d	\bar{D} ^d
P(DTS-DAP)	1	1	0	∞	----	----	----	1.5
P(DTS-DAP)-NH ₂	1	0.95	0.1	10	10,000	6	4500	1.6

^a molar equivalent, ^b calculated from the Carothers equation based on the hypothesis of 100% conversion, ^c calculated from ¹H NMR and ^d measured by SEC using UV detector at 720 nm

For the synthesis, all the materials were weighed in a glovebox, in which DTS was mixed under inert atmosphere in a microwave tube with DAP and 4-bromoaniline in anhydrous chlorobenzene. Tris(dibenzylideneacetone) dipalladium (0) Pd₂(dba)₃ and tri(*o*-tolyl)phosphine P(*o*-tolyl)₃ ligand were then added as shown in **Scheme V-3**. Again, the choice of the catalyst was due to the high air stability of Pd₂(dba)₃ and the steric hindrance of P(*o*-tolyl)₃. This may lead to a faster reaction coupling as reported in literature.^{34,35} The mixture was kept under inert atmosphere and stirred at 110 °C for 1 hour until the product became viscous. The polymer was then precipitated in cold methanol and filtrated. Soxhlet successive extractions were performed in acetone, ethanol, and cyclohexane.

Finally, the product was recovered in chloroform. The chloroform was concentrated and the dark black aniline-terminated P(DTS-DAP) (named P(DTS-DAP)-NH₂ from now on) was collected with an 80% yield.



Scheme V-3: Stille coupling polymerization for synthesizing P(DTS-DAP)-NH₂.

Meanwhile, P(DTS-DAP) was also prepared by the same polymerization conditions but without the introduction of the end-capper reagent.

The chemical structures of the synthesized P(DTS-DAP)-NH₂, P(DTS-DAP) and 4-bromoaniline as references were identified by Fourier Transform Infrared Spectroscopy (FT-IR) (**Figure V-7a**). The characteristic peaks of 4-bromoaniline appeared as twin peaks at around 3380 and 3475 cm⁻¹ which are assigned to the symmetric and asymmetric stretching of N-H bond. Additionally, a shoulder peak appeared at around 1600 cm⁻¹ which is consistent with primary amine N-H bending. Regarding both copolymers, the spectra revealed their characteristic peaks including aromatic C-H stretching bond (2960 cm⁻¹), symmetric and asymmetric CH₂ bonds (2850 and 2920 cm⁻¹, respectively), C-S stretching (1058 cm⁻¹ and 785 cm⁻¹), C=C (1500 cm⁻¹) and other peaks which are characteristics of P(DTS-DAP).^{36,37} A slight difference appeared when comparing the spectrum of P(DTS-DAP)-NH₂ to that of P(DTS-DAP) due to the presence of a single broad absorption peak between 3300 and 3500 cm⁻¹ as shown in **Figure V-7b**. This could be assigned to the N-H stretching bond as it is only a single end-unit with respect to a polymer chain.

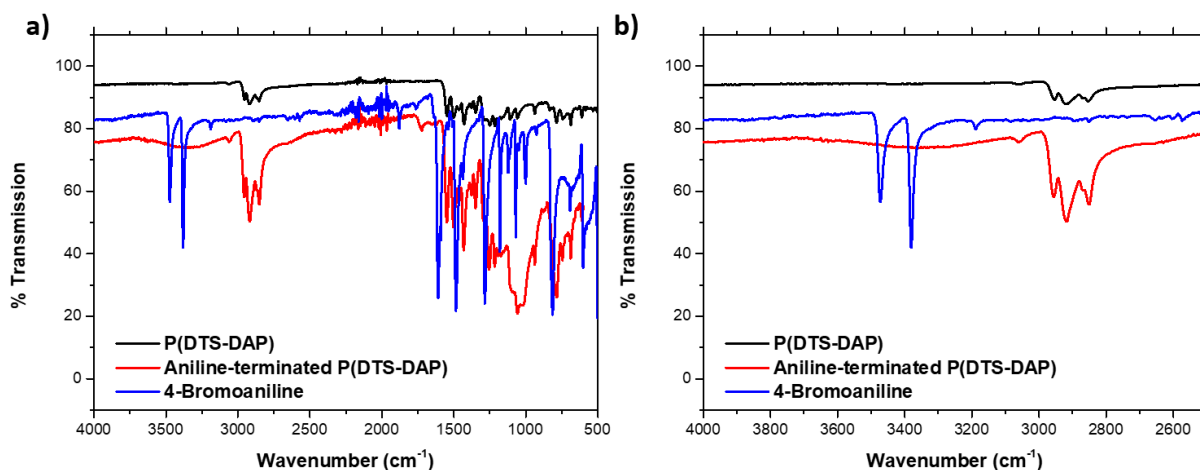


Figure V-7: FT-IR spectra of (a) the synthesized P(DTS-DAP)-NH₂, P(DTS-DAP) and 4-bromoaniline. (b) A zoom in between 2500 and 4000 cm⁻¹.

The synthesized P(DTS-DAP) and P(DTS-DAP)-NH₂ were also characterized by ¹H NMR. The analysis was performed in deuterated tetrachloroethane (TCE) at high temperature (80 °C) to overcome the difficulty of observing the aromatic peaks at room temperature. The spectra of both copolymers shown in **Figure V-8** revealed same peaks that could be assigned to the aromatic protons of the repetitive DTS and DAP units; proton **b** (8.08 ppm) and protons **a**, **c** (between 7.39 and 7.2 ppm). The peaks between 3.61 and 3.59 ppm were assigned to the alkyl (CH₂) substituent in the α-sulfur position (protons **d**). The aliphatic protons in the alkyl chain (CH, CH₂ and CH₃) appear between 2.59 and 0.72 ppm.

Regarding specifically the ¹H NMR analysis of P(DTS-DAP)-NH₂, we could not attest the presence of amino proton because of the overlapping with the protons of the alkyl (CH₂) chains in the α-sulfur position (protons **d**). Nevertheless, additional peaks can be observed in the aromatic region at 6.8 and 7.7 ppm that could be assigned to the aromatic protons of the aniline group (**e** and **f** in **Figure V-8**).

In addition to the verification of the proton structure of the polymer, it was then possible to calculate the ratio between the repetitive units and the end-group (N_{DTS-DAP}/N_{EC}). To do so, a comparison between the integral of the peak at 7.65 ppm (**e**) corresponding to the aromatic protons of the aniline group to that of the peak at 8.08 ppm (**b**) which corresponds to the aromatic protons of the DAP monomer unit was determined. Therefore, in this case by using a 0.1 molar equivalent of the end-capper, the ratio was found to be 6 (reported in **Table V-1**).

Following the Carothers equation (**Equation 6** in **Chapter II**), at 100% conversion, the theoretical DP_n of DTS-DAP should be 40, corresponding to 20 DTS-DAP repetitive units. Since the end-capper has been included in stoichiometry, the end-capper should be present at both ends of the P(DTS-DAP) macromolecules (at 100% conversion). Therefore, the theoretical $N_{DTS-DAP}/N_{EC}$ ratio is 20/2 or 10 (reported in **Table V-1**). The difference between the theory and the experiment could be attributed to an incomplete conversion.

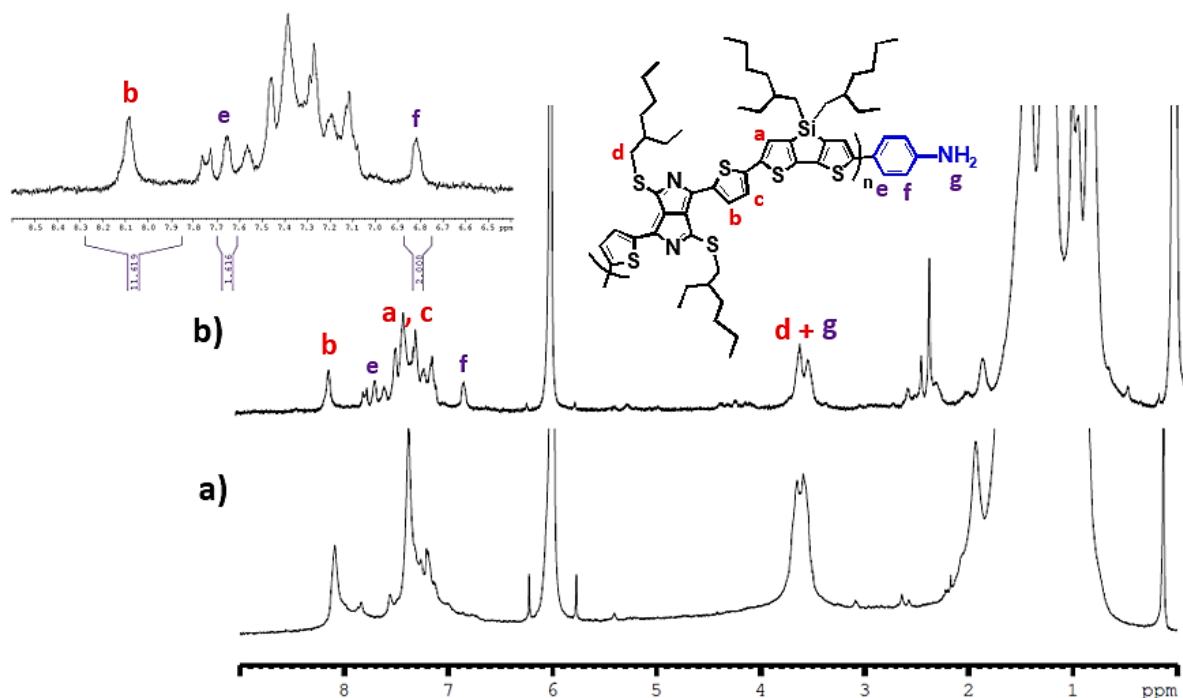


Figure V-8: 1H NMR spectra of (a) P(DTS-DAP) and (b) P(DTS-DAP)- NH_2 ($C_2D_2Cl_4$, 400 MHz).

DOSY NMR was used to determine if the signals at 6.8 and 7.7 ppm belong to the polymer or to an impurity. As shown in **Figure V-9**, the end-capped polymer, P(DTS-DAP)- NH_2 , shows only one diffusion coefficient for all aromatic protons including the one assigned to the aromatic benzene ring in the aniline end-capper. For example, when comparing the diffusion coefficient of protons **b** to that of the aromatic peaks of the benzene group (**e** or **f**), it is clearly confirmed that they are equal.

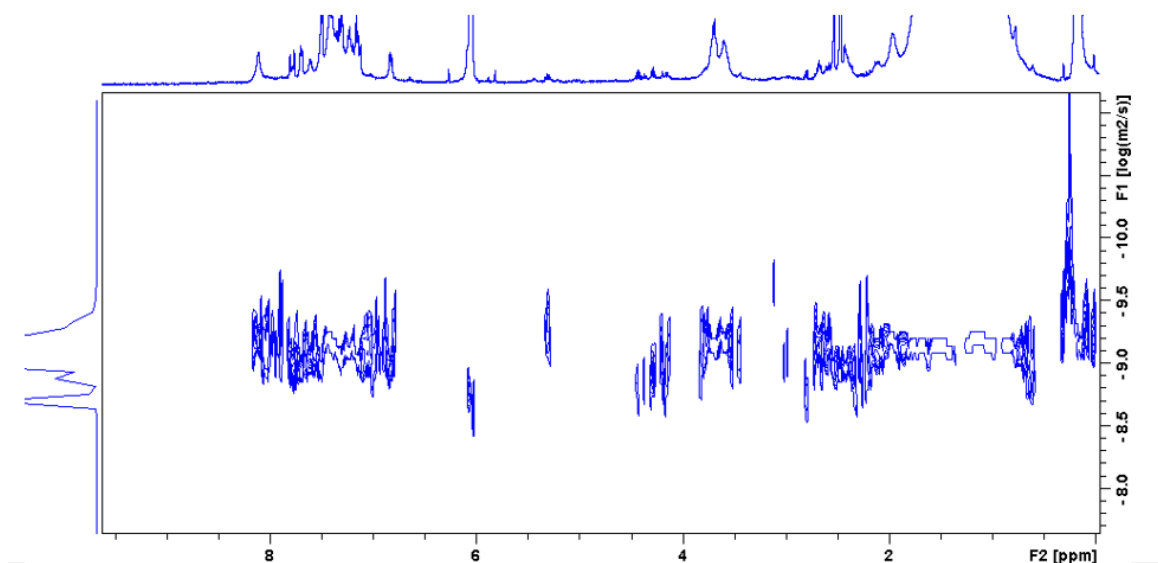


Figure V-9: DOSY NMR of $P(\text{DTS-DAP})\text{-NH}_2$ ($\text{C}_2\text{D}_2\text{Cl}_4$, 400 MHz).

$P(\text{DTS-DAP})\text{-NH}_2$ polymer was completely soluble in tetrahydrofuran (THF). This allows estimating its number average molar mass by using SEC with THF as the eluent. SEC analysis was performed using a UV detector (set at 720 nm) with a conventional polystyrene calibration. The chromatogram shown in **Figure V-10** revealed a narrow peak distribution represented by a monomodal symmetrical shape chromatogram with a number average molar mass (M_n) of $4500 \text{ g}\cdot\text{mol}^{-1}$, molar mass peak maximum (M_p) of $4525 \text{ g}\cdot\text{mol}^{-1}$ and dispersity (D) of 1.6.

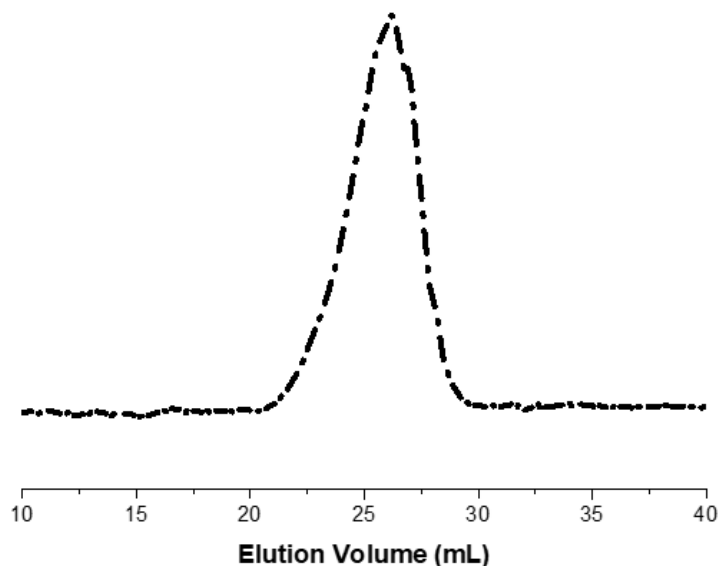
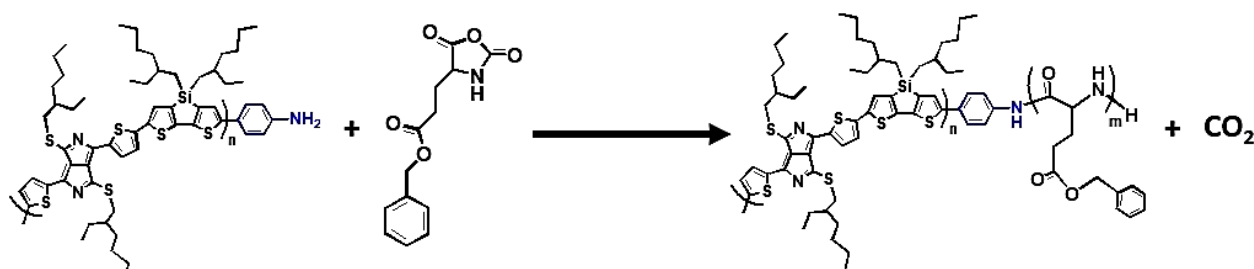


Figure V-10: Size exclusion chromatograms of $P(\text{DTS-DAP})\text{-NH}_2$ against polystyrene calibration (UV detector at 720 nm).

IV. Diblocks with γ -Benzyl-*L*-Glutamate monomer unit

a. Synthesis of P(DTS-DAP)-*b*-P(BLG)

In self-assembly, polypeptides with secondary structures are used for their rod-like structure.²⁴ Among polypeptides, poly(γ -benzyl-*L*-glutamate) (PBLG) is known to exhibit a well-defined rod-like α -helical structure in both film and solution.³⁸ With the aim of preparing P(DTS-DAP)-*b*-P(BLG), P(DTS-DAP)-NH₂ macroinitiator was first dissolved in dry THF solvent in a Schlenk flask equipped with a magnetic stirrer and containing BLG-NCA monomer (**Scheme V-4**). This reaction was performed in an open system to eliminate the formed CO₂ and avoid overpressure. After two days, the polymer was precipitated in methanol and collected as sediments after centrifugation. Two different degrees of polymerization were targeted by setting the monomer to macroinitiator molar ratio (M/I) to 50 and 100. It is worth noting that the synthesis of the hybrid diblock copolymers in this chapter was conducted at the LCPO Laboratory in Bordeaux.



*Scheme V-4: Synthesis of P(DTS-DAP)-*b*-P(BLG).*

The final polymer, recovered after precipitation and drying, was first analyzed by SEC-THF. **Figure V-11** shows the superposition of the chromatograms for the macroinitiator (P(DTS-DAP)-NH₂) and the block copolymer P(DTS-DAP)-*b*-P(BLG) with M/I=50 and 100 using UV detector at 720 nm to screen the presence of the low-bandgap polymer. In both cases, a bimodal chromatogram was obtained with approximately the same features. By comparing the macroinitiator and both diblocks, we could observe 60% of residual P(DTS-DAP)-NH₂ homopolymer and 40% of a second population at lower elution volume pertaining to the diblocks. This shift reveals an increase in the molar mass. The presence of residual P(DTS-DAP) can be explained by the possible presence of P(DTS-DAP) that does not bear an amine moiety or a slow initiation of NCA. The dispersity was increased from 1.6 to 3.03 and 3.3 for M/I=50 and 100, respectively. Meanwhile, the molar mass peak maximum (M_p) value was increased from 4525 g.mol⁻¹ for the macroinitiator to 5600 and 6200 g.mol⁻¹ for M/I=50 and 100, respectively.

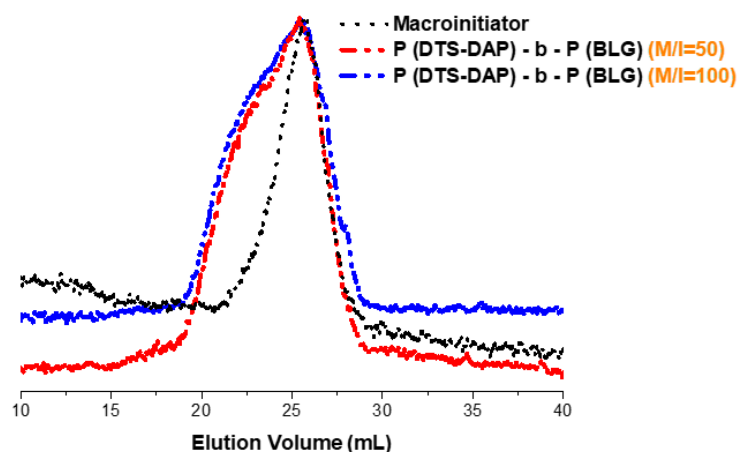


Figure V-11: Normalized size exclusion chromatograms using UV detector at 720 nm for $P(\text{DTS-DAP})\text{-}b\text{-}P(\text{BLG})$ in comparison with the starting $P(\text{DTS-DAP})\text{-NH}_2$.

$P(\text{DTS-DAP})\text{-}b\text{-}P(\text{BLG})$ block copolymers with $M/I=100$ and 50 were then analyzed by ^1H NMR in $\text{C}_2\text{D}_2\text{Cl}_4$ at 80°C (Figure V-12). It was possible to distinguish the resonance peaks attributed to the protons of PBLG block (e, f, g, h, i, j) in addition to those of the macroinitiator $P(\text{DTS-DAP})$ (a, b, c, d). The average degree of polymerization of the peptide chain can be estimated by comparing the integration of the peak signal (a) at 3.55–3.65 ppm, attributed to $P(\text{DTS-DAP})$, to that of PBLG, (g) at 3.98 ppm. Accordingly, average degrees of polymerization of 94 and 42 were calculated for the synthesized block copolymers with $M/I=100$ and 50 , respectively. Thus, the experimental degree of polymerization is close to the theoretical one at full conversion. The naming of the blocks was in accordance to the experimental DP_n calculated from ^1H NMR. However, if we consider that 60% of the first block chains did not initiate polymerization then the real polypeptide DP_n are 235 and 105 for the synthesized block copolymers with $M/I=100$ and 50 , respectively.

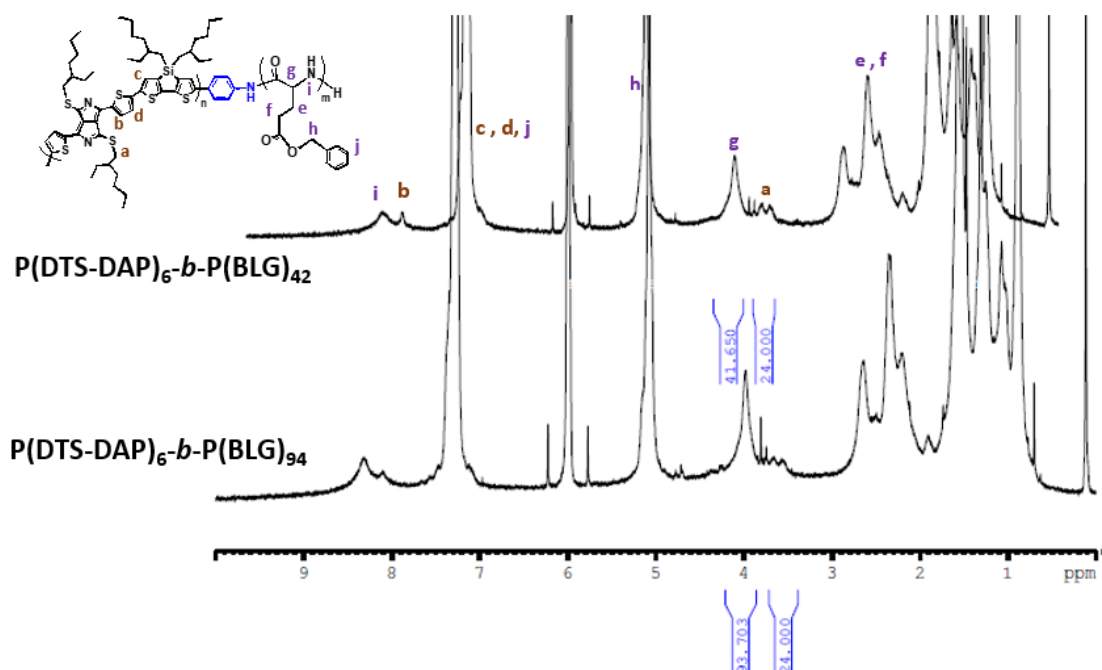


Figure V-12: ^1H NMR spectra of the synthesized $P(\text{DTS-DAP})\text{-}b\text{-}P(\text{BLG})$ block copolymer ($\text{C}_2\text{D}_2\text{Cl}_4$, 400 MHz).

The optical properties of the P(DTS-DAP)-NH₂ and P(DTS-DAP)-*b*-P(BLG) hybrid block copolymers were investigated in THF solution. The absorption spectra shown in **Figure V-13** revealed that the diblock copolymers exhibited very similar absorption properties compared to the conjugated homopolymer. For both, the macroinitiator and the diblocks, a broad absorption in the near-IR region extending from 400 nm to 1200 nm was observed. As discussed in **Chapter II**, this absorption is characterized by two bands. The first one is at a low wavelength (between 400 to 530 nm) corresponding to the π - π^* transition while the other peak found at a higher wavelength (between 600 to 1200 nm) is due to the intramolecular charge transfer from the donor unit to the acceptor unit. The mentioned absorption bands are referred as high energy and low energy absorption bands, respectively.³⁹ Concerning the macroinitiator, the maximum absorption is at $\lambda_{\text{max}}=855$ nm, while as, for the diblock, it was slightly blue-shifted and found at 835 nm. Accordingly, the slight blue-shift of the diblock copolymer could be related to the effect of the PBLG block in slightly disturbing the effective conjugation length of the P(DTS-DAP) planar segment.²⁵

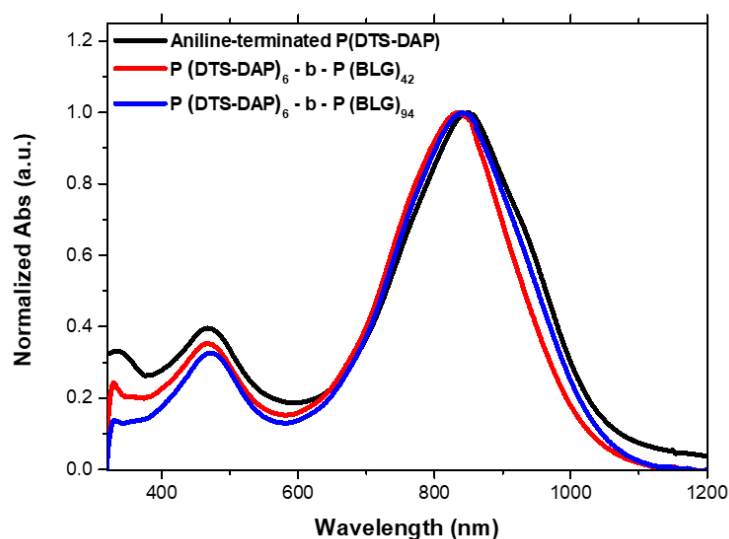


Figure V-13: Normalized UV-vis-NIR absorption spectra of P(DTS-DAP)-NH₂ and P(DTS-DAP)-*b*-P(BLG) in THF solution.

The chemical and secondary structures of the PBLG-based diblocks were then investigated by FT-IR. As shown in **Figure V-14a**, in addition to the peak characteristics of P(DTS-DAP) that were previously discussed, N-H stretching peaks appeared clearly in the diblock spectra at 3300 cm⁻¹. Moreover, the signal at 1730 cm⁻¹ which is assigned to the C=O stretching of the benzyl ester protecting group of the PBLG block appeared after the diblock formation (**Figure V-14b**).⁴⁰ The PBLG is known for its ability to form three different secondary structures: α -helix, β -sheets and random coil conformation.⁴¹ In general, two major bands of the protein infrared spectrum can be identified, amide I and II. The amide I, more intense, is mainly associated with the C=O stretching vibration and directly related to the backbone conformation. On the other hand, amide II band, more complex than amide I, results from the N-H bending vibration and the C-N stretching vibration. In this regard, the position of amide-I and amide-II bands can be an efficient sensor for determining the corresponding conformation. Thus, as shown in the high-resolution spectra of **Figure V-14b**, the amide-I and amide-II located at 1647 and 1545 cm⁻¹, respectively are the characteristic peaks associated to the α -helical conformations.¹²

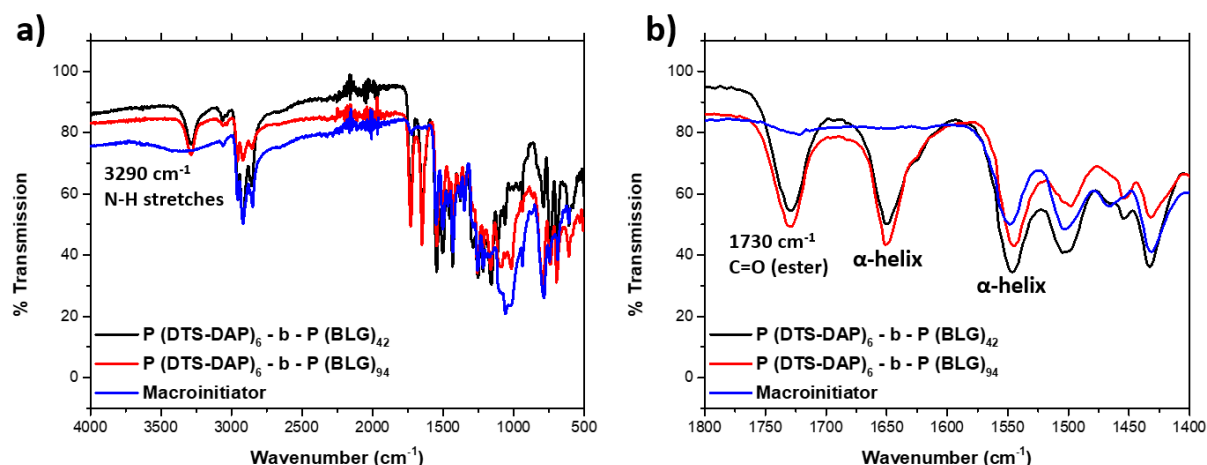
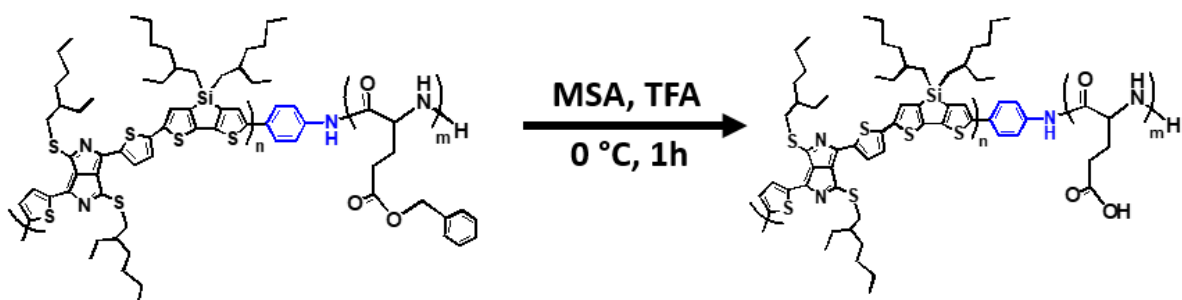


Figure V-14: (a) FT-IR spectra of $P(\text{DTS-DAP})\text{-NH}_2$ and $P(\text{DTS-DAP})\text{-}b\text{-}P(\text{BLG})$ block copolymers and (b) a zoom in spectra between 1400 and 1800 cm^{-1} .

b. Deprotection of $P(\text{DTS-DAP})\text{-}b\text{-}P(\text{BLG})$

For the aim of obtaining an amphiphilic block copolymer by cleaving the benzyl group in the BLG repetitive unit of the hybrid block copolymer, deprotection of $P(\text{DTS-DAP})\text{-}b\text{-}P(\text{BLG})$ was performed according to literature.⁴² As shown in **Scheme V-5**, $P(\text{DTS-DAP})\text{-}b\text{-}P(\text{BLG})$ was dissolved in trifluoroacetic acid (TFA) under agitation using an ice bath at $0\text{ }^\circ\text{C}$. Anisole and methanesulfonic acid (MSA) were then added, after which the solution mixture was stirred for 20 minutes at $0\text{ }^\circ\text{C}$ followed by another 20 minutes at room temperature. The deprotected polymer was then precipitated twice in diethyl ether (Et_2O) and finally collected by centrifugation with a speed of 2000 rpm. The precipitate was then suspended in water and saturated sodium bicarbonate (NaHCO_3) solution. The resulting mixture was dialyzed against milliQwater (MWCO 1 kDa) and lyophilized to obtain the amphiphilic block copolymer.



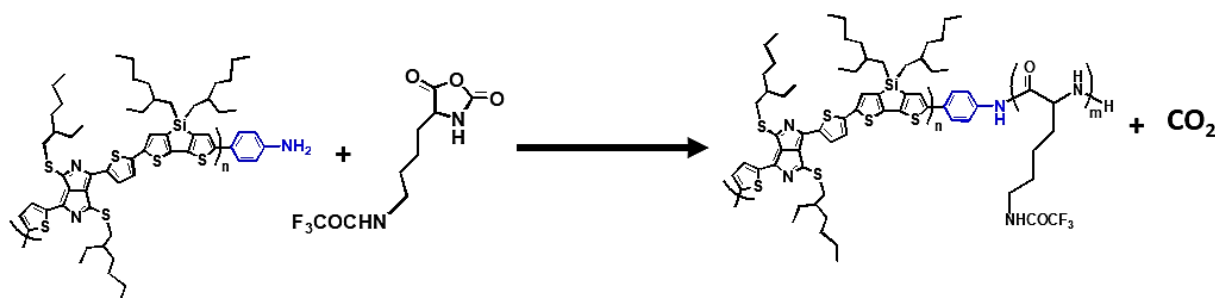
Scheme V-5: Synthesis of the amphiphilic $P(\text{DTS-DAP})\text{-}b\text{-}P(\text{GA})$ after hydrolyzing the benzyl group.

Some experimental conditions lie behind losing the product as it was not possible to recover the final debenzylated polymer, maybe due to solubility problems or an unsuccessful deprotection.

V. Diblocks with TFA-Lysine NCA repetitive unit

a. Synthesis of P(DTS-DAP)-*b*-P(TFA-Lys)

The same procedure used for the elaboration of P(DTS-DAP)-*b*-P(BLG) was also followed for synthesizing P(DTS-DAP)-*b*-P(TFA-Lys) diblock copolymers with two targeted degrees of polymerization represented by the monomer/macroiinitiator (M/I) equal to 50 and 100 as shown in **Scheme V-6**. The only difference is that after two days, the polymer was precipitated in cyclohexane rather than methanol where the polymer was hardly precipitating.



*Scheme V-6: Synthesis of P(DTS-DAP)-*b*-P(TFA-Lys).*

Figure V-15a shows the superposition of the SEC chromatograms of P(DTS-DAP)-NH₂ (macroinitiator) and P(DTS-DAP)-*b*-P(TFA-Lys) with M/I=100 using a UV detector set at 720 nm. The chromatogram of the block copolymer (red curve) is made up of two overlapped peaks. One peak corresponding to the diblock (50%) is located at a lower elution volume in comparison to the macroinitiator and the other is at higher elution volume attributed to the presence of unreacted P(DTS-DAP) homopolymer (50%). In this case, it was possible to purify the P(DTS-DAP)-*b*-P(TFA-Lys) block copolymer by successive washing in toluene in order to remove the unreacted P(DTS-DAP) homopolymer.

After washing, the peak corresponding to the macroinitiator impurities decreased in intensity (20%) in which the majority of the product was made up of the diblock copolymer (80%) which is eluted at a low elution volume (**Figure V-15a**, blue curve). Therefore, it was proved that the successive washing by toluene is an efficient way to purify P(DTS-DAP)-*b*-P(TFA-Lys) block copolymer from the unreacted macroinitiator. In this case, M_n was increased from 4500 (for the macroinitiator) to 13,000 g.mol⁻¹ with an increase in the M_p value from 4225 g.mol⁻¹ to 49,000 g.mol⁻¹. A similar procedure was followed to purify P(DTS-DAP)-*b*-P(TFA-Lys) having M/I=50. As shown in **Figure V-15b**, the same behavior was observed in which the majority of the product after washing constitutes the diblock with a small portion of the macroinitiator revealed by the presence of a small shoulder (at an elution volume of 25 mL). Similarly, M_n was increased from 4500 g.mol⁻¹ to 17,000 g.mol⁻¹ with an increase in the M_p value from 4225 g.mol⁻¹ to 48,000 g.mol⁻¹. This is accompanied by an increase in the dispersity from 1.6 to 3.8 and 3.3 for M/I=100 and 50, respectively. In general, these results represent a direct evidence for the block copolymerization.

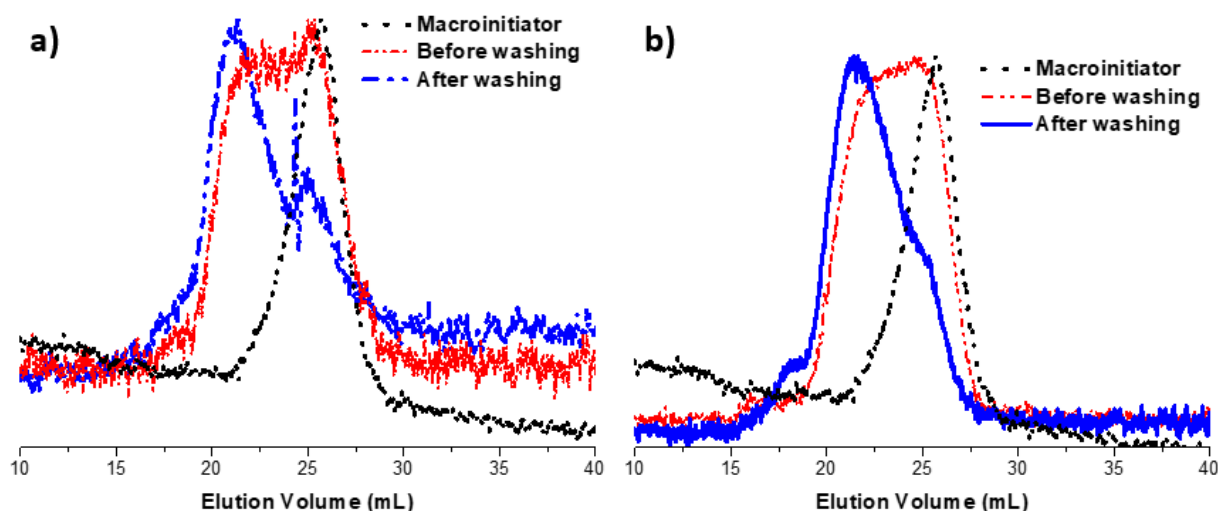


Figure V-15: Normalized size exclusion chromatograms using UV detector at 720 nm for $P(\text{DTS-DAP})\text{-}b\text{-}P(\text{TFA-Lys})$ with $M/I=$ (a) 100 and (b) 50 before and after washing in comparison with the $P(\text{DTS-DAP})\text{-NH}_2$.

The ^1H NMR of the synthesized $P(\text{DTS-DAP})\text{-}b\text{-}P(\text{TFA-Lys})$ block copolymers were performed in THF_d for both $M/I=100$ and 50 (**Figure V-16**). Peaks attributed to $P(\text{TFA-Lys})$ block were clearly identified and assigned. However, despite the appearance of some resonance peaks in the aromatic range (6.8–7.6 ppm), it was difficult to assign them to the protons of $P(\text{DTS-DAP})$ due to solubility problems. Thus, it was difficult to determine the experimental degree of polymerization of these block copolymers by ^1H NMR.

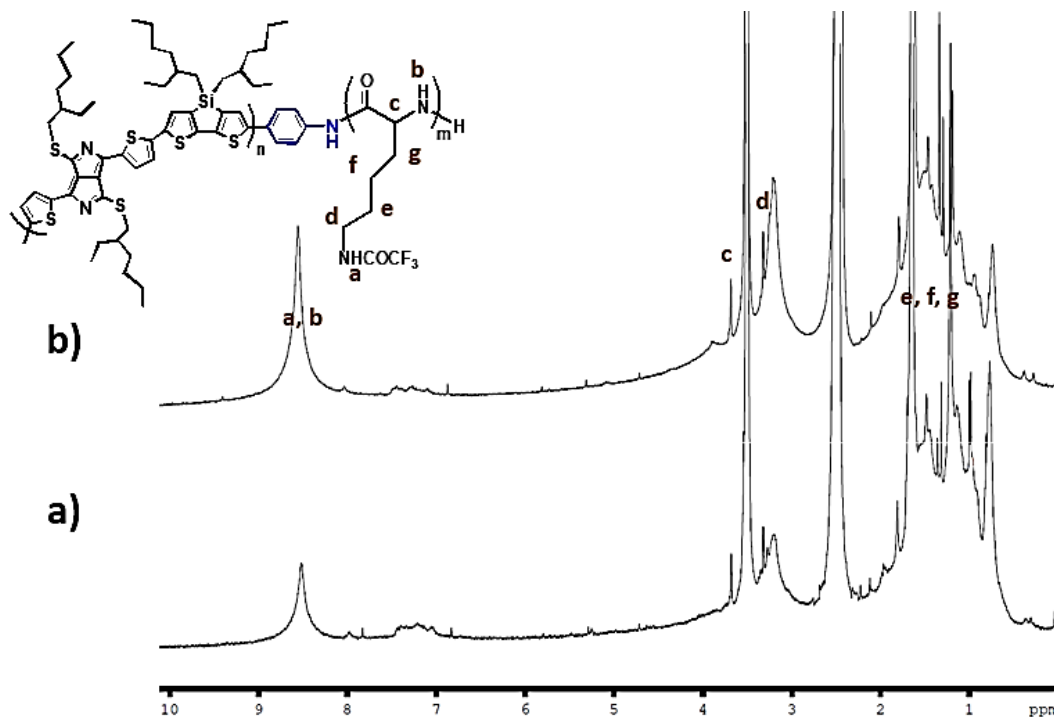


Figure V-16: ^1H NMR spectra of the synthesized $P(\text{DTS-DAP})\text{-}b\text{-}P(\text{TFA-Lys})$ block copolymer with (a) $M/I=50$ and (b) $M/I=100$ (THF_d , 400 MHz).

The optical properties of P(DTS-DAP)-*b*-P(TFA-Lys) were also investigated in THF solution and compared to those of P(DTS-DAP)-NH₂. The diblock copolymers had very similar absorption properties to those of the conjugated homopolymer. *i.e.* the absorption spectra shown in **Figure V-17** revealed the same optical behavior that is characterized by a broad absorption made up of two bands in the near-IR region. It is worth noting that in the case of P(DTS-DAP)-*b*-P(TFA-Lys) diblock, the absorption is not blue-shifted as was observed for P(DTS-DAP)-*b*-P(BLG). Thus, in this case, the presence of the P(TFA-Lys) block did not decrease the conjugation length of the P(DTS-DAP) segment.²⁵

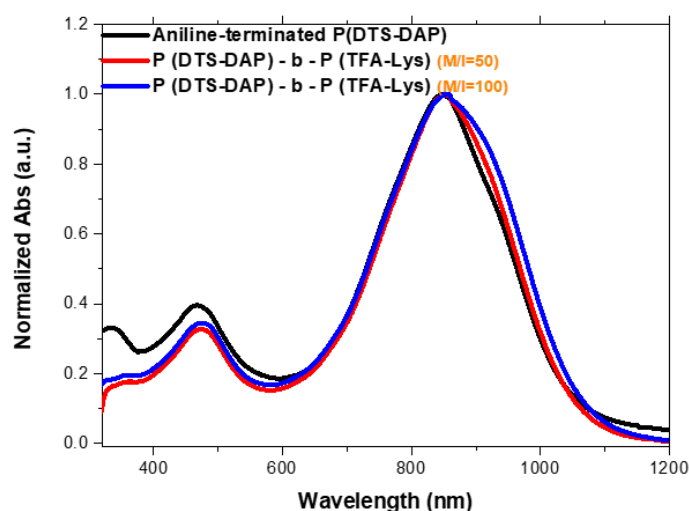


Figure V-17: Normalized UV-vis-NIR absorption spectra of P(DTS-DAP)-NH₂ and P(DTS-DAP)-*b*-P(TFA-Lys) in THF solution.

The chemical functions of the TFA-Lys-based diblocks were revealed by FT-IR. Again, in addition to the characteristic peaks of P(DTS-DAP), N-H stretching peaks appeared clearly in the diblock spectra at 3290 cm⁻¹ as shown in **Figure V-18a**. Additionally, the main characteristic peak associated to the vibration of the C-F bond of the TFA group in the diblock appeared at 1150 cm⁻¹. The latter appeared clearer in the diblock with M/I=100 as shown in **Figure V-18b**. The signal appearing at 1650 cm⁻¹ could be assigned to the C=O stretching of amide ((C=O)-N) while that at 1700 cm⁻¹ is attributed to the ester group in the Lysine repetitive unit which were also more pronounced in the diblock with M/I=100.⁷ Accordingly, the presence of a polypeptide block in the materials was confirmed.

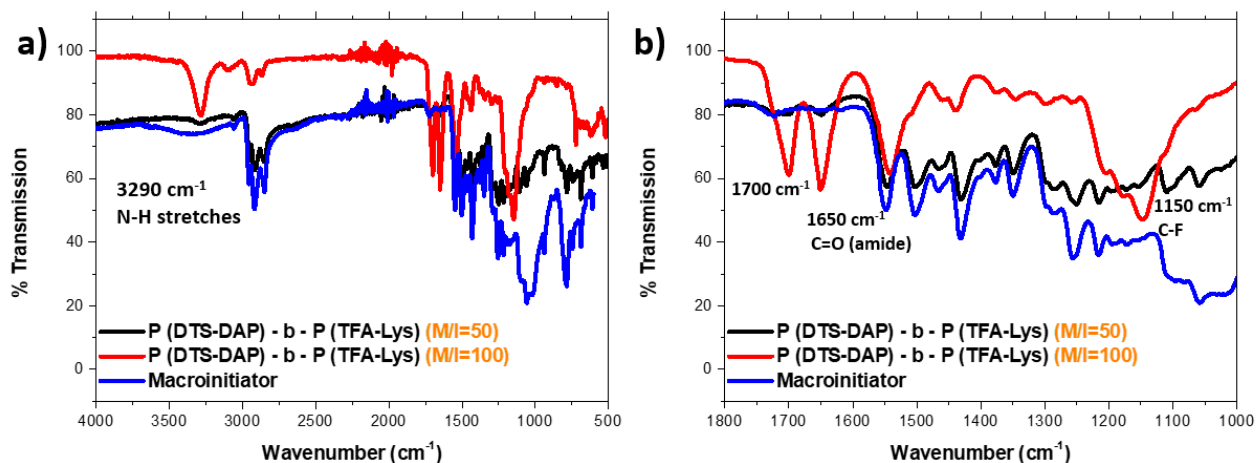


Figure V-18: (a) FT-IR spectra of P(DTS-DAP)-NH₂ and P(DTS-DAP)-*b*-P(TFA-Lys) block copolymers. (b) Zoom in spectra between 1000 and 1800 cm⁻¹.

TGA was also conducted to investigate the thermal stability of the synthesized P(DTS-DAP)-*b*-P(TFA-Lys) diblock copolymers. The study was carried out under nitrogen atmosphere starting from 50 to 600 °C with a ramp of 10 °C/min. As shown in the thermograms of **Figure V-19**, P(DTS-DAP)-NH₂ presented a degradation temperature starting from 230 °C. The degradation was characterized by two stages, the first one between 250 to 300 °C with a residual mass of 80% and the second one between 420 and 500 °C with a 50% residual mass (same as the case of P(DTS-DAP) discussed in **Chapter II**). Such decomposition was attributed to the alkyl chain attached to the dithienosilole unit.⁴³ On the other hand, the decomposition of P(DTS-DAP)-*b*-P(TFA-Lys) was a three-steps process with 80% loss starting from around 250 °C to 450 °C for both blocks with a residual mass between 17 and 20%. In addition to the degradation characteristics of the macroinitiator, an additional stage appeared between 365 °C to 400 °C which was attributed to the P(TFA-Lys) block. Thus, both blocks showed an identical thermal behavior.

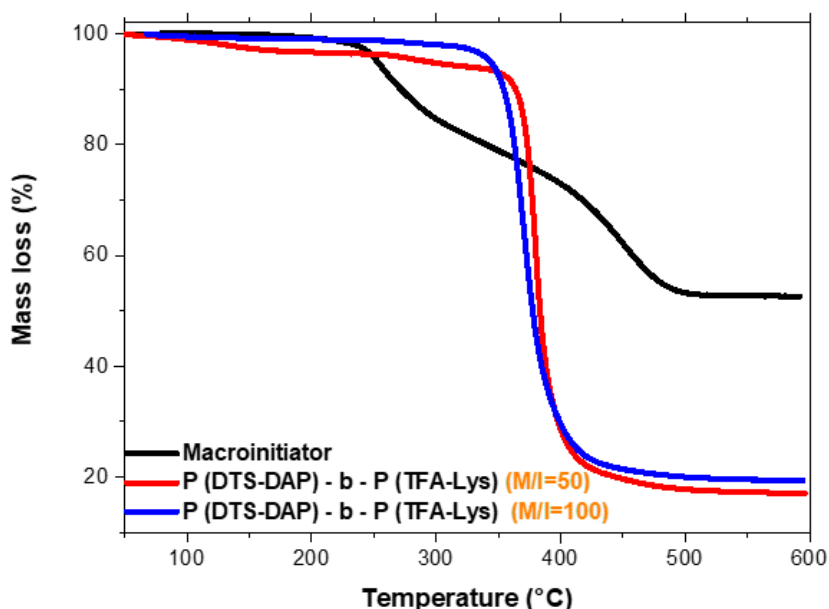
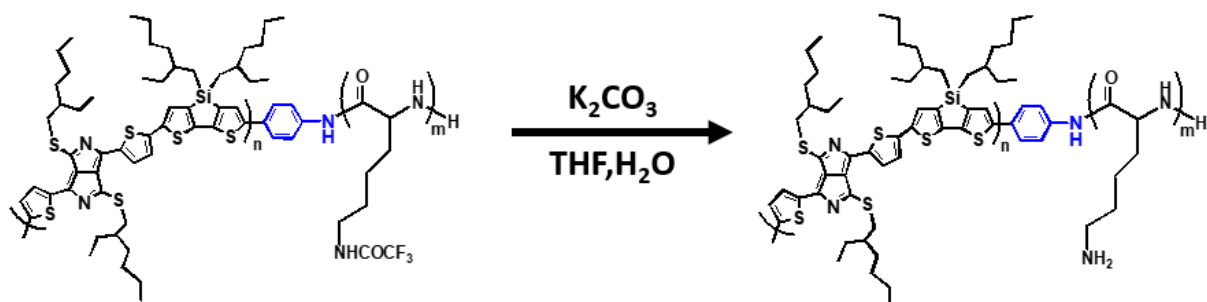


Figure V-19: Thermograms of P(DTS-DAP)-*b*-P(TFA-Lys) in comparison to that of the macroinitiator.

b. Deprotection of P(DTS-DAP)-*b*-P(TFA-Lys)

In order to obtain an amphiphilic block copolymer by hydrolyzing the amide group in the TFA functional group of the hybrid block copolymer, deprotection of this hybrid block copolymer was performed according to literature.²² As shown in **Scheme V-7**, the polymer with M/I=100 was dissolved in a mixture of 1:9 by volume H₂O and THF (as the polymer was only soluble in THF). The solution was heated at 50 °C under reflux where potassium carbonate (K₂CO₃) was then added. After 4 hours of continuous stirring, THF was then removed using a rotary evaporator. The residual polymer was suspended in water-saturated sodium bicarbonate (NaHCO₃) solution. The final product was then dialyzed against milliQwater (MWCO 1 kDa) and lyophilized to obtain the amphiphilic block copolymer.



Scheme V-7: Synthesis of the amphiphilic $P(DTS-DAP)-b-P(Lys)$ after hydrolyzing the amide group.

In general, one of the important concerns with the deprotection of polypeptides is whether a complete removal of the protecting group was achieved or not. A small amount of the protecting group could influence the resulting properties of the polypeptide such as hydrophilicity.⁴⁴ The FT-IR spectra were analyzed to study the deprotection. As shown in **Figure V-20a**, the spectra before and after deprotection were almost the same with slight differences. The peaks attributed to C-F bond vibration of the TFA group and the peak attributed to the ester functional group in the Lysine repetitive unit which were supposed to disappear are still appearing at around 1150 cm^{-1} and 1700 cm^{-1} , respectively. This may indicate that an incomplete deprotection took place. Thus, it could be more efficient in further experiments to increase the amount of K_2CO_3 initially added in the medium.

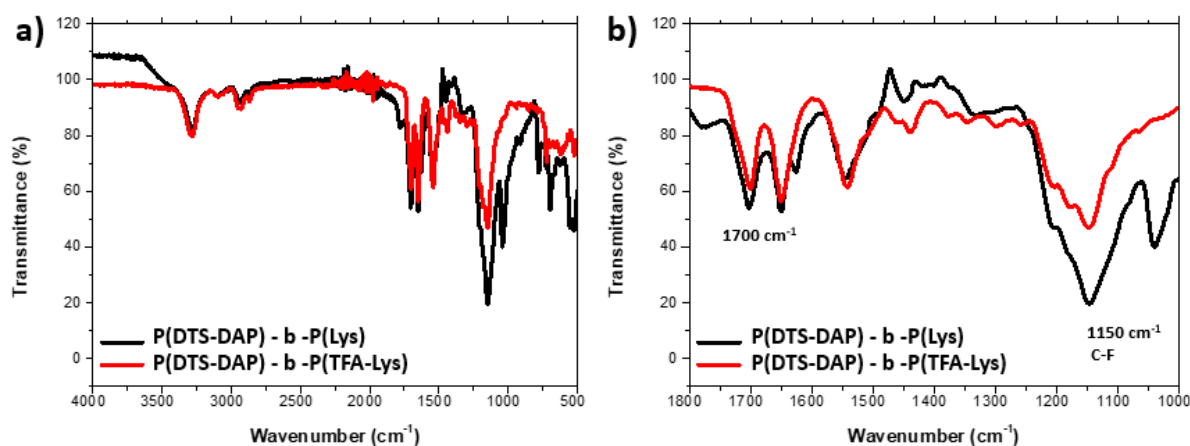


Figure V-20: (a) FT-IR spectra of the synthesized $P(DTS-DAP)-b-P(TFA-Lys)$ block copolymer (red) and $P(DTS-DAP)-b-P(Lys)$ (black). (b) A zoom in between 1000 and 1800 cm^{-1} .

To better confirm the deprotection, ^{19}F NMR was performed on both $P(DTS-DAP)-b-P(TFA-Lys)$ block copolymer and $P(DTS-DAP)-b-P(Lys)$ block copolymer which results from deprotection. As shown in the typical ^{19}F NMR spectra of **Figure V-21**, a resonance peak with a shoulder appeared between -76.57 and -76.06 ppm which could be attributed to the CF_3 functional group of the protected diblock copolymer. This peak disappeared in $P(DTS-DAP)-b-P(Lys)$ which could be an indication of the successful deprotection.

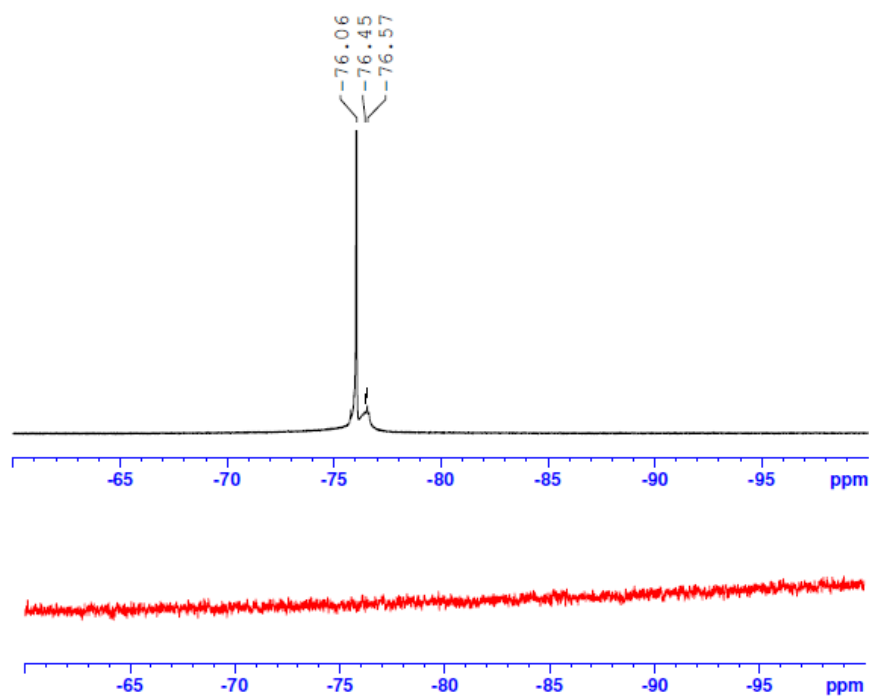


Figure V-21: ^{19}F NMR spectra of $\text{P}(\text{DTS-DAP})\text{-}b\text{-P}(\text{TFA-Lys})$ (black) and $\text{P}(\text{DTS-DAP})\text{-}b\text{-P}(\text{Lys})$ (red) block copolymers (D_2O , 376.53 MHz).

Before deprotection, the polymer was not water soluble (soluble in THF), while after deprotection, it became soluble in water. This is a strong indication of a significant deprotection. Thus, the UV-vis-NIR analysis of the deprotected polymer was performed in water. As shown in **Figure V-22**, the spectrum of $\text{P}(\text{DTS-DAP})\text{-}b\text{-P}(\text{Lys})$ (black) was blue-shifted to a lower wavelength with a maximum absorption at $\lambda_{\text{max}} = 760$ nm. This could be related to a different conformation of the block copolymer in different solvents. Indeed, if $\text{P}(\text{Lys})$ is well solvated in water, it could induce a high steric hindrance which is disturbing the π -stacking and planarity of the conjugated block.

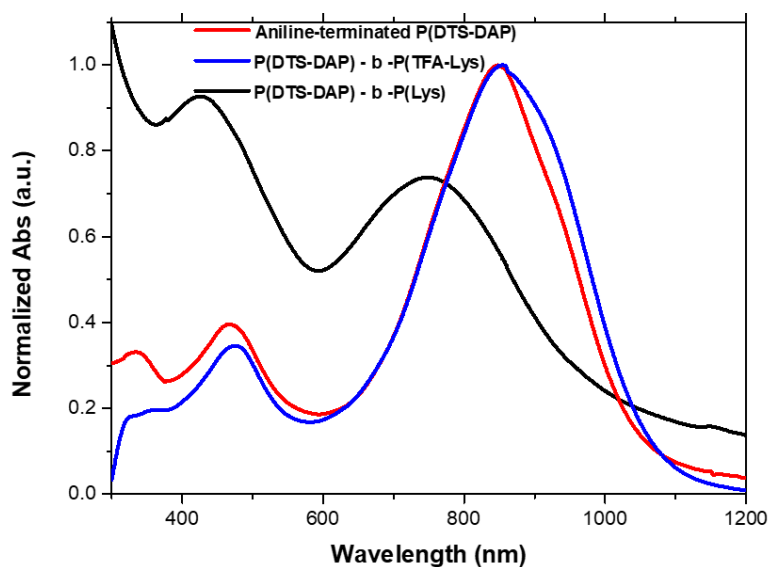


Figure V-22: Normalized UV-vis-NIR absorption spectra of $\text{P}(\text{DTS-DAP})\text{-NH}_2$ (red), $\text{P}(\text{DTS-DAP})\text{-}b\text{-P}(\text{TFA-Lys})$ (blue) in THF and $\text{P}(\text{DTS-DAP})\text{-}b\text{-P}(\text{Lys})$ (black) in water.

The size distribution of the synthesized P(DTS-DAP)-*b*-P(Lys) was determined by Dynamic Light Scattering (DLS). For this, a solution of the polymer was dispersed in water with the addition of few drops of THF. After evaporating THF, the solubility was maintained with a small proportion of aggregates. DLS analysis showed a broad, unimodal distribution with an average hydrodynamic diameter for P(DTS-DAP)-*b*-P(Lys) objects around 157 nm and a polydispersity index (PDI) of 0.1008 (**Figure V-23**).

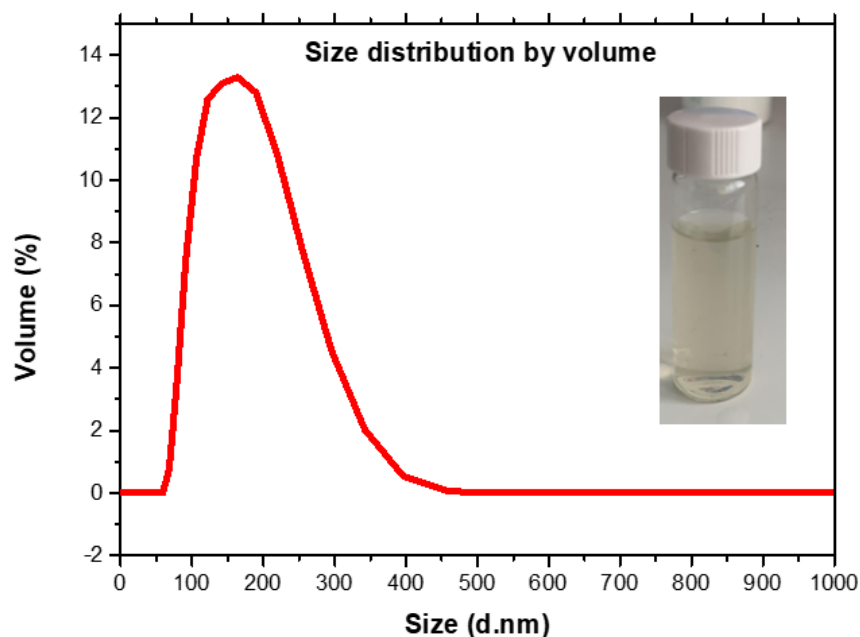


Figure V-23: DLS analysis of P(DTS-DAP)-*b*-P(Lys) in aqueous solution. Inset is the image of the dispersion in water.

c. Photothermal effect of P(DTS-DAP)-*b*-P(Lys) in aqueous solution

The formation of water dispersible objects from this hybrid block copolymer opens the door to study its photothermal behavior. The photothermal performance of P(DTS-DAP)-*b*-P(Lys) in water upon laser irradiation (800 nm) was investigated with a power density of 2 W.cm⁻². The pure water without materials showed slight change in temperature from 24 °C to 30 °C within 15 min of irradiation. On the contrary, a significant temperature increase of 15 °C was detected for P(DTS-DAP)-*b*-P(Lys) solution (0.05 g.L⁻¹) within the same time range (**Figure V-24a**).

A solution of P(DTS-DAP) homopolymer in toluene (0.1 g.L⁻¹) was prepared to compare its photothermal response with P(DTS-DAP)-*b*-P(Lys) (**Figure V-24b**). Under the same conditions, the temperature change was almost null (2 °C) for a pure toluene system, however, for P(DTS-DAP) homopolymer, the temperature variation was 27 °C which is higher compared to that of the hybrid diblock copolymer. The lower photothermal response of P(DTS-DAP)-*b*-P(Lys) could be explained by both the lower solubility of the diblock in aqueous solution when compared to the solubility of P(DTS-DAP) homopolymer in toluene, and the smaller concentration of the chromophore DTS-DAP in the copolymer solution than in the homopolymer one.

To investigate the photothermal stability and reversibility of the hybrid diblock copolymer, multiple cycles of laser irradiation were conducted. As shown in **Figure V-24c**, after 4 heating/cooling cycles, the temperature changes were almost consistent for both P(DTS-DAP)-*b*-P(Lys) and P(DTS-DAP) which is an indication of a good photothermal stability of the hybrid diblock.

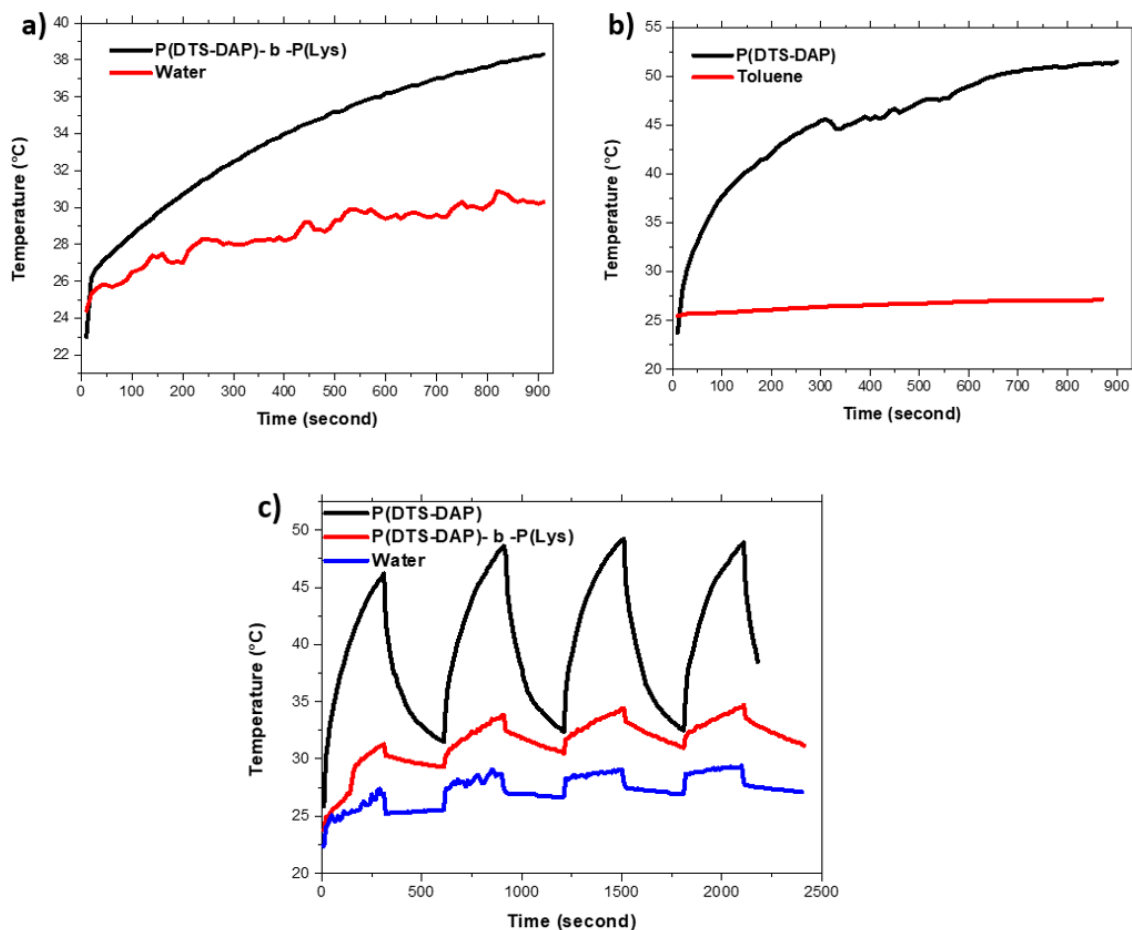


Figure V-24: Photothermal conversion behavior of (a) P(DTS-DAP)-*b*-P(Lys) in water and (b) P(DTS-DAP) in toluene. (c) Temperature variations of P(DTS-DAP)-*b*-P(Lys) and P(DTS-DAP) over four cycles of heating and natural cooling.

VI. Conclusion

The synthesis of block copolymers constituting of a polypeptide segment and a conjugated block absorbing in the near-IR region was investigated in order to create water dispersible, biocompatible and IR absorbing objects. Aniline-terminated P(DTS-DAP) was chosen as the conjugated block to initiate the ROP of the NCA functional group of the corresponding peptide monomers, γ -benzyl-*L*-glutamate (BLG) and trifluoroacetyl-*L*-lysine (TFA-Lys).

In this regard, two different hybrid block copolymers, P(DTS-DAP)-*b*-P(BLG) and P(DTS-DAP)-*b*-P(TFA-Lys), were formed and purified by successive washing in toluene which was more efficient for P(TFA-Lys)-based block copolymers. SEC-THF using a UV detector at 720 nm revealed the existence of 50 to 60% of unreacted P(DTS-DAP) homopolymer chains. ¹H NMR for P(DTS-DAP)-*b*-P(BLG) proved resonance peaks for both blocks while as for P(DTS-DAP)-*b*-P(TFA-Lys), it was difficult to identify the resonance peaks attributed to the conjugated block due to solubility problems. However, the analysis of the diblocks by FT-IR supported the successful synthesis in which peak characteristics for both P(DTS-DAP) block and polypeptide segment were observed. Additionally, the synthesized hybrid block copolymers showed very similar absorption properties to those of the conjugated homopolymer.

For achieving the main goal behind this synthesis, deprotection reactions were performed to cleave the benzyl group and hydrolyze the amide of the TFA functional group for P(DTS-DAP)-*b*-P(BLG) and P(DTS-DAP)-*b*-P(TFA-Lys), respectively. If the deprotection of P(DTS-DAP)-*b*-P(BLG) was not successful and could not be investigated due to time shortage, a nice P(DTS-DAP)-*b*-P(Lys) copolymer was obtained and characterized. After deprotection of the TFA-Lys, the dispersion of P(DTS-DAP)-*b*-P(Lys) in aqueous solution revealed the presence of a mixture of nanoobjects (157 nm) and a small proportion (15 w%) of bigger aggregates due to incomplete deprotection or to a low ratio of hydrophilic block/hydrophobic block. Interestingly, the photothermal behavior of the filtrated solution with 157 nm objects showed a promising photothermal behavior translated by a 15 °C increase in the solution's temperature within 15 min of irradiation.

Thus, future work will be dedicated to the synthesis of a larger batch of P(DTS-DAP)-*b*-P(TFA-Lys) bearing a longer block of polypeptide. The deprotection will be carried out with an increase in the amount of K₂CO₃ to insure a complete hydrolysis. Finally, transmission electron microscopy (TEM) will be used in addition to light scattering experiments to determine the morphology and the size of the synthesized amphiphilic block copolymers.

References

- (1) Cheng, Y.-J.; Yang, S.-H.; Hsu, C.-S. Synthesis of Conjugated Polymers for Organic Solar Cell Applications. *Chem. Rev.* **2009**, *109* (11), 5868–5923.
- (2) Botiz, I.; Darling, S. B. Optoelectronics Using Block Copolymers. *Mater. Today* **2010**, *13* (5), 42–51.
- (3) Iovu, M. C.; Craley, C. R.; Jeffries-EL, M.; Krankowski, A. B.; Zhang, R.; Kowalewski, T.; McCullough, R. D. Conducting Regioregular Polythiophene Block Copolymer Nanofibrils Synthesized by Reversible Addition Fragmentation Chain Transfer Polymerization (RAFT) and Nitroxide Mediated Polymerization (NMP). *Macromolecules* **2007**, *40* (14), 4733–4735.
- (4) Scherf, U.; Gutacker, A.; Koenen, N. All-Conjugated Block Copolymers. *Acc. Chem. Res.* **2008**, *41* (9), 1086–1097.
- (5) Hollinger, J.; Jahnke, A. A.; Coombs, N.; Seferos, D. S. Controlling Phase Separation and Optical Properties in Conjugated Polymers through Selenophene–Thiophene Copolymerization. *J. Am. Chem. Soc.* **2010**, *132* (25), 8546–8547.
- (6) Huang, C.-J.; Chang, F.-C. Polypeptide Diblock Copolymers: Syntheses and Properties of Poly(N-Isopropylacrylamide)-b-Polylysine. *Macromolecules* **2008**, *41* (19), 7041–7052.
- (7) Zhang, X.; Monge, S.; In, M.; Giani, O.; Robin, J.-J. Thermo- and PH-Sensitive Aggregation Behavior of PDEAm-b-P(L-Lysine) Double Hydrophilic Block Copolymers in Aqueous Solution. *Soft Matter* **2012**, *9* (4), 1301–1309.
- (8) Kong, X.; Jenekhe, S. A. Block Copolymers Containing Conjugated Polymer and Polypeptide Sequences: Synthesis and Self-Assembly of Electroactive and Photoactive Nanostructures. *Macromolecules* **2004**, *37* (22), 8180–8183.
- (9) Osada, K.; Christie, R. J.; Kataoka, K. Polymeric Micelles from Poly(Ethylene Glycol)–Poly(Amino Acid) Block Copolymer for Drug and Gene Delivery. *J. R. Soc. Interface* **2009**, *6* (suppl_3), S325–S339.
- (10) Jia, X.; Kiick, K. L. Hybrid Multicomponent Hydrogels for Tissue Engineering. *Macromol. Biosci.* **2009**, *9* (2), 140–156.
- (11) Tsai, H.-K. A.; Moschou, E. A.; Daunert, S.; Madou, M.; Kulinsky, L. Integrating Biosensors and Drug Delivery: A Step Closer Toward Scalable Responsive Drug-Delivery Systems. *Adv. Mater.* **2009**, *21* (6), 656–660.
- (12) Bonduelle, C. Secondary Structures of Synthetic Polypeptide Polymers. *Polym. Chem.* **2018**, *9* (13), 1517–1529.
- (13) Top, A.; Zhong, S.; Yan, C.; Roberts, C. J.; Pochan, D. J.; Kiick, K. L. Controlling Assembly of Helical Polypeptides via PEGylation Strategies. *Soft Matter* **2011**, *7* (20), 9758–9766.
- (14) Lee, M.; Cho, B.-K.; Zin, W.-C. Supramolecular Structures from Rod–Coil Block Copolymers. *Chem. Rev.* **2001**, *101* (12), 3869–3892.
- (15) Papadopoulos, P.; Floudas, G.; Klok, H.-A.; Schnell, I.; Pakula, T. Self-Assembly and Dynamics of Poly(γ -Benzyl-L-Glutamate) Peptides. *Biomacromolecules* **2004**, *5* (1), 81–91.
- (16) Klok, H.-A.; Langenwalter, J. F.; Lecommandoux, S. Self-Assembly of Peptide-Based Diblock Oligomers. *Macromolecules* **2000**, *33* (21), 7819–7826.
- (17) Idelson, M. Poly(γ -Benzyl-L-Glutamate) and Other Glutamic-Acid-Containing Polymers. *Sci. Polym. Lett. Ed.* **1985**, *23* (11), 604–604.
- (18) Kim, K. T.; Vandermeulen, G. W. M.; Winnik, M. A.; Manners, I. Organometallic–Polypeptide Block Copolymers: Synthesis and Properties of Poly(Ferrocenyldimethylsilane)-b-Poly- (γ -Benzyl-L-Glutamate). *Macromolecules* **2005**, *38* (12), 4958–4961.
- (19) Rubatat, L.; Kong, X.; Jenekhe, S. A.; Ruokolainen, J.; Hojiej, M.; Mezzenga, R. Self-Assembly of Polypeptide/ π -Conjugated Polymer/Polypeptide Triblock Copolymers in Rod–Rod–Rod and Coil–Rod–Coil Conformations. *Macromolecules* **2008**, *41* (5), 1846–1852.
- (20) Wallace, G. G.; Kane-Maguire, L. a. P. Manipulating and Monitoring Biomolecular Interactions with Conducting Electroactive Polymers. *Adv. Mater.* **2002**, *14* (13–14), 953–960.
- (21) Schmidt, C. E.; Shastri, V. R.; Vacanti, J. P.; Langer, R. Stimulation of Neurite Outgrowth Using an Electrically Conducting Polymer. *Proc. Natl. Acad. Sci.* **1997**, *94* (17), 8948–8953.
- (22) Piedra-Arroñi, E.; Makni, F.; Severac, L.; Stigliani, J.-L.; Pratiel, G.; Bonduelle, C. Smart Poly(Imidazolyl-L-Lysine): Synthesis and Reversible Helix-to-Coil Transition at Neutral PH. *Polymers* **2017**, *9* (7).
- (23) Rodriguez Hernandez, J.; Klok, H.-A. Synthesis and Ring-Opening (Co) Polymerization of L-Lysine N-Carboxyanhydrides Containing Labile Side-Chain Protective Groups. *J. Polym. Sci. Part -Polym. Chem. - J POLYM SCI -POLYM CHEM* **2003**, *41*, 1167–1187.
- (24) Deming, T. J. Methodologies for Preparation of Synthetic Block Copolypeptides: Materials with Future Promise in Drug Delivery. *Adv. Drug Deliv. Rev.* **2002**, *54* (8), 1145–1155.

- (25) Hundt, N.; Hoang, Q.; Nguyen, H.; Sista, P.; Hao, J.; Servello, J.; Palaniappan, K.; Alemseghed, M.; Biewer, M. C.; Stefan, M. C. Synthesis and Characterization of a Block Copolymer Containing Regioregular Poly(3-Hexylthiophene) and Poly(γ -Benzyl-L-Glutamate). *Macromol. Rapid Commun.* **2011**, *32* (3), 302–308.
- (26) Zhao, W.; Gnanou, Y.; Hadjichristidis, N. Fast and Living Ring-Opening Polymerization of α -Amino Acid N-Carboxyanhydrides Triggered by an “Alliance” of Primary and Secondary Amines at Room Temperature. *Biomacromolecules* **2015**, *16* (4), 1352–1357.
- (27) Wu, Z.-Q.; Ono, R. J.; Chen, Z.; Li, Z.; Bielawski, C. W. Polythiophene–Block–Poly(γ -Benzyl L-Glutamate): Synthesis and Study of a New Rod–Rod Block Copolymer. *Polym. Chem.* **2011**, *2* (2), 300–302.
- (28) Kim, M.; Lee, J.-H.; Nam, J.-M. Plasmonic Photothermal Nanoparticles for Biomedical Applications. *Adv. Sci.* **2019**, *6* (17), 1900471.
- (29) Abbas, M.; Zou, Q.; Li, S.; Yan, X. Self-Assembled Peptide- and Protein-Based Nanomaterials for Antitumor Photodynamic and Photothermal Therapy. *Adv. Mater.* **2017**, *29* (12), 1605021.
- (30) Avci, P.; Gupta, A.; Sadasivam, M.; Vecchio, D.; Pam, Z.; Pam, N.; Hamblin, M. R. Low-Level Laser (Light) Therapy (LLLT) in Skin: Stimulating, Healing, Restoring. *Semin. Cutan. Med. Surg.* **2013**, *32* (1), 41–52.
- (31) Yao, H.; Sheng, K.; Sun, J.; Yan, S.; Hou, Y.; Lu, H.; Olsen, B. D. Secondary Structure Drives Self-Assembly in Weakly Segregated Globular Protein–Rod Block Copolymers. *Polym. Chem.* **2020**, *11* (17), 3032–3045.
- (32) Zhang, Q. T.; Tour, J. M. Alternating Donor/Acceptor Repeat Units in Polythiophenes. Intramolecular Charge Transfer for Reducing Band Gaps in Fully Substituted Conjugated Polymers. *J. Am. Chem. Soc.* **1998**, *120* (22), 5355–5362.
- (33) Devasagayaraj, A.; Tour, J. M. Synthesis of a Conjugated Donor/Acceptor/Passivator (DAP) Polymer. *Macromolecules* **1999**, *32* (20), 6425–6430.
- (34) Koldemir, U.; Puniredd, S. R.; Wagner, M.; Tongay, S.; McCarley, T. D.; Kamenov, G. D.; Müllen, K.; Pisula, W.; Reynolds, J. R. End Capping Does Matter: Enhanced Order and Charge Transport in Conjugated Donor–Acceptor Polymers. *Macromolecules* **2015**, *48* (18), 6369–6377.
- (35) Asawapirom, U.; Güntner, R.; Forster, M.; Farrell, T.; Scherf, U. Dialkylfluorene-Oligothiophene and Dialkylfluorene-Dithienylvinylene Alternating Copolymers. *Synthesis* **2002**, *2002* (9), 1136–1142.
- (36) Ramani, R.; Srivastava, J.; Alam, S. Application of Model-Free Kinetics to the Thermal and Thermo-Oxidative Degradation of Poly(3-Hexyl Thiophene). *Thermochim. Acta* **2010**, *499* (1), 34–39.
- (37) Mishra, S. P.; Palai, A. K.; Patri, M. Synthesis and Characterization of Soluble Narrow Band Gap Conducting Polymers Based on Diketopyrrolopyrrole and Propylenedioxythiophenes. *Synth. Met.* **2010**, *160* (23), 2422–2429.
- (38) Schatz, C.; Louguet, S.; Le Meins, J.-F.; Lecommandoux, S. Polysaccharide-Block-Polypeptide Copolymer Vesicles: Towards Synthetic Viral Capsids. *Angew. Chem. Int. Ed.* **2009**, *48* (14), 2572–2575.
- (39) Wood, S.; Wade, J.; Shahid, M.; Collado-Fregoso, E.; Bradley, D. D. C.; Durrant, J. R.; Heeney, M.; Kim, J.-S. Natures of Optical Absorption Transitions and Excitation Energy Dependent Photostability of Diketopyrrolopyrrole (DPP)-Based Photovoltaic Copolymers. *Energy Environ. Sci.* **2015**, *8* (11), 3222–3232.
- (40) Ibarboue, E.; Rodríguez-Hernández, J.; Papon, E. Thermotropic Liquid Crystal Behavior on PBLG-PDMS-PBLG Triblock Copolymers. *J. Polym. Sci. Part Polym. Chem.* **2006**, *44* (15), 4668–4679.
- (41) Sen, A. C.; Keiderling, T. A. Vibrational Circular Dichroism of Polypeptides. III. Film Studies of Several α -Helical and β -Sheet Polypeptides. *Biopolymers* **1984**, *23* (8), 1533–1545.
- (42) Aujard-Catot, J.; Nguyen, M.; Bijani, C.; Pratviel, G.; Bonduelle, C. Cd²⁺ Coordination: An Efficient Structuring Switch for Polypeptide Polymers. *Polym. Chem.* **2018**, *9* (30), 4100–4107.
- (43) David, J.; Weiter, M.; Vala, M.; Vyňuchal, J.; Kučerík, J. Stability and Structural Aspects of Diketopyrrolopyrrole Pigment and Its N-Alkyl Derivatives. *Dyes Pigments* **2011**, *89* (2), 137–143.
- (44) Cheng, J.; Deming, T. J. Synthesis of Polypeptides by Ring-Opening Polymerization of α -Amino Acid N-Carboxyanhydrides. In *Peptide-Based Materials*; Deming, T., Ed.; Topics in Current Chemistry; Springer: Berlin, Heidelberg, 2012; pp 1–26.

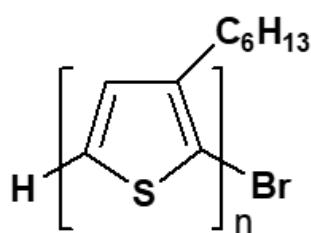
Chapter VI: Experimental Procedures and Characterization Techniques

I. Materials

All the reactions were performed under pre-dried nitrogen using a flame-dried glassware. The syringes used to transfer the reagents or solvents were first purged with nitrogen prior their use. Glassware were washed in organic solvents and dried in an oven at 150 °C overnight before their use. All chemicals and reagents were used as received from Aldrich (France) and ABCR (Germany) companies and stored in the glovebox. Except P3HT₂₄₀ and DTS monomer were purchased from Solaris-Chem and 1-Materials, respectively in which they were also used as received.

II. Synthetic procedures of Chapter II

a. Synthesis of P3HT-Br



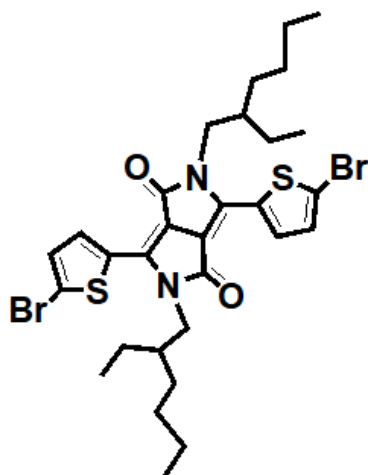
P3HT was prepared by a Grignard metathesis polymerization following the procedure described by McCullough *et al.*¹ In a dry 100 mL round bottom flask equipped with a magnetic bar, 1 g (3.066 mmol) of the 2,5-dibromo-3-hexyl-thiophene monomer was added with 40 mL dry THF. The mixture was flushed with nitrogen and kept under agitation for 30 minutes at room temperature. After then, 1.5 mL (3.066 mmol) of isopropyl magnesium chloride was added to the reaction mixture that was

stirred for 2 hours at room temperature before the addition of 0.040 g (0.075 mmol) of Ni(dppp)Cl₂. After agitating for 15 minutes, the P3HT-Br polymer was quenched by adding 5 mL of methanol. Then, it was precipitated in cold methanol. After filtration, the crude polymer was purified by Soxhlet successive extractions in methanol, hexane and acetone. Finally, the polymer was collected by Soxhlet in chloroform with a yield between 50% to 60%. The same procedure was followed to synthesize P3HT-Br having different molar masses by changing the ratio of the monomer to catalyst depending on the desired degree of polymerization as shown in Table VI-1.

¹H NMR (CDCl₃, 400 MHz) δ (ppm) = 6.97 (s, 1H), 2.80 (t, 2H), 1.70-1.34 (m, 8H), 0.91 (t, 3H).

Table VI-1: P3HTs synthesized with different desired degree of polymerization.

polymer	n Ni(dppp)Cl ₂ (mmol)	$\frac{n \text{ Monomer}}{n \text{ Ni(dppp)Cl}_2}$
P3HT ₂₅	0.075	40
P3HT ₃₇	0.06	50
P3HT ₉₆	0.03	100

b. Synthesis of diketopyrrolopyrrole monomer (DPP)

Di-brominated DPP monomer was synthesized according to the synthetic route developed in literature.² The synthesis is based on three steps.

i. 3,6-Dithiophene-2-yl-2,5-dihydropyrrolo[3,4-c]pyrrole-1,4-dione (DPP)

In a 250 mL double necked round bottom flask with a magnetic stirring bar, 3.5 g (0.15 mol) of sodium were added to 60 mL t-amyl alcohol with 0.05 g (0.3 mmol) of anhydrous iron(III) chloride. The mixture was stirred under inert atmosphere (N₂) at 110 °C for 1 hour, until complete dissolution of sodium. The mixture was then cooled to 80 °C and 9.5 g (0.87 mol) of 2-thiophene-carbonitrile were added in one shot. Then, a solution of di-isopropylsuccinate (7.092 g, 0.35 mol) in t-amyl alcohol was added dropwise using a dropping funnel. When the addition of the solution was completed, the reaction was left at 85 °C for 5 hours. The brown-red mixture was cooled at room temperature and filtered using Buchner funnel. The brown-red solid filtrate was washed several times with warm deionized water and methanol (yield = 80%).

¹H NMR (400 MHz, d₆-DMSO) δ (ppm) = 11.22 (s, 2H), 8.19 (d, 2H), 7.94 (d, 2H), 7.28 (dd, 2H).

ii. 2,5-bis-(2-ethyl-hexyl)-3,6-dithiophen-2-ylpyrrolo[3,4-c]pyrrole-1,4-dione (DPP-eH)

The product was alkylated using 2-ethylhexyl bromide C₈H₁₇Br. In this regard, 1 eq (2g, 6.6 mmol) of the obtained product in step 1 was stirred in anhydrous DMF under inert atmosphere (N₂) for 1 hour. 3.5 eq of anhydrous K₂CO₃ (3.2 g, 23 mmol), 3 eq of C₈H₁₇Br (3.8 g, 19.8 mmol) and 0.01 eq of 18-crown-6 (20.8 mg, 0.1 mmol) were added to the initial solution. The mixture was stirred overnight at 120 °C and then filtered using a Buchner funnel. The filtrate was washed several times with warm deionized water and methanol. The crude product was purified using a classical column chromatography using a 1:1 ratio of hexane and dichloromethane as an eluent. After purification, the product was dried under vacuum to obtain a dark red solid with a yield of 80%.

¹H NMR (400 MHz, CDCl₃) δ (ppm) = 8.88 (d, 2H), 7.62 (d, 2H), 7.27 (m, 2H), 4.02 (m, 4H), 1.85 (m, 2H), 1.56-1.24 (m, 16H), 1.10-0.85 (m, 12H).

iii. 1,4-bis(5-bromothiophen-2-yl)-3,6-bis(Ethylhexylthio)pyrrolo[3,4-c]pyrrole (DPP-Br₂)

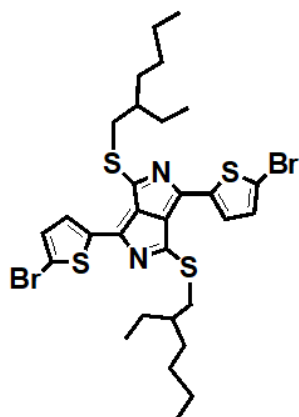
To brominate the thiophene unit after alkylation, 1 eq (2g, 2.9 mmol) of the product obtained in step 2 was placed in 50 mL dry chloroform. After stirring for 30 minutes at room temperature, 2.2 eq of N-bromosuccinimide (NBS) (1.13 g, 6.38 mmol) were added in small portions. The mixture was stirred at 60 °C for 4 hours in the dark. Then, the chloroform was evaporated where the product was precipitated in cold methanol and the resulting dark red solid was purified by column chromatography using a 2:1 ratio of hexane and dichloromethane as an eluent. The final product was dried under vacuum until complete solvent removal (yield = 70%).

¹H NMR (400 MHz, CDCl₃) δ (ppm) = 8.62 (d, 2H), 7.22 (d, 2H), 3.97-3.92 (m, 4H), 1.82 (s, 2H), 1.81-1.26 (m, 16H), 0.86 (m, 12H).

¹³C NMR (100 MHz, CDCl₃) δ (ppm) = 161.39, 139.40, 135.37, 131.46, 131.16, 119.01, 108.00, 46.00, 39.10, 30.17, 28.31.

c. Synthesis of 2,5-diazapentalene monomer (DAP)

Di-brominated DAP monomer was synthesized starting from the product obtained in step 1 of the DPP monomer. This synthetic route was performed according to literature.³



i. 3,6-di(thiophen-2-yl)-2,5-dihydropyrrolo[3,4-c]pyrrole-1,4-dithione (DTPP)

1 g (3.3 mmol) of the non-alkylated DPP was mixed with 2.82 g (6.7 mmol) of Lawesson's reagent in 70 mL anhydrous chlorobenzene. After stirring overnight at 140 °C under inert atmosphere (N₂), the crude product was precipitated in cold methanol. A dark green color was observed as an indication for the formation of thiolactam intermediate. The solution was precipitated in cold methanol and purified using Soxhlet in ethanol to remove the phosphorous residues. The dark green solid was then collected and dried under vacuum in dark to obtain a yield of 85%.

¹H NMR (400 MHz, DMSO-*d*₆) δ (ppm) = 12.92 (s, 2H), 9.12 (dd, 2H), 8.18 (dd, 2H), 7.52 (dd, 2H).

ii. 1,4-bis((2-ethylhexyl)thio)-3,6-di(thiophen-2-yl) pyrrolo[3,4-c]pyrrole (DAP-eH)

The dark green solid (DTPP) was alkylated also using 2-ethylhexyl bromide. To perform this alkylation step, 2 g (6.03 mmol) of DTPP were mixed with 2.8 g (20 mmol) of K_2CO_3 and 75 mL of dry acetone. The solution was bubbled with N_2 for 10 minutes before the addition of 3 eq of $C_8H_{17}Br$ (3.4g, 18 mmol). The mixture was heated at 60 °C overnight. The solvent was then evaporated and the crude product was extracted with chloroform. $MgSO_4$ was used in a drying process. Then, the crude product was purified using a classical column chromatography with a 0.6:0.4 ratio of hexane:dichloromethane (CH_2Cl_2) to separate the desired dark green product with a yield of 45%.

1H NMR (400 MHz, $CDCl_3$) δ (ppm) = 8.10 (d, 2H), 7.62 (d, 2H), 7.27 (m, 2H), 3.57-3.48 (m, 4H), 1.85-1.79 (m, 2H), 1.52-1.30 (m, 16H), 1.00-0.89 (m, 12H).

iii. 1,4-bis(5-bromothiophen-2-yl)-3,6-bis(Ethylhexylthio) pyrrolo[3,4c] pyrrole (DAP-Br₂)

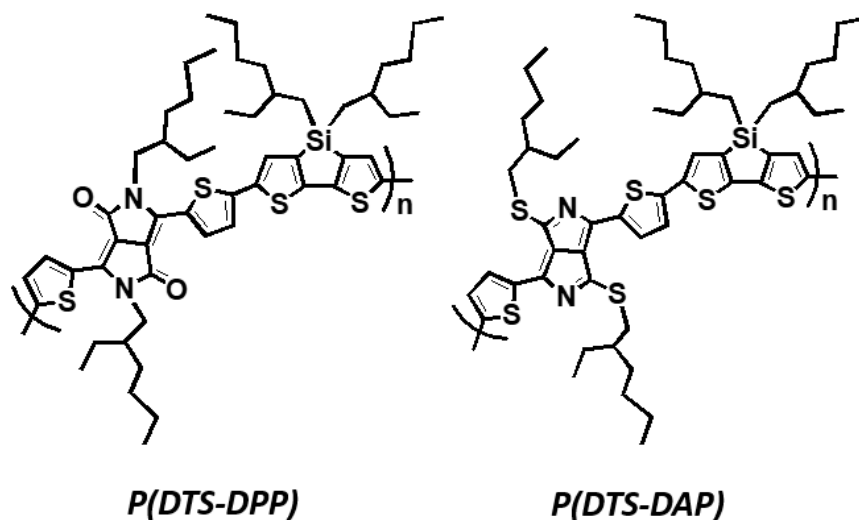
To brominate the thiophene, 1 eq (2 g, 3.6 mmol) of the alkylated product obtained in step 2 was mixed with 2.2 eq of NBS (1.5 mg, 8 mmol) in 80 mL dry chloroform. The mixture was bubbled in N_2 for 10 minutes. The reaction was kept in dark for 3 hours at room temperature. TLC was used to follow the reaction that was quenched with 10 mL distilled water. The aqueous phase was extracted with dichloromethane (CH_2Cl_2). The organic phase was then dried with $MgSO_4$ to remove the traces of water. Column chromatography was used for purification with a 1:1 ratio of hexane and dichloromethane. The final dark solid product was dried under vacuum until complete solvent removal (experimental yield is 82%).

1H NMR (400 MHz, $CDCl_3$) δ (ppm) = 7.79 (d, 2H), 7.21 (d, 2H), 3.52-3.45 (m, 4H), 1.80-1.77 (m, 2H), 1.49-1.25 (m, 16H), 0.97-0.91 (m, 12H).

^{13}C NMR (100 MHz, $CDCl_3$) δ (ppm) = 166.68, 151.02, 140.78, 132.59, 132.15, 121.12, 39.80, 36.66, 32.68, 29.04, 25.84, 23.05, 14.15, 11.01.

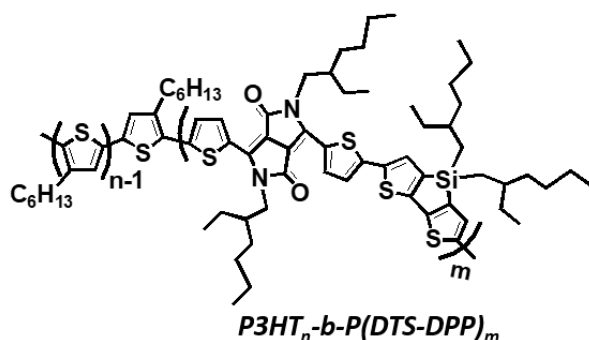
d. Synthesis of P(DTS-DPP) and P(DTS-DAP) copolymers

The various copolymers of (DTS-DPP) and (DTS-DAP) were prepared by following the conventional Stille polycondensation with a metal catalyst following the procedure of Khelifi *et al.*⁴



For the synthesis of P(DTS-DPP)_n and P(DTS-DAP)_n, all materials were weighed in the glovebox, 1 eq of 4,4'-bis(2-ethyl-hexyl)-5,5'-bis(trimethyltin)-dithieno[3,2-b:2',3'-d]silole, DTS (120 mg, 0.16 mmol) was mixed under inert atmosphere in a microwave tube with 1 eq of DPP (110 mg, 0.16 mmol) or DAP (115mg, 0.16 mmol) in 2 mL anhydrous chlorobenzene. Tris(dibenzylideneacetone) dipalladium(0), Pd₂(dba)₃ (6.00 mg, 0.0065 mmol) and tri(*o*-tolyl)phosphine, P(*o*-tolyl)₃ ligand (8 mg, 0.026 mmol) were then added. The mixture was kept under inert atmosphere and stirred at 110 °C for 2 hours until the product became viscous. It is worth mentioning that the synthesis of P(DTS-DAP) was observed to be faster where the polymer became viscous after 20 minutes of the polymerization. The polymers were precipitated in cold methanol and then filtrated. Soxhlet successive extractions were performed in acetone, methanol and cyclohexane. The product was finally recovered in chloroform. The chloroform was concentrated and the final dark black polymers P(DTS-DPP) and P(DTS-DAP) were collected with a yield of 75 to 82%, dried under high vacuum, then stored in the glovebox.

e. Synthesis of all-conjugated block copolymers



A Stille polycondensation with a metal catalyst was used to synthesize all the studied conjugated block copolymers. The main difference was only the ratio of P3HT-Br with respect to the second block. The synthesis of the CBCPs was performed depending on the Carothers equation to determine the amount of the starting material to be added according to the desired degree of polymerization.

i. General procedure for synthesizing $P3HT_n\text{-}b\text{-}P(DTS\text{-}DPP)_m$

The molar composition between P3HT and the monomer reagents was calculated from the Carothers equations used in step-growth polymerization by considering a 100% conversion.⁵ The stoichiometry of both monomers (DTS and DPP) and the end-capping agent (P3HT-Br) in such reactions is an essential factor that allow the determination of the length of the second block (low-bandgap block). In our study, the stoichiometry of the species was maintained according to **Equation 1**.

$$2N_{DTS} = 2N_{DPP} + N_{P3HT} \quad \text{Equation 1}$$

where N_{DTS} , N_{DPP} and N_{P3HT} represent the number of equivalent of DTS, DPP and P3HT end-capper, respectively.

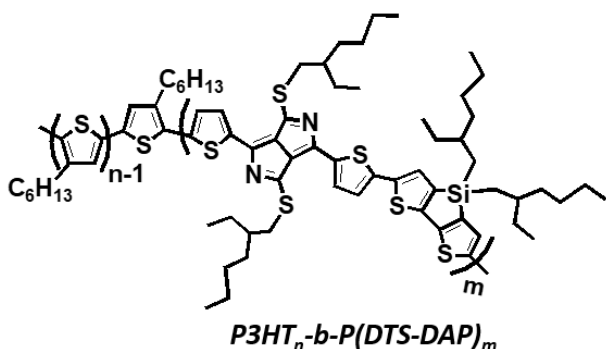
For the synthesis of $P3HT_n\text{-}b\text{-}P(DTS\text{-}DPP)_m$, P3HT-Br was mixed in the glovebox with the distannylated DTS and di-brominated DPP monomers. $Pd_2(dba)_3$ catalyst (4 mg, 0.0043 mmol) and $P(o\text{-tolyl})_3$ ligand (5 mg, 0.016 mmol) were added to the reaction mixture. A flow of N_2 was applied for 15 minutes followed by the addition of 15 mL dry toluene. The mixture was bubbled with N_2 for 10 minutes before heating at 110 °C. After 24 hours, the mixture was cooled down and the crude conjugated block copolymer was precipitated in cold methanol and then filtrated. The obtained polymer was purified using Soxhlet successive extractions in acetone, methanol, cyclohexane and finally collected in chloroform. The final polymer with a yield of 70 to 85% was dried under vacuum and stored in the glovebox.

The same procedure was used to synthesize $P3HT_{25}\text{-}b\text{-}P(DTS\text{-}DPP)_8$, $P3HT_{37}\text{-}b\text{-}P(DTS\text{-}DPP)_4$, $P3HT_{37}\text{-}b\text{-}P(DTS\text{-}DPP)_{19}$, $P3HT_{240}\text{-}b\text{-}P(DTS\text{-}DPP)_{11}$ and $P3HT_{96}\text{-}b\text{-}P(DTS\text{-}DPP)_{13}$ by simply changing the ratio between the starting monomers as shown in **Table VI-2**.

Table VI-2: Molecular ratios used for the synthesis of the DPP-based CBCPs where N is number of equivalent, n is number of moles and m is the corresponding mass.

Polymer	N DTS	N DPP	N P3HT-Br	nDTS ^(mmol)	nDPP ^(mmol)	nP3HT-Br ^(mmol)
				mDTS ^(mg)	mDPP ^(mg)	mP3HT-Br ^(mg)
P3HT ₂₅ - <i>b</i> -P(DTS-DPP) ₈	1	0.96	0.08	0.134	0.12	0.01
				100	82	45
P3HT ₃₇ - <i>b</i> -P(DTS-DPP) ₄	1	0.92	0.16	0.134	0.123	0.02
				100	84	131
P3HT ₃₇ - <i>b</i> -P(DTS-DPP) ₁₉	1	0.98	0.04	0.134	0.131	0.00536
				100	90	33
P3HT ₉₆ - <i>b</i> -P(DTS-DPP) ₁₃	1	0.98	0.04	0.134	0.132	5.3x10 ⁻³
				100	90	85
P3HT ₂₄₀ - <i>b</i> -P(DTS-DPP) ₁₁	1	0.98	0.04	0.067	0.061	0.0026
				50	42	107

ii. General procedure for synthesizing P3HT_{*n*}-*b*-P(DTS-DAP)_{*m*}



The same procedure was applied for synthesizing P3HT_{*n*}-*b*-P(DTS-DAP)_{*m*} by using the same equations in which DPP was replaced by DAP monomer. For this synthesis, P3HT-Br was mixed in the glovebox with di-stannylated DTS and di-brominated DAP monomers. Pd₂(dba)₃ catalyst (4 mg, 0.0043 mmol) and P(*o*-tolyl)₃ ligand (5 mg, 0.016 mmol) were added to the reaction mixture. A flow of N₂ was applied

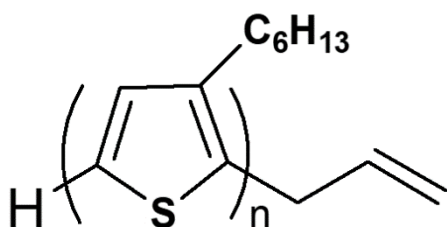
for 15 minutes followed by the addition of 15 mL of dry toluene. The mixture was bubbled with N₂ for 10 minutes before heating at 110 °C. After 24 hours, the mixture was cooled down and the crude conjugated block copolymer was precipitated in cold methanol and then filtrated. The obtained polymer was purified using Soxhlet successive extractions in acetone, methanol, cyclohexane and finally collected in chloroform. The final polymer with a yield of 70 to 85% was dried under vacuum and stored in the glovebox. The same procedure was used to synthesize P3HT₂₅-*b*-P(DTS-DAP)₉, P3HT₃₇-*b*-P(DTS-DAP)₄ and P3HT₃₇-*b*-P(DTS-DAP)₁₁ by changing the ratio between the starting monomers as shown in **Table VI-3**.

Table VI-3: Molecular ratios used for the synthesis of the DAP-based CBCPs where N is number of equivalent, n is number of moles and m is the corresponding mass.

Polymer	N DTS	N DPP	N P3HT-Br	nDTS ^(mmol)	nDPP ^(mmol)	nP3HT-Br ^(mmol)
				mDTS ^(mg)	mDPP ^(mg)	mP3HT-Br ^(mg)
P3HT ₂₅ - <i>b</i> -P(DTS-DAP) ₉	1	0.96	0.08	0.134	0.12	0.01
				100	91	45
P3HT ₃₇ - <i>b</i> -P(DTS-DAP) ₄	1	0.92	0.16	0.134	0.123	0.02
				100	88	131
P3HT ₃₇ - <i>b</i> -P(DTS-DAP) ₁₁	1	0.98	0.04	0.134	0.131	0.00536
				100	93	33

III. Synthetic procedures of Chapter IV

a. Synthesis of allyl-terminated P3HT

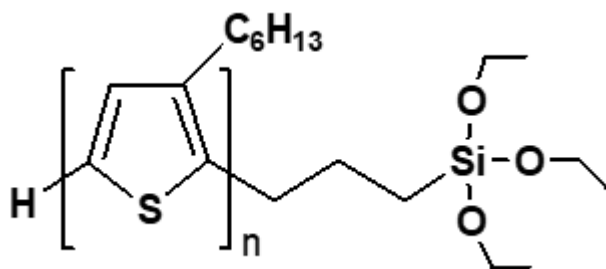


Allyl-terminated P3HT of high regioregularity was synthesized according to the literature work using Kumada catalyst-transfer polycondensation (KCTP) known as GRIM polymerization that yields an end-functionalized allyl group.⁶ This reaction was performed in a dry 100 mL round bottom flask under inert atmosphere at ambient temperature being sensitive to water and oxygen.

1 g (3.06 mmol) of 2,5-dibromo-3-hexyl-thiophene was stirred for 15 minutes in 10 mL dried THF. Then, 1 eq (0.3 g, 3.06 mmol) of isopropyl magnesium chloride was added and the reaction mixture was stirred for 2 hours at ambient temperature. 0.055 g (0.102 mmol) of Ni(dppp)Cl₂ were then added after diluting the reaction mixture with 40 mL dry THF. The reaction mixture was stirred for 10 minutes to proceed the polymerization before the addition of 0.154 g (1.53 mmol) allyl magnesium chloride. After stirring for 30 minutes at ambient temperature, the reaction was quenched with methanol, precipitated in cold methanol and then filtrated. The obtained dark solid product was purified by Soxhlet successive extractions in ethanol and acetone, then finally recovered in chloroform with a yield of 55%.

¹H NMR (CDCl₃, 400 MHz) δ (ppm) = 6.97 (s, 1H), 5.96 (m, 1H), 5.12 (m, 2H), 3.50 (d, 2H), 2.50 (t, 2H), 1.70 (q, 2H), 1.54-1.34 (m, 6H), 0.91 (t, 3H).

b. Synthesis of triethoxysilane-terminated P3HT (P3HT-Si)



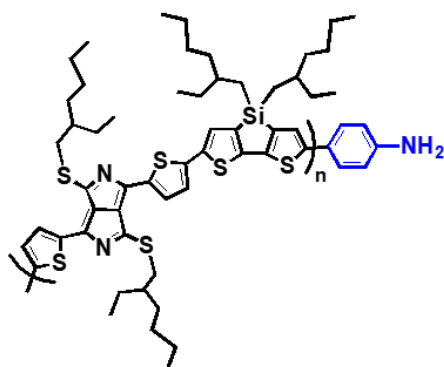
In a 50 mL round bottom flask, 2 eq (100 mg, 0.027 mmol) of allyl-terminated P3HT were mixed with 1 eq (6 mg, 0.013 mmol) of chloroplatinic acid, H_2PtCl_6 in 15 mL dry THF before degassing for 20 minutes. 0.3 mL (100 eq) of triethoxysilane were then added dropwise while the reaction was kept under agitation. The reaction mixture was

then stirred for 30 minutes at ambient temperature before increasing the temperature to 55 °C for 5 hours. The obtained solid powder was precipitated twice in dry ethanol under nitrogen, then filtrated and dried for complete solvent removal. The polymer with 90% yield was stored in the glovebox to avoid hydrolysis of the end-chain.⁷

^1H NMR (CDCl_3 , 400 MHz) δ (ppm) = 6.97 (s, 1H), 3.72 (q, 6H), 2.79 (t, 2H), 1.69 (q, 2H), 1.34 (m, 6H), 1.22 (t, 9H), 0.90 (t, 3H).

IV. Synthetic procedures of Chapter V

a. Synthesis of aniline-terminated P(DTS-DAP)



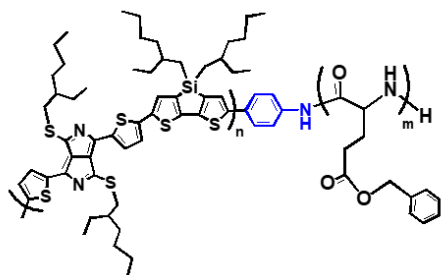
For the synthesis of P(DTS-DAP), all the materials were weighed in the glovebox, 1 eq (120 mg, 0.16 mmol) of DTS was mixed under inert atmosphere in a microwave tube with 0.95 eq (109 mg, 0.153 mmol) of DAP and 0.1 eq (3 mg, 0.016 mmol) of 4-bromoaniline in 2 mL anhydrous chlorobenzene. $\text{Pd}_2(\text{dba})_3$ (6.00 mg, 0.0065 mmol) and $\text{P}(\text{o-tolyl})_3$ ligand (8 mg, 0.026 mmol) were then added. The mixture was kept under inert atmosphere and stirred at 110 °C for 1 hour until the product became viscous. The polymer was then precipitated in cold

methanol and filtrated. Soxhlet successive extractions were performed in acetone, ethanol and cyclohexane. The product was finally recovered in chloroform. The chloroform was concentrated and the final dark black P(DTS-DAP) was collected with an 80% yield, dried under vacuum, then stored in the glovebox.

^1H NMR (400 MHz, $\text{C}_2\text{D}_2\text{Cl}_4$) δ (ppm): 8.08 (s, 12H), 7.65 (s, 2H), 7.09-7.516 (m, 24H), 6.81 (s, 2H), 3.48-3.76 (m, 26H), 2-0.65 (m, 384H).

b. Synthesis of Benzyl-L-Glutamate NCA-based hybrid copolymers

i. Synthesis of P(DTS-DAP)-*b*-P(BLG)



For the synthesis of the diblock, all the reactants were weighed in the glovebox. 30 mg of aniline-terminated P(DTS-DAP) were first dissolved as a macroinitiator in 5 mL THF solvent. The prepared solution was then transferred into the schlenk flask equipped with a magnetic stirrer and containing the benzyl-L-glutamate NCA repetitive monomer with different amounts depending on the desired degree of polymerization

(Monomer/Initiator) as shown in **Table VI-4**.

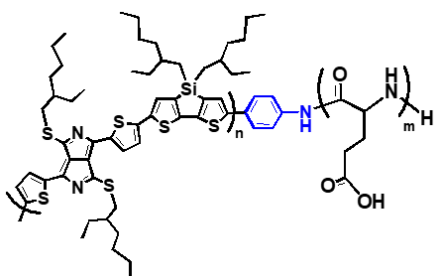
Table VI-4: Masses used in the synthesis of P(DTS-DAP)-*b*-P(BLG) hybrid copolymers with different degrees of polymerization.

Polymer	n of initiator m of initiator	n of monomer (mmol) m of monomer (mg)	DP _n (Monomer/Initiator)
Polymer 1	7.5x10 ⁻³ mmol	0.375 mmol	50
	30 mg	98.6 mg	
Polymer 2	7.5x10 ⁻³ mmol	0.75 mmol	100
	30 mg	197.25 mg	

The reaction mixture was then left under argon while agitating for 48 hours. The polymers were precipitated in methanol and collected as sediments after centrifugation with a speed of 2000 rpm.

¹H NMR: (400 MHz, C₂D₂Cl₄) δ (ppm): P(DTS-DAP) block: 8.10 (s, 12H), 7.41-7.16 (m, 24H), 3.55-3.65 (m, 24H), 1.9-0.80 (m, 384H). PBLG block: (400 MHz, C₂D₂Cl₄) δ (ppm): 8.30 (s, 1H), 5.10 (2H), 4-3.86 (s, 1H), 2.76-1.97 (m, 4H).

ii. Deprotection of P(DTS-DAP)-*b*-P(BLG)



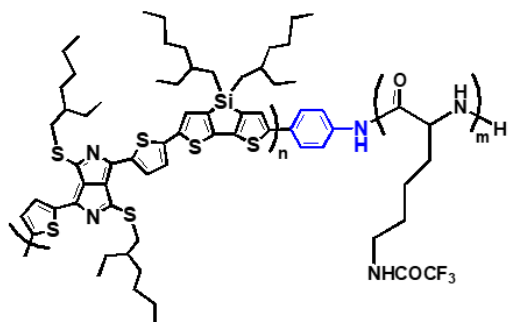
100 mg (0.007 mmol) of P(DTS-DAP)-*b*-P(BLG) were dissolved in 5 mL trifluoroacetic acid (TFA) and stirred in an ice bath at 0 °C. 1 mL of anisole and 5 mL of methanesulfonic acid were then added to the solution mixture. The mixture was first stirred for 20 minutes at 0 °C then at room temperature for another 20 minutes.

The deprotected polymer was then precipitated twice in diethyl ether (Et₂O) and finally collected by centrifugation with a speed of 2000 rpm. The precipitate was suspended in 8 mL water and 9.5 mL saturated sodium bicarbonate (NaHCO₃) solution. The resulting mixture was dialyzed against milliQwater (MWCO 1 kDa) and lyophilized yielding P(DTS-DAP)-*b*-P(GA).

Certain experimental problems were associated with this reaction in which it was difficult to recover the final desired polymer. Additionally, due to the limited amount of the protected polymer it was difficult to repeat it again.

c. Synthesis of TFA-Lysine NCA-based hybrid copolymers

i. Synthesis of P(DTS-DAP)-*b*-P(TFA-Lys)

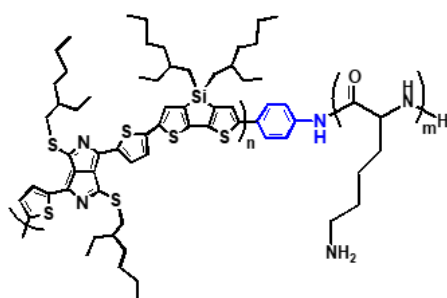


The same procedure used for the synthesis of P(DTS-DAP)-*b*-P(BLG) was applied for synthesizing P(DTS-DAP)-*b*-P(TFA-Lys) diblock copolymer with two different degrees of polymerization as shown in **Table VI-5**. The only difference is that after 48 hours, the polymers were precipitated in cyclohexane and then collected as sediments after centrifugation with a speed of 2000 rpm.

Table VI-5: Masses used in the synthesis of P(DTS-DAP)-*b*-P(TFA-Lys) hybrid copolymers with different degrees of polymerization.

Polymer	n of initiator m of initiator	n of monomer (mmol) m of monomer (mg)	DP _n (Monomer/Initiator)
Polymer 1	7.5x10 ⁻³ mmol	0.375 mmol	50
	30 mg	107 mg	
Polymer 2	7.5x10 ⁻³ mmol	0.75 mmol	100
	30 mg	214 mg	

ii. Deprotection of P(DTS-DAP)-*b*-P(TFA-Lys)



100 mg of the protected polypeptide was dissolved in 20 mL of a 1:9 (v/v) mixture of H₂O and THF. The solution was heated to 50 °C, before the addition of K₂CO₃ (2 eq/peptide chain) to the reaction mixture. After 4 hours under reflux, the reaction mixture was cooled to room temperature and THF was removed by rotary evaporator. The residue was then suspended in 8 mL water and 9.5 mL saturated sodium bicarbonate (NaHCO₃) solution. The resulting mixture was dialyzed against milliQwater (MWCO 1 kDa) and lyophilized yielding P(DTS-DAP)-*b*-P(Lys).

V. Fabrication of organic solar cells

a. Preparation of ITO substrates

The ITO substrates ($10 \Omega/\text{sq}$) were pre-cleaned before use. Cleaning the substrates is a mandatory process to remove any residual dusts or organic contaminants. The handling of the substrates was done using metal tweezers to avoid any further contamination. The cleaning process of the ITO substrates consists of several steps. At first, a digital multimeter was used to check the conductivity of the ITO surface, thus to ensure that the spin-coating is done on the ITO and not on the glass side. The substrates were then placed in a specific holder as shown in **Figure VI-1**. The holder was immersed in a beaker filled with deionized water to be ultrasonicated at room temperature for 15 minutes. This step removes any residual contaminants that can be physisorbed on the surface of the ITO substrate. The holder was then placed in a beaker filled with acetone and ethanol successively and ultrasonicated at room temperature for 15 minutes. Finally, the holder was immersed in isopropanol for the last 15 minutes of ultrasonication. The purpose behind this step is to remove any traces of acetone and ethanol that might appear after drying the ITO substrates with air flow. The last step is placing the substrates inside a UV-O₃ cleaner chamber for 15 minutes at 80 °C.



Figure VI-1: ITO substrates placed in a sample holder.

b. Device fabrication

The spin-coating process was used for the deposition of all the solution-processed layers. As shown in **Figure VI-2**, this process was done by first depositing the solution on top of the substrate followed by spinning at a specific speed for a period of time to obtain the desired thickness. The last step is the solvent evaporation either by thermal annealing or under vacuum.

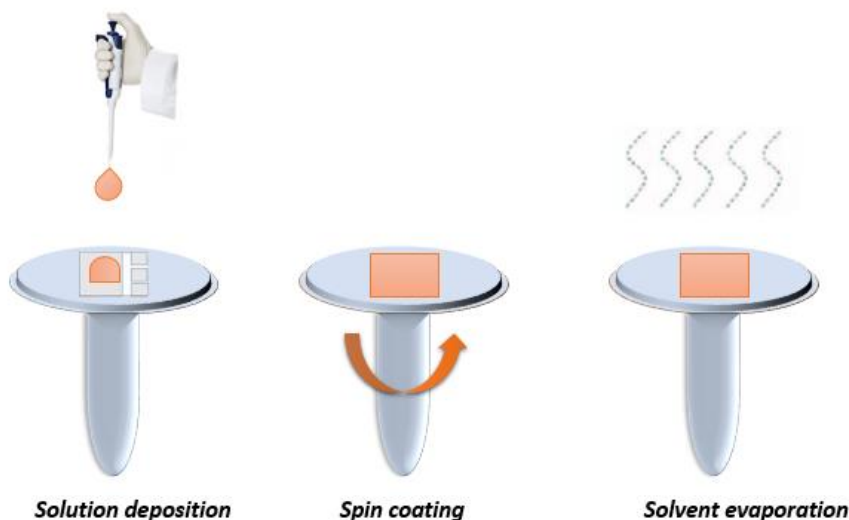


Figure VI-2: The steps of the spin-coating process.

i. Inverted device structures

All the solar cells mentioned in **Chapter III** were based on the inverted device architectures. For their preparation, we proceed as follows: 0.15 mol.L⁻¹ ZnO solution was prepared by mixing 66 mg zinc acetate in 2 mL absolute ethanol and 18 μ L ethanolamine. The solution was stirred at 55 °C for 30 minutes before it was cooled down and spin-coated on top of the pre-cleaned ITO substrates at 2000 rpm/1 minute. The 35 nm-thick layers were annealed at 195 °C for 30 minutes in air. PEIE solution (600 μ L PEIE in 50 mL deionized water) was then spin-coated on top of the ZnO layer at 5000 rpm/1 minute then annealed at 100 °C for 10 minutes in air. The substrates were then transferred into a nitrogen filled glovebox ($O_2 < 1$ ppm; $H_2O < 1$ ppm) to proceed with the photoactive layer deposition. Blend solutions having different ratios and solvents were prepared and annealed at 70 °C overnight. The active layer was then deposited on top of the PEIE layer at 800 rpm/50 seconds followed by 1000 rpm/3 seconds. The layers were then annealed at different temperatures. Then, the substrates were placed into an evaporator inside the glovebox as shown in **Figure VI-3a**, in which a 10 nm-thick MoO₃ layer and a 70 nm-thick Ag anode layer were thermally evaporated at 8×10^{-6} Torr pressure through a shadow mask defining 10 mm² active area (**Figure VI-3b**). The current density-voltage (J-V) characteristics of the cells were measured under N₂ using a K.H.S. SolarCelltest-575 solar simulator with HMI source and under illumination using an AM1.5 filters (ATLAS). The metal halide was set at 100 mW.cm⁻² and using an IL1400BL calibrated radiometer.

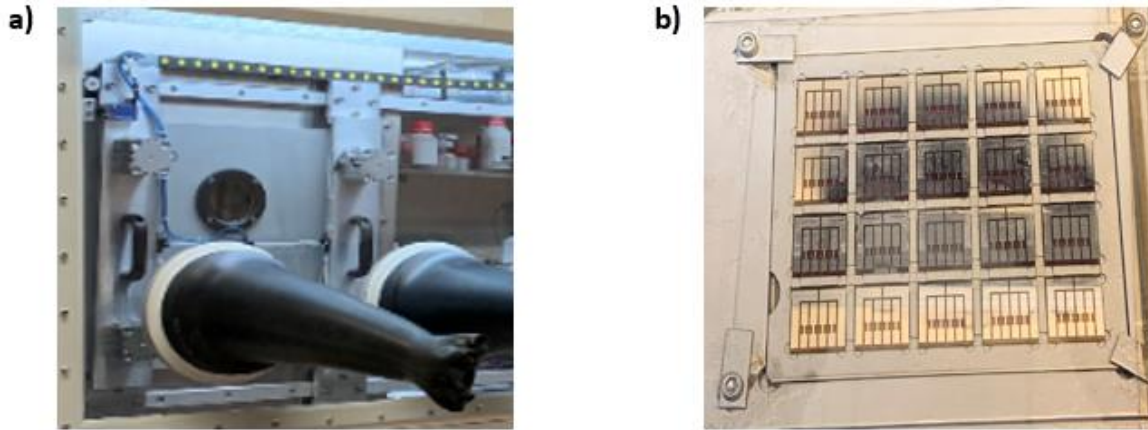


Figure VI-3: Images of (a) the evaporator and (b) the used shadow mask.

ii. Normal device structures

All the solar cells mentioned in **Chapter IV** were based on the normal device structures. For the preparation of the hole transport layers, different solutions having different ratios of P3HT-Si and PTES were used. For the preparation of the mother P3HT-Si solution, 15 mg of the synthesized P3HT-Si polymer were dissolved in 1.8 mL toluene (referred as Moth sol P3HT). The PTES mother solution was prepared by adding 74 μL of PTES into 3mL toluene (referred as Moth sol PTES). The desired solutions were then composed by varying the ratio of the P3HT-Si polymer and the PTES molecule as shown in **Table VI-6**.

Table VI-6: The prepared solutions having different mole fractions of P3HT and PTES.

Number	Moth sol P3HT-Si	Moth sol PTES	Added Toluene	Mol f P3HT-Si	Mol f PTES	P3HT-Si/PTES
1	0.3 mL	0 mL	0.2 mL	1	0	1/0
2	0.3 mL	0.0035 mL	0.1965 mL	0.75	0.25	1/0.33
3	0.3 mL	0.01 mL	0.19 mL	0.5	0.5	1/1
4	0.3 mL	0.032 mL	0.168 mL	0.25	0.75	1/3
5	0.3 mL	0.1 mL	0.1 mL	0.1	0.9	1/10
6	0.3 mL	0.2 mL	0 mL	0.05	0.95	1/20
7	0 mL	0.2 mL	0 mL	0	1	0/1

The prepared solutions were then transferred into the glovebox to proceed with the deposition on top of the pre-cleaned ITO substrates. P3HT-Si, PTES and the mixed solutions (solutions 1 to 7) were spin-coated from toluene at 1200 rpm/90 seconds and the layers were subsequently annealed at 150 °C for 3 hours under inert atmosphere. Then, the grafted substrates were subjected to ultrasonic agitation in chloroform for 10 minutes. This step was done three times to remove the free (ungrafted) silane before drying the layers. The substrates were stored in the glovebox under nitrogen to prevent any degradation of the SAMs. A P3HT:PC₆₀BM blend solution with a 1:1 weight ratio and a total concentration of 40 mg.mL⁻¹ in 1,2 dichlorobenzene was deposited on top of the grafted layers using two steps; the first at 1000 rpm/50 seconds then at 3000 rpm/3 seconds. The layers were directly transferred into a petri dish to undergo solvent vapor annealing for 2 hours. Then, the substrates were transferred to an evaporator inside the glovebox, in which a 30 nm-thick Ca layer and a 100 nm-thick Al layer were thermally evaporated at 3×10^{-6} Torr pressure through a shadow mask. The reference cells were prepared following the same procedure but depositing PEDOT:PSS at 4000 rpm/60 seconds instead of the grafted layer. These PEDOT:PSS layers were annealed on a hot plate 100 °C for 30 minutes.

VI. Characterization techniques

a. Fourier Transform Infrared Spectroscopy (FT-IR spectroscopy)

Principle: IR spectroscopy deals with the infrared light of the electromagnetic spectrum that has a longer wavelength than the visible light. This spectroscopy involves the interaction of the infrared radiation with the matter under study. This technique is mainly used to identify the composition of a substance by providing information on the nature of the chemical bonds and the functional groups present in both organic and inorganic species. Samples of several physical states (solid, liquid and gas) can be analyzed by IR spectroscopy. The measurements are conducted using an infrared spectrometer capable of producing an infrared spectrum. This IR spectrum can be obtained by simply plotting the intensity of the infrared light absorbed or transmitted vs. wavenumbers in (cm⁻¹) or wavelength (μm). The energy required to excite and vibrate the bonds of a molecule occurs in the infrared region, where the sample is subjected to a frequency range between 400 and 4000 cm⁻¹. When the frequency of the IR radiation is the same as the vibrational frequency of a bond, the energy of the incident wave is absorbed with respect to the selection rules. Different functional groups absorb specific frequencies of IR radiation, hence give the characteristics peak value; thus, the IR spectrum is the fingerprint of the molecule.⁸

Apparatus: The infrared region covered by the Nicolet IS50 de ThermoFischer Scientific, used in this study, ranges from near-infrared region (7000 cm⁻¹) to mid-infrared region (400 cm⁻¹).

b. ^1H Nuclear Magnetic Resonance (^1H NMR) and Diffusion order spectroscopy (DOSY)

Principle: The NMR spectroscopy is an analytical technique used for the structural analysis. This is based on the collection of physical, chemical and structural information about molecules in relation with the chemical shift of the resonance frequencies of the nuclear spins within the sample. The principle of NMR involves three sequential steps including the alignment (polarization) of the magnetic nuclear spins, the radio-frequency (RF) pulse and the detection of the NMR signal during or after the RF pulse. Studying the NMR peaks makes it efficient to determine the structure of many compounds.

The NMR analysis is based on the nuclei that possess a nonzero spin in a strong magnetic field. This spinning causes a small energy difference in the spin-up and spin-down states. The ^1H NMR shift is sensitive to the surrounding electronic environment so it depends on the binding environment of the corresponding nucleus. As a result of the change in the neighboring spin position, a chemical shift occurs. The most commonly used nuclei are the ^1H and ^{13}C , although isotopes of many other nuclei such as ^3He , ^{17}O , ^{19}F and ^{31}P can be studied as well.⁹ Beside the ^1H NMR which allows 1-D measurements, the diffusion-ordered spectroscopy (DOSY) is considered to be powerful in characterization. The DOSY analysis aims to separate the NMR signals of the different species depending on their diffusion coefficient as a result of the different sizes. The different diffusion coefficient can be measured by pulsed field gradient resulting in a 2-D DOSY diagram in which each compound can show an individual trace representing the spectrum. DOSY is a useful technique in polymer analysis by providing micellization properties and confirming the structural information about the polymers. The rate of diffusion is inversely proportional to the molar mass of the polymer. This technique is of great interest to confirm the successful coupling in diblock polymeric systems.^{8,10}

Apparatus: All the NMR experiments were characterized using a Bruker 400 MHz instrument in different solvents either at room or at a high temperature. Samples were prepared by weighing 3 mg of the analyzed sample in 0.5 mL of the good deuterated solvent. Experiments related to the diblock study were performed in tetrachloroethane at 60 °C. All spectra were recorded on a Bruker AVANCE 400 MHz spectrometer. Chemical shifts are reported as ppm downfield from Tetramethyl silane (TMS).

c. Gel Permeation Chromatography (GPC)

Principle: The GPC is a type of Size Exclusion Chromatography (SEC) that separates the analytes based on their hydrodynamic volume in a solvent. It is often used in the study of polymers to analyze them and/or to purify the desired product. The separation is based on the size or on the hydrodynamic volume of the analytes based on the use of porous beads packed in a column. Smaller analytes enter the pores easily and therefore spend more time in the columns. This increases their retention time, slowing down their elution. In contrast, larger analytes spend less time in the pores and are quickly eluted. This technique allows the determination of the dispersity (D), the number average molar mass (M_n), the weight average molar mass (M_w), the size average molar mass (M_z), and the viscosity molar mass (M_v).

Polystyrene standards with dispersities less than 1.1 are typically used in the calibration. It is obvious that the eluent or the mobile phase should be a good solvent for the polymer. The concentration by weight of the analyzed polymer in the eluent can be detected using a detector. Many detectors are available such as the concentration sensitive detectors which include differential refractometer (RI), UV absorption, infrared (IR) absorption and density detectors.¹¹

Apparatus: SEC analysis was performed using a bank of 4 columns (Shodex KF801, 802.5, 804 and 806) each 300 mm x 8 mm at 30 °C with THF eluent at a flow rate of 1.0 mL.min⁻¹ controlled by a Malvern pump (Viskotec, VE1122) and connected to Malvern VE3580 refractive index (RI) and Malvern VE3210 UV-Visible detectors. Calibration was performed against polystyrene standards.

d. X-ray Photoelectron Spectroscopy (XPS)

Principle: XPS is a surface-sensitive quantitative spectroscopic technique that is used to measure the surface elemental composition, the empirical formula (which is the integer ratio of the atoms found in a chemical compound), the chemical state (known as the oxidation state when referred to metal cations) and the density of the electronic states of the elements that exist within a material. It is mainly used to analyze inorganic compounds, semiconductors, polymers and others. In principle, XPS detects all elements with an atomic number (Z) above or equal to 3, thus hydrogen ($Z = 1$) or helium ($Z = 2$) cannot be easily detected. XPS is used to analyze the surface chemistry of a material as it is or after some treatments and exposures to heat or UV. The principle is based on the simultaneous measurement of the kinetic energy and the number of electrons escaping from the sample surface after being irradiated with a beam of X-rays. Thus, the XPS spectrum is a plot of the number of electrons detected as function of the binding energy of the electrons.

XPS requires high vacuum ($P \sim 10^{-8}$ millibar) or ultra-high vacuum (UHV; $P < 10^{-9}$ millibar) conditions. Each element produces a characteristic set of XPS peaks at characteristic binding energy values that directly identify each element existing in or on the surface of the material under study. These characteristic spectral peaks correspond to the electron configuration of the electrons within the atoms, e.g., 1s, 2s, 2p, 3s, etc. XPS can detect only the electrons that escape from the sample surface into the vacuum of the instrument and reach the detector. However, the photo-emitted electrons can undergo recombination or can be trapped in various excited states within the material, all of which can reduce the number of escaping photoelectrons. Thus, the results depend on the thickness of the layers.¹²

Apparatus: XPS measurements were performed using a Thermo K-alpha spectrometer with a hemispherical analyzer and a microfocused (400 μm diameter microspot) monochromated radiation (Al $K\alpha$, 1486.6 eV) operating at 72 W under a residual pressure of $1 \cdot 10^{-9}$ mbar. The pass energy was set to 20 eV. All spectra were calibrated using the hydrocarbon peak at a binding energy of 285.0 eV. Spectra were mathematically fitted with Casa XPS software using a least squares algorithm and a nonlinear Shirley-type background.

e. Matrix Assisted Laser Desorption Ionization-Mass Spectrometry MALDI-MS (MALDI-TOF) (Time of Flight)

Principle: MALDI-TOF is a kind of mass spectrometry. It is an analytical technique used for the determination of the mass of a corresponding molecule or polymer. The chemical compounds are ionized into charged molecules in which their mass to charge ratio m/z is measured. The polymers are converted into ions by either the loss or the addition of one or more protons. The high throughput and speed associated with complete automation and the production of single charged ions has made MALDI-TOF mass spectrometer an obvious and easy choice for the mass determination. The analyzed samples are usually mixed with a solution of an energy-absorbent, organic compound called matrix which crystallizes together with the sample entrapped within, causing a homogeneous co-crystallization of sample and matrix molecules. A beam is then used for ionizing the sample in an automated mode that yields to the formation of the singly protonated ions. The latter accelerate at a fixed potential and separate from each other according to their mass to charge ratio (m/z). Time of flight analyzer (TOF) then detects the charged samples where the m/z ratio of an ion is measured by determining the time required for it to travel the length of the flight tube.¹³

Apparatus: MALDI-MS spectra were performed by the CESAMO (Bordeaux, France) on a Voyager mass spectrometer (Applied Biosystems). The instrument was equipped with a pulsed N_2 laser (337 nm) and a time-delayed extracted ion source. Spectra were recorded in the positive-ion mode using the reflectron and with an accelerating voltage of 20 kV. Samples were dissolved in THF at 10 mg.mL^{-1} . The DCTB matrix {T-2-[3-(4-tbutylphenyl)22-methyl-2-propenylidene] malononitrile} solution was prepared at a concentration of 10 mg.mL^{-1} in THF. The solutions were combined in a 10:1 volume ratio of matrix to sample. One to two microliters of the obtained solution were deposited to the sample target and vacuum dried.

f. UV-Visible Spectroscopy (UV-vis)

Principle: UV-visible spectrophotometry is the study of the interaction of the visible and part of the UV radiations with a chemical species. Visible light consists of wavelengths ranging from 380 nm (blue violet) to 720 nm (red). Light travels in packets of energy called photons. Each single photon is characterized by having a specific energy related to a certain frequency or wavelength ($E = h\nu = hc/\lambda$). When the white light falling on a substance is totally reflected, the substance appears white and when it is totally absorbed, the substance appears black. On the other hand, if only a portion of the light is absorbed and the rest is transmitted, the color of the sample is determined by the transmitted light. Moreover, for the colorless substances, the absorption spectrum takes place in the infrared or in the ultraviolet region and not in the visible region. **Table VI-7** illustrates the relationship between the light absorbed by a sample and its corresponding color.¹⁴ It is important to mention that the light energy absorbed by a compound must match exactly the energy required to cause the movement of an electron from the ground state to the excited state. This phenomenon is known as electronic transition. The lower the energy gap between the occupied and the non-occupied levels, the easier the electrons are excited and consequently the longer the wavelength of light can be absorbed.

Table VI-7: The general relation between the color of a substance and the absorbed light.

Colour of light absorbed	Approx. λ ranges / nm	Colour of light transmitted
Red	700-620	Green
Orange	620-580	Blue
Yellow	580-560	Violet
Green	560-490	Red
Blue	490-430	Orange
Violet	430-380	Yellow

Apparatus: UV-vis spectroscopy measurements used for the polymer's characterization were carried out in spectrum mode using a SHIMADZU UV-2450 spectrophotometer. The samples were solubilized properly and analyzed in a quartz cell with an optical path length of 1 cm while the films were deposited onto glass substrates (IPREM-EPCP laboratory in Pau). UV-vis spectroscopy measurements studied in **Chapter III** were recorded with SAFAS UVmc spectrometer (IMS laboratory in Bordeaux).

g. Photoluminescence Spectroscopy (PL)

Principle: PL is a type of luminescence that corresponds to the light emitted from a material after the absorption of photons. The photoexcitation causes an electron to move from the ground state to the excited state. Various relaxation processes typically occur after the excitation and may include either radiative processes like the emission of light or non-radiative processes. The emitted light is usually of a lower energy compared to the absorbed light ($E_{exc} > E_{PL}$) (Stokes shift), thus it is of higher wavelength. However, anti-Stokes exists too.⁸

Apparatus: The PL measurements were recorded using a photon counting Edinburgh FLS920 fluorescence spectrometer using a xenon lamp in a 1 cm quartz fluorescence cell (Hellma).

h. Thermal Gravimetric Analysis (TGA)

Principle: TGA is a method used for the thermal analysis of a sample. The thermogravimetric analyzer detects the mass change of a sample over time under the effect of the temperature. The effect of the temperature on the mass loss of a sample can be detected under a variety of atmospheres including: ambient air, vacuum, inert gas and others. TGA provides information about both the physical and the chemical phenomena. In general, the instrument is equipped with a precision balance inside a furnace with a control temperature program. The collected data are plotted in terms of mass or percentage of initial mass loss versus either temperature or time. This technique is important for analyzing a variety of polymeric materials.¹⁵

Apparatus: The TGA measurements were performed on a TGA Q50, TA instrument at a heating rate of 10 °C/min and under nitrogen.

i. Differential Scanning Calorimetry (DSC)

Principle: DSC is a thermo-analytical technique applied on a reference and a sample. Both the sample and the reference must be maintained at the same temperature throughout the experiment. During analysis, DSC is equipped with a temperature program in which the sample's holder starts to increase the temperature linearly as function of time. The basic principle behind the analysis is the measurement of the enthalpy changes due to changes in chemical and physical properties of a material as a function of temperature or time. In DSC, the observation of the heat difference between the sample and the reference enables the measurement of the amount of heat absorbed or released during the transitions.¹⁶ In general, DSC is useful for measuring the transitions including the glass transition, melting and crystallization. Additionally, the chemical reaction such as thermal curing, specific heat capacity, heat history and purity analysis can be also measured.¹⁷

Apparatus: DSC analysis was performed using a Q100 from TA instruments under N₂ atmosphere. For each analysis, the same temperature programming was followed by increasing the temperature from 40 to 300 °C with a ramp of 10 °C/min, then cooled to room temperature at the same ramp. A second cycle was needed for some samples.

j. Atomic Force Microscopy (AFM)

Principle: AFM is an apparatus used to characterize the surface morphology of a deposited layer. The principle is based on a probe which constitutes a cantilever accompanied with a sharp tip that interacts with the sample to scan the surface. The cantilever can be either silicon or silicon nitride with a tip having a nanometric radius. Once the tip is in contact with the surface of the sample, the forces between the tip and the sample deflect the cantilever according to Hooke's law. Thus, AFM measures the mechanical contact forces, van der Waals forces, chemical bonding, electrostatic forces, magnetic forces, and others. The reaction of the probe to the forces imposed by the sample contributes to form a three-dimensional image (topography) of the sample surface at a high resolution. AFM can be also used to measure the surface roughness over a wide range: from Ra = 0.03 nm to 500 nm.⁸

Apparatus: AFM images were obtained on a microscope Veeco, di-Innova model "fashion tapping".

k. Profilometry

Principle: Profilometry is an instrument used to measure the thickness of the layers. It consists of a diamond stylus with a radius ranging from 20 nm up to 50 μm. To scan the surface of the sample, this stylus moves laterally across the sample with a specified distance and speed by applying a specific contact force. By the vertical stylus displacement as function of the position, a profilometer can measure small surface variations. The height position of the diamond stylus generates an analogue signal which is converted into a digital signal that is stored, analyzed, and displayed.¹⁸

Apparatus: Film thickness was measured using a Detktak surface profilometer. All the values mentioned were calculated as an average of three values (IMS laboratory in Bordeaux).

l. Contact Angle measurements

Principle: Studying the interaction between a solid and a liquid is important to characterize the surface of the solid and to determine the ability of the liquid phase to spread onto the substance. For the aim of determining the surface characteristic of a solid, it is essential to study the wettability that can give an information about the surface free energy. Wettability is defined as the ability of a liquid droplet to form boundary surfaces when it is deposited on a solid surface. Adhesive characteristics can be determined by Van der Waals forces generated by the equilibrium of a liquid droplet on a solid surface. It is then possible to measure the contact angle between the solid and the liquid. Thus, the angle formed between the liquid/solid interface and between the liquid/vapor interface is defined as the contact angle. In general, a wetting liquid is the one that can have a contact angle of 90 °C or less on the solid surface while the non-wetting is the one that creates an angle between 90 °C and 180 °C.¹⁹

Apparatus: The contact angle measurements were performed on a Krüss DSA 100 goniometer at 20 °C in static mode. The results mentioned in the manuscript correspond to the mean of at least two measurements. The droplet of distilled water was deposited at room temperature by a syringe which was subjected vertically down into the surface of the sample, where a high resolution camera was used to capture the image. The contact angle was measured using a specific image analysis software.

m. Cyclic Voltammetry (CV)

Principle: The cyclic voltammetry is an electrochemical technique which is commonly used to understand the mechanism behind the electron transfer among molecules. This determines processes related to the oxidation and reduction of a molecule or a polymer. The voltammetry is the study of the current versus the corresponding potential where the curve is referred as voltammogram. Using CV, it is possible to estimate the HOMO-LUMO energy levels and the bandgap energy of molecules depending on specific calculations based on the oxidation/reduction properties as shown in the equations derived from literature.²⁰

$$E_{\text{HOMO}} \text{ (eV)} = -(\text{E}_{\text{onset OX}} + 4.70) \quad \text{Equation 2}$$

$$E_{\text{LUMO}} \text{ (eV)} = -(\text{E}_{\text{onset Red}} + 4.70) \quad \text{Equation 3}$$

$$E_{\text{g}}^{(\text{cv})} = E_{\text{HOMO}} - E_{\text{LUMO}} \quad \text{Equation 4}$$

Three electrodes are used to conduct the experiment, counter, reference and working electrodes. These are immersed in an electrolyte solution that provides the sufficient conductivity. The analysis is based on varying the applied potential at a working electrode in both forward and reverse directions while observing the current.²¹ In general, the current is recorded when the electrons are moving from the working and the counter electrodes.

During the CV analysis, electron transfer takes place where ions migrate in the solution to compensate the charges, achieving electrical neutrality. Salt electrolyte is needed to decrease the solution resistance. Ferrocene is used as an internal standard and it is recommended to plot the data versus the ferrocene couple at 0 V vs Fc⁺/Fc.

Electrochemical experiments must be performed in inert atmosphere avoiding O₂ which can alter the experimental conditions. To avoid this, all the electrolyte solutions must be purged with inert gases such as nitrogen.²²

Apparatus: All the electrochemical experiments were conducted using a standard three-electrode electrochemical setup (AUTOLAB PGSTAT 101) made up of a glassy carbon or a platinum disk with 2 mm diameter working electrode, a platinum foil functioning as the counter electrode, and an AgCl/Ag reference electrode. It was important to clean the electrodes prior to the analysis by sonication and rinsing with deionized water followed by an electrochemical cleaning in a solution of 0.5 M aqueous H₂SO₄. Experiments were performed in CH₃CN/Bu₄NPF₆ with 0.1 M concentration. A standard potential of the ferrocenium/ferrocene couple, E_{Fc+/Fc}, was measured after each experiment and all potentials were referenced against SCE using a previous determination of E_{Fc+/Fc} = 0.41 V versus SCE in CH₃CN. The solutions were purged with N₂ gas prior to use. The samples were referenced to an external ferrocene solution.

n. External Quantum Efficiency (EQE)

Principle: Quantum efficiency (QE) measurements is the most popular characterization technique for solar cell characterization that allows quantifying the efficiency of the devices by converting the light into electrons in terms of wavelength. QE are of two types, internal (IQE) and external quantum efficiency (EQE). The EQE is the ratio between the number of charge carriers collected by a solar device with the number of incident photons, while the IQE considers only the absorbed photons. Therefore, the EQE depends on the absorption of light and the collection of charges.

If the quantum efficiency of a corresponding photonic device is integrated over the whole solar electromagnetic spectrum, then it is possible to evaluate the amount of current that the cell can produce when exposed to a light of specific intensity. EQE of a solar device can be calculated according to **Equation 5**.

$$\text{EQE} (\lambda) = \frac{\text{number of electrons}}{\text{number of photons}} = \frac{1240 \cdot \text{JSC}}{\lambda \cdot \text{Pin}} \quad \text{Equation 5}$$

The procedure behind this analysis is explained by the fact that once the photon is absorbed, an electron-hole is generated where the two charges must be separated and collected at the junction avoiding the charge recombination. Therefore, for a good material, the recombination of the two charges must be avoided.²³

Apparatus: For the EQE measurements, the setup used is built with a 500 W Xe lamp and Triax 180 monochromator purchased from Horiba Scientific and a Keithley 6487 picoammeter (IMS laboratory in Bordeaux).

o. Dynamic Light Scattering (DLS)

Principle: DLS is a non-destructive technique that determines the size distribution profile and the zeta potential of small dispersed particles in a diluted suspension. The principle is based on bombarding the particles within the solution with a monochromatic light source. If the particles are small compared to the wavelength (below 250 nm), light will be scattered in all directions. Therefore, DLS measures the intensity of light scattered by the particles over time. Although the light source is monochromatic and coherent, the scattering intensity fluctuates over time causing a change in the distance between scatterers in solution. By analyzing the variations of light intensity, specific characteristics of these particles such as their sizes can be determined. It is worth noting that the determined size by DLS may include any other molecules surrounding the particles such as the solvent.⁸

Apparatus: The size distribution of the hybrid block copolymers in aqueous solution was determined using Zetasizer Nano ZS instrument (Malvern Instruments).

References

- (1) Iovu, M. C.; Sheina, E. E.; Gil, R. R.; McCullough, R. D. Experimental Evidence for the Quasi-“Living” Nature of the Grignard Metathesis Method for the Synthesis of Regioregular Poly(3-Alkylthiophenes). *Macromolecules* **2005**, *38* (21), 8649–8656.
- (2) Iqbal, A.; Jost, M.; Kirchmayr, R.; Pfenninger, J.; Rochat, A.; Wallquist, O. The Synthesis and Properties of 1,4-Diketo-Pyrrolo[3,4-C]Pyrroles. *Bull. Sociétés Chim. Belg.* **1988**, *97* (8–9), 615–644.
- (3) Qian, G.; Qi, J.; Davey, J. A.; Wright, J. S.; Wang, Z. Y. Family of Diazapentalene Chromophores and Narrow-Band-Gap Polymers: Synthesis, Halochromism, Halofluorism, and Visible–Near Infrared Photodetectivity. *Chem. Mater.* **2012**, *24* (12), 2364–2372.
- (4) Khelifi, W.; Awada, H.; Brymora, K.; Blanc, S.; Hirsch, L.; Castet, F.; Bousquet, A.; Lartigau-Dagron, C. Halochromic Switch from the 1st to 2nd Near-Infrared Window of Diazapentalene–Dithienosilole Copolymers. *Macromolecules* **2019**, *52* (13), 4820–4827.
- (5) Carothers, W. H. Polymers and Polyfunctionality. *Trans. Faraday Soc.* **1936**, *32* (0), 39–49.
- (6) Osaka, I.; McCullough, R. D. Advances in Molecular Design and Synthesis of Regioregular Polythiophenes. *Acc. Chem. Res.* **2008**, *41* (9), 1202–1214.
- (7) Awada, H.; Medlej, H.; Blanc, S.; Delville, M.-H.; Hiorns, R. C.; Bousquet, A.; Dagron-Lartigau, C.; Billon, L. Versatile Functional Poly(3-Hexylthiophene) for Hybrid Particles Synthesis by the Grafting onto Technique: Core@shell ZnO Nanorods. *J. Polym. Sci. Part Polym. Chem.* **2014**, *52* (1), 30–38.
- (8) Mourdikoudis, S.; Pallares, R. M.; Thanh, N. T. K. Characterization Techniques for Nanoparticles: Comparison and Complementarity upon Studying Nanoparticle Properties. *Nanoscale* **2018**, *10* (27), 12871–12934.
- (9) Tognarelli, J. M.; Dawood, M.; Shariff, M. I. F.; Grover, V. P. B.; Crossey, M. M. E.; Cox, I. J.; Taylor-Robinson, S. D.; McPhail, M. J. W. Magnetic Resonance Spectroscopy: Principles and Techniques: Lessons for Clinicians. *J. Clin. Exp. Hepatol.* **2015**, *5* (4), 320–328.
- (10) Groves, P. Diffusion Ordered Spectroscopy (DOSY) as Applied to Polymers. *Polym. Chem.* **2017**, *8* (44), 6700–6708.
- (11) Size exclusion chromatography (SEC) Gel Permeation Chromatography (GPC) Guide: Waters [https://www.waters.com/waters/en_US/Size-exclusion-chromatography-\(SEC\)-Gel-Permeation-Chromatography-\(GPC\)-Guide](https://www.waters.com/waters/en_US/Size-exclusion-chromatography-(SEC)-Gel-Permeation-Chromatography-(GPC)-Guide)
- (12) Surface Spectroscopy: UPS vs XPS <https://www.azooptics.com/Article>.
- (13) Nielen, M. W. F. Maldi Time-of-Flight Mass Spectrometry of Synthetic Polymers. *Mass Spectrom. Rev.* **1999**, *18* (5), 309–344.
- (14) Unit 4 - Introduction to Solutions <http://forestchemistry.weebly.com/unit-4---introduction-to-solutions>.
- (15) Bottom, R. Thermogravimetric Analysis. In *Principles and Applications of Thermal Analysis*; John Wiley & Sons, Ltd, 2008; pp 87–118.
- (16) Gill, P.; Moghadam, T. T.; Ranjbar, B. Differential Scanning Calorimetry Techniques: Applications in Biology and Nanoscience. *J. Biomol. Tech. JBT* **2010**, *21* (4), 167–193.
- (17) Höhne, G. W. H.; Hemminger, W.; Flammersheim, H.-J. Differential Scanning Calorimetry: An Introduction for Practitioners; *Springer-Verlag: Berlin Heidelberg*, 1996.
- (18) Optical Profilometry. *Nanoscience Instruments*.
- (19) Dwivedi, C.; Pandey, I.; Pandey, H.; Ramteke, P. W.; Pandey, A. C.; Mishra, S. B.; Patil, S. Chapter 9 - Electrospun Nanofibrous Scaffold as a Potential Carrier of Antimicrobial Therapeutics for Diabetic Wound Healing and Tissue Regeneration. In *Nano- and Microscale Drug Delivery Systems*; Grumezescu, A. M., Ed.; Elsevier, 2017; pp 147–164.
- (20) Alfassi, Z. General aspects of the chemistry of radicals, **1999**.
- (21) Marken, F.; Neudeck, A.; Bond, A. M. Cyclic Voltammetry. In *Electroanalytical Methods: Guide to Experiments and Applications*; Scholz, F., Bond, A. M., Compton, R. G., Fiedler, D. A., Inzelt, G., Kahlert, H., Komorsky-Lovrić, Š., Lohse, H., Lovrić, M., Marken, F., Neudeck, A., Retter, U., Scholz, F., Stojek, Z., Eds.; Springer: Berlin, Heidelberg, 2010; pp 57–106.
- (22) Elgrishi, N.; Rountree, K. J.; McCarthy, B. D.; Rountree, E. S.; Eisenhart, T. T.; Dempsey, J. L. A Practical Beginner’s Guide to Cyclic Voltammetry. *J. Chem. Educ.* **2018**, *95* (2), 197–206.
- (23) Ananda, W. External Quantum Efficiency Measurement of Solar Cell; 2017; pp 450–456.

General Conclusion and Perspectives

This PhD is part of the worldwide effort to find ways to increase solar cell efficiency and stability, and is dedicated to the synthesis and functionalization of conjugated polymers.

In the first study of this PhD, new materials for the solar cell active layers were developed with the idea to extend the range of light absorption and possibly use a single donor-acceptor component. To do so, well-defined P3HT polymers, along with DPP and DAP acceptor monomers were successfully synthesized and were involved in a Stille coupling polymerization to prepare all-conjugated block copolymers. For this, a ternary blend of P3HT, DTS and either DPP or DAP monomers was used. An attractive feature of such a synthetic strategy is the high degree of flexibility afforded to the structure and chemical composition of the synthesized block copolymers. In agreement with the Carothers theory, the conversion p and monomer ratio r predetermined both the molar mass and the topology of the obtained macromolecules. Indeed, the block length of the corresponding block copolymers was tailored by varying the molecular weight and amount of P3HT end-capper. For instance, systems with a low monofunctional reagent molar equivalent ($N_{\text{P3HT}} = 0.04$ eq) have contributed to the formation of diblock copolymers with a higher length of the low-bandgap block, P(DTS-DXP), when compared to the block copolymers with high molar equivalent of P3HT ($N_{\text{P3HT}} = 0.16$ eq). The synthesized diblock copolymers ($\text{P3HT}_n\text{-}b\text{-P(DTS-DPP)}_m$ and $\text{P3HT}_n\text{-}b\text{-P(DTS-DAP)}_m$) were purified by Soxhlet successive extractions in different solvents and finally collected in chloroform. The structural, thermal, morphological and optical properties of the synthesized block copolymers were examined by different characterization techniques. The spectrophotometric investigation revealed that the block molar composition was in agreement with the absorption profile in which the polymer's absorption is extended to the near-IR region with two complementary broad absorption bands in the 350-550 and 600-950 nm ranges assigned to the P3HT and the low-bandgap blocks (P(DTS-DPP) or P(DTS-DAP)), respectively. Moreover, the strong donor character of DAP monomer has contributed to lower bandgaps when compared to the DPP-based diblock copolymers. The synthesized block copolymers showed high thermal stability which is an important property for materials used in photovoltaic applications.

Although the estimated energy levels of both blocks calculated from cyclic voltammetry could mean a donor-acceptor behavior, single components active layer solar cells presented very poor efficiency in an inverted device architecture. Therefore, the addition of PC₆₀BM as an electron acceptor in the blend of the photoactive layer ($\text{P3HT}_n\text{-}b\text{-P(DTS-DXP)}_m\text{:PC}_{60}\text{BM}$) was necessary. For the fabricated devices, the performances were block composition dependent. Accordingly, long block of P(DTS-DPP) or P(DTS-DAP) impeded the crystallization of P3HT, thus, lowering the short circuit current density and the power conversion efficiency. For DPP-based copolymers, the highest PCE obtained (2%) was with the copolymer presenting the highest molar mass of P3HT ($\text{P3HT}_{240}\text{-}b\text{-P(DTS-DPP)}_{11}$). In this case, the photoactive layer morphology was optimized with a 1:1 blend ratio in an *o*-xylene solvent and a pre-annealing step at 150 °C. External quantum efficiency measurements revealed that both P3HT and the low-bandgap blocks contributed to the charge collection mechanism.

Under the same processing conditions, P3HT:PC₆₀BM-based reference cells were fabricated for comparison in which they showed almost similar efficiencies. In general, DAP-based block copolymers showed lower performances in which the highest PCE (1.2%) was for devices fabricated with P3HT₃₇-*b*-P(DTS-DAP)₄:PC₆₀BM photoactive layer processed in chlorobenzene.

Based on these results, future work will be focused on the optimization of DAP-based devices. This could be achieved either by changing the processing solvent to better improve morphology or by increasing the molar mass of P3HT block in the diblock copolymer. Additionally, given the D-A design of the block copolymers, replacing PC₆₀BM with a non-fullerene acceptor may enhance the interaction between the acceptor entities and boost the performances. On the other hand, the discussed synthetic approach and framework could be useful in the future for synthesizing more advanced and interesting low-bandgap block copolymers that even rely or not on P3HT polymer. More specifically, changing the nature of the low-bandgap block could be an efficient approach for improving the photon absorption and thus the device efficiency.

In the second study of this manuscript, we used our knowledge in functionalizing conjugated polymers to introduce at the end of P3HT a silane moiety, able to bind metal oxides. With this, ITO substrates were modified by self-assembled monolayers of PTES, P3HT-Si or P3HT-Si/PTES as PEDOT:PSS alternatives. The grafting of the SAM molecules was proved by different techniques including XPS (elemental analysis), UV-vis (absorption) and contact angle measurements (hydrophobicity). Despite the successful grafting, photovoltaic performances of the P3HT:PC₆₀BM-based normal devices did not achieve high efficiencies using the SAM hole transport layers (2% with PTES) when compared to PEDOT:PSS layers (2.7%) but higher efficiencies than the ones using bare ITO (1.34%). In general, the low efficiency was attributed to the low conductivity caused by the high thickness of the grafted layers (around 20 nm).

Therefore, as important prospects for the future, doping the grafted materials and solving the wettability problems between the substrate and the photoactive layer could be useful in improving the low mobility and poor charge transport issues. This eventually could improve the power conversion efficiency in such SAMs-based devices. Trying other conjugated polymers (rather than P3HT) could also pave the way for further work.

In the last part of this PhD, we were interested to extend the application of the IR absorbing polymer we developed, P(DTS-DAP), for photothermal bioapplications. Therefore, hybrid block copolymers constituting of this conjugated block and a polypeptide segment were investigated. Aniline-functionalized P(DTS-DAP) reacted *via* ROP to the NCA functional group of the corresponding peptide monomers, γ -benzyl-*L*-glutamate (BLG) and trifluoroacetyl-*L*-lysine (TFA-Lys). In this regard, P(DTS-DAP)-*b*-P(BLG) and P(DTS-DAP)-*b*-P(TFA-Lys) were synthesized and purified by successive washing in toluene. Structural analysis by ¹H NMR and FT-IR revealed the successful synthesis of the corresponding block copolymers having similar absorption properties to those of P(DTS-DAP). However, for both hybrid blocks, 50 to 60% of unreacted P(DTS-DAP) macroinitiator were detected by SEC-THF (using a UV detector at 720 nm).

To obtain the corresponding amphiphilic block copolymers, deprotection reactions were conducted resulting in the formation of water-soluble P(DTS-DAP)-*b*-P(Lys) solution revealing a mixture of nanoobjects with a small proportion (15 w%) of bigger aggregates. Finally, a promising photothermal behavior was shown with a 15 °C increase in the solution's temperature within 15 min of irradiation.

For further optimization, P(DTS-DAP)-*b*-P(BLG) deprotection can be performed in basic conditions. While, in general, the solubility problems could be overcome by synthesizing block copolymers having longer peptide length segments. Finally, additional characterization by transmission electron microscopy (TEM) might be useful for determining the morphology and the size of the synthesized amphiphilic block copolymers.

Conclusion Générale et Perspectives

Des polymères fonctionnalisés en bout de chaîne de P3HT bien définis, ainsi que des monomères accepteurs DPP et DAP ont été synthétisés avec succès pour être impliqués dans une polymérisation par couplage Stille. Pour cela, un mélange ternaire des monomères P3HT, DTS et soit DPP ou soit DAP, a été utilisé dans la synthèse de copolymères à blocs entièrement conjugués. Une caractéristique intéressante d'une telle stratégie synthétique est le degré élevé de flexibilité accordé à la structure et à la composition chimique des copolymères à blocs (copolymères séquencés) synthétisés. En accord avec la théorie de Carothers, la conversion p et le rapport des monomères r pré-déterminent à la fois la masse molaire et la topologie des macromolécules obtenues. En effet, la longueur de bloc correspondant a été adaptée en faisant varier la masse molaire et la quantité de l'agent de terminaison P3HT. Par exemple, les systèmes avec un faible équivalent molaire du réactif monofonctionnel (NP3HT = 0,04 eq) ont contribué à la formation de copolymères diblocs avec une longueur plus élevée du bloc à faible bande interdite, P(DTS-DXP), par rapport aux CBCP à équivalent molaire élevé de P3HT (NP3HT = 0,16 eq). Les copolymères diblocs synthétisés (P3HT_n-*b*-P(DTS-DPP)_m et P3HT_n-*b*-P(DTS-DAP)_m) ont été purifiés par extractions successives Soxhlet dans différents solvants et finalement collectés dans du chloroforme. Les propriétés structurales, thermiques, morphologiques et optiques des CBCP synthétisés ont été examinées par différentes techniques de caractérisation. L'étude par spectrophotométrie a révélé que la composition molaire du bloc était en accord avec le profil d'absorption dans lequel l'absorption du polymère est étendue à la région proche infrarouge, avec deux larges bandes d'absorption complémentaires dans les gammes 350-550 et 600-950 nm attribuées au P3HT et aux blocs à faible bande interdite (P(DTS-DPP) ou P(DTS-DAP)), respectivement. Cependant, le fort caractère donneur du monomère DAP a contribué à réduire les bandes interdites par rapport aux copolymères diblocs à base de DPP. Les copolymères en blocs synthétisés ont montré une stabilité thermique élevée qui est une propriété importante pour les matériaux utilisés dans les applications photovoltaïques.

Bien que les niveaux d'énergie estimés des deux blocs calculés par voltamétrie cyclique puissent signifier un comportement donneur-accepteur, les cellules solaires à couche active à un seul composant ont présenté une très mauvaise efficacité dans une architecture de dispositif inversé. Cependant, l'ajout de PC₆₀BM comme accepteur d'électrons s'est révélée bénéfique dans le mélange de la couche photoactive (P3HT_n-*b*-P(DTS-DXP)_m:PC₆₀BM. Pour les dispositifs fabriqués, les performances dépendaient de la composition du bloc. Par conséquent, un long bloc de P(DTS-DPP) ou P(DTS-DAP) a empêché la cristallisation du P3HT, abaissant ainsi le courant de court-circuit et l'efficacité de conversion de puissance. Pour les copolymères à base de DPP, le PCE le plus élevé obtenu (2%) a été obtenu avec le copolymère présentant la masse molaire la plus élevée de P3HT (P3HT₂₄₀-*b*-P(DTS-DPP)₁₁). Dans ce cas, la morphologie de la couche photoactive a été optimisée avec un rapport de mélange 1:1 dans un solvant *o*-xylène et une étape de pré-recuit à 150°C. Des mesures externes de l'efficacité quantique ont révélé que la P3HT et le bloc à faible bande interdite contribuaient tous deux au mécanisme de collecte de charges. Dans les mêmes conditions de traitement, des cellules de référence à base de P3HT:PC₆₀BM ont été fabriquées à des fins de comparaison dans lesquelles elles présentent des

efficacités presque similaires. En général, les copolymères à blocs à base de DAP ont montré des performances inférieures avec une PCE maximale à 1,2% pour les dispositifs fabriqués avec une couche photoactive P3HT₃₇-*b*-P(DTS-DAP)₄ : PC₆₀BM traitée dans du chlorobenzène.

Basé sur ces résultats, le futur travail portera sur l'optimisation des appareils à base de DAP. Ceci pourrait être réalisé soit en changeant le solvant de traitement pour mieux améliorer la morphologie, soit en augmentant la masse molaire du bloc P3HT dans le copolymère diblocs. Le remplacement du PC₆₀BM par un accepteur ayant un niveau d'énergie LUMO plus profond pourrait également être efficace pour améliorer les performances de l'appareil. D'autre part, l'approche et le cadre synthétique discutés pourraient être utiles à l'avenir pour synthétiser des copolymères séquencés plus avancés et intéressants même qui ne reposent pas sur le P3HT.

En ce qui concerne les études sur la couche de transport de trous, des substrats ITO modifiés par des monocouches auto-assemblées de PTES, P3HT-Si ou P3HT-Si / PTES ont été incorporés comme alternatives au PEDOT : PSS. Le greffage des molécules SAM a été démontré par différentes techniques dont les mesures XPS (analyse élémentaire), UV-vis (absorption) et d'angle de contact (hydrophobicité). Malgré le succès du greffage, les performances photovoltaïques des dispositifs classiques à base de P3HT/PC₆₀BM n'ont pas atteint des rendements (efficacités) plus élevés en utilisant les couches de transport de trous SAM (2% avec PTES) par rapport au couches PEDOT:PSS (2,7%) mais des rendements plus élevés que ceux en utilisant l'ITO seul (1,34%). En général, le faible rendement a été attribué à la faible conductivité causée par la forte épaisseur des couches greffées (environ 20 nm).

Par conséquent, comme perspectives d'avenir importante, le dopage des matériaux greffés et la résolution des problèmes de mouillabilité entre le substrat et la couche photoactive pourraient être utiles pour améliorer les problèmes de faible mobilité et de faible transport de charge. Cela pourra améliorer l'efficacité de la conversion de puissance dans ces appareils à base de SAMs. Essayer d'autres polymères conjugués (plutôt que le P3HT) pourrait également ouvrir la voie à d'autres travaux.

Profitant de la propriété d'absorption du P(DTS-DAP) dans le proche IR, des copolymères à blocs hybrides composés d'un segment polypeptidique ont été étudiés. Des homopolymères de P(DTS-DAP) ont été fonctionnalisés par l'aniline qui a permis un amorçage par polymérisation par ouverture de cycle (ROP) de N-carboxyanhydride de monomères peptidiques : le γ -benzyl-*L*-glutamate (BLG) and trifluoroacetyl-*L*-lysine (TFA-Lys). A cet égard, P(DTS-DAP)-*b*-P(BLG) et P(DTS-DAP)-*b*-P(TFA-Lys) ont été synthétisés et purifiés par lavages successifs avec du toluène. L'analyse structurale par RMN de proton et FT-IR a révélé la réussite de la synthèse des copolymères en blocs correspondants ayant des propriétés d'absorption similaires à celles du P(DTS-DAP). Cependant, pour les deux blocs hybrides, 50 à 60% du macro-amorceur P(DTS-DAP) non réagi ont été détectés par SEC-THF (en utilisant un détecteur UV à 720 nm). Pour obtenir les copolymères blocs amphiphiles finaux, des réactions de déprotection ont été effectuées, aboutissant à la formation de P(DTS-DAP)-*b*-P(Lys) soluble dans l'eau.

Suite à la déprotection, le P(DTS-DAP)-*b*-P(Lys) est dispersable dans l'eau, formant des objets d'environ 157 nm de diamètre montrant un comportement photothermique intéressant avec une augmentation de 15 ° C en 15 min d'irradiation.

Pour une optimisation supplémentaire, des copolymères à blocs ayant des segments de longueur peptidique plus longs devront être synthétisés pour optimiser la dispersion dans l'eau et l'efficacité photothermale. Enfin, une caractérisation supplémentaire par microscopie électronique à transmission (MET) pourrait être utile pour déterminer la morphologie et la taille des objets amphiphiles synthétisés.

List of publications

- Complementary Absorption versus Morphology in All-Conjugated Block Copolymers Solar Cells
Hisham Idriss et al. *Macromolecules*, 2020, 53, 20, 9043–9053
- Low Band-Gap Polymer Brushes: Influence of the End-group on the Morphology of Core-Shell Nanoparticles
Adèle Gapin, Hisham Idriss et al. *Reactive and Functional Polymers*, 2020, 155,104700

Abstract

Solar cells, known as photovoltaic cells, are considered as an important source of renewable energy achieved by converting solar energy into electric energy. More specifically, organic solar cells are one of the most promising generations. They are characterized by their semi-transparency, low weight, flexibility, solution processability, low temperature processing and rapid energy payback time. Thus, they combine all the requirements for low-cost and large-scale production. Among organic semiconductors, low-bandgap polymers are considered as promising families used in electronic applications. In general, the combination of an electron-rich monomer and an electron deficient one as alternating moieties in the polymer backbone is an efficient strategy for lowering the bandgap of the corresponding polymer. Nowadays, in solar cells development strategies, the topic of interest is the usage of polymers with broad absorption extended to the near-infrared region in order to harvest photons more effectively.

Thus, we focused our studies on an efficient and simple “end-functional coupling method” for synthesizing all-conjugated diblock copolymers. This method is based on the Stille coupling polycondensation of A-A (dithienosilole, DTS) and B-B (diketopyrrolopyrrole, DPP or diazapentalene, DAP) monomers with P3HT as a macro end-capping agent. Diblock and triblock copolymers were produced with a molar composition tuned *via* the macromonomer molar mass and feed ratio. The molar mass and topology of the macromolecules obtained are discussed on the basis of the Carothers equation, conversion and monomer ratio. Structural analysis such as ¹H NMR, DOSY NMR and GPC revealed the successful formation of the desired block copolymers. Moreover, spectrophotometry and cyclic voltammetry were used to highlight the complementarity of block absorption and the donor-acceptor nature of copolymers.

DPP and DAP-based diblock copolymers were incorporated as donor materials with PC₆₀BM fullerene acceptors in inverted devices structured organic solar cells. In general, DPP-based block copolymers showed enhanced power conversion efficiencies when compared to DAP-based ones. The device performances were molar composition dependent and revealed that efficiency enhancement provided by the low-bandgap block absorption was balanced by the copolymer nano-structuration that shrinks the charge collection at electrodes. An optimized efficiency around 2% was obtained using a 1:1 blend ratio of P3HT_{240-b}-P(DTS-DPP)₁₁:PC₆₀BM photoactive layer.

As for the interfacial layer studies, surface engineering of indium tin oxide (ITO) substrate was investigated. For this aim, P3HT and 1H,1H,2H,2H-perfluorooctyltriethoxysilane (PTES), bearing a triethoxysilane function at their end-chains were grafted as self-assembled monolayers (SAMs) onto ITO to replace the commonly used PEDOT:PSS hole transport layer. The optimized grafting methodology was proved by UV-visible, X-ray photoemission spectroscopy and contact angle measurements. Unfortunately, the anchoring of those SAM materials did not bring any improvement to the P3HT:PC₆₀BM-based normal device structures in terms of efficiency as the highest performance obtained was with PTES solution (2%) which was lower than that obtained using PEDOT:PSS (2.7%) but higher than that using bare ITO (1.34%).

Résumé

De nos jours, dans le cadre de développement des cellules solaires, un sujet d'intérêt est l'utilisation de polymères à large absorption étendue au proche infrarouge afin de collecter plus efficacement les photons. Ainsi, nous avons concentré notre étude sur une méthode de couplage simple et efficace pour synthétiser des copolymères diblocs tout conjugués. Cette méthode est basée sur la polycondensation de Stille de monomères A-A (dithiénosilole, DTS) et B-B (dicétopyrrolopyrrole, DPP ou diazapentalène, DAP) avec du P3HT comme agent de terminaison. Les copolymères diblocs et triblocs ont été synthétisés en ajustant la composition molaire initiale des monomères et du macromonomère. La masse molaire et la topologie des macromolécules obtenues sont discutées en se référant à l'équation de Carothers, à la conversion et au rapport des monomères. Des analyses structurales de RMN de proton et DOSY, de FT-IR et de GPC ont montré la bonne formation des copolymères à blocs. De plus, la spectrophotométrie et la voltamétrie cyclique ont été utilisées pour mettre en évidence la complémentarité de l'absorption des blocs et la nature donneur-accepteur des copolymères.

Dans le but d'étudier le potentiel photovoltaïque des matériaux synthétisés, ces copolymères diblocs ont été incorporés comme matériaux donneurs avec des accepteurs de fullerène PC₆₀BM dans des dispositifs à structure inverse. En général, les copolymères à blocs à base de DPP ont montré des efficacités de conversion de puissance améliorées par rapport à ceux à base de DAP. Les performances ont révélé une dépendance à la composition molaire des blocs et une diminution de l'efficacité. La principale cause est la nanostructuration du copolymère qui réduit la collecte des charges au niveau des électrodes, malgré l'amélioration de l'efficacité fournie par l'absorption du bloc à faible bande interdite. Une efficacité optimisée d'environ 2% a été obtenue en utilisant un rapport massique 1:1 de la couche photoactive P₃HT_{240-b}-P(DTS-DPP)₁₁:PC₆₀BM.

En ce qui concerne les études de couche interfaciale, l'ingénierie de surface du substrat d'oxyde d'indium et d'étain (ITO) a été étudiée. Dans ce but, le P3HT et le 1H,1H,2H,2H-perfluorooctyltriéthoxysilane (PTES), portant une fonction triéthoxysilane en extrémité de chaîne ont été greffés en monocouches auto-assemblées (SAM) sur ITO pour remplacer la couche de transport de trous PEDOT:PSS couramment utilisée. La méthodologie de greffage optimisée a été prouvée par spectroscopie UV-visible, photoémission aux rayons X et mesures d'angle de contact. Malheureusement, l'ancrage de ces matériaux SAM n'a apporté aucune amélioration aux structures des dispositifs classiques à base de P3HT:PC₆₀BM en termes d'efficacité en raison de l'épaisseur des couches. En effet, les performances les plus élevées ont été obtenues avec la solution PTES (2%) et se sont révélées inférieures à celles obtenues avec PEDOT:PSS (2,7%) mais supérieures à celles avec l'ITO nu (1,34%).